SAPIENZA
UNIVERSITÀ DI ROMA

Unveiling the phase diagram of high-pressure Hydrogen

Dipartimento di Fisica

Dottorato di Ricerca in Fisica – XXXII Ciclo

Candidate

Lorenzo Monacelli
ID number 1478892

Thesis Advisor

Prof. Francesco Mauri

November 2019

Thesis defended on 7 February 2020
in front of a Board of Examiners composed by:

Prof. Sandro Scandolo (chairman)

Prof. Eugenio Del Re

Prof. Marco Barbieri

Unveiling the phase diagram of high-pressure Hydrogen
Ph.D. thesis. Sapienza – University of Rome

This thesis has been typeset by LaTeX and the Sapthesis class.

Version: February 12, 2020

Author's email: lorenzo92monacelli@gmail.com

Abstract

Production of metallic hydrogen is one of the top three open quests of physics[1]. Three different experimental groups claim to have obtained metallic hydrogen at different pressures, with contradicting results. The firsts [2, 3] measured a transition from phase III to a new insulator molecular phase at 360 GPa, then to a shiny metallic phase at 490 GPa. Another work[4] showed how phase III becomes a metal through indirect bandgap closure at about 360 GPa and it remains stable up to at least 440 GPa. Lastly, a different work[5] measured the infrared transmission up to 430 GPa, claiming that phase III transforms to a new metallic state at about 420 GPa through a first-order phase transition. In this scenario, experimental data need the support from theoretical simulations to correctly understand the hydrogen phase-diagram, as experiments provide only indirect measurements: optical absorption, reflectivity, and vibrational spectroscopy.

In this thesis, I feature the paramount role played by nuclear quantum fluctuations in the phase-diagram and the optical and vibrational properties of high-pressure hydrogen. In the first part of the thesis, I develop a new technique to simulate the quantum character of nuclei, able to correctly describe both phonon-phonon and electron-phonon interactions. In this way, the crystal structure can be relaxed, including lattice parameters, considering quantum and thermal fluctuations. By optimizing also the lattice with quantum fluctuations, I discover new crystalline structures, good candidates for high pressure hydrogen phases. Thanks to the advances I introduce here, it is possible to simulate the anharmonic IR and Raman spectra with phonon lifetimes, allowing for an unprecedented theoretical accuracy, enabling the direct comparison with experiments. I simulate also the optical properties of the high-pressure hydrogen, including the electron-phonon interaction. By computing the direct and indirect bandgap closure of phase III, I conciliate the apparent contradicting scenario revealed by experiments[4, 5].

Contents

Introduction

The high-pressure Hydrogen quest

Controlled nuclear fusion, production of metallic hydrogen, and high-temperature superconductivity have been listed as the top three open problems of physics[1].

All these issues involve atomic hydrogen and its isotopes. Hydrogen is the simplest and most abundant of all elements. Under ambient conditions, hydrogen is found in its molecular phase, thanks to the H-H bond, one of the strongest bonds in chemistry. 80 years ago, Wigner and Huntington[6] theorized the atomic metallic state of hydrogen (MH), stable over 25 GPa. MH is predicted to be superconductor[7] above room temperature.

Until now, MH has been undoubtedly observed only at very high temperatures (over 3000 K) in shock-wave experiments[8]; the main goal of high-pressure solid-state physics is to produce stable MH at room temperature (300 K). This can be achieved using diamond-anvil-cells (DAC).

To simplify the task of reaching metallic hydrogen, Ashcroft proposed to combine hydrogen with heavier ions[7]. This route led to the discovery of other hydrogen-based high temperature superconductors: in 2015 Drozdov et. al.[9] synthesized a new metallic state of a hydrogen compound (H_3S), beating the high-temperature superconductor record with a critical temperature of 203 K (the old record was held by cuprates for decades and was 70 degrees lower). This record has been very recently broken in another hydrogen compound (lanthanum hydride) at 250 K[9]. Even more recently, the superconductive temperature of 243 K was observed in YH_9[10].

Pure hydrogen metalization in DAC, however, is more challenging than expected. Hydrogen at high pressures exhibits a very rich phase diagram, that stabilizes other pre-metallic phases before undergoing into a true atomic metallic state. Four distinct molecular solid phases have been observed experimentally (there are claims about the existence of two other phases[11, 12]). However, full characterization of these phases is challenging since both X-ray and neutron scattering are noneffective on high-pressure hydrogen. Thus, the structural information must be inferred from optical and vibrational spectroscopy (Raman and IR). Furthermore, the interaction between the sample, the diamonds and the coating (used to suppress the quantum diffusion of hydrogen into the diamond structure), interferes with the measurements, hampering their interpretation[13].

Recently, Dias and Silvera[3] claimed to have observed the very first example of MH in static DAC, at pressures about 495 GPa. However, most of the scientific community is sceptical about this outstanding result[13, 14, 15]. The reason for

the scepticism is mainly related to the weakness of the experimental measurements reported, due to the fragility of the sample.

Under these extreme conditions, experiments alone cannot establish if MH has been synthesized; a detailed theoretical analysis is required.

Numerical “ab-initio” simulations play a fundamental role in structure prediction and identification. The atomic structures of the hydrogen phases are elucidated up to phase II. Good crystalline candidates for phase III and IV have been proposed[16, 17], while existences of phase V and VI are still under debate. However, anharmonicities and quantum nuclear zero-point motion are often neglected by computer simulation. They are essential for correctly grasping the energy of the structures and their optical/vibrational features. Hydrogen is the lightest atom and, in its molecular state, it has a strong covalent bond. The high vibrational energy results in a Debye temperature of more than 5000 K. In this regime, classical simulation cannot give quantitative correct results, even at room temperature, as fluctuations are strongly dominated by quantum zero-point motion.

The goal of this thesis is the "ab-initio" reconstruction of hydrogen phase-diagram and the disclosure of the experimental puzzle of the high-pressure phases.

The experimental phase-diagram

Solid hydrogen has a very rich phase-diagram. At low pressure and ambient temperature, hydrogen is in phase I: a hexagonal closed packet crystal where H_2 molecules rotate freely in the lattice sites. Upon increasing pressure (about 100 GPa) and decreasing temperature (under 100 K), hydrogen changes into a new molecular solid phase, phase II, where the rotations of molecules are frozen in an ordered broken symmetry phase[18]. These two structures have been experimentally disclosed. If the pressure increases over 150 GPa, hydrogen transforms into phase III. This phase is characterized by a strong IR activity and an intense vibron whose peak position depends drastically on pressure. When increasing temperature from phase III, hydrogen changes structure to phase IV (above 250 GPa)[19]. Thanks to computer simulation for systematic structure search, we have very good candidates for both phase III[16] and phase IV[17]. Recent experiments claim the existence of a room temperature phase V when increasing further the pressure (at about 330 GPa)[11]. A structure candidate has been proposed recently[20] for this phase. At low temperature, there are claims about another high-pressure phase VI. However, different experiments report contradicting results: Diaz and Silvera[2] claim phase III transforms into another insulator molecular phase VI, distinguishable by the IR spectrum, at 350 GPa. Eremets et. al.[4] claim that phase III remains stable until 440 GPa by observing a continuous evolution of the Raman spectrum, but by measuring the conductivity report the metalization of phase III due to an indirect gap closure. Loubeyre et. al.[5] measured the IR spectrum of phase III until 430 GPa, and observed a sharp transition to a metallic state at 415 GPa: a first-order phase transition to phase VI. A structure has been proposed for phase VI[2, 5] only based on the theoretical computation of the phase-diagram, but no spectroscopic signatures pinpoint this identification.

A sketch of the possible diagram of molecular solid hydrogen is reported in Figure 0.1.

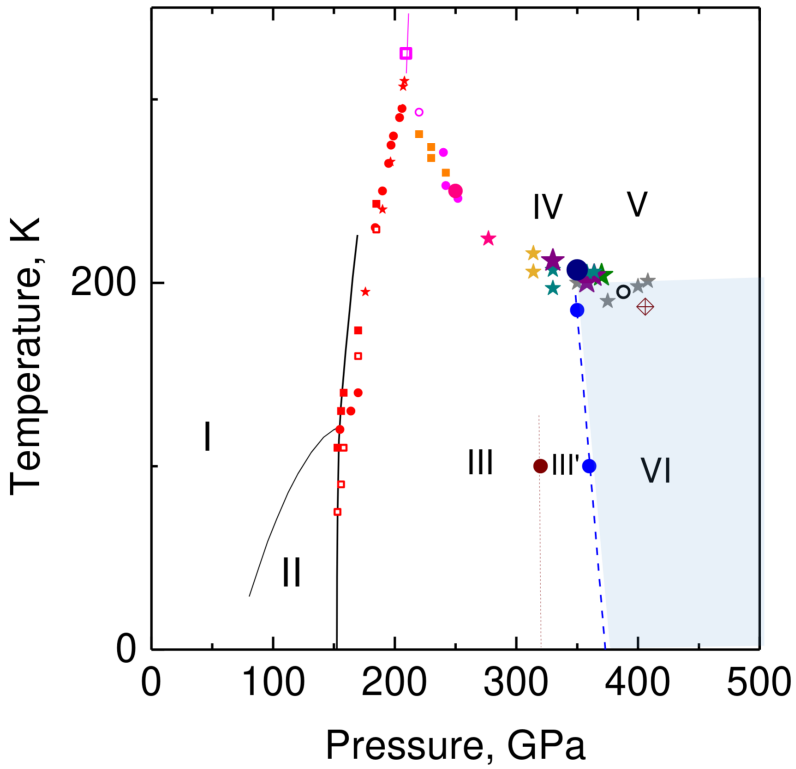

Figure 0.1. Experimental phase-diagram of high-pressure hydrogen, taken from ref.[12]. The existence of phase VI is still strongly debated.

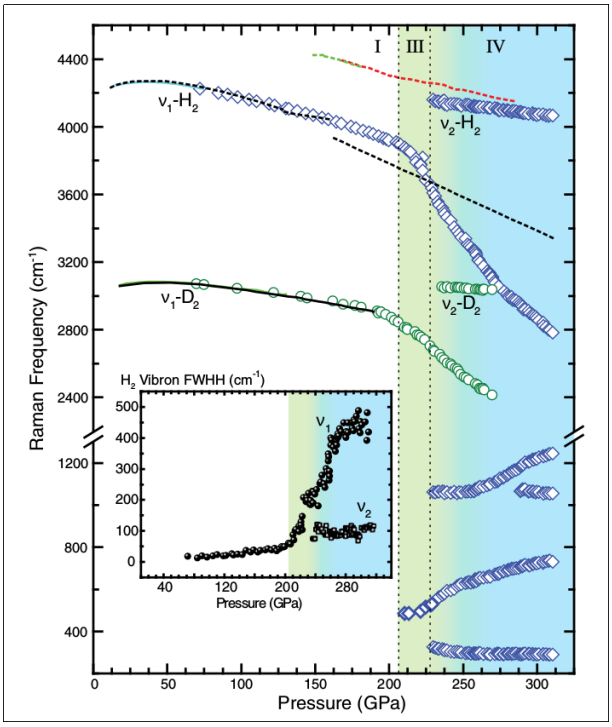

Figure 0.2. Raman active vibrations in molecular hydrogen as a function of pressure. The discontinuity of the vibrational frequencies and kinks in their pressure dependence are the signatures of phase-transitions. Data from Ref.[19].

Experimental signatures of the phases

The difficulties in studying pre-metallic phases of hydrogen are due to both the technological challenges involved in pressurizing hydrogen to such extreme conditions and the measurement of structural properties.

Hydrogen, the lightest element in the universe, has no core electrons. The resulting X-ray cross-section is small, inhibiting the use of the most successful technique in crystallography for crystal structure detection. Moreover, the small size of the sample at high-pressure prevents us from using neutron beams. The only accessible experimental data are optical and vibrational properties, as Raman and IR spectroscopy. They are indirectly related to the structure and strongly affected by anharmonicity. Phase transitions are identified through sharp changes in the vibrational spectrum (see Figure 0.2, where the Raman spectrum is shown during the transition from phase I to III and IV) or in optical properties.

However, often experiments describe contradicting scenarios[2, 12, 5, 4].

No direct measurement of the structure is available. We must solve an inverse problem to correctly assign the crystal structure to the experimental phase. First, a good crystalline candidate must be provided. Then, optical and spectroscopic properties are computed and matched with the experiments. Finding good candidates is possible thanks to the random structure searches algorithms, that provide structures optimizing the enthalpy at fixed thermodynamic conditions. However, it is computationally very expensive to include quantum nuclear effects in both the

structure search and the prediction of optical and vibrational properties. Almost every structure prediction and spectroscopic calculation in the literature relies on the classical nuclei or the harmonic approximation. This, unavoidably, leads to mismatches between experiments and theory and hampers the correct structure-phase identification.

The goal of this thesis is the development and deploy of new computational techniques to study high-pressure solid phases of hydrogen considering thermal and quantum fluctuations of nuclei.

Structure of the Thesis

In this thesis, I present the technique I developed to simulate the phase-diagram of high-pressure Hydrogen and the results I have obtained.

Each chapter is anticipated by a small introduction and followed by a conclusion section with the take-home messages. All the details of mathematical demonstrations are demanded in appendices, while the text contains the logical steps to get to the result.

Chapters from 1 to 4 are theoretical works, in which I progressively develop all the theory and algorithms used to study the hydrogen. In chapters 5 and 6, I deploy the theoretical developments on the high-pressure hydrogen. Each chapter relates to different problems. However, the theoretical chapters should be read sequentially. In particular, Chapter 4 is a direct continuation of 3.

In Chapter 1, I introduce the theoretical framework used in the thesis: the Stochastic Self-Consistent Harmonic Approximation (SCHA). Chapter 2 extends the SCHA to compute the stress tensor and relax the lattice parameters. In Chapter 3, I devise a time-dependent theory, based on the SSCHA, that allows simulating out-of-equilibrium phenomena. In Chapter 4, the time-dependent SCHA (TD-SCHA) is developed to compute the linear response to periodic perturbations and the Raman or IR dynamical response functions. All these new theoretical developments are applied on phase III of high-pressure hydrogen in Chapter 5. There, also a new way to compute the electron-phonon interaction on optical properties is discussed and applied to assess the recent discrepancies in experimental data[5, 4]. Chapter 6 exploits all the theoretical advances to compute the whole phase-diagram of high-pressure hydrogen. In this chapter, I discuss the impact of quantum fluctuations, isotope and temperature effects. In particular, I focus on the contrasting claims of the presence of a new phase of hydrogen at very high pressure and low temperature. The final conclusions are presented in Chapter 7.

All the new theoretical developments introduced are not limited to the study of high-pressure hydrogen, but are applied on a wide variety of systems, among them, charge density waves, thermoelectric materials, high-pressure hydrates and muon spectroscopy. In App. A, I will describe these work that are already (or that are up to be) published.

The complete details about simulation parameters and procedures to reproduce the data reported in each figure or table are discussed in App. E.

Chapter 1

The Stochastic Self-Consistent Harmonic Approximation

1.1 Introduction

The Stochastic Self-Consistent Harmonic Approximation (SSCHA) is a computational tool to efficiently study the thermodynamics of nuclear motion, even including their quantum nature.

The idea behind it is to describe the nuclear probability distribution as a Gaussian, that includes both quantum uncertainty and thermal motion. This nuclear probability distribution is optimized to minimize the Helmholtz free-energy. The method is stochastic: we sample the real energy landscape with random nuclear configurations, extracted from the probability distribution.

The main advantages include:

- Both quantum kinetic energy and entropy are analytical
- Random configurations to sample the space are extracted from a Gaussian distribution (fast and easy).
- Symmetries: in contrast with both classical and quantum molecular dynamics, we can impose crystal symmetries directly on the probability distribution, reducing a lot the number of degrees of freedom, accelerating convergence and distinguishing between different phases.
- The free-energy is analytical, no thermodynamic integral needed. This allows comparing directly free energies of different phases and enables the computation of the phase-diagram.
- The method is unbiased by the starting point: Since the real energy landscape is randomly explored, the results of SSCHA calculations do not depend on the starting point. This is not the case of other approximation, where the energy landscape is fitted around the starting point[21].

In the next section, I discuss the theoretical derivation of the method, introducing the fundamental notations used in the thesis.

The main references of the theoretical derivation of the SSCHA are [22, 23, 24, 25].

In Sec. 1.3, I present a very simple application on a 1D system, showing how SSCHA performs on highly anharmonic systems.

In Sec. 1.5, I discuss the limits of the current implementation of the SSCHA and how to overcome them. This last section is part of the original work I published[25].

1.2 Theory

The SCHA is a variational principle on the Bohr-Oppenheimer (BO) free energy. The nuclear quantum Hamiltonian of a generic system can be defined in the BO approximation as

$$H = \sum_{n=1}^{N} \sum_{\alpha=1}^{3} \frac{p_n^{\alpha 2}}{2m_n} + V(\vec{R}, \{\vec{a}_i\}), \tag{1.1}$$

where V is the BO energy surface, m_n is the mass of the n-th atom, p_n^α and $\vec{R}$ (R_n^α) are the momentum and position operators of the nuclei in the periodic cell (or super-cell), N is the number of atoms, and $\{\vec{a}_i\}$ are the 3 unit-cell vectors. The α index identifies the Cartesian coordinate. Fixed the temperature T and the volume (i.e. the cell vectors $\{\vec{a}_i\}$), the free energy of the ionic Hamiltonian H is:

$$F = U - TS$$

$$F(\{\vec{a}_i\}) = \langle H \rangle_{\rho_H} + k_b T \langle \ln \rho_H \rangle_{\rho_H}, \tag{1.2}$$

where ρ_H is the equilibrium density matrix

$$\rho_H = \frac{e^{-\beta H}}{\mathrm{Tr}\, e^{-\beta H}} \qquad \beta = \frac{1}{k_b T}, \tag{1.3}$$

and the brackets $\langle O \rangle_{\rho_H}$ indicate the average of the observable O according to the ρ_H density matrix:

$$\langle O \rangle_{\rho_H} = \mathrm{Tr}\left[\rho_H O\right]. \tag{1.4}$$

The equilibrium density matrix satisfies the free energy least principle. Given a trial density matrix $\rho_{\mathcal{H}}$, we can define a free energy functional whose minimum is the free energy:

$$\mathcal{F}(\{\vec{a}_i\})[\rho_{\mathcal{H}}] = \langle H \rangle_{\rho_{\mathcal{H}}} + k_b T \langle \ln \rho_{\mathcal{H}} \rangle_{\rho_{\mathcal{H}}}, \tag{1.5}$$

$$F(\{\vec{a}_i\}) = \min_{\rho_{\mathcal{H}}} \mathcal{F}(\{\vec{a}_i\})[\rho_{\mathcal{H}}]. \tag{1.6}$$

The SCHA approximation consists in the restriction of all the possible trial density matrices to solutions of harmonic Hamiltonians:

$$\mathcal{H}_{\vec{\mathcal{R}},\mathbf{\Phi}} = \sum_{n=1}^{N} \sum_{\alpha=1}^{3} \frac{p_n^{\alpha 2}}{2m_n} + \mathcal{V}_{\mathbf{\Phi},\vec{\mathcal{R}}}(\vec{R}), \text{ where} \tag{1.7a}$$

$$\mathcal{V}_{\mathbf{\Phi},\vec{\mathcal{R}}}(\vec{R}) = \frac{1}{2} \sum_{\substack{n=1 \\ m=1}}^{N} \sum_{\substack{\alpha=1 \\ \beta=1}}^{3} u_n^\alpha \Phi_{nm}^{\alpha\beta} u_m^\beta, \text{ and} \tag{1.7b}$$

$$u_n^\alpha = R_n^\alpha - \mathcal{R}_n^\alpha. \tag{1.7c}$$

$$\rho_{\mathcal{H}} = \rho_{\vec{\mathcal{R}},\mathbf{\Phi}} = \frac{e^{-\beta\mathcal{H}_{\vec{\mathcal{R}},\mathbf{\Phi}}}}{\mathrm{Tr}\, e^{-\beta\mathcal{H}_{\vec{\mathcal{R}},\mathbf{\Phi}}}}. \tag{1.7d}$$

Here, u_a^α is the displacement of a-th atom along the α direction with respect to the central position $\vec{\mathcal{R}}$, and $\Phi_{nm}^{\alpha\beta}$ is the matrix element of the real space force constant matrix (we use the bold font to indicate tensors and matrices). This auxiliary harmonic Hamiltonian is just a mathematical artifact to describe the density matrix. In this way, we solve the representation problem (the density matrix is not completely free, it must satisfy all the constraint imposed by a real physical system). Also, we can exploit some features of the harmonic Hamiltonian: we know how to compute analytically both the kinetic and the entropy for this density matrix. To this aim, it is better to recast the total free energy as

$$\mathcal{F}(\vec{\mathcal{R}}, \mathbf{\Phi}, \{\vec{a}_i\}) = F_{\mathbf{\Phi}} + \left\langle V - \mathcal{V}_{\mathbf{\Phi},\vec{\mathcal{R}}} \right\rangle_{\rho_{\vec{\mathcal{R}},\mathbf{\Phi}}}, \tag{1.8}$$

where $F_{\mathbf{\Phi}}$ is the exact free energy of the auxiliary harmonic Hamiltonian and includes both the kinetic and entropic contribution of the real free energy, as well as a part of the potential energy:

$$F_{\mathbf{\Phi}}(T) = \sum_{\mu=1}^{3N} \left[\frac{\hbar\omega_\mu}{2} + \frac{1}{\beta} \ln\left(1 - e^{-\beta\hbar\omega_\mu}\right) \right], \tag{1.9}$$

where ω_μ and $\vec{e}_\mu$ are, respectively, the eigenvalues and eigenvectors of the $\mathbf{\Phi}$ matrix divided by the atomic masses:

$$\sum_{t=1}^{N} \sum_{\beta=1}^{3} \frac{\Phi_{st}^{\alpha\beta}}{\sqrt{m_s m_t}} e_{\mu t}^{\ \beta} = \omega_\mu^2 e_{\mu s}^{\ \alpha}. \tag{1.10}$$

Note that the only part of Eq. (1.8) to be computed numerically is the "anharmonicity", i.e. how much the real energy landscape deviates from the auxiliary harmonic potential inside the nuclear probability distribution. This also drastically reduces the stochastic noise in energy estimation.

The real free energy can be approximated as the minimum of the free energy functional (Eq. 1.8) with respect to $\vec{\mathcal{R}}$ and $\mathbf{\Phi}$:

$$\mathcal{F}(\vec{\mathcal{R}}, \{\vec{a}_i\}) = \min_{\mathbf{\Phi}} \mathcal{F}(\vec{\mathcal{R}}, \mathbf{\Phi}, \{\vec{a}_i\}), \tag{1.11a}$$

$$\mathcal{F}(\{\vec{a}_i\}) = \min_{\mathbf{\Phi},\vec{\mathcal{R}}} \mathcal{F}(\vec{\mathcal{R}}, \mathbf{\Phi}, \{\vec{a}_i\}). \tag{1.11b}$$

From now on, when we drop one of $\vec{\mathcal{R}}$ or $\mathbf{\Phi}$ symbols, we mean the quantity computed in the value of that variable that minimizes the free energy. For example, the equilibrium SCHA density matrix is just ρ.

One of the advantages of using the harmonic Hamiltonian to restrict the $\rho_{\mathcal{H}}$ space is that we have a trivial physical interpretation of the minimization parameters. In fact $\vec{\mathcal{R}}$ represents the centroid positions of the atoms, i.e. the anharmonic average positions as measured by, e.g., diffraction experiments:

$$\vec{\mathcal{R}} = \langle \vec{R} \rangle_\rho. \tag{1.12}$$

In the same way, $\mathbf{\Phi}$ is related to the thermal and quantum fluctuations and defines the real space density matrix broadening. Within the harmonic auxiliary Hamiltonian, the probability distribution function defined by the real space density matrix is a product of Gaussians:

$$\rho_{\vec{\mathcal{R}},\mathbf{\Phi}}(\vec{u}) = \langle \vec{u} | \rho_{\vec{\mathcal{R}}\mathbf{\Phi}} | \vec{u} \rangle$$

$$\rho_{\vec{\mathcal{R}},\mathbf{\Phi}}(\vec{u}) = \sqrt{\det\left(\mathbf{\Upsilon}/2\pi\right)} \exp\left(-\frac{1}{2} \sum_{st\alpha\beta} \Upsilon_{st}^{\alpha\beta} u_s^\alpha u_t^\beta \right) \tag{1.13a}$$

where

$$\Upsilon_{st}^{\alpha\beta} = \sqrt{m_s m_t} \sum_\mu \frac{2\omega_\mu}{(1+2n_\mu)\hbar} e_{\mu s}^{\ \alpha} e_{\mu t}^{\ \beta} \tag{1.13b}$$

and n_μ are the boson average occupation number for the μ mode. It is important to notice that ω_μ and $\vec{e}_\mu$ (Eq. 1.10) are not directly equal to the physical phonons, as we will explore in more details in Chapter 3. They are constrained to be positive defined[24] and are related to quantum and thermal fluctuations.

It is possible to define the SCHA force as the derivative of the free energy (Eq. 1.11a) with respect to the nuclear average positions,

$$-\frac{\partial \mathcal{F}}{\partial \mathcal{R}_n^\alpha}(\vec{\mathcal{R}}, \{\vec{a}_i\}) = \langle f_n^\alpha - f_{\mathcal{H}n}^{\ \alpha} \rangle_{\rho_{\vec{\mathcal{R}}}} , \tag{1.14}$$

where $\vec{f}$ and $\vec{f_{\mathcal{H}}}$ are, respectively, the BO and harmonic forces:

$$f_n^\alpha = -\frac{\partial V}{\partial R_n^\alpha}(\vec{R}, \{\vec{a}_i\}) \tag{1.15}$$

$$f_{\mathcal{H}n}^{\ \alpha} = -\frac{\partial \mathcal{V}_{\vec{\mathcal{R}},\mathbf{\Phi}}}{\partial R_n^\alpha} = -\sum_{m=1}^{N} \sum_{\beta=1}^{3} \Phi_{nm}^{\alpha\beta} u_m^\beta \tag{1.16}$$

To numerically minimize the SCHA free energy it is possible to use the steepest descent (SD) or conjugate gradient (CG) methods[26], both based on the knowledge of the gradient of the function to minimize. This can be expressed as a function of the averages of the BO and harmonic forces[22, 24]:

$$\frac{\partial \mathcal{F}(\vec{\mathcal{R}}, \mathbf{\Phi}, \{\vec{a}_i\}))}{\partial \Phi_{ab}} = -\frac{1}{2} \sum_{cdq} \frac{\partial \Upsilon^{-1}{}_{cd}}{\partial \Phi_{ab}} \Upsilon_{cq} \left\langle u_q \left[\vec{f}_d - \vec{f}_{\mathcal{H}_d} \right] \right\rangle_{\rho_{\vec{\mathcal{R}},\mathbf{\Phi}}} \tag{1.17a}$$

$$\frac{\partial \mathcal{F}(\vec{\mathcal{R}}, \mathbf{\Phi}, \{\vec{a}_i\})}{\partial \mathcal{R}_a} = -\left\langle f_a - f_{\mathcal{H}a} \right\rangle_{\rho_{\vec{\mathcal{R}},\mathbf{\Phi}}} , \tag{1.17b}$$

The derivation of Eq. (1.17a) and (1.17b) is reported in App. B.1. From now on, we will adopt a short notation, where one index replaces the 3N Cartesian and atomic coordinates: $a \leftrightarrow {}_s^\alpha$.

1.3 A practical example

In this section, I apply the SSCHA to a one-dimension particle in an external potential at $T = 0\,\mathrm{K}$, to benchmark the algorithm against the exact solution. At $T = 0\,\mathrm{K}$, the free energy is the ground state energy of the wave function.

$$H\,|\psi\rangle = E\,|\psi\rangle\,. \tag{1.18}$$

The SSCHA consists of minimizing the energy constraining the wave-function to a Gaussian. The energy functional is (given that $|\psi\rangle$ is normalized):

$$E[|\psi\rangle] = \langle\psi|H|\psi\rangle\,. \tag{1.19}$$

The Gaussian wave-function in the position basis is parameterized by the average position x_0 and the variance σ^2:

$$\langle x|\psi\rangle = \sqrt[4]{\frac{1}{2\pi\sigma^2}}\exp\left[-\frac{(x-x_0)^2}{4\sigma^2}\right], \tag{1.20}$$

The Hamiltonian can also be expressed in the position basis:

$$\langle x|H|x'\rangle = -\delta(x-x')\frac{\hbar^2}{2m}\frac{\partial^2}{\partial x^2} + V(x)\delta(x-x'). \tag{1.21}$$

Substituting Eq. (1.20) and (1.21) into (1.19) we have:

$$E(x_0,\sigma) = \int_{-\infty}^{\infty} dx\,|\psi(x)|^2\,\frac{\hbar^2}{4m\sigma^2}\left[\frac{(x-x_0)^2}{2\sigma^2} - 1\right]dx + \int_{-\infty}^{\infty} V(x)|\psi(x)|^2 dx\,, \tag{1.22}$$

$$E(\sigma,x_0) = \frac{\hbar^2}{8m\sigma^2} + \int_{-\infty}^{\infty} V(x)|\psi(x)|^2 dx\,. \tag{1.23}$$

To solve the SSCHA, we must find the minimum of Eq. 1.23 with respect to σ and x_0. To benchmark the SSCHA, we take a highly anharmonic potential $V(x)$, like the one in Figure 1.1.

We compare three different methods:

- the Quasi-Harmonic Approximation (QHA)
- the Self-Consistent Harmonic Approximation (SSCHA)
- the numerical solution (Exact diagonalization with Lanczos).

The QHA free energy is the minimum of the $V(x)$ plus the free energy of the quantum harmonic oscillator obtained by the second-order Taylor series of the BO potential in the minimum[1]. The Lanczos is an iterative algorithm performing the exact (numerical) diagonalization of the Hamiltonian. More details on the Lanczos algorithm are given in Chapter 4.

The results are reported in Figure 1.1. The SCHA correctly assesses both the average nuclear position and the ground state energy, even when strong anharmonicities are present and the real wave-function is not Gaussian.

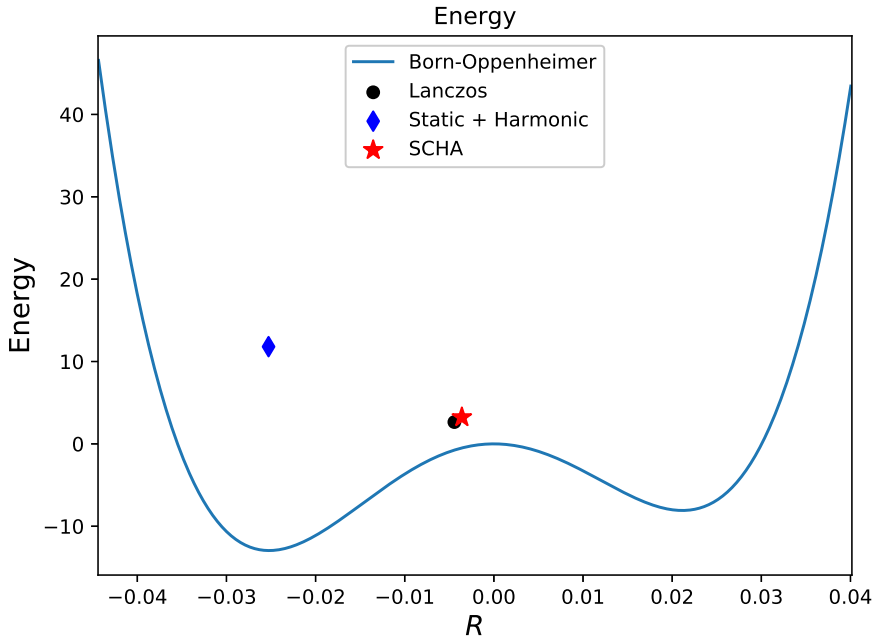

Figure 1.1. Example of the 1D anharmonic potential energy landscape. The solid line is the Born-Oppenheimer energy landscape $V(x)$, the scatter points are the solution of QHA, SSCHA and Lanczos (exact). The x coordinate of the points represents the average atomic position in the ground state, while the y coordinate is the ground state energy. QHA scores badly both in energetic and in the average position. SCHA is very good, as it almost overlaps with the exact solution. Here we used Hartree atomic units, with $m = 1$.

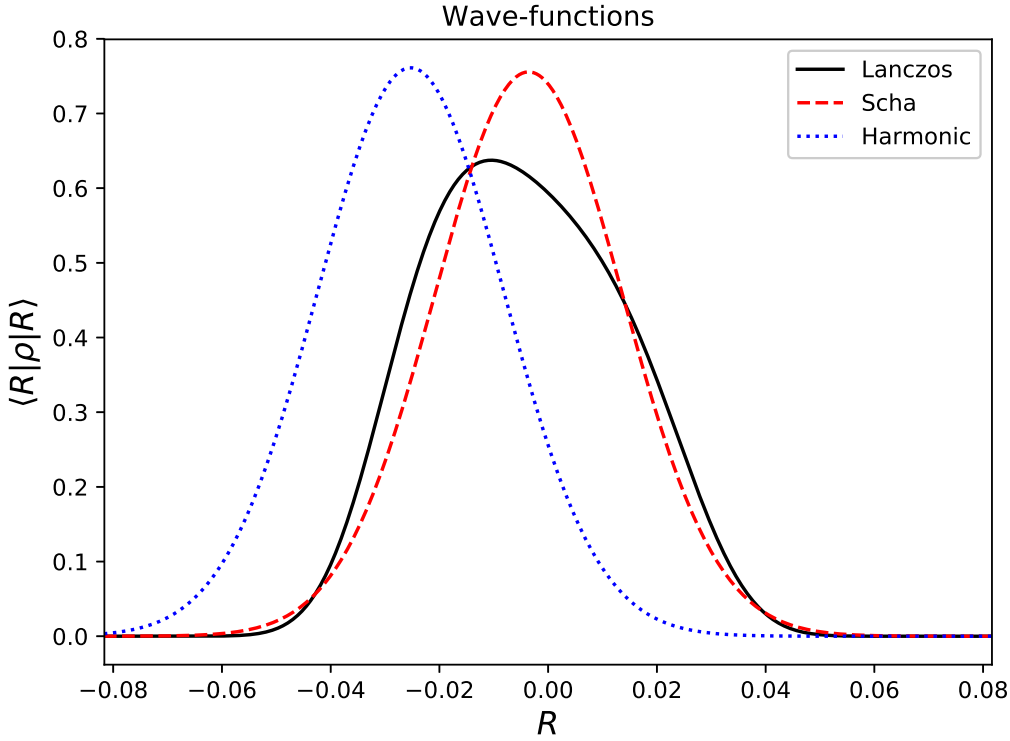

Figure 1.2. Probability distributions of the nuclear ground-state wave-function. Lanczos is the exact diagonalization.

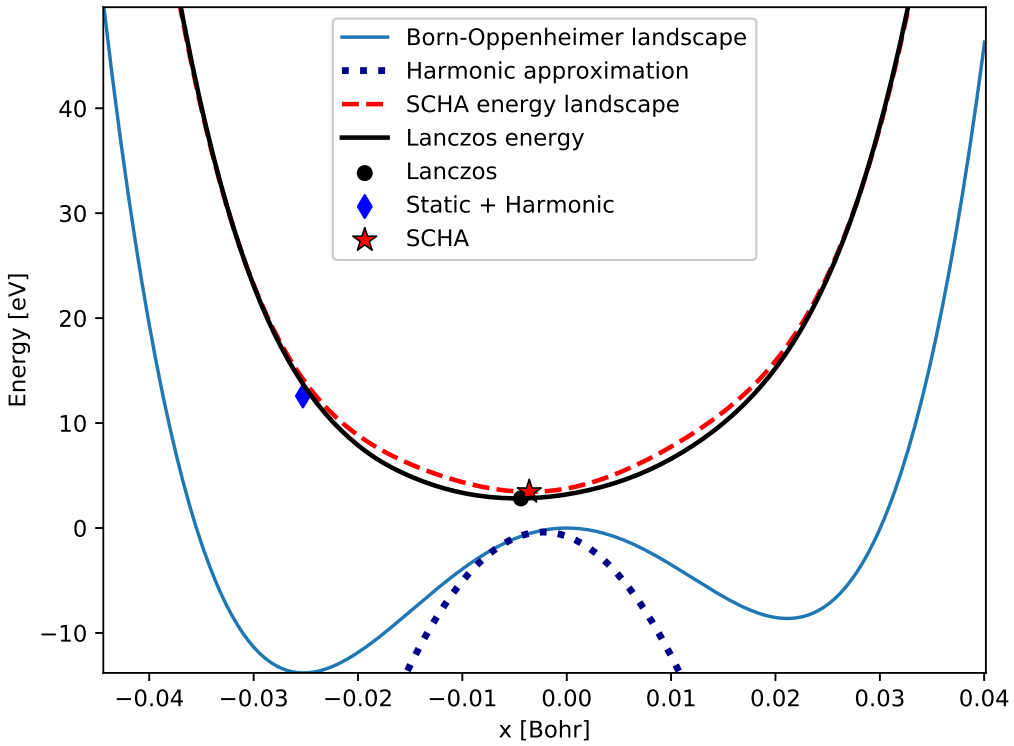

Figure 1.3. The quantum energy landscape. This is defined as the quantum ground state constraining the average nuclear position. The blue solid line is the classical energy landscape $V(x)$, the blue dotted curve is QHA approximation around the exact solution, the red dashed curve is the SSCHA quantum energy landscape while the solid black curve is the Lanczos (exact diagonalization) curve.

In Figure 1.2, I report the ground-state wave-functions. The SSCHA wave-function is, by construction, a Gaussian, whether the real wave-function present an asymmetric shape.

The stability of a structure is related to changes in the free energy under small atomic displacements. We can define a quantum energy landscape, that can be used to assess the structural stability, performing a constrained optimization of the wave-function on the average atomic position using Lagrange multipliers. The Lagrange multiplier term is equivalent to a uniform electric field on the Hamiltonian of Eq. 1.23.

The harmonic, SSCHA and exact quantum energy landscapes are reported in Figure1.3.

From this figure, it can be seen how the quantum energy landscape is more smooth than the classical BO energy landscape. The SSCHA reproduces very well the quantum landscape. It is a perfect tool to study structure stability. The harmonic approximation is not valid around the exact solution and the harmonic frequency is imaginary (it predicts that the system is unstable).

[1] An advanced version of Quasi-harmonic consists in optimizing the central position around which expanding the Taylor series[27], however, it is much computational heavier than the SCHA

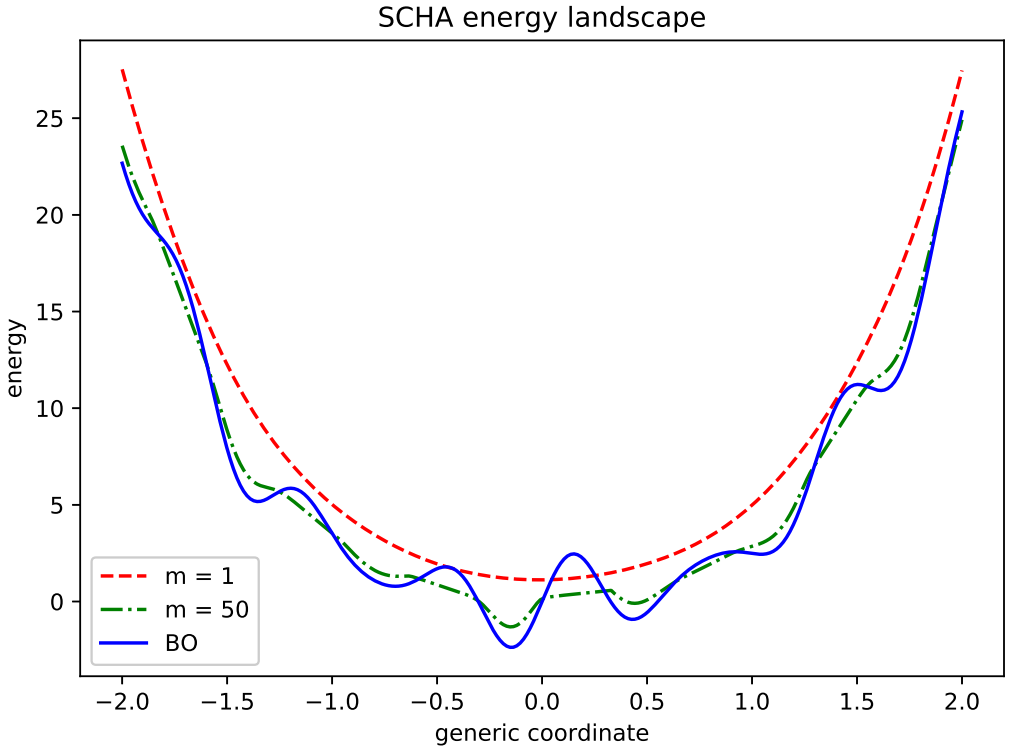

Figure 1.4. SCHA solution using different masses for the nucleus. As can be seen, the many minima are canceled out by the quantum effects.

The SCHA is a good tool for "ab-initio" structure search, as it can overcome energy barriers thanks to quantum tunnelling: the quantum landscape is smoother than the classical one. This result holds even when we pick an irregular $V(x)$ with many local minima, as in Figure 1.4.

The same result applies to real systems. For example, in LaH_{10} the quantum landscape is much more regular than the classical one, and above 130 GPa only one minimum is present (while the BO landscape has many local minima until 250 GPa)[28] (see Figure 1.5). To regularize the quantum landscape also the lattice must be relaxed. I introduce the lattice relaxation through SCHA in the next chapter.

1.4 The stochastic implementation

In the SSCHA, we only need to compute averages of the BO energy and forces on the Gaussian distribution. This can be done in many ways. The Self-Consistent-Phonons (SCP)[29] implementation, for example, fits the BO energy landscape with the polynomial regression. In this way, all Gaussian integrals can be evaluated analytically, and the SSCHA algorithm does not consume CPU time at all. The expensive computation is, indeed, the high-order force constants tensors required by the polynomial fit.

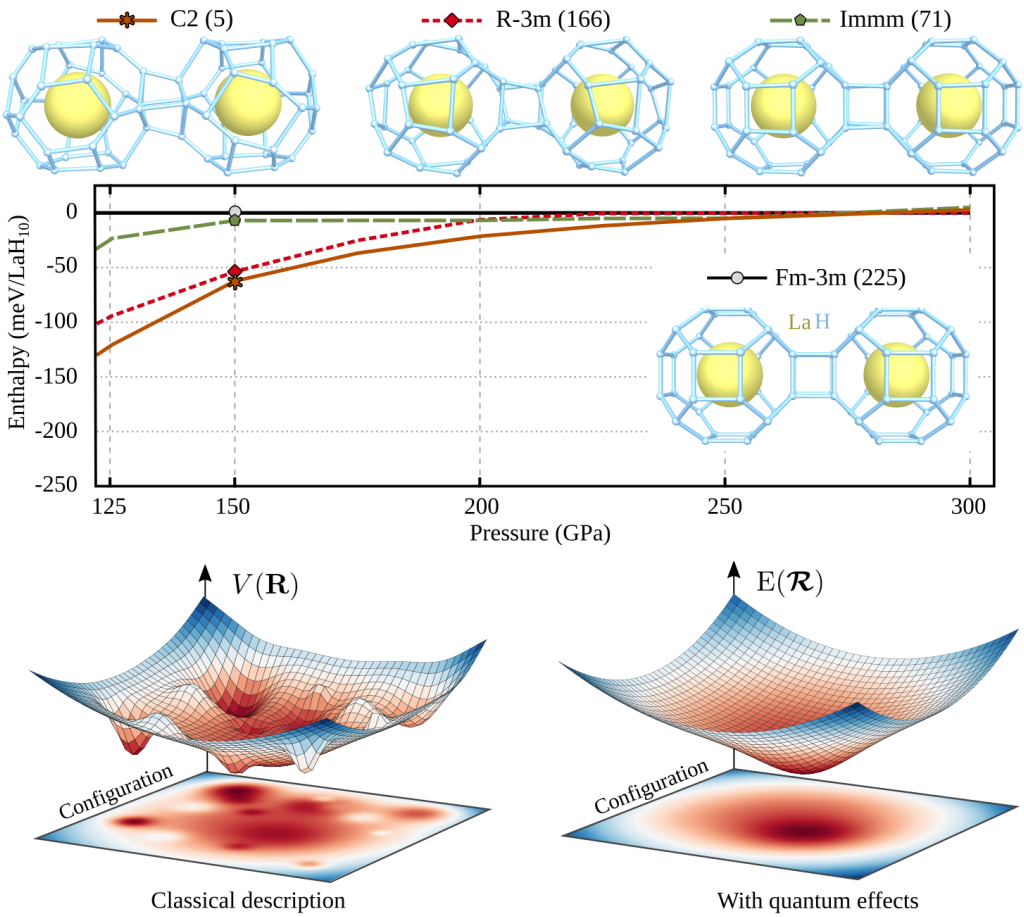

Figure 1.5. Classical vs quantum energy landscape in LaH_{10}. Many local minima of the classical BO surface disappear when quantum effects are turned on.

Another clever way to perform these averages is a Monte Carlo approach. We can extract very quickly Gaussian randomly distributed configurations, without any need of a Markov chain or a thermalization process. In this approach, each integral is evaluated numerically and comes with a controlled stochastic error that can be improved systematically by increasing the number of configurations. With this approach, no approximation is made on the BO landscape.

Indeed, we pay the improved accuracy on the BO landscape with a higher computational cost: we cannot solve the SSCHA equations analytically, and we must recompute the averages after each minimization step. This involves, in principle, the extraction of a new ensemble and the computation of energies and forces. This is a very heavy procedure.

However, we can exploit some tricks from the Monte Carlo community, as the importance sampling. We can recycle the ensemble computed at a previous iteration by changing the probability distribution.

Let me introduce the concept with a one-dimensional distribution: we must compute the average of the observable o on the distribution p, but we have generated an ensemble distributed according to q. We can recast the average as:

$$\langle o \rangle_p = \int dx o(x) p(x) = \int dx o(x) \frac{p(x)}{q(x)} q(x).$$

Then, this is equivalent to the average of the q extracted ensemble:

$$\langle o \rangle_p = \langle o \frac{p}{q} \rangle_q .$$

With this technique, we can recycle the ensemble in following iterations, limiting the number of ab-initio calculations. If we express this integral with the Monte Carlo summation, p/q is the weight ρ_i of the configuration.

In the SSCHA this is equal to:

$$\rho_i = \frac{\rho_{\vec{\mathcal{R}},\mathbf{\Phi}}(\vec{R}_i)}{\rho_{\vec{\mathcal{R}}_0,\mathbf{\Phi}_0}(\vec{R}_i)}, \tag{1.24}$$

where, $\mathbf{\Phi}_0$ and $\vec{\mathcal{R}}_0$ are the parameters used to generate the original ensemble. The averages can be computed as:

$$\langle O \rangle_{\vec{\mathcal{R}},\mathbf{\Phi}} = \frac{\sum_{i=1}^{N} \rho_i O(\vec{R}_i)}{\sum_i \rho_i}. \tag{1.25}$$

If the two probability distributions $p(x)$ and $q(x)$ are too different, then the stochastic average will be affected by a large error.

In particular, we can define the effective number of configurations N_{eff} as the number of configurations that would produce the same stochastic error if the ensemble was generated with the optimal distribution. Therefore, we can define the effective sample size N_eff as Ref.[30]

$$N_{eff} = N \frac{\left(\sum_{i=1}^{N} \rho_i\right)^2}{\sum_{i=1}^{N} . \rho_i^2}. \tag{1.26}$$

Therefore, we can reuse the ensemble until N_{eff}/N is greater than a given threshold η.

The full SSCHA algorithm is represented in the flowchart of Figure 1.6.

1.5 The free-energy condition problem

In Sec. 1.3, we applied SSCHA on a one-dimensional toy model, where a trivial implementation with random moves solves the problem quickly.

However, real systems are not one dimensional; we have $3N$ degrees of freedom in the centroid position (N is the number of atoms in the unit cell) plus $(3N_{sc})(3N_{sc}+1)/2$ degrees of freedom for the Gaussian covariance matrix (N_{sc} is the number of atoms in the super-cell). The number of degrees of freedom of centroids depends only on the atoms on the unit cell (not the supercell) thanks to the translational symmetries. For real systems, it is essential to have an efficient minimization algorithm.

In Eq. (1.17a) and 1.17b, we computed the gradients of the free energy. Any gradient-based technique can be used for the minimization. The performances of a gradient-based algorithm depend on the spectrum of the Hessian matrix of the landscape close to the minimum. The convergence is more difficult if there are both steep and flat valleys. Gradient methods optimize fast steep directions but they are inefficient on flat ones, especially if stochastic noise is present. A schematic representation of a 2D ill-conditioned surface is reported in Figure 1.7.

The condition number is a quantitative measurement of the steepest and the flattest direction. It is the ratio between the highest and smallest eigenvalue (in modulus) of the Hessian matrix around the minimum.

$$C = \frac{\max_\lambda |\lambda|}{\min_\lambda |\lambda|} \geq 1 \tag{1.27}$$

The number of iterations needed to approximate the solution to a given threshold is proportional to the condition number for the steepest descent and its square root for the conjugate gradient[31].

$$N_{sdes} \sim C \qquad N_{cgrad} \sim \sqrt{C}$$

Indeed, the optimal value for the condition number is 1.

The condition number of the SSCHA can be computed analytically for a perfectly harmonic system. The details of the calculation are reported in appendix B.2[25].

The condition number is:

$$\lim_{T\to 0} C_\Phi = \left(\frac{\omega_{max}}{\omega_{min}}\right)^3 \qquad \lim_{T\to\infty} C_\Phi = \left(\frac{\omega_{max}}{\omega_{min}}\right)^4, \tag{1.28}$$

where $\omega_{max/min}$ are the highest/lowest harmonic frequencies of phonons and T is the temperature. Therefore, SSCHA is particularly challenging in molecular crystals, where the typical vibrational energy of covalent bonds is two or more orders of magnitude greater than inter-molecular interactions. This is also a problem in

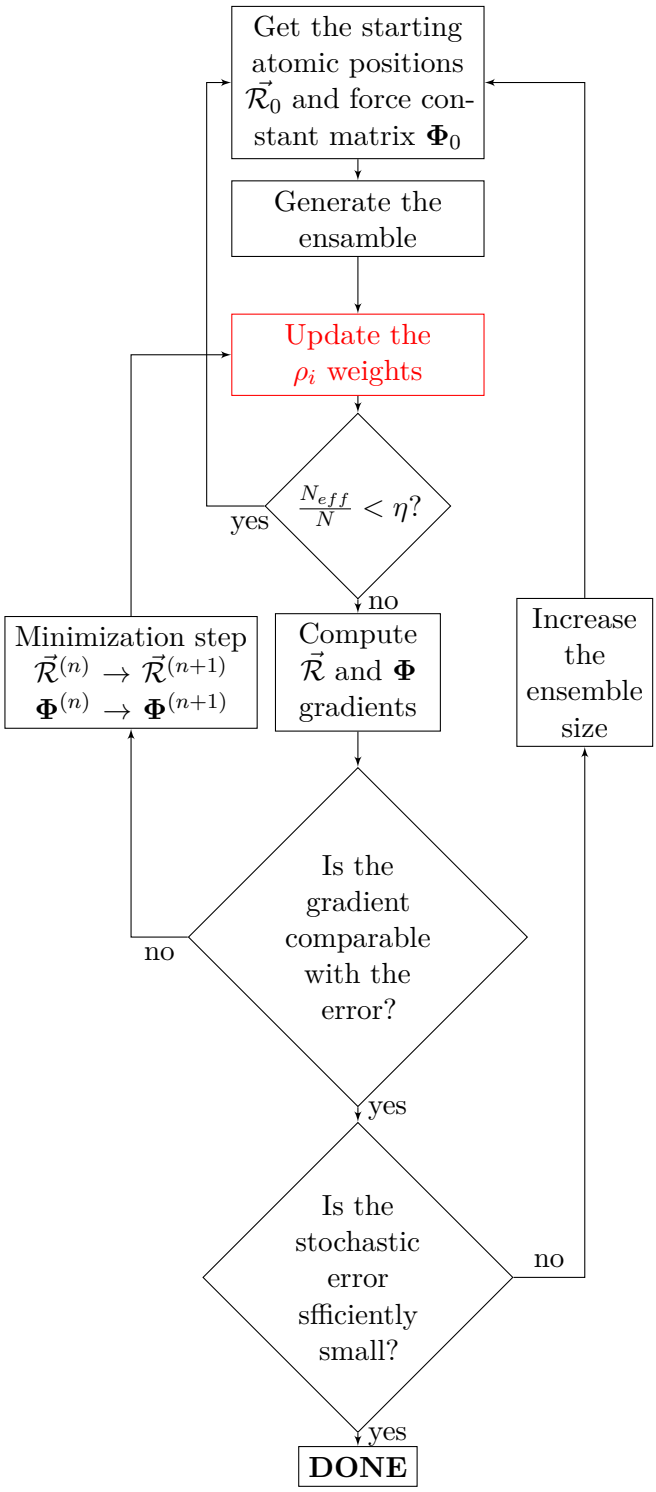

Figure 1.6. Flowchart of the SSCHA implementation. The red box indicates the most expensive computational part of the SSCHA: the calculation of forces and energies for the configurations.

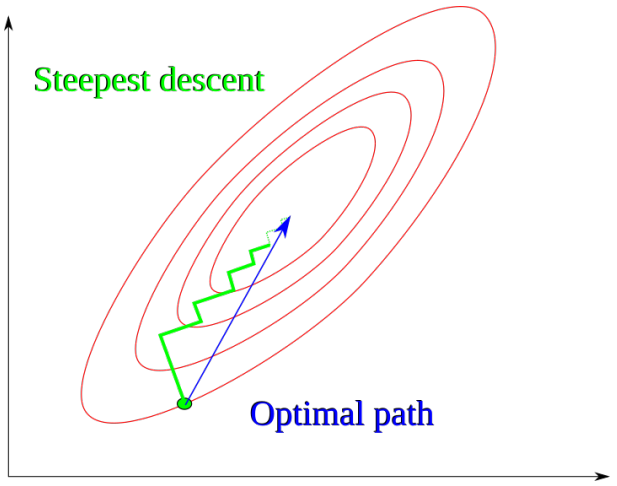

Figure 1.7. Minimization of an ill-conditioned problem. Here, I show the level curves of the 2D function to be minimized. The green path is the best path followed by the steepest descent, that is much worse than the optimal path.

materials that are close to structural instability. In correspondence of the second-order phase transition, the phonon mode associated with the order parameter becomes imaginary passing through 0, introducing a divergence in Eq. (1.28).

In high-pressure phases of hydrogen, for example, we have:

$$C_{hyd}(T = 0\,\mathrm{K}) = \left(\frac{5000\,\mathrm{cm}^{-1}}{100\,\mathrm{cm}^{-1}}\right)^3 = 125000 \gg 1,$$

with this big condition number, there is no surprise that the SSCHA has been applied in past only to very small or simple crystals with many symmetries.

Another numerical issue of the SSCHA is the possibility of incurring in nonphysical run-away solutions during the minimization. In fact, Eq. (1.17a) is stochastic and the dynamical matrix is updated with following scheme:

$$\mathbf{\Phi}^{(n+1)} = \mathbf{\Phi}^{(n)} - \lambda \nabla_{\mathbf{\Phi}} \mathcal{F}(\vec{\mathcal{R}}, \mathbf{\Phi}, \{\vec{a}_i\}) + \boldsymbol{d}^{(n)}, \tag{1.29}$$

where $d^{(n)}$ is 0 for steepest descent algorithm, or accounts for the gradient at the previous step in the conjugate gradient. The $\mathbf{\Phi}$ matrix must be positive definite, otherwise, the density matrix diverges. However, there is no way to guarantee that $\mathbf{\Phi}^{(n+1)}$ is positive definite for a finite step size λ. If this happens during a minimization, the simulation must be discarded and the ensemble increased to reduce the stochastic noise.

1.5.1 Solution to the condition problem

Here, I discuss the two workarounds that I implemented to solve both the ill-conditioning and the runaway solutions. Thanks to these improvements, now the SSCHA can be applied efficiently in all crystals[25, 32, 33, 34, 35, 28, 36].

The simplest solution to get rid of runaway solutions is a nonlinear change of variables that constrains $\mathbf{\Phi}$ to be always positive definite. For example, we optimize

$\sqrt[2n]{\mathbf{\Phi}}$ instead of $\mathbf{\Phi}$.

$$\mathbf{\Phi}^{(i)} = \left(\sqrt[2n]{\Phi}^{(i)} \right)^{2n}$$

We analyze two cases: $n = 1$ (square root) and $n = 2$ (fourth root). The gradient of $\mathcal{F}$ with respect to $\sqrt{\mathbf{\Phi}}$ is obtained from the chain rule:

$$\nabla_{\sqrt{\mathbf{\Phi}}} \mathcal{F} = \sqrt{\mathbf{\Phi}} \nabla_{\mathbf{\Phi}} \mathcal{F} + \nabla_{\mathbf{\Phi}} \mathcal{F} \sqrt{\mathbf{\Phi}} \tag{1.30}$$

The $\sqrt{\mathbf{\Phi}}$ matrix is updated with the gradient descend:

$$\sqrt{\mathbf{\Phi}}^{(n+1)} = \sqrt{\mathbf{\Phi}}^{(n)} - \lambda \nabla_{\sqrt{\mathbf{\Phi}}} \mathcal{F} + \boldsymbol{d}^{(n)}, \tag{1.31}$$

In this way, at each step of the minimization, the $\mathbf{\Phi}$ matrix is defined as:

$$\mathbf{\Phi} = \sqrt{\mathbf{\Phi}} \cdot \sqrt{\mathbf{\Phi}}, \tag{1.32}$$

and it is positive definite by construction. This definitively solves the problem of nonphysical runaway solutions. Moreover, the landscape in $\sqrt{\mathbf{\Phi}}$ is distinct from the $\mathbf{\Phi}$ one: the condition numbers are different. We can prove (see appendix B.3) that the condition number for the square root is:

$$\lim_{T \to 0} C_{\sqrt{\Phi}} = \left(\frac{\omega_{max}}{\omega_{min}} \right) \qquad \lim_{T \to \infty} C_{\sqrt{\Phi}} = \left(\frac{\omega_{max}}{\omega_{min}} \right)^2$$

For the hydrogen we have:

$$C_{hyd,\sqrt{\mathbf{\Phi}}}(T = 0\,\mathrm{K}) = \left(\frac{5000\,\mathrm{cm}^{-1}}{100\,\mathrm{cm}^{-1}} \right) = 50 \ll C_{hyd,\mathbf{\Phi}}(T = 0\,\mathrm{K})$$

This is an acceptable condition number (three orders of magnitude better than the original). it can be further improved using the fourth root. The implementation is straightforward:

$$\nabla_{\sqrt[4]{\mathbf{\Phi}}} \mathcal{F} = \sqrt[4]{\mathbf{\Phi}} \nabla_{\sqrt{\mathbf{\Phi}}} \mathcal{F} + \nabla_{\sqrt{\mathbf{\Phi}}} \mathcal{F} \sqrt[4]{\mathbf{\Phi}}, \tag{1.33}$$

$$\sqrt[4]{\mathbf{\Phi}}^{(n+1)} = \sqrt[4]{\mathbf{\Phi}}^{(n)} - \lambda \nabla_{\sqrt[4]{\mathbf{\Phi}}} \mathcal{F} + \boldsymbol{d}^{(n)}. \tag{1.34}$$

$$\mathbf{\Phi}^{(n+1)} = \sqrt[4]{\mathbf{\Phi}}^{(n+1)} \cdot \sqrt[4]{\mathbf{\Phi}}^{(n+1)} \cdot \sqrt[4]{\mathbf{\Phi}}^{(n+1)} \cdot \sqrt[4]{\mathbf{\Phi}}^{(n+1)} \tag{1.35}$$

In this case the condition number is:

$$\lim_{T \to 0} C_{\sqrt{\Phi}} = 1 \qquad \lim_{T \to \infty} C_{\sqrt{\Phi}} = \left(\frac{\omega_{max}}{\omega_{min}} \right)$$

This completely solves the problem for $T = 0\,\mathrm{K}$ and strongly improves the finite temperature case.

We can do even better. Thanks to the analytical guess on the hessian matrix (see App. B.3), we can modify the gradient direction to point directly to the minimum, compensating for the different steepness of the dimensions. This is a second-order

Newton's method for optimization. The minimum position of a quadratic function is:

$$\boldsymbol{\Phi}_{min} = \boldsymbol{\Phi}_0 - \boldsymbol{A}_{\Phi}^{-1} \nabla_{\boldsymbol{\Phi}} \mathcal{F}., \tag{1.36}$$

where $\boldsymbol{A}_{\boldsymbol{\Phi}}$ is the hessian matrix in the $\boldsymbol{\Phi}$ variable. With this algorithm we solve any quadratic problem, no matter the condition number, in one step (following the blue path in Figure 1.7). Indeed, this method can be combined with the change of variables:

$$\sqrt[4]{\boldsymbol{\Phi}}_{min} = \sqrt[4]{\boldsymbol{\Phi}_0} - \boldsymbol{A}_{\sqrt[4]{\Phi}} \nabla_{\sqrt[4]{\boldsymbol{\Phi}}} \mathcal{F}.$$

In this way, we solve the condition problem for any temperature and avoid runaway solutions at the same time.

1.6 Conclusions

In this chapter, I introduced the SCHA theory and its numerical implementation. This theory is based on the free energy variational principle.

I showed how well the SSCHA reproduces the total energy, average nuclear positions and structural stability, even in anharmonic systems with strong quantum fluctuations.

Since the SSCHA does not rely on a particular fit of the BO energy landscape, its result is equally valid even if the solution is very far from the original guess. Moreover, all the errors in the BO sampling are only due to the stochastic sampling. They are controlled and can be progressively reduced.

This is a key ingredient to search for new structures including quantum fluctuations or relax an unstable structure to see where we fall in. In these cases, the final result can be very far from the starting guess.

In the last section, I showed the SSCHA is affected by unphysical runaway solutions. Moreover, the free energy landscape is ill-conditioned. These issues prevented its application in systems with many degrees of freedom. Thanks to the combination of a nonlinear change of variables and the preconditioning, we solved both, enabling for the first time the application of SSCHA to more complex systems, as high-pressure molecular phases of hydrogen.

Chapter 2

Pressure and variable cell relaxation within Stochastic Self-Consistent Harmonic Approximation

2.1 Introduction

In this chapter, I derive an equation for the pressure and the stress tensor within the SCHA theory. I show how the full stress tensor can be computed after a standard SSCHA calculation with no additional computational effort. This is in contrast with what is usually done in other approximations, like the quasi-harmonic (QHA), where one must compute the stress using a finite difference numerical approach. The efficient evaluation of the stress enables the relaxation of the lattice degrees of freedom even when thermal and quantum fluctuations cannot be neglected.

I present an application computing the thermal expansion of common ice, comparing the SSCHA with the QHA.

This novel result has already been applied in numerous works[25, 28, 32, 33, 35] and it is of great importance to study high-pressure hydrogen.

2.2 Pressure and stress tensor

The stress tensor is the free energy response to strain perturbations. The strain is a deformation of the lattice that affects all the atoms in the system.

The most simple strain is the isotropic volume expansion/contraction. The free energy response to an isotropic volume contraction is the pressure:

$$P = -\frac{dF}{d\Omega}, \tag{2.1}$$

where F is the Helmholtz free energy per unit cell, P is the pressure and Ω is the volume of the unit cell. Indeed, more general strains are possible; for example, one can expand the volume only along one Cartesian axis, or change the angle between two lattice parameters. All the possible infinitesimal strains that excludes rotations

can be represented by a symmetric 3x3 dimensionless tensor $\boldsymbol{\varepsilon}$. A vector in 3D space $\vec{r}$ is strained into $\vec{r'}$ to $\boldsymbol{\varepsilon}$ as follows:

$$r'_a = \vec{r}_a + \sum_{b=x,y,z} \varepsilon_{ab} r_b \tag{2.2}$$

The change of the free energy with respect to any possible strain is a 3x3 tensor:

$$P_{\alpha\beta} = -\frac{1}{\Omega}\frac{dF}{d\varepsilon_{\alpha\beta}}, \tag{2.3}$$

here, $P_{\alpha\beta}$ is the "stress tensor".

A system in equilibrium at constant pressure (that is the condition of many experiments) must have an isotropic stress tensor. The pressure and the stress are tightly related each other. In fact, the pressure is equal to the average of the diagonal elements of the stress:

$$P = \frac{1}{3}\left(P_{xx} + P_{yy} + P_{zz}\right) \tag{2.4}$$

The stress indicates what strain must be applied to the lattice to reduce the free energy. However, while the Helmann-Feynman theorem provides a way to compute the stress efficiently from ab-initio DFT calculations, the vibrational contribution of the stress is usually computed using the finite difference approach, i.e. computing the free energy for any possible strain. This is the standard procedure for the QHA (Quasi Harmonic Approximation). It presents several issues, for example, it requires a highly converged result to dissect different free energies of similar systems. This is particularly annoying for the SSCHA, as a stochastic error affects the free energy and huge ensembles are required.

2.3 The SCHA stress-tensor equation

Since the SCHA, as the DFT, is a variational technique, we can exploit the Helmann-Feynman theorem to compute the derivative of the free energy in the minimum.

The stress tensor is defined as:

$$P_{\alpha\beta}(\vec{\mathcal{R}}, \{\vec{a}_i\}) = -\frac{1}{\Omega}\left.\frac{\partial \mathcal{F}(\vec{\mathcal{R}}, \{\vec{a}_i\})}{\partial \varepsilon_{\alpha\beta}}\right|_{\boldsymbol{\varepsilon}=0}, \tag{2.5}$$

where Ω is the volume of the system and the strain tensor $\varepsilon_{\alpha\beta}$ identifies a generic deformation in which both lattice parameters and centroid positions are affected:

$$a_i'^{\alpha} = a_i{}^{\alpha} + \sum_{\beta=1}^{3} \varepsilon_{\alpha\beta} a_i{}^{\beta}, \tag{2.6a}$$

$$\mathcal{R}'^{\alpha}_{n} = \mathcal{R}^{\alpha}_{n} + \sum_{\beta=1}^{3} \varepsilon_{\alpha\beta} \mathcal{R}^{\beta}_{n}. \tag{2.6b}$$

The final result can be divided into two main contributions (see Appendix C for the proof):

$$P_{\alpha\beta}(\vec{\mathcal{R}}, \{\vec{a}_i\}) = P^{H}_{\alpha\beta}(\vec{\mathcal{R}}, \{\vec{a}_i\}) + P^{\mathrm{FLC}}_{\alpha\beta}(\vec{\mathcal{R}}, \{\vec{a}_i\}), \tag{2.7}$$

where the $P^H_{\alpha\beta}(\vec{\mathcal{R}})$ is the static contribution, i.e. the stress tensor without quantum and thermal fluctuations, while $P^{\text{FLC}}_{\alpha\beta}$ accounts for fluctuations.

$$P^H_{\alpha\beta}(\vec{R}, \{\vec{a}_i\}) = -\frac{1}{\Omega} \left. \frac{\partial V(\vec{R}, \{\vec{a}_i\})}{\partial \varepsilon_{\alpha\beta}} \right|_{\varepsilon=0}, \tag{2.8a}$$

$$P^{\text{FLC}}_{\alpha\beta}(\vec{\mathcal{R}}, \{\vec{a}_i\}) = \langle P^H_{\alpha\beta}(\vec{R}, \{\vec{a}_i\}) \rangle_{\rho_{\vec{\mathcal{R}}}} - P^H_{\alpha\beta}(\vec{\mathcal{R}}, \{\vec{a}_i\}) - \frac{1}{2\Omega} \sum_{s=1}^{N} \langle \left(f_{\mathcal{H}_s}{}^{\alpha} u_s^{\beta} + f_{\mathcal{H}_s}{}^{\beta} u_s^{\alpha} \right) \rangle_{\rho_{\vec{\mathcal{R}}}}, \tag{2.8b}$$

Eq. (2.8) requires the the atomic forces $f^{\alpha}_s(\vec{R}, \{\vec{a}_i\})$ and the electronic stress tensors $P^H_{\alpha\beta}(\vec{R}, \{\vec{a}_i\})$ for each ionic displacement $\vec{R}$ in the ensemble distributed according to $\rho_{\vec{\mathcal{R}}}(\vec{R})$. These parameters are first derivatives of the ground state electronic energy and can be evaluated in the same DFT calculation.

Computing Eq. (2.8) is very fast and it does not add any extra computational cost to a SCHA minimization. In fact the most CPU expensive part of a SCHA run is the ab-initio calculation of $V(\vec{R}, \{\vec{a}_i\})$, $f^{\alpha}_s(\vec{R}, \{\vec{a}_i\})$ and $P^H_{\alpha\beta}(\vec{R}, \{\vec{a}_i\})$ for each configuration. All these quantities are needed also by the SCHA minimization.

2.4 Application: Thermal expansion of common ice

In this section, I will show how the pressure can be used to estimate the thermal expansion of common ice and how the SCHA outperforms the QHA in this system compared with the experiments.

Thanks to Eq. (2.7), it is possible to compute the pressure as a function of temperature at a fixed volume with a single SCHA calculation.

As an application, I will compute the thermal expansion of ice. This is a very interesting problem: the ice thermal expansion is anomalous (negative) for $T \leq 80\,\text{K}$. This anomalous expansion is a pure quantum effect, and is not reproduced by classical molecular dynamics. Moreover, the thermal expansion at higher temperature $T \geq 150\,\text{K}$ is also affected by entropic terms related to the topological defects that may arise due to high mobility of the hydrogen ions. So, up to now, all the failures in reproducing experimental data at high temperature by using the QHA have been addressed to entropic effects that are very difficult to simulate. Here, I show how QHA itself fails in describing the high temperature thermal expansion of ice compared to the SSCHA. This finding resizes the real impact of topological disorder in the ice crystal in the thermal expansion. The result of the SSCHA simulation, compared with both the QHA and the experiments, is reported in Figure 2.1.

The experimental data[37], measured at constant pressure, are converted to constant volume using the experimental bulk modulus[37].

While the QHA seems to reproduce well the low-temperature behavior, it fails in the high-temperature regime. This has been ascribed[38] to the disorder induced by water molecule dissociation occurring in common ice, that is taken into account by neither the QHA nor the SSCHA. However, the SCHA overlaps almost completely with the experimental points, indicating that the discrepancy with QHA is more likely due to not properly accounting for anharmonicity.

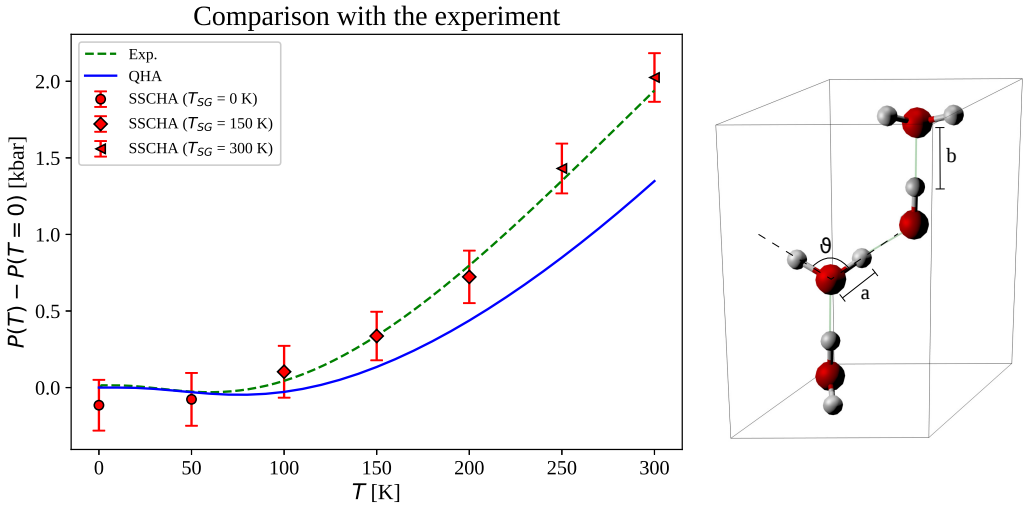

Figure 2.1. Thermal expansion of ice XI, a prototype model of common ice, at fixed volume. Experimental data are from ref.[37]. Error bars are the stochastic uncertainty of the SCHA calculation. Different markers for the SCHA points are obtained with the reweighing from different temperatures. Details of the calculations parameters reported in App. E.1. Here T_{SG} is the temperature used for the importance sampling for each simulation, for more details see Ref.[25].

2.5 The constant pressure relaxation

The direct computation of the stress tensor opens the way to constant pressure simulations. Here, the Helmholtz free energy must be replaced by the Gibbs free energy, that is obtained by a Legendre transform:

$$G(P^*) = \min_{\{\vec{a}_i\}} \left[\mathcal{F}(\{\vec{a}_i\}) + P^*\Omega(\{\vec{a}_i\})\right] \tag{2.9}$$

where P^* here is the target pressure

Since we know how to derive the Helmholtz free energy (and the volume) with respect to the strain, we can minimize the right-hand side of Eq. (2.9). In particular, the strain that we must apply is proportional to:

$$\varepsilon_{xy} = A\left[\Omega P_{xy} - P^*\delta_{xy}\right] \tag{2.10}$$

where A is the strain step. The convenient way is to use a guess of the static bulk modulus B_0 of the material to determine the best strain size to converge in one iteration.

$$A = \frac{1}{3\Omega B_0} \qquad B_0 = \Omega\frac{dP^H}{d\Omega}. \tag{2.11}$$

Then, if convergence is not achieved in one step, A can be updated using standard minimization algorithms like line-optimization.

We can formulate an iterative algorithm for the constant pressure SSCHA:

1. Perform a SCHA relaxation at fixed volume.

2. Compute the stress P_{xy} using Eq. (2.3).

3. Compute the optimal strain using Eq. (2.10)

4. Update the lattice vector and inner position according to Eq. (2.6):

$$\begin{pmatrix} \vec{a}_1' \\ \vec{a}_2' \\ \vec{a}_3' \end{pmatrix} = \begin{pmatrix} \vec{a}_1 \\ \vec{a}_2 \\ \vec{a}_3 \end{pmatrix} \cdot \left[I + \boldsymbol{\varepsilon}^T \right]. \tag{2.12}$$

5. Repeat from step 1 until convergence is achieved.

2.5.1 Constant volume cell relaxation

The ability to run constant pressure simulations is a big step forward. However, in many cases, it is preferable to deal with constant volume quantities. In DFT calculations, the pressure is always affected by a small convergence error due to the use of a finite cutoff for the basis set, the K point sampling, and the threshold for self-consistency, while the volume is known with arbitrary precision, as it does not change during the self-consistent iterations. To compare quantities, it is more precise to deal with a constant volume between different simulations rather than constant pressure, as it is more likely to exploit error cancellations.

However, even a constant volume calculation needs to optimize the lattice parameters, so we can exploit the cell relaxation algorithm also in this case. To redefine the algorithm for the constant volume and variable cell we need to apply the fixed volume constrain to Eq. (2.10).

A strain that does not change the volume must have a zero trace. Since zero trace symmetric matrices form a linear space, we can simply project Eq. (2.10) into the subspace of symmetric matrices with a zero trace.

It is easy to prove that this is equal to replace P^* with P in Eq. (2.10), where we recall that

$$P = \frac{1}{3} \sum_{\alpha} P_{\alpha\alpha}.$$

It is still possible that the volume changes a bit, as the zero trace strain preserves the volume only if the strain step is infinitesimal. To preserve the volume even with finite steps, we can further force the volume conservation after the new lattice vectors have been computed (2.12), multiplying each lattice vector by:

$$[\Omega^*]^{1/3} \left[\det \begin{pmatrix} \vec{a}_1' \\ \vec{a}_2' \\ \vec{a}_3' \end{pmatrix} \right]^{-1/3},$$

with Ω^* being the target (original) volume.

2.6 Conclusions

In this chapter, I introduced the equations to compute the stress tensor. This method does not require any extra computational cost, as all the needed ingredients are shared with the SSCHA minimization. I applied the stress equation to simulate the thermal expansion of common ice, showing an important difference with the quasi-harmonic approximation when compared with experiments.

In the last sections, I introduced the constant pressure and constant volume full relaxation, that includes the lattice parameters.

The lattice relaxation is essential to see the relative stability of two structures, especially in presence of a second order phase transition. In fact, if we are relaxing a low symmetry phase, with a cell distortion, we are not able to recover a higher symmetry if we do not relax also the lattice (allowing, for example, a monoclinic lattice to become a orthorombic or hexagonal). This is exactly what happens in LaH_{10}, where the monoclinic distorted phases of groups $C/2$ or $R-3m$, local minima in the BO surface, must change their lattice parameters in order to recover the orthorombic symmetry $Fm-3m$[28].

Chapter 3

Dynamical theory for the Self-Consistent Harmonic Approximation

3.1 Introduction

The self-consistent harmonic approximation (SCHA) is a static theory. It is a good technique to compute equilibrium quantities. However, many interesting physical properties are dynamical or arise from out-of-equilibrium processes, as transport. This is the case of many emerging fields. In photochemistry, for example, very short (few femtoseconds) laser pulses are used to shock the sample, inducing a chemical reaction that can result in a structural deformation[39]. Typical examples are the retinal isomerization photodynamics[40] (the mechanism through which photons interact with the retina triggering the mechanism of vision), the intermolecular vibrational motion in liquid CS_2 [41] or the photoinduced dynamics in the green florescence protein [42].

Other important systems that cannot be studied with equilibrium simulations are those close to a second-order phase transition. The response function diverges close to the critical point, leading to strong fluctuations. Experiments in this regime are very interesting, as the observed photoinduced superconductivity above T_c in $YBa_2Cu_3O_x$[43] and organic K_3C_{60}[44]. These are cases where the experimental probe induces a strong deviation from the equilibrium configuration that is not sampled through an equilibrium simulation.

Moreover, even when the probe does not bring the system out of equilibrium, phonons are dynamical properties, that are generated and measured during the interaction of the atoms with an external field that changes in time. Therefore, to study the vibrational spectra emerging from IR or Raman experiments, dynamics must be taken into account.

In this chapter, I will extend the SCHA theory, formulating it on the Dirac least action principle, to obtain a time-dependent equation of motion for the nuclear wave-function.

This enables the application of SSCHA to out-of-equilibrium problems and paves the way to the formulation the Raman/IR response functions in the SSCHA

framework (that is derived in the next chapter).

3.2 The stationary action principle

In this section, I present the stationary action principle to derive the quantum equation of motions. The Schrödinger equation can be derived by imposing that the wavefunction is a stationary solution of the Dirac action. The Dirac action is a functional of the time dependent wavefunction, defined as:

$$A[\psi(t)] = \frac{1}{t_1 - t_0} \int_{t_0}^{t_1} dt \, \langle \psi(t)| \left[H - i\hbar \frac{d}{dt} \right] |\psi(t)\rangle \tag{3.1}$$

Deriving the Schrödinger equation is quite easy from this expression. We can do the variation in $\delta |\psi(t)\rangle$ and $\delta \langle \psi(t)|$:

$$\begin{aligned} \delta A = & \frac{1}{t_1 - t_0} \int_{t_0}^{t_1} dt \delta \langle \psi(t)| \left[H |\psi(t)\rangle - i\hbar \frac{d}{dt} |\psi(t)\rangle \right] + \\ & + \frac{1}{t_1 - t_0} \int_{t_0}^{t_1} \left[\langle \psi(t)| H \left(\delta |\psi(t)\rangle \right) - i\hbar \langle \psi(t)| \left(\delta \frac{d}{dt} |\psi(t)\rangle \right) \right] \end{aligned} \tag{3.2}$$

The last term of Eq. (3.2) can be integrated by parts.

$$\begin{aligned} \delta A = & \frac{1}{t_1 - t_0} \int_{t_0}^{t_1} dt \delta \langle \psi(t)| \left[H |\psi(t)\rangle - i\hbar \frac{d}{dt} |\psi(t)\rangle \right] + \\ & + \frac{1}{t_1 - t_0} \int_{t_0}^{t_1} \left[\langle \psi(t)| H \left(\delta |\psi(t)\rangle \right) + i\hbar \left(\frac{d}{dt} \langle \psi(t)| \right) \delta |\psi(t)\rangle \right], \end{aligned} \tag{3.3}$$

where we imposed the condition:

$$\langle \psi(t_1)| \left(\delta |\psi(t_1)\rangle \right) - \langle \psi(t_0)| \left(\delta |\psi(t_0)\rangle \right) = 0.$$

This is true in periodic motions (i.e. $|\psi(t_0)\rangle = |\psi(t_1)\rangle$) or in presence of an adiabatic perturbation.

Imposing $\delta A = 0$ in Eq. (3.3) we get two independent equations:

$$H |\psi(t)\rangle - i\hbar \frac{d}{dt} |\psi(t)\rangle = 0 \tag{3.4}$$

$$\langle \psi(t)| H + i\hbar \frac{d}{dt} \langle \psi(t)| = 0. \tag{3.5}$$

Here, $\langle \psi(t)|$ is the complex conjugate of $|\psi(t)\rangle$, and the equation that solves $|\psi(t)\rangle$ is exactly the Schrödinger equation.

If the wave-function does not depend on time, the time derivative in Eq. 3.1 disappears and the least action becomes the least energy principle.

3.2.1 The SCHA ansatz for the wavefunction

In the previous section, we found that the Dirac action is stationary if the $|\psi\rangle$ solves the Schrödinger equation. We can use this principle to construct a variational theory. We can make the same ansatz on the wavefunction as in the static SSCHA: the wavefunction is a Gaussian during the whole time evolution.

$$\psi(\vec{R},t) = \sqrt[4]{\frac{\det \boldsymbol{\Upsilon}(t)}{2\pi}} \exp\left\{-\frac{1}{4}\sum_{ab}\Upsilon_{ab}(t)[R_a - \mathcal{R}_a(t)][R_b - \mathcal{R}_b(t)]\right\}\cdot$$
$$\cdot \exp\left\{i\sum_a Q_a(t)[R_a - \mathcal{R}_a(t)] + i\sum_{ab}\mathcal{C}_{ab}(t)[R_a - \mathcal{R}_a(t)][R_b - \mathcal{R}_b(t)]\right\}. \tag{3.6}$$

This wave-function reproduces the same density probability as Eq. (1.13a), however, it includes twice as many degrees of freedom, as it contains the phase information $\vec{Q}_a(t)$ and $\boldsymbol{\mathcal{C}}(t)$.

This information is necessary when dealing with dynamics. Let us take the simple one dimensional example and compare two Gaussians with a different phase:

$$\psi_1(x) = \sqrt[4]{\frac{1}{2\pi\sigma^2}} e^{-\frac{(x-x_0)^2}{4\sigma^2}} \tag{3.7}$$

$$\psi_2(x) = \sqrt[4]{\frac{1}{2\pi\sigma^2}} e^{iqx} e^{-\frac{(x-x_0)^2}{4\sigma^2}} \tag{3.8}$$

Both of them share the same density probability $\rho(x) = |\psi(x)|^2$, however, their free time evolution is very different. The average position of ψ_2 will change in time, as it has a positive q momentum, while ψ_1 will not move.

The phase modulation plays the role of the velocity. A uniform phase modulation, like the one of ψ_2 in Eq. (3.8), leads to a drift of the wave-function without deforming it, while more complex x dependence of the phase deforms the wave-function envelope.

In particular, the quadratic dependence in Eq. (3.6), parameterized by the matrix $\boldsymbol{\mathcal{C}}$, changes the variance of the Gaussian.

This is the most general wave-function whose free dynamic remains Gaussian.

For the reasons just discussed, I will refer to $\vec{Q}$ as the momentum of the wave-function, and $\boldsymbol{\mathcal{C}}$ as the "chirp", in analogy to the well studied "chirp" in signal propagation[39].

3.3 The SCHA equation of motion

To derive the motion of our trial wave-function, parameterized by $\vec{\mathcal{R}}$, $\vec{Q}$, $\boldsymbol{\Upsilon}$ and $\boldsymbol{\mathcal{C}}$, we must insert the ansatz of Eq. (3.6) into the Dirac's action Eq. (3.1) and look for the dynamical equations that make the action stationary.

The details of the calculation are reported in App. D.4.

The final equations we get are:

$$\begin{cases} -\langle f_a \rangle + \hbar \dot{Q}_a = 0 \\ -\hbar \dot{\mathcal{R}}_a + \hbar^2 \dfrac{Q_a}{m_a} = 0 \\ \dfrac{\partial \mathcal{F}(\vec{\mathcal{R}}, \mathbf{\Phi}, \{\vec{a}_i\})}{\partial \Phi_{ab}} + \displaystyle\sum_{cde} \frac{2\hbar^2}{m_c} \frac{\partial \Upsilon^{-1}_{de}}{\partial \Phi_{ab}} \mathcal{C}_{cd}\mathcal{C}_{ce} + \hbar \sum_{cd} \dot{\mathcal{C}}_{cd} \frac{\partial (\Upsilon^{-1})_{cd}}{\partial \Phi_{ab}} = 0 \\ -\hbar \displaystyle\sum_{cd} \frac{\partial (\Upsilon^{-1})_{ab}}{\partial \Phi_{cd}} \dot{\Phi}_{cd} + \frac{4\hbar^2}{m_a} \sum_c (\Upsilon^{-1})_{bc} \mathcal{C}_{ca} = 0 \end{cases} . \tag{3.9}$$

To simplify the equations, Eq. 3.9 describe the time evolution for $\mathbf{\Phi}$ instead of $\mathbf{\Upsilon}$. This $\mathbf{\Phi}$ matrix is the same from the static theory, uniquely liked to $\mathbf{\Upsilon}$. This is a convenient choice, as we will see in the next section, it makes possible to define a time-dependent non-linear Schrödinger equation that our wave-function follows in analogy to what it is done for the static case, and also to keep the same degrees of freedom as the static case. The term $\frac{\partial \mathcal{F}(\vec{\mathcal{R}}, \mathbf{\Phi}, \{\vec{a}_i\})}{\partial \Phi_{ab}}$ is the static gradient in Eq. (1.17a).

The first two equations are exactly Newton's equation of motion. If we derive the second equation and substitute the first into the second we get:

$$m_a \ddot{\mathcal{R}}_a = \langle f_a \rangle . \tag{3.10}$$

Here, $\langle f_a \rangle$ is the average force that acts on the a-th atom in the corresponding Cartesian coordinate[1].

This is a very elegant way also to see how the Newton's dynamic law emerges naturally from quantum mechanics.

The last two equations determine how the spread of the wave-function depends on time. It is interesting to notice how this is proportional to the static free energy gradient, in a similar way as the centroid positions $\vec{\mathcal{R}}$ are related to their static gradient (the average of the force). These dynamical equations contain inertia.

We can manipulate them a bit: in both cases the time derivative is row by column multiplied by the same super-operator. This means that, if we are able to invert the super-operator, we can write an explicit equation for both. In particular we can multiply both equations times

$$\frac{\partial \Phi_{ab}}{\partial (\Upsilon^{-1})_{hk}}$$

and we get:

$$\dot{\mathcal{C}}_{hk} = -\sum_{ab} \frac{1}{\hbar} \frac{\partial \Phi_{ab}}{\partial (\Upsilon^{-1})_{hk}} \frac{\partial \mathcal{F}_{SCHA}}{\partial \Phi_{ab}} - \sum_c \frac{2\hbar}{m_c} \mathcal{C}_{kc}\mathcal{C}_{ch} \tag{3.11}$$

In the same way it is possible to invert also the last equation:

$$\dot{\Phi}_{hk} = \sum_{abc} \frac{\partial \Phi_{ab}}{\partial (\Upsilon^{-1})_{hk}} \frac{4\hbar}{m_a} \Upsilon^{-1}_{bc} \mathcal{C}_{ca} \tag{3.12}$$

[1]Here, I am using compression notation, where both atomic and Cartesian coordinates are written with one index for brevity.

Moreover, we can define the $\mathbf{\Lambda}$ tensor as:

$$\Lambda^{abcd} = \frac{1}{2}\frac{\partial(\Upsilon^{-1})_{cd}}{\partial\Phi_{ab}} \tag{3.13}$$

The explicit calculation of $\mathbf{\Lambda}$ is computed in App. D.1, where it is also proved that it is the same tensor introduced in [24, 25].

Then the static free energy gradient is (Eq. 1.17a)

$$\frac{\partial\mathcal{F}(\vec{\mathcal{R}}, \mathbf{\Phi}, \{\vec{a}_i\})}{\partial\Phi_{ab}} = -\sum_{cdn}\Lambda^{cdab}\Upsilon_{cn}\left\langle u_n(f_d - f_d^{\mathcal{H}})\right\rangle \tag{3.14}$$

Then the chirp equation simplifies a lot:

$$\dot{\mathcal{C}}_{hk} = \frac{1}{2\hbar}\sum_a \Upsilon_{ha}\left\langle u_a \Delta f_k\right\rangle - \sum_a \frac{2\hbar}{m_a}\mathcal{C}_{ka}\mathcal{C}_{ah} \tag{3.15}$$

where $\Delta f_k = f_k - f_k^{\mathcal{H}}$ and $f_k^{\mathcal{H}} = -\sum_b \Phi_{kb}(R_b - \mathcal{R}_b)$ in analogy with what introduced for the static theory.

And the $\mathbf{\Phi}$ equation becomes:

$$\dot{\Phi}_{hk} = \sum_{abc}\Lambda^{-1}_{abhk}\frac{2\hbar}{m_a}\Upsilon^{-1}_{bc}\mathcal{C}_{ca} \tag{3.16}$$

These equations are explicit and compact and can be evolved by a symplectic algorithm, as a leap-frog.

A useful check of the consistency of the equations is that, if we insert the static solution inside the equation of motion, we get a stationary point:

$$\dot{\vec{\mathcal{R}}} = 0 \qquad \dot{\vec{Q}} = 0 \tag{3.17}$$

$$\dot{\boldsymbol{\mathcal{C}}} = 0 \qquad \dot{\mathbf{\Phi}} = 0 \tag{3.18}$$

3.4 The dynamical effective Hamiltonian

In this section, I will show how the equations of motion introduced in Sec. 3.3 are equivalent of solving an effective time-dependent self-consistent Schrödinger equation. This puts the dynamical SCHA in the same framework as dynamical Hartree-Fock or Time-Dependent Density Functional Theory (TDDFT), and justifies the name of Time-Dependent Self-Consistent Harmonic Approximation (TDSCHA).

A self-consistent time dependent Schrödinger equation has the following form:

$$i\hbar\frac{d}{dt}\left|\psi\right\rangle = \mathcal{H}[\left|\psi\right\rangle]\left|\psi\right\rangle \tag{3.19}$$

Where $\mathcal{H}[\left|\psi\right\rangle]$ is a non-linear operator, functional of the wave-function itself.

It is not surprising that the new Hamiltonian is a simple extension of the static SCHA effective Hamiltonian:

$$\mathcal{H}[\left|\psi\right\rangle] = \sum_a \frac{p_a^2}{2m_a} + \frac{1}{2}\sum_{ab}\left\langle\frac{d^2V}{dR_a dR_b}\right\rangle(R_a - \mathcal{R}_a)(R_b - \mathcal{R}_b) - \sum_a\left\langle f_a\right\rangle(R_a - \mathcal{R}_a), \tag{3.20}$$

The only difference with the static effective Hamiltonian is the presence of a linear term in $(\vec{R} - \vec{\mathcal{R}})$:

$$\sum_a \langle f_a \rangle \left(R_a - \mathcal{R}_a \right) \tag{3.21}$$

This term was not necessary in the static case, as it is always zero at equilibrium, however, here we are describing an out-of-equilibrium system and it must be taken into account.

In order to prove Eq. (D.73), we must substitute it in Eq. (3.19) and substitute the wave-function with our trial wave-function defined in Eq. (3.6).

The detailed calculation is reported in App. D.5. This procedure leads to the same equations of motion derived from the least-action principle (Eq. 3.9).

3.5 Conclusions

In this chapter, I derived a dynamical formulation of the SCHA, based on the Dirac least action principle.

The wave-function is constrained to be a Gaussian whose parameters depend explicitly on time. The evolution of these parameters has been derived from the Dirac least action principle.

This new theory is analogue to the time-dependent Hartree-Fock or density functional theory, as it can be obtained by a self-consistent time-dependent Scrödinger equation.

This theory allows recovering classical physics from quantum mechanics, as the dynamics of the average position of the Gaussian wave-function follows a Newton-like equation:

$$m\ddot{\mathcal{R}}_a = \langle f_a \rangle ,$$

where the force f is averaged over the time dependent wave-function.

The new theory is expected to correctly describe out-of-equilibrium dynamics, as the response of a system close to a second order phase-transition, where the linear response diverges.

An important application is illustrated in the following chapter, where the dynamical equations are linearized with respect to a small perturbation, to obtain the dynamical Green functions.

Chapter 4

The dynamical linear-response theory

4.1 Introduction

In the previous chapter, we derived the TD-SCHA equations. They can be used to study the most general out-of-equilibrium system. In this chapter, we use the dynamical equations to derive the linear response to time-dependent probes. This is very useful to simulate dynamical properties like IR and Raman spectra. This paves the way for comparing the simulations with experiments even when strong anharmonicity and quantum fluctuations are present. In particular, the TD-SCHA describes how excited vibrational quasiparticles interact and scatter, leading to finite lifetimes and energy shifts. This is the reason why the ω_μ frequencies, obtained as eigenvalues of the force constants matrix $\mathbf{\Phi}$, are not the energy of the anharmonic phonons (see Eq. (1.10)). They do not include the dynamical effects, like finite lifetimes and the energy shifts resulting from the Kramers–Kronig relations.

To emphasize this point, in Sec. 4.2 I introduce a simple anharmonic toy-model, showing how phonon-phonon scattering introduces a finite lifetime when dynamical effects are considered. Then, I apply perturbation theory on the TD-SCHA equations and derive the linear response. I prove that this coincides with the dynamical ansatz formulated for the SCHA by Bianco et. al.[24]. In Sec. 4.5, I derive a new algorithm for the computation of the dynamical results, based on the Lanczos continued fraction. This new algorithm outperforms the one described in[24] and accounts also for the four phonon scattering. This enables the study of new systems, like hydrogen, where four phonon scattering terms cannot be neglected.

Moreover, I prove that it is possible to correctly recover also the static limit, providing a new way for efficiently computing the order parameters of second-order phase-transitions[24].

4.2 Anharmonic phonon scattering

In this section, I show how the phonon-phonon scattering is responsible for both the shift and broadening of the vibrational spectrum.

We study a simple system made by two phonons that we probe with an external perturbation of finite frequency ω. This perturbation interacts with the two phonons exciting both of them. They then recombine and we probe the resulting reaction of the system.

This process is represented by the Feynman diagram in Figure 4.1.

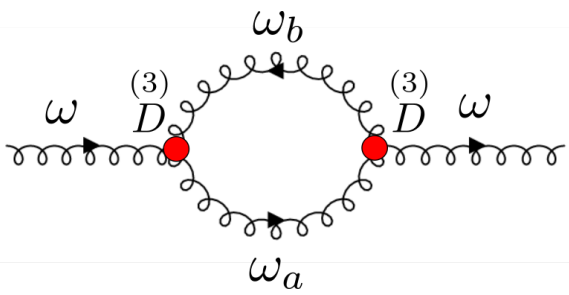

Figure 4.1. Dynamical anharmonic three phonon scattering diagram.

.

So our system is described by a toy potential

$$V(\vec{u}) = \frac{1}{2}\sum_{ab} \overset{(2)}{\tilde{\Phi}}_{ab}\, u_a u_b + \frac{1}{6}\sum_{abc} \overset{(3)}{\Phi}_{abc}\, u_a u_b u_c \tag{4.1}$$

Here we introduce the quantities:

$$\overset{(2)}{\tilde{D}}_{\mu\nu} = \sum_{ab} \frac{\overset{(2)}{\tilde{\Phi}}_{ab}\, e^a_\mu e^b_\nu}{\sqrt{m_a m_b}} = \omega^2_\mu \delta_{\mu\nu} \tag{4.2}$$

$$\overset{(3)}{D}_{\mu\nu\eta} = \sum_{abc} \frac{\overset{(3)}{\Phi}_{ab}\, e^a_\mu e^b_\nu e^c_\eta}{\sqrt{m_a m_b m_c}} \tag{4.3}$$

Since we know the solution for the harmonic potential, we can treat $\overset{(3)}{\boldsymbol{D}}$ as the anharmonic perturbation, and deal with it using Feynman diagrams. The unperturbed result is the following response function (see App. D.2):

$$\tilde{G}_{ab}(\omega) = \frac{1}{\omega^2 - \overset{(2)}{\tilde{D}}_{ab}} = \frac{\delta_{ab}}{\omega^2 - \omega^2_a} \tag{4.4}$$

So it has poles at $\pm\omega_{a/b}$, that are the two frequencies of our toy model system. The harmonic Green function has no imaginary part and phonons have an infinite lifetime.

The diagram reported in Figure 4.1, the bubble, is the lowest order non zero process that involves the perturbation $\overset{(3)}{\boldsymbol{D}}$. This diagrams adds the following contribution to the self-energy:

$$\Pi_{ab}(z) = \sum_{cd} \overset{(3)}{D}_{acd} \left(-\frac{1}{2}\chi_{cd}(z)\right) \overset{(3)}{D}_{cdb} \tag{4.5}$$

Here, $-\frac{1}{2}\chi(z)$ is the two phonons propagator, and it is equal to (see App. D.3):

$$\chi_{ab}(z) = \frac{\hbar}{2}\frac{1}{\omega_a\omega_b}\left[\frac{(\omega_a+\omega_b)(1+n_a+n_b)}{(\omega_a+\omega_b)^2-z^2} - \frac{(\omega_a-\omega_b)(n_a-n_b)}{(\omega_a-\omega_b)^2-z^2}\right] \tag{4.6}$$

The first term represents the original frequency z that splits in $\omega_a+\omega_b$, while the second negative term represents a phonon scattering, where z absorbs ω_b and emits ω_a (the process depicted in Figure 4.1).

Another process is present at smallest order of perturbation in $\overset{(3)}{\boldsymbol{D}}$, the tadpole diagram (see App. D.3), however, it is always positive definite and it does not depend on the perturbation frequency ω (therefore, it does not introduce an imaginary part for the Krames-Kronig relations). Since it shifts only the harmonic frequency (and changes the harmonic polarization vectors), it can be included in the definition of $\overset{(2)}{\tilde{\boldsymbol{D}}}$. This corresponds exactly in substituting the harmonic $\overset{(2)}{\tilde{\boldsymbol{D}}}$ with the SCHA $\overset{(2)}{\boldsymbol{D}}$). The overall response function is

$$G^{-1}_{ab}(\omega) = \omega^2 - \overset{(2)}{D}_{ab} - \Re\Pi_{ab}(\omega+i0^+) - i\Im\Pi_{ab}(\omega+i0^+) \tag{4.7}$$

The new phonon frequencies are the poles of the response functions. So $\Re\Pi(\omega+i0^+)$ causes a shift of the phonon frequency, while $\Im\Pi(q,\omega+i0^+)$ introduces the lifetime.

Now, if Π_{ab} is not zero with $a \neq b$, the direction identified by a and b, i.e. the polarization vectors of the harmonic phonons, are no more the directions in which the green function is diagonal. This is called the "mode-mixing" process.

Let us have a look at how this can profoundly modify the shape of the spectrum. Here we assume $\omega_a = 100\,\mathrm{cm}^{-1}$ and $\omega_b = 200\,\mathrm{cm}^{-1}$. The two phonons ω_a and ω_b have an anharmonic scattering factor d:

$$\overset{(3)}{D}_{aab} = \overset{(3)}{D}_{abb} = \overset{(3)}{D}_{aba} = \overset{(3)}{D}_{baa} = \overset{(3)}{D}_{bba} = \overset{(3)}{D}_{bab} = d \tag{4.8}$$

The spectral function of such a system is reported on Figure 4.2. Even if there are only 2 phonon modes, there are 3 peaks. This is due to the Fermi resonance: a process that takes place when there is a strong anharmonic coupling between two modes and one is in resonance with an overtone of the other. In this case, the anharmonic coupling opens a gap between the two levels (the overtone and the other mode) and both become poles of the spectral function. This is one mechanism that allows anharmonicity to make overtones visible in Raman/IR spectra.

We can even go further, looking what happens to the spectral function as we increase the anharmonic coefficient (Figure 4.3)

When d is zero, the spectrum coincides with the harmonic only two phonon modes are visible. However, while increasing the anharmonicities the mode at $200\,\mathrm{cm}^{-1}$ starts splitting (Fermi resonance). As we further increase the anharmonicity the $200\,\mathrm{cm}^{-1}$ mode goes to zero and becomes imaginary. This is a marker of a second-order phase transition, driven by the anharmonicity. This means that our representation is no more accurate, as the excited states of our phonons have lower energy than the ground state.

The $200\,\mathrm{cm}^{-1}$ mode is much more affected by the anharmonic factor, as it can decay into two modes of $100\,\mathrm{cm}^{-1}$, while the $100\,\mathrm{cm}^{-1}$ needs to scatter with itself to

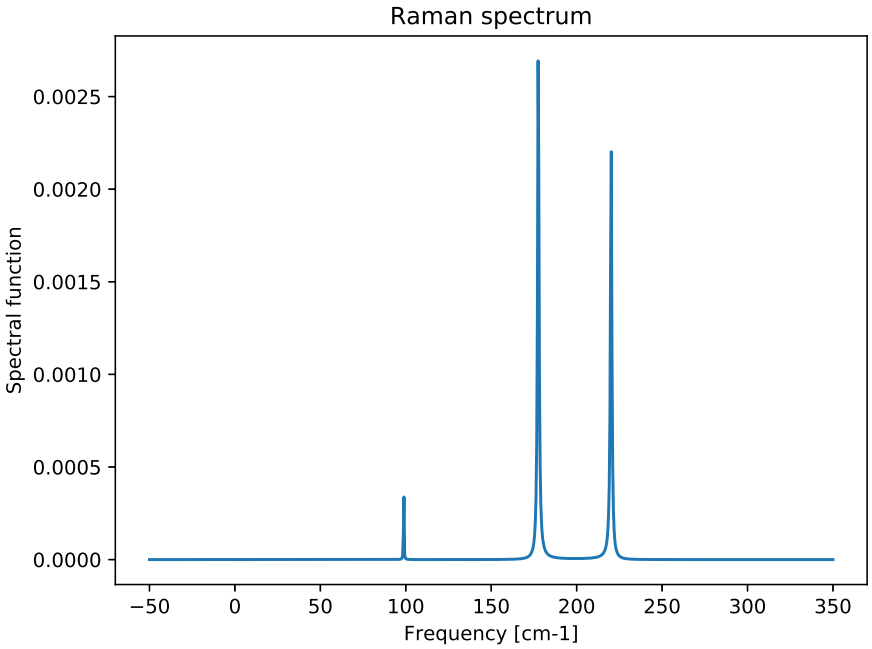

Figure 4.2. Spectral function of a system with two phonons whose harmonic frequencies are $100\,\mathrm{cm}^{-1}$ and $200\,\mathrm{cm}^{-1}$ that have a very strong anharmonic coupling ($T = 0\,\mathrm{K}$). The resonance between one overtone of the lowest mode and the upper mode makes the overtone visible and causes a level splitting. This gives rise to 3 peaks in the spectral function instead of 2. This process is called Fermi resonance.

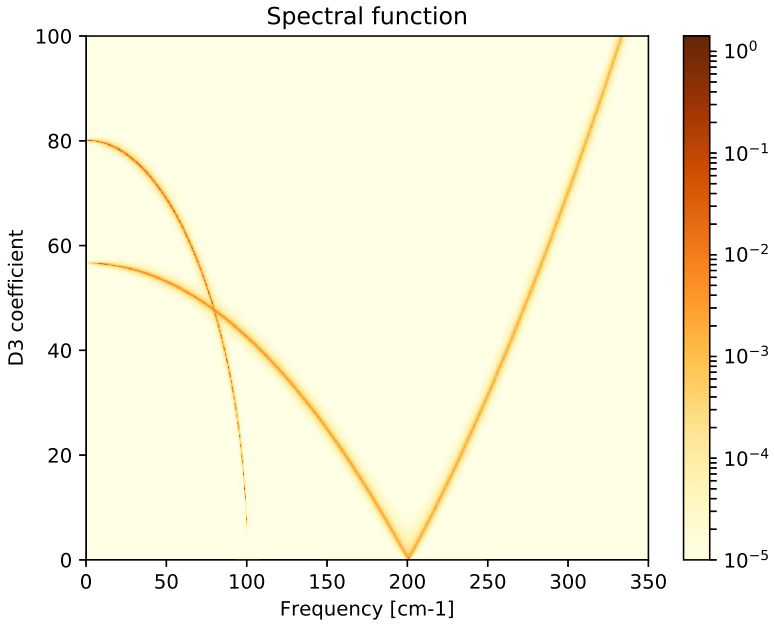

Figure 4.3. Spectral function of a system with the Fermi resonance as a function of the anharmonic coupling between the two modes.

create the mode of $200\,\mathrm{cm}^{-1}$. This second process requires the presence of thermally excited modes at $100\,\mathrm{cm}^{-1}$ and it is suppressed at low temperatures.

In this simple toy model, we neglected the dependence of the SCHA $\overset{(2)}{\boldsymbol{D}}$ matrix from the d coefficient (that is the tadpole diagram). However, this just shifts the poles and it is positive definite. It cannot alone trigger a phase-transition and the qualitative picture provided in this chapter remains valid.

4.3 IR and Raman probe

To derive the linear response to an external dynamical probe we need to linearize the TD-SCHA equations.

We study how a system in equilibrium reacts to small external time-dependent perturbations. These are forces that act on nuclei. This is trivially the case of an IR probe, where an external electromagnetic field is modulated with the same frequency of the phonons. The atoms with a dipole moment react to the time-dependent electric field. In this case, the IR probe interacts directly with the nuclear charge plus the electronic shell that surrounds it. The coupling between the phonon mode and the IR probe is described by the "effective charge" Z_{ab}.

In the BO approximation, the "effective charges" indicate how the atoms displace when an external electric field is applied. This is related to the second derivative of the electronic total energy E_{el}:

$$Z_{ab} = \frac{d^2 E_{el}}{d\mathcal{E}_a dR_b}, \tag{4.9}$$

where $\vec{\mathcal{E}}$ is the applied electric field.

The infrared intensity of a particular mode μ is:

$$I_\mu^{(IR)} = \left| \sum_{ab} \hat{\epsilon}_a Z_{ab} \frac{e_\mu^b}{\sqrt{m_b}} \right|^2 \tag{4.10}$$

where $\hat{\epsilon}_a$ is the polarization of the light used as a probe. Here I sketch the derivation, that is not rigorous but gives an insight into the phenomenon. The IR response can be modeled as the dipole-dipole correlation function:

$$I_{ir}(\omega) \sim \int_{-\infty}^{\infty} \langle \vec{M}(t)\vec{M}(0)\rangle \, e^{i\omega t}$$

$$\vec{M}(t) = \frac{dE_{el}}{d\vec{\mathcal{E}}}$$

We make the approximation that the dipole moment depends linearly on the atomic displacements.

$$M_b(t) = \sum_a \left.\frac{dE_{el}}{d\mathcal{E}_b dR_a}\right|_{R_a = R_a^{(0)}} [R_a(t) - R_a^{(0)}] = Z_{ba}[R_a(t) - R_a^{(0)}] \tag{4.11}$$

$$\langle M_a(t) M_b(0)\rangle = \sum_{cd} \langle \frac{Z_{ac}}{\sqrt{m_c}} \sqrt{m_c}[R_c(t) - R_c^{(0)}][R_d(0) - R_d^{(0)}]\sqrt{m_d}\frac{Z_{db}}{\sqrt{m_d}}\rangle \tag{4.12}$$

This is related to the phonon Green function:

$$G_{cd}(t) = \langle \sqrt{m_c}[R_c(t) - R_c^{(0)}][R_d(0) - R_d^{(0)}]\sqrt{m_d}\rangle$$

$$\langle M_a(\omega)M_b(0)\rangle = \sum_{cd} \frac{Z_{ac}Z_{bd}}{\sqrt{m_c m_d}} G_{cd}(\omega) = \sum_{cd} \frac{Z_{ac}Z_{bd}}{\sqrt{m_c m_d}} \sum_{\mu} \frac{e_\mu^c e_\mu^d}{(\omega + i0^+)^2 - \omega_\mu^2} \quad (4.13)$$

If we look at the coefficient on the intensity of the μ using a field polarized along $\hat{\epsilon}$:

$$I_\mu \sim \sum_{abcd} \hat{\epsilon}_a \hat{\epsilon}_b \frac{Z_{ac}Z_{bd}}{\sqrt{m_c m_d}} e_\mu^c e_\mu^d = \left| \sum_{ac} \hat{\epsilon}_a Z_{ac} \frac{e_\mu^c}{\sqrt{m_c}} \right|^2 \quad (4.14)$$

The Raman works similarly. The incoming photon with frequency ω_0 is scattered by the sample into a new photon of frequency $\omega_0 \pm \omega_{vib}$ where ω_{vib} is the energy of the phonon. The Raman, therefore, involves the interaction between two fields: the incoming light and the outcoming radiation with a different frequency. In this case, the system feels a force on the atoms with a frequency modulation given by the beatings between the two fields that are inside the sample. The polarizability of the system transforms the resulting electric field with amplitude modulation of frequency ω_{vib} into a force that pulls the atoms. The Raman intensity can be derived in the same way we did for the infrared, but this time it is related to the correlation function of the polarizability. The polarizability $\boldsymbol{\alpha}$ reacts to the two external electric fields:

$$V_{ext}(t) = \frac{1}{2}\mathcal{E}_a^{(in)}(t)\alpha_{ab}\mathcal{E}_b^{(out)}(t)$$

$$\alpha_{ab} = \frac{d^2 E_{el}}{d\mathcal{E}_a d\mathcal{E}_b}$$

We assume $\boldsymbol{\alpha}$ linearly dependent on the atomic displacements:

$$\alpha_{ab}(t) = \alpha_{ab}^{(0)} + \sum_c \left.\frac{d\alpha_{ab}}{dR_c}\right|_{\vec{R}=\vec{R}^{(0)}} [R_c(t) - R_c^{(0)}] \quad (4.15)$$

The coupling between the two fields and the sample is described by the Raman tensor:

$$A_{abc} = \frac{dE_{el}}{d\mathcal{E}_a d\mathcal{E}_b dR_c} \quad (4.16)$$

The Raman intensity of a particular mode in the harmonic approximation is:

$$I_\mu^{(R)} = \left| \sum_{abc} \hat{\epsilon}_a^{(in)} \hat{\epsilon}_b^{(out)} A_{abc} \frac{e_\mu^c}{\sqrt{m_c}} \right|^2 . \quad (4.17)$$

Eq. (4.17) can be derived in the same way as the IR.

Note that in experiments usually only one laser field is directed toward the sample and the output electric field is automatically generated and scattered. This phenomenon is the spontaneous Raman. Like spontaneous emission, it is a pure quantum phenomenon. Here the incoming radiation beats with the vacuum state of the outcoming radiation. When this interaction is in resonance with a phonon mode, energy is transferred between the incoming field and the vacuum state of the outcoming field.

4.4 The linear response of TD-SCHA

Linearizing Eq. (3.9) is straightforward. We study how a small perturbation from the static solution evolves in time.

We indicate with $\langle\cdot\rangle_0$ the averages on the equilibrium ensemble, while with $\langle\cdot\rangle_1$ the average on the perturbed ensemble. In the same way, we enumerate with apex $^{(1)}$ the perturbed quantities and $^{(0)}$ the static quantities. When we drop the notation, we refer to static quantities.

We can recognize that $\boldsymbol{\mathcal{C}} = 0$ in equilibrium, therefore the quadratic term in $\boldsymbol{\mathcal{C}}$ can be neglected. In equilibrium, the SCHA gradient must be zero

$$\frac{\partial \mathcal{F}(\vec{\mathcal{R}}, \boldsymbol{\Phi}, \{\vec{a}_i\})}{\partial \Phi_{ab}} = -\sum_{cdq} \Lambda^{abcd} \Upsilon_{cq} \left\langle u_q \left[\vec{f}_d - \vec{f}_{\mathcal{H}_d} \right] \right\rangle_0 = 0 \tag{4.18}$$

Both $-\boldsymbol{\Lambda}$ and $\boldsymbol{\Upsilon}$ are positive defined:

$$\langle u_a \Delta f_b \rangle_0 = 0 \tag{4.19}$$

Keeping only linear quantities in the perturbed variables, we derive the system:

$$\begin{cases} m_a \ddot{\mathcal{R}}_a^{(1)} = \langle f_a^{(1)} \rangle_0 + \langle f_a^{(0)} \rangle_1 \\ \dot{\mathcal{C}}_{hk}^{(1)} = \dfrac{1}{2\hbar} \displaystyle\sum_a \Upsilon_{ha} \left[\langle u_a f_k^{(1)} \rangle_0 + \langle u_a \Delta f_k \rangle_1 \right] + \dfrac{1}{2\hbar} \Phi_{hk}^{(1)} \\ \displaystyle\sum_{cd} \Lambda^{cdab} \dot{\Phi}_{cd}^{(1)} = \sum_c \frac{2\hbar}{m_a} \Upsilon_{bc}^{-1} \mathcal{C}_{ca}^{(1)} \end{cases} \tag{4.20}$$

External perturbations are:

$$-\frac{\partial V^{(1)}}{\partial \mathcal{R}_a} = \langle f_a^{(1)} \rangle_0 \qquad \frac{\partial^2 V^{(1)}}{\partial \mathcal{R}_h \partial \mathcal{R}_k} = \sum_a \Upsilon_{ha} \langle u_a f_k^{(1)} \rangle \tag{4.21}$$

where $f_k^{(1)}$ is the force of the external perturbation. For infrared spectroscopy, the perturbing potential is:

$$V_{IR}^{(1)}(\vec{R}) = -\vec{M}(\vec{R}) \cdot \vec{\mathcal{E}} \qquad \frac{dM_a}{dR_b} = Z_{ab}(\vec{R})$$

$$-\frac{\partial V^{(1)}}{\partial \mathcal{R}_a} = \langle f_a^{(1)} \rangle = \sum_h \mathcal{E}_h \langle Z_{ha} \rangle_0 \tag{4.22}$$

$$\frac{\partial^2 V^{(1)}}{\partial \mathcal{R}_a \partial \mathcal{R}_b} = \sum_h \Upsilon_{ah} \langle u_h f_b^{(1)} \rangle = \sum_{hk} \mathcal{E}_k \Upsilon_{ha} \langle u_h Z_{kb} \rangle_0 \tag{4.23}$$

while the Raman external potential is:

$$\vec{V}_{Raman}^{(1)}(\vec{R}) = \frac{1}{2} \sum_{ab} \mathcal{E}_a^{(in)} \alpha_{ab}(\vec{R}) \mathcal{E}_b^{(out)} \qquad \frac{d\alpha_{ab}}{dR_c} = A_{abc}(\vec{R})$$

$$\langle f_k^{(1)} \rangle_0 = \frac{1}{2} \sum_{ab} \mathcal{E}_a^{(in)} \mathcal{E}_b^{(out)} \langle A_{abk} \rangle_0 \tag{4.24}$$

$$\frac{\partial^2 V^{(1)}}{\partial \mathcal{R}_a \partial \mathcal{R}_b} = \sum_h \Upsilon_{ah} \langle u_h f_b^{(1)} \rangle = \frac{1}{2} \sum_{hkl} \mathcal{E}_k^{(int)} \mathcal{E}_l^{(out)} \Upsilon_{ha} \langle u_h A_{klb} \rangle_0 \tag{4.25}$$

If the effective charges and the Raman tensor are independent on the configuration (harmonic approximation), we can bring them outside the averages and get:

$$\frac{\partial^2 V^{(1)}}{\partial \mathcal{R}_a \partial \mathcal{R}_b} = 0.$$

Then the equations of motion can be rewritten in the following way:

$$\begin{cases} \ddot{\mathcal{R}}_a^{(1)} = \dfrac{1}{m_a} \left[\langle f_a^{(1)} \rangle - \displaystyle\sum_b \Phi_{ab} \mathcal{R}_b^{(1)} - \sum_{pqd} \overset{(3)}{\Phi}_{dea} \Lambda^{pqde} \Phi_{pq}^{(1)} \right] \\ \displaystyle\sum_{cd} \Lambda^{cdab} \ddot{\Phi}_{cd}^{(1)} = - \sum_c \frac{\Upsilon_{bc}^{-1}}{m_a} \Big[- \Phi_{ac}^{(1)} + \sum_h \overset{(3)}{\Phi}_{cah} \mathcal{R}_h^{(1)} + \sum_{rstd} \overset{(4)}{\Phi}_{cars} \Lambda^{tdrs} \Phi_{td}^{(1)} \Big] \end{cases} \tag{4.26}$$

The passages that lead to these equations are reported in App. D.6. In analogy with ref.[24], we defined:

$$\overset{(3)}{\Phi}_{abc} = \Big\langle \frac{\partial^3 V}{\partial R_a \partial R_b \partial R_c} \Big\rangle_0 ,$$

$$\overset{(4)}{\Phi}_{abcd} = \Big\langle \frac{\partial^4 V}{\partial R_a \partial R_b \partial R_c \partial R_d} \Big\rangle_0 .$$

Since our perturbation is a Dirac delta in Fourier space and the time-derivatives become algebraic products, it is convenient to recast this system in the frequency domain:

$$\begin{cases} -\omega^2 \tilde{\mathcal{R}}_a(\omega) = \tilde{f}_a^{(1)}(\omega) - \dfrac{1}{m_a} \displaystyle\sum_b \Phi_{ab} \tilde{\mathcal{R}}_b(\omega) - \frac{1}{m_a} \sum_{pqd} \overset{(3)}{\Phi}_{dea} \Lambda^{pqde} \tilde{\Phi}_{pq}(\omega) \\ \omega^2 \displaystyle\sum_{cd} \Lambda^{cdab} \tilde{\Phi}_{cd}(\omega) = \sum_c \frac{\Upsilon_{bc}^{-1}}{m_a} \Big[- \tilde{\Phi}_{ac} + \sum_h \overset{(3)}{\Phi}_{ach} \tilde{\mathcal{R}}_h + \sum_{rstd} \overset{(4)}{\Phi}_{cars} \Lambda^{tdrs} \tilde{\Phi}_{td} \Big] \end{cases} , \tag{4.27}$$

where we indicate with a ˜ the Fourier-transformed quantities that are ω dependent. To simplify a bit the notation, we drop the (ω) explicit dependence of these quantities.

Defining the 4-rank tensor:

$$A^{cdab} = - \frac{\delta_{ad} \Upsilon_{bc}^{-1}}{\sqrt{m_a m_d}}, \tag{4.28}$$

we can rewrite the second equation from (4.27) as:

$$\sum_{cd} \left(A^{cdab} - \omega^2 \Lambda^{cdab} \right) \tilde{\Phi}_{cd} = \sum_{cd} A^{cdab} \left[\sum_h \overset{(3)}{\Phi}_{cdh} \tilde{\mathcal{R}}_h + \sum_{rstd} \overset{(4)}{\Phi}_{cdrs} \Lambda^{tdrs} \tilde{\Phi}_{td} \right] \tag{4.29}$$

The final system that solves the linear response theory of the TD-SCHA is:

$$\begin{cases} -\omega^2 \tilde{\mathcal{R}}_a(\omega) + \dfrac{1}{m_a} \sum_b \Phi_{ab} \tilde{\mathcal{R}}_b(\omega) + \dfrac{1}{m_a} \sum_{pqd} \overset{(3)}{\Phi}_{dea} \Lambda^{pqde} \tilde{\Phi}_{pq}(\omega) = f_a^{(1)}(\omega) \\ \\ \sum_{cd} \left(A^{cdab} - \omega^2 \Lambda^{cdab} \right) \tilde{\Phi}_{cd} - \sum_{cd} A^{cdab} \left[\sum_h \overset{(3)}{\Phi}_{cdh} \tilde{\mathcal{R}}_h + \sum_{rstd} \overset{(4)}{\Phi}_{cdrs} \Lambda^{tdrs} \tilde{\Phi}_{td} \right] = 0 \end{cases} \tag{4.30}$$

In App. D.7, I prove that the solution of this system is equivalent to the $T = 0\,\mathrm{K}$ dynamical ansatz of the SCHA proposed in [24]. This ansatz was previously not demonstrated and based on an analytical continuation at finite ω of the static response function of SCHA. However, our new formulation of the dynamical problem provides also a much more efficient way of computing the dynamical results that we will explore in the next section.

4.5 The Lanczos algorithm for the dynamical Green functions

Even if we proved that Eq. (4.30) is equivalent to the ansatz reported in ref. [24], the formulation of the dynamical solution as a linear system where no operator is function of ω allows us to write an algorithm able to compute the exact response for any frequency with just one inversion of the system.

We can write the system in Eq. (4.30) in matrix notation as:

$$\left(\boldsymbol{\mathcal{L}} - \omega^2 \boldsymbol{I} \right) \vec{v} = \vec{p}, \tag{4.31}$$

where $\vec{p}$ is the perturbation and $\vec{v}$ is the responce of the system.

$$\vec{v} = \begin{pmatrix} \vec{\tilde{\mathcal{R}}} \\ \vec{\tilde{\boldsymbol{\Phi}}} \end{pmatrix} \qquad \vec{p} = \begin{pmatrix} \vec{f}^{(1)} \\ 0 \end{pmatrix} \tag{4.32}$$

. The $\boldsymbol{\mathcal{L}}$ matrix is:

$$\boldsymbol{\mathcal{L}} = \begin{pmatrix} \frac{1}{m} \boldsymbol{\Phi} & \frac{1}{m} \overset{(3)}{\boldsymbol{\Phi}} \boldsymbol{\Lambda} \\ -\boldsymbol{\Lambda}^{-1} \boldsymbol{A} \overset{(3)}{\boldsymbol{\Phi}} & \boldsymbol{\Lambda}^{-1} \boldsymbol{A} (\boldsymbol{I} - \overset{(4)}{\boldsymbol{\Phi}} \boldsymbol{\Lambda}) \end{pmatrix} \tag{4.33}$$

The solution is:

$$\vec{v} = \left(\boldsymbol{\mathcal{L}} - \omega^2 \boldsymbol{I} \right)^{-1} \vec{p}. \tag{4.34}$$

We are interested in the response of position displacement with respect to perturbations.

$$\chi_{vp}(\omega) = \langle v | \left(\boldsymbol{\mathcal{L}} - \omega^2 \boldsymbol{I} \right)^{-1} | p \rangle \tag{4.35}$$

In both Raman, IR or the spectral function, we always have to compute only the diagonal elements of the response function:

$$\chi_{vv}(\omega) = \langle v | \left(\boldsymbol{\mathcal{L}} - \omega^2 \boldsymbol{I} \right)^{-1} | v \rangle \tag{4.36}$$

Luckily, the right-hand side of Eq. (4.36) is computable very efficiently using the well known Lanczos continued fraction algorithm if $\boldsymbol{\mathcal{L}}$ is symmetric. The explicit calculation of $\boldsymbol{\mathcal{L}}$ and the change of variable that allows us to write it as a symmetric matrix are reported in App. D.8.

4.5.1 The Lanczos continued fraction

Now we describe the Lanczos procedure to calculate the Green's function. First of all, we can define the Krilov subspace of order N as the vector space spanned by the perturbation plus all the vectors generated by the application of the $\boldsymbol{\mathcal{L}}$ matrix $N-1$ times:

$$\mathcal{K}_{\boldsymbol{\mathcal{L}}}^{N} = \mathrm{Span}\left\{ |v\rangle, \boldsymbol{\mathcal{L}}\,|v\rangle, (\boldsymbol{\mathcal{L}})^2\,|v\rangle, \cdots, (\boldsymbol{\mathcal{L}})^{N-1}\,|v\rangle \right\}. \tag{4.37}$$

A good basis of this space is the orthogonal basis generated by the Gram-Schmidt procedure starting from the first vector:

$$|e_1\rangle = \frac{|v\rangle}{\sqrt{\langle v|v\rangle}}, \tag{4.38}$$

$$|e_2\rangle = \frac{\boldsymbol{\mathcal{L}}\,|e_1\rangle - |e_1\rangle\,\langle e_1|\boldsymbol{\mathcal{L}}|e_1\rangle}{\sqrt{\langle e_1|\boldsymbol{\mathcal{L}}^2|e_1\rangle - \langle e_1|\boldsymbol{\mathcal{L}}|e_1\rangle^2}}, \tag{4.39}$$

$$|e_3\rangle = \frac{\boldsymbol{\mathcal{L}}\,|e_2\rangle - |e_2\rangle\,\langle e_2|\boldsymbol{\mathcal{L}}|e_2\rangle - |e\rangle_1\,\langle e_1|\boldsymbol{\mathcal{L}}|e_2\rangle}{\sqrt{\langle e_2|\boldsymbol{\mathcal{L}}^2|e_2\rangle - \langle e_2|\boldsymbol{\mathcal{L}}|e_2\rangle^2 - \langle e_1|\boldsymbol{\mathcal{L}}|e_2\rangle^2}}, \tag{4.40}$$

and so on. In this basis the $\boldsymbol{\mathcal{L}}$ matrix is tridiagonal, i.e. all the elements farther from the diagonal by more than one position are zero. This is easy to prove, as the vector $\boldsymbol{\mathcal{L}}\,|e_k\rangle$ is, by construction, inside the subspace of the first $k+1$ vectors of the basis and it is, therefore, orthogonal to all the vectors $|e_{k+2}\rangle \cdots |e_N\rangle$:

$$\langle e_a|\boldsymbol{\mathcal{L}}|e_b\rangle = 0 \qquad \text{if } \; a > b+1 \tag{4.41}$$

But since the $\boldsymbol{\mathcal{L}}$ matrix is symmetric, the same must be true if we change the indices:

$$\langle e_a|\boldsymbol{\mathcal{L}}|e_b\rangle = \langle e_b|\boldsymbol{\mathcal{L}}|e_a\rangle = 0 \qquad \text{if } \; a > b+1 \tag{4.42}$$

Therefore we have

$$\langle e_a|\boldsymbol{\mathcal{L}}|e_b\rangle = 0 \qquad \text{if } \; b-1 > a > b+1 \tag{4.43}$$

This also allows us to write the general element of the basis in a much easier way:

$$|e_{a+1}\rangle = \frac{\boldsymbol{\mathcal{L}}\,|e_a\rangle - |e_a\rangle\,\langle e_a|\boldsymbol{\mathcal{L}}|e_a\rangle - |e_{a-1}\rangle\,\langle e_{a-1}|\boldsymbol{\mathcal{L}}|e_a\rangle}{\sqrt{\langle e_a|\boldsymbol{\mathcal{L}}^2|e_a\rangle - \langle e_a|\boldsymbol{\mathcal{L}}|e_a\rangle^2 - \langle e_{a-1}|\boldsymbol{\mathcal{L}}|e_a\rangle^2}} \tag{4.44}$$

So the full basis can be written iteratively. If we define the succession:

$$a_n = \langle e_n|\boldsymbol{\mathcal{L}}|e_n\rangle \qquad b_n = \langle e_{n+1}|\boldsymbol{\mathcal{L}}|e_n\rangle \tag{4.45}$$

$$\boldsymbol{\mathcal{L}} = \begin{pmatrix} a_1 & b_1 & 0 & 0 & \cdots & 0 \\ b_1 & a_2 & b_2 & 0 & \cdots & 0 \\ 0 & b_2 & a_3 & b_3 & \cdots & 0 \\ \vdots & \vdots & \ddots & \ddots & \ddots & \vdots \end{pmatrix} \tag{4.46}$$

we can rewrithe the matrix in symbolic notation, leaving explicitely the first row and column and indicating the remaining block as $(\boldsymbol{L} - \omega^2 I)_{2\cdots N, 2\cdots N}$

$$\left(\boldsymbol{\mathcal{L}} - \omega^2 I\right) = \begin{pmatrix} a_1 - \omega^2 & \vec{b}_1 \\ \vec{b}_1 & \left(\boldsymbol{\mathcal{L}} - \omega^2 I\right)_{2\cdots N, 2\cdots N} \end{pmatrix} \tag{4.47}$$

$$\vec{b}_1 = \begin{pmatrix} b_1 \\ 0 \\ 0 \\ \vdots \end{pmatrix} \qquad \left(\boldsymbol{\mathcal{L}} - \omega^2 I\right)_{2\cdots N, 2\cdots N} = \begin{pmatrix} a_2 - \omega^2 & b_2 & 0 & \cdots & 0 \\ b_2 & a_3 & b_3 - \omega^2 & \cdots & 0 \\ \vdots & \ddots & \ddots & \ddots & \vdots \end{pmatrix}$$

Since the perturbation vector is the first element of our basis, must compute the first element of the inverse of this matrix:

$$\langle v| \left(\boldsymbol{\mathcal{L}} - \omega^2 I\right)^{-1} |v\rangle = \left[\begin{pmatrix} a_1 - \omega^2 & \vec{b}_1 \\ \vec{b}_1 & \left(\boldsymbol{\mathcal{L}} - \omega^2 I\right)_{2\cdots N, 2\cdots N} \end{pmatrix}^{-1} \right]_{11} \tag{4.48}$$

Where $|v\rangle$ is the vector we must use to initialize the Lanczos algorithm, so that the $\langle v| \cdot |v\rangle$ element is the 11-th one. We can perform this inversion iteratively with the Kramer technique:

$$\langle v| \left(\boldsymbol{\mathcal{L}} - \omega^2 I\right)^{-1} |v\rangle = \frac{\det \left(\boldsymbol{\mathcal{L}} - \omega^2 I\right)_{2\cdots N, 2\cdots N}}{(a_1 - \omega^2) \det \left(\boldsymbol{\mathcal{L}} - \omega^2 I\right)_{2\cdots N, 2\cdots N} - b_1^2 \det \left(\boldsymbol{\mathcal{L}} - \omega^2 I\right)_{3\cdots N, 3\cdots N}} \tag{4.49}$$

$$\langle v| \left(\boldsymbol{\mathcal{L}} - \omega^2 I\right)^{-1} |v\rangle = \frac{1}{(a_1 - \omega^2) - \frac{b_1^2 \det(\boldsymbol{\mathcal{L}} - \omega^2 I)_{3\cdots N, 3\cdots N}}{\det(\boldsymbol{\mathcal{L}} - \omega^2 I)_{2\cdots N, 2\cdots N}}} \tag{4.50}$$

Since the $\boldsymbol{\mathcal{L}}$ matrix is tridiagonal, we can also rewrite the $1\cdots N \times 1\cdots N$ block in the same way, and obtain:

$$\frac{\det \left(\boldsymbol{\mathcal{L}} - \omega^2 I\right)_{3\cdots N, 3\cdots N}}{\det \left(\boldsymbol{\mathcal{L}} - \omega^2 I\right)_{2\cdots N, 2\cdots N}} = \frac{1}{a_2 - \omega^2 - \frac{b_2^2 \det(\boldsymbol{\mathcal{L}} - \omega^2 I)_{4\cdots N, 4\cdots N}}{\det(\boldsymbol{\mathcal{L}} - \omega^2 I)_{3\cdots N, 3\cdots N}}} \tag{4.51}$$

Therefore we have the iterative procedure:

$$\langle v| \left(\boldsymbol{\mathcal{L}} - \omega^2 I\right)^{-1} |v\rangle = \cfrac{1}{a_1 - \omega^2 - \cfrac{b_1^2}{a_2 - \omega^2 - \cfrac{b_2^2}{a_3 - \omega^2 - \cfrac{b_3^2}{\ddots}}}} \tag{4.52}$$

Each iteration of the Lanczos procedure introduces a new pole in the Green function. We can use a terminator to reach the limit $N \to \infty$. We can imagine that the last

coefficients do not depend on N any more:

$$\cfrac{1}{a_L - \omega^2 - \cfrac{b_L}{a_L - \omega^2 - \cfrac{b_L}{a_L - \omega^2 - \ddots}}} = f(\omega) \tag{4.53}$$

This continued fraction is the solution of the following equation:

$$\frac{1}{f(\omega)} = a_L - \omega^2 - b_L f(\omega) \tag{4.54}$$

From which we have the following two solutions:

$$f(\omega) = \frac{a_L - \omega^2 \pm \sqrt{(a_L - \omega^2)^2 - 4b_L^2}}{2b_L^2} \tag{4.55}$$

Here there is an ambiguity in the sign of the square root, however if one looks carefully, the square root is the source of the imaginary part in the green function. The two solutions correspond to the backward and forward green functions. To be consistent with our convention, we can chose $\Im G(\omega) < 0$ for $\omega \to a_L$ in correspondence of the $L - th$ pole.

$$f(\omega) = \frac{a_L - \omega^2 - \sqrt{(a_L - \omega^2)^2 - 4b_L^2}}{2b_L^2} \tag{4.56}$$

In this way, we are able to add an imaginary part of the Green function even without explicitly including a smearing parameter.

The direct comparison of the Lanczos with the static theory of SCHA to study response to static perturbation as derived by ref. [24] is reported in App. D.9.

4.6 Convergence of the algorithm

To show the power of the algorithm, I calculate the example of the Raman response function in the C2/c-24 phase of hydrogen, at 250 GPa.

The detailed description of the properties of this phase is demanded in Chapter 5. This section is just an anticipation of the results that will be discussed in detail there.

In Figure 4.4 and 4.5 the Raman signals are reported as a function of the number of Lanczos steps, to show the convergence of the algorithm. Figure 4.5 has the terminator, while Figure 4.4 not.

The use of the terminator (Eq. 4.56) is fundamental to achieve a good convergence with few steps of the algorithm. Without a terminator, the Lanczos algorithm adds a new pole for each iteration. Many iterations are needed to have poles with distances lower than the smearing to obtain a smooth curve. This is particularly true for systems with a huge anharmonicity and strong deviations from the Lorentzian shape, as in Figure 4.4 and Figure 4.5.

Moreover, from Figure 4.5 is also clear as the first part of the spectrum to converge is the high-frequency, while the low frequencies are the hardest to converge

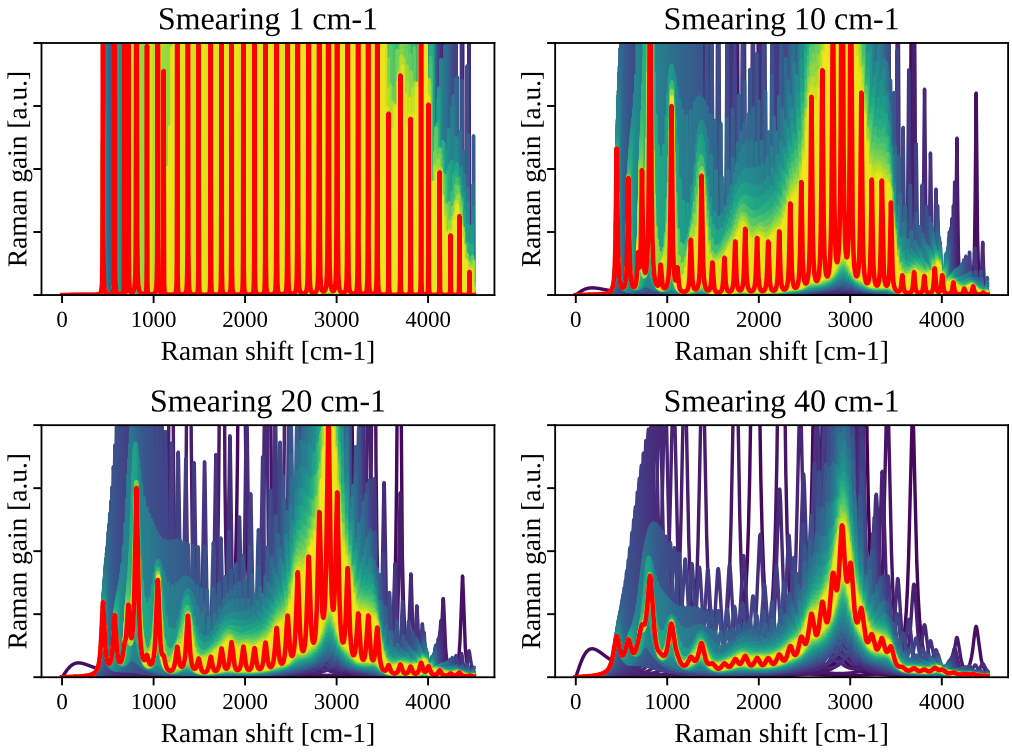

Figure 4.4. Raman dynamical green function using the Lanczos algorithm. Colors scales from dark purple to yellow as we increase the number of Lanczos iterations. The last (100th) iteration is shown in bold red. This simulation has been carried without a terminator. Very big smearing is required to achieve a good convergence of the spectrum. Data obtained with 10000 configurations.

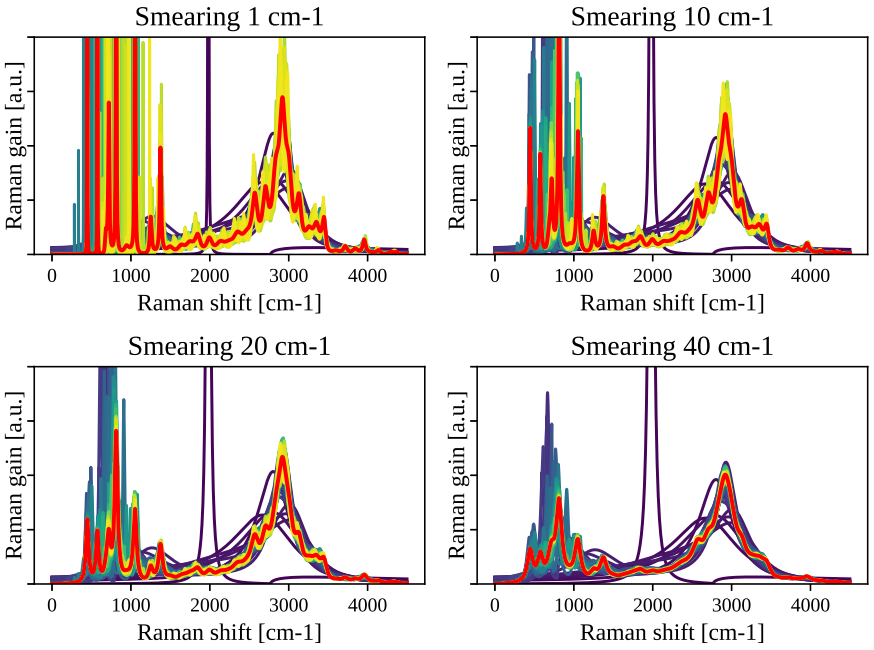

Figure 4.5. Raman dynamical green function using the Lanczos algorithm. Colors scales from dark purple to yellow as we increase the number of Lanczos iterations. The last (100th) iteration is shown in bold red. Here, I used the terminator to extrapolate the $N \to \infty$, averaging over the last 5 values of the coefficients a_n and b_n. Thanks to the terminator, a much smaller number of steps are required to achieve the convergence even with very small smearing. Data obtained with 10000 configurations.

(the shaded area converges faster in the high-frequency region). This is a drawback of the Lanczos algorithm, as it is a power-method (based on the application of the $\boldsymbol{\mathcal{L}}$ matrix several times on the perturbation vector). In this way, the highest eigenvalues of $\boldsymbol{\mathcal{L}}$ will be the first one to converge in the Krilov subspace, followed by all the others.

Indeed, it is possible to overturn the $\boldsymbol{\mathcal{L}}$ matrix to do the opposite. In particular, we can perform the Lanczos algorithm using the following matrix:

$$\boldsymbol{\mathcal{L}}' = \lambda_{max} I - \boldsymbol{\mathcal{L}}$$

where λ_{max} is an estimation of the maximum (in modulus) of the eigenvalues of $\boldsymbol{\mathcal{L}}$. This is, for an harmonic case, $2\omega_{max}$. Then the $\boldsymbol{\mathcal{L}}$ matrix in the new Krilov subspace is again tridiagonal, where the coefficients are:

$$a_i = \lambda_{max} - a_i' \qquad b_i = -b_i'$$

The highest eigenvalues of the $\boldsymbol{\mathcal{L}}'$ are the lowest eigenvalues of the $\boldsymbol{\mathcal{L}}$.

To further show the potentiality of the new algorithm, I show how it can be deployed to study the structural stability.

A structure is stable or meta-stable if it is in a local minimum of the free energy landscape. In other words, the Hessian of the free energy of the atomic coordinates must be positive definite.

This is a static property, and can be computed inside the standard SCHA framework, as done in ref. [24].

$$\frac{d\mathcal{F}(\vec{\mathcal{R}}, \boldsymbol{\Phi}, \{\vec{a}_i\})}{d\mathcal{R}_a d\mathcal{R}_b} = \overset{(2)}{\Phi}_{ab} + \sum_{hklmpq} \overset{(3)}{\Phi}_{ahk} \left[1 - \boldsymbol{\Lambda} \overset{(4)}{\boldsymbol{\Phi}}\right]^{-1}_{hklm} \Lambda_{lmpq} \overset{(3)}{\Phi}_{pqb} \tag{4.57}$$

This requires to store and compute the inverse of the 4-rank matrix $1 - \boldsymbol{\Lambda} \overset{(4)}{\boldsymbol{\Phi}}$, that has $(3N)^4$ elements, where N is the number of atoms in the supercell.

In most applications up to now, it has been considered $\overset{(4)}{\boldsymbol{\Phi}} = 0$. This allows one to avoid storing in memory such a big matrix and performing its inversion. However, this is impossible for high-pressure hydrogen, where the $\overset{(4)}{\boldsymbol{\Phi}}$ has a major impact on Eq. 4.57. It is fundamental to determine whether the structure is stable or not.

For example, neglecting $\overset{(4)}{\boldsymbol{\Phi}}$ in Eq. (4.57) leads the phase III of hydrogen to be unstable at all pressures.

To have an idea of how difficult is the calculation in a real case: for the 2x2x1 super-cell of the C2/c structure with 24 atoms in the unit cell (96 in total), one would require to invert a matrix of 82944x82944 elements. Only to store such a matrix in the memory with double precision requires more than 50 Gb of RAM. Its inversion is a very expensive computation, as it is, in principle, a dense matrix.

This calculation was impossible before I introduced the Lanczos algorithm. In fact, the Hessian matrix is equal to the inverse of the static green function:

$$\frac{d\mathcal{F}(\vec{\mathcal{R}}, \boldsymbol{\Phi}, \{\vec{a}_i\})}{d\mathcal{R}_a d\mathcal{R}_b} = \sqrt{m_a m_b} G^{-1}_{ab}(\omega = 0)$$

Therefore, in practice, since Lanczos is very good in computing the diagonal element of the Green function, we can directly take the polarization vector that leads to instability and compute the response function as:

$$\chi^{-1}_{\mu\mu}(\omega = 0) = \tilde{\omega}^2_\mu \tag{4.58}$$

Here, $\tilde{\omega}^2_\mu$ is the eigenvalue of the hessian matrix associated with the $\vec{e}_\mu$ eigenvector.

The lowest static frequency $\tilde{\omega}_\mu$ of the free energy hessian, as a function of the number of the Lanczos iterations, is reported in Figure 4.6. To further spot on the importance of the fourth-order $\overset{(4)}{\mathbf{\Phi}}$ I performed two computations, one neglecting it and one not.

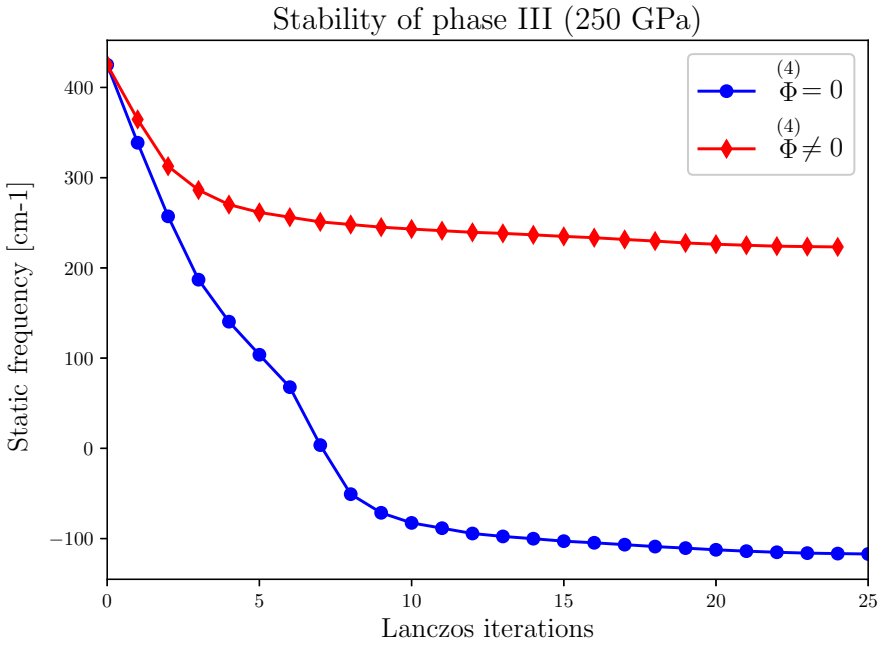

Figure 4.6. The lowest frequency of the static hessian of phase III of Hydrogen. I report the two result neglecting or considering $\overset{(4)}{\mathbf{\Phi}}$. The inclusion of the fourth order force constant makes this phase stable at 250 GPa. This simulation is computed with 40000 configurations to converge the $\overset{(4)}{\mathbf{\Phi}}$

This plot shows clearly how the high order $\overset{(4)}{\mathbf{\Phi}}$ cannot be neglected when studying the stability of the structure. In this system, it is the dominant term that stabilizes the phase. This term has, up today, always been neglected in all anharmonic calculation, as it was believed to be zero. Moreover, before the Lanczos algorithm, dynamical computations including the fourth-order were never carried out. Moreover, the inversion at Eq. 4.57 cannot be performed using a geometric series as the eigenvalue of $\mathbf{\Lambda}\ \overset{(4)}{\mathbf{\Phi}}$ are higher than 1, and the series diverges. This spots on the power of the Lanczos algorithm, that can correctly handle even very extreme cases like this one, where anharmonicity cannot be treated at any level with perturbation theory.

4.7 Conclusions

In this chapter, I derived the dynamical linear response theory from TD-SCHA. I proved, at $T = 0\,\mathrm{K}$, the dynamical ansatz formulated by Bianco et. al.[24] based on the analytical continuation of the static response at finite frequency.

I formulated a new algorithm to compute the static and dynamic response based on the Lanczos continued fraction. This algorithm outperforms the previous one, being able to compute the whole dynamical response function with just one calculation, and provides a natural way to interpolate the result in the thermodynamic limit, introducing a finite life-time even without (or at least with very small) smearings. Moreover, the algorithm proved to be very efficient also for static calculations, where it allows computing the response including four phonons scattering. This element is essential to describe complex (dirty) crystals like high-pressure hydrogen phases.

Now, we can compute in a very efficient way all the dynamical phonon response functions in strongly anharmonic systems. This includes Raman and IR spectroscopy. The perturbation theory on TD-SCHA, in contrast with the dynamical ansatz, allows one to formulate responses to more complex perturbations, accounting also for the case in which effective charges or the Raman tensor depend on the atomic displacements.

In the next chapter, I will show all the potentiality of the newly introduced technique to simulate phase III of hydrogen.

Chapter 5

The anharmonicity and quantum nuclear effects on hydrogen phase III

5.1 Introduction

In this chapter, I apply the theoretical framework developed in Chapter 1,2 and 4 to study phase III of hydrogen.

Phase III is found experimentally to be stable at low temperatures (under 200 K) and high pressure (above 150 GPa).

Here, I discuss how quantum effects completely reshape the structure: atomic positions, lattice parameters, and collective excitations, like phonon spectrum and electronic bands structure.

I compute the Raman and IR spectra within the full quantum/anharmonic approach developed in Chapter 4, strongly improving the agreement with experiments. I deploy the SSCHA to simulate the optical transmittance and reflectivity of the sample including the electron-phonon beyond perturbation theory. In this way, I can conciliate the apparent contradiction in recent experimental results[4, 5].

5.2 How do we solve the electronic problem?

In principle, the SCHA can be coupled with any energy-force engine. However, thanks to the very efficient implementations available, high accuracy and affordable computational cost, density functional theory (DFT) is the state of art tool to solve the electronic problem.

5.2.1 Density functional theory

DFT is a tool to solve the electronic problem in the BO approximation (i.e. dealing with nuclei as a fixed external electrostatic potential). In DFT, the interacting many-body electronic problem is mapped into a non interacting one, that shares the

same density $\rho(\vec{r})$ with the original.

$$\rho(\vec{r}) = \langle\psi| \sum_{i=1}^{N_{el}} \delta(\vec{r} - \vec{r}_i)|\psi|\,,$$

where $|\psi\rangle$ is the many-body electron wave-function. This mapping is universal: it does not depend on the particular external potential, i.e. does not depend on the nuclear position or species[45, 46]. However, unfortunately, this mapping is unknown. It is encoded into the so called "exchange-correlation" functional $V_{xc}[\rho]$. The non interacting Hamiltonian can be written as:

$$H_{KS}[\rho] = -\int d^3r \frac{e^2\rho(\vec{r})}{|\vec{r} - \vec{r}_1|} |r_1\rangle \langle r_1| + \frac{P^2}{2m_e} + V_{xc}[\rho](\vec{r}_1) |r_1\rangle \langle r_1| + V_{ext}(\vec{r}_1) |r_1\rangle \langle r_1| \tag{5.1}$$

Here, ρ is the self-consistent electron density, found by solving H_{KS}, V_{ext} is the external potential.

In past years, many efforts were made in modeling an approximate form of $V_{xc}[\rho]$, based on exact calculations performed with Quantum Monte Carlo[47] or Coupled Clusters[48] on prototypical systems. One of the most successful classes of functionals is the generalized gradient approximation (GGA), where the V_{xc} is assumed to be a function only of the local density and its gradient. The exchange correlation energy functional is:

$$E_{xc}[\rho] = \int dr \rho(\vec{r}) f[\rho(\vec{r}), \vec{\nabla}\rho(\vec{r})]$$

$$V_{xc}[\rho](\vec{r}) = f[\rho(\vec{r}), \vec{\nabla}\rho(\vec{r})] + \rho(\vec{r})\frac{\partial f}{\partial \rho} - \vec{\nabla} \cdot \left[\rho(\vec{r})\frac{\partial f}{\partial(\vec{\nabla}\rho)}\right]$$

The GGA exchange-correlation functional is defined with $f[\rho, \vec{\nabla}\rho]$. Some of the most successful GGA functionals are PBE[49] or BLYP[50]. Indeed, more complex, accurate, and time-consuming approximations of the exchange-correlation were also carried out, as hybrid functional, that includes Hartree-Fock exchange explicitly, or meta-GGA. It is even possible to explicitly account for the van der Waals interactions.

5.2.2 Is DFT good for studying high-pressure Hydrogen?

Many works focus DFT accuracy in simulation high-pressure phases of hydrogen.

Hydrogen is the most simple atom in the universe. Each nucleus carries only one electron. This means that it is a prototypical system in which DFT can be tested against more accurate (and much more expensive) methods.

All the correlation effects in hydrogen are encoded in the covalent bonds between two atoms, the H_2 molecule, and the long-range van der Waals forces.

However, most common functionals (like BLYP) are trained to solve the isolated molecule, and long-range van der Waals forces can be included in a DFT calculation. Therefore, DFT is a perfect tool for this task, in principle.

However, recent studies underlined limitations of DFT calculations compared with more accurate methods[51, 52, 53, 54].

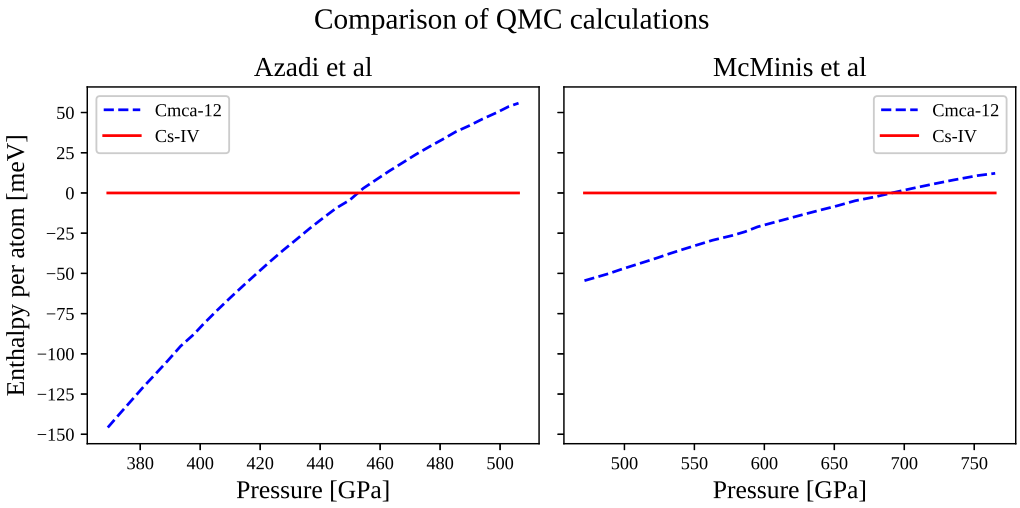

Figure 5.1. Two different QMC static enthalpy calculations, performed by indipendent groups. On the left the PRL published by Azadi et al on 2014[55], on the right the PRL published by McMinis et al[56] the following year. The two calculations strongly disagree, predicting a transition pressure between these two phases respectively at 460 and 700 GPa.

These difficulties do not arise by the intrinsic correlation of hydrogen that DFT is not able to grasp but, rather, from the high variety of structures very close in energy discovered. Dissecting the most stable structure requires an accuracy higher than 1 meV per atom in the energy difference. This small energy difference is behind the accuracy achievable with standard DFT, therefore, large errors occur in the determination of phase stability with DFT.

Many studies[51, 52, 20] indicate that BLYP is the semilocal DFT functional that reproduces best the energy differences between structures versus quantum Monte Carlo. The error in energy differences between structures of BLYP functional reduces to less than 1 meV per atom in many cases. So, in the following discussion, we will always refer to DFT-BLYP as a force engine. More details on the simulation parameters are discussed in App. E.

5.2.3 Is Quantum Monte Carlo reliable?

In the previous section, we discussed the precision of the DFT functionals. To overcome the DFT limitations, many works relax the structure using DFT, then they compute energies using Quantum Monte Carlo (QMC). However, even between different QMC implementations there are huge discrepancies.

As an example, I report the comparison of the static enthalpies from ref.[55] and ref.[56] in Figure 5.1. As clearly shown, results lead to completely different phase diagrams.

This massive failure is justified in the work of McMinis[56] by the different DFT functional used for the structural optimization upon which QMC energetics are computed (even if some of the authors of the original work[55] argued this to be not so effective in a later paper[52]).

This, indeed, makes most of QMC predictions based on the use of a constant scissor operator not reliable. As we will see in the next sections, the anharmonic effects completely change the structural properties of these phases, with differences that are larger than those between the static relaxation of two DFT functionals and strongly pressure dependent.

5.3 Phase III in the theoretical literature

Phase III is found experimentally to be stable at low temperatures (under 200 K) and high pressure (above 150 GPa).

The first models of this phase identified a hexagonal close packet structure with molecules arranged in layers[57]. The currently most supported structure is an almost hexagonal phase with C2/c group symmetry and 24 atoms in the unit cell[16], divided into 4 layers, with stacking ABCD.

This phase is supported by both ab-initio energetic and comparison between harmonic simulated Raman/IR spectra with experiments. However, the most important experimental signature of this phase is the characterization of the H_2 vibron, located above 3500 cm. This vibration cannot be thermally populated, even at room temperature, as the corresponding excitation energy is above 5000 K. This makes impossible to correctly simulate the vibron using classical molecular dynamics and requires a more sophisticated approach like path-integral. The prediction of Raman and IR using path-integral is, however, extremely time-demanding. Up to now, spectroscopic signatures that include anharmonic effects have been computed mainly within classical molecular dynamics[58, 59], thus strongly underestimating the fluctuations affecting the crystal structure.

The difficulties in dealing with quantum nuclei lead to the existence of strange twists in the theoretical literature: while it is commonly recognized that the PBE exchange-correlation functional performs poorly for high-pressure hydrogen[51, 52, 60, 56, 20], it is still the first choice for comparing vibrational features with experiments[16, 17, 58, 61, 20]. This is a clear sign that current theoretical methods lack the precision necessary to compare with experiments, and this is compensated with the "ad-hoc" choice of the XC functional that best fits with experimental data. However, in this way, calculations cannot be predictive and the correct assessment of the crystalline phase is built on the hope of a big error cancellation between exchange-correlation and quantum nuclear effects.

In this chapter, we will focus on a completely unbiased prediction of the experimental signatures of phase III using one of the most reliable GGA functional that we have, the BLYP[50].

Even if this functional has the same computational cost of PBE, it has been proven to strongly outperform the other compared to more accurate methods like Quantum Monte Carlo[51] or Coupled-Cluster when simulating high-pressure hydrogen.

Nevertheless, if BLYP is used to predict Raman/IR spectra with classical molecular dynamic or harmonic approximation, it spectacularly fails when compared to experiments. We will show that this failure is mostly due to anharmonicities activated by quantum fluctuations, therefore, the apparent good agreement of PBE is only due to casual error cancellation, and cannot be used to accurately compare

with experiments.

5.4 The quantum anharmonic effect on the phase III crystalline structure

In this section, I report how the structure changes as we introduce quantum effects. I perform the constant pressure quantum relaxation at 150 GPa, 250 GPa, 350 GPa, and 450 GPa, to cover the whole pressure range spanned by experiments. We can compare the very recent X-ray measurements[62] up to 250 GPa with our simulations of phase III. The results on the structural relaxation are shown in Figure 5.2. Quantum effects expand the volume at fixed pressure and act mainly on the out-of-plane lattice parameter c. In fact, quantum stress is strongly non isotropic, and progressively pushes away the layers as we increase the pressure, as reported in the c/a ratio. We found that quantum fluctuations progressively increase the H_2 bond length up to a 6 % in comparison to classical nuclei (see Figure 5.2). Such an extreme effect was also shown in Cmca-4[63], even if in that case it shows an opposite trend with pressure. In particular, in C2/c-24, a classical treatment of nuclei completely misses the H_2 dependence on pressure.

The stretching of the H_2 molecule has a big impact on physical properties. The vibron frequency depends strongly on the molecular bond length in both Raman and IR spectra. If structures are relaxed with classical nuclei, no matter the exchange correlation functional, the H_2 distance is ill-reproduced as its stretching is a pure quantum effect. This leads to a strong error in both the vibrational frequency and energy. This error affects also the static phase diagram computed with Quantum Monte Carlo (QMC). Different QMC calculation on reference structures obtained by different DFT functionals led to discrepancies[55, 56] of more than 200 GPa on the transition pressures. Under these conditions, no calculation that deals with classical nuclei can predict correctly neither spectroscopic features nor the relative energy of the phases.

The quantum effect on the cell shape are less pronounced, but still important: at 450 GPa the c/a ratio deviates from the static result by about a 0.9%. This effect is smaller than the H_2 bond stretching in percentage, but it is on the same order of the typical cell shape difference predicted by different DFT exchange correlation functionals.

The overall effect of anharmonicity is to expand the volume at fixed pressure (or increase the pressure at fixed volume). This is reported in Table 5.1, where the quantum contribution to the stress tensor is reported at fixed cell (calculated on the static cell). These data show a strong anisotropy in the quantum stress that increases with pressure.

We can compare the cell obtained by the lattice relaxation with the very recent experimental results obtained for phase I-III-IV at room temperature[62]. Since X-ray data cannot distinguish the molecular orientation, they see a primitive cell with higher periodicity, therefore the measured a' and c' must be rescaled with the parameters of the 24 atoms structure Figure 5.2:

$$a' = \frac{a}{\sqrt{3}} \qquad c' = \frac{c}{2}$$

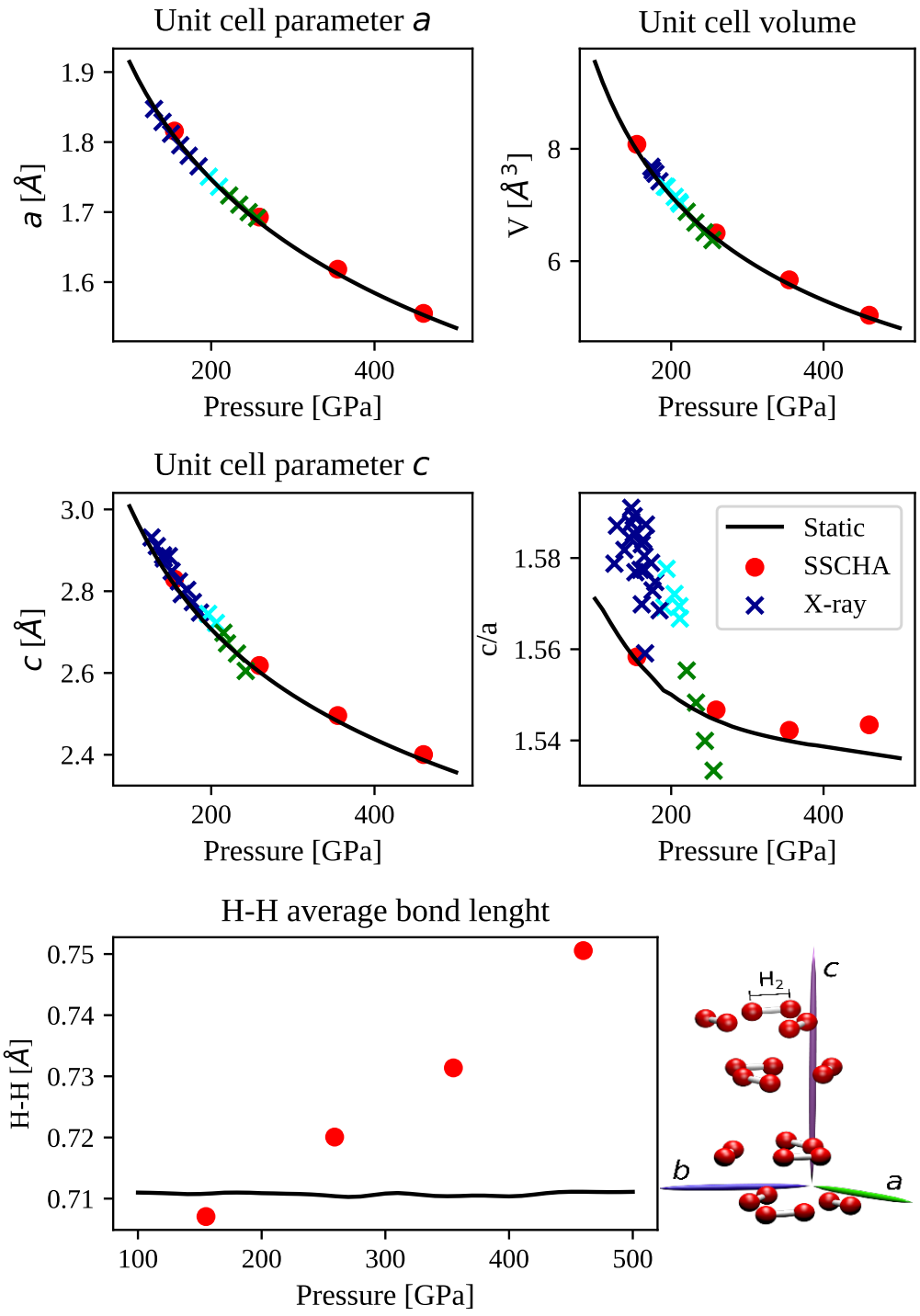

Figure 5.2. Structure of the C2/c-24. Top panel: in-plane a and out-of-plane c lattice parameters, equation of states $V(P)$, and c/a ratios are shown with and without quantum effects. The crosses are experimental data obtained with X-Ray[62] (Only the cyan points represent the phase III). On the bottom, the H_2 average distance as a function of pressure with and without quantum effects. Bottom-right, the C2/c-24 structure with its unit cell. Parameters of the simulation discussed in App. E.2.1.

P_{static}	$\frac{1}{2}(P_{xx}+P_{yy})$	P_{zz}
250 GPa	6.0 GPa	12.2 GPa
350 GPa	5.0 GPa	15.7 GPa
450 GPa	4.6 GPa	18.3 GPa

Table 5.1. Table with the static pressure (on the left) and the corresponding quantum contribution, on the inplane direction, and the one in the out-of-plane direction for the C2/c-24 structure. This data are obtained on the 1x1x1 phonon mesh. The stochastic error is about 0.5 GPa, however the overall error is dominated by cell-size effects

Taking care of this we get a very good comparison with experiments (see Figure 5.2).

5.5 Raman and IR of phase III

To simulate the vibrational spectrum of phase III, we employed a new dynamical extension of the SSCHA, introduced in Chapter 3 and 4.

In Figure 5.3, we show the comparison between the Harmonic result, the dynamical SSCHA green function, and the experiments for both the IR and the Raman vibrons.

The dynamical SSCHA green function strongly improves the experimental accuracy, and it introduces the phonon lifetime. The data have been simulated only with one polarization light, without averaging on all the possible crystal orientations. This can explain the different peak intensities in the Raman spectrum of the libron region. To get a complete result, we should average this green function over all the possible polarizations.

In the case of Raman, we can accurately grasp the spectrum shape and broadening. The Raman signal shows a significant deviation from the natural Lorentzian shape. This behavior is due to the huge anharmonicity in the BO landscape along the mode coordinate. The vibron is the only peak to acquire a non-negligible broadening due to phonon-phonon scattering. On the other hand, the IR vibron in our simulation is much more definite than the experimental results (as the full width half maximum). Here, the experimental broadening may be explained either as nonhomogeneous or a consequence of the anharmonicity in the effective charges, that change during the atomic displacements. This kind of broadening was not considered in our simulation, as we computed the vibrational spectrum contracting the dynamical green function of the displacements with the effective charges computed in the average position. This was obtained taking the effective charges as constant outside averages in Eq. 4.22 and Eq. 4.23.

To test that this is not an artifact of using a single crystal orientation, we report the result of the IR spectrum averaged on the principal crystal orientations neglecting the $\overset{(4)}{\mathbf{\Phi}}$ contribution (Figure 5.4).

Indeed, the average over the possible polarization slightly increases the width of the peak, however, this effect is not sufficient to explain the disagreement with experiments.

To test if the peak broadening is due to anharmonicity in the effective charges,

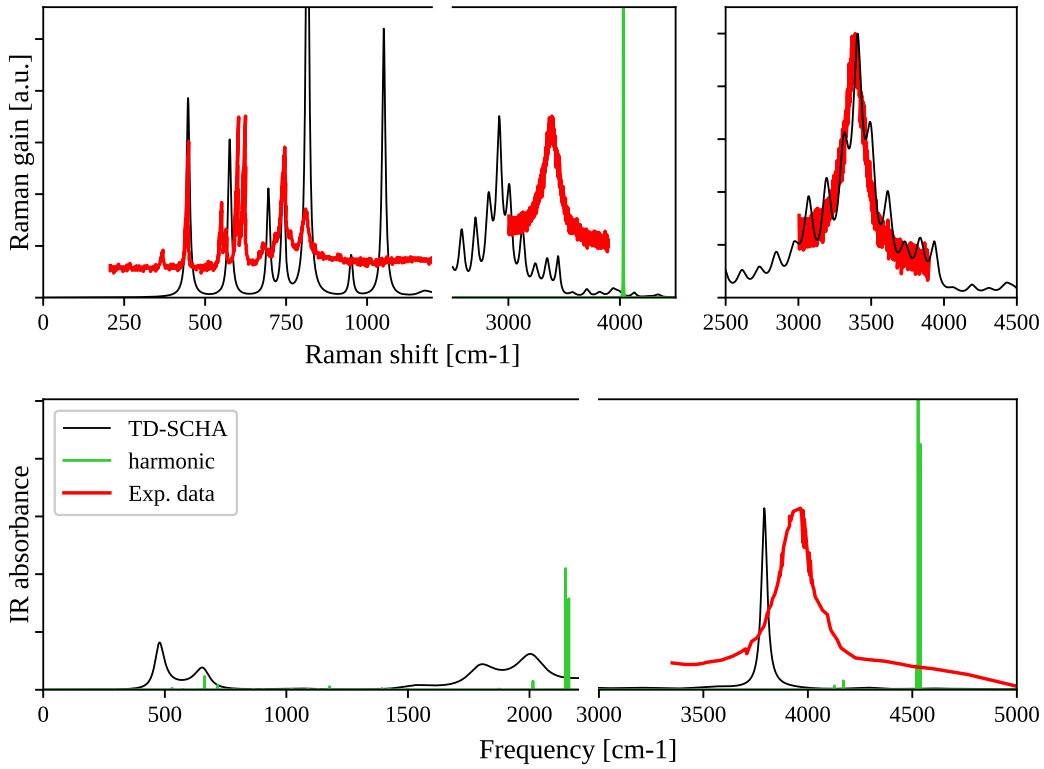

Figure 5.3. Raman (top panels) and IR (bottom panel) spectra of phase III at 350 GPa. Experimental data for the Raman spectrum have been taken from ref.[64], while the IR data from ref.[5]. On the top left panel, the Raman signal has been shifted to overlap the simulated and the measured vibron peak. Simulation details in App. E.2.1

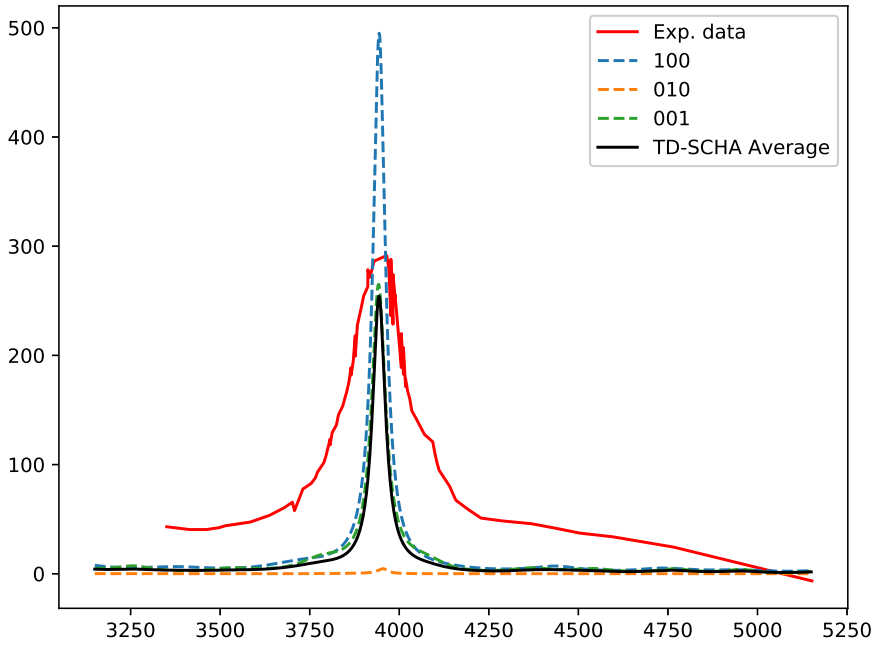

Figure 5.4. Comparison of the IR vibron spectrum obtained with the different direction for the polarization light (or, equivalently, the different orientations of the crystal). Details of the simulation in App. E.2.1

I computed the effective charges in 10 displaced atomic configurations randomly distributed according to the SSCHA density matrix in a supercell 2x2x1. In this way I simulated the IR spectrum with Eq. 4.22 neglecting the contribution arising from Eq. 4.23. The comparison of the IR simulated on the static SSCHA dynamical matrix using Eq. (4.22) and the effective charge in the undisplaced configuration is reported in Figure 5.5. The result does not change much, however, the contribution of Eq. (4.23), here neglected, should be greater, as it is affected by first-order corrections to the effective charges on atomic displacements while the lowest order correction on Eq. (4.22) is the second order.

In Figure 5.6, we report the IR vibron peak and the full-width at half maximum only due to phonon-phonon scattering (Figure 5.7) as a function of the pressure.

The improvement in the experimental agreement compared to the Harmonic result is impressive, in both the slope of the vibron and the absolute value. The FWHM is underestimated by the TD-SSCHA. On the other side, the SSCHA improves the decrease of the vibron life-time when increasing the pressure.

The Raman vibron energy as a function of pressure is reported in Figure 5.8. The TD-SSCHA shows a very good improvement in contrast with the Harmonic case.

Both in Raman and IR, quantum effects correct the slope of the vibron, increasing the match with the experiments. However, in both the simulations, the SSCHA result is systematically underestimating the vibrational energy. This effect could be related to DFT accuracy.

In this work, we used the BLYP functional. This functional is often referred as

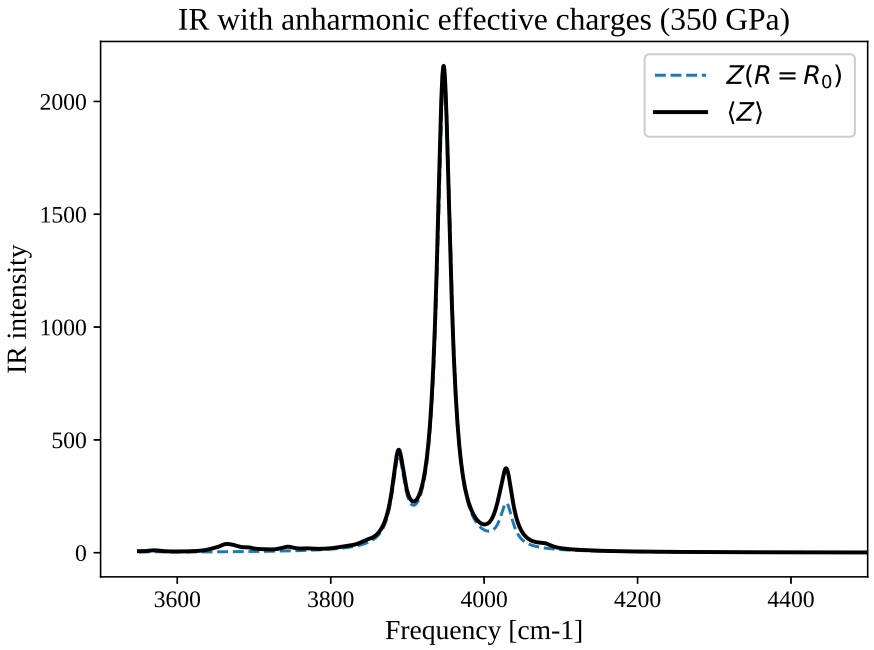

Figure 5.5. IR vibron intensity computed with effective charges obtained averaging randomly displaced configurations and on the reference average position. Details of the simulation reported in App. E.2.1

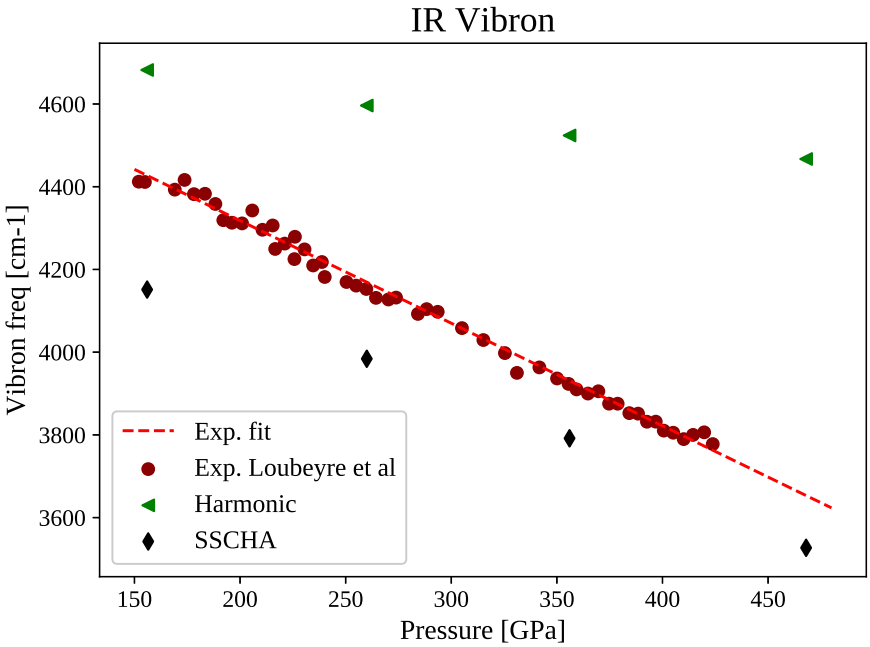

Figure 5.6. IR vibron frequency peak as a function of pressure. Comparison between experimental data[5], Harmonic approximation and the dynamical SSCHA green function. Simulation details in App. E.2.1

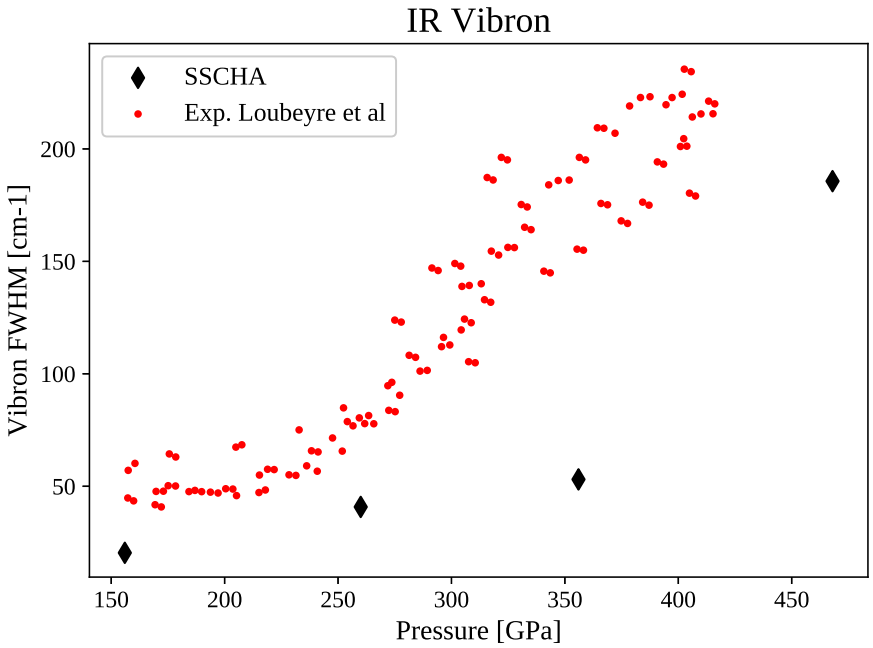

Figure 5.7. IR vibron lifetimes as a function of pressure. Comparison between experimental data[5] and the dynamical SSCHA green function. Here, only the phonon-phonon scattering has been taken into account. The mismatch with experiment is due to anharmonicity in the effective charges, as shown in Figure 5.5

state-of-art DFT-GGA accuracy accuracy for predicting energetics in high-pressure hydrogen together with vdW-DF1[51, 52, 20], whether for the prediction of the vibrational spectra PBE is typically used[16, 17, 58, 20]. The reason is that, as shown in Figure 5.6 and 5.8, the Harmonic result of BLYP is completely off with respect to experiment. PBE, instead, which is known to score poorly in energetics[51, 52, 20, 56], overestimates the H_2 equilibrium bond length at static level[52, 65]. This exchange-correlation error mimics the effect of quantum nuclei (see Figure 5.2) and leads to the partial fortuitous error cancellation that makes the Harmonic result of PBE closer to experiment than the BLYP functional. Indeed, the Harmonic vibrons of BLYP have a much higher frequency than the experiments, as it should, since quantum effects strongly suppress it. The good agreement with experiments of classical molecular dynamics[58, 61] using the PBE functional is a clear indication that anharmonicity on vibron is strongly underestimated by considering only thermal fluctuations even at room temperature and reflects the quite good agreement of PBE harmonic phonons. The thermal energy necessary to excite the vibron (and to sample its anharmonicity) is 5000 K, much above the simulated temperatures. In this regime, the main source of nuclear dispersion is quantum uncertainty, while the temperature plays only a very marginal role.

5.6 The band gap closure of phase III

Here we discuss how anharmonic phonons affect the electronic band structure.

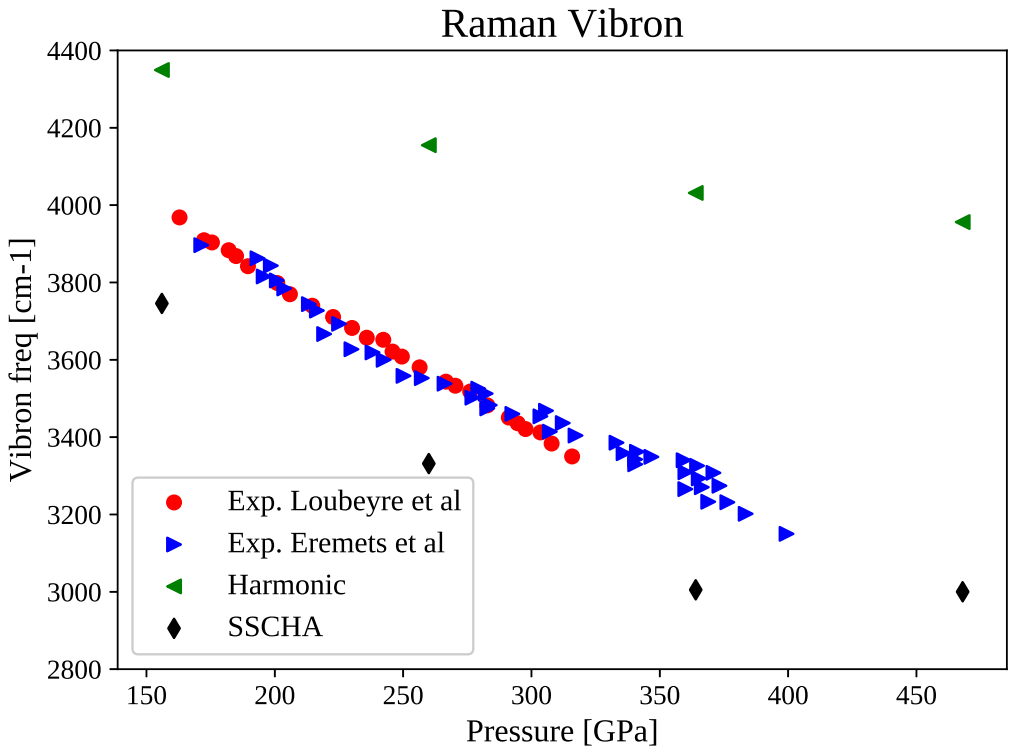

Figure 5.8. The Raman vibron frequency as a function of pressure, comparison between Harmonic, dynamical SSCHA and experiments. Experimental data are taken at 100 K from ref[64, 4]

I compute the optical properties of phase III, comparing the results with two experiments in apparent contradiction[4, 5]. Eremets et. al.[4] (EDWK) observe an indirect band gap closure of phase III at about 360 GPa, but they continue to see the Raman spectrum up to 440 GPa, claiming that no phase-transition occurs up to these very high pressures. On the other side, Loubeyre et. al.[5] (LOD) observe the IR transmission of the sample up to 430 GPa and claim that the structure remains an insulator until about 420 GPa, when the transmission drops down very sharply to zero, indicating a first-order phase transition to a new metallic phase. We will discuss more in detail this phase transition in Chapter 6, while here we focus our attention only on the simulation of the IR transmittance and the indirect gap closure, to verify which experiment is closer to the theoretical prediction.

Moreover, a recent calculation by Azadi et. al.[60] claimed that C2/c-24 cannot be the experimentally observed phase, as electron-phonon closes the gap very early (before 300 GPa) inducing metallization, while all the experiments concord phase III to be insulator up to at least 350 GPa. Their very accurate calculation includes both exact exchange-correlation effects (a variable scissor correction on the band gap computed with Diffusion Monte Carlo) and quantum nuclear effects (Path Integral Molecular Dynamics). To shed light on this observation and assess eventual finite-size effects in their simulation, we repeated the calculation using SSCHA with a much bigger cell.

To compute the optical properties we calculate the bare density-density electronic response $\chi(\omega)$ at fixed nuclei. Nuclear motion is included averaging the dynamical dielectric constant over several atomic configurations, displaced according to the quantum wave-function as obtained by the SCHA relaxation.

In this way, we neglect the non-adiabatic effects of the electron-phonon interaction. Even if in many systems they have a not so high impact, they could play a role in high-pressure hydrogen, as the phonon energy can reach 0.5 eV.

Since hydrogen is not a strongly correlated system, we do not expect excitons to dominate optical properties; we used the independent particle approximation for computing the dielectric constant, and we included the electron-phonon effects within the William-Lax framework[66].

To obtain the electronic contribution to the susceptibility tensor $\chi_{\alpha\beta}$ at each nuclear configuration we employed the following equation:

$$\chi_{\alpha\beta}(\omega + i0^+) = -4\left(\frac{e}{m}\right)^2 \frac{1}{\Omega N_k} \sum_{\vec{k}} \sum_{ij} \frac{f(\varepsilon_{i\vec{k}}) - f(\varepsilon_{j\vec{k}})}{\varepsilon_{i\vec{k}} - \varepsilon_{j\vec{k}}} \frac{M^{\alpha}_{\vec{k}ij} M^{\beta}_{\vec{k}ji}}{(\varepsilon_{i\vec{k}} - \varepsilon_{j\vec{k}})^2 - (\omega + i0^+)^2} \tag{5.2}$$

where

$$M^{\alpha}_{\vec{k}ij} = \langle u_{i\vec{k}} | (-i\nabla_\alpha + k_\alpha) | u_{j\vec{k}} \rangle \,,$$

N_k is the total number of k points, $f(\varepsilon)$ is the Fermi occupation number, $\varepsilon_{i\vec{k}}$ is the i-th Kohn-Scham energy level at $\vec{k}$.

The details of the derivation of this equation are reported in App. F.

The advantage of Eq. (5.2) is that it does not account separately between inter-band and intra-band contributions, it is well defined even in a disordered system with many spaghetti-like bands and a very small Brillouin zone. This is the case

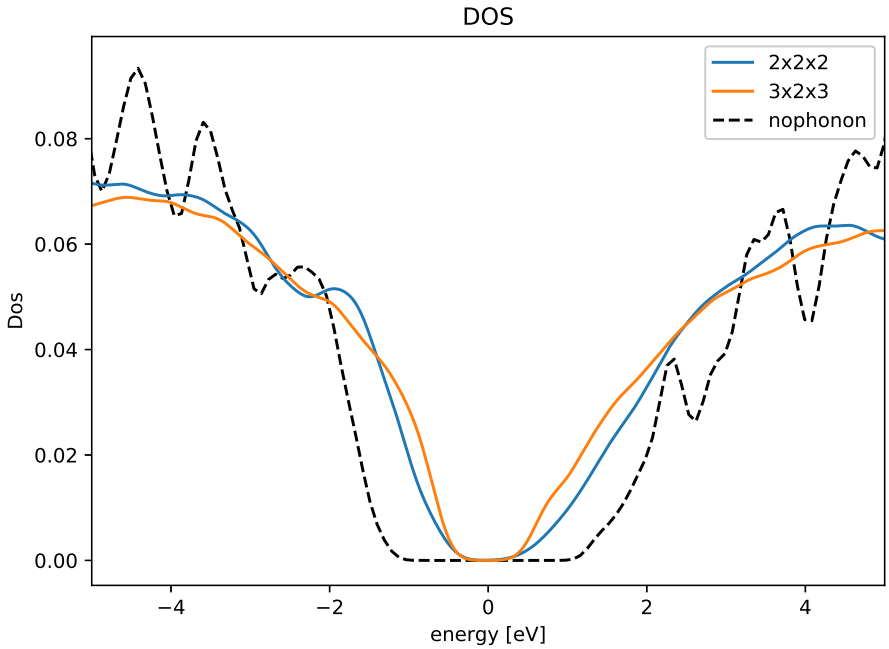

Figure 5.9. Electron DOS including electron-phonon interaction as a function of the simulation cell size. This simulation corresponds to a pressure of 260 GPa.

of a distorted configuration due to nuclear motion. Moreover, Eq. (5.2) is well defined both for metals and insulators, allowing us to blindly compute the dielectric properties (at finite frequencies) without too much care if we are dealing with metals or insulators.

To carry out these calculations, I implemented Eq. (5.2) inside the Quantum ESPRESSO[67, 68] software suite.

The electronic density of states (DOS) averaged over many phonon displaced configurations is reported in Figure 5.9, 5.10 and 5.11 for 250, 350, and 450 GPa.

Here, we confirm the astonishing effect of electron-phonon coupling, that closes the gap by about 2.3 eV. However, physical properties depend critically on the simulation cell size. For example, if we look at the DOS at 355 GPa (Figure 5.10, we can see that using a 2x2x1 (96 atoms) simulation cell leads to an overestimation of the metallic character of the phase. More details in App. E.2.1.

Since the metallic properties depend critically on the DOS close to the Fermi energy, a big simulation cell is required to correctly describe these effects. Interestingly, Azadi et. al.[60] used a simulation cell of only 96 atoms and measured the metallicity by looking at the differences between highest occupied - lowest unoccupied energy levels. In this way, they classify a phase as metallic even if an infinitesimal DOS is present close to the Fermi level. Their observable is very sensitive to the simulation cell.

From our simulations in bigger cells, the indirect band-gap closes just before 350 GPa. This is in good agreement with recent measurements of resistivity[4], considering that DFT is known to favor metallization.

However, in all our simulations, the DOS close to the Fermi energy is very small.

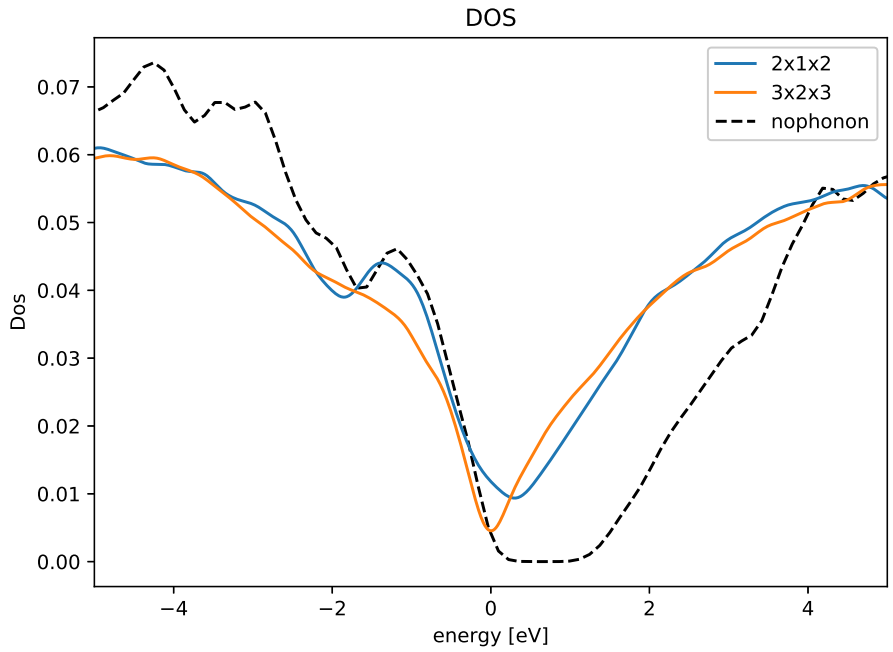

Figure 5.10. Electron DOS including electron-phonon interaction as a function of the simulation cell size. This simulation corresponds to a pressure of 356 GPa.

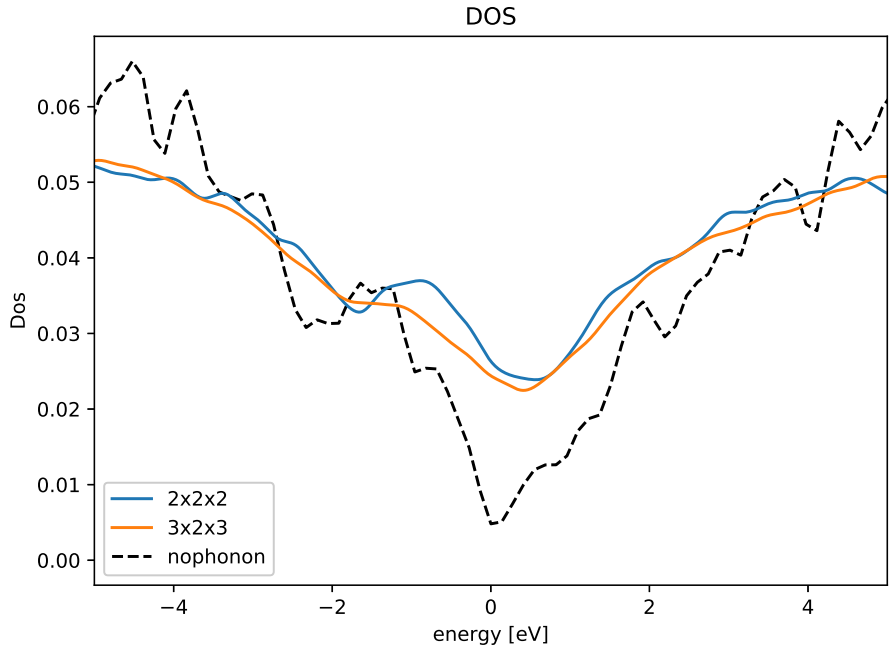

Figure 5.11. Electron DOS including electron-phonon interaction as a function of the simulation cell size. This simulation corresponds to a pressure of 465 GPa.

This means that the physical behavior of this phase is similar to a semi-metal. This is confirmed by measuring the transmitted intensity in the IR regime, as we report in Figure 5.12.

Also here, the transmittance depends critically on the simulation cell size. To compare the optical gap with those reported in the experiment it is important to define a coherent protocol. In structures with many atoms as the C2/c-24 it is in principle wrong to look at the lowest vertical transition in the band structure. This is because in disordered systems (or systems with few symmetries like molecular phases of hydrogen) matrix elements play a crucial role. In particular, C2/c-24 is a structure made of layers, an electron jump between states that belongs to different layers is more likely to give a negligible contribution to the transmittance, and thus not to be revealed experimentally. To properly account all the effects, we compute the transmittance across a sample of 1.5 µm thick, looking at the first energy value where the transmittance drops below the 2%. Reflectivity is computed from the dielectric function as:

$$R(\omega) = \left| \frac{\sqrt{\varepsilon(\omega)} - n_d}{\sqrt{\varepsilon(\omega)} + n_d} \right|^2 , \tag{5.3}$$

where n_d is the diamond refractive index, equal to 2.33 when $0.1 \leq \omega \leq 4\,\text{eV}$. The transmittance is computed as:

$$T(\omega) = [1 - R(\omega)] \exp\left[-2\omega \Im \sqrt{\varepsilon(\omega)} \frac{d}{c} \right] , \tag{5.4}$$

where d is the sample thickness. Here, we ignore the interference due to multiple reflections inside the sample.

The computed direct band gap is in good agreement with experiments but slightly underestimated. Again, this effect could be explained by the fact that DFT usually underestimates the gap.

To include effect beyond DFT we used the HSE0 hybrid functional to assess how much we are underestimating the gap.

The comparison of the band structure at the centroid position between BLYP and HSE0 is reported in Figure 5.13.

From this calculation, we can estimate an error of 0.8 eV on the direct gap at gamma. If we add this to the direct band gap estimation, we improve a lot the comparison with the experiments (Figure 5.14).

Therefore, also the experiment by Loubeyre et. al.[5] is strongly supported by our simulation.

The last interesting observable is the reflectivity, which can be measured by experiments, and provides a signature of the metallic character of the phase.

In Figure 5.15, 5.16 and 5.17 we report the simulation of the reflectivity for C2/c-24 at 260 GPa, 356 GPa and 465 GPa.

Here is evident how the reflectivity gradually increases with pressure, showing that no sharp transition appears when the structure metallizes due to the indirect band gap closure. Also here, electron-phonon coupling and the simulation cell size play a major role for a quantitative accurate prediction.

To separate between the effect of the stochastic noise with the effect on the cell size, we report the calculations of the reflectivity and the transmittance for the 355 GPa case of 5 configurations (Figure 5.18).

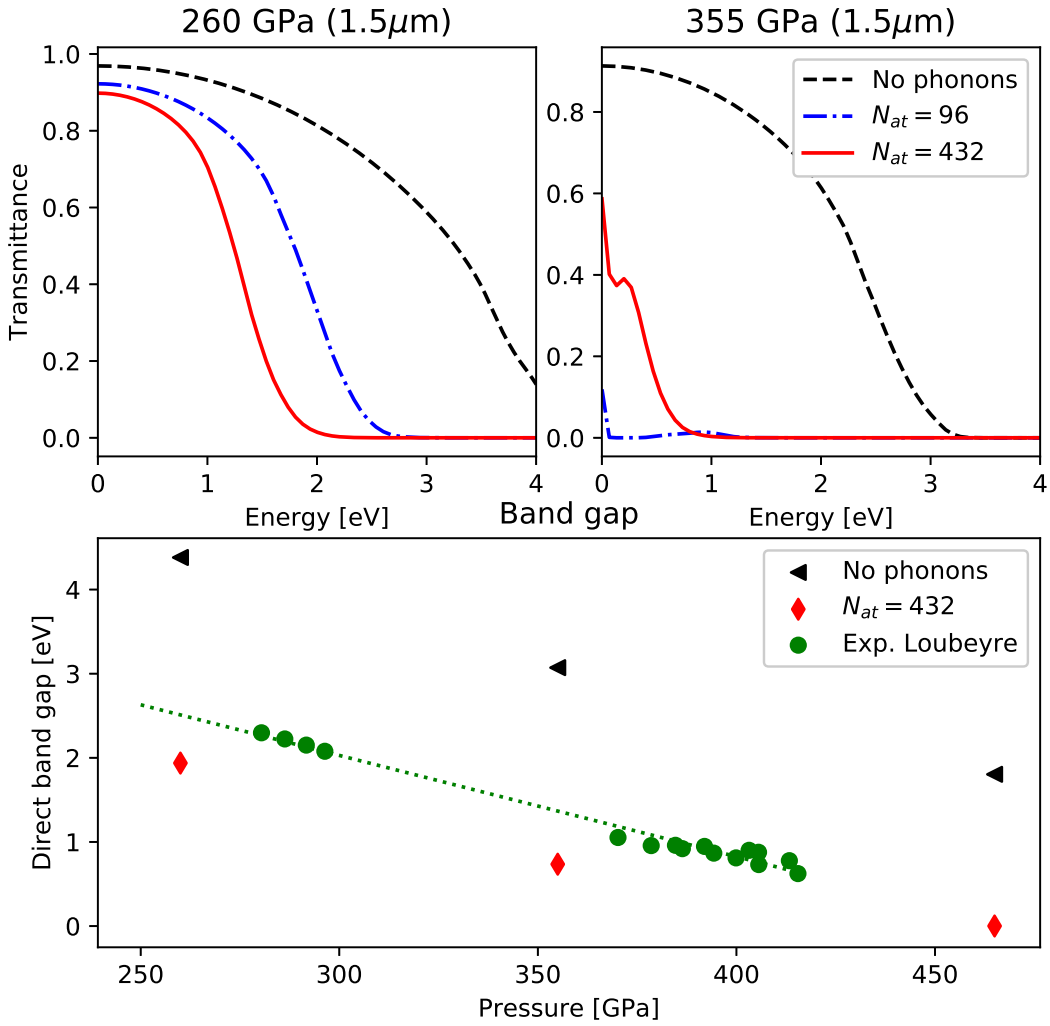

Figure 5.12. Transmittance as a function of the frequency. As can be seen in the 355 GPa panel, even if the phase is metallic (see the DOS of Figure 5.10) still a small amount of IR signal passes through the sample. This occurs because the system behaves as a very bad metal, with a very low plasma frequency. The transmittance is used to calculate the direct gap, as done by experiments[5]. The size effect is strongly pressure depenedent, however, this is a consequence of the induced metallization at 355 GPa in the 96 atoms system. The comparison between experimental direct band-gap and the theoretical simulation is reported in the lower panel. The "No phonons" curve refers to the electronic structure computed in the average position after the SSCHA relaxation. The reported direct (optical) gap is not the lowest possible direct transition in the band structure, as it is properly weighed on the dipole matrix elements between the states.

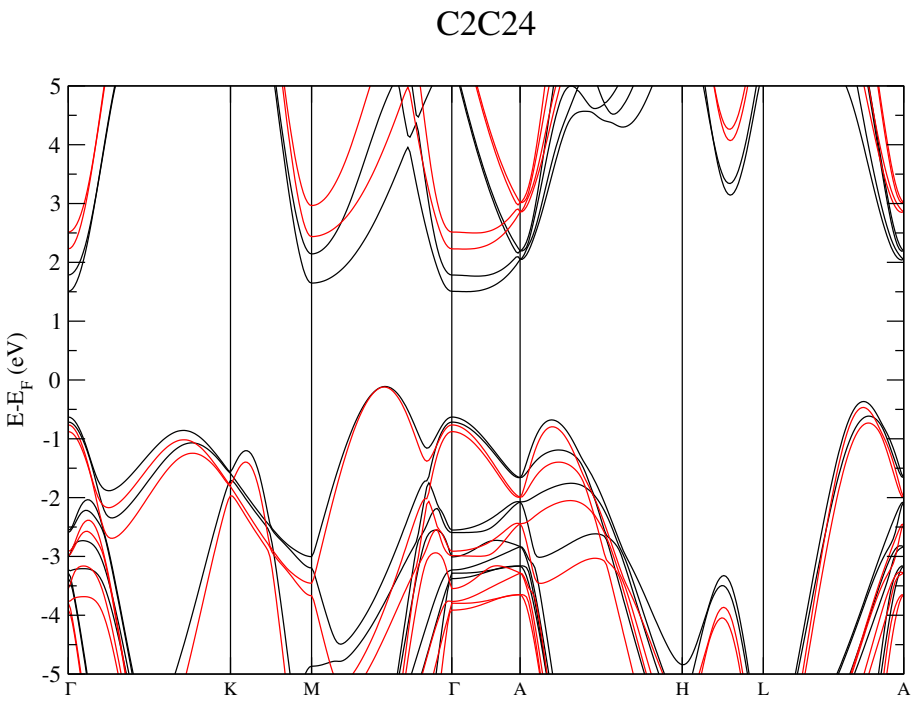

Figure 5.13. Comparison between BLYP (in black) and HSE0 (in red) band structure for the C2/c-24, at 356 GPa. The structure is the average structure after quantum effects have been relaxed.

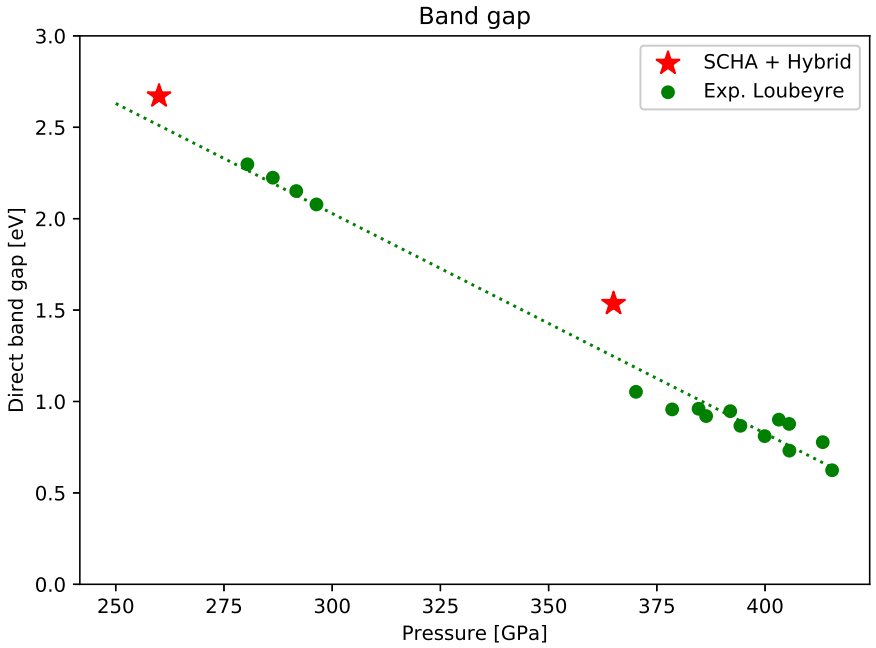

Figure 5.14. Direct band gap calculation of C2/c-24 vs experimental data for phase III[5]. This calculation includes also exact exchange effects using a scissor operator of 0.8 eV as computed in Figure 5.13.

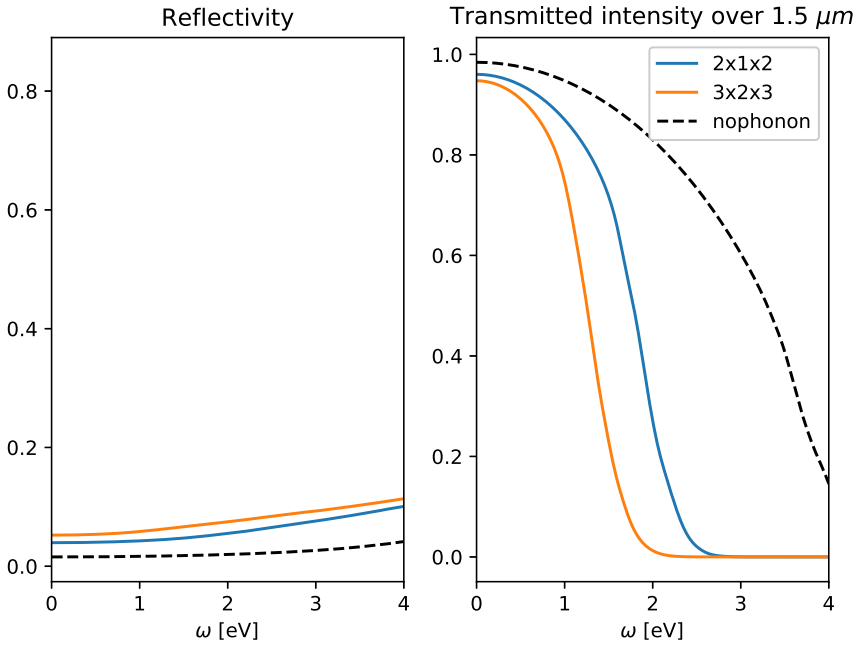

Figure 5.15. Reflectivity and Transmittance for the C2/c-24 at 260 GPa

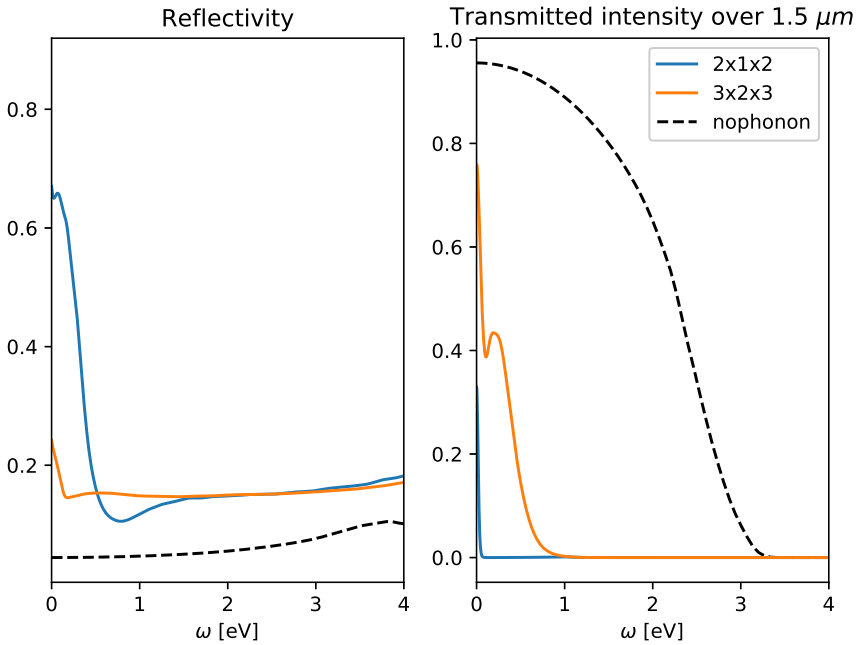

Figure 5.16. Reflectivity and Transmittance for the C2/c-24 at 356 GPa

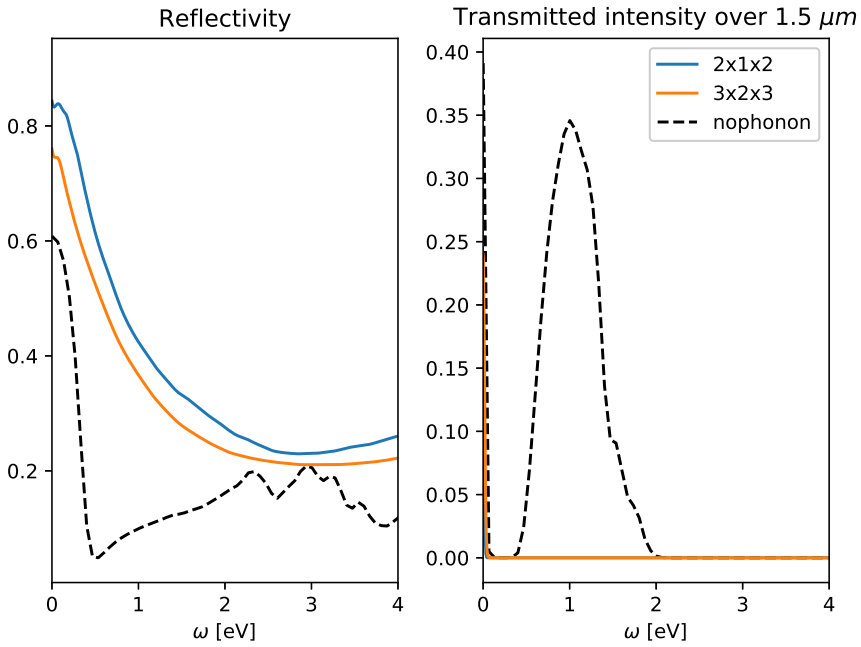

Figure 5.17. Reflectivity and Transmittance for the C2/c-24 at 465 GPa

The optical gap accuracy can be estimated by comparing the results with different configurations to be of about 0.08 eV for the 96 atoms cell and 0.04 eV for the 432 atoms. This can be neglected if compared with the 0.6 eV of difference between the optical gaps obtained with 96 and 432 atoms. Figure 5.18 also shows why the effect of the cell on the optical gap seems to be opposite in the 355 GPa and the 260 GPa case (the 432 atoms-cell has a lower gap at 260 GPa but an higher one at 355 GPa than the 96 atoms-cell): in both cases the interband transition contribution to the absorbtion are higher in energy in the cell with less atoms, however, the presence of a stronger Drude peak at 355 GPa (due to the higher DOS at the Fermi level in the 96 atoms cell, see Figure 5.10) causes an higher value of the reflectivity that makes the transmittance to drop down and cover the gap. In fact, interband contribution is visible for 2 out of 5 configurations for the 96 atoms-cell, where the transmittance drops below 2% at about 1.2 eV; 0.6 eV higher than the 432 atoms-cell.

All these results argue that the experiments[4, 5] are not in contradiction, at least regarding the measurements they presented for phase III. However, also the claim of a first-order phase transition observed by LOD is not in contradiction, as the two experiments use a different pressure calibration scale. Indeed, LOD used the 2006 Akahama scale[69], while EDKW used the 2010 Akahama scale[70]. In their supporting materials, LOD compare the results of the two scales concluding that the use of the 2010 scale leads to the overestimation of about 30 GPa of the pressure above 300 GPa for hydrogen (to Akahama 2006).

This mismatch is well represented both by overlapping their Raman vibron frequency as a function of pressure (Figure 5.8) or by looking at the resonance in the Raman vibration as a function of the frequency of the laser used to irradiate the sample (Figure 5.19).

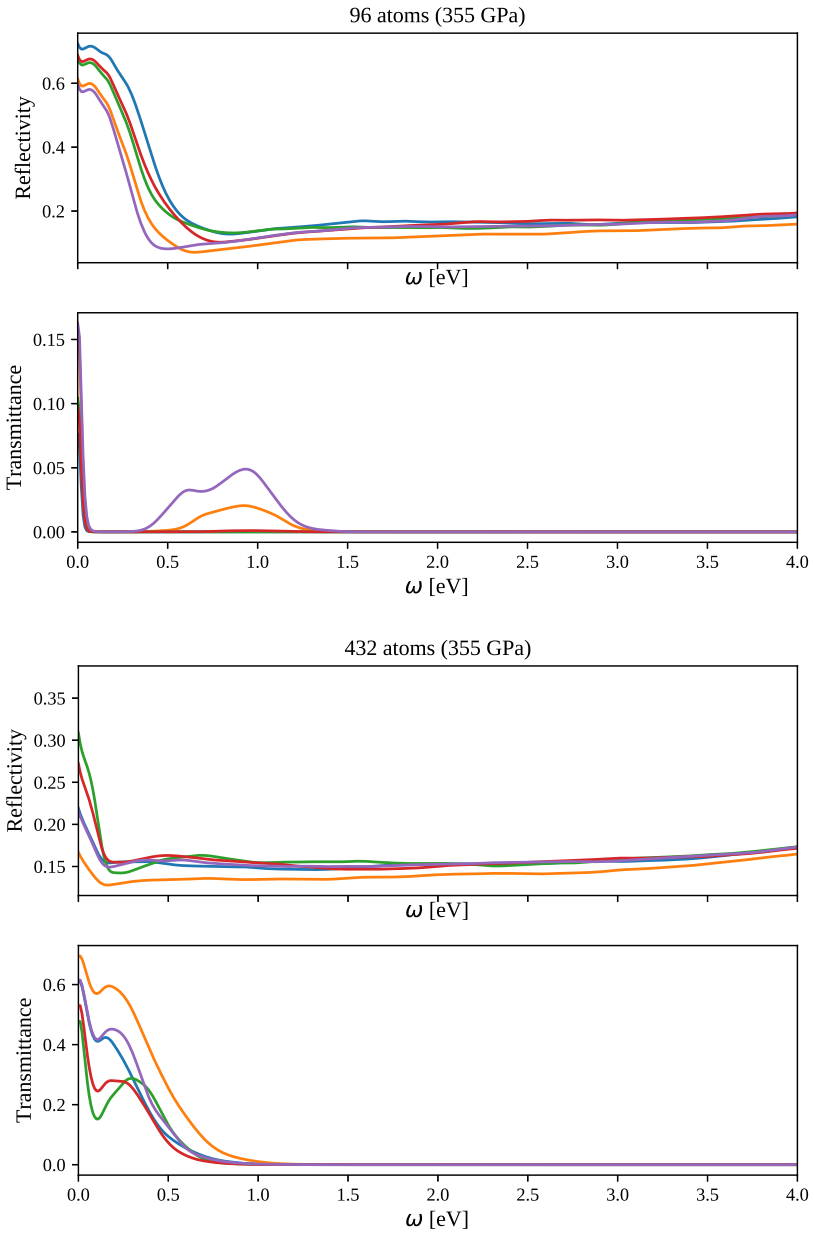

Figure 5.18. Reflectivity and transmitted intensity for the 355 GPa case computed with 5 different configurations for the two cell-size of 96 and 432 atoms respectively. The cell size error dominates over the stochastic noise.

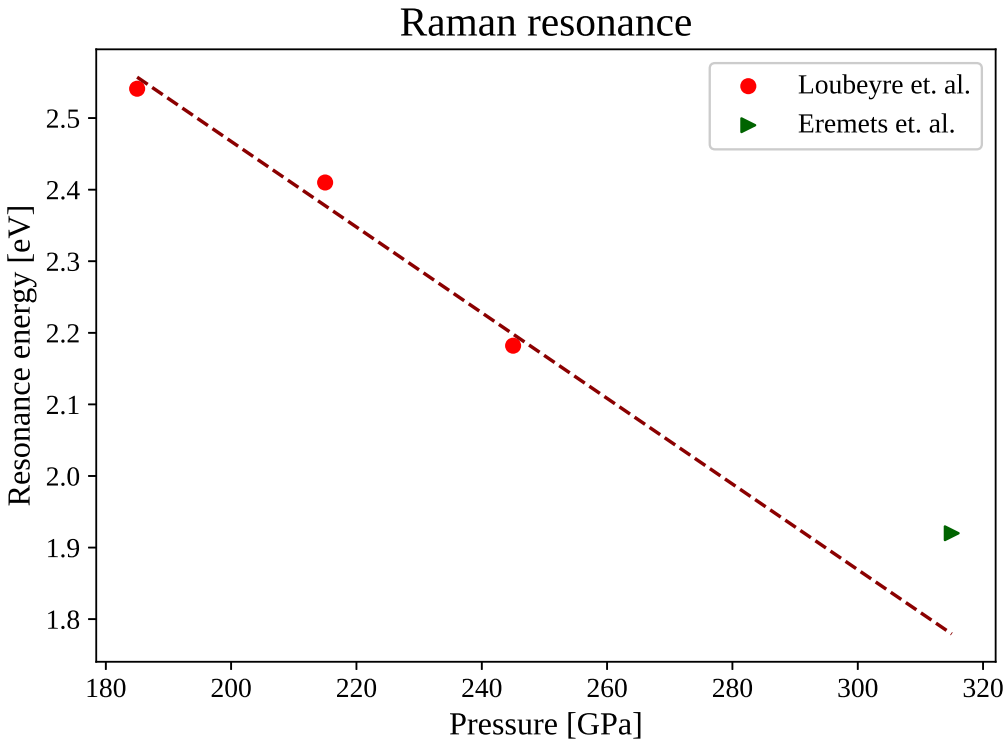

Figure 5.19. Pressure of the Raman resonance using different lights to irradiate the sample. A comparison between data by Loubeyre et. al.[64] and EDWK[4].

Therefore, we conclude that the two experiments report consistent results, in particular, EDKW measured the increase of conductivity related to the indirect band gap closure, while LOD measured the direct band gap closure, which occurs at much higher pressure.

However, LOD saw evidence for a first-order phase transition at 425 GPa, which is above the last pressure at which EDKW see the Raman to disappear after converting the two pressure scales.

5.7 Conclusions

In this chapter, I used the SCHA and its time-dependent extension to simulate the properties of phase III.

I showed how this structure is reshaped by the anharmonicity induced by quantum fluctuations of light hydrogen atoms.

In particular, the H_2 molecular bond increases linearly with pressure up to a 6% value at 450 GPa. This effect is not only absent at the static level, but profoundly change the properties of the atomic vibrations and the energetics.

I simulated the Raman and IR vibrations, showing how TD-SCHA significantly improves the agreement with experiments. Moreover, we are able to simulate also the peak broadening. We showed how the Raman broadening affects almost only the vibron and is dominated by phonon-phonon scattering. On the other side, the IR broadening is dominated by the anharmonicity on the effective charges or inhomogeneous effects.

We used the SCHA theory to compute the electronic and optical properties with the electron-phonon interaction.

We showed how the C2/c-24 structure reproduces remarkably well the experimental direct and indirect band-gap closure, in opposition with previous results[60]. We showed how the use of a big simulation cell is essential to correctly describe the electronic DOS close to the Fermi energy.

These results establish the C2/c-24 as a very good candidate for phase III. In the next chapter, I simulate the whole P-T phase diagram.

Chapter 6

The Hydrogen Phase-Diagram

6.1 Introduction

In the previous chapter, I simulated phase III of hydrogen, showing how anharmoncity and quantum fluctuations change structural properties and experimental features, hampering the correct crystal structure assignment. In this scenario, it is impossible to predict the correct phase-diagram of high-pressure hydrogen accounting for the zero point energy only within the harmonic approximation. For this reason, in this chapter, I compute the full phase-diagram of hydrogen using the SSCHA theory.

In the first section, I review the experimental phase-diagram. I show how it is strongly affected by quantum zero-point motion. This favours high-symmetry structures that are saddle points of the static energy landscape. The ability of the SSCHA algorithm to explore the configuration phase in an unbiased way allows us to identify three new structures, unknown previously.

The transition to the atomic metallic state, the expected room temperature superconductor and the isotope effect in the phase diagram are discussed.

Exploiting the new algorithm introduced in Chapter 4, I predict the quantum melting of phase III, leading the discovery of a new crystal structure, candidate for phase VI. In the last section, I focus on phase III→VI transition, claimed by Loubeyre et. al.[5] and contested by other works[4, 71].

6.2 Experimental phase-diagram

Hydrogen presents a very rich phase-diagram. At low pressures and ambient temperature, hydrogen is in a solid molecular phase where H_2 molecules are situated in the sites of a hexagonal closed packed lattice. This is commonly known as phase I. Upon increasing pressure (about 100 GPa) and decreasing temperature (under 100 K), hydrogen transits into a new molecular solid phase, phase II, where the rotations of molecules are frozen in an ordered broken symmetry phase[18]. These two structures are disclosed and are not topics of this thesis. If pressure increases over 150 GPa a new structure is found, known as phase III. This phase is characterized by a strong IR activity and an intense vibron. The structure linked to this phase has been disclosed by computer simulations and Ab-Initio Random Structure Search (AIRSS) [16], and it is the one we discussed in Chapter 5. Thanks to the progress in the

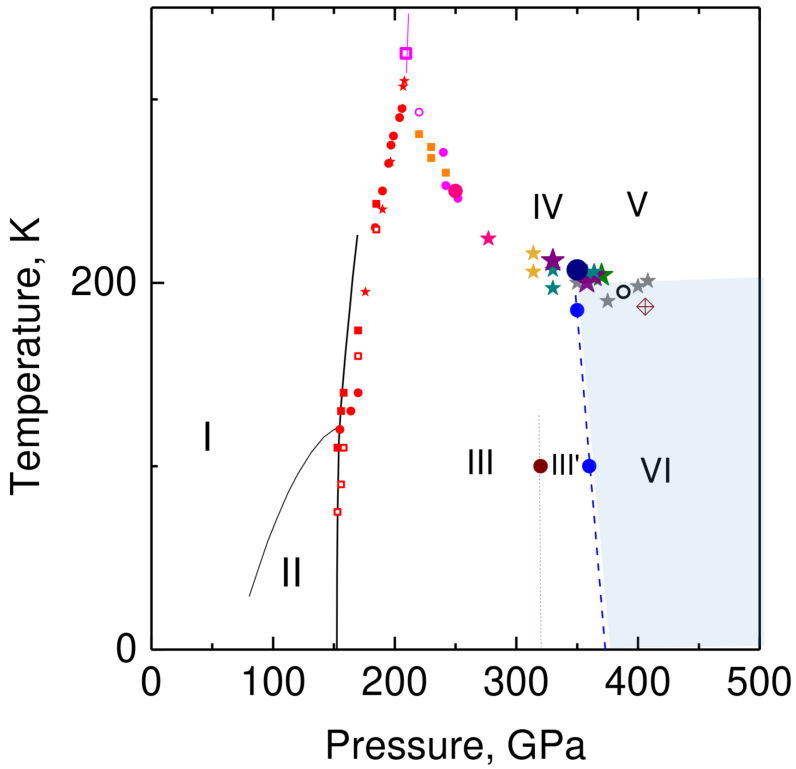

Figure 6.1. Experimental phase-diagram of high-pressure hydrogen, taken from ref [12]. The work by Loubeyre et. al.[5] reports a transition to a new phase at higher pressure (around 420 GPa), while a more recent experiment by Eremets et. al.[4] reports no transition to phase VI up to 480 GPa

field of AIRSS, many different structures have been proposed since that moment. Also for phase IV[19] (obtained in the same pressure range of phase III but at room temperature), a candidate structure has been identified by simulations[17].

New experiments claimed the existence of two new phases, respectively V and VI at pressures above 330 Gpa (room and low temperature)[11, 2, 12, 5], but still, no definitive structure has been found for them, and measurements are still controversial. Recently, a new experiment claimed that no transition from phase III occurs up to 480 GPa[4]. New structures have been proposed for both phase V and VI[20, 53].

The proposed experimental phase diagram is reported in Figure 6.1.

6.2.1 Phase III to VI transition (low temperature)

Addressing the existence of a molecular phase at low temperature and high pressure (phase VI) is a target of this thesis.

Phase VI has been claimed experimentally by three competing groups, but all of them report different signatures. A work by Eremets et. al.[12] (ETD from now on) was the first one to claim the existence of a semi-metallic phase at low temperatures above 380 GPa. They guessed this transition by the disappearance of the Raman spectrum and a simultaneous drop in the measured resistivity when cooling. A

few months later, a work by Dias et al[2] (DNS from now on) measured the IR absorption spectrum, showing a sharp transition in the vibrational signatures at low temperatures above 355 GPa. Very recently, Loubeyre et al[5] (LOD) reported the measurement of direct band gap closure due to a sharp transition at 415 GPa with IR absorption measurement, however, the sample remained black (low reflectivity). This last experiment managed to return to phase III by further reducing the pressure, showing no hysteresis on this transition. Very recently, another experiment by Eremets et al[4] (EDKW) contradicted their previous results (ETD), showing the Raman spectrum in back reflection until 440 GPa, claiming that no transition occurs until that pressure. Their resistivity data are in agreement with a scenario of metallization due to indirect band gap closure.

The first three measurements seem to agree on the existence of another phase above III. This phase cannot be identified as the pure atomic metallic phase, as it has too low conductivity to be a good metal[12] and it is not shiny[12, 2]. The ETD and LOD measurements agree in identifying it as a very bad metal, as the drop of Raman, the increase of conductivity (ETD), and the direct band gap closure (LOD) point to. On the contrary, the DNS measured an IR vibrational spectrum, that is observable in transmission only under the hypothesis that the phase is an insulator.

Recently, the Harvard group criticized the LOD claims of metallization for the lacking of reflectivity measurements and the dark appearance of their sample, incompatible with a metal[71].

EDKW shows that phase III becomes a metal after 350 GPa, but they did not identify a transition to a new phase. This is in contradiction with the IR measurement of DNS.

The apparent contradiction between EDKW and LOD could be possibly explained by a mismatch between their pressure scale, as already discussed in Chapter 5.

This seems to indicate that at high-pressure, the EDKW pressure data are overestimated by about 30 GPa compared to LOD's one. This is within experimental errors on pressure uncertainty due to calibration. The EDKW Raman signal disappears at 440 GPa, while the LOD IR absorption drops to zero at 420 GPa.

6.3 The static theoretical phase-diagram

In this section, we show the static high-pressure hydrogen phase diagram, i.e. neglecting both quantum and thermal fluctuations.

To be consistent with the literature, I name the phases with the symmetry group followed by the atoms in the unit cell. This nomenclature is, indeed, ambiguous, especially for symmetry groups with very low symmetries. Sometimes, I will name a structure according to a specific feature or similarities with other elements.

The most important candidates found by crystal structure search are:

- C2/c-24: This is the commonly accepted candidate for phase III of hydrogen[16], stable at low temperature between 150 and 420 GPa, composed by layers of molecules in imperfect rings. A top/side view is shown in Figure 6.2.

- Cmca-12: This is a candidate for phase VI, a high-pressure phase composed by layers of molecules in imperfect rings, very similar to C2/c-24, but more

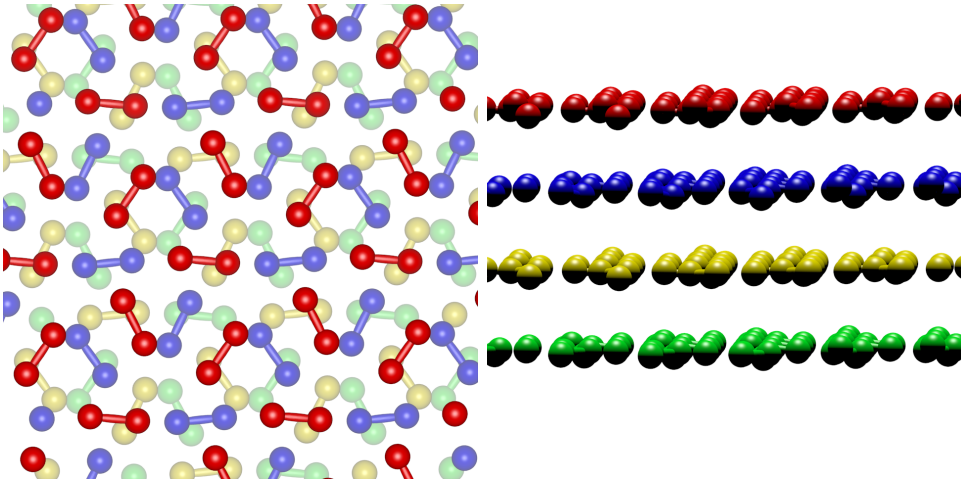

Figure 6.2. Top and side view of C2c-24 phase of hydrogen. This phase has a stacking ABCD

symmetric. Shown in Figure 6.3.

- P62/c-24: This is a new phase we introduce that we will show to be highly favored by quantum motion. It is composed of mixed graphene and molecular layers. Molecular layers are very similar to C2c-24.
- Pc-48: This is a candidate for phase IV[17]. It is a mixed structure of distorted graphene layers and strongly bonded molecular layers. Shown in Figure 6.5.
- Ibam-8: This is a prototype for the Pc-48 phase, as it has more symmetries. Shown in Figure 6.6
- P2/c-48: This is a new phase. It is obtained from the quantum relaxation of Pc-48 at 250 GPa. Shown in Figure 6.7.
- C2/c-16: This is a new phase. It is obtained from P2/c-48 when relaxing with quantum effect at 350 GPa. Shown in Figure 6.8.
- Cs-IV. This is the accepted candidate for the metallic superconductive hydrogen. The phase-group is I4-amd with 2 atoms per cell, however, it has the same structure as Cesium IV, this allows us to better identify structural properties. Shown in Figure 6.9.

The most stable crystal structure at fixed pressure and $T = 0\,\mathrm{K}$ is the one with the lowest enthalpy H, defined as:

$$H_{el} = E_{el} + P\Omega,$$

where E is the electronic energy per cell, P is the pressure and Ω is the volume of the unit cell.

The H_{el} as a function of pressure is reported in Figure 6.10. We used DFT-BLYP as energy and force engine, the convergence parameters are discussed in App. E.

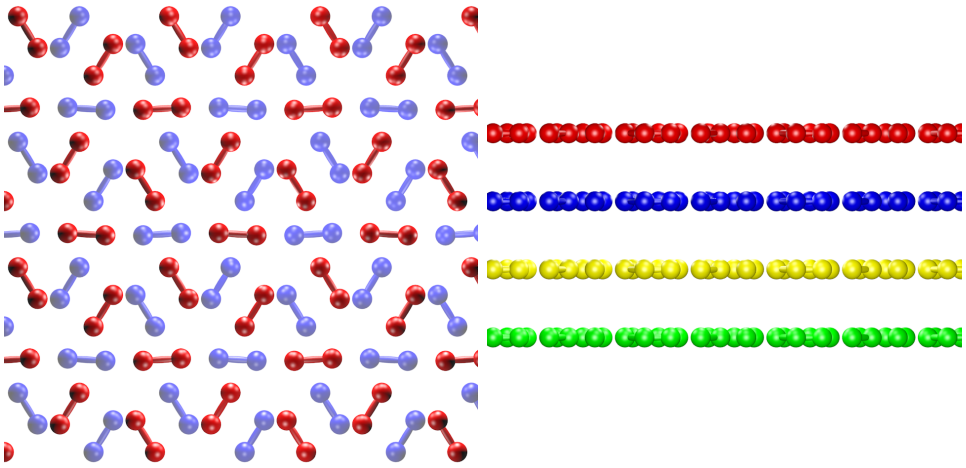

Figure 6.3. Top and side view of Cmca-12 phase of hydrogen. This phase has a stacking ABAB

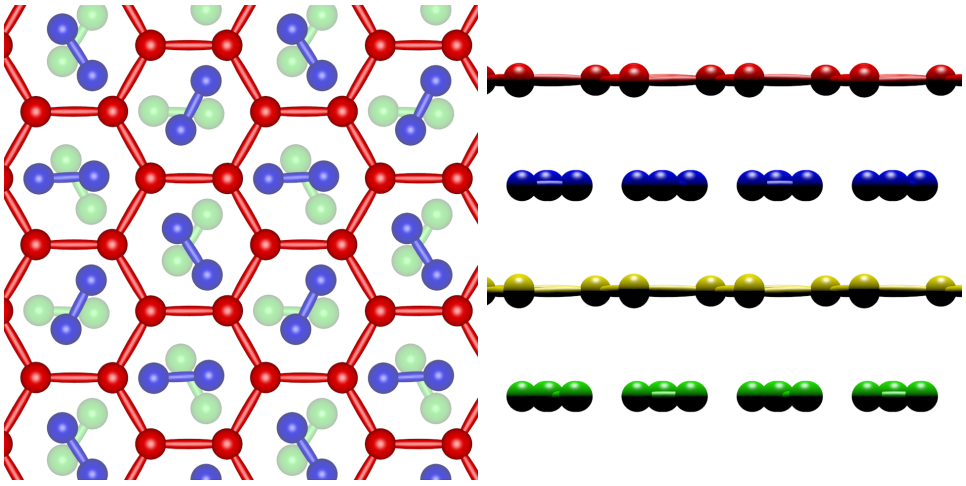

Figure 6.4. Top and side view of P62c-24 phase of hydrogen. This phase has a stacking ABAC

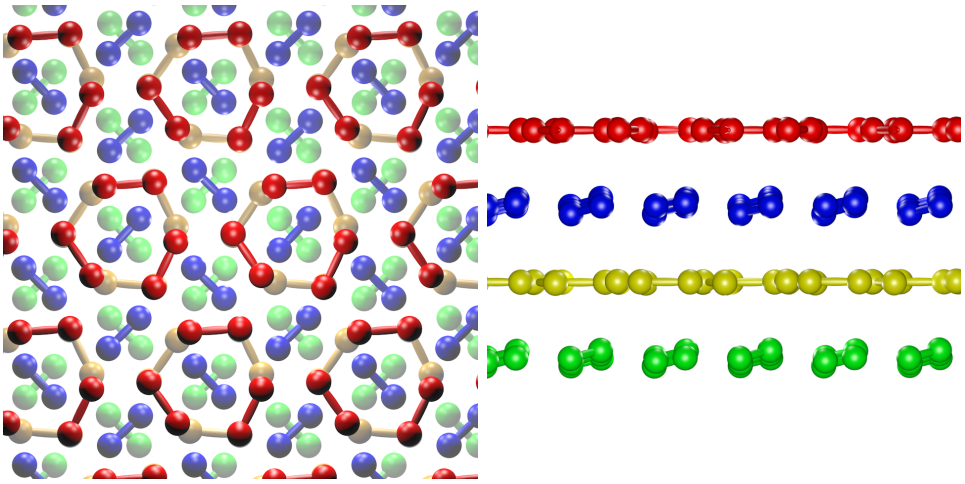

Figure 6.5. Top and side view of Pc-48 phase of hydrogen. This phase has a stacking ABCD.

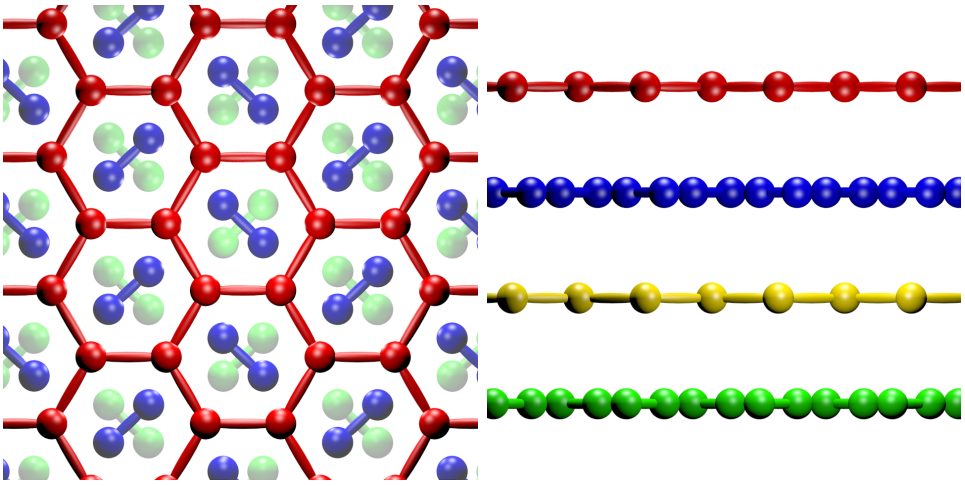

Figure 6.6. Top and side view of Ibam-8 phase of hydrogen. This phase has a stacking ABAC. It is prototype for Pc-48

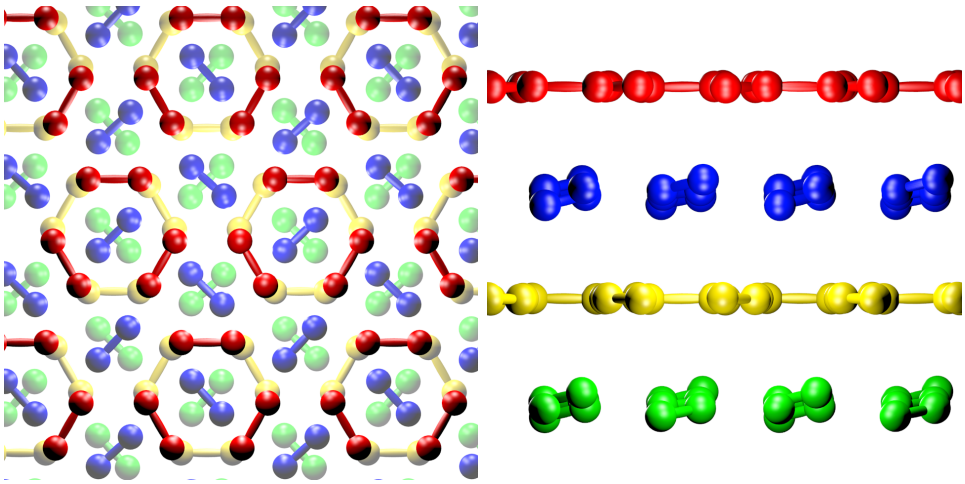

Figure 6.7. Top and side view of P2/c-48 phase of hydrogen. This phase has a stacking ABCD. It is obtained after a quantum relaxation of Pc-48 at 250 GPa.

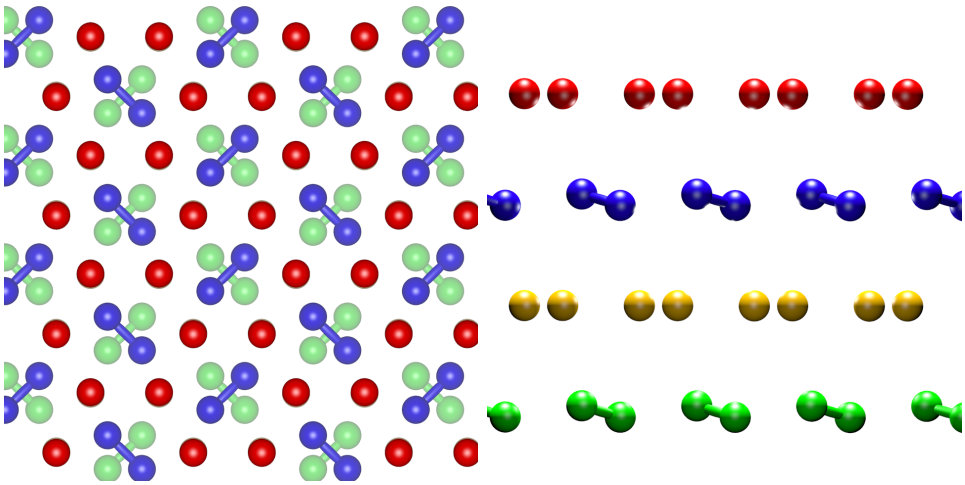

Figure 6.8. Top and side view of C2/c-16 phase of hydrogen. This phase has a stacking ABAC. It is obtained after a quantum relaxation of Pc-48 at 350 GPa. Not to be mistaken with C2/c-24, that is the candidate for phase III.

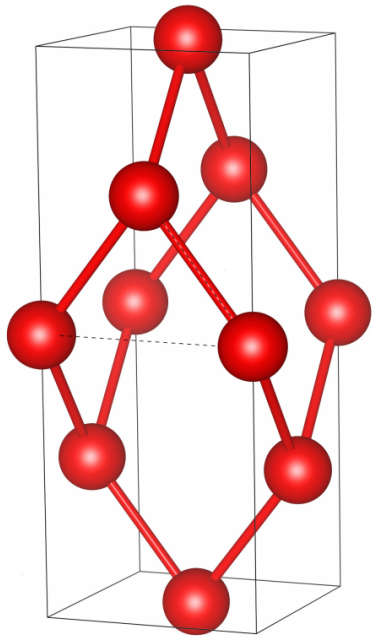

Figure 6.9. The atomic metallic hydrogen phase CS-IV. This is the only phase considered not made by layers. Figure from ref.[72].

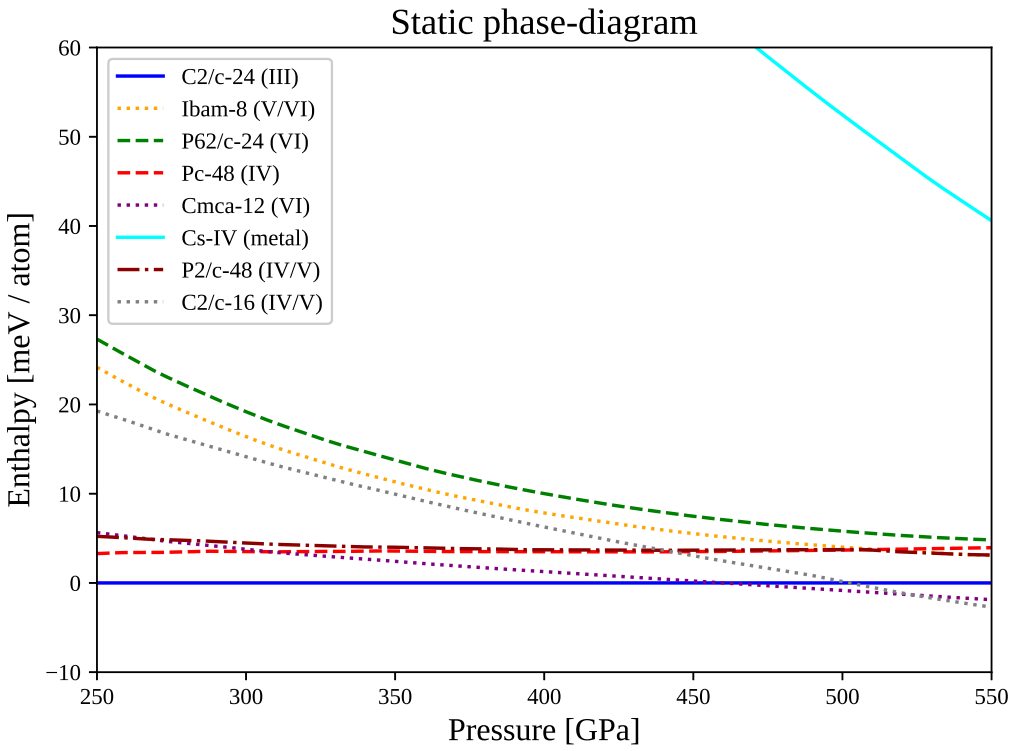

Figure 6.10. Static enthalpy vs pressure diagram. For each pressure, the stable structure is the one with the lowest enthalpy per atom.

C2/c-24 is the most stable structure up to 460 GPa. Cs-IV, the expected room-temperature superconductor, has an extremely high enthalpy and it is out of reach of the current experimental facilities.

DFT-BLYP reproduces a phase-diagram more in agreement with QMC data of McMinis et al[56], see Figure 5.1.

However, here the main ingredient is still missing: the effect of lattice motion. Without lattice dynamics, we are not even able to compute the temperature dependence of the phase diagram.

Both Ibam-8, P62/c-24, P2/c-48 and C2/c-16 are saddle points of the BO energy landscape. They are unstable and cannot exist in the simulated pressure range.

6.4 The full anharmonic phase-diagram at $T = 0\,\mathrm{K}$

Anharmonic quantum effects can be included with all the methodology presented in Chapter 1 and Chapter 2.

At low temperatures, we are interested in the transition between phase III, the eventual unknown phase VI, and the metallic superconductive phase. We report the full quantum anharmonic phase diagram for the low temperature candidates, C2/c-24, P62/c-24, Cmca-8, Ibam-8, and the atomic metal Cs-IV, in Figure 6.11. In Figure 6.12, we report a zoom on the transition to Cs-IV, the expected room temperature superconductor.

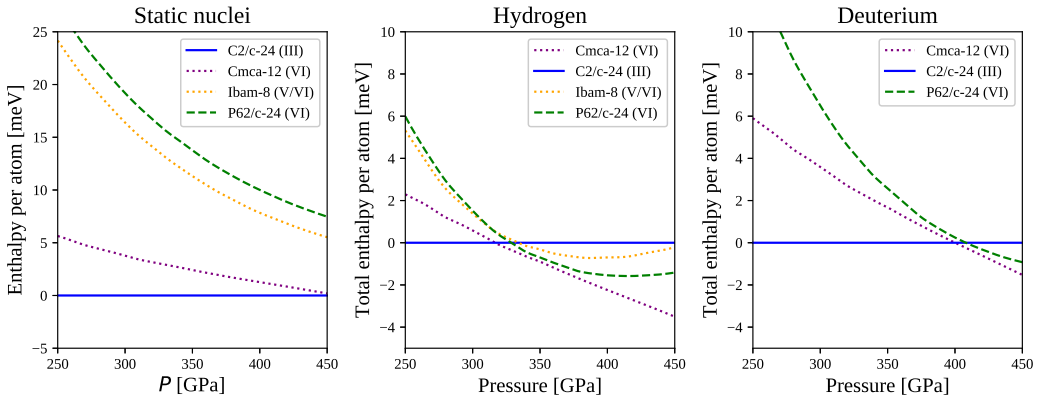

Figure 6.11. Phase diagram of the molecular phases at low temperature. The static diagram is on the left, the quantum phase diagram on the middle, the phase-diagram of deuterium on the right. In opposition to the static phase diagram, all the structures have similar enthalpies.

The phase diagram drastically changes when quantum fluctuations are included. The saddle point structures, Ibam-8 and P62/c-24, become stable and competitive in energy. The C2/c-24, ground state up to 450 GPa in the static case, transit to a new phase at about 325 GPa. Between 325 and 370 GPa, Cmca-12 and P62/c-24 are almost degenerate in energy, then the Cmca-12 dominates at higher pressures. This transition from phase III to a new phase presents an impressive isotope effect: it is shifted at about 400 GPa in Deuterium (70 GPa higher).

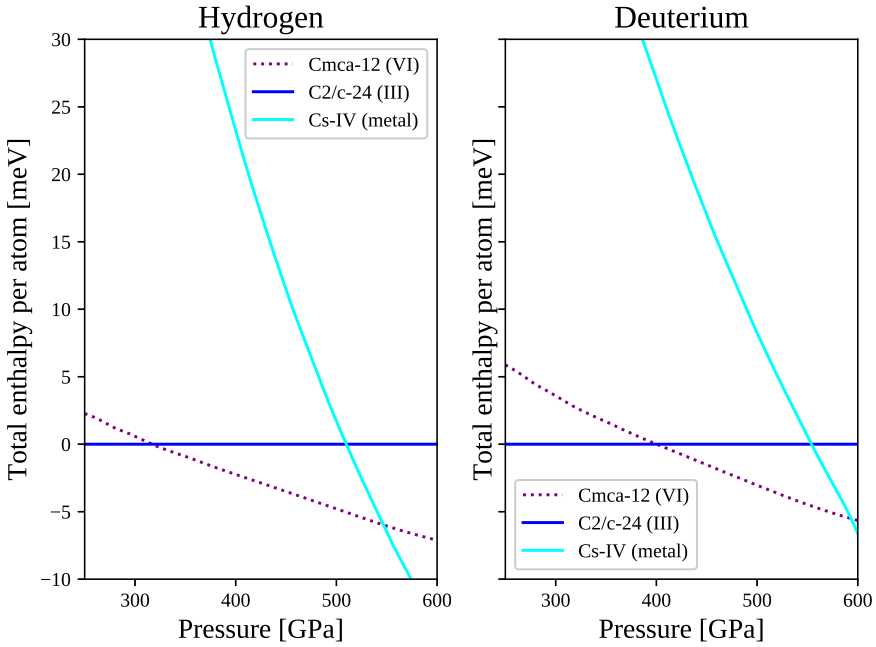

Figure 6.12. Phase diagram at high pressure. The metal transition is predicted to occur at 550 GPa from the Cmca-12 phase

Cmca-12 remains ground state up to 550 GPa, where the Cs-IV phase becomes less energetic (Figure 6.12). This transition also shows a big isotope effect, being shifted to about 600 GPa for Deuterium. Here we neglected Cmca-4, another phase competitive in DFT calculations, but unfavored by QMC[52].

6.4.1 Instability of C2/c-24

The transition from phase III to phase VI is immediately followed by an instability in the C2/c-24. This means that this phase is no more a local minimum after the transition.

The calculation of the stability of phase III can be done with the newly introduced Lanczos algorithm (see Chapter 3).

The unstable mode is an infrared active mode. Its static eigenvalue is reported as a function of pressure in Figure 6.13

This is a very important result, that has two consequences on experimental observations:

- Phase III→VI transition should not have hysteresis, phase III cannot exist above the transition.
- The first-order phase transition is anticipated by a detectable IR mode that decreases its energy before the transition.

The first evidence for phase III instability has been measured by LOD[5]. They notice a transition from phase III to a new metallic phase at about 415 GPa. They

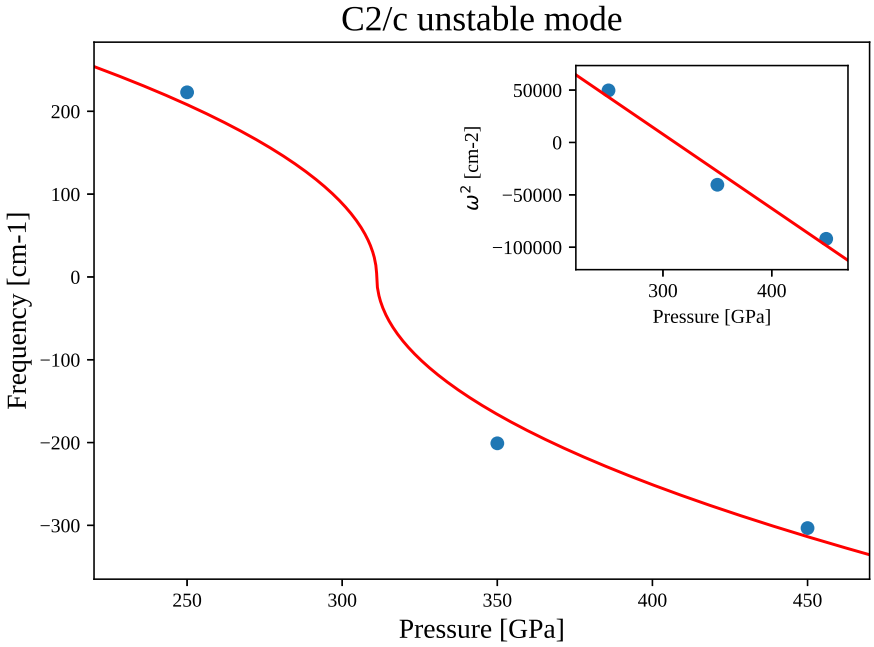

Figure 6.13. Static frequency of the unstable mode in phase C2/c-24. Negative values means imaginary (instability). In the inset, ω^2 (eigenvalue of the free energy Hessian), that is expected to be linear around the transition. Phase III becomes unstable at about 320 GPa, immediately after the first order phase transition (see Figure 6.11).

returned to phase III unloading pressure without hysteresis. The soft IR mode has still not been observed, however, no data have been reported in the low energy infrared region.

The instability of C2/c-24 could be enhanced by the DFT exchange-correlation error, as pointed out by Rillo et. al.[53], who perform a mixed path-integral with QMC as energy engine to compare with a standard PIMD-DFT. Another approximation that can overestimate the melting is the adiabatic approximation. Here, the vibron has an energy of about 0.5 eV. This value is comparable with the direct band gap. Therefore, phonons can induce electronic transition, and their degrees of freedom can mix with electronic ones. Up to now, there is no calculation pointing out the role of non-adiabatic effects in low-temperature hydrogen crystals.

6.5 The room temperature phases

The experimental phase diagram presents interesting features also at room temperature. Above 200 GPa, phase III transforms to phase VI. This is believed to be a mixed molecular/atomic phase.

The most supported candidate for this phase is a very low symmetric structure, Pc-48[17] (48 atoms in the unit cell, and only 2 symmetry operations). I studied this structure at 250 GPa, 350 GPa and 450 GPa in a 2x1x1 supercell (96 atoms).

The phase diagram is reported in Figure 6.14. During the SSCHA relaxation of the Pc-48 with quantum effect, I discovered two new crystal structures, namely

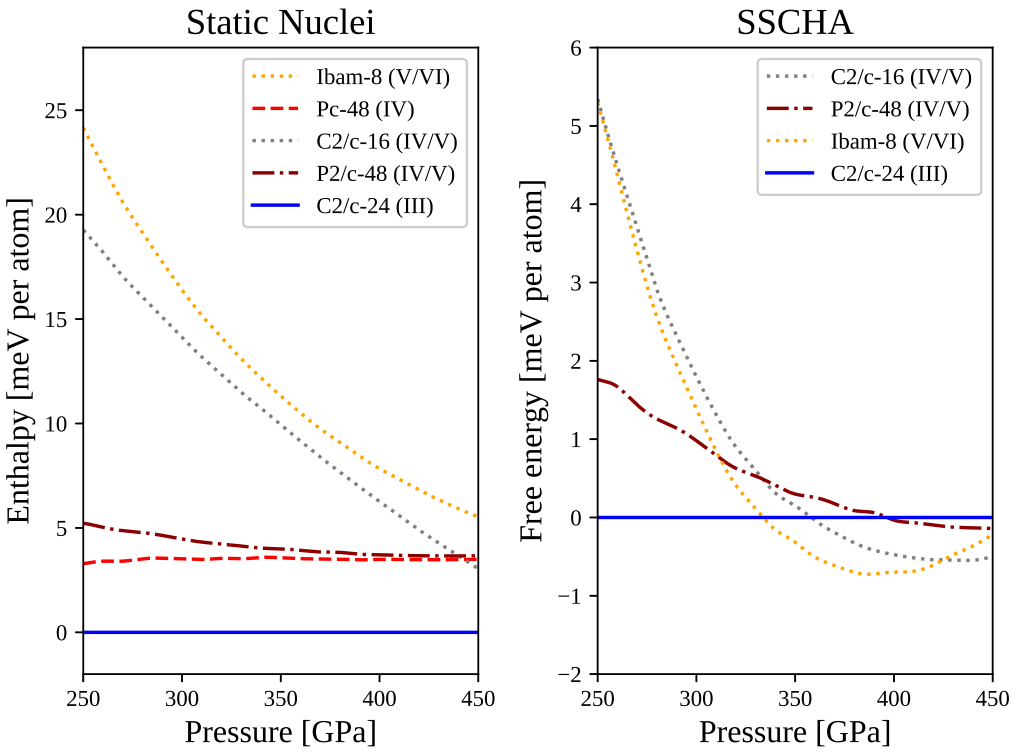

Figure 6.14. Free energy of the mixed phases. The Pc-48 disappears in the SCHA phase diagram as, even at the lowest pressure, it spontaneously transits into the P2/c-48. In the right panel the temperature of the calculation was 0 K, however it resulted to be almost unaffected up to 400 K.

P2/c-48 (at 250 GPa) and C2/c-16 (at 350 GPa).

I found quantum effects to suppress Pc-48 even at the lowest pressure simulated (250 GPa). When I perform the quantum relaxation, the structure recovers automatically more symmetries and atoms arrange themselves in the P2/c-48 structure. When increasing pressure to 350 GPa, the P2/c-48 further acquires more symmetries, even recovering a smaller unit cell. This new phase is C2/c-16 (not to be mistaken with C2/c-24, the candidate for phase III). The transitions Pc-48→P2/c-48→C2/c-16 are compatible with a second-order type by group-subgroup relationships. It is a progressive gain of symmetries.

This partially agrees with Monserrat et. al.[20]. Also in their diagram Pc-48 results destabilized in energy compared to a more symmetric phase ($Pca2_1$), identified using high-symmetry constraints for AIRSS. Interestingly, $Pca2_1$ is very similar to my new P2/c-48. The methodology they used to include quantum effects is the vibrational self-consistent field (VSCF), a theory developed by Monserrat et. al[21]. They claim $Pca2_1$ to be phase V, even if this result is not directly supported by the free energies they computed. Their claim is mainly based on Raman/IR calculation at the harmonic level using the PBE exchange-correlation and the static band gap of the structure. However, in Chapter 5, I show how these observables are strongly affected by quantum effects and anharmonicity. A more detailed discussion is necessary to correctly assess whether these structures describe phase IV or V.

Limiting our analysis only on the SSCHA+BLYP free energies, we predict the P2/c-48 to be a good candidate for phase IV, while Ibam-8 or C2/c-16 good candidates for the transition to phase V. The free energy difference in Figure 6.14 between C2/c-16 and Ibam-8 is compatible with the stochastic noise of the SSCHA. Ibam-8 is very similar to C2/c-16, but with 4 times more symmetries. This is the reason why their energy is very similar.

The Ibam-8 SSCHA+BLYP calculation is in sharp contrast with VSCF+BLYP[20]. I found Ibam-8 to be favored by quantum fluctuations compared to C2/c-24. Monserrat et al show the opposite behavior. This difference is probably due to the uncontrolled source of error in VSCF arising by the fit in the BO energy landscape. This can introduce very big errors in free energy differences[73]. Moreover, they did not include the effect on lattice relaxation.

However, both SCHA and VSCF show that temperature plays a very little role in stabilizing these phases compared to C2/c-24.

The free energy difference between C2/c-24 and both Pc-48, P2/c-48, Ibam-8 and C2/c-16 changes less than 1 meV per atom between 0 and 400 K.

This seems to contradict the fact that these phases are responsible for the observed phase IV, which should be favored at room-temperature.

However, this can be a failure of SCHA, as Pc-48 was shown to have one layer of molecules that can rotate[58, 53]. Rotation of molecules is ill-represented by a Gaussian wave-function. The SCHA can underestimate the free energy drop due to thermal activation of molecular rotations of mixed phases.

6.6 The electron-phonon on optical properties in the phase III→ VI transition

Here, we analyze the candidates for the phase III→VI transition observed at low temperatures while increasing pressure (355 GPa DNS[2], 380 GPa ETD[12], 415 GPa LOD[5], 440 GPa EDKW[4]).

ETD and LOD agree in identifying this phase as a bad metal, LOD show that this phase is opaque in the full IR spectrum down to 600 cm^{-1}, in contrast with what observed by DNS measuring the IR vibrational spectrum at high frequency. More recently, EDKW showed that phase III resistance drops above 350 GPa, indicating an indirect band gap closure, and behavior similar to those of a semi-metal. Their Raman measurement show no sharp transition until 440 GPa, where the Raman definitively disappears.

From the phase diagram simulation in Chapter 6 we showed that C2/c-24 structure, candidate for phase III, is stable only up to 325 GPa, then it transforms into a new phase, that could be either P62/c-24 or Cmca-12. Path-Integral with coupled electron-ion Monte Carlo showed that DFT calculations underestimates the barrier between C2/c-24 and other phases[53], therefore we may underestimate the transition pressure.

In this section, I simulate the optical properties including the electron-phonon scattering of C2/c-24, Cmca-12, and P62/c-24 to assess if this transition is in agreement with experimental results.

6.6.1 The dark metallic Hydrogen

In the previous chapter, our theoretical analysis conciliated the EDKW and LOD experimental results in phase III. Then, LOD showed that, at high pressure, phase III transits into an opaque new phase VI. This phase cannot be the shiny atomic metal[71], as it appears black. Thus, it must be another molecular metallic phase. LOD suggested it to be Cmca-12, basing on the DMC phase-diagram. Our more accurate phase-diagram agrees with this possibility but indicates also another possible candidate, P62/c-24.

The two phases are topologically very different. P62/c-24 (Figure 6.4) has graphene-like layers alternated by molecular layers, while Cmca-12 (Figure 6.3) is a pure molecular phase.

P62/c-24 is a metal protected by topology, thanks to the Dirac cones of the honeycomb layers. Cmca-12 is a metal with a closed indirect gap, similar to C2/c-24.

Both phases are bad metals, as they have a vanishing density of states (DOS) close to the Fermi level. This is in agreement with the requirements for phase VI.

The simulations of transmittance and reflectivity are reported in Figure 6.15 and 6.16 for Cmca-12 , while in Figure 6.17 and 6.18 for P62/c-24.

The two phases have very different behavior without electron-phonon effects. Cmca-12 has a very low plasma frequency, and it becomes transparent at low pressure for frequencies above 0.6 eV. This phase would have been a transparent metal. However, phonons affect the band structure and this phase becomes opaque due to the closure of its direct band gap, smaller to the one of C2/c-24. So this phase remains opaque at all pressures.

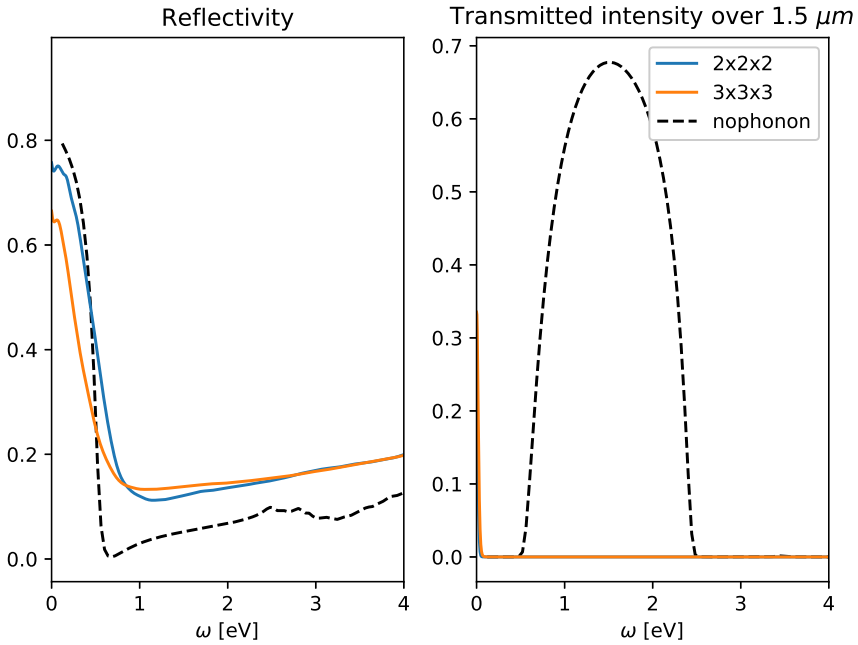

Figure 6.15. Reflectivity and transmittance for Cmca-12 at 360 GPa.

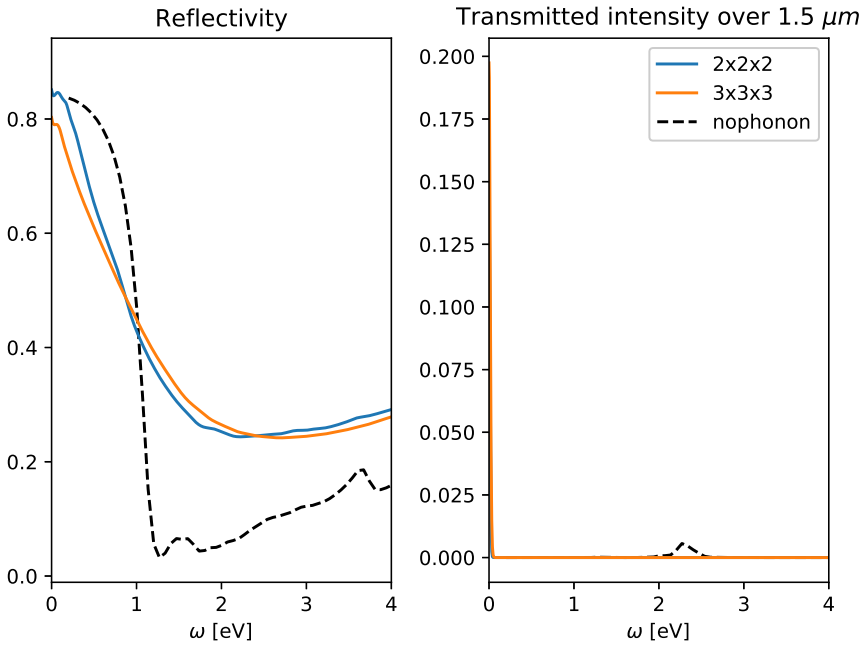

Figure 6.16. Reflectivity and transmittance for Cmca-12 at 465 GPa.

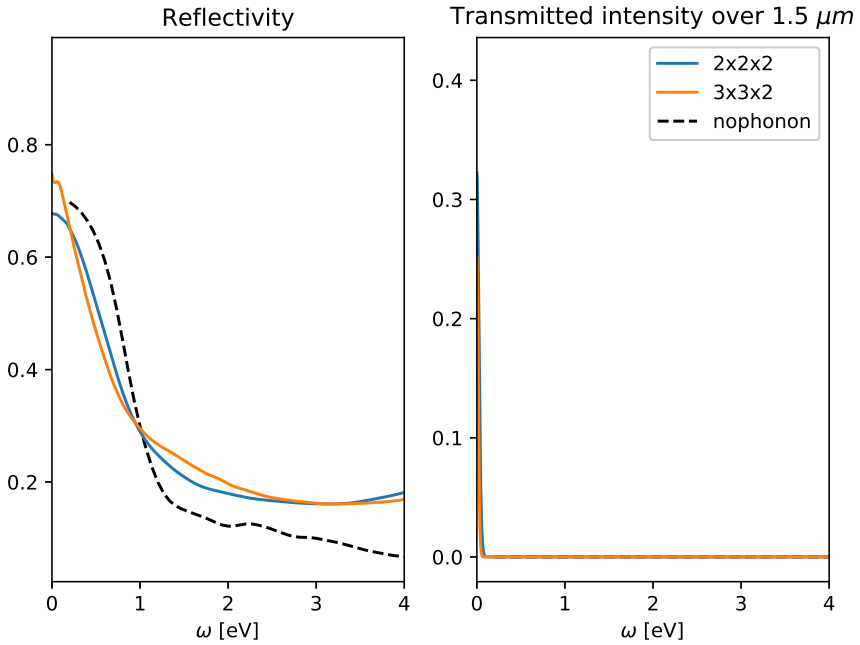

Figure 6.17. Reflectivity and transmittance for P62c-24 at 360 GPa.

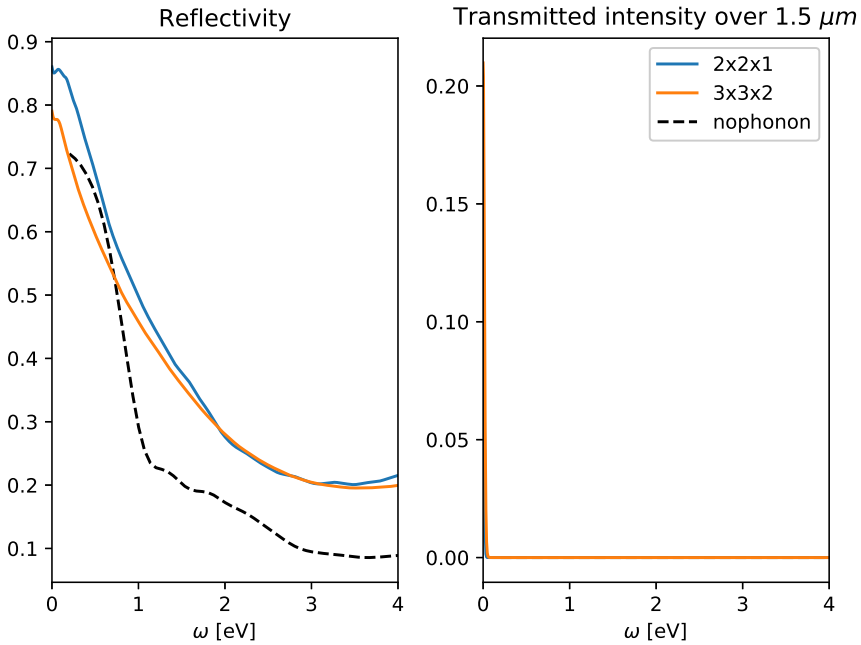

Figure 6.18. Reflectivity and transmittance for P62c-24 at 465 GPa.

The P62/c-24 is opaque by definition, as interband transitions are possible at any energies due to the presence of the Dirac cones close to the Fermi surface. Like graphite, it is black. Both phases have very low reflectivity, between 0.2 and 0.3 in the visible range, a very small value if compared to typical metals. This explains why this phase is not shiny and overcomes some of the critics made to the LOD's experiment[71].

Unfortunately, after electron-phonon is added, the two phases have very similar optical properties. One difference is in the reflectivity: the Cmca-12 reflectivity rises above 2 eV, while P62/c-24 decreases.

The only hope to distinguish between the two phases is the possibility to check their vibrational spectrum. This can be achieved by looking at the IR in reflection, or with Raman, tuning the laser wave-length to have a resonant transition.

In their work[2], DOS claimed to found a new insulator phase above 355 GPa, by seeing a sharp transition in the IR spectrum. They claim this phase to be Cmca-12. Here we completely rule out this hypothesis, as Cmca-12 is opaque at all the pressures when electron-phonon interaction is considered. Neither P62/c-24 nor Cmca-12 are compatible with the IR data reported by DNS, as IR light is completely absorbed by the sample at any pressure.

6.7 Conclusions

In this chapter, I simulated the phase-diagram of high-pressure hydrogen, fully accounting for both anharmonicity and quantum fluctuations.

I showed how the quantum effects and anharmonicity are important, and cannot be neglected to achieve the experimental precision. They stabilize high symmetric structures. Most of them are saddle points of the Born-Oppenheimer energy landscape where the harmonic approximation breaks down. By relaxing with SSCHA the C2/c-24 and the Pc-48, candidates for phase III and IV, I found three new structures competitive in energy more symmetric: P62/c-24, P2/c-48, and C2/c-16.

Moreover, C2/c-24 is unstable above 320 GPa and spontaneously breaks the C2/c symmetry group to fall into the hexagonal P62/c-24. We predict, therefore, phase III to transit to a new phase without hysteresis. This structure is competitive with the Cmca-12 in a broad range of pressures, up to 400 GPa, above which the Cmca-12 dominates. This transition has an impressive isotopic effect: it is shifted by 70 GPa to higher pressures in deuterium. The optical properties of both P62/c-24 and Cmca-12 are compatible with recent experiments[5, 4, 71] on phase VI, but rule out the possible insulator phase H2-PRE proposed by Dias et.al.[2].

Chapter 7

Conclusions

This thesis is focused on disclosing the experimental puzzle of the high-pressure phase diagram of hydrogen.

This is achieved through both theoretical developments and computer simulations. To fully account for the strong anharmonic character of the lightest element at high pressures, I employed the stochastic self-consistent harmonic approximation (SSCHA). In the first part of the thesis, I solve the condition problem in the free energy optimization algorithm. Thanks to this advance, I was able to simulate systems with many atoms and few symmetries, like high-pressure molecular phases of hydrogen. Then, I extend the SSCHA theory to compute the stress tensor and perform the variable cell optimization. This enables for the very first time to account for the quantum effects on the stress and relax using a full quantum treatment of the lattice parameters. The novelty of this approach is very important in hydrates, like LaH_{10}, where static simulations find a monoclinic ground state crystal. When quantum fluctuations are considered, the lattice transforms into an orthorhombic cell, recovering many symmetries and stabilizing a very strong electron-phonon coupling. This guarantees LaH_{10} to be the superconductor with the highest critical temperature known. This continuous transition cannot be described if the lattice is not allowed to relax with quantum effects[28]. Thanks to this mechanism, LaH_{10} is a superconductor more than 100 GPa below what predicted by harmonic calculations.

I also formulated the time-dependent generalization of the SCHA. Throughout the least action principle, I derived the quantum equation of motion for the nuclear wave-function. This new theory enables the study of out-of-equilibrium processes. Using linear response theory, I compute the dynamical Green functions to simulate the anharmonic Raman and IR spectra. High order force constants (beyond third order) can be included in the calculation of the Green functions with this new algorithm very efficiently.

Thanks to all these developments, I simulate the phase diagram of hydrogen. In particular, I show how phase III is deformed by quantum effects. The H_2 bonds grow as pressure increases and the unit cell is anisotropically deformed. These effects are bigger than the typical differences between DFT functionals and cannot be neglected.

Exploiting the new developments, I simulated the vibrational Raman/IR spectrum for phase III. Here, anharmonicity changes the spectral features, especially the

vibrons, introducing a finite life-time and shifting the average frequency of about $800\,\mathrm{cm}^{-1}$ to the harmonic simulation. This is an impressive result if we consider that most of the effort to identify the structures is currently based on harmonic calculations. After anharmonicity is considered, I showed how the simulated spectra for the C2/c-24 increase the agreement with the experimental data for phase III.

I also computed the direct/indirect band-gap closure and the impact of electron-phonon coupling, that affect the electronic properties by about 2.3 eV. The results I found conciliate the two apparent contradicting experiments[4, 5]. I found the sample to metalize by an indirect band gap closure at about 360 GPa (in agreement with[4]), but the sample remains transparent in the IR until 450 GPa due to the very small density of states close to the Fermi energy. The direct band gap closure, that can be measured by IR transmittance, is in excellent agreement with the experiments[5].

My simulations of the full phase-diagram underline how quantum effects favor high-symmetry phases. In particular, many unstable structures are stabilized by quantum fluctuations. I show how the most supported candidate for phase IV (Pc-48) acquires more symmetries even at the lowest simulated pressure of 250 GPa, and it continues gaining symmetries as pressure is increased. We conclude that a more symmetric partner of Pc-48 is phase IV and, probably, phase V is due by a new symmetrization of the atomic layer.

On the other hand, my new algorithm highlights the instability of phase III at 320 GPa. Following the soft mode, I found a new structure, namely P62/c-24, made by alternating layers of graphene-like honeycomb and molecules. This phase is competitive with the previously known Cmca-12. This unstable mode is IR active and it should be measured experimentally.

In general, I showed how quantum fluctuations smear out the strong differences between phases that are evident in the static calculation.

I also simulated phase III→VI transition at low temperatures and high-pressure. My findings show that there is no contradiction between recent experiments[5, 4]. Moreover, I found two candidates compatible with the experimental signatures of this phase[5]: the Cmca-12 (already proposed as a candidate for this phase) and P62/c-24 (a new phase proposed here). Moreover, P62/c-24 is connected by no barrier with phase III, in opposition to Cmca-12; this could explain the lack of hysteresis observed.

The novel techniques I developed during these three years have a high impact on quantum atomistic computer simulations. The big number of new phases I found for high-pressure hydrogen simply relaxing the nuclear wave-functions without any systematic search is a clear indication of how the SSCHA could strongly improve common structure search algorithms. These new tools will pave the way to ab-initio random structure search with fluctuations even at finite temperatures, pushing forward the field of material design and discovery.

Appendix A

Other published works

In this appendix, I attach all my works, published or preprinted. Here a list of the works that are directly related to this thesis:

1. **Pressure and stress tensor of complex anharmonic crystals**. It is the work referenced in Chapter 1 and 2. This work focuses on improvements I introduced in the SCHA algorithm (the preconditioning and the non-linear change of variables) as well as the stress tensor derivation. These tools are applied to shed light on the anharmonic effect on the ice thermal expansion.

2. **Quantum Crystal Structure in the 250 K Superconducting Lanthanum Hydride**. This work is currently under revision, and a preprint has been published. Here, we show how quantum effects completely reshape the free energy landscape of LaH_{10}, stabilizing a high symmetry structure with astonishing electron-phonon coupling (responsible for the very high-temperature superconductivity). Thanks to quantum effect, this structure remains the ground state more than 100 GPa under what predicted by classical simulations. This strengthens the hope of finding high-temperature superconductivity at a lower pressure than those predicted by current ab-initio structure searches.

3. **Phonon collapse and second-order phase transition in thermoelectric SnSe**. Here we use the SSCHA to prove that the phase transition between the high symmetry Cmcm and the charge density wave Pnma is a second-order phase transition, driven by a phonon-softening in the Y point of the Brillouin space. The strong anharmonicity is the main reason why this compound exhibits such high thermoelectric efficiency.

4. **Quantum Enhancement of Charge Density Wave in NbS2 in the Two-Dimensional Limit**. Here we clarified the difference between NbS_2 bulk and monolayer. Only the latter exhibits a 3x3 charge density wave, while anharmonicity completely suppresses it in the bulk. Moreover, we proved that a very small strain can switch off charge-density-wave in the monolayer, proposing a device that can easily tune on-off charge ordering with controlled electric fields.

5. **Quantum effects in muon spin spectroscopy within the stochastic self-consistent harmonic approximation**. Here we proved how the SSCHA

can perform very well in interpreting the results of muon spectroscopy. Antimuons behave like very light hydrogen ions. They are similar to defects and can be detected with magnetic fields. The intrinsically quantum and anharmonic behavior of the muon wave-function makes the SSCHA the best tool for interpreting the result of this technique.

6. **Strong anharmonicity and high thermoelectric efficiency in high-temperature SnS from first-principles**. Here, we analyze how anharmonicity affects the structural stability and the thermal transport of SnS. Similarly to SnSe, we proved that also this element displays a second-order phase transition. It is an optimal candidate for cheap and efficient thermoelectric material.

7. **Anharmonic melting of the charge density wave in single-layer $TiSe_2$**. Here, we study the charge density wave on $TiSe_2$. We show how excitons play no role in the single-layer $TiSe_2$ charge density wave ordering, even if correlation effects strongly affect the electronic properties of the material. This is achieved by simulating the melting temperature of the charge density wave by using both hybrid and semi-local functionals within the SSCHA, showing no difference. Moreover, we prove the doping of the substrate to play a relevant role in suppressing the temperature of the charge density wave, obtaining values very similar to the experimental ones.

Besides these works, during my PhD, I also collaborated to other projects:

1. **Manipulating impulsive stimulated Raman spectroscopy with a chirped probe pulse**. This is a mixed theoretical and experimental work, that I performed during my master thesis in the Femtoscopy lab and finished during the first year of my PhD. Here, I developed a theoretical model to describe the impulsive stimulated Raman scattering. Thanks to this model, I was able to interpret the experimental result and design a novel technique to increase the experimental accuracy. My findings were supported by experiments that I contributed to perform.

2. **Entropy evaluation sheds light on ecosystem complexity**. This is a work I did with my friend and colleague Mattia Miotto (a PhD student of my same year). We introduced a novel technique to measure entropy in out-of-equilibrium processes, as the dynamics of a toy-model ecosystem. Our findings shed new light on the dynamical phase transition of the ecosystem, as well as a change in the spatial ordering when predator hunting efficiency overcomes a fixed threshold.

3. **Gene heterogeneity drives the evolution of species**. Here we show how heterogeneity in gene expression affects the evolution of species. This is an important open quest in evolutionary biology. Most of the DNA that composes a complex organism (more than 98%) is non-coding and defined as *junk*. Even in the coding part, there is a strong differentiation between genes. This enormous source of heterogeneity that emerges from biology must be linked to the evolutionary process; however, the way is still unknown. In this work, we

identify heterogeneity in gene relevance as the control parameter that allows species to improve their fitness and originate new species. We also show how the absence of heterogeneity favors the mutational meltdown of the population causing the extinction of the species due to the slow accumulation of deleterious mutations in the genes. These findings are obtained by simulating a novel minimal model of an ecosystem on a lattice in which two species struggle for survival. Specimens carry a genome that codes the phenotype of each individual. Random mutations affect the genes in the genome. Heterogeneity is introduced by changing the weight of each gene on the overall individual phenotype. The results we present point out how this heterogeneity is fundamental for assuring survival, adaptability and sympatric speciations of populations.

Pressure and stress tensor of complex anharmonic crystals within the stochastic self-consistent harmonic approximation

Lorenzo Monacelli,[1] Ion Errea,[2,3] Matteo Calandra,[4] and Francesco Mauri[1,5]

[1]*Department of Physics, University of "La Sapienza", Rome, Italy*

[2]*Fisika Aplikatua 1 Saila, Bilboko Ingeniaritza Eskola, University of the Basque Country (UPV/EHU), Bilbao, Basque Country, Spain*

[3]*Donostia International Physics Center, Donostia-San Sebastian, Basque Country, Spain*

[4]*Sorbonne Université, Centre National de la Recherche Scientifique, Institut des Nanosciences de Paris, UMR7588, F-75252 Paris, France*

[5]*Graphene Labs, Fondazione Istituto Italiano di Tecnologia, Genova, Italy*

(Received 18 April 2018; revised manuscript received 14 June 2018; published 26 July 2018)

The self-consistent harmonic approximation (SCHA) allows the computation of free energy of anharmonic crystals considering both quantum and thermal fluctuations. Recently, a stochastic implementation of the SCHA has been developed, tailored for applications that use total energy and forces computed from first principles. In this paper, we extend the applicability of the stochastic SCHA to complex crystals, i.e., systems in which symmetries do not fix the inner coordinates and require the optimization of both the lattice vectors and the atomic positions. To this goal, we provide an expression for the evaluation of the pressure and stress tensor within the stochastic SCHA formalism. Moreover, we develop a more robust free-energy minimization algorithm, which allows us to perform the SCHA variational minimization very efficiently in systems having a broad spectrum of phonon frequencies and many degrees of freedom. We test and illustrate the approach with an application to the phase XI of water ice using density-functional theory. We find that the SCHA reproduces extremely well the experimental thermal expansion of ice in the whole temperature range between 0 and 270 K, in contrast with the results obtained within the quasiharmonic approximation, that underestimates the effect by about 25%.

DOI: 10.1103/PhysRevB.98.024106

I. INTRODUCTION

Atomic vibrations play a main role in many branches of physics and chemistry, as they are involved in thermodynamic, transport, and superconducting proprieties of materials and molecules. Many spectroscopic techniques, such as Raman and IR, measure how atoms vibrate. The standard approach to describe vibrations is the harmonic approximation, in which the Born-Oppenheimer (BO) energy surface is approximated as a $3N$-dimensional paraboloid around the ionic positions. The solutions of the harmonic Hamiltonian are well-defined noninteracting vibrational quasiparticles, phonons with an infinite lifetime and temperature-independent spectrum. Anharmonic effects, due to higher orders in the BO energy surface, introduce interactions between phonons. As a result, phonons acquire a finite lifetime that is responsible for thermal transport. Furthermore, phonon spectra become temperature dependent.

Anharmonic effects are commonly accounted for by perturbation theory, the validity range of which is limited only when the harmonic contribution dominates in the range defined by the quantum zero-point motion (ZPM). This is not the case of many interesting phenomena, such as systems undergoing a displacive second-order structural phase transition in which a phonon branch softens as a function of temperature, e.g., charge-density waves and ferroelectrics [1–12], or in solids largely affected by the ZPM, for example in hydrides or in molecular crystals containing H, like water and high-pressure phases of hydrogen [13–18]. Classical molecular dynamics (MD) for ions or methods based on it can be used to extract the nonperturbative anharmonic renormalized phonon dispersion [19–27]. However, within these approaches, quantum effects on nuclei are neglected. These methods are then inappropriate below the Debye temperature.

In order to correctly account for both quantum and anharmonic effects, the ideal technique is path-integral molecular dynamics (PIMD) [28–30], but its demanding computational cost limits its applicability to systems with few atoms or to the use of empirical potentials. To overcome these problems many self-consistent approximations have been developed [31,32]. Among them, the self-consistent harmonic approximation (SCHA) allows one to describe anharmonicity through a full-quantum variational theory. The stochastic implementation of the SCHA [16] (SSCHA) allows us to apply the powerful variational SCHA method to many systems with a lower numerical effort than MD and PIMD, making possible the calculation of nonperturbative anharmonic effects from first principles.

So far, the applications of the SSCHA method [15–17,33–35] have been limited to simple systems with high symmetry. The main reason is that the variational minimization as formulated in Ref. [16] can yield "runaway solutions" and become very inefficient in complex crystals that show a wide range of phonon frequencies and many degrees of freedom. Another limitation of the original SSCHA formulation is that it needs finite-difference approaches to estimate the effect of ionic fluctuations in the stress tensor, as it happens in the quasiharmonic approximation (QHA), which is extremely cumbersome for noncubic crystals. This hinders cell relaxation within the SSCHA.

In this paper, we efficiently overcome these difficulties by developing an equation for the stress tensor within the SCHA. Furthermore, we develop a more robust minimization algorithm based on an analytical preconditioner combined with a nonlinear change of variables that allows for efficient many-variables minimizations. Our developments pave the way to primitive cell relaxations including quantum and anharmonic effects avoiding finite difference approaches. Thanks to the improvements, we are able to drop the symmetry constraints and to study systems with little or no symmetry, as it is in molecular crystals.

We illustrate and benchmark the method with the phase XI of ice (H_2O), the perfect prototype of a complex molecular crystal. Ice XI is the ordered phase of common ice formed below 72 K in the presence of a small amount of an alkali-metal hydroxide [36]. It is commonly used to study quantum effects in water thanks to its great similarity to normal ice (Ih) [37,38]. Ice is characterized by the interplay between intramolecular covalent OH bonds and intermolecular hydrogen bonds. The great difference in strength of intermolecular and intramolecular forces makes ice phases acquire a very broad spectrum for their vibrational energies, from the very low-energy rotons to the large-energy vibrons. Moreover, this structure of ice experimentally exhibits at low temperature negative thermal expansion [39] and the "anomalous isotope volume effect" [37–40]: if hydrogen is replaced by deuterium, the crystal volume expands by about a 0.1%. This is the opposite behavior of what is usually observed when a heavier isotope is substituted in the crystal. These features make the XI phase of crystal ice a perfect benchmark for the here developed SSCHA algorithm (Secs. VI and VII).

This paper is organized as follows. We recall the basis of the SCHA algorithm in Sec. II. We introduce the stress tensor in the SCHA formalism in Sec. III. We discuss the stochastic implementation of the algorithm in Sec. IV. We face the issues of the SSCHA minimization algorithm in Sec. V: we get an ansatz on the condition number of the minimization process (Sec. V A), and provide two changes of variables that suppress it (Secs. V B and V C). Then, we benchmark the SCHA algorithm in ice XI in Sec. VI. Finally, Sec. VII reports the results computed with density functional theory (DFT) in the unit cell of ice XI, compared with the QHA. In Sec. VIII we summarize the main results of this paper. The paper is completed with three appendices, where the mathematical derivations of the presented equations are provided.

II. THE SELF-CONSISTENT HARMONIC APPROXIMATION

The SCHA is a variational principle on the BO free energy. The nuclear quantum Hamiltonian of a generic system can be defined in the BO approximation as

$$H = \sum_{n=1}^{N} \sum_{\alpha=1}^{3} \frac{p_n^{\alpha 2}}{2M_n} + V(\vec{R}, \{\vec{a}_i\}), \tag{1}$$

where V is the BO energy surface, M_n is the mass of the nth atom, p_n^α and $\vec{R}$ (R_n^α) are the momentum and position operators of the nuclei in the periodic cell (or supercell), N is the number of atoms, and $\{\vec{a}_i\}$ are the three unit-cell vectors. The α index identifies the Cartesian coordinate. Fixing the temperature T and the volume (i.e., the cell vectors $\{\vec{a}_i\}$), the free energy of the ionic Hamiltonian H is

$$F(\{\vec{a}_i\}) = \langle H \rangle_{\rho_H} + k_b T \, \langle \ln \rho_H \rangle_{\rho_H}, \tag{2}$$

where ρ_H is the equilibrium density matrix

$$\rho_H = \frac{e^{-\beta H}}{\mathrm{Tr}\, e^{-\beta H}}, \qquad \beta = \frac{1}{k_b T}, \tag{3}$$

and the brackets $\langle O \rangle_{\rho_H}$ indicate the average of the observable O according to the ρ_H density matrix:

$$\langle O \rangle_{\rho_H} = \mathrm{Tr}\,[\rho_H O]. \tag{4}$$

The equilibrium density matrix satisfies the free-energy least principle. Given a trial density matrix $\rho_{\mathcal{H}}$, we can define a free-energy functional the minimum of which is the free energy:

$$\mathcal{F}(\{\vec{a}_i\})[\rho_{\mathcal{H}}] = \langle H \rangle_{\rho_{\mathcal{H}}} + k_b T \, \langle \ln \rho_{\mathcal{H}} \rangle_{\rho_{\mathcal{H}}}, \tag{5}$$

$$F(\{\vec{a}_i\}) = \min_{\rho_{\mathcal{H}}} \mathcal{F}(\{\vec{a}_i\})[\rho_{\mathcal{H}}]. \tag{6}$$

The SCHA consists in the restriction of the possible trial density matrices to the equilibrium one obtained from a harmonic Hamiltonian:

$$\mathcal{H}_{\vec{\mathcal{R}},\mathbf{\Phi}} = \sum_{n=1}^{N} \sum_{\alpha=1}^{3} \frac{p_n^{\alpha 2}}{2M_n} + \mathcal{V}_{\mathbf{\Phi},\vec{\mathcal{R}}}(\vec{R}), \text{ where} \tag{7a}$$

$$\mathcal{V}_{\mathbf{\Phi},\vec{\mathcal{R}}}(\vec{R}) = \frac{1}{2} \sum_{\substack{n=1 \\ m=1}}^{N} \sum_{\substack{\alpha=1 \\ \beta=1}}^{3} u_n^\alpha \Phi_{nm}^{\alpha\beta} u_m^\beta, \text{ and} \tag{7b}$$

$$u_n^\alpha = R_n^\alpha - \mathcal{R}_n^\alpha, \tag{7c}$$

$$\rho_{\mathcal{H}} = \rho_{\vec{\mathcal{R}},\mathbf{\Phi}} = \frac{e^{-\beta \mathcal{H}_{\vec{\mathcal{R}},\mathbf{\Phi}}}}{\mathrm{Tr}\, e^{-\beta \mathcal{H}_{\vec{\mathcal{R}},\mathbf{\Phi}}}}. \tag{7d}$$

Here u_a^α is the displacement of the ath atom along the α direction with respect to a central position $\vec{\mathcal{R}}$, and $\Phi_{nm}^{\alpha\beta}$ is the matrix element of the real-space force constant matrix (we use bold font to indicate tensors and matrices). With the introduction of the auxiliary harmonic Hamiltonian it is possible to recast the free energy as

$$\mathcal{F}(\vec{\mathcal{R}}, \mathbf{\Phi}, \{\vec{a}_i\}) = F_{\mathbf{\Phi}} + \langle V - \mathcal{V}_{\mathbf{\Phi},\vec{\mathcal{R}}} \rangle_{\rho_{\vec{\mathcal{R}},\mathbf{\Phi}}}, \tag{8}$$

where $F_{\mathbf{\Phi}}$ is the exact free energy of the harmonic Hamiltonian:

$$F_{\mathbf{\Phi}}(T) = \sum_{\mu=1}^{3N} \left[\frac{\hbar \omega_\mu}{2} + \frac{1}{\beta} \ln\left(1 - e^{-\beta \hbar \omega_\mu}\right) \right], \tag{9}$$

where ω_μ and $\vec{e}_\mu$ are, respectively, the eigenvalues and eigenvectors of the $\mathbf{\Phi}$ matrix divided by the atomic masses:

$$\sum_{t=1}^{N} \sum_{\beta=1}^{3} \frac{\Phi_{st}^{\alpha\beta}}{\sqrt{M_s M_t}} e_{\mu t}^{\ \beta} = \omega_\mu^2 e_{\mu s}^{\ \alpha}. \tag{10}$$

The real free energy can, therefore, be approximated as the minimum of the free-energy functional [Eq. (8)] with respect

to $\vec{\mathcal{R}}$ and $\mathbf{\Phi}$:

$$\mathcal{F}(\vec{\mathcal{R}},\{\vec{a}_i\}) = \min_{\mathbf{\Phi}} \mathcal{F}(\vec{\mathcal{R}},\mathbf{\Phi},\{\vec{a}_i\}), \tag{11a}$$

$$\mathcal{F}(\{\vec{a}_i\}) = \min_{\mathbf{\Phi},\vec{\mathcal{R}}} \mathcal{F}(\vec{\mathcal{R}},\mathbf{\Phi},\{\vec{a}_i\}). \tag{11b}$$

From now on, when we drop either the $\vec{\mathcal{R}}$ or $\mathbf{\Phi}$ symbol, we mean the quantity computed in the value of that variable that minimizes the free energy. For example, the equilibrium SCHA density matrix is just ρ.

One of the advantages of using the harmonic Hamiltonian to restrict the $\rho_{\mathcal{H}}$ space is that we have a trivial physical interpretation of the minimization parameters. In fact $\vec{\mathcal{R}}$ represents the centroid positions of the atoms, i.e., the anharmonic average positions as measured by, e.g., diffraction experiments:

$$\vec{\mathcal{R}} = \langle \vec{R} \rangle_{\rho} . \tag{12}$$

In the same way, $\mathbf{\Phi}$ is related to the thermal and quantum fluctuations and defines the real-space density matrix broadening. Within the harmonic auxiliary Hamiltonian, the probability distribution function defined by the real-space density matrix is a product of Gaussians:

$$\rho_{\vec{\mathcal{R}},\mathbf{\Phi}}(\vec{u}) = \langle \vec{u} | \rho_{\vec{\mathcal{R}}\mathbf{\Phi}} | \vec{u} \rangle ,$$

$$\rho_{\vec{\mathcal{R}},\mathbf{\Phi}}(\vec{u}) = \sqrt{\det\left(\mathbf{\Upsilon}/2\pi\right)} \exp\left(-\frac{1}{2}\sum_{st\alpha\beta} \Upsilon_{st}^{\alpha\beta} u_s^{\alpha} u_t^{\beta}\right) \tag{13a}$$

where

$$\Upsilon_{st}^{\alpha\beta} = \sqrt{M_s M_t} \sum_{\mu} \frac{2\omega_{\mu}}{(1+2n_{\mu})\hbar} e_{\mu_s}^{\ \alpha} e_{\mu_t}^{\ \beta} \tag{13b}$$

and n_{μ} are the boson average occupation number for the μ mode. It is important to notice that ω_{μ} and $\vec{e}_{\mu}$ [Eq. (10)] are not directly equal to the physical phonons since they are constrained to be positive defined [35]. Instead, they are related to quantum and thermal fluctuations: they uniquely define the $\mathbf{\Upsilon}$ tensor.

It is possible to define the SCHA force as the derivative of the free energy [Eq. (11a)] with respect to the nuclear average positions:

$$-\frac{\partial \mathcal{F}}{\partial \mathcal{R}_n^{\alpha}}(\vec{\mathcal{R}},\{\vec{a}_i\}) = \left\langle f_n^{\alpha} - f_{\mathcal{H}_n}^{\alpha} \right\rangle_{\rho_{\vec{\mathcal{R}}}} , \tag{14}$$

where $\vec{f}$ and $\vec{f}_{\mathcal{H}}$ are, respectively, the BO and harmonic forces:

$$f_n^{\alpha} = -\frac{\partial V}{\partial R_n^{\alpha}}(\vec{R},\{\vec{a}_i\}), \tag{15}$$

$$f_{\mathcal{H}_n}^{\alpha} = -\frac{\partial \mathcal{V}_{\vec{\mathcal{R}},\mathbf{\Phi}}}{\partial R_n^{\alpha}} = -\sum_{m=1}^{N}\sum_{\beta=1}^{3} \Phi_{nm}^{\alpha\beta} u_m^{\beta}. \tag{16}$$

It is interesting to notice how the harmonic potential $\mathcal{V}_{\vec{\mathcal{R}},\mathbf{\Phi}}$ does not depend explicitly on the unit-cell vectors $\{\vec{a}_i\}$, while the BO energy $V(\vec{R},\{\vec{a}_i\})$ does.

To numerically minimize the SCHA free energy it is possible to use the steepest descent (SD) or conjugate gradient (CG) methods [41], both based on the knowledge of the gradient of the function to minimize. This can be expressed as a function of the averages of the BO and harmonic forces [16]:

$$\nabla_{\mathbf{\Phi}} \mathcal{F}(\vec{\mathcal{R}},\mathbf{\Phi},\{\vec{a}_i\}) = -\sum_{st\alpha\beta\mu} \sqrt{\frac{M_t}{M_s}} \left(e_{\mu_s}^{\ \alpha} \nabla_{\mathbf{\Phi}} \ln a_{\mu} + \nabla_{\mathbf{\Phi}} e_{\mu_s}^{\ \alpha}\right) \times \left\langle \left[f_s^{\alpha}(\vec{u}) - f_{\mathcal{H}_s}^{\alpha}(\vec{u})\right] u_t^{\beta} \right\rangle_{\rho_{\vec{\mathcal{R}},\mathbf{\Phi}}} e_{\mu_t}^{\ \beta}, \tag{17a}$$

$$\nabla_{\mathcal{R}_s^{\alpha}} \mathcal{F}(\vec{\mathcal{R}},\mathbf{\Phi},\{\vec{a}_i\}) = -\left\langle f_s^{\alpha} - f_{\mathcal{H}_s}^{\alpha} \right\rangle_{\rho_{\vec{\mathcal{R}},\mathbf{\Phi}}} . \tag{17b}$$

In the next section, we show how to implement the SCHA in an isobaric ensemble, allowing for the relaxation also of the unit cell. This is achieved thanks to the introduction of the stress tensor in the SCHA framework.

III. THE STRESS TENSOR IN THE SELF-CONSISTENT STOCHASTIC APPROXIMATION

To minimize the free energy with respect to the lattice parameters in a periodic system, knowledge of the stress tensor is crucial. The SCHA stress can be defined as

$$P_{\alpha\beta}(\vec{\mathcal{R}},\{\vec{a}_i\}) = -\frac{1}{\Omega} \left.\frac{\partial \mathcal{F}(\vec{\mathcal{R}},\{\vec{a}_i\})}{\partial \varepsilon_{\alpha\beta}}\right|_{\boldsymbol{\varepsilon}=0} , \tag{18}$$

where Ω is the volume of the system and the strain tensor $\varepsilon_{\alpha\beta}$ identifies a generic deformation, where both the lattice parameters and the average central position are affected:

$$a_i'^{\alpha} = a_i^{\ \alpha} + \sum_{\beta=1}^{3} \varepsilon_{\alpha\beta} a_i^{\ \beta}, \tag{19a}$$

$$\mathcal{R}_n'^{\alpha} = \mathcal{R}_n^{\alpha} + \sum_{\beta=1}^{3} \varepsilon_{\alpha\beta} \mathcal{R}_n^{\beta}. \tag{19b}$$

This is equivalent to performing a strain keeping fixed the internal crystal coordinates of the system. The final result can be divided into three main contributions (see Appendix A for the proof):

$$P_{\alpha\beta}(\vec{\mathcal{R}},\{\vec{a}_i\}) = P_{\alpha\beta}^{H}(\vec{\mathcal{R}},\{\vec{a}_i\}) + P_{\alpha\beta}^{\mathrm{FLC}}(\vec{\mathcal{R}},\{\vec{a}_i\}) + P_{\alpha\beta}^{\mathrm{FRC}}(\vec{\mathcal{R}},\{\vec{a}_i\}), \tag{20}$$

where the $P_{\alpha\beta}^{H}(\vec{\mathcal{R}})$ is the static contribution, i.e., the stress tensor computed without quantum and thermal fluctuations (classical with $T = 0$), $P_{\alpha\beta}^{\mathrm{FLC}}$ is the contribution of the fluctuations to the stress, and $P_{\alpha\beta}^{\mathrm{FRC}}$ is an extra term that takes into account the work necessary to move the centroids according to the applied strain $\boldsymbol{\varepsilon}$:

$$P_{\alpha\beta}^{H}(\vec{R},\{\vec{a}_i\}) = -\frac{1}{\Omega} \left.\frac{\partial V(\vec{R},\{\vec{a}_i\})}{\partial \varepsilon_{\alpha\beta}}\right|_{\boldsymbol{\varepsilon}=0} , \tag{21a}$$

$$P_{\alpha\beta}^{\mathrm{FLC}}(\vec{\mathcal{R}},\{\vec{a}_i\}) = \langle P_{\alpha\beta}^{H}(\vec{R},\{\vec{a}_i\}) \rangle_{\rho_{\vec{\mathcal{R}}}} - P_{\alpha\beta}^{H}(\vec{\mathcal{R}},\{\vec{a}_i\}) - \frac{1}{2\Omega}\sum_{s=1}^{N} \left\langle \left(f_{\mathcal{H}_s}^{\alpha} u_s^{\beta} + f_{\mathcal{H}_s}^{\beta} u_s^{\alpha}\right) \right\rangle_{\rho_{\vec{\mathcal{R}}}} , \tag{21b}$$

$$P^{\mathrm{FRC}}_{\alpha\beta}(\vec{\mathcal{R}},\{\vec{a}_i\}) = \frac{1}{2\Omega}\sum_{s=1}^{N}\left(\mathcal{R}^{\beta}_{s}\left\langle f^{\alpha}_{s} - f_{\mathcal{H}^{\alpha}_{s}}\right\rangle_{\rho_{\vec{\mathcal{R}}}} + \mathcal{R}^{\alpha}_{s}\left\langle f^{\beta}_{s} - f_{\mathcal{H}^{\beta}_{s}}\right\rangle_{\rho_{\vec{\mathcal{R}}}}\right). \tag{21c}$$

The last term in Eq. (21b) makes fluctuations on pressure disappear in a pure harmonic crystal (see Appendix A). The force term, i.e., Eq. (21c), is nonzero only if the SCHA centroids $\vec{\mathcal{R}}$ are not in the equilibrium configuration, i.e., the SCHA force Eq. (14) on each atom is not zero, and it is independent of the choice of the origin (the sum of the forces over atom indices is zero).

Equation (21) can be computed once we know the BO surface $V(\vec{R},\{\vec{a}_i\})$, the atomic force $f^{\alpha}_{s}(\vec{R},\{\vec{a}_i\})$, and the stress tensors $P^{H}_{\alpha\beta}(\vec{R},\{\vec{a}_i\})$ for each ionic displacement $\vec{R}$ in the ensemble of the configurations distributed according to $\rho_{\vec{\mathcal{R}}}(\vec{R})$. In Sec. IV we discuss an efficient stochastic implementation to numerically compute this average.

The computation of the SCHA stress tensor enables the complete unit-cell relaxation in isobaric conditions (fixing the external P^* pressure). This is done by minimizing the Gibbs free energy, that is obtained from the Helmholtz free energy through the Legendre transform:

$$\mathcal{G}(\vec{\mathcal{R}},P^*) = \mathcal{F}(\vec{\mathcal{R}},\{\vec{a}_i\}) + P^*\,\Omega(\{\vec{a}_i\}). \tag{22}$$

IV. THE STOCHASTIC IMPLEMENTATION

The SCHA algorithm can be implemented by performing the stochastic evaluation of all the averages. Thanks to the fact that the density matrix is a multidimensional Gaussian function [Eq. (13a)], it is possible to generate an ensemble distributed according to $\rho_{\vec{\mathcal{R}},\mathbf{\Phi}}$ without any Metropolis algorithm [16], and the average of a generic observable $O(\vec{R})$ can be computed through Monte Carlo integration:

$$\langle O(\vec{R})\rangle_{\rho_{\vec{\mathcal{R}},\mathbf{\Phi}}} = \frac{1}{N_c}\sum_{\vec{R}_I} O(\vec{R}_I), \tag{23}$$

where N_c and $\vec{R}_I$ are, respectively, the dimension and the configurations of the ensemble. To avoid regenerating the ensemble at each minimization step it is convenient to introduce the importance sampling reweighting [16]:

$$\rho_I = \frac{\rho_{\vec{\mathcal{R}},\mathbf{\Phi}}(\vec{R}_I)}{\rho_{\vec{\mathcal{R}}_{\mathrm{SG}},\mathbf{\Phi}_{\mathrm{SG}}}(\vec{R}_I)} \tag{24}$$

where $\rho_{\vec{\mathcal{R}}_{\mathrm{SG}},\mathbf{\Phi}_{\mathrm{SG}}}(\vec{R}_I)$ is the density matrix used to extract the ensemble configurations, i.e., computed with the starting guess for the centroid positions $\vec{\mathcal{R}}_{\mathrm{SG}}$ and the auxiliary dynamical matrix $\mathbf{\Phi}_{\mathrm{SG}}$. Then, the average of the observable O in a generic value of $\vec{\mathcal{R}}$ and $\mathbf{\Phi}$ can be computed through

$$\langle O(\vec{R})\rangle_{\rho_{\vec{\mathcal{R}},\mathbf{\Phi}}} = \frac{1}{N_c}\sum_{\vec{R}_I}\rho_I\,O(\vec{R}_I). \tag{25}$$

The reweighting procedure allows us to overtake the usually high computational effort required by the SSCHA minimization. In fact, the computation of the SCHA free-energy gradient [16], as well as the SCHA stress tensor [Eq. (21)], requires only the knowledge of the first derivative of the BO energy in the ensemble, that can be obtained just in one total-energy calculation per configuration thanks to the Hellmann-Feynman theorem. Moreover, the total-energy calculation can be computed only one time in the starting ensemble of configurations $\vec{R}_I$, and then recycled on the whole minimization thanks to the reweighting. When the new variables $\vec{\mathcal{R}}$ and $\mathbf{\Phi}$ are too distant from the initial ones, $\vec{\mathcal{R}}_{\mathrm{SG}}$ and $\mathbf{\Phi}_{\mathrm{SG}}$, the ensemble is no longer able to provide a good estimation of the stochastic averages and it must be reextracted. Thus, the overall computational effort to run an *ab initio* SSCHA calculation is given by the number of times the initial ensemble is regenerated.

It is crucial to improve the reliability of the ensemble, in order to minimize the number of times the initial ensemble is regenerated during the SSCHA free-energy optimization. To this purpose, we adopt both a *symmetrized sampling* and a stochastic threshold to evaluate the important sampling accuracy.

The real-space density matrix is a symmetric distribution, $\rho_{\vec{\mathcal{R}},\mathbf{\Phi}}(\vec{u}) = \rho_{\vec{\mathcal{R}},\mathbf{\Phi}}(-\vec{u})$, and all observables required in the SSCHA free-energy minimization are purely even or odd terms of the Taylor expansion of $V(\vec{R},\{\vec{a}_i\})$ in $(\vec{R}-\vec{\mathcal{R}})$. To reduce the stochastic noise we implemented the symmetrized sampling [42]: for each displacement $\vec{u}$ generated, also its opposite $-\vec{u}$ is included in the ensemble. This analytically cancels all the noncontributing terms in the Taylor expansion of the BO energy. It is important to notice that this advantage is lost when $\vec{\mathcal{R}} \neq \vec{\mathcal{R}}_{\mathrm{SG}}$. However, we still find the symmetrized sampling to be convenient to reduce the stochastic noise even if the centroids do not match perfectly the starting guess.

The previous estimator of the importance sampling accuracy used by Errea *et al.* [16] was the check on the ρ_I normalization:

$$\left|\frac{1}{N_c}\sum_{I=1}^{N_c}\rho_I - 1\right| < \eta. \tag{26}$$

However, this threshold can be exceeded if all the weight constantly drifts from the uniform value, or it can remain satisfied if they spread a lot. Thus, a much better estimator that considers the spreading of the different configuration weights can be implemented. In order to improve the reliability of the reweighting procedure we found more reliable the Kong-Liu effective sample size [43]:

$$N_{\mathrm{eff}} = \frac{\left(\sum_I \rho_I\right)^2}{\sum_I \rho_I^2} < N_c. \tag{27}$$

A critical threshold η' can be defined as

$$\frac{N_{\mathrm{eff}}}{N_c} > \eta'. \tag{28}$$

If the weight ρ_I of a configuration goes to zero, it does not contribute to the averages. The effective sample size counts how many configurations are actually contributing to the Monte Carlo average [Eq. (25)], even if the ρ_I are properly normalized.

We set $\eta' = 0.6$ in all the simulations reported in this paper. If the critical threshold is overcome, the minimization

is stopped and an ensemble is generated with the final trial density matrix $\rho_{\vec{\mathcal{R}},\mathbf{\Phi}}$.

V. MINIMIZATION INSTABILITIES AND RUNAWAY SOLUTIONS

The SSCHA algorithm consists in minimizing the free energy through the stochastic evaluation of its gradient [Eq. (17)], employing the SD or CG algorithm, and taking advantage of reweighting to perform multiple SD or CG steps without recomputing energies and forces of the ensemble at each step. However, this minimization procedure was empirically found to be very difficult in some systems, especially in those near a structural instability, where a phonon mode frequency softens to zero, while all the other modes are substantially higher in energy, or molecular crystals, in which hard intermolecular vibrations coexist with low-energy intramolecular modes. In these cases, of very great physical interest, the stochastic free-energy minimization requires a large number of ensemble regenerations (and consequently a large number of first-principles force calculations) to converge. Moreover, the minimization can lead to runaway solutions: fake nonphysical solutions of the SCHA self-consistency where the auxiliary dynamical matrix $\mathbf{\Phi}$ is not positive defined.

To understand the convergence properties we consider the SCHA free energy close to the minimum. It can be approximated as a quadratic form in the minimization variables ($\vec{\mathcal{R}}$ and $\mathbf{\Phi}$). Under this condition, the SCHA free energy is expressed by the Hessian matrix $\boldsymbol{A}$ with respect to those variables. From the Hessian matrix it is possible to define the condition number [44] C, as

$$C = \frac{\max \lambda_{\boldsymbol{A}}}{\min \lambda_{\boldsymbol{A}}}, \tag{29}$$

where $\lambda_{\boldsymbol{A}}$ is a generic eigenvalue of the $\boldsymbol{A}$ matrix. In the limit in which the number of degrees of freedom is much greater than the number of minimization steps, the SD and the CG algorithms converge into a fixed threshold with almost N steps proportional [41] to

$$N_{\mathrm{SD}} \propto C, \tag{30a}$$

$$N_{\mathrm{CG}} \propto \sqrt{C}. \tag{30b}$$

In the SCHA case, the number of minimization steps is proportional to the number of times the critical threshold η' is overcome. Then, this number must be carefully optimized, since each time the ensemble is reextracted the *ab initio* energies and forces for each configuration must be computed. This calculation is the overall computational cost of the algorithm. In the next sections, we provide an ansatz for the condition number, unveiling that it dramatically diverges in the aforesaid cases. We further provide two ways to prevent this divergence, paving the way for the application of SSCHA in these systems.

A. Hessian matrix

In this section, we provide an analytical guess of the free-energy Hessian matrix $\boldsymbol{A}$ with respect to the minimization variable $\mathbf{\Phi}$. In general, this is not possible, since computing the real Hessian matrix corresponds to solving exactly the problem. However, we can perform the computation in an analytical test case that, hopefully, will enclose all the physics of the minimization problems incurred so far. This is a purely harmonic system, described by a harmonic Hamiltonian. From now on we introduce a compact notation to describe both Cartesian and atomic indices ($v_a = v_s^\alpha$):

$$H = \frac{1}{2}\sum_a \frac{(p_a)^2}{2M_a} + \frac{1}{2}\sum_{ab} u_a K_{ab} u_b. \tag{31}$$

The free-energy Hessian matrix with respect to the $\mathbf{\Phi}$ variable can be computed analytically. The steps that lead to the following result are reported in Appendix B:

$$A^{abcd}_{\mathbf{\Phi}} = \left.\frac{\partial^2 \mathcal{F}(\vec{\mathcal{R}},\mathbf{\Phi},\{\vec{a}_i\})}{\partial \Phi_{ab}\partial \Phi_{cd}}\right|_{\mathbf{\Phi}=\mathbf{K}} = \frac{1}{2}\mathcal{P}_{ab}\mathcal{P}_{cd}(\Lambda^{abcd} + \Lambda^{abdc}), \tag{32}$$

where the $\mathbf{\Lambda}$ rank-4 tensor is the same as that introduced by Bianco *et al.* [35], and $\mathcal{P}$ is a symmetrization factor:

$$\Lambda^{abcd} = -\frac{\hbar}{4}\sum_{\mu\nu}\frac{1}{\omega_\mu\omega_\nu}\frac{e^a_\nu e^b_\mu e^c_\nu e^d_\mu}{\sqrt{M_a M_b M_c M_d}} \times \begin{cases} \dfrac{2n_\nu+1}{2\omega_\nu} - \dfrac{dn_\nu}{d\omega_\mu} & \omega_\nu = \omega_\mu \\ \dfrac{n_\mu + n_\nu + 1}{\omega_\mu + \omega_\nu} - \dfrac{n_\mu - n_\nu}{\omega_\mu - \omega_\nu} & \omega_\nu \neq \omega_\mu \end{cases}, \tag{33}$$

$$\mathcal{P}_{ab} = \sqrt{2}(1-\delta_{ab}) + \delta_{ab}. \tag{34}$$

Here the ω_μ and $\vec{e}_\mu$ are the frequencies and polarization vectors of the $\boldsymbol{K}$ matrix. These are, indeed, equal to the $\mathbf{\Phi}$ matrix in the minimum of the SCHA free energy, and represent the real phonons of the system.

The $\mathbf{\Lambda}$ matrix can be diagonalized analytically if we consider the case of all equal masses:

$$\sum_{cd}\Lambda^{abcd} e^c_\mu e^d_\nu = \tilde{\lambda}_{\mu\nu} e^a_\mu e^b_\mu. \tag{35}$$

We can obtain an easy expression of the spectrum of the Hessian matrix in the pure quantum limit $T \to 0$ and the pure classical limit $T \to \infty$:

$$\lim_{T\to 0}\tilde{\lambda}_{\mu\nu} = -\frac{\hbar}{4M^2}\frac{1}{\omega_\mu\omega_\nu(\omega_\mu+\omega_\nu)}, \tag{36a}$$

$$\lim_{T\to\infty}\tilde{\lambda}_{\mu\nu} = -\frac{1}{4\beta M^2}\frac{1}{\omega_\mu^2\omega_\nu^2}\left[1 + \frac{\omega_\mu\omega_\nu}{(\omega_\mu+\omega_\nu)^2}\right]. \tag{36b}$$

Therefore, the Hessian matrix spectrum goes as ω_μ^{-3} in the quantum limit and ω_ν^{-4} in the classical one. We can compute the condition numbers, as defined in Eq. (29):

$$C_{\mathbf{\Phi},T=0} \approx \left(\frac{\omega_{\max}}{\omega_{\min}}\right)^3, \tag{37a}$$

$$C_{\mathbf{\Phi},T\to\infty} \approx \left(\frac{\omega_{\max}}{\omega_{\min}}\right)^4. \tag{37b}$$

This unveils the pathology in the SSCHA minimization if the gradient is taken with respect to $\mathbf{\Phi}$ as presented in

Ref. [16] for the mentioned systems: when we have a structural instability, there is a phonon mode that softens to zero ($\omega_{\text{min}} \to 0$), producing a diverging condition number $C \to \infty$. In the same way, molecular crystals have a broad spectrum, with a very large difference between the highest vibron modes and the lowest intermolecular ones (for example, in common ice we have $\omega_{\text{max}}/\omega_{\text{min}} \sim 10^3$). This yields extremely high values of the condition numbers, that makes the minimization really difficult and requires lots of energy and force recalculations to achieve a good minimization. This obviously hinders the fully *ab initio* application of the SSCHA method in complex systems.

B. Nonlinear change of variable

The condition number is a function of the minimization variables. Therefore, a simple change of variables can result in a powerful improvement in the minimization algorithm. In this section, we show that it is possible to almost completely solve the divergences occurring in the condition numbers [Eq. (37)] with a simple nonlinear change in the $\boldsymbol{\Phi}$ auxiliary matrix. Moreover, we can also completely cancel the aforesaid runaway solutions. The runaway solutions are fake nonphysical solutions of the SCHA that may arise during the minimization if the $\boldsymbol{\Phi}$ matrix is not positive definite. In order to avoid this problem, one could perform a constrained minimization. It is difficult to implement this kind of constraint with the SD or CG algorithm. We find it much more convenient to introduce a nonlinear change of variables, where we replace the auxiliary dynamical matrix $\boldsymbol{\Phi}$ with one of its even roots:

$$\boldsymbol{\Phi} \to \sqrt[2n]{\boldsymbol{\Phi}}. \tag{38}$$

This mathematically constrains the minimization to have only positive defined matrices $\boldsymbol{\Phi}$. Does this nonlinear change improve the condition number on the minimization?

We can compute the Hessian matrix $\boldsymbol{A}_{\sqrt{\boldsymbol{\Phi}}}$ with respect to the square root of $\boldsymbol{\Phi}$ where $\boldsymbol{\Phi}$ minimizes the free energy:

$$\boldsymbol{A}_{\sqrt{\boldsymbol{\Phi}}} = \frac{\partial^2 \mathcal{F}(\vec{\mathcal{R}}, \boldsymbol{\Phi}, \{\vec{a}_i\})}{\partial \sqrt{\boldsymbol{\Phi}} \partial \sqrt{\boldsymbol{\Phi}}} = \boldsymbol{\Phi} \boldsymbol{A}_{\boldsymbol{\Phi}} + 2\sqrt{\boldsymbol{\Phi}} \boldsymbol{A}_{\boldsymbol{\Phi}} \sqrt{\boldsymbol{\Phi}} + \boldsymbol{A}_{\boldsymbol{\Phi}} \boldsymbol{\Phi}, \tag{39}$$

where $\boldsymbol{A}_{\boldsymbol{\Phi}}$ is the rank-4 Hessian with respect to $\boldsymbol{\Phi}$ [Eq. (32)]. The procedure can be iterated to obtain any even root of $\boldsymbol{\Phi}$. Here we report also the $\sqrt[4]{\boldsymbol{\Phi}}$ expression, since, as we will show, it has a very favorable condition number:

$$\boldsymbol{A}_{\sqrt[4]{\boldsymbol{\Phi}}} = \sqrt{\boldsymbol{\Phi}} \boldsymbol{A}_{\sqrt{\boldsymbol{\Phi}}} + 2\sqrt[4]{\boldsymbol{\Phi}} \boldsymbol{A}_{\sqrt{\boldsymbol{\Phi}}} \sqrt[4]{\boldsymbol{\Phi}} + \boldsymbol{A}_{\sqrt{\boldsymbol{\Phi}}} \sqrt{\boldsymbol{\Phi}}. \tag{40}$$

We can easily compute the condition numbers in the new variables if all the masses are equal substituting Eq. (32) into Eqs. (39) and (40) (recalling that $\boldsymbol{\Phi} \sim \omega^2$):

$$C_{\sqrt[2]{\boldsymbol{\Phi}}, T=0} \sim \left(\frac{\omega_{\text{max}}}{\omega_{\text{min}}}\right), \qquad C_{\sqrt[2]{\boldsymbol{\Phi}}, T\to\infty} \sim \left(\frac{\omega_{\text{max}}}{\omega_{\text{min}}}\right)^2, \tag{41}$$

$$C_{\sqrt[4]{\boldsymbol{\Phi}}, T=0} \sim 1, \qquad C_{\sqrt[4]{\boldsymbol{\Phi}}, T\to\infty} \sim \left(\frac{\omega_{\text{max}}}{\omega_{\text{min}}}\right). \tag{42}$$

The nonlinear change of variable $\boldsymbol{\Phi} \to \sqrt[4]{\boldsymbol{\Phi}}$ both avoids the nonphysical runaway solutions constraining the minimization space to admit only positive defined matrices and strongly suppress the condition number, making it independent on the phonon frequencies in the $T = 0$ case and suppressing it by a fourth root in the classical case.

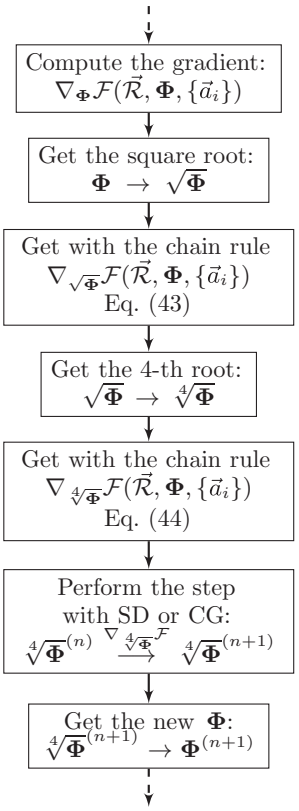

FIG. 1. Flowchart on a minimization step with the $\boldsymbol{\Phi} \to \sqrt[4]{\boldsymbol{\Phi}}$ change of variables.

In practice, the minimization in the $\sqrt[4]{\boldsymbol{\Phi}}$ is performed by computing the free-energy gradient with respect to the new variable adopting the chain rule on the derivatives:

$$\nabla_{\sqrt{\boldsymbol{\Phi}}} \mathcal{F}(\vec{\mathcal{R}}, \boldsymbol{\Phi}, \{\vec{a}_i\}) = \sqrt{\boldsymbol{\Phi}} \nabla_{\boldsymbol{\Phi}} \mathcal{F}(\vec{\mathcal{R}}, \boldsymbol{\Phi}, \{\vec{a}_i\}) + \nabla_{\boldsymbol{\Phi}} \mathcal{F}(\vec{\mathcal{R}}, \boldsymbol{\Phi}, \{\vec{a}_i\}) \sqrt{\boldsymbol{\Phi}}, \tag{43}$$

$$\nabla_{\sqrt[4]{\boldsymbol{\Phi}}} \mathcal{F}(\vec{\mathcal{R}}, \boldsymbol{\Phi}, \{\vec{a}_i\}) = \sqrt[4]{\boldsymbol{\Phi}} \nabla_{\sqrt{\boldsymbol{\Phi}}} \mathcal{F}(\vec{\mathcal{R}}, \boldsymbol{\Phi}, \{\vec{a}_i\}) + \nabla_{\sqrt{\boldsymbol{\Phi}}} \mathcal{F}(\vec{\mathcal{R}}, \boldsymbol{\Phi}, \{\vec{a}_i\}) \sqrt[4]{\boldsymbol{\Phi}}. \tag{44}$$

The minimization step is updated as described by the flowchart reported in Fig. 1.

C. Preconditioning

Even if the fourth root change of variable considerably improves the condition number, for high-temperature calculations it still depends on the phonon frequencies linearly, which could be problematic when a phonon mode goes close to zero near a structural phase transition. The SSCHA minimization algorithm corresponds to finding the zeros of the free-energy gradient:

$$\nabla_{\boldsymbol{\Phi}} \mathcal{F}(\vec{\mathcal{R}}, \boldsymbol{\Phi}, \{\vec{a}_i\}) = 0. \tag{45}$$

From the above system, the SD and the CG algorithms are derived. However, since $\boldsymbol{A}_{\boldsymbol{\Phi}}$ is a positive defined matrix, the

solution of the SCHA equation coincides with the solution of the auxiliary problem:

$$\boldsymbol{A}_{\boldsymbol{\Phi}}^{-1}\nabla_{\boldsymbol{\Phi}}\mathcal{F}(\vec{\mathcal{R}},\boldsymbol{\Phi},\{\vec{a}_i\}) = 0. \tag{46}$$

It can be shown [41,44] that the condition number on the problem defined by Eq. (46) is equal to 1 if $\boldsymbol{A}$ is the exact Hessian matrix of $\mathcal{F}(\vec{\mathcal{R}},\boldsymbol{\Phi},\{\vec{a}_i\})$. We can, therefore, use the analytic guess of the Hessian matrix $\boldsymbol{A}$ provided in Eq. (32) to redefine the minimization algorithm. The SD algorithm on the problem of Eq. (46) becomes

$$\boldsymbol{\Phi}^{(n+1)} = \boldsymbol{\Phi}^{(n)} - \lambda \boldsymbol{A}_{\boldsymbol{\Phi}}^{-1}\nabla_{\boldsymbol{\Phi}}\mathcal{F}(\vec{\mathcal{R}}^{(n)},\boldsymbol{\Phi}^{(n)},\{\vec{a}_i\}), \tag{47}$$

where λ is the minimization step. Another advantage of using the auxiliary problem is that, if $\boldsymbol{A}$ is exact and $\mathcal{F}(\vec{\mathcal{R}},\boldsymbol{\Phi},\{\vec{a}_i\})$ is quadratic, the minimization arrives in the minimum of the free energy in only one step with $\lambda = 1$. In a very similar way also the CG algorithm can be redefined for the auxiliary problem:

$$\boldsymbol{d}^{(0)} = 0, \tag{48a}$$

$$\boldsymbol{d}^{(n+1)} = \boldsymbol{A}_{\boldsymbol{\Phi}}^{-1}\nabla_{\boldsymbol{\Phi}}\mathcal{F}^{(n+1)} + \frac{\nabla_{\boldsymbol{\Phi}}\mathcal{F}^{(n+1)}\boldsymbol{A}_{\boldsymbol{\Phi}}^{-1}\nabla_{\boldsymbol{\Phi}}\mathcal{F}^{(n+1)}}{\nabla_{\boldsymbol{\Phi}}\mathcal{F}^{(n)}\boldsymbol{A}_{\boldsymbol{\Phi}}^{-1}\nabla_{\boldsymbol{\Phi}}\mathcal{F}^{(n)}}\boldsymbol{d}^{(n)}, \tag{48b}$$

$$\boldsymbol{\Phi}^{(n+1)} = \boldsymbol{\Phi}^{(n)} - \lambda \boldsymbol{d}^{(n)}. \tag{48c}$$

Here, we omit the explicit dependence of the free energy $\nabla_{\boldsymbol{\Phi}}\mathcal{F}^{(n)} = \nabla_{\boldsymbol{\Phi}}\mathcal{F}(\vec{\mathcal{R}}^{(n)},\boldsymbol{\Phi}^{(n)},\{\vec{a}_i\})$ for simplicity.

Since we can compute the Hessian matrix even of the fourth root problem, we can combine the two approaches of the nonlinear change of variable and the preconditioner to achieve a minimization constrained only on the positive defined $\boldsymbol{\Phi}$ with the smallest condition number.

D. Hessian in the $\vec{\mathcal{R}}$ vector

The analysis on the minimization conducted so far investigates only the minimization problems faced with the $\boldsymbol{\Phi}$ parameter of the free energy. This is usually the most problematic part of the minimization, since, being a matrix, $\boldsymbol{\Phi}$ has many more degrees of freedom than the centroid positions. Furthermore, the centroid positions are defined in the unit cell, while the force constant matrix is a supercell quantity. However, for generality, it is very easy to provide an approximation also for the Hessian matrix of the free energy with respect to the $\vec{\mathcal{R}}$ variables:

$$A_{\vec{\mathcal{R}}}^{ab} = \left.\frac{\partial^2\mathcal{F}(\vec{\mathcal{R}},\boldsymbol{\Phi},\{\vec{a}_i\})}{\partial\mathcal{R}_a\partial\mathcal{R}_b}\right|_{\boldsymbol{\Phi}}. \tag{49}$$

Differences and similarities between this expression and the free-energy Hessian studied in Ref. [35] are discussed in Appendix C. Since we are both neglecting mixed terms in the Hessian, and we are taking an approximated Hessian also for the $\boldsymbol{\Phi}$ minimization, we chose

$$\boldsymbol{A}_{\vec{\mathcal{R}}} = \boldsymbol{\Phi}_{\mathrm{SG}}. \tag{50}$$

This expression is correct when the $\vec{\mathcal{R}}$ and the $\boldsymbol{\Phi}$ degrees of freedom are simultaneously minimized. Moreover, Eq. (50) provides a good preconditioner as it is always positive defined, and it does not require any additional computational effort to the algorithm.

The eigenvalues of $\boldsymbol{\Phi}$ are related to the square of the phonon frequencies for harmonic systems, therefore we can approximate the condition number on the $\vec{\mathcal{R}}$ variables as

$$C_{\vec{\mathcal{R}}} \sim \left(\frac{\omega_{\max}}{\omega_{\min}}\right)^2. \tag{51}$$

This is not as pathological as the condition number seen on the $\boldsymbol{\Phi}$ minimization. However, we can introduce a preconditioner in the same way as described in Sec. V C to handle easier minimization in low-symmetry systems, as molecular crystals, where also many centroid degrees of freedom must be optimized, and the condition number (51) can be of the order of 10^6. Preconditioning also the $\vec{\mathcal{R}}$ variables allows one to have a dimensionless step λ for the minimization algorithms [Eqs. (47) and (48c)], with a clear advantage of reducing the human time necessary to optimize the two λ steps for the $\boldsymbol{\Phi}$ and $\vec{\mathcal{R}}$ minimizations. We remark that the terms in the Hessian matrix obtained by the mixed derivatives in $\vec{\mathcal{R}}$ and $\boldsymbol{\Phi}$ are neglected.

The new SCHA algorithm flowchart is shown in Fig. 2.

VI. TESTS ON ICE XI (H_2O)

In order to present the impressive enhancement in the minimization procedure obtained thanks to the combination of the preconditioning with the root representation, we report the calculation on phase XI of ice. The difficulties of applying the SSCHA to this structure arise due to the presence of both hard covalent intramolecular bonds and soft intermolecular H bonds, resulting in a broad phonon spectrum.

Ice XI is the proton ordered phase of common ice [36] that is stable below 72 K. This is a typical prototype of a molecular crystal also for the low symmetry of the structure. It belongs to the $Cmc2_1$ group, with four symmetry operations. The unit cell contains four water molecules (12 atoms). The number of symmetry independent SCHA degrees of freedom is 11 for the inner coordinates (Wyckoff positions) and 159 for the unit-cell force-constant matrix. All the 11 inner coordinates, as well as the 159 parameters in the force-constant matrix, are allowed to move in the SSCHA.

We restricted the calculation to the unit cell, as we presented this example as a test case; however, all the methods developed here (both the minimization strategy and the stress tensor computation) are defined on an arbitrary large supercell.

In this section, we use a classical force field that explicitly includes anharmonicity of the water molecule to compute energies and forces. The model is q-SPC/FW+anh [45].

A. Stress tensor test

Here we test the anharmonic effects on the stress tensor with q-SPC/FW+anh. Equation (20) can be checked by performing the numerical derivative of the SCHA free energy at different volumes. In Fig. 3 we report the SCHA free energy as a function of the system volume, with a polynomial fit. The cell is deformed with an isotropic expansion of the volume so that the obtained pressure as the derivative of the free energy versus the volume can be compared with 1/3 of the stress tensor trace

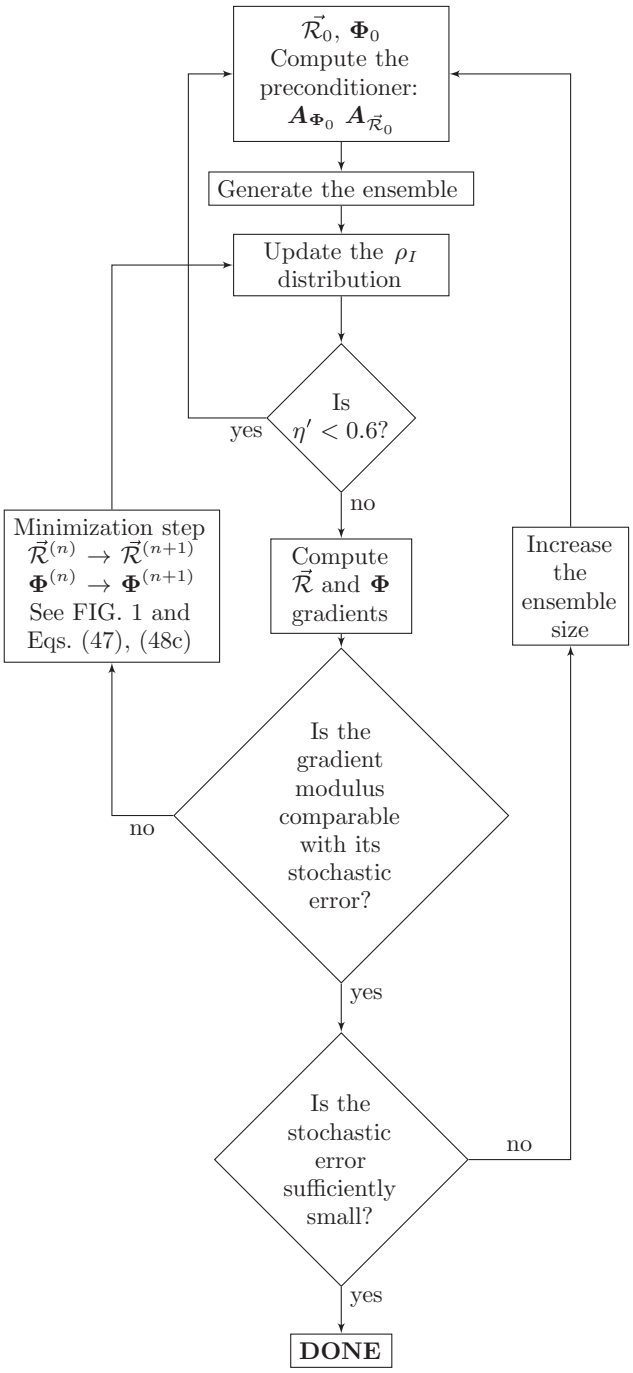

FIG. 2. Flowchart of the new SSCHA implementation. The minimization step can be expanded by using the root4 algorithm shown in Fig. 1. In this case, the preconditioner $\boldsymbol{A}_{\boldsymbol{\Phi}_0}$ should be replaced with $\boldsymbol{A}_{\sqrt[4]{\boldsymbol{\Phi}_0}}$ in the initial step. The minimization step is performed using the CG algorithm as long as the error is much greater than the stochastic noise, then the last steps are performed using SD. This prevents error propagation in the conjugation due to the correlated noise introduced by the importance sampling reweighting procedure.

of Eq. (20). The fit on the SCHA free energy is then used to evaluate the pressure as a function of the volume:

$$P = -\frac{d\mathcal{F}}{d\Omega} = \frac{1}{3}\sum_{\alpha=x,y,z} P_{\alpha\alpha}. \tag{52}$$

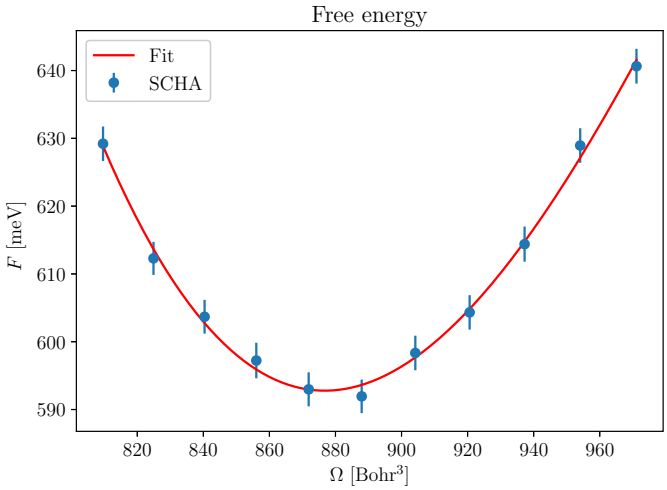

FIG. 3. SCHA free energy as a function of the volume. The unit cell is kept fixed, while only an isotropic scaling factor is considered. The solid line represents a cubic fit. The simulation is performed at $T = 100$ K.

In Fig. 4 we compare the SCHA pressure obtained both as indicated in Eq. (52) and as the opposite of the total derivative of the free energy. The stochastic average of the stress tensors $\langle P^H_{\alpha\beta}(\vec{R},\{\vec{a}_i\})\rangle_\rho$ is also reported, showing how the pressure cannot be considered as a physical observable to be computed in analogy to what is done for general operators: $P_{\alpha\beta} \neq \langle P^H_{\alpha\beta}\rangle_\rho$; in fact, this neglects the kinetic contribution of the vibrations. It is necessary to compute it as the derivative of the free energy, as done in Eq. (20). The pressure P_{cla} without quantum effects at $T = 0$ is also reported, and can be computed as 1/3 of the trace of the stress tensor in the classical equilibrium centroid

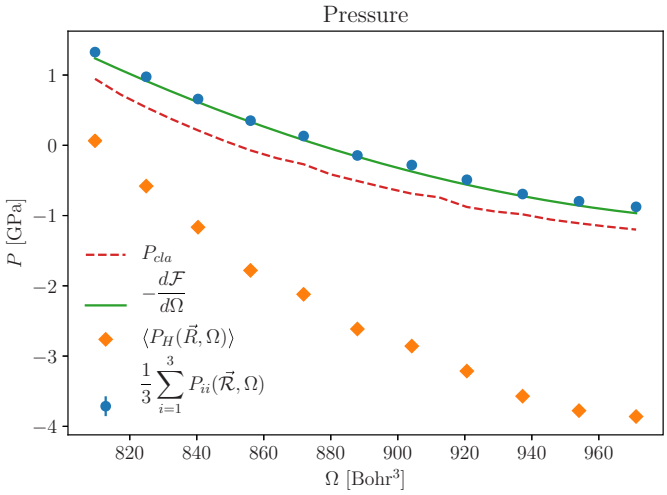

FIG. 4. The figure compares the pressure computed with Eq. (20) (blue circles), the classical pressure P_{cla} obtained neglecting thermal and quantum fluctuations (red dashed line), the average of the classical pressures over the SCHA ensemble (orange diamonds), and the analytical derivative of the free energy fit reported in Fig. 3 (solid green line). The simulation is performed at $T = 100$ K.

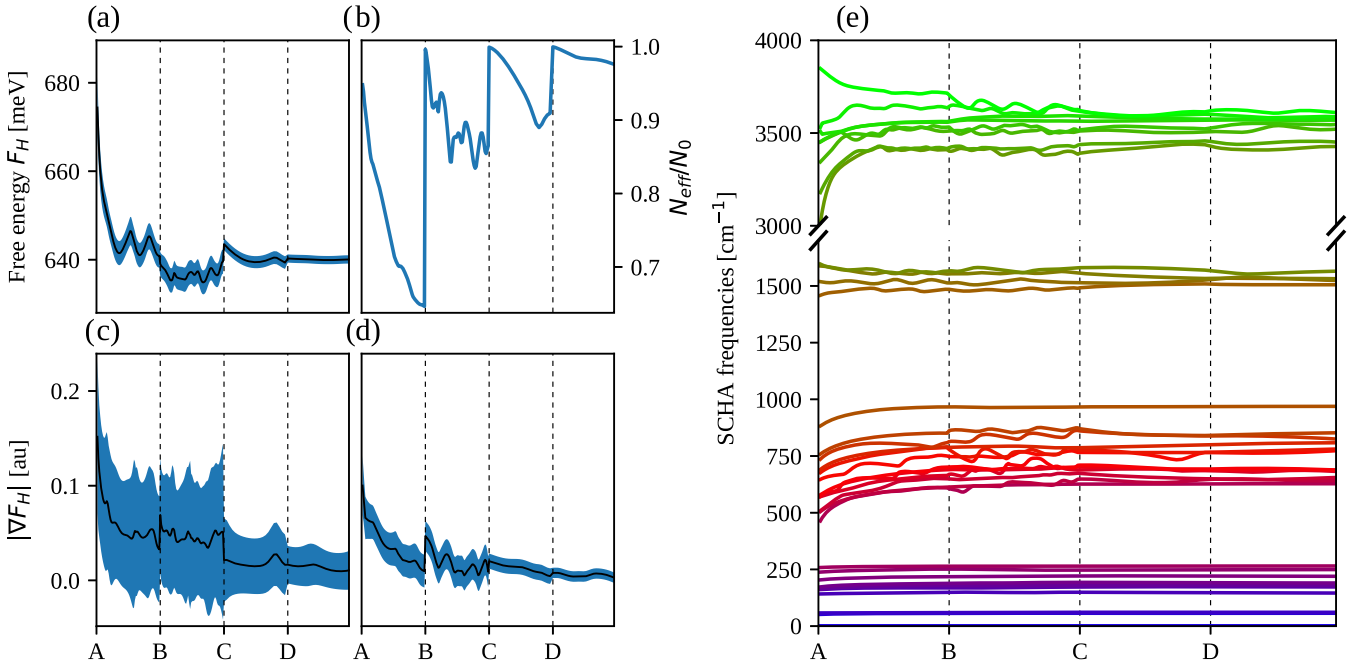

FIG. 5. Minimization progress starting from the harmonic result with the preconditioning linear change of variables. (a) The free energy. (b) The Kong-Liu effective sample size ratio, defined in Eq. (27). (c) Modulus of the free-energy gradient with respect to the dynamical matrix $\mathbf{\Phi}$. (d) Modulus of the free-energy gradient with respect to the centroids $\vec{\mathcal{R}}$. (e) Frequencies obtained from the eigenvalues of the SCHA $\mathbf{\Phi}$ matrix, as they evolve during the minimization. Preconditioning uniformly converges all the frequencies, achieving the final result much faster. Panels (a), (c), and (d) contain the stochastic error. For the two gradients, the error is computed as the norm of the error on each component of the gradient, to make it invariant with respect to the basis used to describe the $\mathbf{\Phi}$.

positions:

$$P_{\text{cla}} = -\frac{1}{3}\sum_{\alpha=x,y,z}\frac{1}{\Omega}\frac{\partial V(\vec{R}_0,\{\vec{a}_i\})}{\partial \varepsilon_{\alpha\alpha}}, \tag{53}$$

where $\vec{R}_0$ is defined as

$$\left.\frac{\partial V(\vec{R},\{\vec{a}_i\})}{\partial \vec{R}}\right|_{\vec{R}=\vec{R}_0} = 0. \tag{54}$$

B. Tests on the new minimization algorithm

A typical SCHA run with the precondition is reported in Fig. 5. The $\rho_{\vec{\mathcal{R}},\mathbf{\Phi}}$ ensemble is reextracted four times. The first two times (A and B) 2500 configurations were used, 10 000 were used in the C step, and 20 000 were used in D. As clearly reported, the frequencies of the dynamical matrix converge uniformly to the final result, as we expect from the preconditioning, and we achieve a converged good result after only two steps.

The comparison of the performances between the nonlinear change $\mathbf{\Phi} \to \sqrt[4]{\mathbf{\Phi}}$ and the preconditioning is reported in Fig. 6. As a reference, the SCHA run without the nonlinear change of variable and without preconditioning is also reported. The simulations are compared at $T = 100$ K. It is clear that both methods greatly outperform the standard algorithm. The harmonic dynamical matrix around the static equilibrium positions (neglecting quantum and thermal fluctuations) is used as a starting point, according to what is usually done in *ab initio* calculations [16,17,34]. The q-SPC/FW+anh harmonic dynamical matrix is close to the SCHA result, as seen by the low value of the free-energy gradient with respect to $\mathbf{\Phi}$,

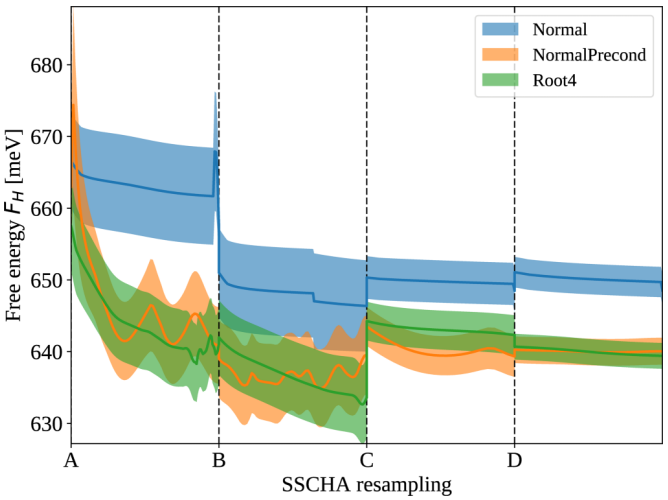

FIG. 6. Comparison between the different methods described here. The free energy is shown as a function of the number of configurations used for the stochastic evaluation together with its stochastic error. The first two calculations have 2500 configurations each. The third (C) is with 10 000. A final calculation is performed as a reference (D) with 20 000 configurations to check the convergence of the previous ones. As shown, the minimization without the preconditioning or the nonlinear change of variables is not able to get a converged result even using an overall of 35 000 configurations, preventing the old SCHA from being used with any *ab initio* technique in this kind of system.

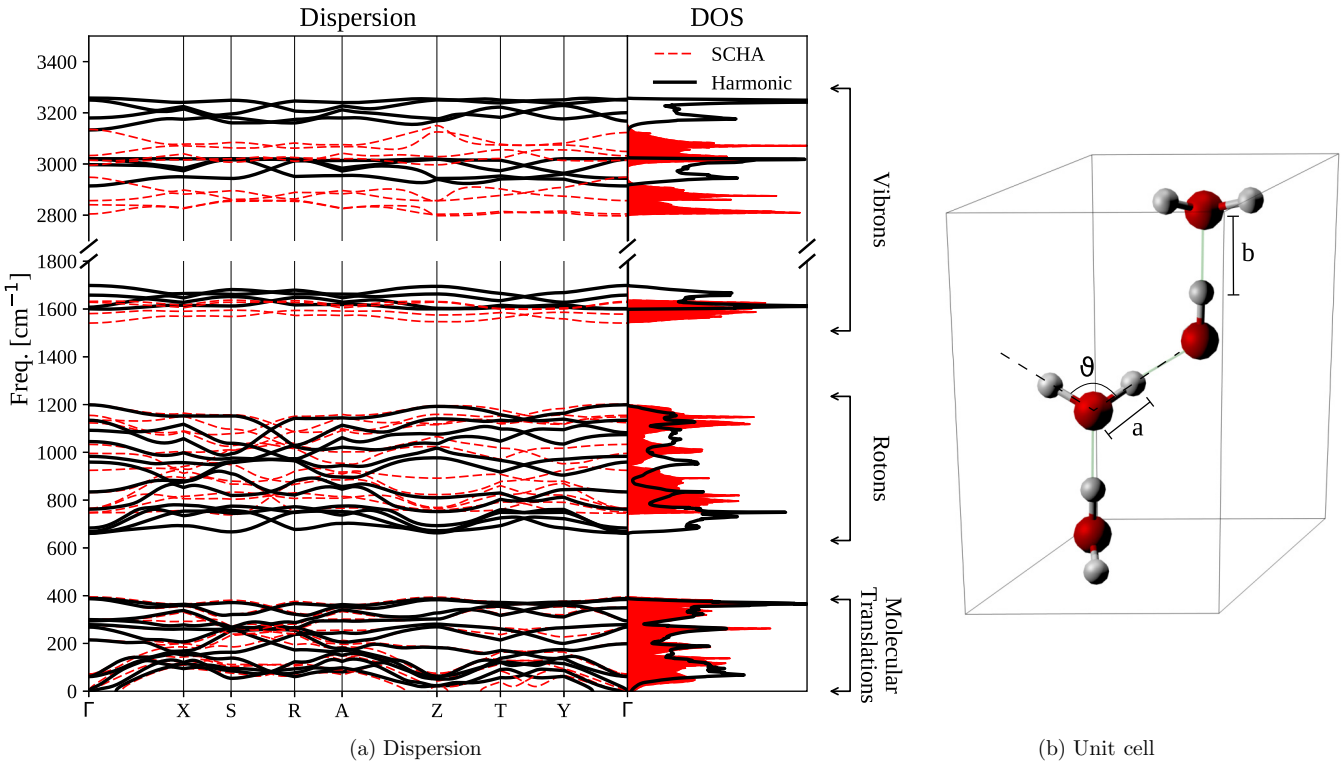

(a) Dispersion (b) Unit cell

FIG. 7. (a) Comparison between harmonic (black solid lines) and SCHA (red dashed lines) dispersion and density of states. (b) Unit cell of the ice XI structure. The parameters a, b, and ϑ represent, respectively, the covalent OH bond, the hydrogen bond, and the molecule angle. Their average value as a function of the temperature is reported in Table I.

compared with its stochastic error, already in the first step of Fig. 5. However, the standard minimization is not able to further minimize the system.

The success of the SCHA implementation on this force field paves the way to its systematic utilization for the study of water and any other complex system with many degrees of freedom.

In the next section, we show the capabilities of our method in a more realistic first-principles potential.

VII. *AB INITIO* SIMULATION ON ICE XI

Encouraged by the success of the SCHA implementation on the q-SPC/FW+anh force field, we report also the SCHA results on a realistic DFT potential. The converged SCHA phonon dispersion ($T = 0$ K) is compared to the harmonic one in Fig. 7. The calculation of energies and forces required to minimize the SCHA free energy, as well as the computation of the harmonic dynamical matrix, are performed *ab initio* with DFT, Perdew-Burke-Ernzerhof (PBE) exchange-correlation functional [46], and ultrasoft pseudopotentials [47] from the *pslibrary* [48], as implemented in the QUANTUMESPRESSO suite [49,50]. The SCHA dispersion is computed in the unit cell with 13 000 overall configurations and a wave-function cutoff of 45 Ry (360 Ry being the charge density cutoff), then the difference between the harmonic and anharmonic dynamical matrices is extrapolated in a $3 \times 3 \times 3$ supercell, and the harmonic dispersion $\mathbf{\Phi}_0$ is added:

$$\mathbf{\Phi}^{(3\times3\times3)} = \mathbf{\Phi}_0^{(3\times3\times3)} + \left(\mathbf{\Phi}^{(1\times1\times1)} - \mathbf{\Phi}_0^{(1\times1\times1)}\right)^{(3\times3\times3)}. \quad (55)$$

The harmonic phonon dispersion obtained interpolating the dynamical matrices converges already in a $2 \times 2 \times 2$ supercell, with a wave-function cutoff of 80 Ry (640 Ry being the charge density cutoff). The SCHA auxiliary dynamical matrix $\mathbf{\Phi}$ is not directly related to the anharmonic phonon dispersion and, in general, a more sophisticated calculation is required to extract the real phonon frequencies in the SCHA approximation [35]. However, it is found [35] that the static phonon dispersion can be obtained as a perturbative series, the leading order of which is given by the $\mathbf{\Phi}$ matrix itself plus a "bubble" correction. It has been found in many systems with hydrogen [34,51] that the bubble correction is much lower than the $\mathbf{\Phi}$ contribution. As an explicative case, here we neglect this correction. It is, however, worth noticing that the developments presented in Sec. V A do not affect the bubble computation as reported in Ref. [35] since it depends only on the converged result and not on the particular minimization strategy. Therefore, we report the anharmonic phonon dispersion and density of states approximated by directly interpolating the $\mathbf{\Phi}$ matrix after the SSCHA optimization in Fig. 7.

All phonon modes below 500 cm^{-1} (molecular translations) are almost unaffected by the anharmonicity. The two upper bands corresponding to symmetric and asymmetric stretching suffer a redshift, together with the band around 1600 cm^{-1} (molecular bending). These modes are well described by molecular vibrons, and the observed redshift is a general property of the water molecule [52]. Also, the lowest part of the molecular rotations (the bands between 600 and 1200 cm^{-1}) are blueshifted. This blueshift of the lowest modes is indeed very interesting since it involves intermolecular modes. Such

TABLE I. Anharmonic effects on the crystal structure predicted by the DFT-PBE at three temperatures. The average intramolecular OH distance (covalent bond), the average H-bond distance, and the water molecule mean angle, as reported in Fig. 7.

	Harmonic	0 K	150 K	300 K
a (OH-covalent)	1.00835 Å	1.0159 Å	1.0148 Å	1.0131 Å
b (H-bond)	1.6769 Å	1.673 Å	1.674 Å	1.6765 Å
ϑ (HOH angle)	106.715°	106.950°	106.951°	106.886°

an effect of anharmonicity is typical of this solid structure of ice, and cannot be predicted just studying anharmonicity in the isolated water molecule or the dimer. Moreover, the Debye temperature of these bands is far above room temperature, invalidating the dispersion obtained with classical molecular dynamics since zero-point motion has a predominating role in these lattice oscillations.

Also the average atomic positions are affected as reported in Table I. Here, the quantum fluctuations slightly stretch the water molecule, each covalent OH bond increases its length by almost 0.7%, and the molecular angle widens by 0.2%.

Even if the anharmonic molecular stretch can seem negligible compared to what it has been predicted to be for a high-pressure molecular phase of hydrogen [33], a difference of 1% in the OH covalent bond has a great contribution to the energy. As a test, the SCHA average structure can be used for a classical DFT calculation, where the classical pressure is found to be 1 GPa lower (negative) than its value in the equilibrium positions, suggesting that the anharmonic relaxation of the centroid positions may significantly affect the pressure and, consequently, the equilibrium volume.

The stress tensor calculation can be used to optimize the unit cell considering both thermal and quantum effects. The most advanced calculations to include these effects without involving PIMD in water have been performed within the QHA [37,38]. In this scheme the total pressure is obtained expanding the BO energy surface as a quadratic function around its minimum at each volume. Then the exact free energy of the approximated BO surface can be computed analytically:

$$\mathcal{F}_{\mathrm{QHA}}(\vec{R}_c,\{\vec{a}_i\}) = V(\vec{R}_c,\{\vec{a}_i\}) + \sum_{\mu=1}^{3N}\left[\frac{\hbar\tilde{\omega}_\mu(\vec{R}_c,\{\vec{a}_i\})}{2} + \frac{1}{\beta}\ln(1-e^{-\beta\hbar\tilde{\omega}_\mu(\vec{R},\{\vec{a}_i\})})\right], \tag{56}$$

where $\tilde{\omega}_\mu$ are the harmonic frequencies of the BO surface. The QHA free energy F_{QHA} is obtained minimizing the functional $\mathcal{F}_{\mathrm{QHA}}$ at fixed volume and temperature:

$$F_{\mathrm{QHA}}(T,\{\vec{a}_i\}) = \min_{\vec{R}_c}\mathcal{F}_{\mathrm{QHA}}(T,\vec{R}_c,\{\vec{a}_i\}). \tag{57}$$

The QHA pressure is obtained by differentiating the free energy with respect to a uniform volume deformation:

$$P_{\mathrm{QHA}} = -\frac{dF_{\mathrm{QHA}}}{d\Omega}. \tag{58}$$

In complex systems with many degrees of freedom, like in ice, the minimization in Eq. (57) is computationally very expensive, since it requires the calculation of the gradient of the free energy (that depends on the harmonic dynamical matrix) with respect to any possible atomic displacement. This involves the calculation of a third-order derivative of the BO total energy for each minimization step [53]. Differences and analogies of QHA and SCHA approaches are discussed in Appendix D. The QHA implementation with the full atomic coordinates relaxation in H_2O system has never been performed, and usually the QHA free energy is approximated with $\vec{R}_c = \vec{R}_0$: the minimum of the BO energy. The pressure in Eq. (57) is computed numerically taking finite differences between the QHA free energies at several volumes. A more convenient way to compute the QHA pressure is to consider the harmonic frequencies as a linear function of the volume:

$$\tilde{\omega}_k(\Omega) = \tilde{\omega}_k(\Omega_0)\left[1 - \frac{\Omega-\Omega_0}{\Omega_0}\gamma_k\right], \tag{59}$$

where the γ_k are the Grüneisen parameters. Then the QHA pressure can be easily obtained at any temperature:

$$P_{\mathrm{QHA}} = P_H(\Omega) - \sum_{\mu=1}^{3N}\frac{\hbar\omega_\mu\gamma_\mu}{2\Omega}\frac{1}{\tanh\left(\frac{\beta\hbar\omega_\mu}{2}\right)}. \tag{60}$$

The comparison between QHA and the SSCHA pressure calculations as a function of temperature is reported in Fig. 8(a). Both the calculations have been performed in the unit cell, allowing for a direct comparison between the SCHA and the QHA result. Moreover, we checked the QHA pressure convergence versus the supercell size, and found that the difference between the QHA in a $3\times3\times2$ supercell and in the unit cell was much lower than the SCHA stochastic error itself.

The experimental fit on the elastic bulk modulus and the volume expansivity have been used to compare the QHA and SSCHA pressures at a fixed volume. As clearly shown, the QHA pressure is shifted by about 4 kbars with respect to the SSCHA result. This is two times bigger than the whole pressure range between 0 and 300 K. In Fig. 8(b) the comparison between the QHA, the SSCHA, and the experimental results is reported. All the pressures are shifted with respect to their zero-temperature value. The SSCHA zero-temperature pressure has been obtained by fitting the SSCHA points with the experimental curve. The experimental data have been obtained from the fit reported in Ref. [54].

The QHA grasps the qualitative behavior of the pressure, including the low-temperature negative thermal expansion [55], but it deviates from the experiments at temperatures above 80 K. This effect has been associated with the entropy contribution of the proton disorder of the ice Ih with respect to the ice XI, that is not accounted for in the simulations [55]. However, the SSCHA result corrects the QHA estimation of the pressure by a significant amount, matching perfectly the experiments, suggesting that the underestimation of the pressure at high temperature can be simply explained as a failure of the QHA. This indicates that anharmonic effects beyond QHA play an important role in reproducing the physical properties of ice at temperatures above 80 K.

We computed also the whole SCHA anharmonic stress tensor. The effect of fluctuations on pressure anisotropy is much smaller than that on the isotropic pressure. Indeed, the

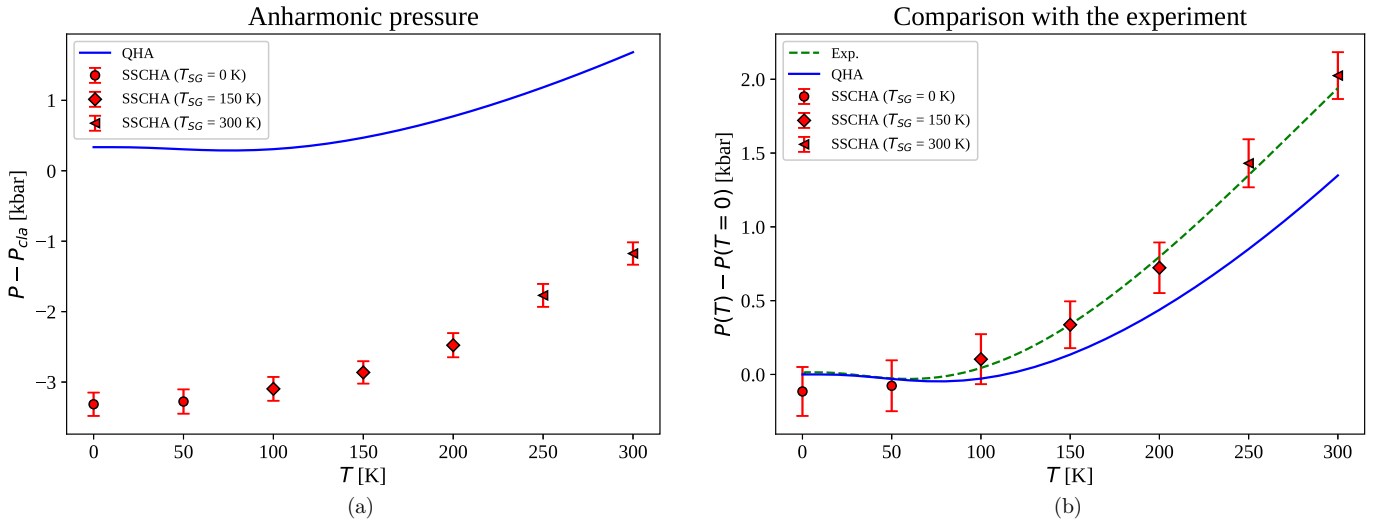

FIG. 8. (a) Comparison between the QHA and the SSCHA pressure as a function of the temperature at fixed volume. The zero value of the pressure is P_{cla}, obtained as $1/3$ of the stress tensor trace at $T = 0$ neglecting quantum fluctuations. (b) Comparison between QHA and SSCHA simulations and the fit of the experimental results from Ref. [54] (ice Ih). The SSCHA results are computed at temperatures of 0, 150, and 300 K with 40 000 stochastic configurations. The other temperatures reported have been obtained through reweighting [16], therefore their stochastic error is correlated.

computed pressure anisotropy is comparable with the statistical error bars.

Another interesting feature of ice at low temperature is the anomalous volume isotope effect: the D_2O equilibrium volume is bigger than the H_2O one. This effect has been recently studied within the QHA [37,38]. In particular, Pamuk *et al.* [37] showed how the QHA result systematically overestimates this effect with several DFT functionals but it depends slightly on the chosen functional, on the difference between ice Ih and XI, and on the q-grid interpolation. The experimental [39] difference between the two volumes at 10 K is about 0.09%, while the difference between the QHA equilibrium volume and the SSCHA one is 1.8%. Therefore, the isotope volume effect is a tiny correction with respect to the ZPE contribution on the equilibrium volume and the difference between the SSCHA and the QHA.

VIII. CONCLUSIONS

The study of quantum anharmonic effects in complex crystals with lots of degrees of freedom, e.g., molecular crystals, is a major challenge that impacts many domains of physics and chemistry, including high-pressure phases of hydrogen, water anomalies, thermoelectric materials, charge-density waves, ferroelectrics, multiferroics, and so on. In this paper, we derive an expression for the anharmonic contribution to the stress tensor in the SCHA theory. This correction is very important for accurate pressure estimations and phase-diagram computations and paves the way for isobaric unit-cell relaxation. We further improved the stochastic implementation of the SCHA theory to apply it in complex crystals with a large number of degrees of freedom. This aim has been achieved thanks to a preconditioning on the free-energy minimization algorithm, based on an analytical guess of the Hessian matrix of both the force-constant matrix and the central nucleus positions, and with a nonlinear change of variables that restricts the space of allowed dynamical matrices only to the positive defined ones.

The algorithm is benchmarked with the phase XI of ice, the proton-ordered phase of common ice, a prototype molecular crystal. The quantum ZPM and anharmonicity are proven to affect the phonon dispersion both in the molecular and in the intermolecular modes. Also, the O-H and H-H bound distances are slightly affected by anharmonicity. The importance of the nonperturbative SCHA contribution to the pressure in this system has been benchmarked in q-SPC/FW+anh and calculated with *ab initio* DFT PBE, where the quantum fluctuations at 0 K are shown to affect the equilibrium volume by 1.8%.

The thermal expansion of the system has been computed within both the QHA and the SSCHA. The QHA is found to miscalculate both the ZPM contribution to the equilibrium volume (with the wrong sign) and the effect of the thermal fluctuations at temperatures above 80 K. The latter discrepancy was associated with the proton disorder of phase Ih of ice. However, we found the SSCHA to correct this effect, and to exhibit an excellent agreement with the experiments, unveiling that anharmonic effects behind QHA are crucial to correctly describe the thermodynamic properties of ice.

The cell-relaxation and stress calculation here developed paves the way to a refreshed quantitative and accurate study of anharmonic effects on water, like the anomalous isotope volume, the equilibrium isotope fraction, the negative thermal expansion, and the high-pressure phase diagram. More generally, the developed stress tensor derivation and the improved minimization algorithm make the SSCHA an efficient method to calculate quantum and thermal anharmonic effects on complex systems with many degrees of freedom.

ACKNOWLEDGMENTS

I.E. acknowledges financial support from the Spanish Ministry of Economy and Competitiveness (Grant No. FIS2016-

76617-P). We acknowledge a CINECA award under the ISCRA initiative (Grant No. HP10BLTB9A); PRACE; IDRIS; CINES; and TGCC under EDARI Project No. A0030901202 for the use of high-performance computing resources and support.

APPENDIX A: STRESS TENSOR DERIVATION

To easily compute the derivative of the SCHA free-energy functional with respect to the strain tensor it is convenient to use the formalism introduced by Bianco *et al.* [35]. The average of a generic observable can be written as

$$\langle O\rangle_{\rho_{\vec{\mathcal{R}},\mathbf{\Phi}}} = \sqrt{\det\left(\frac{\boldsymbol{\Upsilon}}{2\pi}\right)}\int O(\vec{\mathcal{R}}+\vec{u},\{\vec{a}_i\}) \times \exp\left(-\frac{1}{2}\vec{u}\,\boldsymbol{\Upsilon}\,\vec{u}\right) d^{3N}u. \tag{A1}$$

In order to normalize the Gaussian integral a change of variable can be applied, so that

$$u_s^\alpha = \sum_\mu J_{\mu_s}^{\ \alpha} y_\mu, \qquad J_{\mu_s}^{\ \alpha} = \frac{e_{\mu_s}^{\ \alpha}}{\sqrt{M_s}}\sqrt{\frac{\hbar(1+n_\mu)}{2\omega_\mu}},$$
$$(\boldsymbol{\Upsilon}^{-1})_{st}^{\alpha\beta} = \sum_\mu J_{\mu_s}^{\ \alpha} J_{\mu_t}^{\ \beta}. \tag{A2}$$

Then we have

$$\langle O\rangle_{\rho_{\vec{\mathcal{R}},\mathbf{\Phi}}} = \int O(\vec{\mathcal{R}}+\mathbf{J}\vec{y},\{\vec{a}_i\})[dy],$$
$$[dy] = \prod_{\mu=1}^{3N}\frac{\exp\left(\frac{-y_\mu^2}{2}\right)}{\sqrt{2\pi}}dy_\mu. \tag{A3}$$

Since we are deriving the $\mathcal{F}_{\vec{\mathcal{R}}}$ functional [Eq. (9)], the Hellman-Feynman theorem allows us to neglect the changes introduced by the strain on the dynamical matrix. Only $\vec{\mathcal{R}}$ is affected by the deformation, according to Eq. (19). Therefore we have

$$\frac{d\,\langle O(\vec{R},\{\vec{a}_i\})\rangle_{\rho_{\mathcal{R}}}}{d\varepsilon_{\alpha\beta}} = \left.\frac{\partial\,\langle O(\vec{R},\{\vec{a}_i\})\rangle_{\rho_{\vec{\mathcal{R}}}}}{\partial\varepsilon_{\alpha\beta}}\right|_{\mathbf{\Phi}=\mathbf{\Phi}(\vec{\mathcal{R}})}, \tag{A4}$$

$$\frac{\partial\,\langle O\rangle_{\rho_{\vec{\mathcal{R}}}}}{\partial\varepsilon_{\alpha\beta}} = \frac{\partial}{\partial\varepsilon_{\alpha\beta}}\int O(\vec{\mathcal{R}}(\boldsymbol{\varepsilon})+\boldsymbol{J}\vec{y},\{\vec{a}_i(\varepsilon)\})[dy]$$
$$= \int\left(\sum_{s\gamma}\frac{\partial O}{\partial R_s^\gamma}\frac{\partial\mathcal{R}_s^\gamma}{\partial\varepsilon_{\alpha\beta}} + \sum_{i\gamma}\frac{\partial O}{\partial a_i^\gamma}\frac{\partial a_i^\gamma}{\partial\varepsilon_{\alpha\beta}}\right)[dy]. \tag{A5}$$

Note that the observable $O(\vec{R})$ is derived with respect to its argument, i.e., the atom positions in the ensemble configuration $\vec{R}$, not the centroid position $\vec{\mathcal{R}}$. This happens because the $\vec{\mathcal{R}}(\boldsymbol{\varepsilon})$ appears linearly in the configuration position of O after the change of variable:

$$\frac{\partial\,\langle O\rangle_{\rho_{\vec{\mathcal{R}}}}}{\partial\varepsilon_{\alpha\beta}} = \frac{1}{2}\sum_s\left(\mathcal{R}_s^\beta\left\langle\frac{\partial O}{\partial R_s^\alpha}\right\rangle_{\rho_{\vec{\mathcal{R}}}} + \mathcal{R}_s^\alpha\left\langle\frac{\partial O}{\partial R_s^\beta}\right\rangle_{\rho_{\vec{\mathcal{R}}}}\right) + \left\langle\sum_{i\gamma}\frac{\partial O}{\partial a_i^\gamma}\frac{\partial a_i^\gamma}{\partial\varepsilon_{\alpha\beta}}\right\rangle_{\rho_{\vec{\mathcal{R}}}}. \tag{A6}$$

The free-energy functional is

$$\mathcal{F}_{\vec{\mathcal{R}}} = F_{\mathbf{\Phi}(\vec{\mathcal{R}})} + \langle V - \mathcal{V}_{\vec{\mathcal{R}},\mathbf{\Phi}(\vec{\mathcal{R}})}\rangle_{\rho_{\vec{\mathcal{R}}}}, \tag{A7}$$

where $\mathbf{\Phi}(\vec{\mathcal{R}})$ is the dynamical matrix that minimizes $\mathcal{F}(\vec{\mathcal{R}},\mathbf{\Phi},\{\vec{a}_i\})$ fixing the average atomic positions. The first term, $F_{\mathbf{\Phi}(\vec{\mathcal{R}})}$ is an explicit function only of the SCHA dynamical matrix, and therefore does not contribute to the derivative. The latter average can be derived thanks to Eq. (A6):

$$\frac{\partial\,\langle V\rangle_{\rho_{\vec{\mathcal{R}}}}}{\partial\varepsilon_{\alpha\beta}} = -\frac{1}{2}\sum_{s=1}^{N}\left(\mathcal{R}_s^\beta\left\langle f_s^\alpha\right\rangle_{\rho_{\vec{\mathcal{R}}}} + \mathcal{R}_s^\alpha\left\langle f_s^\beta\right\rangle_{\rho_{\vec{\mathcal{R}}}}\right) - \Omega\left\langle P_{\alpha\beta}^H\right\rangle_{\rho_{\vec{\mathcal{R}}}}, \tag{A8}$$

where $P_{\alpha\beta}^H$ is the BO stress tensor. In fact the last term of Eq. (A6) is the average of the derivatives of the BO energy when the strain is applied to the unit cell. The "harmonic" term can be computed in a similar way:

$$\left.\frac{\partial\,\langle\mathcal{V}_{\vec{\mathcal{R}},\mathbf{\Phi}}\rangle_{\rho_{\vec{\mathcal{R}}}}}{\partial\varepsilon_{\alpha\beta}}\right|_{\mathbf{\Phi}} = \frac{1}{2}\sum_s\left(\mathcal{R}_s^\beta\left\langle\frac{\partial\mathcal{V}_{\vec{\mathcal{R}},\mathbf{\Phi}}}{\partial R_s^\alpha}\right\rangle_{\rho_{\vec{\mathcal{R}}}} + \mathcal{R}_s^\alpha\left\langle\frac{\partial\mathcal{V}_{\vec{\mathcal{R}},\mathbf{\Phi}}}{\partial R_s^\beta}\right\rangle_{\rho_{\vec{\mathcal{R}}}}\right) + \left\langle\frac{\partial\mathcal{V}_{\vec{\mathcal{R}},\mathbf{\Phi}}}{\partial\varepsilon_{\alpha\beta}}\right\rangle. \tag{A9}$$

In the same way as done for the BO energy surface, it is possible to introduce the harmonic stress tensor as

$$P_{\alpha\beta}^{\mathcal{H}} = -\frac{1}{\Omega}\left\langle\frac{\partial\mathcal{V}_{\vec{\mathcal{R}},\mathbf{\Phi}}}{\partial\varepsilon_{\alpha\beta}}\right\rangle_{\rho_{\vec{\mathcal{R}}}} = \frac{1}{2\Omega}\sum_s\left\langle f_{\mathcal{H}_s}^\alpha u_s^\beta + f_{\mathcal{H}_s}^\beta u_s^\alpha\right\rangle_{\rho_{\vec{\mathcal{R}}}}$$
$$= -\frac{1}{\Omega}\sum_{\mu=1}^{3N}\sum_{s=1}^{N}\frac{\hbar\omega_\mu}{2\tanh\left(\frac{\beta\hbar\omega_\mu}{2}\right)}e_{\mu_s}^{\ \alpha}e_{\mu_s}^{\ \beta}, \tag{A10}$$

$$\frac{\partial\,\langle\mathcal{V}\rangle_{\rho_{\vec{\mathcal{R}}}}}{\partial\varepsilon_{\alpha\beta}} = -\frac{1}{2}\sum_{s=1}^{N}\left(\mathcal{R}_s^\beta\left\langle f_{\mathcal{H}_s}^\alpha\right\rangle_{\rho_{\vec{\mathcal{R}}}} + \mathcal{R}_s^\alpha\left\langle f_{\mathcal{H}_s}^\beta\right\rangle_{\rho_{\vec{\mathcal{R}}}}\right) - \Omega P_{\alpha\beta}^{\mathcal{H}}. \tag{A11}$$

The first term is zero (the harmonic forces $\vec{f}_{\mathcal{H}}$ are odd, while the probability distribution $\rho_{\vec{\mathcal{R}}}$ is even). However, we keep it as it helps to increase the numerical accuracy [16], as we can combine it with Eq. (A8) to exploit the correlation between f_s^α and $f_{\mathcal{H}_s}^\alpha$ to reduce the statistical noise on the average. In a pure harmonic crystal also the quantities $P_{\alpha\beta}^H$ and $P_{\alpha\beta}^{\mathcal{H}}$ are correlated. Therefore, the final expression of the pressure can be written as follows:

$$P_{\alpha\beta} = \left\langle P_{\alpha\beta}^H - \frac{1}{2\Omega}\sum_{s=1}^{N}\left(f_{\mathcal{H}_s}^\alpha u_s^\beta + f_{\mathcal{H}_s}^\beta u_s^\alpha\right)\right\rangle_{\rho_{\vec{\mathcal{R}}}} + \frac{1}{2\Omega}\sum_{s=1}^{N}\left(\mathcal{R}_s^\beta\left\langle f_s^\alpha - f_{\mathcal{H}_s}^\alpha\right\rangle_{\rho_{\vec{\mathcal{R}}}} + \mathcal{R}_s^\alpha\left\langle f_s^\beta - f_{\mathcal{H}_s}^\beta\right\rangle_{\rho_{\vec{\mathcal{R}}}}\right). \tag{A12}$$

The last term is zero if the free energy has been minimized also with respect to the $\vec{\mathcal{R}}$ variables (as the average of the BO forces is the SCHA force acting on each atom, it is zero in the equilibrium).

APPENDIX B: DETAILED CALCULATION FOR THE HESSIAN MATRIX

The real and trial classical forces acting on each configuration identified by the displacements $\vec{u}$ are

$$f_s^\alpha = -\frac{\partial V}{\partial u_s^\alpha} = -\sum_{t\beta} K_{st}^{\alpha\beta} u_t^\beta, \tag{B1a}$$

$$f_{\mathcal{H}_s}^\alpha = -\frac{\partial \mathcal{V}_{\vec{\mathcal{R}},\mathbf{\Phi}}}{\partial u_s^\alpha} = -\sum_{t\beta} \Phi_{st}^{\alpha\beta} u_t^\beta. \tag{B1b}$$

Defining $\delta\vec{f} = \vec{f} - \vec{f}_{\mathcal{H}}$ we have

$$\left\langle \delta f_s^\alpha u_t^\beta \right\rangle_{\rho_{\mathcal{H}}} = -\sum_{n\eta} \left(K_{sn}^{\alpha\eta} - \Phi_{sn}^{\alpha\eta}\right) \left\langle u_n^\eta u_t^\beta \right\rangle_{\rho_{\vec{\mathcal{R}},\mathbf{\Phi}}}. \tag{B2}$$

From now on, we drop the subscript $\rho_{\vec{\mathcal{R}},\mathbf{\Phi}}$ for each average, and consider all the averages computed with respect to the trial density matrix. We further simplify the notation, introducing one index for each Cartesian and atomic coordinate, so $v_s^\alpha \to v_a$. In this new notation Eq. (B2) reads

$$\langle \delta f_a u_b \rangle = -\sum_{c=1}^{3N} (K_{ac} - \Phi_{ac}) \langle u_c u_b \rangle. \tag{B3}$$

The average of the product between two displacements of a Gaussian distributed variable is the covariance between the two displacements [Eq. (13a)]:

$$\langle u_c u_b \rangle = \left(\mathbf{\Upsilon}^{-1}\right)_{cb} = \frac{1}{\sqrt{M_c M_b}} \sum_{\nu=1}^{3N} e_\nu^c e_\nu^b a_\nu^2, \tag{B4}$$

where we introduce the mode length a_μ:

$$a_\mu = \sqrt{\frac{\hbar}{2\omega_\mu}\left(1 + 2n_\mu\right)}. \tag{B5}$$

The gradient of the SCHA free-energy functional with respect to $\mathbf{\Phi}$ is [16]

$$\nabla_{\mathbf{\Phi}} \mathcal{F}_{\vec{\mathcal{R}},\mathbf{\Phi}} = -\sum_{ab\mu} \sqrt{\frac{M_a}{M_b}} \left(e_\mu^b \nabla_{\mathbf{\Phi}} \ln a_\mu + \nabla_{\mathbf{\Phi}} e_\mu^b\right) e_\mu^a \langle \delta f_b u_a \rangle. \tag{B6}$$

Substituting the explicit expression of the forces we have

$$\nabla_{\mathbf{\Phi}} \mathcal{F}(\vec{\mathcal{R}},\mathbf{\Phi},\{\vec{a}_i\}) = \sum_{abc\mu\nu} (K_{ac} - \Phi_{ac}) \left(e_\mu^a \nabla_{\mathbf{\Phi}} \ln a_\mu + \nabla_{\mathbf{\Phi}} e_\mu^a\right) \times \frac{e_\mu^b e_\nu^c e_\nu^b a_\nu^2}{\sqrt{M_c M_a}}. \tag{B7}$$

It is clear from Eq. (B7) that in the minimum $\mathbf{\Phi} = \mathbf{K}$. Therefore, it is convenient to compact all the other terms into a symbol:

$$\frac{\partial \mathcal{F}(\vec{\mathcal{R}},\mathbf{\Phi},\{\vec{a}_i\})}{\partial \Phi_{cd}} = \sum_{ab} (K_{ab} - \Phi_{ab}) \mathcal{L}_{abcd}. \tag{B8}$$

Here $\boldsymbol{\mathcal{L}}$ is a rank-4 tensor. Since we sum on all a and b indices and the $\boldsymbol{\mathcal{L}}$ rank-4 tensor multiplies a symmetrical matrix, it is convenient to recast it into a symmetrical form:

$$L_{abcd} = \sum_{k,\mu\nu} \left(e_\mu^a \frac{\partial \ln a_\mu}{\partial \Phi_{cd}} + \frac{\partial e_\mu^a}{\partial \Phi_{cd}}\right) e_\mu^k e_\nu^b e_\nu^k a_\nu^2, \tag{B9}$$

$$\mathcal{L}_{abcd} = \frac{\mathcal{P}_{ab}}{\sqrt{M_a M_b}} \frac{L_{abcd} + L_{bacd}}{2}, \tag{B10}$$

$$\mathcal{P}_{ab} = \sqrt{2}(1 - \delta_{ab}) + \delta_{ab}, \tag{B11}$$

$$\mathcal{L}_{abcd} = \frac{\mathcal{P}_{ab}}{\sqrt{M_a M_b}} \sum_\mu \left[e_\mu^a e_\mu^b \frac{\partial \ln a_\mu}{\partial \Phi_{cd}} + \frac{1}{2} \frac{\partial (e_\mu^a e_\mu^b)}{\partial \Phi_{cd}}\right] a_\mu^2. \tag{B12}$$

In the minimum the only nonzero term of the Hessian matrix is given by

$$\left.\frac{\partial^2 \mathcal{F}(\vec{\mathcal{R}},\mathbf{\Phi},\{\vec{a}_i\})}{\partial \Phi_{ab} \partial \Phi_{cd}}\right|_{\mathbf{\Phi}=\mathbf{K}} = -\mathcal{L}_{abcd}, \tag{B13}$$

$$\frac{\partial^2 \mathcal{F}(\vec{\mathcal{R}},\mathbf{\Phi},\{\vec{a}_i\})}{\partial \Phi_{ab} \partial \Phi_{cd}} = -\frac{\mathcal{P}_{ab}}{\sqrt{M_a M_b}} \times \sum_\mu \left[a_\mu e_\mu^a e_\mu^b \frac{\partial a_\mu}{\partial \Phi_{cd}} + \frac{1}{2} a_\mu^2 \frac{\partial (e_\mu^a e_\mu^b)}{\partial \Phi_{cd}}\right]. \tag{B14}$$

Let us start with the term inside the square brackets. The derivative of a_μ can be obtained with the chain rule:

$$\frac{\partial a_\mu}{\partial \Phi_{cd}} = \frac{\partial a_\mu}{\partial \omega_\mu} \frac{\partial \omega_\mu}{\partial \Phi_{cd}} = \frac{\mathcal{P}_{cd}}{2\omega_\mu} \frac{e_\mu^c e_\mu^d}{\sqrt{M_c M_d}} \frac{\partial a_\mu}{\partial \omega_\mu}. \tag{B15}$$

The derivative of the polarization versors can be computed with first-order perturbation theory:

$$\frac{\partial \left(e_\mu^a e_\mu^b\right)}{\partial \Phi_{cd}} = e_\mu^a \frac{\partial e_\mu^b}{\partial \Phi_{cd}} + e_\mu^b \frac{\partial e_\mu^a}{\partial \Phi_{cd}} = \frac{\mathcal{P}_{cd}}{\sqrt{M_c M_d}} \sum_\nu^{\nu\neq\mu} \frac{\left(e_\mu^a e_\nu^b + e_\mu^b e_\nu^a\right)\left(e_\nu^c e_\mu^d + e_\mu^c e_\nu^d\right)}{2\left(\omega_\mu^2 - \omega_\nu^2\right)}. \tag{B16}$$

We have a complete expression for the Hessian matrix:

$$\frac{\partial^2 \mathcal{F}(\vec{\mathcal{R}},\mathbf{\Phi},\{\vec{a}_i\})}{\partial \Phi_{ab} \partial \Phi_{cd}} = -\frac{\mathcal{P}_{ab}\mathcal{P}_{cd}}{\sqrt{M_a M_b M_c M_d}} \left[\sum_\mu \frac{e_\mu^a e_\mu^b e_\mu^c e_\mu^d}{4\omega_\mu} \frac{\partial a_\mu^2}{\partial \omega_\mu} + \sum_{\mu\nu}^{\mu\neq\nu} \frac{e_\mu^a e_\nu^b (e_\mu^c \varepsilon_\nu^d + e_\nu^c e_\mu^d)}{4} \left(\frac{a_\mu^2}{\omega_\mu^2 - \omega_\nu^2} + \frac{a_\nu^2}{\omega_\nu^2 - \omega_\mu^2}\right)\right]. \tag{B17}$$

We can use the bosonic occupation number and write a_μ as a function of n_μ:

$$a_\mu = \sqrt{\frac{\hbar}{\omega_\mu}\left[n_\mu(\beta)+\frac{1}{2}\right]}, \tag{B18a}$$

$$\frac{a_\mu}{2\omega_\mu}\frac{\partial a_\mu}{\partial \omega_\mu} = -\frac{\hbar}{8\omega_\mu^3}\left(2n_\mu+1+2\beta\hbar\omega_\mu n_\mu^2+2\beta\hbar\omega n_\mu\right). \tag{B18b}$$

Therefore we have

$$\frac{\partial^2\mathcal{F}(\vec{\mathcal{R}},\mathbf{\Phi},\{\vec{a}_i\})}{\partial\Phi_{ab}\partial\Phi_{cd}} = \frac{\hbar\,\mathcal{P}_{ab}\mathcal{P}_{cd}}{\sqrt{M_aM_bM_cM_d}}\Bigg[\sum_\mu e_\mu^a e_\mu^b e_\mu^c e_\mu^d \frac{2n_\mu+1+2\beta\hbar\omega_\mu n_\mu^2+2\beta\hbar\omega_\mu n_\mu}{8\omega_\mu^3} - \sum_{\mu\nu}^{\mu\neq\nu}\frac{e_\mu^a e_\nu^b(e_\mu^c e_\nu^d+e_\nu^c e_\mu^d)}{8(\omega_\mu^2-\omega_\nu^2)}\left(\frac{2n_\mu+1}{\omega_\mu}-\frac{2\omega_\nu+1}{\omega_\nu}\right)\Bigg]. \tag{B19}$$

It is clear from Eq. (B19) that a $\mathbf{\Lambda}$ matrix can be introduced so that

$$\frac{\partial^2\mathcal{F}(\vec{\mathcal{R}},\mathbf{\Phi},\{\vec{a}_i\})}{\partial\Phi_{ab}\partial\Phi_{cd}} = \frac{1}{2}\mathcal{P}_{ab}\mathcal{P}_{cd}\sum_{\mu\nu}\left(\Lambda_{\mu\nu}^{abcd}+\Lambda_{\mu\nu}^{abdc}\right), \tag{B20}$$

where

$$\Lambda_{\mu\mu}^{abcd} = \frac{\hbar e_\mu^a e_\mu^b e_\mu^c e_\mu^d}{\sqrt{M_aM_bM_cM_d}}\frac{2n_\mu+1+2\beta\hbar\omega_\mu n_\mu^2+2\beta\hbar\omega_\mu n_\mu}{8\omega_\mu^3}, \tag{B21a}$$

$$\Lambda_{\mu\nu}^{abcd} = -\frac{\hbar}{\sqrt{M_aM_bM_cM_d}}\frac{e_\mu^a e_\nu^b e_\mu^c e_\nu^d}{(\omega_\mu-\omega_\nu)(\omega_\mu+\omega_\nu)}\frac{2n_\mu\omega_\nu-2\omega_\mu n_\nu+\omega_\nu-\omega_\mu}{4\omega_\mu\omega_\nu}. \tag{B21b}$$

To conclude the proof it is sufficient to show that the $\mathbf{\Lambda}$ matrix of Eq. (32) is equal to

$$\Lambda^{abcd} = \sum_{\mu\nu}\Lambda_{\mu\nu}^{abcd}. \tag{B22}$$

First, we introduce an auxiliary function $f(\omega_\mu,\omega_\nu)$ as

$$f(\omega_\mu,\omega_\nu) = \frac{2\omega_\nu n_\mu-2\omega_\mu n_\nu+\omega_\nu-\omega_\mu}{4\omega_\mu\omega_\nu(\omega_\mu+\omega_\nu)(\omega_\mu-\omega_\nu)} = -\frac{1}{4\omega_\mu\omega_\nu}\left[\frac{n_\mu+n_\nu+1}{\omega_\mu+\omega_\nu}-\frac{n_\mu-n_\nu}{\omega_\mu-\omega_\nu}\right]. \tag{B23}$$

In the limit $\omega_\nu\to\omega_\mu$ we get

$$f(\omega_\mu) = \lim_{\omega_\nu\to\omega_\mu} f(\omega_\mu,\omega_\nu) = -\frac{2n_\mu+1+2\hbar\beta\omega_\mu n_\mu^2+2\hbar\beta n_\mu\omega_\mu}{8\omega_\mu^3}, \tag{B24}$$

$$f(\omega_\mu) = -\frac{1}{4\omega_\mu^2}\left[\frac{2n_\mu+1}{2\omega_\mu}-\frac{\partial n}{\partial\omega}\right]. \tag{B25}$$

So $\Lambda_{\mu\mu}^{abcd}$ is obtained as the continuous limit of $\Lambda_{\mu\nu}^{abcd}$ when $\mu\to\nu$:

$$\Lambda_{\mu\nu}^{abcd} = -\frac{\hbar e_\mu^a e_\mu^b e_\mu^c e_\mu^d}{\sqrt{M_aM_bM_cM_d}}f(\omega_\mu,\omega_\nu), \qquad \Lambda_{\mu\mu}^{abcd} = -\frac{\hbar e_\mu^a e_\mu^b e_\mu^c e_\mu^d}{\sqrt{M_aM_bM_cM_d}}f(\omega_\mu). \tag{B26}$$

Substituting Eqs. (B23) and (B25) we finally get

$$\Lambda_{\mu\nu}^{abcd} = \frac{\hbar}{4\omega_\mu\omega_\nu}\frac{e_\mu^a e_\nu^b e_\mu^c e_\nu^d}{\sqrt{M_aM_bM_cM_d}}\times\begin{cases}\dfrac{n_\mu+n_\nu+1}{\omega_\mu+\omega_\nu}-\dfrac{n_\mu-n_\nu}{\omega_\mu-\omega_\nu} & \omega_\mu\neq\omega_\nu\\ \dfrac{2n_\mu+1}{2\omega_\mu}-\dfrac{\partial n_\mu}{\partial\omega_\mu} & \omega_\mu=\omega_\nu\end{cases}. \tag{B27}$$

APPENDIX C: HESSIAN IN THE CENTROIDS

The Hessian matrix approximation that we provide for the centroids is compared with the free-energy Hessian calculated in Ref. [35]. In particular, the correct preconditioner should be chosen according to the minimization strategy. If the inner degrees of freedom are optimized simultaneously with the force constant matrix, then the correct preconditioner should be

the complete Hessian matrix between any couple of degrees of freedom while the others are fixed. Therefore we are neglecting the mixed derivatives between the force constant and the centroids. However, the centroids preconditioner we provided is the correct one, since the second derivative of the free energy is computed at a fixed force constant matrix.

The free-energy Hessian provided by Ref. [35] is, instead, the total derivative of the free energy:

$$\frac{d^2\mathcal{F}(\vec{\mathcal{R}},\boldsymbol{\Phi}(\vec{\mathcal{R}}),\{\vec{a}_i\})}{d\mathcal{R}_a d\mathcal{R}_b} = \frac{\partial^2\mathcal{F}(\vec{\mathcal{R}},\boldsymbol{\Phi},\{\vec{a}_i\})}{\partial\mathcal{R}_a\partial\mathcal{R}_b} + \frac{\partial^2\mathcal{F}(\vec{\mathcal{R}},\boldsymbol{\Phi},\{\vec{a}_i\})}{\partial R_a\partial\boldsymbol{\Phi}}\frac{\partial\boldsymbol{\Phi}}{\partial\mathcal{R}_b} + \frac{\partial^2\boldsymbol{\Phi}}{\partial\mathcal{R}_a\partial\mathcal{R}_b}\frac{\partial\mathcal{F}(\vec{\mathcal{R}},\boldsymbol{\Phi},\{\vec{a}_i\})}{\partial\boldsymbol{\Phi}}. \quad \text{(C1)}$$

The last term is zero in the minimum of the free energy, due to the Hellman-Feynman theorem. This is, indeed, the correct free-energy Hessian to study structural instabilities. It is also the correct preconditioner if the centroids are moved only after the full relaxation of the force constant is performed at each step. This is unpractical: the so-defined minimization algorithm converges slower, as it needs a full force constant minimization, the most expensive one, before starting to move the inner degrees of freedom. Moreover, the computation of the Hessian in Eq. (C1) is more expensive than the one provided in this paper, and it is not always positive defined.

APPENDIX D: QHA IN THE SCHA FRAMEWORK

The QHA can be reformulated in the SCHA framework in order to understand differences between the two approaches. The SCHA free energy is

$$\mathcal{F}(\vec{\mathcal{R}},\boldsymbol{\Phi},\{\vec{a}_i\}) = F_{\boldsymbol{\Phi}} + \langle V - \mathcal{V}_{\vec{\mathcal{R}},\boldsymbol{\Phi}}\rangle_{\rho_{\vec{\mathcal{R}},\boldsymbol{\Phi}}}. \quad \text{(D1)}$$

If the system is perfectly harmonic, then the minimum of the free energy is found when $\mathcal{V}_{\vec{R}_0,\boldsymbol{\Phi}_0} = V$, and we get the QHA free energy:

$$F_{\mathrm{QHA}} = \mathcal{F} = F_{\boldsymbol{\Phi}_0} + V(\vec{R}_0),$$
$$\Phi_{0\alpha\beta} = \left.\frac{\partial^2 V}{\partial R_\alpha \partial R_\beta}\right|_{\vec{R}=\vec{R}_0}, \quad \text{(D2)}$$

where $\vec{R}_0$ is the minimum of the BO energy surface. So QHA is equivalent to SCHA for any harmonic potential. If the system is anharmonic, QHA approximates the potential as the second-order Taylor expansion around the equilibrium position. This makes the QHA theory not a self-consistent approach but a series expansion of the real potential.

If the atomic position coordinates relaxation is allowed, as introduced by Lazzeri and de Gironcoli [53,56], then the QHA free energy becomes

$$\mathcal{F}_{\mathrm{QHA}}(\vec{R}_c) = F_{\tilde{\boldsymbol{\Phi}}(\vec{R}_c)} + V(\vec{R}_c),$$
$$\tilde{\Phi}_{\alpha\beta}(\vec{R}_c) = \left.\frac{\partial^2 V}{\partial R_\alpha \partial R_\beta}\right|_{\vec{R}=\vec{R}_c}. \quad \text{(D3)}$$

This is equivalent to SCHA [Eq. (D1)] keeping Φ fixed to the harmonic dynamical matrix and neglecting the contribution arising from $\langle V - \mathcal{V}\rangle_{\rho_{\vec{R}_c,\tilde{\boldsymbol{\Phi}}(\vec{R}_c)}}$. The anharmonicity is taken into account by the fact that the harmonic dynamical matrix is a function of the atomic positions. This approximation is equivalent to neglecting all the even (from the fourth order) contribution in the BO surface Taylor expansion around the $\vec{R}_c$ that minimizes $\mathcal{F}_{\mathrm{QHA}}$. In this case, the average $\langle V - \mathcal{V}\rangle_{\rho_{\tilde{\boldsymbol{\Phi}}(\vec{R}_c)}}$ is equal to zero, and the harmonic dynamical matrix is the one that minimizes the SCHA free energy [Eq. (17) is exactly zero]. If only odd anharmonicities are present in the system (i.e., they dominate in the region of the quantum and thermal fluctuations), the QHA relaxed free energy coincides with the SCHA. The SCHA, therefore, is a natural extension to the relaxed QHA that assures the self-consistency of the theory for any kind of anharmonicity by explicitly including the average $\langle V - \mathcal{V}\rangle_{\rho_{\vec{\mathcal{R}},\boldsymbol{\Phi}}}$ in the free energy. Indeed, the SSCHA algorithm is much more efficient than the QHA relaxation, since it requires us only to compute energies and forces, while the QHA relaxation requires the third-order derivatives of the energy, and the application of the $2n+1$ theorem for each minimization step [53].

[1] A. A. Volkov, Y. G. Goncharov, G. V. Kozlov, S. P. Lebedev, A. M. Prokhorov, R. A. Aliev, and K. R. Allakhverdiev, Pis'ma Zh. Eksp. Teor. Fiz. **37**, 517 (1983) [JETP Lett. **37**, 615 (1983)].

[2] J. Tsang, J. Smith, Jr., and M. Shafer, Phys. Rev. Lett. **37**, 1407 (1976).

[3] G. Pawley, W. Cochran, R. Cowley, and G. Dolling, Phys. Rev. Lett. **17**, 753 (1966).

[4] O. Delaire, J. Ma, K. Marty, A. F. May, M. A. McGuire, M.-H. Du, D. J. Singh, A. Podlesnyak, G. Ehlers, M. Lumsden *et al.*, Nat. Mater. **10**, 614 (2011).

[5] Y. Luspin, J. Servoin, and F. Gervais, J. Phys. C **13**, 3761 (1980).

[6] F. Weber, S. Rosenkranz, J.-P. Castellan, R. Osborn, G. Karapetrov, R. Hott, R. Heid, K.-P. Bohnen, and A. Alatas, Phys. Rev. Lett. **107**, 266401 (2011).

[7] M. Leroux, I. Errea, M. Le Tacon, S.-M. Souliou, G. Garbarino, L. Cario, A. Bosak, F. Mauri, M. Calandra, and P. Rodière, Phys. Rev. B **92**, 140303 (2015).

[8] M. Holt, P. Zschack, H. Hong, M. Y. Chou, and T.-C. Chiang, Phys. Rev. Lett. **86**, 3799 (2001).

[9] M. Leroux, M. Le Tacon, M. Calandra, L. Cario, M. A. Measson, P. Diener, E. Borrissenko, A. Bosak, and P. Rodiere, Phys. Rev. B **86**, 155125 (2012).

[10] P. S. H. Ghosez, X. Gonze, and J.-P. Michenaud, Ferroelectrics **206**, 205 (1998).

[11] M. Calandra, I. I. Mazin, and F. Mauri, Phys. Rev. B **80**, 241108 (2009).

[12] M. Calandra and F. Mauri, Phys. Rev. Lett. **106**, 196406 (2011).

[13] I. Errea, Euro. Phys. J. B **89**, 237 (2016).

[14] B. Stritzker and W. Buckel, Z. Phys. A **257**, 1 (1972).
[15] I. Errea, M. Calandra, and F. Mauri, Phys. Rev. Lett. **111**, 177002 (2013).
[16] I. Errea, M. Calandra, and F. Mauri, Phys. Rev. B **89**, 064302 (2014).
[17] I. Errea, M. Calandra, C. J. Pickard, J. Nelson, R. J. Needs, Y. Li, H. Liu, Y. Zhang, Y. Ma, and F. Mauri, Phys. Rev. Lett. **114**, 157004 (2015).
[18] J. Schirber and C. Northrup, Jr., Phys. Rev. B **10**, 3818 (1974).
[19] R. Car and M. Parrinello, Phys. Rev. Lett. **55**, 2471 (1985).
[20] C. Z. Wang, C. T. Chan, and K. M. Ho, Phys. Rev. B **42**, 11276 (1990).
[21] I. B. Magdău and G. J. Ackland, Phys. Rev. B **87**, 174110 (2013).
[22] M. P. Ljungberg and J. Íñiguez, Phys. Rev. Lett. **110**, 105503 (2013).
[23] A. M. Teweldeberhan, J. L. Dubois, and S. A. Bonev, Phys. Rev. Lett. **105**, 235503 (2010).
[24] D.-B. Zhang, T. Sun, and R. M. Wentzcovitch, Phys. Rev. Lett. **112**, 058501 (2014).
[25] O. Hellman, I. A. Abrikosov, and S. I. Simak, Phys. Rev. B **84**, 180301 (2011).
[26] O. Hellman, P. Steneteg, I. A. Abrikosov, and S. I. Simak, Phys. Rev. B **87**, 104111 (2013).
[27] O. Hellman and I. A. Abrikosov, Phys. Rev. B **88**, 144301 (2013).
[28] D. Chandler and P. G. Wolynes, J. Chem. Phys. **74**, 4078 (1981).
[29] J. A. Barker, J. Chem. Phys. **70**, 2914 (1979).
[30] M. Ceriotti, M. Parrinello, T. E. Markland, and D. E. Manolopoulos, J. Chem. Phys. **133**, 124104 (2010).
[31] T. Tadano and S. Tsuneyuki, Phys. Rev. B **92**, 054301 (2015).
[32] B. Monserrat, N. D. Drummond, and R. J. Needs, Phys. Rev. B **87**, 144302 (2013).
[33] M. Borinaga, P. Riego, A. Leonardo, M. Calandra, F. Mauri, A. Bergara, and I. Errea, J. Phys.: Condens. Matter **28**, 494001 (2016).
[34] I. Errea, M. Calandra, C. J. Pickard, J. R. Nelson, R. J. Needs, Y. Li, H. Liu, Y. Zhang, Y. Ma, and F. Mauri, Nature (London) **532**, 81 (2016).
[35] R. Bianco, I. Errea, L. Paulatto, M. Calandra, and F. Mauri, Phys. Rev. B **96**, 014111 (2017).
[36] Y. Tajima, T. Matsuo, and H. Suga, Nature (London) **299**, 810 (1982).
[37] B. Pamuk, J. M. Soler, R. Ramírez, C. P. Herrero, P. W. Stephens, P. B. Allen, and M.-V. Fernández-Serra, Phys. Rev. Lett. **108**, 193003 (2012).
[38] K. Umemoto, E. Sugimura, S. de Gironcoli, Y. Nakajima, K. Hirose, Y. Ohishi, and R. M. Wentzcovitch, Phys. Rev. Lett. **115**, 173005 (2015).
[39] K. Röttger, A. Endriss, J. Ihringer, S. Doyle, and W. F. Kuhs, Acta Crystallogr. Sect. B **50**, 644 (1994).
[40] K. Röttger, A. Endriss, J. Ihringer, S. Doyle, and W. F. Kuhs, Acta Crystallogr. Sect. B **68**, 91 (2012).
[41] W. H. Press, *Numerical Recipes: The Art of Scientific Computing*, 3rd ed. (Cambridge University Press, Cambridge, England, 2007).
[42] P. López Ríos, B. Monserrat, and R. J. Needs, Phys. Rev. B **97**, 054104 (2018).
[43] A. Kong, J. S. Liu, and W. H. Wong, J. Am. Stat. Assoc. **89**, 278 (1994).
[44] F. Tassone, F. Mauri, and R. Car, Phys. Rev. B **50**, 10561 (1994).
[45] C. Pinilla, M. Blanchard, E. Balan, G. Ferlat, R. Vuilleumier, and F. Mauri, Geochim. Cosmochim. Acta **135**, 203 (2014).
[46] J. P. Perdew, K. Burke, and M. Ernzerhof, Phys. Rev. Lett. **77**, 3865 (1996).
[47] D. Vanderbilt, Phys. Rev. B **41**, 7892 (1990).
[48] A. D. Corso, Comput. Mater. Sci. **95**, 337 (2014).
[49] P. Giannozzi, S. Baroni, N. Bonini, M. Calandra, R. Car, C. Cavazzoni, D. Ceresoli, G. L. Chiarotti, M. Cococcioni, I. Dabo, A. D. Corso, S. de Gironcoli, S. Fabris, G. Fratesi, R. Gebauer, U. Gerstmann, C. Gougoussis, A. Kokalj, M. Lazzeri, L. Martin-Samos, N. Marzari, F. Mauri, R. Mazzarello, S. Paolini, A. Pasquarello, L. Paulatto, C. Sbraccia, S. Scandolo, G. Sclauzero, A. P. Seitsonen, A. Smogunov, P. Umari, and R. M. Wentzcovitch, J. Phys.: Condens. Matter **21**, 395502 (2009).
[50] P. Giannozzi, O. Andreussi, T. Brumme, O. Bunau, M. B. Nardelli, M. Calandra, R. Car, C. Cavazzoni, D. Ceresoli, M. Cococcioni, N. Colonna, I. Carnimeo, A. D. Corso, S. de Gironcoli, P. Delugas, R. A. DiStasio, A. Ferretti, A. Floris, G. Fratesi, G. Fugallo, R. Gebauer, U. Gerstmann, F. Giustino, T. Gorni, J. Jia, M. Kawamura, H.-Y. Ko, A. Kokalj, E. Küçükbenli, M. Lazzeri, M. Marsili, N. Marzari, F. Mauri, N. L. Nguyen, H.-V. Nguyen, A. O. de-la Roza, L. Paulatto, S. Poncé, D. Rocca, R. Sabatini, B. Santra, M. Schlipf, A. P. Seitsonen, A. Smogunov, I. Timrov, T. Thonhauser, P. Umari, N. Vast, X. Wu, and S. Baroni, J. Phys.: Condens. Matter **29**, 465901 (2017).
[51] L. Paulatto, I. Errea, M. Calandra, and F. Mauri, Phys. Rev. B **91**, 054304 (2015).
[52] M. J. Gillan, D. Alfè, and A. Michaelides, J. Chem. Phys. **144**, 130901 (2016).
[53] M. Lazzeri and S. de Gironcoli, Phys. Rev. B **65**, 245402 (2002).
[54] A. D. Fortes, Acta Crystallogr. Sect. B **74**, 196 (2018).
[55] M. Gupta, R. Mittal, B. Singh, S. Mishra, D. Adroja, A. Fortes, and S. Chaplot, arXiv:1803.08769.
[56] M. Lazzeri and S. de Gironcoli, Phys. Rev. Lett. **81**, 2096 (1998).

Quantum Crystal Structure in the 250 K Superconducting Lanthanum Hydride

Ion Errea,[1,2,3] Francesco Belli,[1,2] Lorenzo Monacelli,[4] Antonio Sanna,[5] Takashi Koretsune,[6] Terumasa Tadano,[7] Raffaello Bianco,[2] Matteo Calandra,[8] Ryotaro Arita,[9,10] Francesco Mauri,[4,11] and José A. Flores-Livas[4]

[1] *Fisika Aplikatua 1 Saila, Gipuzkoako Ingeniaritza Eskola, University of the Basque Country (UPV/EHU), Europa Plaza 1, 20018 Donostia/San Sebastián, Spain*
[2] *Centro de Física de Materiales (CSIC-UPV/EHU), Manuel de Lardizabal Pasealekua 5, 20018 Donostia/San Sebastián, Spain*
[3] *Donostia International Physics Center (DIPC), Manuel de Lardizabal Pasealekua 4, 20018 Donostia/San Sebastián, Spain*
[4] *Dipartimento di Fisica, Università di Roma La Sapienza, Piazzale Aldo Moro 5, I-00185 Roma, Italy*
[5] *Max-Planck Institute of Microstructure Physics, Weinberg 2, 06120 Halle, Germany*
[6] *Department of Physics, Tohoku University, 6-3 Aza-Aoba, Sendai, 980-8578 Japan*
[7] *Research Center for Magnetic and Spintronic Materials, National Institute for Materials Science, Tsukuba 305-0047, Japan*
[8] *Sorbonne Université, CNRS, Institut des Nanosciences de Paris, UMR7588, F-75252, Paris, France*
[9] *Department of Applied Physics, University of Tokyo, 7-3-1 Hongo Bunkyo-ku, Tokyo 113-8656 Japan*
[10] *RIKEN Center for Emergent Matter Science, 2-1 Hirosawa, Wako, 351-0198, Japan*
[11] *Graphene Labs, Fondazione Istituto Italiano di Tecnologia, Via Morego, I-16163 Genova, Italy*

(Dated: July 30, 2019)

The discovery of superconductivity at 200 K in the hydrogen sulfide system at large pressures [1] was a clear demonstration that hydrogen-rich materials can be high-temperature superconductors. The recent synthesis of LaH_{10} with a superconducting critical temperature (T_c) of 250 K [2, 3] places these materials at the verge of reaching the long-dreamed room-temperature superconductivity. Electrical and x-ray diffraction measurements determined a weakly pressure-dependent T_c for LaH_{10} between 137 and 218 gigapascals in a structure with a face-centered cubic (fcc) arrangement of La atoms [3]. Here we show that quantum atomic fluctuations stabilize in all this pressure range a high-symmetry Fm-3m crystal structure consistent with experiments, which has a colossal electron-phonon coupling of $\lambda \sim 3.5$. Even if *ab initio* classical calculations neglecting quantum atomic vibrations predict this structure to distort below 230 GPa yielding a complex energy landscape with many local minima, the inclusion of quantum effects simplifies the energy landscape evidencing the Fm-3m as the true ground state. The agreement between the calculated and experimental T_c values further supports this phase as responsible for the 250 K superconductivity. The relevance of quantum fluctuations in the energy landscape found here questions many of the crystal structure predictions made for hydrides within a classical approach that at the moment guide the experimental quest for room-temperature superconductivity [4–6]. Furthermore, quantum effects reveal crucial to sustain solids with extraordinary electron-phonon coupling that may otherwise be unstable [7].

The potential of metallic hydrogen as a high-T_c superconductor [8, 9] was identified few years after the development of the Bardeen-Cooper-Schrieffer (BCS) theory, which explained superconductivity through the electron-phonon coupling mechanism. The main argument was that T_c can be maximized for light compounds due to their high vibrational frequencies. In view of the large pressures needed to metallize hydrogen [10], chemical pre-compression with heavier atoms [11, 12] was suggested as a pathway to decrease the pressure needed to reach metallicity and, thus, superconductivity. These ideas have bloomed thanks to modern *ab initio* crystal structure prediction methods based on density-functional theory (DFT) [5, 13, 14]. Hundreds of hydrogen-rich compounds have been predicted to be thermodynamically stable at high pressures and, by calculating the electron-phonon interaction parameters, their T_c's have been estimated [4, 5]. The success of this symbiosis between DFT crystal structure predictions and T_c calculations is exemplified by the discovery of superconductivity in H_3S at 200 K [1, 15, 16]. The prospects for discovering warm hydrogen-based superconductors in the next years are thus high, in clear contrast with other high-T_c superconducting families such as cuprates or pnictides [17, 18], where the lack of a clear understanding of the superconducting mechanism hinders an *in silico* guided approach.

DFT predictions in the La-H system proposed LaH_{10} to be thermodynamically stable against decomposition above 150 GPa. A sodalite type-structure with space group Fm-3m and T_c∼280 K was suggested above ∼220 GPa (see Fig. 1), and a distorted version of it below with space group $C2/m$ and a rhombohedral La sublattice [19, 20]. By laser heating a lanthanum sample in a hydrogen-rich atmosphere within a diamond anvil cell (DAC), a lanthanum superhydride was synthesized right after [20]. Based on the unit cell volume obtained by x-ray diffraction, the hydrogen to lanthanum ratio was estimated to be between 9 and 12. An fcc arrangement of the La atoms was determined above ∼160 GPa, and a rhombohedral lattice below with R-3m space group for the La sublattice. Due to the small x-ray cross section of hydrogen, experimentally it is not possible to resolve directly the H sublattice. Early this year, evidences of a superconducting transition at 260 K and 188 GPa were reported in a lanthanum superhydride [2]. These findings were confirmed and put in solid grounds few months later

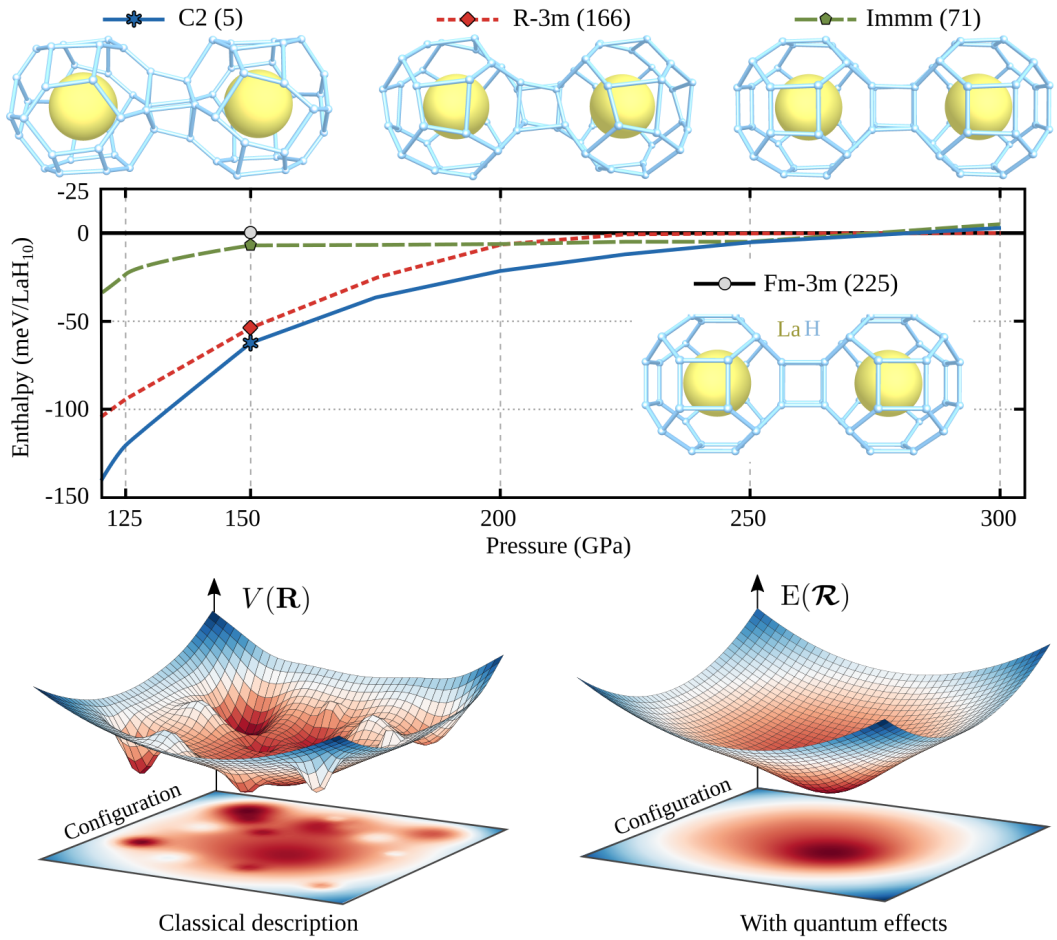

Figure 1. **Quantum effects stabilize the symmetric Fm-3m phase of LaH_{10}.** Top panel: Enthalpy as function of pressure for different structures of LaH_{10} calculated neglecting the zero-point energy. The pressure in the figure is calculated from $V(\mathbf{R})$, neglecting quantum effects on it. The crystal structure of the different phases found are shown. Bottom left: Sketch of a Born-Oppenheimer energy surface $V(\mathbf{R})$ exemplifying the presence of many local minima for many distorted structures. $\mathbf{R}$ represents the positions of atoms treated classically as simple points. Bottom right: sketch of the configurational $E(\boldsymbol{\mathcal{R}})$ energy surface including quantum effects. $\boldsymbol{\mathcal{R}}$ represents the quantum centroid positions, which determine the center of the ionic wave functions, i.e., the average atomic positions. All phases collapse to a single phase, the highly symmetric Fm-3m.

by an independent group that measured a T_c of 250 K from 137 to 218 GPa in a structure with fcc arrangement of the La atoms and suggested a LaH_{10} stoichiometry [3].

Even if it is tempting to assign the record superconductivity to the Fm-3m phase predicted previously [2, 3], there is a clear problem: the Fm-3m structure is predicted to be dynamically unstable in the whole pressure range where a 250 K T_c was observed. This implies that this phase is not a minimum of the Born-Oppenheimer energy surface. Consequently, no T_c has been estimated for this phase in the experimental pressure range. Considering that quantum proton fluctuations symmetrize hydrogen bonds in the high-pressure X phase of ice [21] and in H_3S [22, 23], this contradiction may signal a problem of the classical treatment of the atomic vibrations in the calculations. We show here how quantum atomic fluctuations completely reshape the energy landscape making the Fm-3m phase the true ground state and the responsible for the observed superconducting critical temperature.

We start by calculating with DFT the lowest enthalpy structures of LaH_{10} as a function of pressure with state-of-the-art crystal structure prediction methods [24, 25]. The contribution associated with atomic fluctuations is not included, so that the energy just corresponds to the Born-Oppenheimer energy $V(\mathbf{R})$, where $\mathbf{R}$ represents the position of atoms treated classically as simple points. As shown in Figure 1, different distorted phases of LaH_{10} are thermodynamically more stable than the Fm-3m phase. Above ∼250 GPa all phases merge to the Fm-3m symmetric phase. These results are in agreement with previous calculations [19], even if we identify other possible distorted structures with lower enthalpy such as

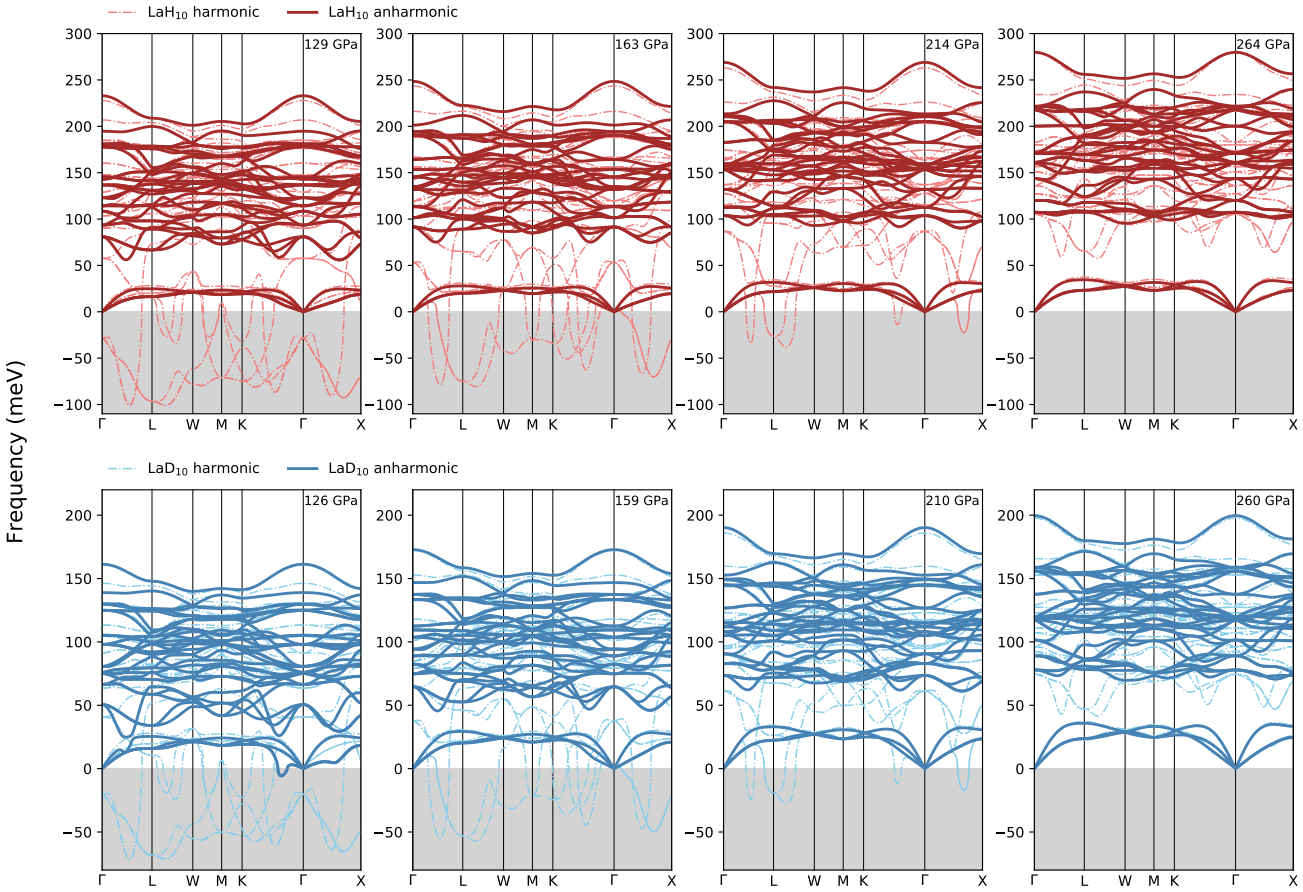

Figure 2. **Phonon band structure of Fm-3m LaH_{10} at different pressures.** The harmonic phonons show large instabilities in several regions of the Brillouin zone. Only at the high-pressure limit, e.g. above 220-250 GPa dynamic (harmonic) stabilization is reached. The anharmonic phonons obtained from the Hessian of the quantum $E(\boldsymbol{\mathcal{R}})$ energy within the SSCHA are dynamically stable in the experimentally relevant range. The case of deuterium develops a instability at low pressures (126 GPa) consistent with experimental evidence. The pressure given corresponds to the calculated from $E(\boldsymbol{\mathcal{R}})$ that considers quantum effects. The grey area marks the region with imaginary phonon frequencies, which are depicted as negative frequencies.

the R-3m, $C2$ and $P1$ (not shown) phases. These phases not only imply a distortion of the H atoms, also show a La sublattice without an fcc arrangement, and thus should be detectable by x-ray. The fact that many structures are predicted underlines that the classical $V(\mathbf{R})$ energy surface is of a multifunnel structure tractable to many different saddle and local minima, as sketched in Figure 1.

This picture completely changes when including the energy of quantum atomic fluctuations, the zero-point energy (ZPE). We calculate the ZPE within the stochastic self-consistent harmonic approximation (SSCHA) [26–28]. The SSCHA is a variational method that calculates the $E(\boldsymbol{\mathcal{R}})$ energy of the system including atomic quantum fluctuations as a function of the *centroid* positions $\boldsymbol{\mathcal{R}}$, which determine the center of the ionic wave functions. The calculations are performed without approximating the $V(\mathbf{R})$ potential, keeping all its anharmonic terms. We perform a minimization of $E(\boldsymbol{\mathcal{R}})$ and determine the centroid positions at its minimum. By calculating the stress tensor from $E(\boldsymbol{\mathcal{R}})$ [28], we relax the lattice parameters seeking for structures with isotropic stress conditions considering quantum effects. We start the quantum relaxation for both R-3m and $C2$ phases with the lattice that yields a classical isotropic pressure of 150 GPa and vanishing classical forces, i.e., calculated from $V(\mathbf{R})$. All quantum relaxations quickly evolve into the Fm-3m phase. This suggests that the quantum $E(\boldsymbol{\mathcal{R}})$ energy landscape is much simpler than the classical $V(\mathbf{R})$ as sketched in Figure 1. And that the sodalite symmetric Fm-3m phase is the ground state for LaH_{10} in all the pressure range of interest. Quantum effects are colossal: reshaping the energy landscape and stabilizing structures by more than 60 meV per LaH_{10}.

Our results further confirm that the structure of LaH_{10} responsible for the 250 K superconductivity is Fm-3m. This is completely consistent with the fcc arrangement of La atoms found experimentally [3]. However, Geballe et al. [20] observed a rhombohedral distortion below ∼160

GPa, with an R-3m space group for the La sublattice and a rhombohedral angle of approximately 61.3°($c/a \sim 2.38$ in the hexagonal representation). Our calculations show that this distortion is compatible with slight anisotropic stress conditions in the DAC. Indeed, performing a SSCHA minimization for our R-3m phase but keeping the rhombohedral angle fixed at 62.3°(the value that yields an isotropic pressure of 150 GPa at the classical level) the quantum stress tensor shows a 6% anisotropy between the diagonal direction and the perpendicular plane. This suggests that anisotropic conditions inside the DAC can produce the R-3m phase, while other experimental stress conditions could favor other crystal phases.

The Fm-3m phonon spectra calculated in the harmonic approximation from the Hessian of $V(\mathbf{R})$ show clear phonon instabilities in a broad region of the Brillouin zone (see Figure 2). These instabilities appear below ∼230 GPa. This is consistent with the fact that below this pressure many possible atomic distortions lower the enthalpy of this phase. On the contrary, as shown in Figure 2, when calculating the phonons from the Hessian of $E(\boldsymbol{\mathcal{R}})$ [27], which effectively captures the full anharmonicity of $V(\mathbf{R})$, no instability is observed. This confirms again that the Fm-3m phase is a minimum in the quantum-energy landscape in the whole pressure range where a 250 K T_c was observed. While the Fm-3m phase of LaH_{10} remains a minimum of $E(\boldsymbol{\mathcal{R}})$ as low as $\sim$ 129 GPa, the case of LaD_{10} shows instabilities at 126 GPa, implying that at this pressure the Fm-3m phase of LaD_{10} distorts to a new phase (as suggested by Drozdov et al. [3]). Below this pressure we also predict that LaH_{10} composition is not longer thermodynamically stable and low-hydrogen compositions are likely to occur.

Flagrantly, the breakdown of the classical harmonic approximation for phonons makes impossible the estimation of T_c below ∼250 GPa in the Fm-3m phase and questions all previous calculations [19, 29]. Indeed, the anharmonic phonon renormalization remains huge also at 264 GPa (see Figure 2). On the contrary, with anharmonic phonons derived from the Hessian of $E(\boldsymbol{\mathcal{R}})$ we can readily calculate the electron-phonon interaction and the superconducting T_c in the experimental range of pressure (120–210 GPa). The superconducting critical temperature is estimated fully *ab initio* –without any empirical parameter– by solving Migdal-Éliashberg (ME) equations and applying SuperConducting DFT (SCDFT). As shown in Figure 3, the numerical solutions of ME equations with anisotropic energy gap are almost on top of the experimental values. SCDFT values systematically show a slightly lower T_c. Our reported values of T_c evidence the phonon-driven mechanism of superconductivity and confirm LaH_{10} in its Fm-3m structure as responsible for the highest-T_c up to date reported. Our calculations for LaD_{10} in the Fm-3m phase are also in agreement with the experimental point reported. Despite the large anharmonic effects at play, the isotope coefficient

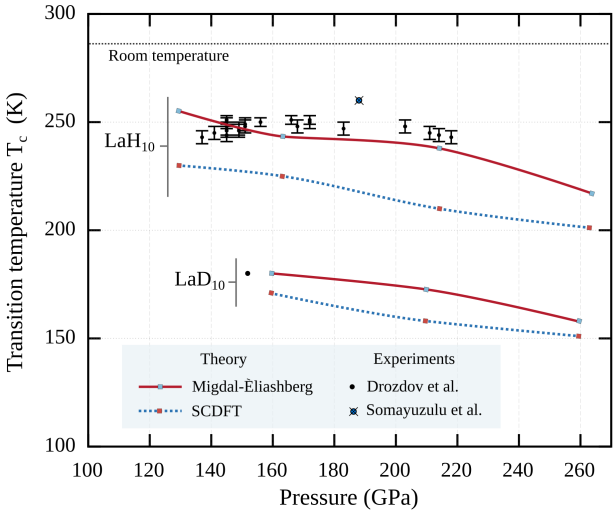

Figure 3. **Summary of experimental and theoretical T_c values.** Superconducting critical temperatures calculated within anisotropic Migdal-Éliashberg equations and SCDFT. In both cases the anharmonic phonons obtained with the SSCHA are used. The results are compared with the experimental measurements by Somayuzulu et al. [2] and Drozdov et al. [3].

$\alpha = -\left[\ln T_c(LaD_{10}) - \ln T_c(LaH_{10})\right] / \ln 2$ is close to 0.5 (0.43 around 160 GPa), the expected value in BCS theory, and it is in agreement with the experimentally reported $\alpha = 0.46$.

We finally check T_c for the subtle rhombohedral distortion that could be induced by anisotropic stress conditions of pressure. Fixing the rhombohedral angle at 62.3° the obtained T_c for the R-3m phase at 160 GPa is a 9% lower than for the Fm-3m. Thus, the observed weak pressure dependence of T_c is consistent with the absence of a rhombohedral distortion, as suggested by the x-ray data [3]. However, as argued above, undesired anisotropic stress conditions in the DAC can induce phase transitions. We thus believe that other experimental T_c measurements with lower values but around 200 K correspond to distorted structures induced by anisotropic conditions of pressure. In fact, we can safely rule out that compositions such as LaH_{11}, proposed to yield a high critical temperature [3], is responsible for any sizable T_c (see Extended Data).

In summary, this work demonstrates how quantum effects are of capital importance in determining the ground state structures of superconducting hydrides, challenging all current predictions and evidencing flaws in standard theoretical methods. It also illustrates that quantum fluctuations are indispensable to sustain crystals with huge λ's (λ reaches a record value of 3.6 at 129 GPa for LaH_{10}) that be otherwise destabilized by the colossal electron-phonon interaction to distorted (low symmetry)

structures reducing the electronic density of states at the Fermi level (see Extended Data) [7]. This is relevant since large λ is required to guarantee high-T_c [5, 6], not simply light atomic masses.

[1] A. P. Drozdov, M. I. Eremets, I. A. Troyan, V. Ksenofontov, and S. I. Shylin. Conventional superconductivity at 203 kelvin at high pressures in the sulfur hydride system. *Nature*, 525:73, 2015.

[2] Maddury Somayazulu, Muhtar Ahart, Ajay K. Mishra, Zachary M. Geballe, Maria Baldini, Yue Meng, Viktor V. Struzhkin, and Russell J. Hemley. Evidence for superconductivity above 260 K in lanthanum superhydride at megabar pressures. *Phys. Rev. Lett.*, 122:027001, 2019.

[3] A. P. Drozdov, P. P. Kong, V. S. Minkov, S. P. Besedin, M. A. Kuzovnikov, S. Mozaffari, L. Balicas, F. F. Balakirev, D. E. Graf, V. B. Prakapenka, E. Greenberg, D. A. Knyazev, M. Tkacz, and M. I. Eremets. Superconductivity at 250 K in lanthanum hydride under high pressures. *Nature*, 569:528, 2019.

[4] Tiange Bi, Niloofar Zarifi, Tyson Terpstra, and Eva Zurek. The search for superconductivity in high pressure hydrides. *arXiv preprint arXiv:1806.00163*, 2018.

[5] José A. Flores-Livas, Lilia Boeri, Antonio Sanna, Gianni Profeta, Ryotaro Arita, and Mikhail Eremets. A Perspective on Conventional High-Temperature Superconductors at High Pressure: Methods and Materials. *arXiv e-prints*, page arXiv:1905.06693, 2019.

[6] Chris J. Pickard, Ion Errea, and Mikhail I. Eremets. *to be published in Annual Review of Condensed Matter Physics*, 2019.

[7] Philip B. Allen and Marvin L. Cohen. Superconductivity and Phonon Softening. *Phys. Rev. Lett.*, 29:1593, 1972.

[8] N. Ashcroft. Metallic hydrogen: A high-temperature superconductor? *Phys. Rev. Lett.*, 21:1748, 1968.

[9] Vitalii L. Ginzburg. Superfluidity and superconductivity in the universe. *Journal of Statistical Physics*, 1:3, 1969.

[10] Ranga P. Dias and Isaac F. Silvera. Observation of the wigner-huntington transition to metallic hydrogen. *Science*, 355:715, 2017.

[11] J. J. Gilman. Lithium dihydrogen fluoride—an approach to metallic hydrogen. *Phys. Rev. Lett.*, 26:546, 1971.

[12] N. W. Ashcroft. Hydrogen dominant metallic alloys: High temperature superconductors? *Phys. Rev. Lett.*, 92:187002, 2004.

[13] Lijun Zhang, Yanchao Wang, Jian Lv, and Yanming Ma. Materials discovery at high pressures. *Nature Reviews Materials*, 2:17005, 2017.

[14] Artem R. Oganov, Chris J. Pickard, Qiang Zhu, and Richard J. Needs. Structure prediction drives materials discovery. *Nature Reviews Materials*, 4:331, 2019.

[15] Yinwei Li, Jian Hao, Hanyu Liu, Yanling Li, and Yanming Ma. The metallization and superconductivity of dense hydrogen sulfide. *The Journal of Chemical Physics*, 140:174712, 2014.

[16] Defang Duan, Yunxian Liu, Fubo Tian, Da Li, Xiaoli Huang, Zhonglong Zhao, Hongyu Yu, Bingbing Liu, Wenjing Tian, and Tian Cui. Pressure-induced metallization of dense $(H_2S)_2H_2$ with high-Tc superconductivity. *Sci. Rep.*, 4:6968, 2014.

[17] A. Schilling, M. Cantoni, J. D. Guo, and H. R. Ott. Superconductivity above 130 K in the Hg–Ba–Ca–Cu–O system. *Nature*, 363:56, 1993.

[18] Yoichi Kamihara, Hidenori Hiramatsu, Masahiro Hirano, Ryuto Kawamura, Hiroshi Yanagi, Toshio Kamiya, and Hideo Hosono. Iron-based layered superconductor: LaOFeP. *Journal of the American Chemical Society*, 128:10012, 2006.

[19] Hanyu Liu, Ivan I. Naumov, Roald Hoffmann, N.W. Ashcroft, and Russell J. Hemley. Potential high-Tc superconducting lanthanum and yttrium hydrides at high pressure. *Proceedings of the National Academy of Sciences*, 114:6990, 2017.

[20] Zachary M. Geballe, Hanyu Liu, Ajay K. Mishra, Muhtar Ahart, Maddury Somayazulu, Yue Meng, Maria Baldini, and Russell J. Hemley. Synthesis and stability of lanthanum superhydrides. *Angewandte Chemie International Edition*, 57:688, 2018.

[21] Magali Benoit, Dominik Marx, and Michele Parrinello. Tunnelling and zero-point motion in high-pressure ice. *Nature*, 392:258, 1998.

[22] Ion Errea, Matteo Calandra, Chris J. Pickard, Joseph R. Nelson, Richard J. Needs, Yinwei Li, Hanyu Liu, Yunwei Zhang, Yanming Ma, and Francesco Mauri. Quantum hydrogen-bond symmetrization in the superconducting hydrogen sulfide system. *Nature*, 532:81, 2016.

[23] Raffaello Bianco, Ion Errea, Matteo Calandra, and Francesco Mauri. High-pressure phase diagram of hydrogen and deuterium sulfides from first principles: Structural and vibrational properties including quantum and anharmonic effects. *Phys. Rev. B*, 97:214101, 2018.

[24] Stefan Goedecker. Minima hopping: An efficient search method for the global minimum of the potential energy surface of complex molecular systems. *The Journal of Chemical Physics*, 120:9911, 2004.

[25] M. Amsler and S. Goedecker. Crystal structure prediction using the minima hopping method. *The Journal of Chemical Physics*, 133:224104, 2010.

[26] Ion Errea, Matteo Calandra, and Francesco Mauri. Anharmonic free energies and phonon dispersions from the stochastic self-consistent harmonic approximation: Application to platinum and palladium hydrides. *Phys. Rev. B*, 89:064302, 2014.

[27] Raffaello Bianco, Ion Errea, Lorenzo Paulatto, Matteo Calandra, and Francesco Mauri. Second-order structural phase transitions, free energy curvature, and temperature-dependent anharmonic phonons in the self-consistent harmonic approximation: Theory and stochastic implementation. *Phys. Rev. B*, 96:014111, 2017.

[28] Lorenzo Monacelli, Ion Errea, Matteo Calandra, and Francesco Mauri. Pressure and stress tensor of complex anharmonic crystals within the stochastic self-consistent harmonic approximation. *Phys. Rev. B*, 98:024106, 2018.

[29] Liangliang Liu, Chongze Wang, Seho Yi, Kun Woo Kim, Jaeyong Kim, and Jun-Hyung Cho. Microscopic mechanism of room-temperature superconductivity in compressed LaH_{10}. *Phys. Rev. B*, 99:140501, 2019.

Acknowledgements. This research was supported by the European Research Council (ERC) under the European Unions Horizon 2020 research and innovation programme (grant agreement No. 802533); the Spanish Ministry of Economy and Competitiveness (FIS2016-76617-P); NCCR MARVEL funded by the Swiss National

Science Foundation; and grant-in-Aid for Scientific Research (No.16H06345, 18K03442 and No. 19H05825) from the Ministry of Education, Culture, Sports, Science and Technology, Japan. Computational resources were provided by the Barcelona Superconducting Center (project FI-2019-1-0031) and the Swiss National Supercomputing Center (CSCS).

Author contributions. The project was conceived by I.E. and J.A.F.-L. The SSCHA was developed by I.E., L.M., R.B., M.C. and F.M. In particular, R.B. developed the method to compute the quantum energy Hessian and the anharmonic phonon dispersions, and L.M. developed the method to perform a quantum relaxation of the lattice parameters. I.E. and F.B. performed the SSCHA calculations. A.S. T.K., T.T., R.A. and J.A.F.-L. conducted studies on structure prediction and superconductivity. All authors contributed to the editing of the manuscript.

Competing interests. The authors declare no competing interests.

Methods

Calculation details. First-principles calculations were performed within DFT and the generalized gradient approximation (GGA) as parametrized by Perdew, Burke, and Ernzerhof (PBE) [30]. Harmonic phonon frequencies were calculated within density functional perturbation theory (DFPT) [31] making use of the Quantum ESPRESSO code [32, 33]. The SSCHA [26–28, 34] minimization requires the calculation of energies, forces and stress tensors in supercells. These were calculated as well within DFT at the PBE level with Quantum ESPRESSO. For the final SSCHA populations, 1000 configurations were used to reduce the stochastic noise. In all these calculations we used ultrasoft pseudopotentials including 11 electrons for the La atoms, a plane-wave cut-off energy of 50 Ry for the kinetic energy and 500 Ry for the charge density.

In the harmonic phonon calculations for the Fm-$3m$ and R-$3m$ phases, we used the primitive and rhombohedral lattices, respectively, with one LaH_{10} formula unit in the unit cell. A 20×20×20 Monkhorst-Pack shifted electron-momentum grid was used for these calculations with a Methfessel-Paxton smearing of 0.02 Ry. The DFT calculations performed for the SSCHA on supercells were performed on a coarser electron-momentum grid, which would correspond to a 12×12×12 grid in the unit cell. We explicitly verified that this coarser mesh yields a fully converged SSCHA gradient with respect to the electron-momentum grid, thus, not affecting the SSCHA minimization. The DFT supercell calculations for the SSCHA minimization on the $C2$ phase were performed keeping the same **k**-point density.

All phonon frequencies for **q**-points not commensurate with the supercell used in the SSCHA minimization were obtained by directly Fourier interpolating the real space force constants obtained in this supercell, which are calculated form the Hessian of $E(\boldsymbol{\mathcal{R}})$. For the Fm-$3m$ phase the SSCHA calculation was performed both on a 2×2×2 and 3×3×3 supercell containing, respectively, 88 and 297 atoms. The phonon spectra shown in Figure 2 for the Fm-$3m$ phase are obtained by Fourier interpolating directly the SSCHA energy Hessian force constants obtained in a 3×3×3 supercell. In Extended Data Figure 2 we show that the phonon spectrum obtained interpolating directly the force constants in a 2×2×2 supercell yields similar results, indicating that the energy Hessian force constants are short-range and can be Fourier interpolated. Indeed, the T_c calculated with the 2×2×2 and 3×3×3 force constants for interpolating phonons only differs in approximately 3 K. Upon this, the SSCHA quantum structural relaxations in the R-$3m$ and $C2$ phases were performed in supercells with 88 atoms.

As shown in Ref. [27], the Hessian of $E(\boldsymbol{\mathcal{R}})$ is

$$\frac{\partial^2 E(\boldsymbol{\mathcal{R}})}{\partial \boldsymbol{\mathcal{R}} \partial \boldsymbol{\mathcal{R}}} = \boldsymbol{\Phi} + \overset{(3)}{\boldsymbol{\Phi}} \boldsymbol{\Lambda} \left[\mathbf{1} - \overset{(4)}{\boldsymbol{\Phi}} \boldsymbol{\Lambda} \right]^{-1} \overset{(3)}{\boldsymbol{\Phi}}. \tag{1}$$

Bold notation represents matrices and tensors in compact notation. In Eq. (1), $\boldsymbol{\Phi}$ are the variational force constants of the SSCHA minimization, $\overset{(n)}{\boldsymbol{\Phi}}$ the quantum statistical averages taken with the SSCHA density matrix of the n-th order derivatives of $V(\mathbf{R})$, and $\boldsymbol{\Lambda}$ a tensor that depends on the temperature and $\boldsymbol{\Phi}$. $\mathbf{1}$ is the identity matrix. As we show in Extended Figure 3, setting $\overset{(4)}{\boldsymbol{\Phi}} = 0$ has a negligible effect on the phonons obtained from the Hessian defined in Eq. (1). Therefore, $\overset{(4)}{\boldsymbol{\Phi}}$ is neglected throughout, and all superconductivity calculations in the Fm-$3m$ and R-$3m$ phases are performed making use of the phonon frequencies and polarization vectors obtained from the Hessian of $E(\boldsymbol{\mathcal{R}})$ with $\overset{(4)}{\boldsymbol{\Phi}} = 0$. We also estimated T_c with the phonon frequencies and polarization vectors obtained instead from $\boldsymbol{\Phi}$, resulting in a critical temperature 12 K lower within Allen-Dynes modified McMillan equation. This difference is small and within the uncertainty of the T_c calculation between SCDFT and anisotropic Migdal-Éliashberg calculations (see Figure 3 and below).

The Éliashberg spectral function, which we used for the T_c calculations, is defined as

$$\alpha^2 F(\omega) = \frac{1}{N_{E_F}} \sum_{n\mathbf{k},m\mathbf{q},\nu} |g^{\nu}_{n\mathbf{k},m\mathbf{k}+\mathbf{q}}|^2 \delta(\epsilon_{n\mathbf{k}} - E_F) \times \delta(\epsilon_{m\mathbf{k}+\mathbf{q}} - E_F) \delta(\omega - \omega_{\mathbf{q}\nu}), \tag{2}$$

where N_{E_F} is the electronic density of states (DOS) at the Fermi energy (E_F), n and m are band indices, $\mathbf{k}$ is a crystal momentum, $\epsilon_{n\mathbf{k}}$ is a band energy, $\omega_{\mathbf{q}\nu}$ is the phonon frequency of mode ν at wavevector $\mathbf{q}$, and $g^{\nu}_{n\mathbf{k},m\mathbf{k}+\mathbf{q}}$ is the electron-phonon matrix element between a state $n\mathbf{k}$ and $m\mathbf{k}+\mathbf{q}$. We calculated $\alpha^2 F(\omega)$ combining

the SSCHA phonon frequencies and polarization vectors obtained from the Hessian of $E(\boldsymbol{\mathcal{R}})$ with the electron-phonon matrix elements calculated with DFPT. For the Fm-$3m$ and R-$3m$ phases, the electron-phonon matrix elements were calculated in a 6×6×6 **q** point grid and a 40×40×40 **k** point grid. These were combined with the SSCHA phonons and polarization vectors obtained by Fourier interpolation to the 6×6×6 **q** point grid from the real space force constants coming from the Hessian of $E(\boldsymbol{\mathcal{R}})$ in a 3×3×3 supercell for the Fm-$3m$ and in a 2×2×2 supercell for the R-$3m$. The Dirac deltas on the band energies are estimated by substituting them with a Gaussian of 0.004 Ry width. The calculated $\alpha^2F(\omega)$ functions for the Fm-$3m$ phase are shown in Extended Figures 4 and 5, while in Extended Figure 6 we show the results for the R-$3m$ phase.

Crystal phase diagram exploration. To sample the enthalpy landscape of LaH_{10} we employed the minima hopping method (MHM) [24, 25], which has been successfully used for global geometry optimization in a large variety of applications including superconducting materials such as H_3S, PH_3, and disilane at high pressure [35, 36]. This composition was thoroughly explored with 1, 2, 3 and 4 formula units simulation cells. Variable composition simulations were also performed for other La-H compositions. Energy, atomic forces and stresses were evaluated at the DFT level with the GGA-PBE parametrization to the exchange-correlation functional. A plane wave basis-set with a high cutoff energy of 900 eV was used to expand the wave-function together with the projector augmented wave (PAW) method as implemented in the Vienna Ab Initio Simulation Package VASP [37]. Geometry relaxations were performed with tight convergence criteria such that the forces on the atoms were less than 2 meV/Å and the stresses were less than 0.1 eV/Å^3. Extended Data Figure 1 shows our calculated convex hull of enthalpy formation without considering the zero-point energy at 100, 150 and 200 GPa. Interestingly, there are many stable compositions in the convex hull. LaH_{10} becomes enthalpically stable at ∼125 GPa and remains in the convex well above 300 GPa. Below 150 GPa, R-$3m$ and $C2$ phases (LaH_{10}) show unstable harmonic phonon at Γ, becoming saddle points of $V(\mathbf{R})$. However, harmonically one can find $P1$ stable structures (decreasing symmetry) by following the instability pattern (softening direction, i.e. along eigenvector polarization). $P1$ structures are degenerate in enthalpy within less 3 meV/LaH_{10} with respect $C2$. Hence, we used the $C2$ as a representative of highly distorted structures for our study.

Superconductivity calculations in the Fm-$3m$ phase. Superconductivity calculations were performed within two different approaches that represent the state-of-the-art of *ab initio* superconductivity: Density functional theory for Superconductors (SCDFT) and the Éliashberg equations with full Coulomb interaction.

SCDFT is an extension to DFT for a superconducting ground state [38, 39]. By assuming that the $n\mathbf{k}$ anisotropy in the electron-phonon coupling is negligible (see Ref. 39 for further details), the critical temperature is computed by solving an (isotropic) equation for the Kohn-Sham gap:

$$\Delta_s(\epsilon) = \mathcal{Z}(\epsilon)\Delta_s(\epsilon) - \int d\epsilon' \mathcal{K}(\epsilon,\epsilon') \frac{\tanh\left[\frac{\beta E(\epsilon')}{2}\right]}{2E(\epsilon')} \Delta_s(\epsilon'), \tag{3}$$

where ϵ is the electron energy and β the inverse temperature. The kernels $\mathcal{K}$ and $\mathcal{Z}$ come from the exchange correlation functional of the theory [39–44] and depend on the properties of the pairing interactions: electron-phonon coupling and screened electron-electron repulsion. Eq. 3 allows us to calculate T_c completely *ab initio*, without introducing an empirical μ^* parameter (Coulomb pseudopotential). Dynamic effects on the Coulomb interaction (plasmon) were also tested and did not show any significant effect. In its isotropic form, the screened Coulomb interaction in SCDFT is accounted for by a function $\mu(\epsilon,\epsilon')$, which is given by the average [45] RPA Coulomb matrix element on the iso-energy surfaces ϵ and ϵ' times the DOS at ϵ' ($N(\epsilon')$):

$$\mu(\epsilon,\epsilon') = \sum_{n,m} \iint d^3(kk') V^{RPA}_{n\mathbf{k},m\mathbf{k}'} \frac{\delta(\epsilon-\epsilon_{n\mathbf{k}})}{N(\epsilon_{n\mathbf{k}})} \delta(\epsilon'-\epsilon_{m\mathbf{k}'}). \tag{4}$$

The full energy dependence of the DOS is accounted in the calculations, while the electron-phonon coupling is described by the $\alpha^2F(\omega)$ of Eq. (2).

The second approach we use to simulate the superconducting state is the anisotropic Éliashberg approach [46]. Here we include, together with the energy dependence of the electron DOS, the anisotropy of the electron-phonon coupling. The Green's function form of the Éliashberg equation [46] we solve is given as

$$\Sigma_{n\mathbf{k}}(i\omega_i) = -\frac{1}{N\beta} \sum_{\mu,\mathbf{q},m} V^{\rm ph}_{mn}(\mathbf{q},i\omega_\mu) G_{m\mathbf{k}+\mathbf{q}}(i\omega_\mu + i\omega_i), \tag{5}$$

$$\Delta_{n\mathbf{k}}(i\omega_i) = -\frac{1}{N\beta} \sum_{\mu,\mathbf{q},m} \{V^{\rm ph}_{mn}(\mathbf{q},i\omega_\mu) + V^{\rm C}_{mn}(\mathbf{q},i\omega_\mu)\} \times |G_{m\mathbf{k}+\mathbf{q}}(i\omega_\mu + i\omega_i)|^2 \Delta_{m\mathbf{k}+\mathbf{q}}(i\omega_\mu + i\omega_i). \tag{6}$$

Here, $\Sigma_{n\mathbf{k}}(i\omega_i)$ and $\Delta_{n\mathbf{k}}(i\omega_i)$ are the normal and anomalous self energy, and $V^{\rm ph}_{mn}(\mathbf{q},i\omega_\mu)$ and $V^{\rm C}_{mn}(\mathbf{q},i\omega_\mu)$ are the **k**-averaged phonon-mediated interaction and Coulomb interaction, respectively. The explicit form of $V^{\rm ph}_{mn}(\mathbf{q},i\omega_\mu)$ is given as

$$V^{\rm ph}_{mn}(\mathbf{q},i\omega_\mu) = \sum_\nu |g^\nu_{nm}(\mathbf{q})|^2 D_\nu(\mathbf{q},i\omega_\mu), \tag{7}$$

where $|g^{\nu}_{nm}(\mathbf{q})|^2$ is a $\mathbf{k}$-averaged electron-phonon matrix element,

$$|g^{\nu}_{nm}(\mathbf{q})|^2 = \frac{\sum_{\mathbf{k}} |g^{\nu}_{n\mathbf{k},m\mathbf{k}+\mathbf{q}}|^2 \delta(\epsilon_{n\mathbf{k}} - E_F)\delta(\epsilon_{m\mathbf{k}+\mathbf{q}} - E_F)}{\sum_{\mathbf{k}} \delta(\epsilon_{n\mathbf{k}} - E_F)\delta(\epsilon_{m\mathbf{k}+\mathbf{q}} - E_F)}, \tag{8}$$

and $D_{\nu}(\mathbf{q}, i\omega_{\mu})$ is a free-phonon Green's function, $D_{\nu}(\mathbf{q}, i\omega_{\mu}) = -2\omega_{\mathbf{q}\nu}/(\omega^2_{\mu} + \omega^2_{\mathbf{q}\nu})$. The electron-phonon matrix elements are calculated through a DFPT calculation with 6×6×6 $\mathbf{q}$ point grid, and are combined with the phonon frequencies and polarization vectors obtained by directly Fourier interpolating to this grid the force constants coming from the $E(\boldsymbol{\mathcal{R}})$ Hessian in the 3×3×3 supercell. For the Coulomb interaction, $V^{\mathrm{C}}_{mn}(\mathbf{q}, i\omega_{\mu})$ is approximated by $\mathbf{k}$-averaged static Coulomb interaction within the random phase approximation, $\frac{1}{N_k}\sum_{\mathbf{k}} V^{\mathrm{RPA}}_{m\mathbf{k},n\mathbf{k}+\mathbf{q}}(i\omega_{\mu} = 0)$. Using Eq. (5), the Dyson equation was solved self-consistently and then Eq. (6) was solved to estimate T_c with 36× 36 × 36 $\mathbf{k}$ point grid and 512 Matsubara frequencies.

In Extended Data Table I we summarize all calculated T_c's within anisotropic ME and isotropic SCDFT. We also include the values obtained with McMillan equation and Allen-Dynes modified McMillan equation (μ^*=0.1). The calculated electron-phonon coupling constant, $\lambda = 2\int_0^{\infty} d\omega \alpha^2F(\omega)/\omega$, and the logarithmic frequency average, $\omega_{log} = \exp\left(\frac{2}{\lambda}\int_0^{\infty} d\omega \frac{\alpha^2F(\omega)}{\omega}\log\omega\right)$, are also included in the table.

Quantum structural relaxations in the R-3m and C2 phases. In Extended Figure 7 we show the evolution of the pressure calculated along the different Cartesian directions for the R-3m throughout the SSCHA minimization but keeping the rhombohedral angle fixed at 62.3°. Thus, the centroid positions $\boldsymbol{\mathcal{R}}$ are optimized only considering the internal degrees of freedom of the R-3m phase. Even if at the classical level the stress is isotropic (within a 0.5%), after the SSCHA quantum relaxation an anisotropic stress of a 6% is created between the z and $x-y$ directions. The phonons obtained at the end of the minimization are shown in Extended Figure 6. Secondly, in Extended Figure 8, we show that starting from the result of this minimization but now relaxing also the lattice, the R-3m phase evolves into the Fm-3m phase. It is clear how the pressure calculated with quantum effects becomes isotropic when the rhombohedral angle becomes 60°, the angle corresponding to a fcc lattice in a rhombohedral description. Also it is evident that the Wyckoff positions of the R-3m phase evolve clearly into the Fm-3m Wyckoff positions, which are summarized in Extended Data Table II.

In Extended Data Figure 9 we show the evolution of the diagonal components of the pressure along the three different Cartesian directions for the monoclininc C2 when the lattice structure is relaxed with the SSCHA. The starting point is obtained by first performing a SSCHA relaxation of only internal atomic coordinates keeping the lattice parameters that yield an isotropic stress of 150 GPa. It is clear that quantum effects create an anisotropic stress if the lattice parameters are not modified. When the quantum relaxation of the lattice is performed, the lattice parameters are modified and an isotropic stress is recovered.

Extended Data Figure 10 shows the structures of the R-3m and C2 phases obtained classically and after the quantum SSCHA relaxation. After the quantum relaxation, the symmetry of both structures is recognized as Fm-3m with a tolerance of 0.001 Å for lattice vectors and 0.005 Å for ionic positions, consistent with the stochastic accuracy of the SSCHA. In the same Figure 10, the electronic density of states (DOS) as a function of pressure is plotted. Highly symmetric motif (Fm-3m) maximizes N_{E_F}, while in distorted structures (R-3m and C2) the occupation at the Fermi level is reduced by more than 20 %. This underlines that the classical distortions would lower N_{E_F}, reducing λ, as expected in a system destabilized by the electron-phonon interaction.

Transition temperatures from other La-H compositions. Different compositions on the La-H phase diagram have been reported as thermodynamically stable. Presumably, the stabilization of these compositions and the measurement of different T_c's (see Drozdov et al. [3]) demonstrate that other stoichiometries are responsible for these measured T_c's. Notably, these T_c's appear substantially lower, for instance the values decrease from 250 K, to 215 K, 110 K and to 70 K. Experimentally there is not a clear correlation between sample preparation, T_c and pressure. In sample preparation of Drozdov et al. pressures can vary from 100 to 200 GPa (gradient inside the diamond anvil cell) and it was proposed that other stoichiometries (low-hydrogen content) are responsible for systematically lower T_c's.

Conversely, in a later publication the same authors suggested other hydrogen rich system that is enthalpically competitive (LaH_{11}) and possibly responsible for other high-T_c phases. In order to explore this possibility, we did consider structure prediction runs with this stoichiometry and found crystalline structures that were previously reported in Ref. [47]. Extended Data Figure 11 shows the structural motif and the corresponding phonons and $\alpha^2F(\omega)$ spectral function. We can rule out the possibility that high-T_c, as measured in different samples, arises from LaH_{11} in its $P4/nmm$ (129) structure (lowest enthalpy structure for this composition at relevant experimental pressures). As seen in Extended Data Figure 11, this phase has a strong molecular crystal character, composed of H_2 units weakly interacting with La-lattice. This phase is indeed a poor metal with low occupation of electrons at the Fermi level due to its molecular character and cannot explain 70 K, or higher values of T_c. Our estimated T_c with Allen-Dynes formula, harmonic phonons and using a μ^*=0.1 is 7 K at 100 GPa.

[30] John P. Perdew, Kieron Burke, and Matthias Ernzerhof. Generalized gradient approximation made simple. *Phys. Rev. Lett.*, 77:3865, 1996.

[31] Stefano Baroni, Stefano de Gironcoli, Andrea Dal Corso, and Paolo Giannozzi. Phonons and related crystal properties from density-functional perturbation theory. *Rev. Mod. Phys.*, 73:515, 2001.

[32] Paolo Giannozzi, Stefano Baroni, Nicola Bonini, Matteo Calandra, Roberto Car, Carlo Cavazzoni, Davide Ceresoli, Guido L Chiarotti, Matteo Cococcioni, Ismaila Dabo, Andrea Dal Corso, Stefano de Gironcoli, Stefano Fabris, Guido Fratesi, Ralph Gebauer, Uwe Gerstmann, Christos Gougoussis, Anton Kokalj, Michele Lazzeri, Layla Martin-Samos, Nicola Marzari, Francesco Mauri, Riccardo Mazzarello, Stefano Paolini, Alfredo Pasquarello, Lorenzo Paulatto, Carlo Sbraccia, Sandro Scandolo, Gabriele Sclauzero, Ari P Seitsonen, Alexander Smogunov, Paolo Umari, and Renata M Wentzcovitch. Quantum espresso: a modular and open-source software project for quantum simulations of materials. *Journal of Physics: Condensed Matter*, 21:395502, 2009.

[33] P Giannozzi, Oliviero Andreussi, T Brumme, O Bunau, M Buongiorno Nardelli, M Calandra, R Car, C Cavazzoni, D Ceresoli, M Cococcioni, et al. Advanced capabilities for materials modelling with quantum espresso. *Journal of Physics: Condensed Matter*, 29:465901, 2017.

[34] Ion Errea, Matteo Calandra, and Francesco Mauri. First-principles theory of anharmonicity and the inverse isotope effect in superconducting palladium-hydride compounds. *Phys. Rev. Lett.*, 111:177002, 2013.

[35] A. José Flores-Livas, Antonio Sanna, and E.K.U. Gross. High temperature superconductivity in sulfur and selenium hydrides at high pressure. *Eur. Phys. J. B*, 89:1, 2016.

[36] José A. Flores-Livas, Maximilian Amsler, Christoph Heil, Antonio Sanna, Lilia Boeri, Gianni Profeta, Chris Wolverton, Stefan Goedecker, and E. K. U. Gross. Superconductivity in metastable phases of phosphorus-hydride compounds under high pressure. *Phys. Rev. B*, 93:020508, 2016.

[37] G. Kresse and J. Furthmüller. Efficiency of ab-initio total energy calculations for metals and semiconductors using a plane-wave basis set. *Comput. Mat. Sci.*, 6:15, 1996.

[38] L. N. Oliveira, E. K. U. Gross, and W. Kohn. Density-functional theory for superconductors. *Phys. Rev. Lett.*, 60:2430, 1988.

[39] M. Lüders, M. A. L. Marques, N. N. Lathiotakis, A. Floris, G. Profeta, L. Fast, A. Continenza, S. Massidda, and E. K. U. Gross. Ab-initio theory of superconductivity. i. density functional formalism and approximate functionals. *Phys. Rev. B*, 72:024545, 2005.

[40] José A. Flores-Livas and Antonio Sanna. Superconductivity in intercalated group-iv honeycomb structures. *Phys. Rev. B*, 91:054508, 2015.

[41] Camilla Pellegrini, Henning Glawe, Antonio Sanna. Density functional theory of superconductivity in doped tungsten oxides. *Phys. Rev. Materials*, 3:064804, 2019.

[42] M. A. L. Marques, M. Lüders, N. N. Lathiotakis, G. Profeta, A. Floris, L. Fast, A. Continenza, E. K. U. Gross, and S. Massida. Ab initio theory of superconductivity. II. Application to elemental metals. *Phys. Rev. B*, 72:024546, 2005.

[43] A. Linscheid, A. Sanna, A. Floris, and E. K. U. Gross. First-principles calculation of the real-space order parameter and condensation energy density in phonon-mediated superconductors. *Phys. Rev. Lett.*, 115:097002, 2015.

[44] S. Massidda, F. Bernardini, C. Bersier, A. Continenza, P. Cudazzo, A. Floris, H. Glawe, M. Monni, S. Pittalis, G. Profeta, A. Sanna, S. Sharma, and E. K. U. Gross. The role of coulomb interaction in the superconducting properties of CaC6 and H under pressure. *Superconductor Science and Technology*, 22:034006, 2009.

[45] Antonio Sanna, José A. Flores-Livas, Arkadiy Davydov, Gianni Profeta, Kay Dewhurst, Sangeeta Sharma, and E. K. U. Gross. Ab initio Eliashberg Theory: Making Genuine Predictions of Superconducting Features. *J. Phys. Soc. Jpn.*, 87:041012, 2018.

[46] W. Sano, T. Koretsune, T. Tadano, R. Akashi, and R. Arita. Effect of Van Hove singularities on high-T_c superconductivity in H_3S. *Phys. Rev. B*, 93:094525, 2016.

[47] Feng Peng, Ying Sun, Chris J. Pickard, Richard J. Needs, Qiang Wu, and Yanming Ma. Hydrogen clathrate structures in rare earth hydrides at high pressures: Possible route to room-temperature superconductivity. *Phys. Rev. Lett.*, 119:107001, 2017.

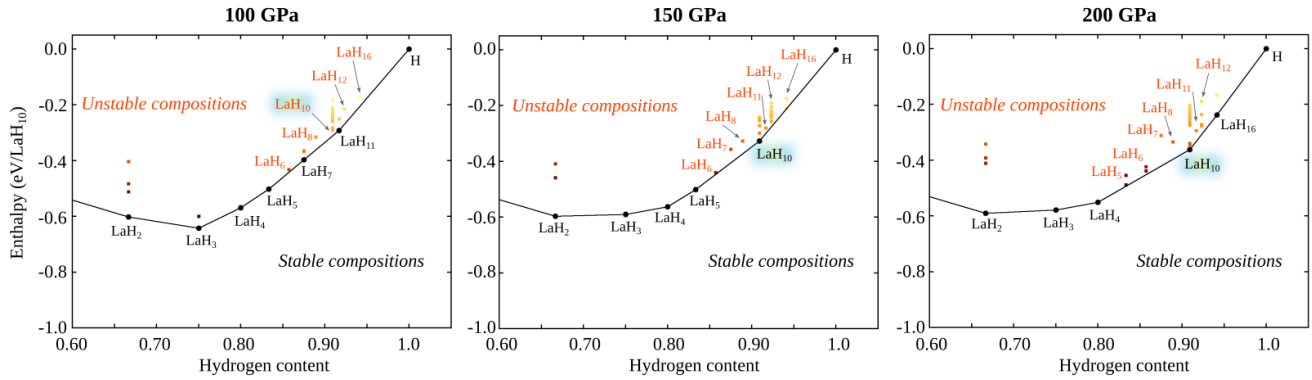

Extended Data Figure 1. **Convex hull of enthalpy formation.** It is noticeable that at low pressure (left panel, 100 GPa) the composition of LaH_{10} is not stable and only develops as stable point in the convex hull above ∼125 GPa.

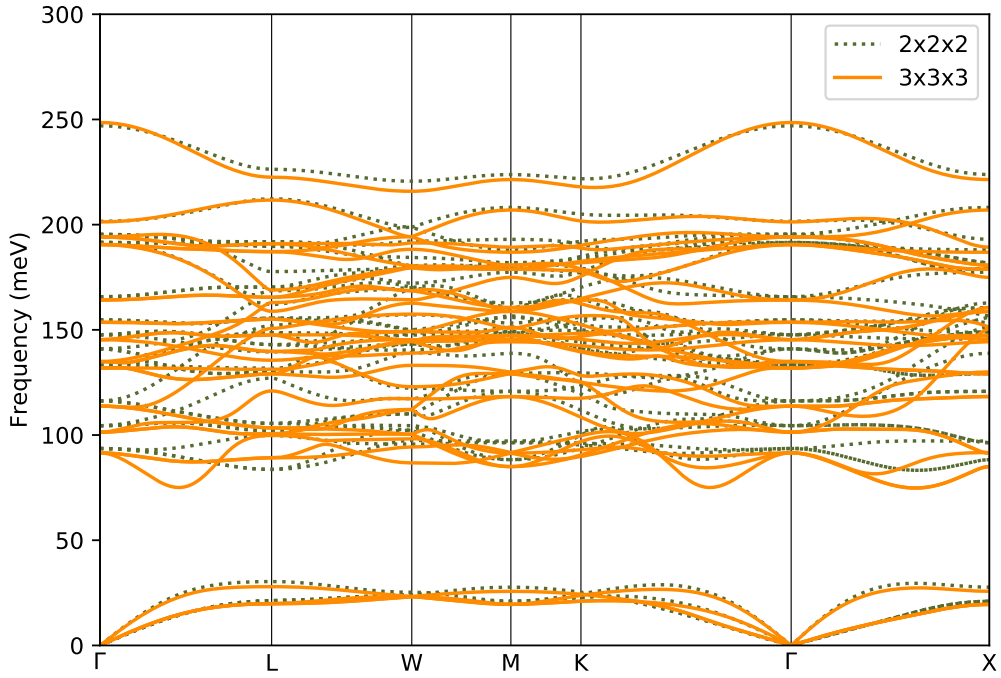

Extended Data Figure 2. **SSCHA phonons supercell convergence for LaH_{10} at 163 GPa.** The phonon spectra shown are calculated by directly Fourier interpolating the force constants obtained from the Hessian of $E(\boldsymbol{\mathcal{R}})$ in a real space $2 \times 2 \times 2$ and a $3 \times 3 \times 3$ supercell. The similarity of both phonon spectrum obtained by Fourier interpolation indicates that these SSCHA force constants are short-ranged and can be Fourier interpolated.

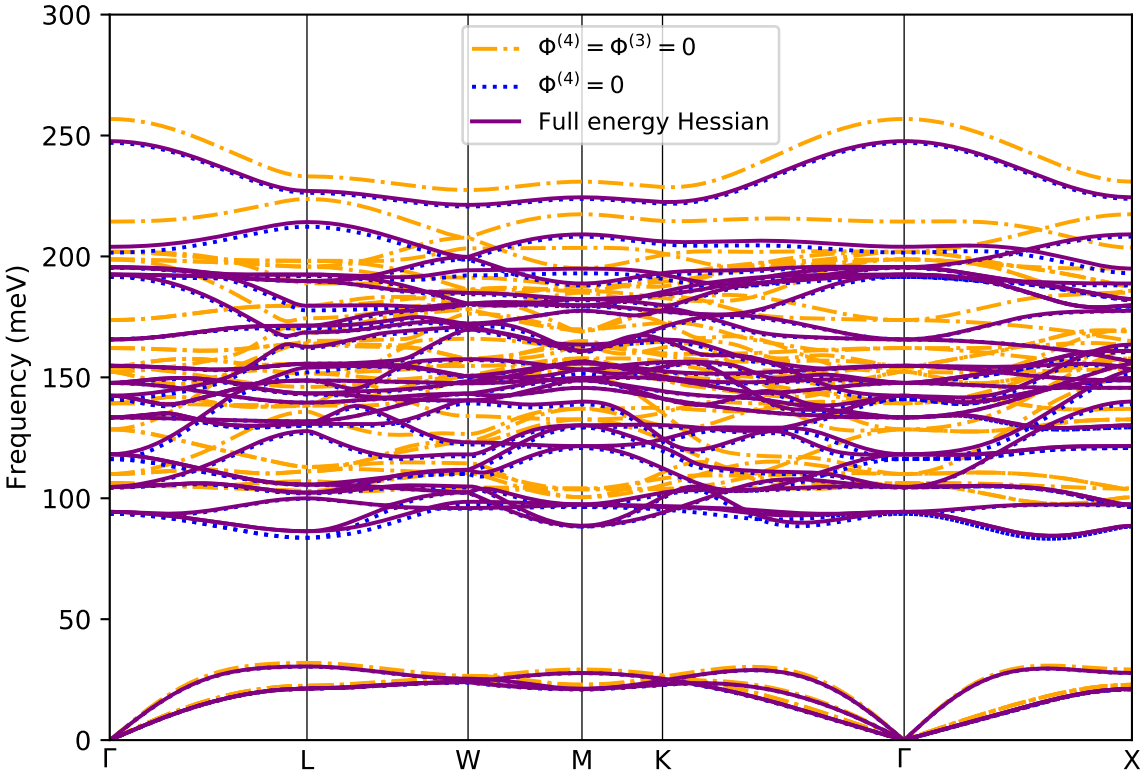

Extended Data Figure 3. **Different anharmonic phonons calculated for LaH_{10} at 163 GPa.** Phonon spectra obtained from the SSCHA energy Hessian of Eq. (1) making different level of approximations. The purple solid line is the phonon spectrum calculated with the full energy Hessian, without any approximation. In the blue dotted spectrum we set $\overset{(4)}{\mathbf{\Phi}} = 0$ in the equation. In the orange dash-dotted line we set $\overset{(3)}{\mathbf{\Phi}} = \overset{(4)}{\mathbf{\Phi}} = 0$, so that the phonon spectra corresponds to the one coming directly from the SSCHA variational force constants $\mathbf{\Phi}$. The results clearly show that while the effect of $\overset{(3)}{\mathbf{\Phi}}$ is important, setting $\overset{(4)}{\mathbf{\Phi}} = 0$ is perfectly safe. All these phonon spectra in the figures are obtained by Fourier interpolating directly the real space anharmonic force constants in a $2 \times 2 \times 2$ supercell.

Extended Data Table I. **Summary of calculated superconducting T_c.** Values are within different approaches ranging from empirical to fully *ab initio*: McMillan equation ($T_{c\mu^*=0.1}^{Mc}$), Allen-Dynes modified McMillan equation ($T_{c\mu^*=0.1}^{AD}$), anisotropic treatment of Migdal-Éliashberg ($T_{c ani}^{ME}$) and SCDFT (T_c^{SCDFT}). Values of λ and ω_{log} are also given.

System	Pressure (GPa)	λ	ω_{log} (meV)	$T_{c\mu^*=0.1}^{Mc}$ (K)	$T_{c\mu^*=0.1}^{AD}$ (K)	$T_{c ani}^{ME}$ (K)	T_c^{SCDFT} (K)
LaH_{10}	129	3.62	76.4	171.8	252.6	255.3	230
LaH_{10}	163	2.67	96.4	197.1	247.0	242.8	225
LaH_{10}	214	2.06	115.5	196.3	235.9	237.9	210
LaH_{10}	264	1.73	126.6	189.5	219.2	216.9	201
LaD_{10}	159	3.14	63.5	135.0	184.2	180.4	171
LaD_{10}	210	2.21	81.7	145.5	176.5	172.9	158
LaD_{10}	260	1.80	92.2	142.2	164.6	157.9	151

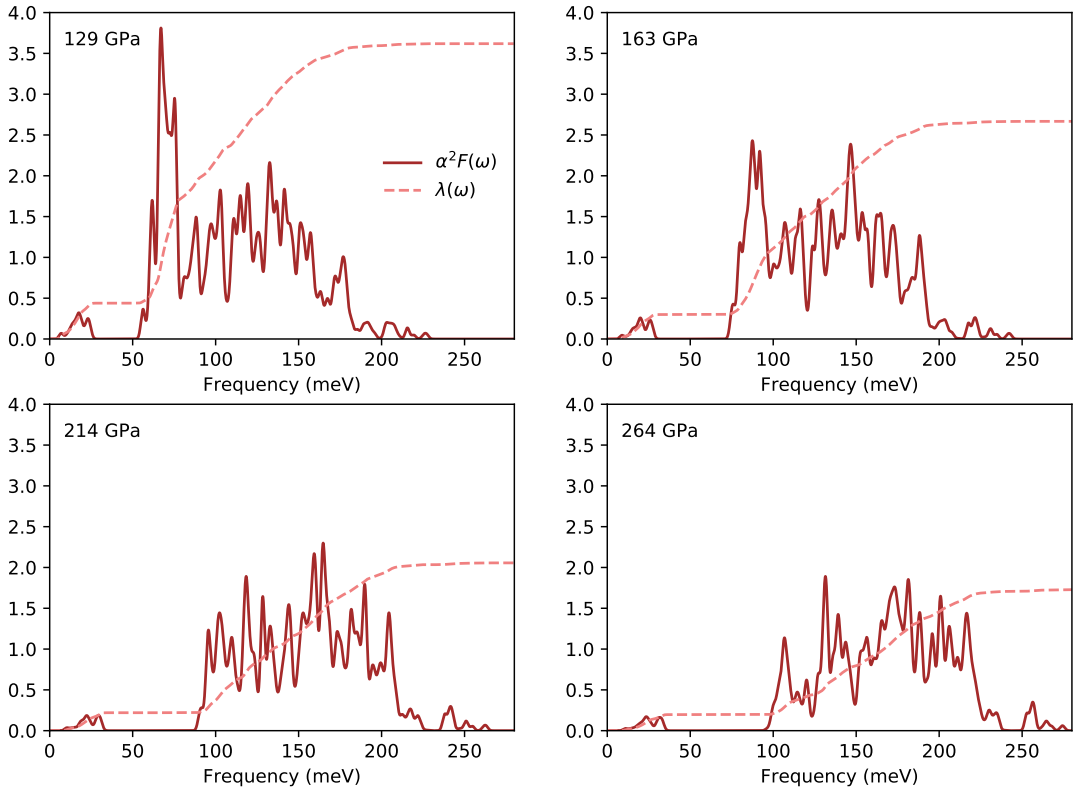

Extended Data Figure 4. $\alpha^2F(\omega)$ **for the** Fm-$3m$ **phase of LaH**$_{10}$**.** Calculated $\alpha^2F(\omega)$ for different pressures together with the integrated electron-phonon coupling constant, which is defined as $\lambda(\omega) = 2\int_0^\omega d\Omega\alpha^2F(\Omega)/\Omega$. The results show that optical modes, who have hydrogen character, are responsible for the large value of the electron-phonon coupling constant λ. It is worth noting, however, that acoustic modes with La character contribute between 0.2 and 0.5 to λ and cannot be neglected to estimate T_c correctly.

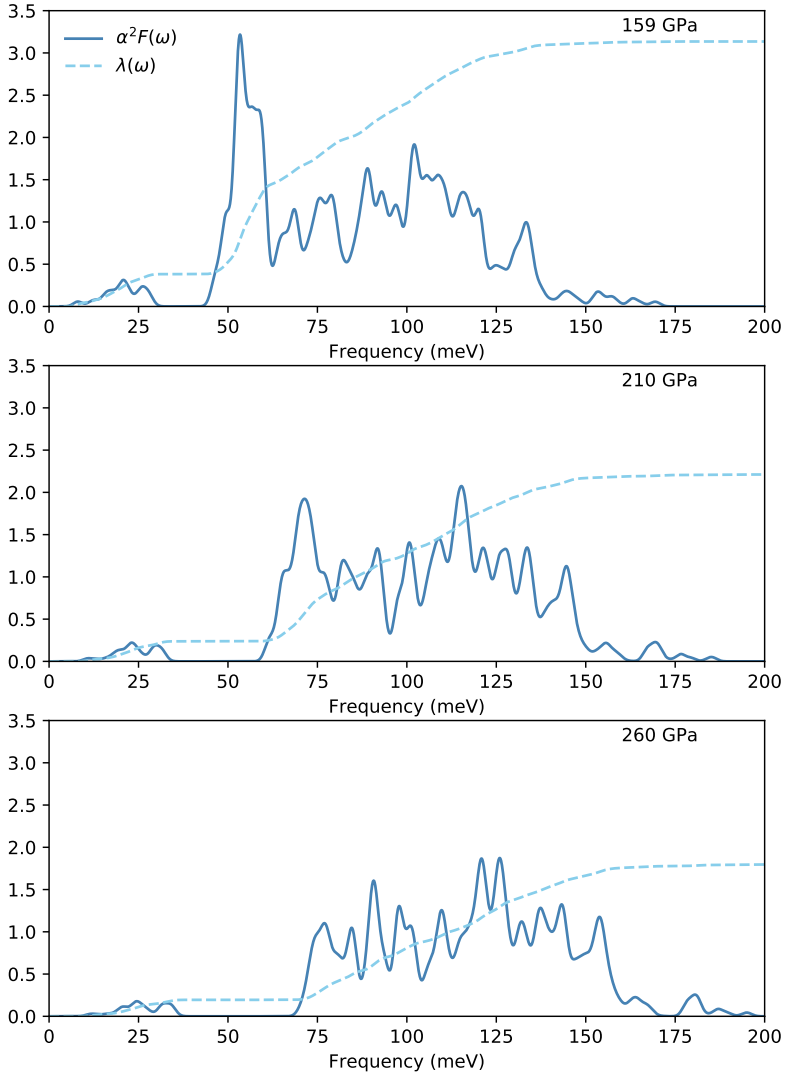

Extended Data Figure 5. $\alpha^2F(\omega)$ **for the** Fm-$3m$ **phase of** $\mathbf{LaD_{10}}$**.** The integrated electron-phonon coupling constant $\lambda(\omega)$ is also shown.

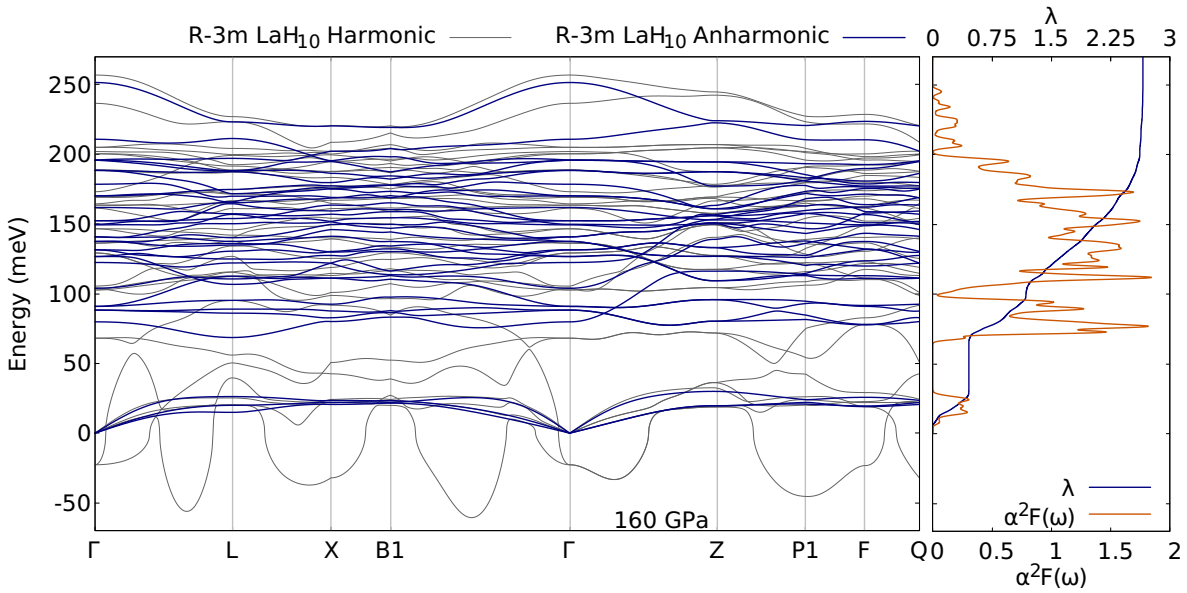

Extended Data Figure 6. **Phonon dispersion of LaH_{10} on the rhombohedral phase.** Harmonic and anharmonic phonon spectrum keeping a 62.3° rhombohedral angle. The harmonic calculation is performed with the internal atomic positions that yield classical vanishing forces. The anharmonic calculation is performed after relaxing with the SSCHA the internal degrees of freedom but keeping the 62.3° rhombohedral angle. At the harmonic level there are unstable phonon modes even at Γ. Symmetry prevents the relaxation of this structure according to the unstable phonon mode at Γ. The harmonic phonons are calculated at a classic pressure of 150 GPa. Quantum effects add an extra ∼10 GPa to the pressure. On the right side of the figure is also shown the behavior of $\lambda(\omega)$ and $\alpha^2F(\omega)$ for the anharmonic calculation.

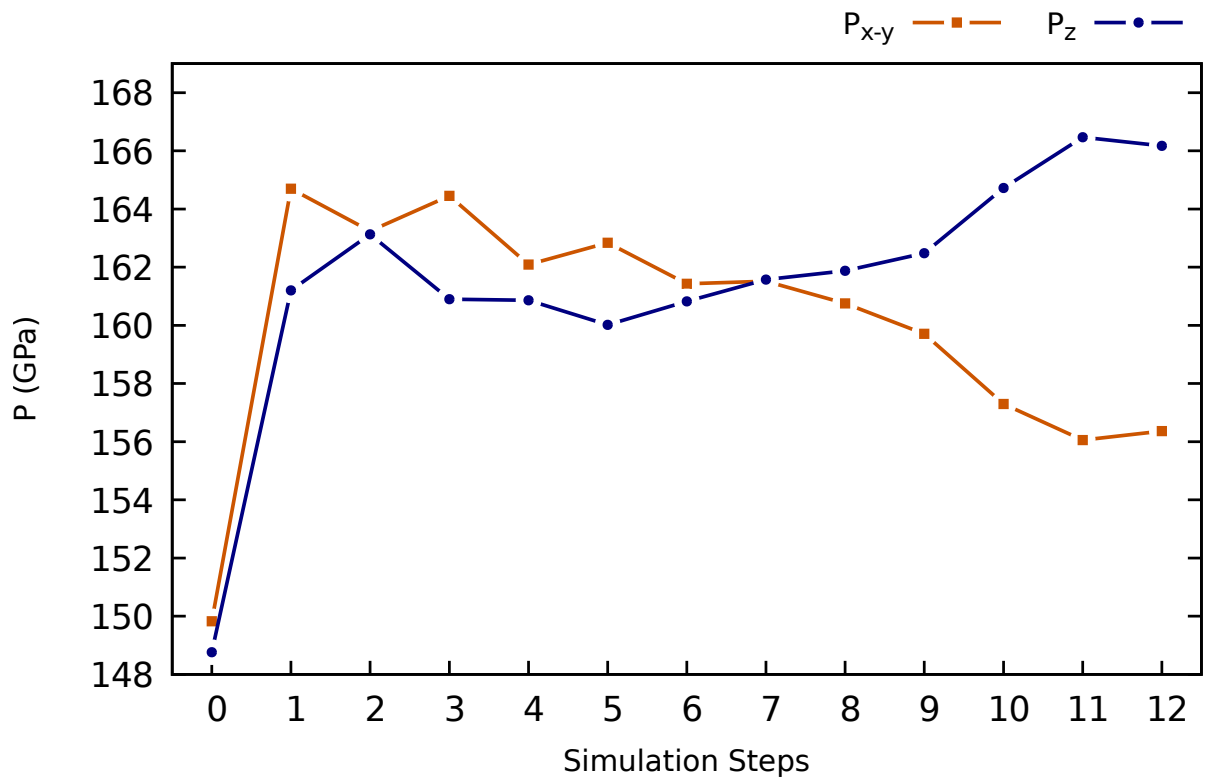

Extended Data Figure 7. **Anisotropic pressure of the R-3m phase of LaH_{10} in a fixed-cell quantum relaxation.** Pressure along the different Cartesian directions during the SSCHA relaxation of the internal parameters keeping the rhombohedral angle at 62.3° fixed. At step 0 the pressure reported is obtained directly from $V(\mathbf{R})$, neglecting quantum effects. It is isotropic within one GPa of difference between the $x-y$ and z directions. At the other steps it is calculated from the quantum $E(\boldsymbol{\mathcal{R}})$ and along the minimization it becomes anisotropic. When the minimization stops at step 12, i.e., the internal coordinates are at the minimum of the $E(\boldsymbol{\mathcal{R}})$ for this lattice, the stress anisotropy between z and $x-y$ directions is about 6%. This clearly indicates that quantum effects want to relax the crystal lattice, in particular, since P_z is larger, by reducing the rhombohedral angle. It is worth noting that quantum effects approximately increase the total pressure by 10 GPa, which is calculated as $P = (P_x + P_y + P_z)/3$. The initial cell parameters before the minimization are $a = 3.5473398$ Å and $\alpha = 62.34158$ ° . The initial values of the free Wyckoff parameters, which yield classical vanishing forces and a 150 GPa isotropic stress, are $\epsilon_a = 0.26043$, $\epsilon_b = 0.09950$, $\epsilon_x = 0.10746$ and $\epsilon_y = 0.12810$. Check the Extended Data Table II for more details.

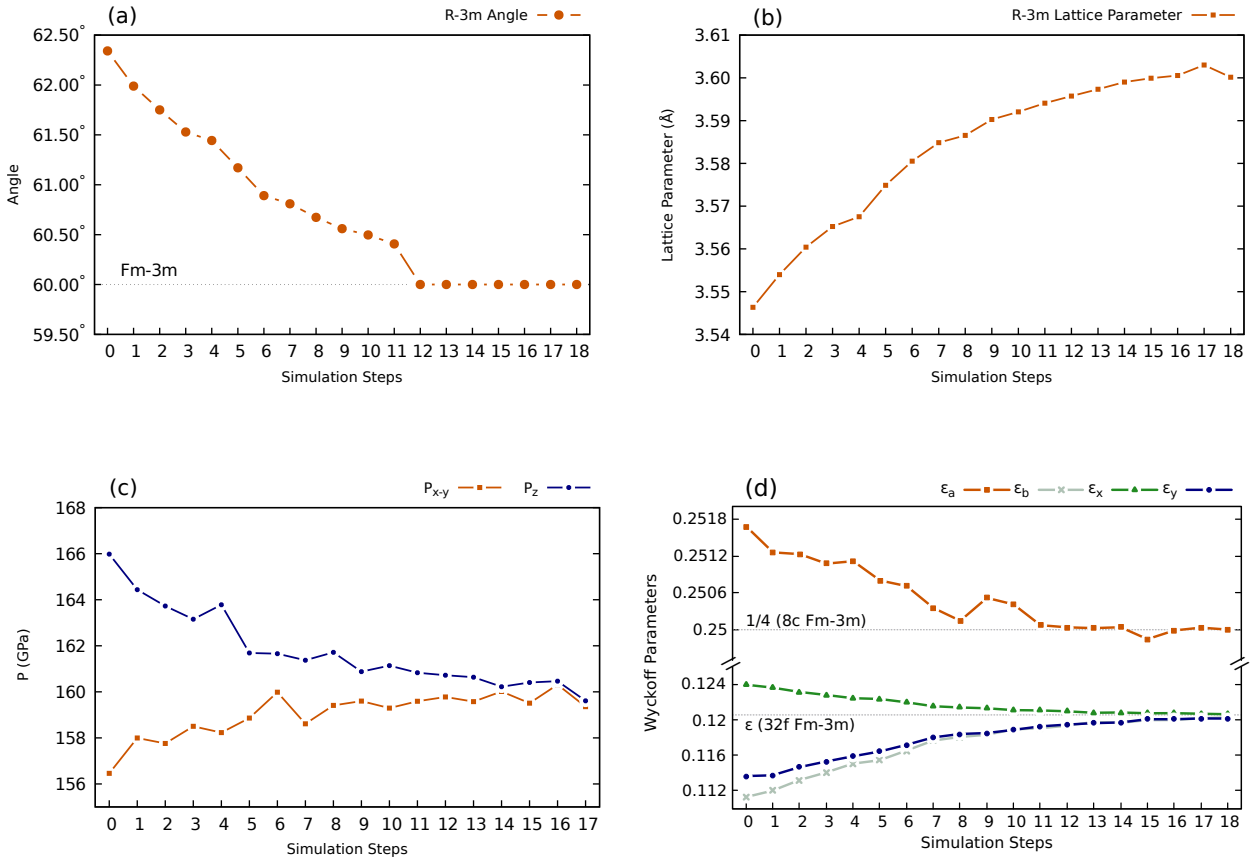

Extended Data Figure 8. **Details on the R-3m LaH_{10} cell relaxation including quantum effects.** The initial point for the relaxation is the output from the previous internal relaxation with fixed angle presented in Extended Figure 7. The R-3m phase in the rhombohedral description is described by three vectors of the same length ($a = b = c$) and by the angle between them ($\alpha = \beta = \gamma$). In panel **(a)** we show the evolution of the rhombohedral angle and in panel **(b)** the evolution of the rhombohedral lattice parameter ($|\mathbf{a}| = |\mathbf{b}| = |\mathbf{c}|$). The evolution of the stress tensor in the quantum SSCHA minimization is shown in panel **(c)**. It is clear that in the end of the minimization the structure obtains a 60° angle, which matches the angle of a fcc lattice, and that in this case the stress is isotropic. In panel **(d)** we show the evolution of the Wyckoff positions in the minimization and we compare it with those of the Fm-3m. The occupied Wyckoff positions for both R-3m LaH_{10} and Fm-3m LaH_{10} are summarized in the Extended Data Table II. Here, it can be seen the evolution of ϵ_a, ϵ_b, ϵ_x, and ϵ_y parameters in the minimization. The atoms in the first set of 6c positions approach the 8c Wyckoff site of the Fm-3m, while the atoms in the second set of 6c positions and those in 18h sites approach the atoms in the 32f Wyckoff site of the Fm-3m, where $\epsilon = 0.12053$.

Extended Data Table II. R-3m **LaH$_{10}$ and** Fm-3m **LaH$_{10}$ Wycokff positions.** The table summarizes the occupied Wyckoff positions for the two structures. We describe the Wyckoff positions in crystal coordinates so that the $[x, y, z]$ coordinate should be understood as a $x\mathbf{a} + y\mathbf{b} + z\mathbf{c}$ atomic position with **a**, **b**, **c** the lattice vectors. For the R-3m phase we use the rhombohedral lattice (R), where the three lattice vectors have the same length ($a = b = c$) and the angle between them is the same ($\alpha = \beta = \gamma$). The Fm-3m phase is described both in this rhombohedral description (R) and, for comparison, in the standard cubic conventional lattice (C). In the Fm-3m the lanthanum atom is described by the **4b** sites, two hydrogen atoms occupy the **8c** sites, and the remaining 8 hydrogen atoms occupy the **32f** sites. Most of the atomic positions are fixed by symmetry and overall the Fm-3m structure can be described by one single free parameter (ϵ). In the R-3m the lanthanum atom is locked in the **3b** sites, two pairs of hydrogen atoms occupy the **6c** sites, and the remaining 6 hydrogen atoms occupy the **18h** sites. In this case symmetry allows for more freedom, and overall the structure of the R-3m phase can be described by 4 free parameters (ϵ_a, ϵ_b, ϵ_x and ϵ_y).

Fm-3m (C)	Fm-3m (R)	R-3m (R)
1 La **4b** $[\frac{1}{2}, \frac{1}{2}, \frac{1}{2}]$	1 La **4b** $[\frac{1}{2}, \frac{1}{2}, \frac{1}{2}]$	1 La **3b** $[\frac{1}{2}, \frac{1}{2}, \frac{1}{2}]$
2 H **8c** $[\frac{1}{4}, \frac{1}{4}, \frac{1}{4}]$	2 H **8c** $[\frac{1}{4}, \frac{1}{4}, \frac{1}{4}]$	2 H **6c** $[\epsilon_a, \epsilon_a, \epsilon_a]$
$[\frac{3}{4}, \frac{3}{4}, \frac{3}{4}]$	$[\frac{3}{4}, \frac{3}{4}, \frac{3}{4}]$	$[-\epsilon_a, -\epsilon_a, -\epsilon_a]$
8 H **32f** $[\epsilon,\epsilon,\epsilon]$	8 H **32f** $[\epsilon,\epsilon,\epsilon]$	2 H **6c** $[\epsilon_b,\epsilon_b,\epsilon_b]$
$[-\epsilon,-\epsilon,-\epsilon]$	$[-\epsilon,-\epsilon,-\epsilon]$	$[-\epsilon_b,-\epsilon_b,-\epsilon_b]$
$[\epsilon,\epsilon,-\epsilon]$	$[-\epsilon,-\epsilon,3\epsilon]$	6 H **18h** $[-\epsilon_x,-\epsilon_x,3\epsilon_y]$
$[\epsilon,-\epsilon,\epsilon]$	$[-\epsilon,3\epsilon,-\epsilon]$	$[-\epsilon_y,3\epsilon_x,-\epsilon_x]$
$[-\epsilon,\epsilon,\epsilon]$	$[3\epsilon,-\epsilon,-\epsilon]$	$[3\epsilon_y,-\epsilon_x,-\epsilon_x]$
$[-\epsilon,-\epsilon,\epsilon]$	$[\epsilon,\epsilon,-3\epsilon]$	$[\epsilon_x,\epsilon_x,-3\epsilon_y]$
$[-\epsilon,\epsilon,-\epsilon]$	$[\epsilon,-3\epsilon,\epsilon]$	$[\epsilon_x,-3\epsilon_y,\epsilon_x]$
$[\epsilon,-\epsilon,-\epsilon]$	$[-3\epsilon,\epsilon,\epsilon]$	$[-3\epsilon_y,\epsilon_x,\epsilon_x]$

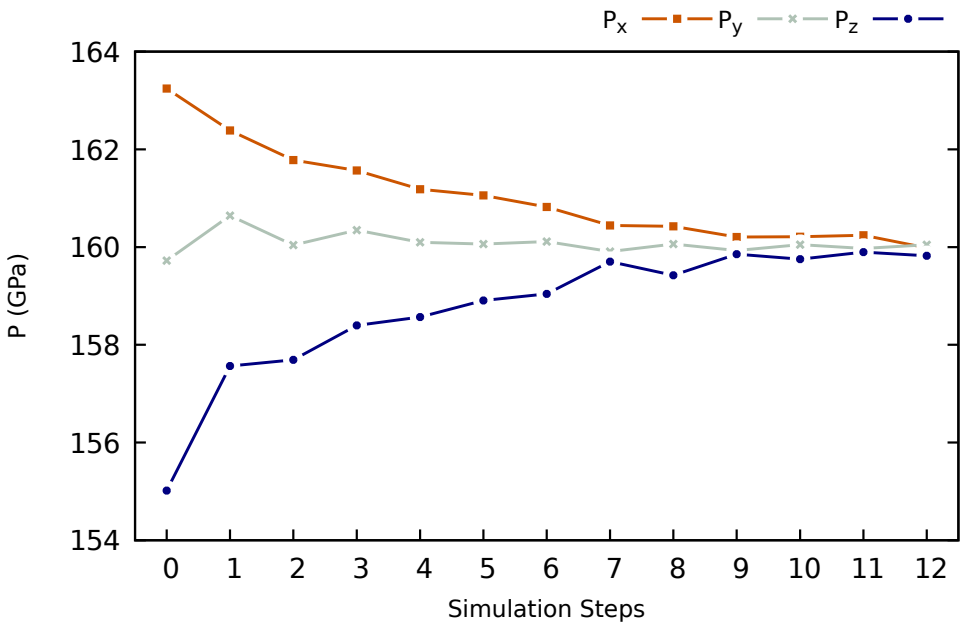

Extended Data Figure 9. **Anisotropic pressure of the** $C2$ **phase of LaH$_{10}$ in a cell quantum relaxation.** The figure shows the pressures along the different Cartesian directions during the SSCHA cell minimization. The target pressure for this minimization is 160 GPa. At the end of the minimization the isotropy of the stress tensor is recovered. A symmetry analysis performed on the structure at the end of the minimization confirms the $C2$ LaH$_{10}$ evolves in the Fm-3m LaH$_{10}$. The initial values $P_x = 163.2$ (GPa), $P_y = 159.7$(GPa), $P_z = 155.0$(GPa) are obtained by an atomic internal relaxation performed using the SSCHA with fixed cell.

Extended Data Table III. **Crystal structure details for relevant phases**. Lattice parameters and atomic coordinates for LaH_{10} ($Immm$) and LaH_{10} ($C2$) at 150 GPa and LaH_{11} $P4/nmm$ at 100 GPa. These pressures are estimated classically. The positions below give vanishing forces at classical level.

Composition (Space group)	Lattice parameters	Wyckoff positions		
LaH_{10} ($Immm$)	$a = 3.58303$ Å	La	**2c**	[0.50000, 0.50000, 0.00000]
	$b = 3.61834$ Å	H	**8m**	[0.75841, 0.00000, 0.11649]
	$c = 5.08749$ Å	H	**8l**	[0.00000, 0.75742, 0.87548]
		H	**4j**	[0.50000, 0.00000, 0.74572]
LaH_{10} ($C2$)	$a = 6.15468$ Å	La	**4c**	[0.49244, 0.00070, 0.25292]
	$b = 3.60628$ Å	H	**4c**	[0.13978, 0.24567, -0.05243]
	$c = 7.23776$ Å	H	**4c**	[0.09798, 0.24122, 0.45027]
	$\beta = 55.71434°$	H	**4c**	[0.36015, 0.25590, 0.05238]
		H	**4c**	[0.40204, 0.26021, 0.54971]
		H	**4c**	[-0.09751, 0.00051, -0.05100]
		H	**4c**	[0.86810, 0.00071, 0.43706]
		H	**4c**	[0.88713, 0.00076, 0.69398]
		H	**4c**	[0.87083, 0.00068, 0.19089]
		H	**4c**	[0.73058, 0.00043, 0.88088]
		H	**4c**	[0.76156, 0.00071, 0.36763]
LaH_{11} ($P4/nmm$)	$a = 3.87435$ Å	La	**2c**	[0.25000, 0.25000, 0.78577]
	$b = 3.87435$ Å	H	**4e**	[0.00000, 0.00000, 0.50000]
	$c = 5.27636$ Å	H	**8i**	[0.25000, -0.02052, 0.17824]
		H	**8i**	[0.25000, 0.55418, 0.35160]
		H	**2a**	[0.75000, 0.25000, 0.00000]

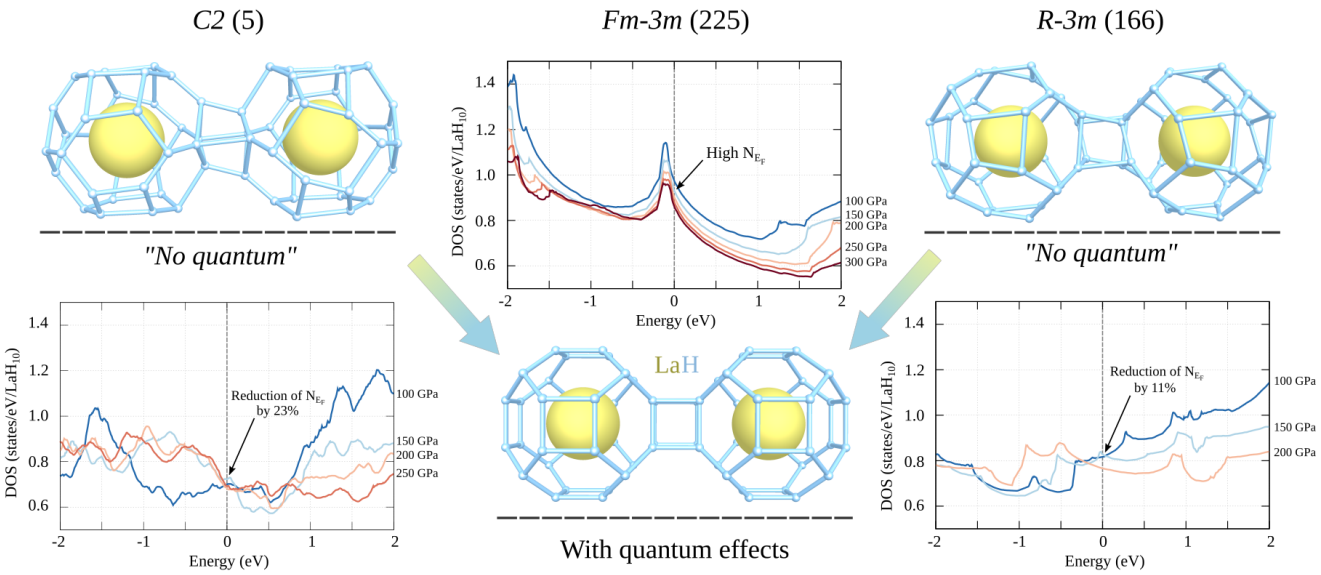

Extended Data Figure 10. **SSCHA minimization on LaH_{10} and DOS.** Top figures: two initial structures ($C2$ and R-$3m$) low enthalpy, considered in our SSCHA simulations. When considering quantum effects both structures evolve towards the Fm-$3m$ structure. Corresponding total electronic density of states (DOS) as a function of pressure are plotted for each structure (for comparison in the same energy scale). Highly symmetric motif (Fm-$3m$) maximizes N_{E_F}, while in distorted structures (R-$3m$ and $C2$) the occupation at the Fermi level is reduced by more than 23 % for $C2$ and by 11 % for R-$3m$, both comparison at 150 GPa w.r.t. Fm-$3m$. Classical pressures are appended for comparison in DOS panels. Note that DOS shape is also strongly modified.

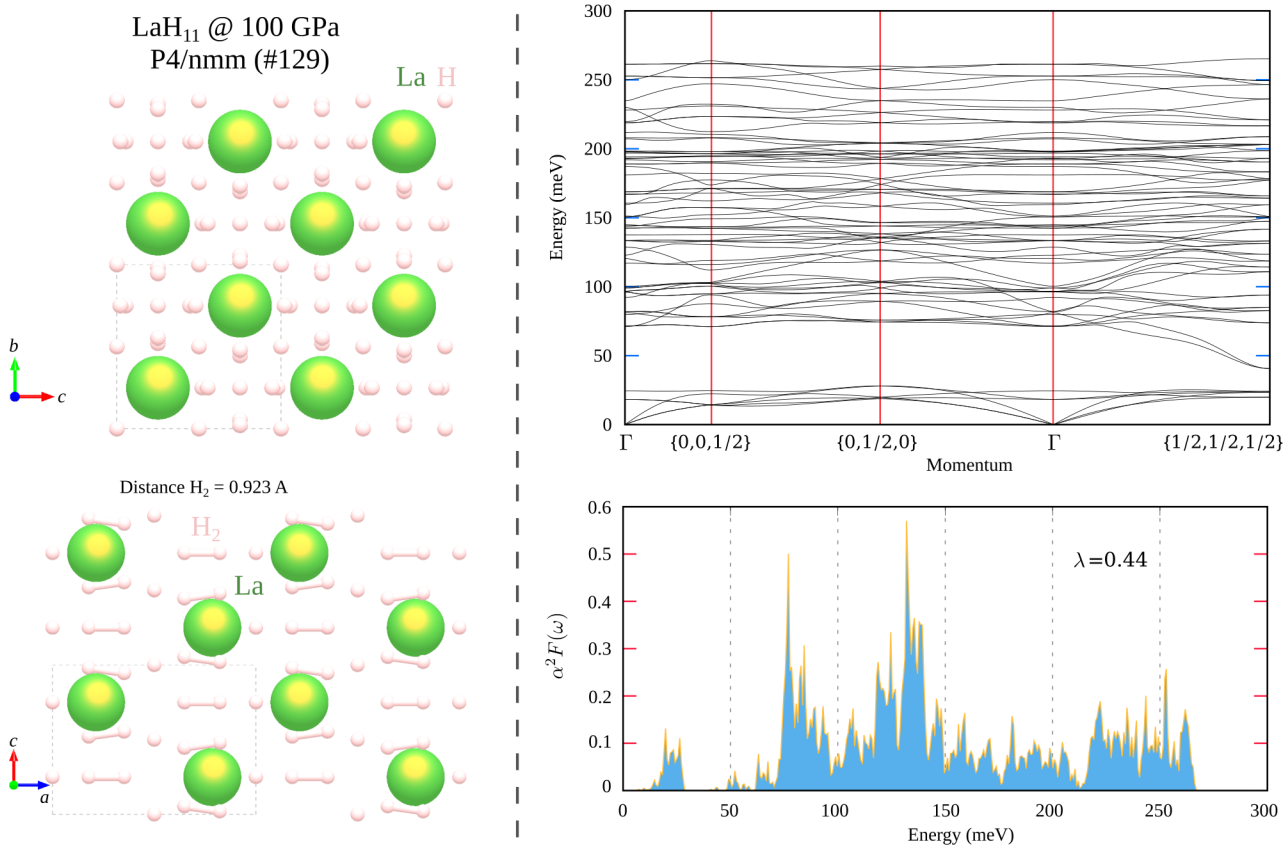

Extended Data Figure 11. **Details on LaH_{11}.** Left: $P4/nmm$ crystal structure of LaH_{11} at 100 GPa thermodynamically stable in the convex hull. Right top: harmonic phonons dispersion along momentum space for this composition: it is dynamically stable. Right bottom: superconducting Éliashberg spectrum function ($\alpha^2F(\omega)$) calculated for this composition at the pressure indicated with harmonic phonons. The estimated T_c with Allen-Dynes formula (μ^*=0.1) is ~7 K at 100 GPa (harmonic phonons).

Phonon Collapse and Second-Order Phase Transition in Thermoelectric SnSe

Unai Aseginolaza,[1,2,3] Raffaello Bianco,[4,5,6] Lorenzo Monacelli,[4] Lorenzo Paulatto,[7] Matteo Calandra,[8] Francesco Mauri,[4,5] Aitor Bergara,[1,2,9] and Ion Errea[2,3]

[1]*Centro de Física de Materiales CFM, CSIC-UPV/EHU, Paseo Manuel de Lardizabal 5, 20018 Donostia, Basque Country, Spain*

[2]*Donostia International Physics Center (DIPC), Manuel Lardizabal pasealekua 4, 20018 Donostia, Basque Country, Spain*

[3]*Fisika Aplikatua 1 Saila, University of the Basque Country (UPV/EHU), Europa Plaza 1, 20018 Donostia, Basque Country, Spain*

[4]*Dipartimento di Fisica, Università di Roma La Sapienza, Piazzale Aldo Moro 5, I-00185 Roma, Italy*

[5]*Graphene Labs, Fondazione Istituto Italiano di Tecnologia, Via Morego, I-16163 Genova, Italy*

[6]*Department of Applied Physics and Material Science, Steele Laboratory, California Institute of Technology, Pasadena, California 91125, USA*

[7]*IMPMC, UMR CNRS 7590, Sorbonne Universités—UPMC Univ. Paris 06, MNHN, IRD, 4 Place Jussieu, F-75005 Paris, France*

[8]*Sorbonne Universités, CNRS, Institut des Nanosciences de Paris, UMR7588, F-75252 Paris, France*

[9]*Departamento de Física de la Materia Condensada, University of the Basque Country (UPV/EHU), 48080 Bilbao, Basque Country, Spain*

(Received 19 July 2018; revised manuscript received 29 November 2018; published 22 February 2019)

Since 2014 the layered semiconductor SnSe in the high-temperature *Cmcm* phase is known to be the most efficient intrinsic thermoelectric material. Making use of first-principles calculations we show that its vibrational and thermal transport properties are determined by huge nonperturbative anharmonic effects. We show that the transition from the *Cmcm* phase to the low-symmetry *Pnma* is a second-order phase transition driven by the collapse of a zone border phonon, whose frequency vanishes at the transition temperature. Our calculations show that the spectral function of the in-plane vibrational modes are strongly anomalous with shoulders and double-peak structures. We calculate the lattice thermal conductivity obtaining good agreement with experiments only when nonperturbative anharmonic scattering is included. Our results suggest that the good thermoelectric efficiency of SnSe is strongly affected by the nonperturbative anharmonicity.

DOI: 10.1103/PhysRevLett.122.075901

Thermoelectric materials can convert waste heat into electricity [1,2]. The thermoelectric efficiency of a material is measured by the dimensionless figure of merit $ZT = S^2\sigma T/\kappa$, where S is the Seebeck coefficient, σ the electrical conductivity, T the temperature, and $\kappa = \kappa_e + \kappa_l$ the thermal conductivity, constituted by electronic κ_e and lattice κ_l contributions. The thermoelectric efficiency can be thus enhanced by decreasing the thermal conductivity while keeping a high power factor $S^2\sigma$. Materials have been doped [3–5] or nanostructured [6,7] in order to get a high power factor combined with a low thermal conductivity, yielding, i.e., $ZT \simeq 2.2$ in PbTe [8]. In the proximity to a phase transition ZT may also soar, as in the case of Cu_2Se [9]. Recently, however, Zhao *et al.* reported for SnSe [10] the highest thermoelectric figure of merit ever reached in a material without doping, material treatment, or without being sharply enhanced by the proximity to a phase transition: $ZT \simeq 2.6$ above 800 K.

SnSe is a narrow gap semiconductor that crystallizes at room temperature in an orthorhombic *Pnma* phase. At $T \simeq$ 800 K [10–13] it transforms into a more symmetric base-centered orthorhombic *Cmcm* structure (see Fig. 1). The

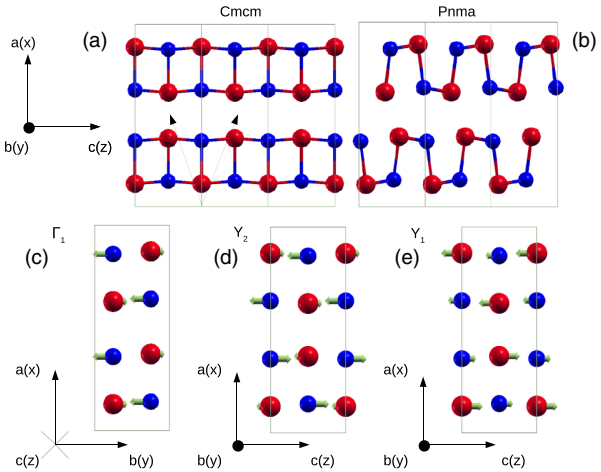

FIG. 1. The primitive lattice vectors of the *Cmcm* structure are $\mathbf{a}_1 = (a/2, 0, c/2)$, $\mathbf{a}_2 = (-a/2, 0, c/2)$, and $\mathbf{a}_3 = (0, b, 0)$, where a (long axis), b, and c are the lattice constants of the conventional cell. (a) XZ face of the *Cmcm* structure. Primitive lattice vectors are denoted with arrows for convenience we show $\mathbf{a}_1$ and $-\mathbf{a}_2$. (b) XZ face of the *Pnma* structure. (c) Atomic displacements of mode Γ_1. (d) Atomic displacements of mode Y_2. (e) Atomic displacements of mode Y_1. Sn atoms are red and Se blue.

order of the transition is not clear: some works [10–12] claim it is a second-order transition and others it has a first-order character [13]. A recent work [14] argues the transition occurs in two steps, where increasing temperature induces first a change in the lattice parameters that induces after a lattice instability. There is no inelastic scattering experiment so far for the high-temperature phase, which should show a prominent phonon collapse at the transition temperature if it belonged to the displacive second-order type [15–17].

The most interesting thermoelectric properties appear in the high-temperature phase, where the reduction of the electronic band gap increases the number of carriers providing a higher power factor, while the thermal conductivity remains very low [10]. The value of the intrinsic κ_l of SnSe remains controversial, as the extremely low isotropic 0.3 W/mK value at 800 K reported by Zhao *et al.* [10] could not be reproduced in other experiments, where a clear anisotropy is shown and the in-plane thermal conductivity is considerably larger [18–20]. The lattice thermal conductivity of the *Pnma* phase has been calculated from first principles solving the Boltzmann transport equation (BTE) using harmonic phonons and third order force-constants (TOFCs) obtained perturbatively as derivatives of the Born-Oppenheimer energy surface [21,22]. The *Cmcm* phase has imaginary phonon frequencies in the harmonic approximation [14,22,23], as expected for the high-symmetry phase in a second-order transition [24–26], and it is stabilized by anharmonicity [14,22], hindering the calculation of κ_l [22].

In this Letter, by performing *ab initio* calculations including anharmonicity at a nonperturbative level, we show that the phonon mode that drives the instability collapses at the transition temperature T_c demonstrating that the transition is second order. Anharmonic effects are so large that the spectral function expected for some in-plane modes deviates from the Lorentzian-like shape and shows broad peaks, shoulders, and satellite peaks, as in other monochalcogenides [25,27]. We calculate the lattice thermal conductivity of the *Cmcm* phase by combining the anharmonic phonon spectra with perturbative and nonperturbative TOFCs. We show here for the first time that nonperturbative anharmonic effects are not only crucial in the phonon spectra, but also in high-order force constants, which have a huge impact on the calculated thermal conductivity: κ_l agrees with experiments [18] only with nonperturbative TOFCs.

The group/subgroup index of the *Cmcm*/*Pnma* transition is 2, making a displacive second-order transition possible [28]. In this scenario, the transition temperature T_c is defined as the temperature at which the second derivative of the free energy F with respect to the order parameter Q that transforms the structure continuously from the *Cmcm* phase ($Q = 0$) into the *Pnma* ($Q \neq 0$) vanishes. As was already pointed out [12], symmetry [29,30] dictates that the amplitude of the transition is dominated by the distortion pattern associated to a nondegenerate mode (Y_1) at the zone border Y point with irreducible representation Y_2^+ (see Fig. 1 for the distortion pattern). This means that $\partial^2 F/\partial Q^2$ is proportional to the eigenvalue of the free energy Hessian matrix associated to this irreducible representation: $\omega^2_{Y_1}$.

In this work we calculate the free energy Hessian using the stochastic self-consistent harmonic approximation (SSCHA) [31,32], which is applied using *ab initio* density-functional theory (DFT) calculations within the Perdew-Burke-Ernzerhof (PBE) [33] or local density approximation (LDA) [34] parametrizations of the exchange-correlation functional (see Supplemental Material [35] for the details of the calculations [40–44]). The SSCHA is based on variational minimization of the free energy using a trial harmonic density matrix $\rho_{\mathcal{R},\mathbf{\Phi}}$ parametrized by centroid positions $\mathcal{R}$ and force constants $\mathbf{\Phi}$ (bold symbols represent tensors in compact notation). The centroids $\mathcal{R}$ determine the most probable position of the atoms and $\mathbf{\Phi}$ is related to the amplitude of their fluctuations around $\mathcal{R}$. The free energy Hessian can be calculated as [32]

$$\frac{\partial^2 F}{\partial \mathcal{R}\partial \mathcal{R}} = \mathbf{\Phi} + \overset{(3)}{\mathbf{\Phi}}\mathbf{\Lambda}(0)[\mathbf{1} - \overset{(4)}{\mathbf{\Phi}}\mathbf{\Lambda}(0)]^{-1}\overset{(3)}{\mathbf{\Phi}}, \tag{1}$$

where $\overset{(3)}{\mathbf{\Phi}}$ and $\overset{(4)}{\mathbf{\Phi}}$ are third- and fourth-order nonperturbative force constants obtained as quantum averages calculated with $\rho_{\mathcal{R},\mathbf{\Phi}}$: $\overset{(n)}{\mathbf{\Phi}} = \langle \partial^n V/\partial \mathbf{R}^n \rangle_{\rho_{\mathcal{R},\mathbf{\Phi}}}$. The $\overset{(n)}{\mathbf{\Phi}}$ force constants are generally different from the $\overset{(n)}{\Phi}$ perturbative ones obtained as derivatives of the Born-Oppenheimer potential V at the minimum: $\overset{(n)}{\boldsymbol{\phi}} = [\partial^n V/\partial \mathbf{R}^n]_0$. $\mathbf{\Lambda}(0)$ in Eq. (1) is a function of the $\tilde{\Omega}_\mu$ SSCHA frequencies and polarization vectors obtained diagonalizing $\Phi_{ab}/\sqrt{M_a M_b}$, with M_a the atomic mass (a labels both an atom and Cartesian index). The ω_μ frequencies obtained instead from the free energy Hessian after diagonalizing $[(\partial^2 F)/(\partial \mathcal{R}_a \partial \mathcal{R}_b)]/\sqrt{M_a M_b}$, e.g., ω_{Y_1}, can be interpreted as the static limit of the physical phonons [32]. The contribution of $\overset{(4)}{\mathbf{\Phi}}\mathbf{\Lambda}$ is negligible with respect to the identity matrix [35] and thus it is neglected throughout.

The calculated temperature dependence of $\omega^2_{Y_1}$ is shown in Fig. 2 for LDA and PBE for two different lattice volumes in each case. In all cases $\omega^2_{Y_1}$ is positive at high temperatures, but it rapidly decreases with lowering the temperature, vanishing at T_c. This phonon collapse is consistent with a second-order phase transition between the *Pnma* and *Cmcm*. We check that a SSCHA calculation at $T > T_c$ ($T = 800$ K) starting from the relaxed low-symmetry *Pnma* phase (relaxed at DFT static level) yields the high-symmetry *Cmcm* atomic positions for the $\mathcal{R}$

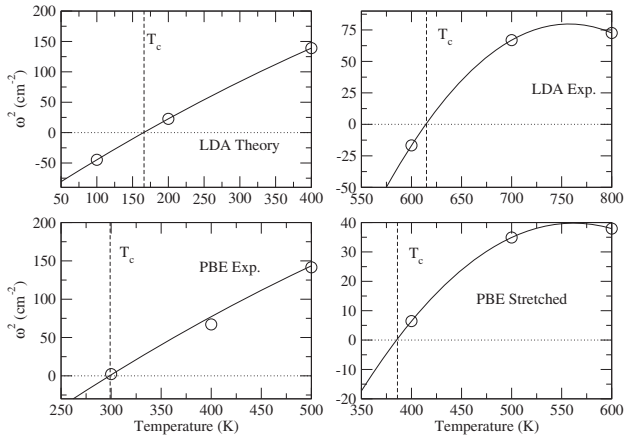

FIG. 2. $\omega^2_{Y_1}$ as a function of temperature within LDA and PBE approximations for different lattice volumes (circles). In the LDA we compare the results obtained with the theoretical and experimental [10] lattice parameters. In the PBE calculation we present the results for the experimental lattice parameters and a stretched unit cell (see Table I for the lattice parameters). The solid lines correspond to a polynomial fit.

centroids. Thus, the *Pnma* is not a local minimum of the free energy above T_c, ruling out the first-order transition. Our result disagrees with the conclusions drawn in Ref. [14]. First, because at the T_c calculated in Ref. [14], which is estimated by comparing the free energies of the two structures, the Y_1 mode of the *Cmcm* phase is stable, which implies this phase is a local minimum at T_c, and, thus, the transition is of first-order type [14]. And second, because it is argued [14] that the instability at Y is produced by a slight change in the in-plane lattice parameters induced by temperature (from $c/b > 1$ to $c/b < 1$), which makes the transition a two-step process. We do not see this sudden appearance of the instability [35].

The obtained transition temperature strongly depends on the exchange-correlation functional and the volume, as it occurs in similar monochalcogenides [25]. Within LDA T_c ranges between 168 K with theoretical lattice parameters and 616 K with experimental lattice parameters [10]. Within PBE T_c barely changes between the experimental and theoretical lattice parameters. We attribute this result to the fact that the in-plane lattice parameters b and c are in perfect agreement with the experimental results within PBE, while LDA clearly underestimates them. The theoretical lattice parameters are estimated neglecting vibrational contributions to the free energy. In order to estimate the role of the thermal expansion, we calculate the stress tensor including vibrational contributions at the anharmonic level [45]. The in-plane contribution of the stress tensor calculated at the temperature closest to T_c, P_{zz}, shows that both theoretical LDA and PBE lattices should be stretched. Within LDA it is clear that stretching the lattice increases T_c. Within PBE, when we take a stretched lattice

TABLE I. Experimental [10] and theoretical (DFT at static level) LDA and PBE lattice parameters used in this work. The stretched cell used in some calculations is also given. a, b, and c lattice parameters are given in Bohr length units (a_0) and the three components of the stress tensor in GPa units. The pressure is calculated including vibrational terms at an anharmonic level at the following temperatures for each case: 200 K (LDA theory), 600 K (LDA Exp.), 400 K (PBE Exp.), 400 K (PBE theory), and 400 K (PBE stretched).

	a	b	c	P_{xx}	P_{yy}	P_{zz}
LDA theory	21.58	7.90	7.90	0.4	0.6	0.7
LDA exp.	22.13	8.13	8.13	−1.1	−2.0	−2.2
PBE theory	22.77	8.13	8.13	0.5	1.1	1.0
PBE exp.	22.13	8.13	8.13	1.8	1.3	1.2
PBE stretched	23.48	8.27	8.27	−0.3	−0.7	−0.7

to reduce P_{zz}, T_c increases from 299 to 387 K. In all cases the other in-plane component of the stress tensor, P_{yy}, is very similar to P_{zz}. The LDA transition temperature with the experimental lattice parameters yields the transition temperature in closest agreement with experiments ($T_c \simeq 800$ K [10–13,46]). The underestimation of the transition temperature may be due to the approximated exchange-correlation or the finite supercell size taken for the SSCHA.

The predicted phonon collapse should be measurable by inelastic neutron scattering (INS) experiments. INS experiments [46] show a softening of a zone-center optical mode of the *Pnma* phase upon heating, which is consistent with the condensation of the Y_1 mode after the transition. By making use of a dynamical ansatz [32], we calculate the mode-projected phonon anharmonic self-energy [35] $\Pi_\mu(\mathbf{q},\omega)$, from which we obtain the phonon spectral function:

$$\sigma(\mathbf{q},\omega) = \frac{1}{\pi}\sum_\mu \frac{-\omega \mathrm{Im}\Pi_\mu(\mathbf{q},\omega)}{[\omega^2 - \tilde{\Omega}^2_\mu(\mathbf{q}) - \mathrm{Re}\Pi_\mu(\mathbf{q},\omega)]^2 + [\mathrm{Im}\Pi_\mu(\mathbf{q},\omega)]^2}. \quad (2)$$

Peaks in $\sigma(\mathbf{q},\omega)$ represent experimental phonon excitations. Replacing $\Pi_\mu(\mathbf{q},\omega) \to \Pi_\mu(\mathbf{q},\tilde{\Omega}_\mu(\mathbf{q}))$ in Eq. (2) the Lorentzian approximation is recovered, in which each peak is represented with a Lorentzian function centered at $\Omega_\mu(\mathbf{q}) = \sqrt{\tilde{\Omega}^2_\mu(\mathbf{q}) + \mathrm{Re}\Pi_\mu(\mathbf{q},\tilde{\Omega}_\mu(\mathbf{q}))}$ with a linewidth proportional to $\mathrm{Im}\Pi_\mu(\mathbf{q},\tilde{\Omega}_\mu(\mathbf{q}))$ [47].

Figure 3 compares the harmonic phonon spectrum with the anharmonic one in the Lorentzian approximation obtained at 800 K within LDA in the experimental lattice (the results below are also obtained within the LDA in the experimental lattice). The anharmonic correction is large

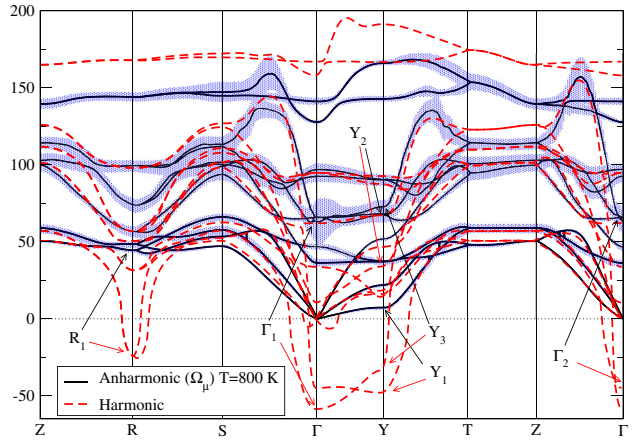

FIG. 3. Harmonic and anharmonic phonons in the Lorentzian approximation [$\Omega_\mu(\mathbf{q})$]. The length of the bars corresponds to the linewidth (full length of the line is the full width at half maximum). The calculations are done within LDA in the experimental structure using $\overset{(3)}{\mathbf{\Phi}}$ at 800 and $\tilde{\Omega}_\mu(\mathbf{q})$ at 800 K.

for most of the modes across the Brillouin zone. Within the harmonic approximation, there are five unstable modes: two (Γ_1, Γ_2) at Γ, two (Y_1, Y_3) at Y, and one (R_1) at R. The instabilities at Γ would cause ferroeletric transitions [22,48], but they suffer an anharmonic renormalization that prevents it. Y_3 and R_1 are also stabilized by anharmonic effects. The Y_1 mode, however, remains unstable at 600 K and it is stabilized after the transition [see Figs. 4(a) and 4(b)].

In highly anharmonic materials [25,27,47,49,50], the spectral functions show broad peaks, shoulders, and satellite peaks, strongly deviating from the Lorentzian picture. In Fig. 4 we show the spectral function keeping the full frequency dependence on the self-energy, without assuming the Lorentzian line shape. The spectral function clearly reproduces the collapse of the Y_1 mode at the transition temperature. The calculated spectral functions show that the strong anharmonicity present on the phonon frequency renormalization is also reflected on the spectral function. The strongly anharmonic features specially affect in-plane modes in the 25–75 cm^{-1} energy range. For instance, at the Γ point the Γ_1 mode, which describes a vibration along the in-plane y axis in opposite direction for the Sn and Se atoms (see Fig. 1) and is stabilized by anharmonicity, shows a double peak structure and a broad shoulder [see Fig. 4(e)]. The mode that describes the same vibration (Γ_2) but in the other in-plane z direction also shows a complex non-Lorentzian shape. The overall $\sigma(\mathbf{q}=\Gamma,\omega)$ consequently has a broad shoulder at $\simeq$25 cm^{-1} as marked in Fig. 4(c), which is less acute as temperature increases. At the Y point there are also two modes, Y_2, whose eigenvector is plotted in Fig. 1, and Y_3, which describes the same displacement but in the other y in-plane direction, that show a strongly anharmonic non-Lorentzian shape. The modes with complex line shapes are those that show the largest linewidth in the Lorentzian limit (see Fig. 3). These modes have strongly anomalous spectral functions and large linewidths because they can easily scatter with an optical mode close in energy and an acoustic mode close to Γ. We identify this by directly analyzing which phonon triplets contribute more to the linewidth. It is interesting to remark that if $\Pi_\mu(\mathbf{q},\omega)$ is calculated by substituting $\overset{(3)}{\mathbf{\Phi}}$ by $\overset{(3)}{\boldsymbol{\phi}}$, the anomalies of these modes become weaker [35]. This underlines that in the *Cmcm* phase the third-order derivatives of V are not sufficient to calculate the phonon linewidths and that higher order terms are important, which are effectively captured by $\overset{(3)}{\mathbf{\Phi}}$.

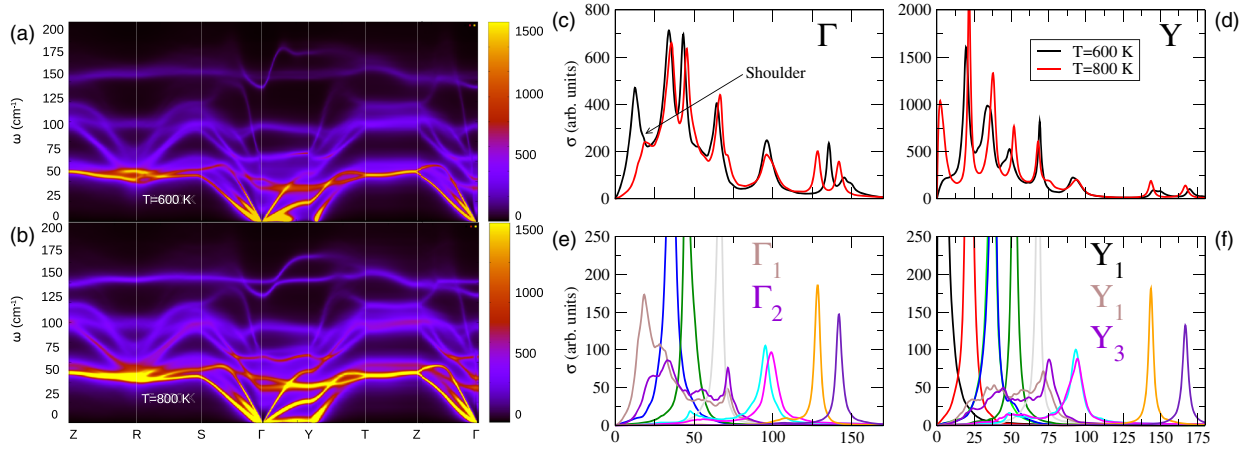

FIG. 4. Spectral function of SnSe in the *Cmcm* phase calculated at (a) 600 and (b) 800 K using $\overset{(3)}{\mathbf{\Phi}}$ at the corresponding temperature. The spectral function at the (c) Γ and (d) Y points at 600 and 800 K. The contribution of each mode to the spectral function is also shown at the Γ point (e) and the Y point (f) at 800 K. Different colors correspond to different modes. All the calculations are performed within LDA in the experimental structure. In each case we use $\tilde{\Omega}_\mu(\mathbf{q})$ calculated at the same temperature as $\overset{(3)}{\mathbf{\Phi}}$.

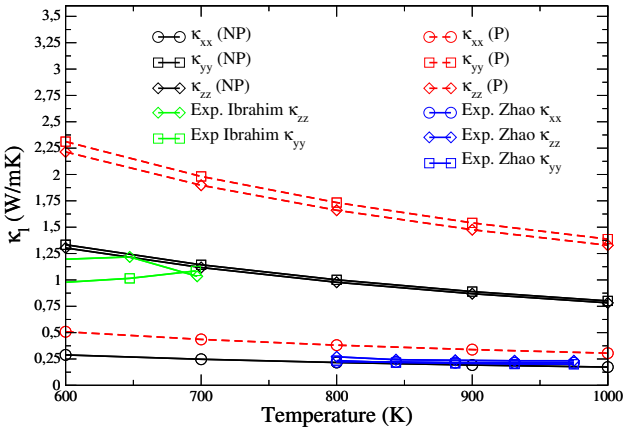

FIG. 5. Lattice thermal conductivity of SnSe calculated with perturbative $\overset{(3)}{\boldsymbol{\phi}}$ (P) and nonperturbative $\overset{(3)}{\boldsymbol{\Phi}}$ (NP) at 800 K compared to the experiments by Ibrahim *et al.* [18] and Zhao *et al.* [10]. We use the $\tilde{\Omega}_\mu(\mathbf{q})$ phonon frequencies calculated at 800 K at all temperatures. Calculations are performed within LDA using the experimental structure. Different volumes or exchange-correlation functionals give consistent results [35].

In Fig. 5 we present the lattice thermal conductivity calculated with the SSCHA frequencies ($\tilde{\Omega}_\mu(\mathbf{q})$) and nonperturbative TOFCs ($\overset{(3)}{\boldsymbol{\Phi}}$). For comparison we also calculate κ_l substituting $\overset{(3)}{\boldsymbol{\Phi}}$ by $\overset{(3)}{\boldsymbol{\phi}}$. The calculation is performed solving the BTE assuming the single-mode relaxation time approximation (SMA). The thermal conductivity of SnSe is very low, mainly because the contribution of optical modes is strongly suppressed by the large anharmonicity and the contribution of acoustic modes is also reduced due to the large scattering among themselves and with the Γ_1 mode. We compare our results with the values obtained by Zhao *et al.* [10] above the transition at 800 K. We also include in the figure the results obtained by Ibrahim *et al.* [18] above 600 K (only the in-plane κ_l is reported at these temperatures) in the *Pnma* phase. Even if the results belong to different phases, comparing our calculations for the *Cmcm* phase with those obtained in the latter work is insightful because the thermal conductivity of these two phases is very similar close to the transition [35], as expected in a second-order phase transition. Though direct comparison should be taken carefully for this reason, the lattice thermal conductivity is in better agreement with experimental results using $\overset{(3)}{\boldsymbol{\Phi}}$ instead of $\overset{(3)}{\boldsymbol{\phi}}$, which overestimates the lattice thermal conductivity along the in-plane directions. This is consistent with the larger phonon linewidths obtained with the nonperturbative TOFCs. The agreement for the in-plane $\kappa_{yy} \sim \kappa_{zz}$ with the measurements by Ibrahim *et al.* [18] is good in the nonperturbative limit, contrary to previous calculations that underestimate it [22]. The calculated out-of-plane κ_{xx} is also in good agreement with the results by Zhao *et al.* [10], but we find that their ultralow results for the in-plane κ_l, in contradiction with the values in Ref. [18] obtained for the low-symmetry phase close to the transition, are underestimated. These results suggest that the thermal conductivity measured by Zhao *et al.* may have nonintrinsic effects as it has already been pointed out [51].

In conclusion, we show that the vibrational properties of SnSe in the *Cmcm* phase are dominated by huge nonperturbative anharmonic effects. We show how the collapse of the Y_1 mode is responsible for the second-order phase transition. The calculated transition temperature is volume and functional dependent. The spectral functions of in-plane modes are characterized by anomalous features deviating from the Lorentzian-like shape. These results will be crucial to interpret future INS experiments for the high-temperature phase. The calculated in-plane thermal conductivity is in good agreement with the experiments by Ibrahim *et al.* [18], but not with those by Zhao *et al.* [10] which show low anisotropy. These results suggest that the isotropic ultralow values by Zhao *et al.* could be the observation of a nonintrinsic property. Our results show for the first time that the inclusion of nonperturbative effects is crucial for obtaining third-order force constants that yield a lattice thermal conductivity in agreement with experiments.

The authors acknowledge fruitful discussions with O. Delaire. Financial support was provided by the Spanish Ministry of Economy and Competitiveness (FIS2016-76617-P), the Department of Education, Universities and Research of the Basque Government and the University of the Basque Country (IT756-13). U. A. is also thankful to the Material Physics Center for support. Computer facilities were provided by the Donostia International Physics Center (DIPC), the Spanish Supercomputing Network (FI-2017-2-0007), and PRACE (2017174186).

[1] H. J. Goldsmid, *Introduction to Thermoelectricity* (Springer, New York, 2010), pp. 1–7.
[2] K. Behnia, *Fundamentals of Thermoelectricity* (OUP, Oxford, 2015).
[3] G.-H. Kim, L. Shao, K. Zhang, and K. P. Pipe, Nat. Mater. **12**, 719 (2013).
[4] Y. Pei, A. D. LaLonde, N. A. Heinz, X. Shi, S. Iwanaga, H. Wang, L. Chen, and G. J. Snyder, Adv. Mater. **23**, 5674 (2011).
[5] J. P. Heremans, V. Jovovic, E. S. Toberer, A. Saramat, K. Kurosaki, A. Charoenphakdee, S. Yamanaka, and G. J. Snyder, Science **321**, 554 (2008).
[6] C. J. Vineis, A. Shakouri, A. Majumdar, and M. G. Kanatzidis, Adv. Mater. **22**, 3970 (2010).
[7] A. Minnich, M. Dresselhaus, Z. Ren, and G. Chen, Energy Environ. Sci. **2**, 466 (2009).
[8] K. F. Hsu, S. Loo, F. Guo, W. Chen, J. S. Dyck, C. Uher, T. Hogan, E. K. Polychroniadis, and M. G. Kanatzidis, Science **303**, 818 (2004).

[9] H. Liu, X. Yuan, P. Lu, X. Shi, F. Xu, Y. He, Y. Tang, S. Bai, W. Zhang, L. Chen *et al.*, Adv. Mater. **25**, 6607 (2013).

[10] L.-D. Zhao, S.-H. Lo, Y. Zhang, H. Sun, G. Tan, C. Uher, C. Wolverton, V. P. Dravid, and M. G. Kanatzidis, Nature (London) **508**, 373 (2014).

[11] K. Adouby, Z. Kristallogr. **213**, 343 (1998).

[12] T. Chattopadhyay, J. Pannetier, and H. Von Schnering, J. Phys. Chem. Solids **47**, 879 (1986).

[13] H. G. Von Schnering and H. Wiedemeier, Z. Kristallogr. Cryst. Mater. **156**, 143 (1981).

[14] A. Dewandre, O. Hellman, S. Bhattacharya, A. H. Romero, G. K. H. Madsen, and M. J. Verstraete, Phys. Rev. Lett. **117**, 276601 (2016).

[15] M. Holt, P. Zschack, H. Hong, M. Y. Chou, and T.-C. Chiang, Phys. Rev. Lett. **86**, 3799 (2001).

[16] F. Weber, S. Rosenkranz, J.-P. Castellan, R. Osborn, R. Hott, R. Heid, K.-P. Bohnen, T. Egami, A. H. Said, and D. Reznik, Phys. Rev. Lett. **107**, 107403 (2011).

[17] C. D. O'Neill, D. A. Sokolov, A. Hermann, A. Bossak, C. Stock, and A. D. Huxley, Phys. Rev. B **95**, 144101 (2017).

[18] D. Ibrahim, J.-B. Vaney, S. Sassi, C. Candolfi, V. Ohorodniichuk, P. Levinsky, C. Semprimoschnig, A. Dauscher, and B. Lenoir, Appl. Phys. Lett. **110**, 032103 (2017).

[19] S. Sassy, C. Candolfi, J.-B. Vaney, V. Ohorodniichuk, P. Masschelein, A. Dauscher, and B. Lenoir, Appl. Phys. Lett. **104**, 212105 (2014).

[20] C.-L. Cheng, H. Wang, Y.-Y. Chen, T. Day, and G. J. Snyder, J. Mater. Chem. A **2**, 11171 (2014).

[21] J. Carrete, N. Mingo, and S. Curtarolo, Appl. Phys. Lett. **105**, 101907 (2014).

[22] J. M. Skelton, L. A. Burton, S. C. Parker, A. Walsh, C.-E. Kim, A. Soon, J. Buckeridge, A. A. Sokol, C. R. A. Catlow, A. Togo *et al.*, Phys. Rev. Lett. **117**, 075502 (2016).

[23] H. Yu, S. Dai, and Y. Chen, Sci. Rep. **6**, 26193 (2016).

[24] M. Iizumi, Y. Hamaguchi, K. F. Komatsubara, and Y. Kato, J. Phys. Soc. Jpn. **38**, 443 (1975).

[25] G. A. S. Ribeiro, L. Paulatto, R. Bianco, I. Errea, F. Mauri, and M. Calandra, Phys. Rev. B **97**, 014306 (2018).

[26] M. Jian, M. Trigo, S. Savíc, S. Fahy, É. Murray, C. Bray, J. Clark, T. Henighan, M. Kozina, M. Chollet *et al.*, Nat. Commun. **7**, 12291 (2016).

[27] C. W. Li, O. Hellam, J. Ma, A. F. May, H. B. Cao, X. Chen, A. D. Christianson, G. Ehlers, D. J. Singh, B. C. Sales, and O. Delaire, Phys. Rev. Lett. **112**, 175501 (2014).

[28] J.-C. Toledano and P. Toledano, *The Landau Theory of Phase Transitions: Application to Structural, Incommensurate, Magnetic and Liquid Crystal Systems* (World Scientific, Singapore, 1987).

[29] D. Orobengoa, C. Capillas, M. I. Aroyo, and J. M. Perez-Mato, J. Appl. Crystallogr. **42**, 820 (2009).

[30] J. M. Perez-Mato, D. Orobengoa, and M. I. Aroyo, Acta Crystallogr. Sect. A **66**, 558 (2010).

[31] I. Errea, M. Calandra, and F. Mauri, Phys. Rev. B **89**, 064302 (2014).

[32] R. Bianco, I. Errea, L. Paulatto, M. Calandra, and F. Mauri, Phys. Rev. B **96**, 014111 (2017).

[33] J. P. Perdew, K. Burke, and M. Ernzerhof, Phys. Rev. Lett. **77**, 3865 (1996).

[34] J. P. Perdew and A. Zunger, Phys. Rev. B **23**, 5048 (1981).

[35] See Supplemental Material at http://link.aps.org/supplemental/10.1103/PhysRevLett.122.075901 for more detailed analysis of crystal structure, theory, and calculation methods, which includes Refs. [36–39].

[36] G. Kresse and J. Hafner, J. Phys. Condens. Matter **6**, 8245 (1994).

[37] P. E. Blöchl, Phys. Rev. B **50**, 17953 (1994).

[38] N. Troullier and J. L. Martins, Phys. Rev. B **43**, 1993 (1991).

[39] G. Fugallo, M. Lazzeri, L. Paulatto, and F. Mauri, Phys. Rev. B **88**, 045430 (2013).

[40] S. Baroni, S. De Gironcoli, A. Dal Corso, and P. Giannozzi, Rev. Mod. Phys. **73**, 515 (2001).

[41] L. Paulatto, F. Mauri, and M. Lazzeri, Phys. Rev. B **87**, 214303 (2013).

[42] P. Giannozzi, S. Baroni, N. Bonini, M. Calandra, R. Car, C. Cavazzoni, D. Ceresoli, G. L. Chiarotti, M. Cococcioni, I. Dabo *et al.*, J. Phys. Condens. Matter **21**, 395502 (2009).

[43] P. Giannozzi *et al.*, J. Phys. Condens. Matter **29**, 465901 (2017).

[44] W. Li, J. Carrete, N. A. Katcho, and N. Mingo, Comput. Phys. Commun. **185**, 1747 (2014).

[45] L. Monacelli, I. Errea, M. Calandra, and F. Mauri, Phys. Rev. B **98**, 024106 (2018).

[46] C. W. Li, J. Hong, A. F. May, D. Bansal, S. Chi, T. Hong, G. Ehlers, and O. Delaire, Nat. Phys. **11**, 1063 (2015).

[47] R. Bianco, I. Errea, M. Calandra, and F. Mauri, Phys. Rev. B **97**, 214101 (2018).

[48] J. Hong and O. Delaire, arXiv:1604.07077.

[49] O. Delaire, J. Ma, K. Marty, A. F. May, M. A. McGuire, M.-H. Du, D. J. Singh, A. Podlesnyak, G. Ehlers, M. Lumsden *et al.*, Nat. Mater. **10**, 614 (2011).

[50] L. Paulatto, I. Errea, M. Calandra, and F. Mauri, Phys. Rev. B **91**, 054304 (2015).

[51] P.-C. Wei, S. Bhattacharya, J. He, S. Neeleshwar, R. Podila, Y. Chen, and A. Rao, Nature (London) **539**, E1 (2016).

NANO LETTERS
Cite This: Nano Lett. 2019, 19, 3098−3103
Letter
pubs.acs.org/NanoLett

Quantum Enhancement of Charge Density Wave in NbS_2 in the Two-Dimensional Limit

Raffaello Bianco,[*,†,‡,§] Ion Errea,[∥,⊥,#] Lorenzo Monacelli,[§] Matteo Calandra,[○] and Francesco Mauri[§,‡]

[†]Department of Applied Physics and Materials Science, California Institute of Technology, Pasadena, California 91125, United States

[‡]Graphene Laboratories, Fondazione Istituto Italiano di Tecnologia, Via Morego, I-16163 Genova, Italy

[§]Dipartimento di Fisica, Università di Roma La Sapienza, Piazzale Aldo Moro 5, I-00185 Roma, Italy

[∥]Fisika Aplikatua 1 Saila, Gipuzkoako Ingeniaritza Eskola, University of the Basque Country (UPV/EHU), Europa Plaza 1, 20018 Donostia-San Sebastián, Basque Country, Spain

[⊥]Centro de Física de Materiales (CSIC-UPV/EHU), Manuel de Lardizabal pasealekua 5, 20018 Donostia-San Sebastián, Basque Country, Spain

[#]Donostia International Physics Center (DIPC), Manuel de Lardizabal pasealekua 4, 20018 Donostia-San Sebastián, Basque Country, Spain

[○]Sorbonne Université, CNRS, Institut des Nanosciences de Paris, UMR7588, F-75252, Paris, France

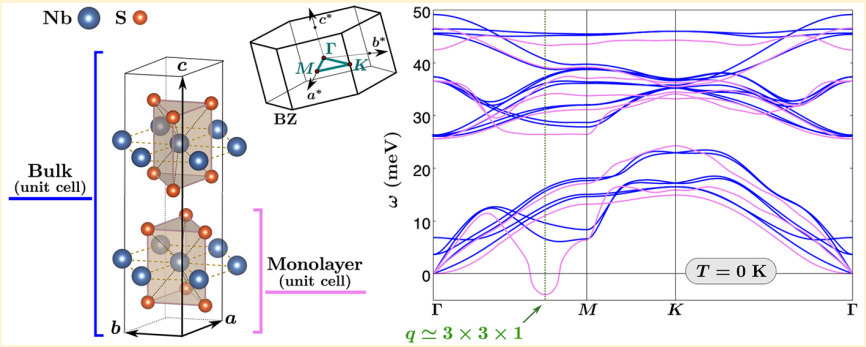

ABSTRACT: At ambient pressure, bulk 2H-NbS_2 displays no charge density wave instability, which is at odds with the isostructural and isoelectronic compounds 2H-$NbSe_2$, 2H-TaS_2, and 2H-$TaSe_2$, and in disagreement with harmonic calculations. Contradictory experimental results have been reported in supported single layers, as 1H-NbS_2 on Au(111) does not display a charge density wave, whereas 1H-NbS_2 on 6H-SiC(0001) endures a 3 × 3 reconstruction. Here, by carrying out quantum anharmonic calculations from first-principles, we evaluate the temperature dependence of phonon spectra in NbS_2 bulk and single layer as a function of pressure/strain. For bulk 2H-NbS_2, we find excellent agreement with inelastic X-ray spectra and demonstrate the removal of charge ordering due to anharmonicity. In the two-dimensional limit, we find an enhanced tendency toward charge density wave order. Freestanding 1H-NbS_2 undergoes a 3 × 3 reconstruction, in agreement with data on 6H-SiC(0001) supported samples. Moreover, as strains smaller than 0.5% in the lattice parameter are enough to completely remove the 3 × 3 superstructure, deposition of 1H-NbS_2 on flexible substrates or a small charge transfer via field-effect could lead to devices with dynamical switching on/off of charge order.

KEYWORDS: *Transition metal dichalcogenide, monolayer, charge density wave, anharmoncity, size-dependent properties, phonons*

Transition metal dichalcogenides (TMDs) are layered materials with generic formula MX_2, where M is a transition metal (Nb, Ta, Ti, Mo, W, ...) and X a chalcogen (S, Se, Te). The layers, made of triangular lattices of transition metal atoms sandwiched by covalently bonded chalcogens, are held together by weak van der Waals forces, and TMDs can be readily exfoliated into thin flakes down to the single layer limit, with mechanical or chemical techniques.[1−4] In TMDs, the interplay between strong electron−electron and electron−phonon interactions gives rise to rich phase diagrams with a wide variety of cooperating/competing collective electronic orderings as charge-density wave (CDW), Mott insulating, and superconductive phases.[5,6] Of the several polytypes, we focus here on the most common one for NbS_2, the H polytype,[7,8] where the transition metal is in trigonal prismatic coordination

Received: February 3, 2019
Revised: March 20, 2019
Published: April 1, 2019

DOI: 10.1021/acs.nanolett.9b00504
Nano Lett. 2019, 19, 3098−3103

with the surrounding chalcogens. In Figure 1 the 1H (monolayer) and 2H (bulk) crystal structures are shown.

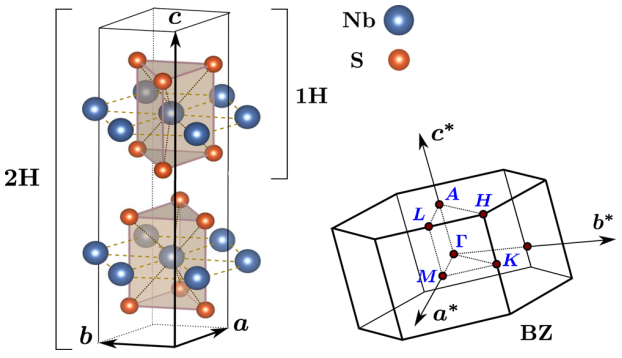

Figure 1. Left-hand side: crystal structure of trigonal NbS_2 in the 1H monolayer and in the 2H (bulk) stacking layer configuration. Right-hand side: corresponding hexagonal BZ with the high-symmetry points (in the monolayer configuration only the points ΓMK are relevant, and they are customarily indicated with a line over the letter).

Among metallic 2H bulk TMDs, NbS_2 occupies a special place as no CDW has been reported,[9,10] contrary to its isoelectronic and isostructural 2H-$TaSe_2$, 2H-TaS_2, and 2H-$NbSe_2$. All these systems have very similar band structures and are conventional (i.e., phonon-mediated) superconductors with critical temperatures T_c that increases from a sub-Kelvin value in 2H-$TaSe_2$ and 2H-TaS_2 (around 0.2 and 0.5 K, respectively) up to 5.7 K in 2H-NbS_2 and 7.2 K in 2H-$NbSe_2$.[11−14] They also show quite a different CDW transition strength.[15,16] 2H-$TaSe_2$, 2H-TaS_2, and 2H-$NbSe_2$ undergo a triple incommensurate CDW transition to a superlattice with hexagonal symmetry corresponding roughly to the same wave vector $\mathbf{q}_{CDW} = \Gamma M(1 - \delta)2/3$ ($\delta \simeq 0.02$ is the incommensurate factor) of the Brillouin zone. However, the transition temperature T_{CDW} increases from 30 K for 2H-$NbSe_2$ to 80 K for 2H-TaS_2 and 120 K for 2H-$TaSe_2$ (2H-$TaSe_2$ actually shows a further commensurate first-order CDW transition at 92 K with δ dropping continuously to zero).[17] Therefore, 2H-NbS_2 considerably stands out as it shows only an incipient instability near $\mathbf{q}_{CDW}$, but it remains stable even at the lowest temperatures. This circumstance is even more surprising if it is considered that 2H-$NbSe_2$ and 2H-NbS_2 display superconductivity at similar temperatures.

In TMDs, the behavior of the CDW ordering in the two-dimensional (2D) limit cannot be inferred from the knowledge of their bulk counterparts, because two competing mechanisms are expected to play a major role. On the one hand, reduced dimensionality strengthens Peierls instabilities (due to Fermi surface nesting) and electron−phonon interactions (due to reduced dielectric screening), thus favoring stronger CDW. On the other hand, stronger fluctuation effects from both finite temperatures and disorders should tend to destroy long-range CDW coherence in low-dimensional systems.[18] In particular, the effect of dimensionality on the CDW ordering in the H polytype is a current active research area. In 1H-TaS_2, the CDW vanishes in the 2D limit,[19] while in 1H-$TaSe_2$ it remains unchanged with respect to the bulk.[20] For 1H-$NbSe_2$ and 1H-NbS_2, the situation is more debated. In the 1H-$NbSe_2$ case, 3 × 3 CDW is observed but some controversy is still present in literature, tentatively attributed either to the sample exposure to air or to the different substrates, concerning the thickness dependence of the T_{CDW} (lower/higher T_{CDW} of the monolayer with respect to the bulk has been reported with bilayer graphene[21]/silicon[18] substrate, respectively). Supported single layers of 1H-NbS_2 have become recently available, and although no traces of CDW have been observed down to 30 K for monolayers grown on top of Au(111),[22] a 3 × 3 CDW ordering has been observed at ultralow temperature (measurements performed below 5 K) for monolayers grown on top of graphitized 6H-SiC(0001).[23]

In this Letter, we investigate from first-principles the vibrational properties of bulk 2H-NbS_2 (at zero and finite pressure) and suspended 1H-NbS_2, taking into account quantum anharmonic effects at nonperturbative level in the framework of the stochastic self-consistent harmonic approximation (SSCHA).[24−27] For bulk 2H-NbS_2, we show that quantum anharmonic effects remove the instability found at harmonic level and give temperature-dependent phonon energies in quantitative agreement with experiment. Previous anharmonic calculations for 2H-NbS_2 anticipated the role of anharmonicity but were limited to a low-dimensional subspace of the total high-dimensional configurations space and did not account for the temperature dependence.[14] We also show that quantum anharmonic effects are noticeable even at high pressure. Moreover, we demonstrate that the difference between 2H-NbS_2 and 2H-$NbSe_2$ is not simply ascribable to the different chalcogen mass. Finally, we analyze the 2D limit and show that freestanding single-layer 1H-NbS_2 undergoes a 3 × 3 CDW instability in agreement with data on 6H-SiC(0001) supported samples. However, strains smaller than 0.5% are sufficient to completely remove the instability, suggesting a strong dependence of the CDW on the environmental conditions (substrate, charge transfer, and so forth) and reconciling the apparent contradiction with supported Au(111) samples.

For bulk 2H-NbS_2, in Figure 2 we compare the computed anharmonic phonon dispersions with the results of the inelastic

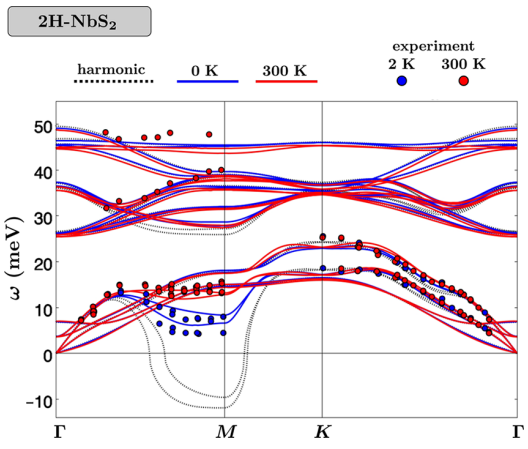

Figure 2. 2H-NbS_2 harmonic (black dashed lines) and SSCHA anharmonic phonon dispersion at 300 K (red solid lines) and 0 K (blue solid lines), calculated using the experimental lattice parameters. The results are compared with the IXS measurements of ref 7 performed at 300 K (red dots) and 2 K (blue dots). The SSCHA dispersion corrects the errors of the pure harmonic result near M: the instability of the two longitudinal acoustic and optical modes is removed and the softening on lowering temperature is well reproduced.

DOI: 10.1021/acs.nanolett.9b00504
Nano Lett. 2019, 19, 3098−3103

X-ray scattering (IXS) experiment of ref 7 at low and ambient temperature. We also show the (temperature-independent) harmonic phonon dispersion. Calculations were performed with the $a^{2H}_{Exp} = b^{2H}_{Exp} = 3.33$ Å and $c^{2H}_{Exp} = 11.95$ Å bulk experimental lattice parameters at zero pressure.[7] The phonon dispersion is almost everywhere well reproduced with the harmonic calculation, except close to M, where it predicts that two longitudinal acoustic and optical modes become imaginary. Experimental phonon energies show a sensible temperature dependence in this region of the Brillouin zone (BZ) and are, obviously, always real. The SSCHA cures the pathology of the harmonic result; the anharmonic phonon dispersions do not show any instability and give a very good agreement with the experiment at both temperatures.

Because SSCHA calculations give dispersions in good agreement with experiments, we can perform a wider analysis. In the upper panel of Figure 3, we show the SSCHA phonon dispersion for different temperatures along the full high-symmetry path of the BZ. As temperature decreases, anharmonicity causes the softening of two acoustic and optical longitudinal modes close to both M and L, but there is no instability. Thus, quantum fluctuations strongly affected by the anharmonic potential stabilize 2H-NbS_2. In the other two panels, we show the effect of hydrostatic pressure on the phonon dispersion. Because there are no available experimental lattice parameters at high pressures, we estimated them by assuming that the ratio between experimental and standard density functional theory (DFT) theoretical lattice parameters (i.e., the lattice parameters that minimize the DFT energy but do not take into account any lattice quantum dynamic effects), $a^{2H}_{Exp}(P)/a^{2H}_{Th-DFT}(P)$ and $c^{2H}_{Exp}(P)/c^{2H}_{Th-DFT}(P)$, are independent of the applied pressure P. Thus, we computed those ratios at zero pressure and for a given pressure P the calculations were performed using as lattice parameters $a = (a^{2H}_{Exp}/a^{2H}_{Th-DFT}) \times a^{2H}_{Th-DFT}(P)$ and $c = (c^{2H}_{Exp}/c^{2H}_{Th-DFT}) \times c^{2H}_{Th-DFT}(P)$. By increasing pressure the anharmonicity of the lowest energy modes around M and L decreases but remains relevant even up to 14 GPa. A similar conclusion was drawn for 2H-$NbSe_2$, where where large anharmonic effects and strong temperature dependence of these phonon modes were observed as high as 16 GPa, in a region of its phase diagram where no CDW transition is observed.[28]

These results confirm the importance of quantum anharmonicity in 2H-NbS_2 to describe experimental data and the absence of a CDW instability. It is tempting at this point to use the same technique to shed light on the different CDW behavior exhibited by the very similar compound 2H-$NbSe_2$. Indeed, as we showed in a previous work,[28] the SSCHA correctly displays the occurrence of CDW in 2H-$NbSe_2$ at ambient pressure. One evident difference between 2H-NbS_2 and 2H-$NbSe_2$ is, of course, the mass of the chalcogen atom. We then performed a SSCHA calculation at 0 K for 2H-NbS_2 with "artificial" S atoms having unaltered electronic configuration but the mass of Se. In other words, we performed a SSCHA calculation where the average displacements of the atoms from the equilibrium position is ruled by the Se mass but for each fixed position of the atoms the electronic structure is computed with the normal S atoms. The results are shown in Figure 4. Also in this case, when quantum anharmonic effects are included the system does not show any CDW instability. Thus, the different behavior of 2H-NbS_2 and 2H-$NbSe_2$ cannot be ascribed to a mass effect but has a more complex origin related to the different electron screening on the ions.

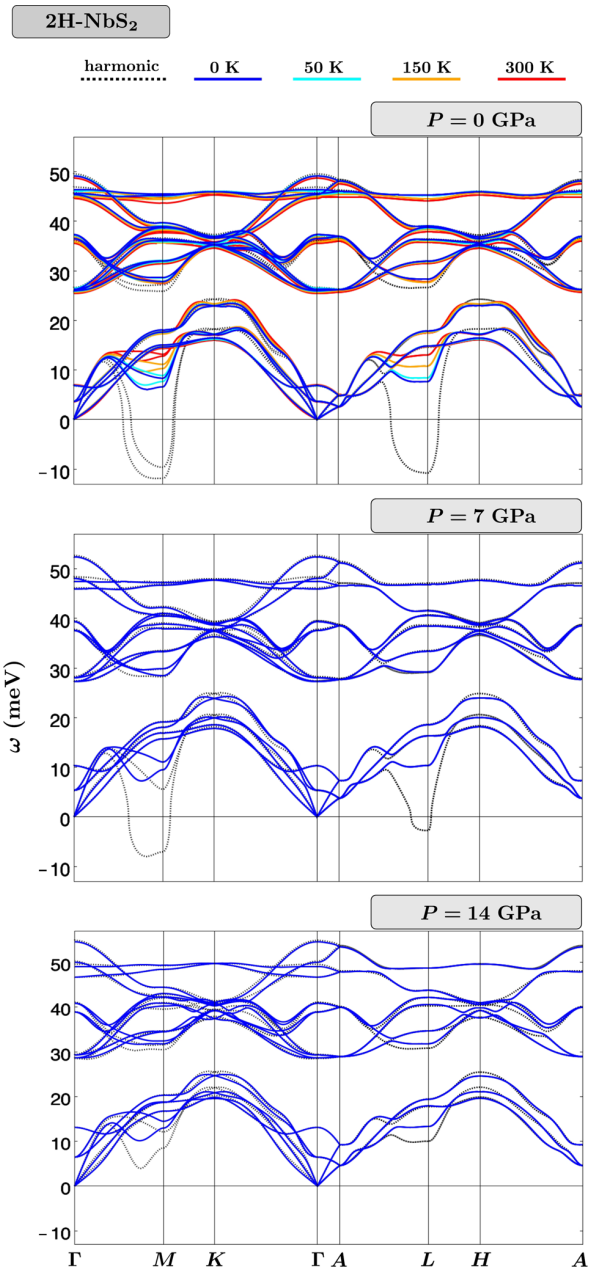

Figure 3. 2H-NbS_2 harmonic phonon dispersion (black dashed lines) and SSCHA anharmonic phonon dispersion at several temperatures (colored solid lines). Results for different pressures are shown. From the top to the bottom panel: 0, 7, and 14 GPa. The zero-pressure results are obtained using the experimental lattice parameters. The high-pressure results are obtained assuming that the ratio between experimental and DFT theoretical lattice parameters are independent of the applied pressure (more details in the main text). Anharmonicity removes the instability, obtained at harmonic level, of the longitudinal acoustic and optical modes near M and L at 0 and 7 GPa. Anharmonicity reduces as the pressure increases but it has a noticeable effect even at 14 GPa.

The validity of the results obtained with the SSCHA method on bulk 2H-NbS_2 gives us confidence that a similar calculation on the 1H-NbS_2 monolayer may shine light about the effects that dimensionality and environmental conditions (substrate, doping) can have on the CDW ordering in metallic TMDs.

DOI: 10.1021/acs.nanolett.9b00504
Nano Lett. 2019, 19, 3098−3103

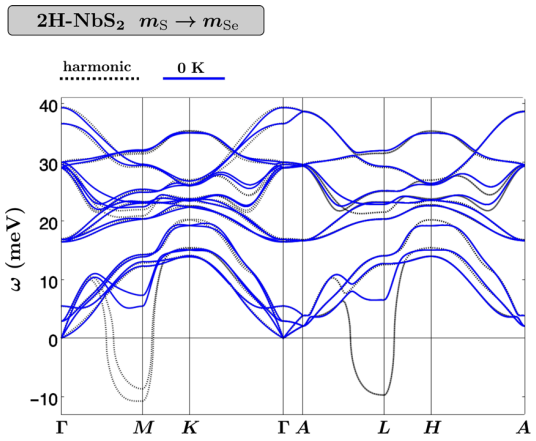

Figure 4. The 2H-NbS_2 harmonic phonon dispersion (black dashed lines) and SSCHA anharmonic phonon dispersion at 0 K (blue solid lines) at zero pressure computed replacing the mass of S with the mass of Se (more details in the main text). Anharmonicity removes the instability also in this case.

The suspended 1H-NbS_2 monolayer was simulated leaving 12.55 Å of vacuum space between a 1H layer and its periodic replica. At conventional static DFT level, we found that the theoretical zero pressure in-plane lattice parameter of the monolayer and the bulk are essentially the same, $a^{2H}_{Th-DFT} \simeq a^{1H}_{Th-DFT} \simeq 3.34$ Å. Therefore, for the suspended monolayer we use as in-plane lattice parameter the bulk experimental one, $a^{2H}_{Exp} = 3.33$ Å. This value is also compatible with the recent experimental measures 3.29 ± 0.03 and 3.34 Å reported for the lattice parameter of monolayer grown on substrate in ref 23 and ref 22, respectively.

In the upper panel of Figure 5, we show the harmonic and SSCHA anharmonic phonon dispersions of suspended 1H-NbS_2 at several temperatures, calculated with the lattice parameter a^{2H}_{Exp}. As in the bulk case, the system is unstable at harmonic level, but it is stabilized by quantum fluctuations strongly sensitive to the anharmonic potential down to 0 K. However, comparing Figures 2 and 5, we observe that even if the used in-plane lattice parameter is the same in both cases, at 0 K the softest theoretical phonon frequency is approximately 20% harder in the bulk than in the single layer case, demonstrating that there is a substantial enhancement of the tendency toward CDW in the 2D limit. In the monolayer, the theoretical phonon softening is localized in $\mathbf{q}_{CDW} = 0.72\ \overline{\Gamma M}$, which is quite close to the $\mathbf{q}_{CDW} \simeq 2/3\ \overline{\Gamma M}$ of the CDW instability experimentally found in 1H-NbS_2 on 6H-SiC(0001)[23] (and in 1H-$NbSe_2$[18,21]). Notice that, since the computed wave vector of the instability may be affected by the finite grids used in the calculations, we do not discard that it may be slightly shifted in the infinite grid limit.

Pressure tends normally to remove CDW ordering. Therefore, considering the proximity of the instability, it cannot be discarded that a tensile dilatation due to the substrate may induce the CDW transition observed for 1H-NbS_2 on graphitized 6H-SiC(0001). However, for the same reason we cannot exclude the more interesting prospect that the observed CDW be an intrinsic property of this system. Indeed, even small variations of the lattice parameter, compatible with the experimental uncertainly, could have a relevant impact on the results of the calculations, and a more accurate theoretical analysis of the monolayer structure is therefore necessary. As

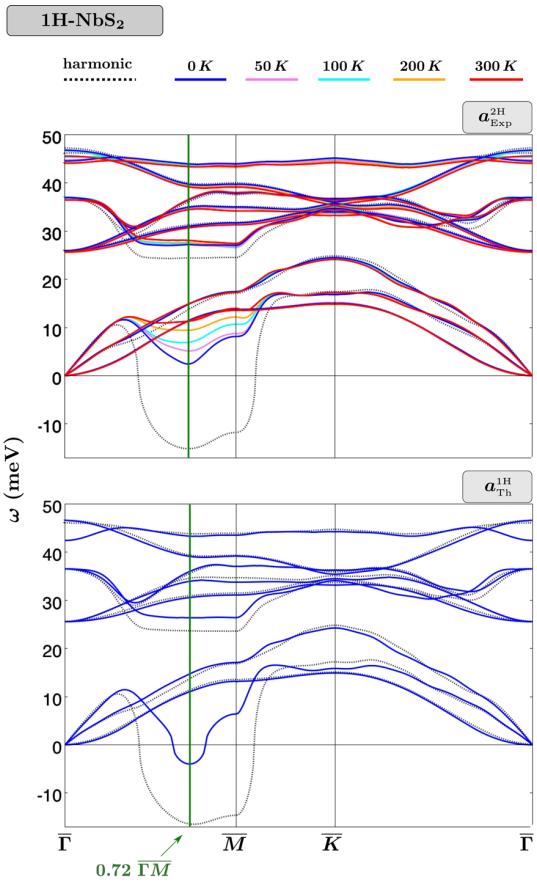

Figure 5. Suspended 1H-NbS_2 harmonic phonon dispersion (black dashed lines) and SSCHA anharmonic phonon dispersion at several temperatures (colored solid lines), at zero pressure. Top panel: results obtained with the experimental in-plane bulk lattice parameter a^{2H}_{Exp}. The softening of the acoustic mode, localized at $\mathbf{q}_{CDW} = 0.72\ \overline{\Gamma M}$, is more pronounced than in the 2H bulk case. However, the frequencies remain real even at 0 K. Bottom panel: results obtained with the theoretical lattice parameter a^{1H}_{Th}, obtained by fully relaxing the structure taking into account quantum anharmonic effects. At 0 K, the frequency at $\mathbf{q}_{CDW} = 0.72\ \overline{\Gamma M}$ becomes imaginary.

the energy of the soft-mode along $\overline{\Gamma M}$ is of the order of ≃58 K, for a proper analysis of the CDW in the monolayer it is important to fully take into account quantum effects. Including quantum anharmonic contributions to strain through the technique introduced in ref 26, we find that with the used lattice parameter a^{2H}_{Exp} the structure is sligthly compressed with an in-plane pressure $P = 0.66$ GPa. Upon relaxation, we obtain the theoretical lattice parameter $a^{1H}_{Th} = 3.35$ Å, approximatively 0.5% larger than a^{2H}_{Exp}.

The harmonic and quantum anharmonic phonons at 0 K calculated with the lattice parameter a^{1H}_{Th} are shown in the bottom panel of Figure 5. Although at harmonic level the phonon dispersion is not substantially different from the one computed with a^{2H}_{Exp}, when quantum anharmonic effects are included the phonon dispersion at 0 K now shows an instability at $\mathbf{q}_{CDW} = 0.72\ \overline{\Gamma M}$ thus in agreement with the CDW observed for 1H-NbS_2 on top of 6H-SiC(0001). The obtained instability is very weak (i.e., the obtained imaginary phonon frequency is very small). Therefore, this result is also compatible with the hypothesis that charge doping from the

DOI: 10.1021/acs.nanolett.9b00504
Nano Lett. 2019, 19, 3098−3103

substrate could be at the origin of the CDW suppression for 1H-NbS_2 on top of Au(111), similarly to what it was proposed for the case of 1H-TaS_2 on top of Au(111).[29] Our results show that if quantum anharmonic effects are included, then even a small compression/dilatation of approximately 0.5% removes/induces the charge density wave instability on 1H-NbS_2. The extreme sensitivity of the CDW on environmental conditions therefore suggests that deposition of 1H-NbS_2 on flexible substrates[30−32] or a small charge transfer via field effect could lead to devices with dynamical on/off switching of the 3 × 3 order.

In conclusion, we have shown that quantum anharmonicity is the key interaction for the stabilization of the crystal lattice in bulk 2H-NbS_2, as it removes the instability found at the harmonic level. The calculated temperature dependence of the phonon spectra are in excellent agreement with inelastic X-ray scattering data. Anharmonicity remains important even at large pressures. Given the good agreement between theory and experiment in bulk 2H-NbS_2, we have studied the behavior of the CDW in the 2D limit by considering single layer 1H-NbS_2. We found that suspended 1H-NbS_2 undergoes a quantum phase transition to a CDW state with approximately 3 × 3 charge ordering in the 2D limit, which is in agreement with experimental results on supported samples on 6H-SiC(0001). However, the CDW is extremely sensitive to environmental conditions, as it is very weak and compressive strains smaller than 0.5% are enough to suppress it. This explains the absence of CDW observed in 1H-NbS_2 on top of Au(111). This also suggest that devices with dynamical on/off switching of the 3 × 3 charge order can be obtained with deposition of 1H-NbS_2 on flexible substrates or through a small charge transfer via field effect.

AUTHOR INFORMATION

Corresponding Author

*E-mail: rbianco@caltech.edu.

ORCID

Raffaello Bianco: 0000-0002-3751-5484

Notes

The authors declare no competing financial interest.

ACKNOWLEDGMENTS

R.B. acknowledges the CINECA award under the ISCRA initiative (Grant HP10BLTB9A). Computational resources were provided by PRACE (Project No. 2017174186) and EDARI (Grant A0050901202). I.E. acknowledges financial support from the Spanish Ministry of Economy and Competitiveness (Grant FIS2016-76617-P). M.C. acknowledges support from Agence Nationale de la Recherche under the reference No. ANR-13-IS10-0003- 01. We acknowledge support from the Graphene Flagship (Grant Agreement 696656-GrapheneCore1 and 785219-GrapheneCore2).

REFERENCES

(1) Novoselov, K. S.; Jiang, D.; Schedin, F.; Booth, T. J.; Khotkevich, V. V.; Morozov, S. V.; Geim, A. K. Two-dimensional atomic crystals. *Proc. Natl. Acad. Sci. U. S. A.* **2005**, *102*, 10451−10453.

(2) Mak, K. F.; He, K.; Shan, J.; Heinz, T. F. Control of valley polarization in monolayer MoS2 by optical helicity. *Nat. Nanotechnol.* **2012**, *7*, 494.

(3) Radisavljevic, B.; Radenovic, A.; Brivio, J.; Giacometti, V.; Kis, A. Single-layer MoS2 transistors. *Nat. Nanotechnol.* **2011**, *6*, 147.

(4) Zeng, Z.; Yin, Z.; Huang, X.; Li, H.; He, Q.; Lu, G.; Boey, F.; Zhang, H. Single-Layer Semiconducting Nanosheets: High-Yield Preparation and Device Fabrication. *Angew. Chem., Int. Ed.* **2011**, *50*, 11093−11097.

(5) Wilson, J.; Salvo, F. D.; Mahajan, S. Charge-density waves and superlattices in the metallic layered transition metal dichalcogenides. *Adv. Phys.* **1975**, *24*, 117−201.

(6) Calandra, M. Phonon-Assisted Magnetic Mott-Insulating State in the Charge Density Wave Phase of Single-Layer 1*T* − $NbSe_2$. *Phys. Rev. Lett.* **2018**, *121*, 026401.

(7) Leroux, M.; Le Tacon, M.; Calandra, M.; Cario, L.; Méasson, M.-A.; Diener, P.; Borrissenko, E.; Bosak, A.; Rodière, P. Anharmonic suppression of charge density waves in 2*H*-NbS_2. *Phys. Rev. B: Condens. Matter Mater. Phys.* **2012**, *86*, 155125.

(8) Leroux, M.; Cario, L.; Bosak, A.; Rodière, P. Traces of charge density waves in NbS_2. *Phys. Rev. B: Condens. Matter Mater. Phys.* **2018**, *97*, 195140.

(9) Fisher, W. G.; Sienko, M. J. Stoichiometry, structure, and physical properties of niobium disulfide. *Inorg. Chem.* **1980**, *19*, 39−43.

(10) Recent diffuse X-ray scattering experiments report faint traces of CDW in the 2H polytype of NbS_2 commensurate with a $\sqrt{13} \times \sqrt{13}$ supercell, therefore identical to the supercell modulation associated with the CDW of 1T-$TaSe_2$ and 1T-TaS_2.[8] However, this is attributed to the presence of isolated rare and dilute octhaedral 1T layers, caused either by diluite amount of Nb in the van der Waals interlayer space of 3R-like stacking faults or rotational disorder in the stacking of 1H layers.

(11) Navarro-Moratalla, E.; Island, J. O.; Mañas-Valero, S.; Pinilla-Cienfuegos, E.; Castellanos-Gomez, A.; Quereda, J.; Rubio-Bollinger, G.; Chirolli, L.; Silva-Guillén, J. A.; Agraït, N.; Steele, G. A.; Guinea, F.; van der Zant, H. S. J.; Coronado, E. Enhanced superconductivity in atomically thin TaS2. *Nat. Commun.* **2016**, *7*, 11043.

(12) Wagner, K. E.; Morosan, E.; Hor, Y. S.; Tao, J.; Zhu, Y.; Sanders, T.; McQueen, T. M.; Zandbergen, H. W.; Williams, A. J.; West, D. V.; Cava, R. J. Tuning the charge density wave and superconductivity in Cu_xTaS_2. *Phys. Rev. B: Condens. Matter Mater. Phys.* **2008**, *78*, 104520.

(13) Harper, J. M. E.; Geballe, T. H.; DiSalvo, F. J. Thermal properties of layered transition-metal dichalcogenides at charge-density-wave transitions. *Phys. Rev. B* **1977**, *15*, 2943−2951.

(14) Heil, C.; Poncé, S.; Lambert, H.; Schlipf, M.; Margine, E. R.; Giustino, F. Origin of Superconductivity and Latent Charge Density Wave in NbS_2. *Phys. Rev. Lett.* **2017**, *119*, 087003.

(15) Naito, M.; Tanaka, S. Electrical Transport Properties in 2H-NbS2, -NbSe2, -TaS2 and -TaSe2. *J. Phys. Soc. Jpn.* **1982**, *51*, 219−227.

(16) Castro Neto, A. H. Charge Density Wave, Superconductivity, and Anomalous Metallic Behavior in 2D Transition Metal Dichalcogenides. *Phys. Rev. Lett.* **2001**, *86*, 4382−4385.

(17) Moncton, D. E.; Axe, J. D.; DiSalvo, F. J. Neutron scattering study of the charge-density wave transitions in 2*H* − $TaSe_2$ and 2*H* − $NbSe_2$. *Phys. Rev. B* **1977**, *16*, 801−819.

(18) Xi, X.; Zhao, L.; Wang, Z.; Berger, H.; Forró, L.; Shan, J.; Mak, K. F. Strongly enhanced charge-density-wave order in monolayer NbSe2. *Nat. Nanotechnol.* **2015**, *10*, 765.

(19) Yang, Y.; Fang, S.; Fatemi, V.; Ruhman, J.; Navarro-Moratalla, E.; Watanabe, K.; Taniguchi, T.; Kaxiras, E.; Jarillo-Herrero, P. Enhanced superconductivity upon weakening of charge density wave transport in 2*H* − TaS_2 in the two-dimensional limit. *Phys. Rev. B: Condens. Matter Mater. Phys.* **2018**, *98*, 035203.

(20) Ryu, H.; Chen, Y.; Kim, H.; Tsai, H.-Z.; Tang, S.; Jiang, J.; Liou, F.; Kahn, S.; Jia, C.; Omrani, A. A.; Shim, J. H.; Hussain, Z.; Shen, Z.-X.; Kim, K.; Min, B. I.; Hwang, C.; Crommie, M. F.; Mo, S.-K. Persistent Charge-Density-Wave Order in Single-Layer TaSe2. *Nano Lett.* **2018**, *18*, 689−694.

(21) Ugeda, M. M.; Bradley, A. J.; Zhang, Y.; Onishi, S.; Chen, Y.; Ruan, W.; Ojeda-Aristizabal, C.; Ryu, H.; Edmonds, M. T.; Tsai, H.-Z.; Riss, A.; Mo, S.-K.; Lee, D.; Zettl, A.; Hussain, Z.; Shen, Z.-X.;

DOI: 10.1021/acs.nanolett.9b00504
Nano Lett. 2019, 19, 3098−3103

Crommie, M. F. Characterization of collective ground states in single-layer NbSe2. *Nat. Phys.* **2016**, *12*, 92.
(22) Stan, R.-M.; Mahatha, S. K.; Bianchi, M.; Sanders, C. E.; Curcio, D.; Hofmann, P.; Miwa, J. A. Epitaxial single layer NbS $_{2}$ on Au(111): synthesis, structure, and electronic properties. 2019, arXiv:1901.03552
(23) Lin, H.; Huang, W.; Zhao, K.; Lian, C.; Duan, W.; Chen, X.; Ji, S.-H. Growth of atomically thick transition metal sulfide filmson graphene/6H-SiC(0001) by molecular beam epitaxy. *Nano Res.* **2018**, *11*, 4722.
(24) Errea, I.; Calandra, M.; Mauri, F. Anharmonic free energies and phonon dispersions from the stochastic self-consistent harmonic approximation: Application to platinum and palladium hydrides. *Phys. Rev. B: Condens. Matter Mater. Phys.* **2014**, *89*, 064302.
(25) Bianco, R.; Errea, I.; Paulatto, L.; Calandra, M.; Mauri, F. Second-order structural phase transitions, free energy curvature, and temperature-dependent anharmonic phonons in the self-consistent harmonic approximation: Theory and stochastic implementation. *Phys. Rev. B: Condens. Matter Mater. Phys.* **2017**, *96*, 014111.
(26) Monacelli, L.; Errea, I.; Calandra, M.; Mauri, F. Pressure and stress tensor of complex anharmonic crystals within the stochastic self-consistent harmonic approximation. *Phys. Rev. B: Condens. Matter Mater. Phys.* **2018**, *98*, 024106.
(27) All the calculations were performed from first-principles with the QUANTUM ESPRESSO package[33] by computing the energy/forces of the configurations used by the SSCHA within density-functional theory and the harmonic dynamical matrices within density-functional perturbation theory. We used the generalized gradient approximation for the exchange-correlation functional, under the Perdew−Burke−Ernzherhof parametrization.[34] For the unit-cell calculation in the bulk and in the monolayer, the integration in reciprocal space was performed on a 24 × 24 × 8 and a 40 × 40 × 1 Monkhorst−Pack grid[35] of the Brillouin zone, respectively. These meshes were adjusted accordingly in the supercell calculations. We used ultrasoft pseudopotentials,[36] a plane-wave cutoff energy of 35 Ry for the kinetic energy and 400 Ry for the charge density, and a Methfessel−Paxton smearing of 0.005 Ry.[37] The SSCHA calculations were performed on a 4 × 4 × 1 supercell for the bulk and on a 6 × 6 × 1 supercell for the monolayer. The short-range part of the anharmonic dynamical matrices were computed with SSCHA in the static approximation for the phonon self-energy, retaining only the so-called "bubble term".[25,38] The long-range part of the anharmonic dynamical matrices were obtained first by Fourier interpolating the difference between the SSCHA and the harmonic dynamical matrices to finer grid and then adding the harmonic contribution calculated on this grid (for 6 × 6 × 4 the bulk and for 16 × 16 × 1 the monolayer). The phonon dispersion along high-symmetry paths were subsequently obtained by Fourier interpolation.
(28) Leroux, M.; Errea, I.; Le Tacon, M.; Souliou, S.-M.; Garbarino, G.; Cario, L.; Bosak, A.; Mauri, F.; Calandra, M.; Rodière, P. Strong anharmonicity induces quantum melting of charge density wave in 2*H* − $NbSe_2$ under pressure. *Phys. Rev. B: Condens. Matter Mater. Phys.* **2015**, *92*, 140303.
(29) Albertini, O. R.; Liu, A. Y.; Calandra, M. Effect of electron doping on lattice instabilities in single-layer 1*H* − TaS_2. *Phys. Rev. B: Condens. Matter Mater. Phys.* **2017**, *95*, 235121.
(30) Wu, W.; Wang, L.; Li, Y.; Zhang, F.; Lin, L.; Niu, S.; Chenet, D.; Zhang, X.; Hao, Y.; Heinz, T. F.; Hone, J.; Wang, Z. L. Piezoelectricity of single-atomic-layer MoS2 for energy conversion and piezotronics. *Nature* **2014**, *514*, 470.
(31) He, K.; Poole, C.; Mak, K. F.; Shan, J. Experimental Demonstration of Continuous Electronic Structure Tuning via Strain in Atomically Thin MoS2. *Nano Lett.* **2013**, *13*, 2931−2936.
(32) Conley, H. J.; Wang, B.; Ziegler, J. I.; Haglund, R. F.; Pantelides, S. T.; Bolotin, K. I. Bandgap Engineering of Strained Monolayer and Bilayer MoS2. *Nano Lett.* **2013**, *13*, 3626−3630.
(33) Giannozzi, P.; Baroni, S.; Bonini, N.; Calandra, M.; Car, R.; Cavazzoni, C.; Ceresoli, D.; Chiarotti, G. L.; Cococcioni, M.; Dabo, I.; Corso, A. D.; de Gironcoli, S.; Fabris, S.; Fratesi, G.; Gebauer, R.; Gerstmann, U.; Gougoussis, C.; Kokalj, A.; Lazzeri, M.; Martin-Samos, L.; Marzari, N.; Mauri, F.; Mazzarello, R.; Paolini, S.; Pasquarello, A.; Paulatto, L.; Sbraccia, C.; Scandolo, S.; Sclauzero, G.; Seitsonen, A. P.; Smogunov, A.; Umari, P.; Wentzcovitch, R. M. QUANTUM ESPRESSO: a modular and open-source software project for quantum simulations of materials. *J. Phys.: Condens. Matter* **2009**, *21*, 395502.
(34) Perdew, J. P.; Burke, K.; Ernzerhof, M. Generalized Gradient Approximation Made Simple. *Phys. Rev. Lett.* **1996**, *77*, 3865−3868.
(35) Monkhorst, H. J.; Pack, J. D. Special points for Brillouin-zone integrations. *Phys. Rev. B* **1976**, *13*, 5188−5192.
(36) Vanderbilt, D. Soft self-consistent pseudopotentials in a generalized eigenvalue formalism. *Phys. Rev. B: Condens. Matter Mater. Phys.* **1990**, *41*, 7892−7895.
(37) Methfessel, M.; Paxton, A. T. High-precision sampling for Brillouin-zone integration in metals. *Phys. Rev. B: Condens. Matter Mater. Phys.* **1989**, *40*, 3616−3621.
(38) Bianco, R.; Errea, I.; Calandra, M.; Mauri, F. High-pressure phase diagram of hydrogen and deuterium sulfides from first principles: Structural and vibrational properties including quantum and anharmonic effects. *Phys. Rev. B: Condens. Matter Mater. Phys.* **2018**, *97*, 214101.

DOI: 10.1021/acs.nanolett.9b00504
Nano Lett. 2019, 19, 3098−3103

Editors' Suggestion

Quantum effects in muon spin spectroscopy within the stochastic self-consistent harmonic approximation

Ifeanyi John Onuorah,[1,*] Pietro Bonfà,[1,2] Roberto De Renzi,[1,†] Lorenzo Monacelli,[3] Francesco Mauri,[3] Matteo Calandra,[4] and Ion Errea[5,6,7]

[1]*Department of Mathematical, Physical and Computer Sciences, University of Parma, Italy*
[2]*Centro S3, CNR-Istituto Nanoscienze, 41125 Modena, Italy*
[3]*Dipartimento di Fisica, Università di Roma Sapienza, Italy*
[4]*Sorbonne Universitè, CNRS, Institut des Nanosciences de Paris, UMR7588, F-75252 Paris, France*
[5]*Fisika Aplikatua 1 Saila, Gipuazkoako Ingeniaritza Eskola, University of the Basque Country (UPV/EHU), Donostia-San Sebastian, Basque Country, Spain*
[6]*Centro de Física de Materiales (CSIC-UPV/EHU), Donostia-San Sebastian, Basque Country, Spain*
[7]*Donostia International Physics Center (DIPC), Donostia-San Sebastian, Basque Country, Spain*

(Received 29 April 2019; revised manuscript received 18 June 2019; published 19 July 2019)

Muon spin rotation experiments involve muons that experience zero-point vibration at their implantation sites. Quantum-mechanical calculations of the host material usually treat the muon as a point impurity, ignoring its zero-point vibrational energy that, however, plays a role in determining the stability of calculated implantation sites and estimating physical observables. As a first-order correction, the muon zero-point motion is usually described within the harmonic approximation, despite the anharmonicity of the crystal potential. Here we apply the stochastic self-consistent harmonic approximation, a quantum variational method devised to include anharmonic effects in total energy and vibrational frequency calculations, in order to overcome these limitations and provide an accurate *ab initio* description of the quantum nature of the muon. We applied this full quantum treatment to the calculation of the muon contact hyperfine field in textbook-case metallic systems, such as Fe, Ni, Co including MnSi and MnGe, improving agreement with experiments. Our results show that there are anharmonic contributions to the muon vibrational frequencies with the muon zero-point energies above 0.5 eV. Finally, in contrast to the harmonic approximation, we show that including quantum anharmonic fluctuations, the muon stabilizes at the octahedral site in bcc Fe.

DOI: 10.1103/PhysRevMaterials.3.073804

I. INTRODUCTION

In muon spin rotation (μSR) experiments, spin-polarized positive (anti)muons are used to probe the microscopic field distribution at the interstitial site(s) where the μ^+ stop inside the sample under investigation. The extreme sensitivity of the muon to small magnetic fields as well as the absence of quadrupolar coupling makes this technique very effective in probing magnetic orders, offering a valuable alternative to neutron scattering. This approach, which shares many similarities with nuclear magnetic resonance, has the advantage of being applicable to virtually any material, but it has the drawback that the interstitial sites where the muon stops and the nature of muon interaction with the host are generally unknown. Here we discuss an improved method to tackle this problem based on computational chemistry methods.

An accurate, *ab initio*, description of the electron-muon interaction in periodic solids has been out of reach until a few years ago. The dramatic increase of both the computational power and the accuracy of first-principles calculations make this goal possible. Self-consistent electronic structure calculations, in particular those based on density functional theory (DFT), are already employed to study the muon implantation site, muon interaction parameters, and for understanding the muon-induced distortion in the lattice [1–7]. This turns out to be a very valuable tool for analyzing experimental data and interpreting the results [8]. The knowledge of the muon implantation site(s) and of the hyperfine field allows very important quantitative information, including the magnetic structure and the moment size, to be obtained from μSR experiments. Moreover, a reliable quantum calculation of the muon embedded in the system under investigation provides an estimate for its induced perturbation; the probe is an impurity and it may in principle alter the local electronic properties. Fortunately this is a very rare case, and yet assessing these rare cases [9,10] is very important.

However, self-consistent DFT calculations often treat the muon as just another atom in the lattice, within the Born-Oppenheimer (BO) approximation [11], without taking into consideration the quantum effect of the muon zero-point vibrations, which is sizable relative to those of heavier nuclei. The embedded muon, by virtue of its very light mass ($\sim$1/9th the proton mass), is characterized by zero-point vibration with amplitude typically of the order of 1 Bohr radius [1]. The neglect of this effect may have two major consequences: inaccurate estimation of the contact hyperfine

*ifeanyijohn.onuorah@unipr.it
†roberto.derenzi@unipr.it

field, and/or incorrect identification of muon implantation sites. The former is due to neglect of the space extent of the muon wave function, whereas the latter happens when the quantum zero-point vibration energy is comparable with the energy difference between the various implantation sites [2,3,5,12].

Earlier approaches toward a quantum-mechanical description of the muon zero-point vibration include calculations within the harmonic approximation [3,13]. However, the muon potential has been discussed and shown to be anharmonic, for instance by total energy calculations with site exploration algorithms [1,12,14,15]. Furthermore, a breakdown of the harmonic approximation takes place when within the range of the muon vibrations the potential is not dominated by the second-order term in its Taylor expansion.

Alternative methods do take into account the anharmonic nature of the crystalline potential. One of them consists in the potential exploration approach [12]. The non-BO methods represent another computationally demanding alternative, employing a linear combination of Gaussian basis functions to realize both the nuclear and the electronic degrees of freedom [16–19], and optimized local potentials to represent the nuclear-electron correlation [20]. One of the most advanced approaches relies on *ab initio* path integral molecular dynamics, which allows for contextual quantization of both the muon and the electrons in the calculation of the electronic structure and of the interatomic forces [15,21,22]. However, computational resources required by this method grow exceedingly with the size of the cell.

In this paper, we describe a stochastic self-consistent harmonic approximation (SSCHA) that allows us to include the effects of anharmonicity in the muon vibrations [23–26]. The SSCHA is a quantum variational method that efficiently calculates anharmonic free energies and phonon frequencies in a nonperturbative way. This approach has been very successful for calculating phonon frequencies and superconducting properties in hydrogen-rich materials, as well as in systems undergoing charge density wave (CDW) transitions, ferroelectrics, and thermoelectrics [23,27–32]. For the muon, the SSCHA is variational in the muon (free) energy, with this energy evaluated stochastically from forces and energies calculated at a sufficient number of random muon configurations. The muon energy is minimized using trial harmonic wave functions that are Gaussian, while the minimization parameter is the width of the Gaussian. From the output of the minimization, muon frequencies including anharmonic contributions and the muon ground-state energy can be extracted.

With this approach, we demonstrate that there are anharmonic contributions to the harmonic muon vibrational modes, as expected for the muon due to its light mass. We further use the SSCHA muon wave function to refine the contact hyperfine field in a series of metals: Fe, Ni, Co, MnSi and MnGe, where the SSCHA improves the agreement of the calculated value with the experimental results with respect to recent point impurity calculations [6]. Finally, the SSCHA together with energy curvature considerations [25] allows the stable occupation of the muon at the octahedral site in bcc Fe, which is unstable within the harmonic regime.

The paper has the following structure: Sec. II discusses the double Born-Oppenheimer approximation, which allows us to separate the muon degrees of freedom from those of the host nuclei and electrons. In Sec. III, we describe the working principles of the SSCHA, including the stochastic implementation. In Sec. IV, we discuss the muon zero-point energy calculation results using the SSCHA together with the stability of the muon at octahedral and tetrahedral sites in Fe(bcc). Finally, in Sec. VI we present the results of the quantum corrections in the calculation of the contact hyperfine field, and then conclusions are given in Sec. VII.

II. DOUBLE BORN-OPPENHEIMER APPROXIMATION

The BO approximation considers the nuclei frozen on the time scale of electron dynamics in view of their sufficiently large mass ratio [11]. Hydrogen is already sufficiently lighter than most other atoms to allow a further separation of time scales, and this holds *a fortiori* true for a positive muon. This allows for the quantum treatment of a single muon *impurity* in the crystal by employing the so-called double Born-Oppenheimer approximation (DBO) [12,14,33]. The muon dynamics ($m_\mu \sim 200 m_e$) is much slower than that of electrons, thus justifying an electron structure obtained by DFT with frozen muon and nuclei. The same muon dynamics is still much faster than that of other nuclei, since transition metals are typically 400 times heavier than a muon (care must be taken when considering, e.g., hydrogen, which is only nine times heavier than a muon). Therefore, it is justified to use total DFT energy versus the muon configuration coordinates as a frozen potential energy landscape in which the muon dynamics takes place on its characteristic time scale. This allows us to consider the zero-point vibration of only the muon within the potential energy surface, *drastically reducing the computational load requirements for the calculations*.

The total Hamiltonian H_{tot} describing the many-body interaction including explicitly the muon coordinates is written as

$$H_{\text{tot}} = T_e + T_\mu + T_N + V(\mathbf{r}_e, \mathbf{r}_\mu, \mathbf{R}_N), \tag{1}$$

with subscript μ describing the muon-related quantities while e and N describe those of the electrons and host nuclei, respectively. T and V are the kinetic and potential energy, respectively. The Schrödinger equation is then written as

$$H_{\text{tot}}|\Psi_{\text{tot}}\rangle = E_{\text{tot}}|\Psi_{\text{tot}}\rangle. \tag{2}$$

This further allows us to write the DBO wave function as a product wave function of the electrons, the muon, and the nuclei in the form

$$|\Psi_{\text{tot}}\rangle = |\psi_e\rangle|\phi_\mu\rangle|\Phi_N\rangle. \tag{3}$$

The Hamiltonian for the electronic problem can be rewritten to specifically point out the presence of the muon position operator as

$$H_e = T_e + V(\mathbf{r}_e; \mathbf{r}_\mu, \mathbf{R}_N). \tag{4}$$

Similar to the BO approximation, only the position operators of the muon and the nuclei enter in the eigenvalue problem of the electrons. The solution of the electronic problem gives the BO potential energy surface, $V(\mathbf{r}_\mu, \mathbf{R}_N)$, dependent on the muon and the nuclei position operators.

Hence, the ground-state Hamiltonian H_μ for the muon can be written as

$$H_\mu = T_\mu + V(\mathbf{r}_\mu; \mathbf{R}_N), \tag{5}$$

where the muon kinetic energy T_μ is defined as

$$T_\mu = \sum_{\lambda=1}^{3} \frac{p_\lambda^2}{2m_\mu},$$

with p the momentum operator along the Cartesian component indexes λ while m_μ is the muon mass.

The acquisition of the DBO potential energy surface $V(\mathbf{r}_\mu; \mathbf{R}_N)$ for the solution of the Schrödinger equation (5) is still a long and difficult task. However, the DBO approximation is advantageous since it allows us to consider separately only the degrees of freedom of the muon. For this reason, in the next section we revisit the SSCHA theory originally presented in Refs. [23,24], specializing its application to muon dynamics.

III. STOCHASTIC SELF-CONSISTENT HARMONIC APPROXIMATION FOR MUONS

To begin with the formal description of the stochastic self-consistent harmonic approximation (SSCHA) restricted only to the muon modes, let us write the muon Hamiltonian H_μ, the muon wave function ϕ_μ, and the DBO potential energy surface $V(\mathbf{r}_\mu; \mathbf{R}_N)$, appearing in the previous section, simply as H, ϕ, and $V(\mathbf{r}_\mu)$, respectively.

The muon zero-point energy from the Hamiltonian H is given as

$$E = \langle\phi|H|\phi\rangle, \tag{6}$$

where $|\phi\rangle$ is the muon ground-state wave function. Calculating E is far from trivial since the form of the muon potential [Eq. (5)] is not known. However, it is possible to establish a quantum variational principle for the muon ground-state energy E by replacing the exact muon wave function $|\phi\rangle$ with the wave function $|\widetilde{\phi}\rangle$ of a trial muon Hamiltonian $\widetilde{H} = T_\mu + \widetilde{V}(\mathbf{r}_\mu)$ with energy

$$\widetilde{E} = \langle\widetilde{\phi}|\widetilde{H}|\widetilde{\phi}\rangle. \tag{7}$$

This is such that one can define an energy functional of the trial Hamiltonian as

$$\widetilde{E}_H[\widetilde{H}] = \langle\widetilde{\phi}|H|\widetilde{\phi}\rangle. \tag{8}$$

The variational form of the muon ground-state energy can be written as

$$E \leqslant \widetilde{E}_H[\widetilde{H}] \tag{9}$$

such that the equality holds when the true and trial potentials are the same.

By adding and subtracting Eq. (7) to and from Eq. (8), $\widetilde{E}_H[\widetilde{H}]$ is written in the form

$$\widetilde{E}_H[\widetilde{H}] = \widetilde{E} + \langle\widetilde{\phi}|(V - \widetilde{V})|\widetilde{\phi}\rangle. \tag{10}$$

The above definitions allow us to formulate a variational principle following the Gibbs-Bogoliubov inequality theorem [34] at zero temperature, similar to the Rayleigh-Ritz inequality [35].

According to the trial wave function, the probability of finding the muon in the position $\mathbf{r}_\mu$ is

$$\widetilde{\rho}(\mathbf{r}_\mu) = \langle\mathbf{r}_\mu|\widetilde{\phi}\rangle\langle\widetilde{\phi}|\mathbf{r}_\mu\rangle = |\widetilde{\phi}(\mathbf{r}_\mu)|^2. \tag{11}$$

Thus, an observable A dependent only on $\mathbf{r}_\mu$ can be averaged statistically within the form of the corresponding Hamiltonian $\widetilde{H}$ as

$$\langle A\rangle_{\widetilde{H}} = \int d\mathbf{r}_\mu A(\mathbf{r}_\mu)\widetilde{\rho}(\mathbf{r}_\mu), \tag{12}$$

and the muon energy in Eq. (10) can be evaluated as

$$\widetilde{E}_H[\widetilde{H}] = \widetilde{E} + \int d\mathbf{r}_\mu \widetilde{\rho}(\mathbf{r}_\mu)[V(\mathbf{r}_\mu) - \widetilde{V}(\mathbf{r}_\mu)]. \tag{13}$$

With the above form of $\widetilde{E}_H[\widetilde{H}]$, the muon energy can be evaluated at each step during the variational minimization. One can directly see that the equality in the form of the variation in Eq. (9) holds if $V = \widetilde{V}$. Hence, with the variational principle, the ground state of the muon is determined if the potential $\widetilde{V}(\mathbf{r}_\mu)$ that minimizes $\widetilde{E}_H[\widetilde{H}]$ is found.

To proceed with the minimization of $\widetilde{E}_H$, in the SSCHA implementation we restrict the muon wave functions only to the Gaussian form. The term *harmonic* in the technique refers to the fact that each Gaussian is the ground state of a trial *harmonic* Hamiltonian, with known analytic solutions (see Appendix A) where the trial potential is expressed in terms of a force-constant matrix. Moreover, using Gaussian functions has the advantage of allowing us to sample the wave function by extracting randomly distributed configurations without any METROPOLIS algorithm that requires long equilibration time and also provides an analytic expression for the kinetic energy.

Finally, the actual minimization is obtained using the conjugate gradient (CG) algorithm [36], which requires an evaluation of the energy gradient, whose analytic form is given in Ref. [24] and in Appendix B for the muon case, and depends on the forces acting on the muon when displaced from the equilibrium position.

The evaluation of the quantities of interest at each minimization step, namely $\widetilde{E}_H$ and its gradient, is performed stochastically. One of the advantages of the stochastic sampling resides in the gradual optimization of the potential felt by the muon during the iterative process. This ensures that the entire BO landscape, beyond the harmonic component around the minimum, is sampled, hence capturing the anharmonic effects.

The stochastic sampling of the BO energy and of the forces acting on the muon and entering the energy gradient (see Appendix B) can be calculated with any *ab initio* method including DFT [37] and Hartree-Fock [38–40] based approaches.

The evaluation of the forces and energies for the random muon configurations in the stochastic sampling represents the most computationally demanding task in the SSCHA minimization cycle. This effort can be partially alleviated with a reweighting procedure based on importance sampling. The reader is referred to Ref. [24] for a detailed description of this additional detail.

When the energy gradient vanishes numerically, the $\widetilde{E}$ that minimizes $\widetilde{E}_H[\widetilde{H}]$ is the zero-point energy of the muon, and the anharmonic vibrational frequencies $\widetilde{\omega}_i$ of the auxiliary

TABLE I. Harmonic muon frequencies ω_i^h along the mode i and harmonic zero-point energy $E^h = \sum_{i=1}^{3} \hbar\omega_i^h/2$, together with the SSCHA muon frequencies $\widetilde{\omega}_i$ and energy $\widetilde{E}$ at the minimum that includes the anharmonic contribution.

Host	ω_x^h (cm^{-1})	ω_y^h (cm^{-1})	ω_z^h (cm^{-1})	E^h (eV)	$\widetilde{\omega}_x$ (cm^{-1})	$\widetilde{\omega}_y$ (cm^{-1})	$\widetilde{\omega}_z$ (cm^{-1})	$\widetilde{E}$ (eV)
Fe-bcc[a]	4364.01	2913.01	4364.62	0.72	4769.08	2572.58	5088.37	0.74
Fe-bcc[b]	1965.08i	1958.72i	6828.00	[c]	2005.24	2005.24	6364.81	0.53
Co-hcp	2930.41	2929.85	2752.25	0.53	3741.10	3741.10	3476.24	0.61
Co-fcc	2607.29	2607.02	2606.66	0.49	3424.16	3424.16	3424.16	0.56
Ni-fcc	2377.62	2377.60	2377.61	0.44	3317.78	3317.78	3317.78	0.53
MnGe	3123.70	3123.67	3123.66	0.58	3470.29	3470.29	3470.29	0.64
MnSi	3296.27	3296.32	3296.11	0.61	3685.25	3685.25	3685.25	0.67

[a]Muon at the tetrahedral site.
[b]Muon at the octahedral site.
[c]The muon is not stable at the octahedral site (imaginary frequencies) within the harmonic regime.

Hamiltonian whose SSCHA wave function is the ground state are obtained, so that

$$\sum_{i=1}^{3} \frac{1}{2}\hbar\widetilde{\omega}_i = \widetilde{E}. \tag{14}$$

A formal description of the trial Hamiltonian and the trial wave function is given in Appendix A.

IV. MUON ZERO-POINT ENERGY

Let us first describe the zero-point energy of the muon obtained in the harmonic approximation, which is later used in comparisons with the anharmonic one.

The harmonic muon frequencies ω_i^h and the corresponding energies $E^h = \sum_{i=1}^{3} \hbar\omega_i^h/2$ were calculated by the finite-difference method [41,42], which allows only the muon frequencies to be singled out, for all the materials under investigation, namely Fe, Co, Ni, MnSi, and MnGe. These were also used to generate the starting wave functions for the SSCHA minimization except for the stability discussion in Sec. V with the muon at the octahedral and tetrahedral site in bcc Fe. Here, the density functional perturbation theory (DFPT) within the QUANTUM ESPRESSO suite of code [43,44] was used to calculate the frequencies of the whole system, including those of the host Fe nuclei. The resulting harmonic muon frequencies from both methods in the two Fe systems are in good agreement.

For the SSCHA minimization and stochastic averaging [see Eq. (17)], hundreds (100–400) of random configurations were generated for the muon while keeping the host atoms fixed to ensure that the muon energy gradient vanishes. Their energies and Hellmann-Feynman forces [45] were calculated by DFT as implemented in the QUANTUM ESPRESSO suite of code [44]. The details of the muon site in these systems and DFT input parameters are contained in Ref. [6]. For all the systems, a $2 \times 2 \times 2$ supercell constructed starting from the conventional unit cell was used for the harmonic frequency calculations, the SSCHA frequency minimization, and the force calculation within DFT. Other DFT computational details are identical to those reported in Ref. [6]. To accommodate the muon impurity in the supercell, the forces introduced by the muon in the system were relaxed by DFT and the relaxed structures were used for the SSCHA calculations. Relaxations were converged with force and energy thresholds of 10^{-3} a.u. and 10^{-4} Ry, respectively.

Figure 1 shows the evolution of the SSCHA muon frequencies and energy during the minimization procedure. Significant anharmonic contributions to the resulting SSCHA frequencies can be deduced from the difference between the initial values, i.e., the starting harmonic guess, and the final converged results (the comparison with the anharmonic correction obtained for host atoms is presented in Appendix C). The anharmonic correction to the harmonic frequencies is found to be in the range of 330–820 cm^{-1} except for the muon at the octahedral site in Fe.

The stochastic implementation ensures that the effect of the muon vibrations, the effect of the chemical environment around the muon, and anharmonic contributions to the forces acting on the muon are all incorporated in the muon ground-state minimum.

Table I contains the harmonic frequencies ω_i^h and energies E^h, obtained with the finite-difference method and used as the starting point of the SSCHA iterative process, and the SSCHA frequencies $\widetilde{\omega}_i$ and energies $\widetilde{E}$ at the end of the minimization. The error estimates of the reported muon energies are within the range of 0.1 meV. The results show the anharmonic effects in the muon vibrational frequencies. Notice that the muon at octahedral implantation site in Fe is unstable in the harmonic regime. For all other cases with positive harmonic frequencies for which E^h can be defined, the difference between the SSCHA muon vibrational energies and the harmonic ones is in the range of 0.02–0.09 eV.

V. TETRAHEDRAL AND OCTAHEDRAL MUON SITE IN Fe

Conflicting experimental and theoretical studies report the muon site in Fe to be either at the tetrahedral (T) or the octahedral (O) interstitial sites [46–51]. From the point of view of the DFT total energy, the T site is 0.184 eV lower that the O site. This would indicate that the T site is the stable one. However, since the calculated muon zero-point energies (above 0.5 eV) are large relative to the DFT energy difference, the possible population of both sites cannot be excluded.

DFPT calculations of the muon frequencies provide further insight into the stability of the two candidate sites. Unphysical *negative* frequencies, generally a signal of instability, are obtained for the muon at the O site, as opposed to those of the

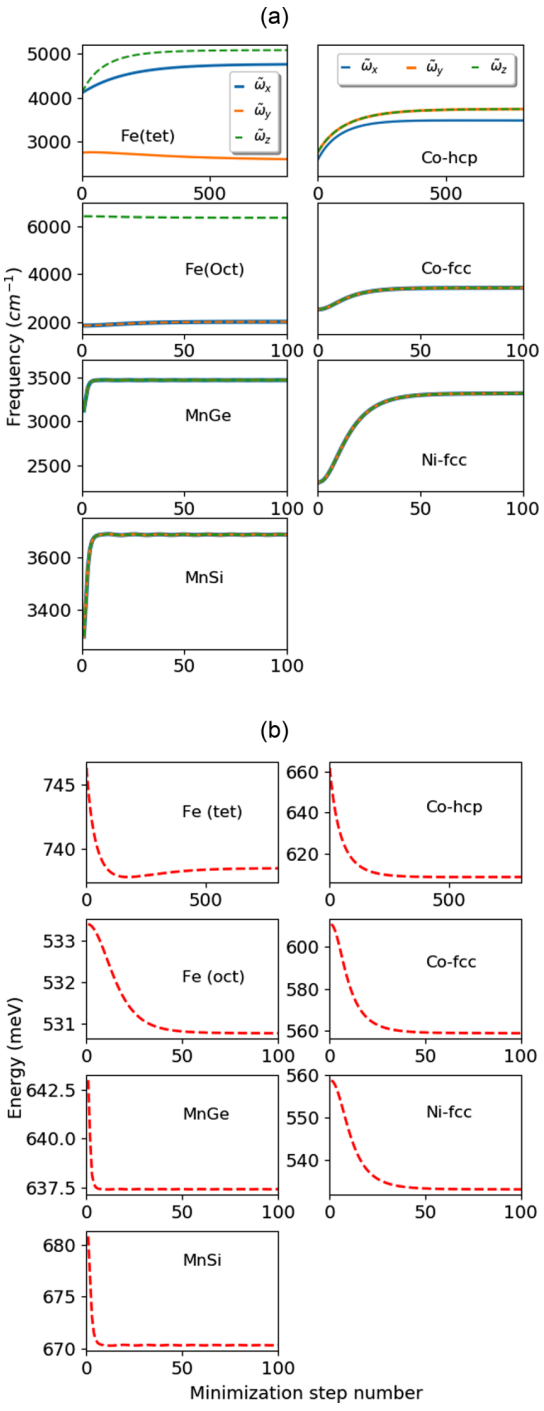

FIG. 1. (a) Evolution of the SSCHA muon frequency during the minimization steps. (b) Evolution of SSCHA muon energy as in Eq. (13) during the minimization steps. In both figures, the starting point for the minimization step number = 0 is that of the harmonic Hamiltonian except for the muon in octahedral site of Fe [Fe (oct)] when the starting potential is arbitrary.

T site, which are always positive. The harmonic approximation then appears to indicate an instability of the muon at the O site.

However, the anharmonic effects, fully captured by the SSCHA, yield positive frequencies also for the O site indicating that the instability is an artifact of the harmonic approximation. As the $\widetilde{\omega}_i$ frequencies are positive-definite by definition, this is not proof that the O site occupation is stable. Obtaining the frequencies from the energy curvature [25], which can correctly describe an instability, confirms, however, that the O site interstitial site is in fact stable. The SSCHA frequencies for the muon in the O site are larger than the frequencies resulting from those obtained from the curvature by only 0.53% along the x, y axis and 0.14% along the z axis.

The quantum correction with the SSCHA shows that both T and O are stable local minima. The vibrational contribution to the energy is 0.21 eV less for the O site than for the T site (see Table I). Adding this to the static DFT contribution makes the O site energetically favored by approximately 0.03 eV over the T site, thus indicating that the two sites are basically degenerate, and possibly both occupied.

VI. QUANTUM CORRECTION ON THE MUON CONTACT HYPERFINE FIELD

The contact hyperfine field $B_c(\mathbf{r}_\mu)$ at the muon position $\mathbf{r}_\mu$ is computed *ab initio* by considering the imbalance in the spin density at the muon site [6] given as

$$B_c(\mathbf{r}_\mu) = \tfrac{2}{3}\mu_0\mu_B[n_\uparrow(\mathbf{r}_\mu) - n_\downarrow(\mathbf{r}_\mu)], \tag{15}$$

where μ_0 is the vacuum permeability, μ_B is the Bohr magneton, and $n_\uparrow - n_\downarrow$ represents the spin polarization at the muon site $\mathbf{r}_\mu$ calculated here by DFT. $B_c(\mathbf{r}_\mu^{\rm eq})$ has been calculated in this way for metals within a point impurity treatment of the muon [6]. We now calculate the effect of the muon quantum delocalization on its contact hyperfine field, using the muon SSCHA wave functions ϕ that already contain the anharmonic contributions.

The quantum expectation value $\langle B_c\rangle$ is given by

$$\langle B_c\rangle = \int d\mathbf{r}_\mu B_c(\mathbf{r}_\mu)|\phi(\mathbf{r}_\mu)|^2, \tag{16}$$

where the probability density $|\phi(\mathbf{r}_\mu)|^2$ has been defined in Eq. (11) and is obtained from the SSCHA muon frequencies $\widetilde{\omega}_i$ according to Eq. (A3).

The above integral can be evaluated in a post-DFT calculation by a statistical average performed stochastically, i.e., according to

$$\int d\mathbf{r}_\mu B_c(\mathbf{r}_\mu)\widetilde{\rho}(\mathbf{r}_\mu) \simeq \frac{1}{N_c}\sum_{n=1}^{N_c} B_c\left(\mathbf{r}_\mu^n\right) \equiv \langle B_c\rangle_{\widetilde{H}}, \tag{17}$$

where the sum extends over a number of muon random configurations N_c displaced from the equilibrium position $\mathbf{r}_\mu^{\rm eq}$ and generated with the probability distribution of the muon wave function [see Eq. (B1)]. The number of muon random configurations used is the same as in the SSCHA minimization of the muon wave function. However, the new muon random positions are generated considering the anharmonic corrected SSCHA muon wave function. Figure 2 shows the distribution of the 100 configurations used for fcc Co in the unit cell.

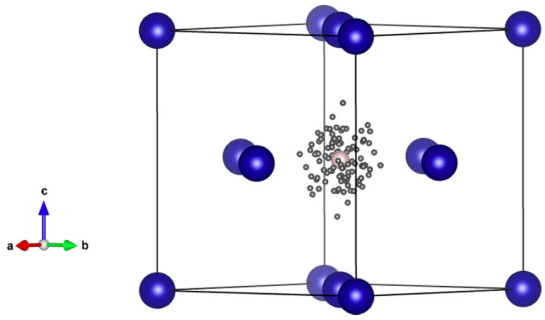

FIG. 2. 100 random position generated using Eq. (B1) for the muon at the octahedral site in the Co-fcc unit cell. The equilibrium octahedral center is depicted by the pink sphere, while the small dark spheres represent the different random muon positions where the muon contact hyperfine field within point impurity treatment $B_c(\mathbf{r}_\mu)$ was also calculated for the purpose of including the quantum effects of the muon.

$B_c(\mathbf{r}_\mu)$ was calculated by DFT for each of these random configurations within a $3 \times 3 \times 3$ supercell for Fe, Co, and Ni and a $2 \times 2 \times 2$ supercell for MnGe and MnSi, while other computational details are the same as reported in Ref. [6].

Table II and Fig. 3 show the calculated contact field $B_c(\mathbf{r}_\mu^{\rm eq})$ for a pointlike muon [6] and its stochastically *averaged* $\langle B_c \rangle$ values together with the experimental values. For all the systems, the statistical error for the stochastic sampling of $\langle B_c \rangle$ is in the range of $\approx$1 mT. The contact hyperfine field including quantum correction within the SSCHA, $\langle B_c \rangle$, improves the agreement with the experiments, thus underlining the importance of considering the finite muon wave function when computing muon hyperfine interactions. Admittedly, the correction to the contact hyperfine field appears to be less relevant than the outcome obtained on the stability of the muon at the octahedral site in Fe, still $|\langle B_c \rangle|$ introduces a correction that ranges between 1% and 18%.

VII. CONCLUSION

In conclusion, we have presented a general, effective, and robust approach, based on the DBO approximation, to obtain the ground-state wave function and zero-point energy of a positive muon embedded in a crystal from first principles. The adaptation of the SSCHA to the muon case allows us to evaluate the delocalized muon wave function including anharmonic contributions that correct harmonic ones.

Moreover, the SSCHA circumvents the problem of directly reconstructing the potential energy surface by replacing this task with a variational problem, and more importantly, it provides a computationally tractable method to describe the zero-point energy of the muon. This leads to a number of important insights concerning the stability of the muon sites and its coupling with the surrounding electrons.

The first point has been discussed by considering the case of the muon site in Fe, where anharmonicity plays a crucial role in establishing the stability of the muon in the tetrahedral and octahedral sites.

We reformulated the calculation of the muon contact hyperfine field by including the effects of its anharmonic zero-point vibration, improving the agreement with experiments with respect to previous estimates based on the point impurity treatment of the muon. Even though the correction is small, in numerous cases the contact field is of the order of tenths of a Tesla, thus making the absolute value of the correction presented here quite relevant.

Finally, the clean iterative procedure of the SSCHA makes it rather straightforward to define standardized work flows to automate the computational procedure. This represents another step toward routinely supporting experimental data analysis with computational simulation results.

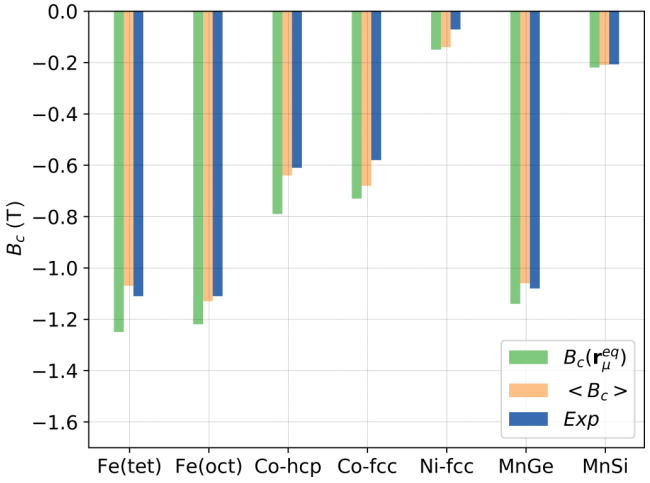

FIG. 3. Contact hyperfine field $B_c(\mathbf{r}_\mu^{\rm eq})$ at the equilibrium muon implantation position $\mathbf{r}_\mu^{\rm eq}$, the muon contact field averaged over the muon wave-function spread, $\langle B_c \rangle$, and experimentally observed values.

TABLE II. Calculated contact hyperfine field for the point muon at the equilibrium position $B_c(\mathbf{r}_\mu^{\rm eq})$, the calculated contact hyperfine field averaged over the spread of the muon wave function, $\langle B_c \rangle$, and experimentally observed values (Expt).

Host metals	$B_c(\mathbf{r}_\mu^{\rm eq})$ (T)[a]	$\langle B_c \rangle$ (T)	Expt.
Fe-bcc[b]	−1.25	−1.07	−1.11 [52]
Fe-bcc[c]	−1.22	−1.13	−1.11 [52]
Co-hcp	−0.79	−0.64	−0.61 [53]
Co-fcc	−0.73	−0.68	−0.58 [48]
Ni-fcc	−0.15	−0.14	−0.071 [54]
MnGe	−1.14	−1.07	−1.08 [55]
MnSi	−0.22	−0.21	−0.207 [56]

[a]Reference [6].
[b]Muon at the tetrahedral site.
[c]Muon at the octahedral site.

ACKNOWLEDGMENTS

R.D.R. acknowledges grants from the European Union's Horizon 2020 research and innovation program under Grant Agreement No. 654000. R.D.R., P.B., and I.J.O. also acknowledge computing resources provided by, the Swiss National Supercomputing Centre (CSCS) under Project ID sm16, CINECA under Project ID IsC58, the STFC Scientific

Computing Department's SCARF cluster, and the HPC resources at the University of Parma, Italy. I.E. acknowledges funding from the Spanish Ministry of Economy and Competitiveness (FIS2016-76617-P). This work is part of the Ph.D. thesis of I.J.O. at the University of Parma, Italy.

APPENDIX A: THE TRIAL MUON HARMONIC HAMILTONIAN

The trial muon harmonic Hamiltonian is of the form

$$\widetilde{H} = \sum_{\lambda=1}^{3} \frac{p_\lambda^2}{2m_\mu} + \frac{1}{2}\sum_{\lambda\nu}^{3} K^{\lambda\nu}\left(r_\mu - r_\mu^{\rm eq}\right)^\lambda \left(r_\mu - r_\mu^{\rm eq}\right)^\nu, \quad \text{(A1)}$$

where λ and ν are Cartesian component indexes, $\mathbf{r}_\mu^{\rm eq}$ is the muon equilibrium position, m_μ is the mass of the muon, and $K^{\lambda\nu}$ is the muon 3×3 force-constant matrix. The force-constant matrix $K^{\lambda\nu}/m_\mu$ can be constructed and diagonalized as

$$\sum_{\nu=1}^{3} \frac{K^{\lambda\nu}}{m_\mu}\widetilde{\epsilon}_i^\nu = \widetilde{\omega}_i^2 \widetilde{\epsilon}_i^\lambda, \quad \text{(A2)}$$

where i is the index of each of the orthogonal modes, $\widetilde{\epsilon}_i^\nu$ is the polarization vector, and $\widetilde{\omega}_i$ is the muon frequency corresponding to the trial Hamiltonian $\widetilde{H}$ for each mode.

Assuming a trial harmonic potential, the probability of finding the muon at $\mathbf{r}_\mu$ can be written simply as

$$\widetilde{\rho}(\mathbf{r}_\mu) = \frac{1}{\prod_{i=1}^{3}\sqrt{2\pi\widetilde{\sigma}_i^2}} \exp\left(-\sum_{\lambda\nu i}^{3} \frac{\widetilde{\epsilon}_i^\lambda \widetilde{\epsilon}_i^\nu}{2\widetilde{\sigma}_i^2}\left(r_\mu - r_\mu^{\rm eq}\right)^\lambda \left(r_\mu - r_\mu^{\rm eq}\right)^\nu\right), \quad \text{(A3)}$$

where $\widetilde{\sigma}_i$, the normal length for each of the modes i, is given as

$$\widetilde{\sigma}_i = \sqrt{\frac{\hbar}{2m_\mu\widetilde{\omega}_i}}. \quad \text{(A4)}$$

Using the quantum statistical averaging defined in Eq. (12), the energy of the trial harmonic Hamiltonian can be calculated as

$$\widetilde{E} = \sum_{i=1}^{3} \frac{1}{2}\hbar\widetilde{\omega}_i. \quad \text{(A5)}$$

APPENDIX B: RANDOM CONFIGURATION SAMPLING AND MINIMIZATION DETAILS

The distribution for the generation of the random muon position configurations is realized using random numbers $\{\xi_{\rm in}\}_{n=1,\ldots,N_c}$ generated with the Gaussian distribution $\widetilde{\rho}(\mathbf{r}_\mu)$ and rescaled by the corresponding normal length modes $\widetilde{\sigma}_i$ and polarization vector $\widetilde{\epsilon}_i^\lambda$. The generated positions are thus obtained as

$$\left(r_\mu^n\right)^\lambda = \left(r_\mu^{\rm eq}\right)^\lambda + \sum_{i=1}^{3} \widetilde{\epsilon}_i^\lambda \widetilde{\sigma}_i \xi_{\rm in}. \quad \text{(B1)}$$

This constitutes the set of points used in the stochastic evaluation of $\widetilde{E}$ and of the gradient of the energy functional,

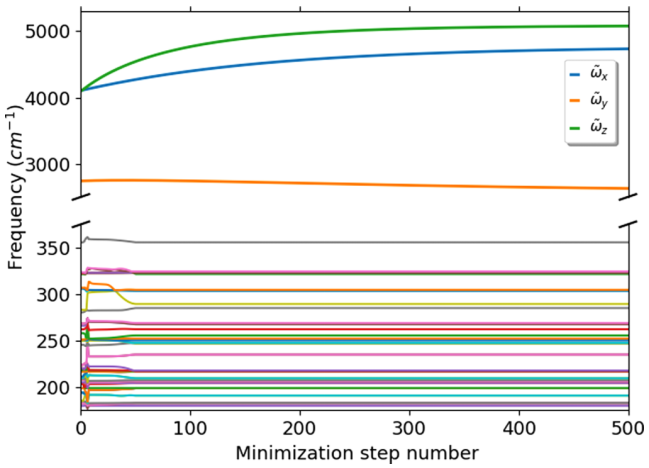

FIG. 4. Evolution of the SSCHA muon frequency ($\tilde{\omega}$ in the upper panel) and those of Fe (nearly static low-frequency lines in the lower panel) during minimization for the muon in the tetrahedral site of bcc Fe. The figure depicts the expected anharmonicity effects on the SSCHA muon frequencies and nearly nonexistent anharmonicity effects on those of Fe, due to the large mass difference of the muon and Fe nuclei. The muon is ≈490 times lighter.

namely $\nabla_K \widetilde{E}_H[\widetilde{H}]$, with respect to the force constant K. The analytic form of this last term is written as (see also Ref. [24])

$$\nabla_K \widetilde{E}_H[\widetilde{H}] = -\sum_{i\lambda\nu}\left(\widetilde{\epsilon}_i^\lambda \nabla_K \ln\widetilde{\sigma}_i + \nabla_K\widetilde{\epsilon}_i^\lambda\right)\widetilde{\epsilon}_i^\nu \times \int d\mathbf{r}_\mu [f^\lambda(\mathbf{r}_\mu) - \widetilde{f}^\lambda(\mathbf{r}_\mu)]\left(r_\mu - r_\mu^{\rm eq}\right)^\nu \widetilde{\rho}(\mathbf{r}_\mu), \quad \text{(B2)}$$

where $f^\lambda(\mathbf{r}_\mu)$ is the muon force component in the λ Cartesian direction for all muon positions $\mathbf{r}_\mu$, and $\widetilde{f}^\lambda(\mathbf{r}_\mu)$ are the forces obtained with the $\widetilde{V}$ potential. The SSCHA minimization is performed with respect to the symmetries of the crystal [24].

We also add that with the SSCHA, it is possible to minimize the energy both with respect to the muon position $\mathbf{r}_\mu$ and also the force-constant matrix $K^{\lambda\nu}$. However, for the materials considered in this paper, there is sufficient knowledge of the equilibrium muon position $\mathbf{r}_\mu^{\rm eq}$. Hence, the muon energy is only minimized with respect to the force-constant matrix K. For the muon in a high symmetry position, the force-constant matrix is a 3×3 matrix, with the diagonal elements of the matrix accounting for the dominant contribution.

Finally, it is important to note that, in order to obtain physical phonons from the ground-state minimized quantities provided by the SSCHA, the second derivative (curvature) of SSCHA energy at the minimum with respect to $\mathbf{r}_\mu$ has to be calculated [25], which includes a correction term to the force-constant matrix $K^{\lambda\nu}/m_\mu$ in Eq. (A2). We verified that for the cases under study here the muon frequencies are affected less than 1% by this extra correction. Thus, we can treat the $\widetilde{\omega}_i$ frequencies as the physical vibrational energies of the muons.

APPENDIX C: EVOLUTION OF MUON AND HOST Fe SSCHA FREQUENCIES

The evolution of the frequencies in the SSCHA calculation including anharmonic effects both for the Fe host nuclei and the muon at the tetrahedral site in a $2 \times 2 \times 2$ supercell is shown in Fig. 4. The figure indicates that there is a significant anharmonic contribution to the muon eigenfrequencies after several iterations (upper panel), whereas the lower frequency modes of the heavier Fe nuclei (lower panel) remain negligibly changed. This consideration together with the DBO approximation discussed in Sec. II also supports separating and concentrating only on the muon degrees of freedom.

[1] M. M. J. Rath, P. Jena, and C. Wang, Solid State Commun. **31**, 1003 (1979).
[2] J. S. Möller, P. Bonfá, D. Ceresoli, F. Bernardini, S. J. Blundell, T. Lancaster, R. D. Renzi, N. Marzari, I. Watanabe, S. Sulaiman, and M. I. Mohamed-Ibrahim, Phys. Scr. **88**, 068510 (2013).
[3] J. S. Möller, D. Ceresoli, T. Lancaster, N. Marzari, and S. J. Blundell, Phys. Rev. B **87**, 121108(R) (2013).
[4] F. Bernardini, P. Bonfà, S. Massidda, and R. De Renzi, Phys. Rev. B **87**, 115148 (2013).
[5] P. Bonfà and R. De Renzi, J. Phys. Soc. Jpn. **85**, 091014 (2016).
[6] I. J. Onuorah, P. Bonfà, and R. De Renzi, Phys. Rev. B **97**, 174414 (2018).
[7] L. Liborio, S. Sturniolo, and D. Jochym, J. Chem. Phys. **148**, 134114 (2018).
[8] S. M. Disseler, Phys. Rev. B **89**, 140413(R) (2014).
[9] F. R. Foronda, F. Lang, J. S. Möller, T. Lancaster, A. T. Boothroyd, F. L. Pratt, S. R. Giblin, D. Prabhakaran, and S. J. Blundell, Phys. Rev. Lett. **114**, 017602 (2015).
[10] P. D. de Réotier, A. Yaouanc, A. Amato, A. Maisuradze, D. Andreica, B. Roessli, T. Goko, R. Scheuermann, and G. Lapertot, Quantum Beam Sci. **2**, 19 (2018).
[11] M. Born and R. Oppenheimer, Ann. Phys. **389**, 457 (1927).
[12] P. Bonfà, F. Sartori, and R. De Renzi, J. Phys. Chem. C **119**, 4278 (2015).
[13] M. A. Boxwell, T. A. Claxton, and S. F. J. Cox, J. Chem. Soc., Faraday Trans. **89**, 2957 (1993).
[14] A. R. Porter, M. D. Towler, and R. J. Needs, Phys. Rev. B **60**, 13534 (1999).
[15] C. P. Herrero, R. Ramírez, and E. R. Hernández, Phys. Rev. B **73**, 245211 (2006).
[16] M. Tachikawa, K. Mori, H. Nakai, and K. Iguchi, Chem. Phys. Lett. **290**, 437 (1998).
[17] H. Nakai, Int. J. Quantum Chem. **86**, 511 (2001).
[18] S. P. Webb, T. Iordanov, and S. Hammes-Schiffer, J. Chem. Phys. **117**, 4106 (2002).
[19] A. Kerridge, A. H. Harker, and A. M. Stoneham, J. Phys.: Condens. Matter **16**, 8743 (2004).
[20] N. I. Gidopoulos and E. K. U. Gross, Philos. Trans. R. Soc. A **372**, 20130059 (2014).
[21] R. Valladares, A. Fisher, and W. Hayes, Chem. Phys. Lett. **242**, 1 (1995).
[22] M. I. J. Probert and M. J. Glover, Ab initio path integral molecular dynamics simulation of hydrogen in silicon, in *Hydrogen in Matter*, edited by G. R. Myneni and B. Hjorvarsson (American Institute of Physics, Melville, New York, 2006), p. 311.
[23] I. Errea, M. Calandra, and F. Mauri, Phys. Rev. Lett. **111**, 177002 (2013).
[24] I. Errea, M. Calandra, and F. Mauri, Phys. Rev. B **89**, 064302 (2014).
[25] R. Bianco, I. Errea, L. Paulatto, M. Calandra, and F. Mauri, Phys. Rev. B **96**, 014111 (2017).
[26] L. Monacelli, I. Errea, M. Calandra, and F. Mauri, Phys. Rev. B **98**, 024106 (2018).
[27] I. Errea, M. Calandra, C. J. Pickard, J. Nelson, R. J. Needs, Y. Li, H. Liu, Y. Zhang, Y. Ma, and F. Mauri, Phys. Rev. Lett. **114**, 157004 (2015).
[28] M. Leroux, I. Errea, M. Le Tacon, S.-M. Souliou, G. Garbarino, L. Cario, A. Bosak, F. Mauri, M. Calandra, and P. Rodière, Phys. Rev. B **92**, 140303(R) (2015).
[29] I. Errea, M. Calandra, C. J. Pickard, J. R. Nelson, R. J. Needs, Y. Li, H. Liu, Y. Zhang, Y. Ma, and F. Mauri, Nature (London) **532**, 81 (2016).
[30] G. A. S. Ribeiro, L. Paulatto, R. Bianco, I. Errea, F. Mauri, and M. Calandra, Phys. Rev. B **97**, 014306 (2018).
[31] U. Aseginolaza, R. Bianco, L. Monacelli, L. Paulatto, M. Calandra, F. Mauri, A. Bergara, and I. Errea, Phys. Rev. Lett. **122**, 075901 (2019).
[32] R. Bianco, I. Errea, L. Monacelli, M. Calandra, and F. Mauri, Nano Lett. **19**, 3098 (2019).
[33] A. V. Soudackov and S. Hammes-Schiffer, Chem. Phys. Lett. **299**, 503 (1999).
[34] A. Isihara, J. Phys. A **1**, 539 (1968).
[35] J. K. L. MacDonald, Phys. Rev. **43**, 830 (1933).
[36] M. R. Hestenes and E. Stiefel, J. Res. Natl. Bur. Stand. **49**, 409 (1952).
[37] W. Kohn and L. J. Sham, Phys. Rev. **140**, A1133 (1965).
[38] V. Fock, Z. Phys. **61**, 126 (1930).
[39] D. R. Hartree, F.R.S., Rep. Prog. Phys. **11**, 113 (1947).
[40] J. C. Slater, Phys. Rev. **81**, 385 (1951).
[41] G. Kresse, J. Furthmüller, and J. Hafner, Europhys. Lett. **32**, 729 (1995).
[42] K. Parlinski, Z. Q. Li, and Y. Kawazoe, Phys. Rev. Lett. **78**, 4063 (1997).
[43] S. Baroni, S. de Gironcoli, A. Dal Corso, and P. Giannozzi, Rev. Mod. Phys. **73**, 515 (2001).
[44] P. Giannozzi, S. Baroni, N. Bonini, M. Calandra, R. Car, C. Cavazzoni, D. Ceresoli, G. L. Chiarotti, M. Cococcioni, I. Dabo, A. Dal Corso, S. de Gironcoli, S. Fabris, G. Fratesi, R. Gebauer, U. Gerstmann, C. Gougoussis, A. Kokalj, M. Lazzeri, L. Martin-Samos, N. Marzari, F. Mauri, R. Mazzarello, S. Paolini, A. Pasquarello, L. Paulatto, C. Sbraccia, S. Scandolo, G. Sclauzero, A. P. Seitsonen, A. Smogunov, P. Umari, and R. M. Wentzcovitch, J. Phys.: Condens. Matter **21**, 395502 (2009).
[45] P. Pulay, Mol. Phys. **17**, 197 (1969).
[46] A. Seeger, Phys. Lett. A **58**, 137 (1976).
[47] H. Graf, G. Balzer, E. Recknagel, A. Weidinger, and R. I. Grynszpan, Phys. Rev. Lett. **44**, 1333 (1980).
[48] B. Lindgren and D. E. Ellis, Phys. Rev. B **26**, 636 (1982).

[49] S. Estreicher and P. F. Meier, Phys. Rev. B **25**, 297 (1982).

[50] E. Yagi, G. Flik, K. Fürderer, N. Haas, D. Herlach, J. Major, A. Seeger, W. Jacobs, M. Krause, M. Krauth, H. J. Mundinger, and H. Orth, Phys. Rev. B **30**, 441 (1984).

[51] W. J. Kossler, M. Namkung, B. Hitti, Y. Li, J. Kempton, C. E. Stronach, L. R. Goode, W. F. Lankford, B. D. Patterson, W. Kündig, and R. I. Grynszpan, Phys. Rev. B **32**, 293 (1985).

[52] N. Nishida, R. S. Hayano, K. Nagamine, T. Yamazaki, J. H. Bewer, D. M. Garner, D. Fleming, T. Takeuchi, and Y. Ishikawa, Solid State Commun. **22**, 235 (1977).

[53] H. Graf, W. Kündig, B. D. Patterson, W. Reichart, P. Roggwiller, M. Camani, F. N. Gygax, W. Rüegg, A. Schenck, H. Schilling, and P. F. Meier, Phys. Rev. Lett. **37**, 1644 (1976).

[54] H. Graf, E. Holzschuh, E. Recknagel, A. Weidinger, and T. Wichert, Hyperfine Interact. **6**, 245 (1979).

[55] N. Martin, M. Deutsch, F. Bert, D. Andreica, A. Amato, P. Bonfà, R. De Renzi, U. K. Rößler, P. Bonville, L. N. Fomicheva, A. V. Tsvyashchenko, and I. Mirebeau, Phys. Rev. B **93**, 174405 (2016).

[56] A. Amato, P. D. de Réotier, D. Andreica, A. Yaouanc, A. Suter, G. Lapertot, I. M. Pop, E. Morenzoni, P. Bonfà, F. Bernardini, and R. De Renzi, Phys. Rev. B **89**, 184425 (2014).

Strong anharmonicity and high thermoelectric efficiency in high temperature SnS from first-principles

Unai Aseginolaza,[1,2,3] Raffaello Bianco,[1,4] Lorenzo Monacelli,[5] Lorenzo Paulatto,[6] Matteo Calandra,[7] Francesco Mauri,[5,8] Aitor Bergara,[1,2,9] and Ion Errea[1,2,3]

[1] *Centro de Física de Materiales CFM, CSIC-UPV/EHU, Paseo Manuel de Lardizabal 5, 20018 Donostia, Basque Country, Spain*
[2] *Donostia International Physics Center (DIPC), Manuel Lardizabal pasealekua 4, 20018 Donostia, Basque Country, Spain*
[3] *Fisika Aplikatua 1 Saila, Gipuzkoako Ingenieritza Eskola, University of the Basque Country (UPV/EHU), Europa Plaza 1, 20018 Donostia, Basque Country, Spain*
[4] *Department of Applied Physics and Material Science, Steele Laboratory, California Institute of Technology, Pasadena, California 91125, United States*
[5] *Dipartimento di Fisica, Università di Roma La Sapienza, Piazzale Aldo Moro 5, I-00185 Roma, Italy*
[6] *IMPMC, UMR CNRS 7590, Sorbonne Universités - UPMC Univ. Paris 06, MNHN, IRD, 4 Place Jussieu, F-75005 Paris, France*
[7] *Sorbonne Universités, CNRS, Institut des Nanosciences de Paris, UMR7588, F-75252, Paris, France*
[8] *Graphene Labs, Fondazione Instituto Italiano di Tecnologia, Italy*
[9] *Departamento de Física de la Materia Condensada, University of the Basque Country (UPV/EHU), 48080 Bilbao, Basque Country, Spain*

(Dated: June 6, 2019)

SnS and SnSe are isoelectronic materials with a common phase diagram. Recently, SnSe was found to be the most efficient intrinsic thermoelectric material in its high-temperature *Cmcm* phase above 800 K. Making use of first-principles calculations, here we show that the electronic and vibrational properties of both materials are very similar in this phase and, consequently, SnS is also expected to have a high thermoelectric figure of merit at high temperature in its *Cmcm* phase. In fact, the electronic power factor and lattice thermal conductivity are comparable for both materials, which ensures a similar figure of merit. As in the case of SnSe, the vibrational properties of SnS in the *Cmcm* phase are far from trivial and are dominated by huge anharmonic effects. Its phonon spectra are strongly renormalized by anharmonicity and the spectral functions of some particular in-plane modes depict anomalous non-lorentzian profiles. Finally, we show that non-perturbative anharmonic effects in the third-order force-constants are crucial in the calculation of the lattice thermal conductivity. Our results motivate new experiments in the high temperature regime to measure the figure of merit of SnS.

I. INTRODUCTION

Thermoelectricity is a technologically interesting material property that allows to transform residual heat into useful electricity[1,2]. The efficiency of this energy transformation is controlled by the dimensionless figure of merit

$$ZT = S^2\sigma T/\kappa, \tag{1}$$

where S is the Seebeck coefficient, σ the electrical conductivity, T the temperature, and $\kappa = \kappa_e + \kappa_l$ the sum of electronic κ_e and lattice κ_l thermal conductivities. Therefore, a good thermoelectric performance requires a high power factor $P_F = S^2\sigma$ together with a low thermal conductivity.

Monochalcogenides have proven to be efficient thermoelectric materials[3–6] mainly due to their strongly anharmonic lattice that implies a low lattice thermal conductivity[7–11]. PbTe is an appropriate example of the potential technological relevance of thermoelectric monochalcogenides: it shows a high ZT in the $600-800$ K temperature range[12], as high as 2.2 when nanostructured[13], and has been successfully applied in spacecrafts[14]. In the last years SnSe has attracted a great deal of attention since it was measured to be the most efficient intrinsic thermoelectric material[15]. Its figure of merit soars to 2.6 after a structural phase transition[15–18] at around 800 K from the low-symmetry *Pnma* phase to the high-symmetry *Cmcm*. In the high-symmetry phase the electronic band gap is reduced without affecting its ultralow thermal conductivity, providing the record ZT. A recent theoretical work shows that the phase transition[19] is second order and non-perturbative anharmonicity is very important to get a thermal conductivity in agreement with experiments.

SnS is isoelectronic to SnSe and shows very similar electronic and vibrational properties[17,18,20] at low temperatures. Experimentally it also shows a phase transition[17,18] from the *Pnma* to the *Cmcm* structure and a very low thermal conductivity in the former[21,22] phase. Therefore, it is expected to be a very efficient thermoelectric material in the high temperature phase, which together with the fact that S is a much more earth abundant element than Se, makes it a very interesting candidate for technological applications. Actually, in Refs. 21 and 22 it is shown how the ZT of undoped SnS increases very fast before the phase transition as in

the case of SnSe. However, as far as we are aware, there are no experimental transport measurements for the high temperature phase of SnS. First-principles calculations of its thermoelectric properties are also absent in the literature, hindered by the unstable modes obtained within the harmonic approximation as in the case of SnSe[23,24].

In this work, by performing *ab initio* calculations we propose that *Cmcm* SnS is expected to be a very efficient intrinsic thermoelectric material, as good as SnSe in this phase. We show that the P_F of SnSe and SnS are expected to be very similar in this phase, as long as the electronic relaxation time is similar in both materials. By including anharmonicity in the phonon calculation at a non-perturbative level within the Stochastic Self-Consistent Harmonic Approximation[25–27] (SSCHA), we show that the phonon spectrum of SnS suffers a strong anharmonic renormalization. The phase transition is driven by the collapse of a zone-border phonon. Anharmonicity is so large that the spectral function of some vibrational modes deviates from the Lorentzian-like shape as it happens in other monochalcogenides[8,11]. Finally, we calculate the lattice thermal conductivity of *Cmcm* SnS obtaining ultralow values below ≈ 1.0 $\mathrm{Wm^{-1}K^{-1}}$. Non-perturbative anharmonic corrections to the third-order force-constants are important in its calculation as it happens in SnSe[19]. There is a clear anisotropy between in-plane and out-of-plane thermal conductivities. The similarity of the power factors and the lattice thermal conductivities of SnSe and SnS suggest that the latter may be an earth abundant efficient thermoelectric material and motivate more experimental effort to measure its ZT in the high-temperature phase.

This article is organized as follows. In section II we briefly review the theoretical background for the calculation of anharmonic phonons, thermal conductivity, and electronic transport properties. In section III we specify the computational details. In section IV we discuss the results of our work. Conclusions are given in section V.

II. THEORETICAL BACKGROUND

A. Electronic transport properties

Within the semiclassical Boltzmann transport theory[28] the electrical conductivity and the Seebeck coefficient can be calculated respectively as

$$\sigma(T,\mu) = e^2 \int_{-\infty}^{\infty} d\varepsilon \left[-\frac{\partial f(T,\mu,\varepsilon)}{\partial \epsilon} \right] \Sigma(\varepsilon) \tag{2}$$

$$S(T,\mu) = \frac{e}{T\sigma(T,\mu)} \int_{-\infty}^{\infty} d\varepsilon \left[-\frac{\partial f(T,\mu,\varepsilon)}{\partial \epsilon} \right] \Sigma(\varepsilon)(\varepsilon-\mu), \tag{3}$$

where e is the electron charge, μ the chemical potential, $f(T,\mu,\varepsilon)$ the Fermi-Dirac distribution function, and $\Sigma(\varepsilon)$ the transport distribution function. The latter is defined as

$$\Sigma(\varepsilon) = \frac{1}{\Omega N_{\mathbf{k}}} \sum_{n\mathbf{k}} \tau^e_{n\mathbf{k}} |\mathbf{v}_{n\mathbf{k}}|^2 \delta(\varepsilon - \varepsilon_{n\mathbf{k}}), \tag{4}$$

where Ω is the unit cell volume, $N_{\mathbf{k}}$ the number of $\mathbf{k}$ points in the sum, and $\varepsilon_{n\mathbf{k}}$, $\mathbf{v}_{n\mathbf{k}}$ and $\tau^e_{n\mathbf{k}}$ are, respectively, the energy, Fermi velocity and relaxation time of the electronic state with band index n and crystal momentum $\mathbf{k}$. Our goal here is to compare the power factors $P_F(T,\mu) = \sigma(T,\mu)S^2(T,\mu)$ of SnSe and SnS coming from their different band structure without explicitly calculating the electronic relaxation times. We thus assume that $\tau^e_{n\mathbf{k}} = \tau^e$ is just the same constant for both compounds. In these conditions it is easy to see from Eqs. (2)-(4) that the power factor is proportional to τ^e. In the following we will limit ourselves to the analysis of $P_F(T,\mu)/\tau^e$, which only depends on the band structure of the compounds.

B. Free energy of strongly anharmonic crystals

We study the vibrational properties of SnS within the Born-Oppenheimer (BO) approximation, in which the Hamiltonian H that determines the dynamics of the ions consists of the ionic kinetic energy and the BO potential $V(\mathbf{R})$. $\mathbf{R}$ denotes $R^{\alpha s}(\mathbf{l})$ in component free notation, which specifies the atomic configuration of the crystal. α is a Cartesian direction, s labels an atom within the unit cell, and $\mathbf{l}$ a lattice vector. From now on, we will use a single composite index $a = (\alpha, s, \mathbf{l})$ and bold letters to indicate quantities in component-free notation. We will keep this composite index for Fourier transformed components adding a bar, $\bar{a}$, to distinguish that in this case $\bar{a}$ just denotes a Cartesian index and an atom in the unit cell.

As it will be shown below and as it happens in *Cmcm* SnSe[19,23,24], the harmonic approximation collapses for *Cmcm* SnS. Truncating the Taylor expansion of $V(\mathbf{R})$ for this phase at second order and diagonalizing the resulting harmonic force-constants $\boldsymbol{\phi}$ large imaginary frequencies are obtained. This makes the calculation of any thermodynamic and transport property involving phonons impossible at the harmonic level. We overcome this problem by solving the ionic Hamiltonian within the SSCHA, a variational method that includes anharmonic effects at a non-perturbative level in the calculation of the vibrational free energy[25–27].

The SSCHA performs a variational minimization of the free energy with respect to a trial density matrix $\rho_{\mathcal{H}}$ that solves an auxiliary harmonic Hamiltonian

$$\mathcal{H} = \sum_a \frac{P_a^2}{2M_a} + \frac{1}{2}\sum_{ab} (\mathbf{R}-\boldsymbol{\mathcal{R}})_a \Phi_{ab} (\mathbf{R}-\boldsymbol{\mathcal{R}})_b, \tag{5}$$

where P is the kinetic energy and M_a the atomic mass of atom a. The variational parameters in the minimization are the $\boldsymbol{\Phi}$ force-constants, which should not be confused with the harmonic force-constants $\boldsymbol{\phi}$, and

the $\boldsymbol{\mathcal{R}}$ positions. The $\boldsymbol{\mathcal{R}}$ positions are referred as the *centroid* positions, i.e., the most probable atomic positions. The $\boldsymbol{\Phi}$ force-constants are related to the broadening of the ionic wave functions around the centroid positions. At the minimum, the SSCHA yields a free energy F that takes into account anharmonicity without approximating the BO potential. The minimization can be performed by calculating atomic forces and energies in stochastic atomic configurations in supercells using importance sampling and reweighting techniques[25–27]. The supercell atomic configurations are created according to the probability distribution function related to $\rho_{\mathcal{H}}$. Since the BO energy landscape is sampled stochastically, the SSCHA method does not use any fit or approximation on the $V(\boldsymbol{R})$. It is, therefore, unbiased by the starting point.

C. Free energy Hessian and second-order phase transition

In a displacive second-order phase transition, at high temperature the free energy F has a minimum in a high-symmetry configuration ($\boldsymbol{\mathcal{R}}_{hs}$), but, on lowering the temperature, $\boldsymbol{\mathcal{R}}_{hs}$ becomes a saddle point at the transition temperature T_c. Therefore, the free energy Hessian evaluated at $\boldsymbol{\mathcal{R}}_{hs}$, $\partial^2 F/\partial\boldsymbol{\mathcal{R}}\partial\boldsymbol{\mathcal{R}}|_{\boldsymbol{\mathcal{R}}_{hs}}$, at high temperature is positive definite but it develops one or multiple negative eigendirections at T_c. The SSCHA free energy Hessian can be computed by using the analytic formula[26]

$$\frac{\partial^2 F}{\partial\boldsymbol{\mathcal{R}}\partial\boldsymbol{\mathcal{R}}} = \boldsymbol{\Phi} + \overset{(3)}{\boldsymbol{\Phi}}\boldsymbol{\Lambda}(0)[\mathbf{1} - \overset{(4)}{\boldsymbol{\Phi}}\boldsymbol{\Lambda}(0)]^{-1}\overset{(3)}{\boldsymbol{\Phi}}, \tag{6}$$

with

$$\overset{(n)}{\boldsymbol{\Phi}} = \left\langle \frac{\partial^n V}{\partial \mathbf{R}^n} \right\rangle_{\rho_{\mathcal{H}}}. \tag{7}$$

Here $\langle\rangle_{\rho_{\mathcal{H}}}$ denotes the quantum statistical average taken with the density matrix $\rho_{\mathcal{H}}$. All these averages are evaluated here stochastically as described in Ref. 26. The $\overset{(n)}{\boldsymbol{\Phi}}$ non-perturbative n-th order force-constants should not be confused with the n-th order perturbative force-constants $\overset{(n)}{\boldsymbol{\phi}}$, which are calculated as derivatives of the BO potential at a reference position 0 and not as quantum statistical averages:

$$\overset{(n)}{\boldsymbol{\phi}} = \left[\frac{\partial^n V}{\partial \mathbf{R}^n}\right]_0. \tag{8}$$

In Eq. (6) the value $z = 0$ of the fourth-order tensor $\boldsymbol{\Lambda}(z)$ is used. For a generic complex number z it is defined, in components, by

$$\Lambda^{abcd}(z) = -\frac{1}{2}\sum_{\mu\nu}\tilde{F}(z,\tilde{\Omega}_\mu,\tilde{\Omega}_\nu)\times \sqrt{\frac{\hbar}{2M_a\tilde{\Omega}_\mu}}e^a_\mu\sqrt{\frac{\hbar}{2M_b\tilde{\Omega}_\nu}}e^b_\nu\sqrt{\frac{\hbar}{2M_c\tilde{\Omega}_\mu}}e^c_\mu\sqrt{\frac{\hbar}{2M_d\tilde{\Omega}_\nu}}e^d_\nu, \tag{9}$$

with $\tilde{\Omega}^2_\mu$ and e^a_μ the eigenvalues and corresponding eigenvectors of

$$D^{(S)}_{ab} = \Phi_{ab}/\sqrt{M_a M_b}, \tag{10}$$

respectively. In Eq. (9)

$$\tilde{F}(z,\tilde{\Omega}_\mu,\tilde{\Omega}_\nu) = \frac{2}{\hbar}\left[\frac{(\tilde{\Omega}_\mu+\tilde{\Omega}_\nu)[1+n_B(\tilde{\Omega}_\mu)+n_B(\tilde{\Omega}_\nu)]}{(\tilde{\Omega}_\mu+\tilde{\Omega}_\nu)^2-z^2} - \frac{(\tilde{\Omega}_\mu-\tilde{\Omega}_\nu)[n_B(\tilde{\Omega}_\mu)-n_B(\tilde{\Omega}_\nu)]}{(\tilde{\Omega}_\mu-\tilde{\Omega}_\nu)^2-z^2}\right], \tag{11}$$

where $n_B(\omega) = 1/(e^{\beta\hbar\omega}-1)$ is the bosonic occupation number. Evaluating through Eq. (6) the free energy Hessian at $\boldsymbol{\mathcal{R}}_{hs}$ and studying its spectrum as a function of temperature, we can predict the occurrence of a displacive phase transition and estimate T_c. This technique has been successful to study phase-transition temperatures in high-pressure hydrides, monochalcogenides, and transition metal dichalcogenides undergoing charge-density wave transitions[11,29,30].

D. Dynamical properties of solids and phonon frequencies

As shown in Ref. 26, even if the SSCHA is a ground-state theory, it is possible to formulate a valid ansatz in order to calculate dynamical properties of crystals such as phonon spectral functions. The one-phonon Green function $\mathbf{G}(z)$ for the variable $\sqrt{M_a}(R_a - \mathcal{R}_a)$ can be calculated as

$$\mathbf{G}^{-1}(z) = z^2\mathbf{1} - \mathbf{M}^{-\frac{1}{2}}\boldsymbol{\Phi}\mathbf{M}^{-\frac{1}{2}} - \boldsymbol{\Pi}(z). \tag{12}$$

With this definition, in the static limit the Green function becomes the dynamical matrix obtained with the free energy Hessian: $\mathbf{G}^{-1}(0) = -\mathbf{D}^{(F)}$, with

$$D^{(F)}_{ab} = \frac{1}{\sqrt{M_a M_b}}\frac{\partial^2 F}{\partial\mathcal{R}_a\partial\mathcal{R}_b}. \tag{13}$$

We will label with ω_μ the eigenvalues of $\mathbf{D}^{(F)}$. The SSCHA self-energy is given by

$$\Pi(z) = \mathbf{M}^{-\frac{1}{2}}\overset{(3)}{\boldsymbol{\Phi}}\boldsymbol{\Lambda}(z)[\mathbf{1} - \overset{(4)}{\boldsymbol{\Phi}}\boldsymbol{\Lambda}(z)]^{-1}\overset{(3)}{\boldsymbol{\Phi}}\mathbf{M}^{-\frac{1}{2}}, \tag{14}$$

where $M_{ab} = \delta_{ab}M_a$ is the mass matrix. We have explicitly verified that neglecting $\overset{(4)}{\boldsymbol{\Phi}}$ in Eq. (6) has a completely

negligible impact on the eigenvalues of $\mathbf{D}^{(F)}$. We consistently neglect $\overset{(4)}{\mathbf{\Phi}}$ in Eq. (12) as well. This reduces the SSCHA self energy to the so-called bubble self energy, namely

$$\mathbf{\Pi}(z) \approx \mathbf{\Pi}^{(B)}(z) = \mathbf{M}^{-\frac{1}{2}} \overset{(3)}{\mathbf{\Phi}} \mathbf{\Lambda}(z) \overset{(3)}{\mathbf{\Phi}} \mathbf{M}^{-\frac{1}{2}}. \quad (15)$$

The cross section in an inelastic, e.g. neutron, experiment is proportional to the spectral function $\sigma(\omega) = -\omega \mathrm{Tr} Im\mathbf{G}(\omega + i0^+)/\pi$[31]. Its peaks signal the presence of collective vibrational excitations (phonons) having certain energies and linewidth. In order to recognize the contribution of each phonon mode to this spectral function, we first take advantage of the lattice periodicity and Fourier transform the spectral function and the self energy, and second we neglect the mixing between phonon modes and assume that $\mathbf{\Pi}(z)$ is diagonal in the basis of the eigenvectors:

$$\Pi_\mu(\mathbf{q}, \omega) = \sum_{\bar{a}\bar{b}} e^{\bar{a}}_\mu(-\mathbf{q}) \Pi_{\bar{a}\bar{b}}(\mathbf{q}, \omega + i0^+) e^{\bar{b}}_\mu(\mathbf{q}). \quad (16)$$

The cross section is then given by

$$\sigma(\mathbf{q}, \omega) = \frac{1}{\pi} \sum_\mu \frac{-\omega Im\Pi_\mu(\mathbf{q}, \omega)}{(\omega^2 - \tilde{\Omega}^2_\mu(\mathbf{q}) - Re\Pi_\mu(\mathbf{q}, \omega))^2 + (Im\Pi_\mu(\mathbf{q}, \omega))^2}. \quad (17)$$

In Eqs. (16) and (17) $\tilde{\Omega}^2_\mu(\mathbf{q})$ and $e^{\bar{a}}_\mu(\mathbf{q})$ are, respectively, the eigenvalues and eigenvectors of $\mathbf{D}^{(S)}(\mathbf{q})$, the Fourier transform of Eq. (10).

The cross section calculated as in Eq. (17) does not have any given lineshape. However, when $\Pi_\mu(\mathbf{q}, \omega)$ is small compared to $\tilde{\Omega}^2_\mu(\mathbf{q})$, it is justified to approximate $\Pi_\mu(\mathbf{q}, \omega) \sim \Pi_\mu(\mathbf{q}, \tilde{\Omega}_\mu(\mathbf{q}))$, which turns $\sigma(\mathbf{q}, \omega)$ into a sum of Lorentzian functions. In this Lorentzian approximation the peaks appear at the $\Omega_\mu(\mathbf{q})$ phonon frequencies, with

$$\Omega^2_\mu(\mathbf{q}) = \tilde{\Omega}^2_\mu(\mathbf{q}) + Re\Pi_\mu(\mathbf{q}, \tilde{\Omega}_\mu(\mathbf{q})), \quad (18)$$

and the linewidths are proportional to $Im[\Pi_\mu(\mathbf{q}, \tilde{\Omega}_\mu(\mathbf{q}))]$.

E. Thermal conductivity

We calculate the lattice thermal conductivity within the single mode relaxation time approximation (SMA)[32] making use of the eigenvalues and eigenvectors of $\mathbf{D}^{(S)}(\mathbf{q})$ (as it will be shown below it is not possible at the harmonic level due to the instabilities obtained) as well as the non-preturbative third-order force-constants $\overset{(3)}{\mathbf{\Phi}}$. In the SMA the lattice thermal conductivity is written as follows[33]:

$$\kappa^{\alpha\beta}_l = \frac{\hbar^2}{\Omega N_\mathbf{q} k_B T^2} \times \sum_{\mathbf{q}\mu} c^\alpha_\mu(\mathbf{q}) c^\beta_\mu(\mathbf{q}) \tilde{\Omega}^2_\mu(\mathbf{q}) n_B(\tilde{\Omega}_\mu(\mathbf{q})) \left[n_B(\tilde{\Omega}_\mu(\mathbf{q})) + 1 \right] \tau_\mu(\mathbf{q}), \quad (19)$$

where, for the phonon mode μ with momentum $\mathbf{q}$, $c^\alpha_\mu(\mathbf{q})$ is the Cartesian component α of its lattice group velocity and $\tau_\mu(\mathbf{q})$ its lifetime. $N_\mathbf{q}$ is the number of $\mathbf{q}$ points used in the sum. The Bose-Einstein occupation of each mode is given by the Boltzmann Transport Equation (BTE) and the inverse phonon lifetime (with $\gamma_\mu(\mathbf{q})$ the half width at half maximum) is calculated as[33]

$$\frac{1}{\tau_\mu(\mathbf{q})} = 2\gamma_\mu(\mathbf{q}) = \frac{\pi}{\hbar^2 N_\mathbf{q}} \sum_{\mathbf{q}'\nu\eta} |\overset{(3)}{\Phi}_{\mu\nu\eta}(\mathbf{q}, \mathbf{q}', \mathbf{q}'')|^2 \times [(1 + n_B(\tilde{\Omega}_\nu(\mathbf{q}')) + n_B(\tilde{\Omega}_\eta(\mathbf{q}'')))\delta(\tilde{\Omega}_\mu(\mathbf{q}) - \tilde{\Omega}_\nu(\mathbf{q}') - \tilde{\Omega}_\eta(\mathbf{q}'')) + 2(n_B(\tilde{\Omega}_\nu(\mathbf{q}')) - n_B(\tilde{\Omega}_\eta(\mathbf{q}'')))\delta(\tilde{\Omega}_\mu(\mathbf{q}) + \tilde{\Omega}_\nu(\mathbf{q}') - \tilde{\Omega}_\eta(\mathbf{q}''))], \quad (20)$$

with $\mathbf{q} + \mathbf{q}' + \mathbf{q}'' = \mathbf{G}$, $\mathbf{G}$ being a reciprocal lattice vector. Here $\overset{(3)}{\Phi}_{\mu\nu\eta}(\mathbf{q}, \mathbf{q}', \mathbf{q}'')$ is the third order force-constants matrix written in the space of the normal modes:

$$\overset{(3)}{\Phi}_{\mu\nu\eta}(\mathbf{q}, \mathbf{q}', \mathbf{q}'') = \sum_{\bar{a}\bar{b}\bar{c}} \sqrt{\frac{\hbar^3}{8 M_{\bar{a}} M_{\bar{b}} M_{\bar{c}} \tilde{\Omega}_\mu(\mathbf{q}) \tilde{\Omega}_\nu(\mathbf{q}') \tilde{\Omega}_\eta(\mathbf{q}'')}} \times e^{\bar{a}}_\mu(\mathbf{q}) e^{\bar{b}}_\nu(\mathbf{q}') e^{\bar{c}}_\eta(\mathbf{q}'') \overset{(3)}{\Phi}_{\bar{a}\bar{b}\bar{c}}(\mathbf{q}, \mathbf{q}', \mathbf{q}''), \quad (21)$$

where $\overset{(3)}{\Phi}_{\bar{a}\bar{b}\bar{c}}(\mathbf{q}, \mathbf{q}', \mathbf{q}'')$ are the Fourier transformed non-perturbative third-order force-constants. We also calculate the thermal conductivity with the perturbative third-order force-constants by substituting the non-perturbative $\overset{(3)}{\mathbf{\Phi}}$ by the perturbative $\overset{(3)}{\boldsymbol{\phi}}$ in Eqs. (20) and (21).

III. COMPUTATIONAL DETAILS

We calculate the electronic bands using *ab initio* Density Functional Theory (DFT) calculations within the local density approximation (LDA)[34] and the generalized gradient approximation in the Perdew Burke Ernzerhof (PBE) parametrization[35] as implemented in the QUANTUM ESPRESSO[36,37] software package. Harmonic phonons and perturbative third-order force-constants $\overset{(3)}{\boldsymbol{\phi}}$ are calculated using Density Functional Perturbation Theory[33,38]. We use projector augmented wave[39] (PAW) pseudopotentials that include $5s^2\ 5p^2\ 4d^{10}$ electrons in the case of Sn and $3s^2\ 3p^4$ in the case of S or Se. For

the perturbative third-order force-constants we use norm-conserving pseudopotentials which were shown[19] to provide very similar third-order force-constants compared to the PAW result. A $16\times16\times16$ sampling of the first Brillouin zone of the primitive cell and an energy cutoff of 70 Ry are employed for the DFT self-consistent calculation. For the electronic transport calculations we use the Boltztrap software package[40]. For the sum in Eq. 4 we perform a non self-consistent DFT calculation in a $30\times30\times30$ sampling of the first Brillouin zone. We use experimental lattice parameters at the transition temperature as we got better agreement with experiments for SnSe in a previous work[19]. The experimental lattice parameters taken from Refs.[16,17] are $a = 22.13$ a$_0$, $b = 8.13$ a$_0$, $c = 8.13$ a$_0$ for SnSe and $a = 21.69$ a$_0$, $b = 7.84$ a$_0$, $c = 7.84$ a$_0$ (a$_0$ is the Bohr length) for SnS. The structures of the high temperature *Cmcm* and low temperature *Pnma* phases are shown in Figure 1.

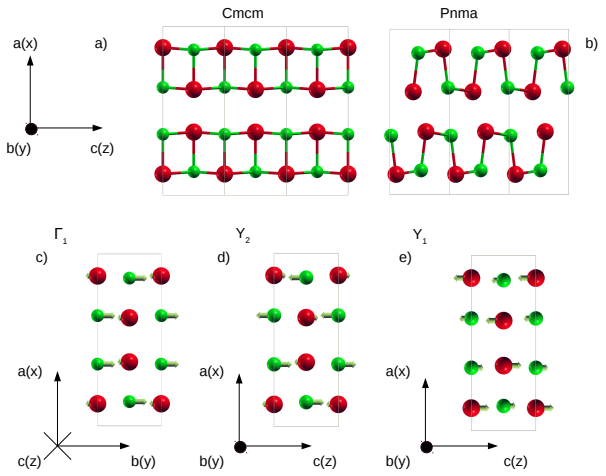

Figure 1. XY face of the a) *Cmcm* and b) *Pnma* structures. Atomic displacements of modes c) Γ_1, d) Y_2 and e) Y_1. Sn atoms are red and S green.

Anharmonic phonons and non-perturbative third-order force-constants are calculated within the SSCHA using a $2\times2\times2$ supercell. For the SSCHA calculation we use forces calculated within DFT. Once we get the anharmonic force-constants, we substract the harmonic ones and interpolate the difference to a $6\times6\times6$ grid. Then, we add this interpolated difference to the harmonic dynamical matrices in a $6\times6\times6$ grid, which yields anharmonic force-constants in a fine grid. By Fourier interpolating the latter we can calculate phonon frequencies at any point in the Brillouin zone. We impose the acoustic sum rule to the third-order force-constants with an iterative method prior to their Fourier interpolation[19,33]. The lattice thermal conductivity is calculated with Eq. (19) using a $10\times10\times10$ grid. For the calculation of the phonon linewidths we use a $20\times20\times20$ mesh in Eq. (20) with a Gaussian smearing of 1 cm^{-1} for the Dirac deltas.

IV. RESULTS AND DISCUSSION

A. Electronic transport

Figure 2 (a) shows the electronic band structures of SnS and SnSe in the high symmetry phase. It shows that the electronic properties of these materials are very similar because their electronic band structures are basically the same as expected for isoelectronic compounds with the same atomic structure. The major difference is that the indirect (the conduction and valence bands that constitute the gap are denoted with an arrow in Figure 2 (a)) energy gap (0.45 eV for SnSe and 0.7 eV for SnS) is bigger in the case of SnS, in agreement with experiments[15,41] and previous calculations[20]. As expected, the calculated electronic gaps within LDA underestimate the experimental values (0.86−0.948 eV for SnSe and 0.9−1.142 eV for SnS). Using these band structures we have calculated the Seebeck coefficient, which within the approximation of a constant electronic relaxation time it is independent of it, and the electrical conductivity over the electronic relaxation time σ/τ^e. The Seebeck coefficient is very similar for both materials, but σ/τ^e is slightly larger in the case of SnSe due to the smaller electronic gap. Using these two quantities we have calculated P_F/τ^e, shown in Figure 2 (b). As we can see, P_F/τ^e is very similar for both materials, but slightly higher in the case of SnSe. As we can see, P_F/τ^e increases as temperature increases and the difference between SnSe and SnS is less than 5% at 1000 K. These results make clear that regarding the electronic transport properties these two materials are very similar in the high temperature phase provided that the relaxation time for the electrons is similar for both materials, which is expected for isoelectronic and isostructural compounds.

B. *Pnma* to *Cmcm* phase transition

As it was already pointed out[17,19], symmetry[42,43] dictates that it is possible to have a second-order phase transition between the *Cmcm* and *Pnma* phases. The transition is dominated by the distortion pattern associated to a non-degenerate mode (Y_1) at the zone border Y point. This means[19] that, in a second-order displacive phase transition scenario, the transition temperature T_c is defined as $\partial^2F/\partial Q^2(T=T_c)=0$ where Q is the order parameter that transforms the system continuously from the *Pnma* ($Q\neq0$) to the *Cmcm* ($Q=0$) phase. As the distortion is dominated by the Y_1 phonon, $\partial^2F/\partial Q^2(T)$ is proportional to $\omega^2_{Y_1}(T)$, which we can calculate diagonalizing $\mathbf{D}^{(F)}$.

Figure 3 shows $\omega^2_{Y_1}(T)$ within the LDA and PBE approximations. As in the case of SnSe[19], the second derivative of the free energy is positive at high temperatures and decreases lowering the temperature. For both approximations, it becomes negative at the critical tem-

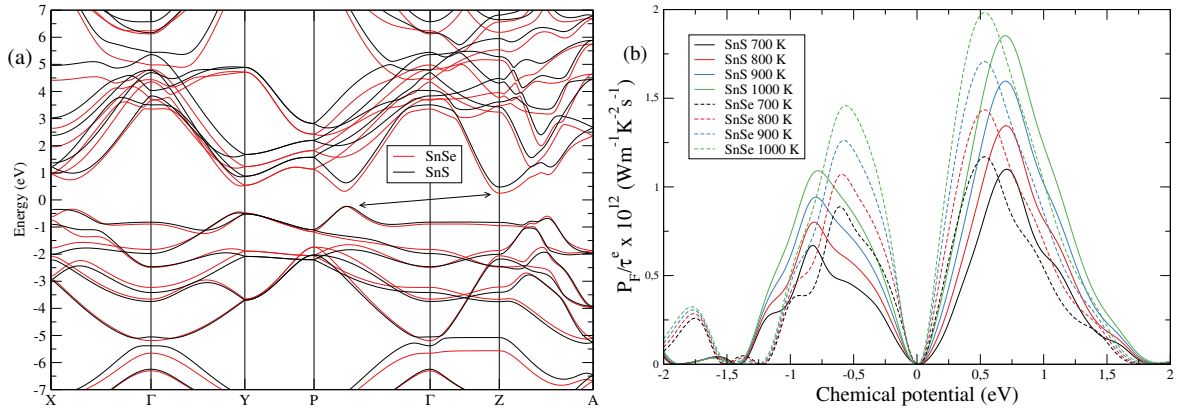

Figure 2. (a) Electronic band structure of *Cmcm* SnS and SnSe using experimental lattice parameters. (b) PF/τ^e of *Cmcm* SnS and SnSe for different temperatures as a function of the chemical potential. The 0 value corresponds to the middle of the gap in both figures.

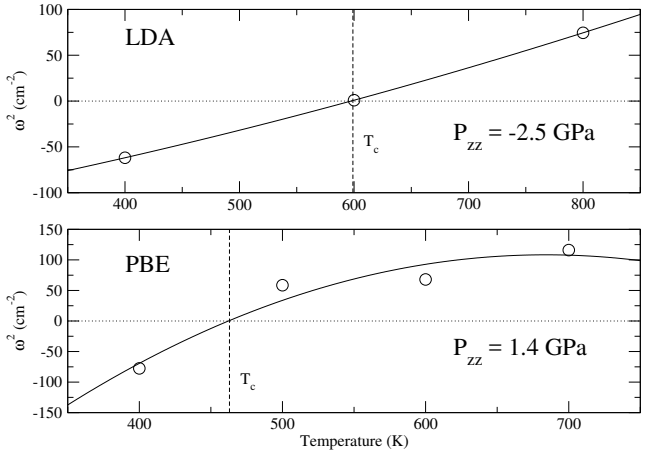

Figure 3. $\omega^2_{Y_1}$ as a function of temperature within LDA and PBE approximations using the experimental lattice parameters (circles). The solid lines correspond to a polynomial fit. We include the pressure component P_{zz}, which is the pressure in the direction where the atoms move in the transition. This pressure is calculated including the anharmonic vibrational energy within the SSCHA as discussed in Ref. 27.

perature T_c, which means that the *Pnma* phase is not any longer a minimum of the free energy and the structure distorts adopting the *Pnma* phase. T_c strongly depends on the approximation of the exchange-correlation functional: it is 600 K for LDA and 465 K for PBE. Our LDA calculation agrees better with the experimental value, around 900 K[17]. We associate the discrepancy between LDA and PBE to the different pressures obtained in the transition direction, P_{zz}. In fact, as shown in the case of SnSe[19], T_c depends strongly on the pressure in this z direction. The pressure in Figure 3 includes anharmonic vibrational effects on the energy following the procedure outlined in Ref. 27. For the same lattice parameter LDA displays a much smaller pressure, as generally LDA predicts smaller lattice volumes than PBE. The underestimation with respect to experiments may be attributed to the small supercell size used for the SSCHA calculations ($2\times2\times2$). Even if experimentally T_c is around 100 K higher in SnS than in SnSe, our LDA calculations give basically the same transition temperature for both materials as T_c = 616 K in SnSe according to our previous calculations[19]. However, within PBE SnSe does show a lower transition temperature since T_c = 299 K for SnSe K[19].

C. Anharmonic phonons

Figure 4 (a) compares the harmonic phonon spectrum with the anharmonic one calculated within the Lorentzian approximation at 800 K within the LDA. In the anharmonic spectrum shown the phonon energies correspond to the $\Omega_\mu(\mathbf{q})$ values of Eq. (18). The linewidth obtained in the Lorentzian approximation is also shown. The phonon spectrum suffers from a huge anharmonic renormalization. The harmonic spectrum shows broad instabilities, which are stabilized by anharmonicity. The Y_1 mode is unstable below the transition temperature, but it is stabilized after the transition. By having a look at the the phonon linewidths, we can see that two modes at the Γ point (Γ_1 and Γ_2) not only suffer a strong anharmonic renormalization, but they also have a large linewidth compared to the rest of the modes in the first Brillouin zone. These modes describe optical in-plane atomic displacements (see Figure 1, Γ_2 has the same atomic displacements as Γ_1 but in the other in-plane direction), which are the same atomic displacements of Y_2 and Y_3 at the point Y with a different periodicity due to the different momentum. The Y_2 and Y_3 in-plane modes also show a very large linewidth. On the contrary, the linewidth of mode Y_1 is not so large even if it is responsible for the phase transition (see Figure 1).

In strongly anharmonic materials[7,8,11,19,29,44], the

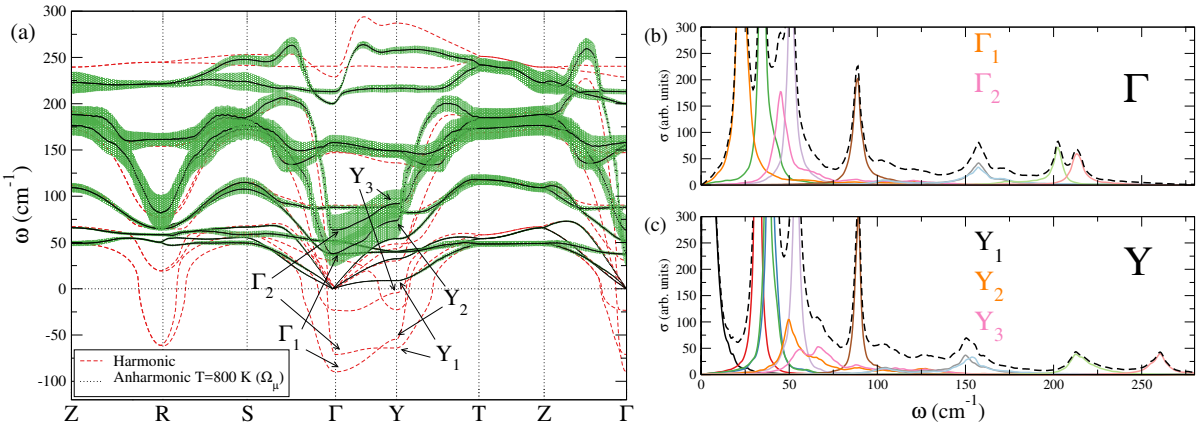

Figure 4. (a) Harmonic and anharmonic $[\Omega_\mu(\mathbf{q})]$ phonon spectra within the Lorentzian approximation. The length of the bars corresponds to the linewidth (full length of the line is the full width at half maximum). The calculations are done within the LDA using $\overset{(3)}{\mathbf{\Phi}}$ at 800 K and $\tilde{\Omega}_\mu(\mathbf{q})$ at 800 K. (b) and (c) $\sigma(\omega)$ spectral functions at the points Γ and Y, respectively, calculated as in Eq. (17). Solid lines correspond to individual modes and dashed lines are the total spectral functions.

phonon spectral functions $\sigma(\mathbf{q},\omega)$ show broad peaks, shoulders, and satellite peaks that cannot be captured by the simple Lorentzian picture. In Figure 4 (b) and (c) we show the spectral function keeping the full frequency dependence on the self-energy (see Eq. (17)). The calculation is done for the Γ and Y points. The great majority of the modes describe a Lorentzian shape. However, the modes with a large linewidth within the Lorentzian approximation (see Figure 4 (a)) are those that clearly deviate from the Lorentzian profile (Γ_1, Γ_2, Y_2, Y_3). This non-Lorentzian shape makes clear that these modes are strongly anharmonic and the frequency dependence of the self-energy is crucial to account for their spectral function. In this case, as we can see in in Figures 4 (b) and (c), the non-Lorentzian shapes of the strongly anharmonic modes do not create appreciable shoulders or satellite peak in the total spectral function, however, their contribution is far from trivial.

D. Lattice thermal transport

In Figure 5 (a) we show the lattice thermal conductivity of *Cmcm* SnS as a function of temperature calculated using $\overset{(3)}{\mathbf{\Phi}}$ and $\overset{(3)}{\boldsymbol{\phi}}$ for solving the BTE within the SMA. We recall that $\overset{(3)}{\mathbf{\Phi}}$ are non-perturbative third-order force-constants calculated using Eq. 7 and $\overset{(3)}{\boldsymbol{\phi}}$ are perturbative third-order force-constants calculated using Eq. 8. In Figure 5 (b) we show the lattice thermal conductivities of *Cmcm* SnS and SnSe using $\overset{(3)}{\mathbf{\Phi}}$. We can see that the non-perturbative calculation using $\overset{(3)}{\mathbf{\Phi}}$ is lower than the perturbative one using $\overset{(3)}{\boldsymbol{\phi}}$ for the three Cartesian directions. This result makes clear that the non-perturbative anharmonicity is very important to calculate the thermal conductivity in this kind of thermoelectric materials. By looking at the values of the lattice thermal conductivity we can see that both materials show very similar ultralow values, below ≈ 1.0 Wm^{-1}K^{-1}. In-plane results are slightly higher for SnSe and out-of-plane calculations higher for SnS, in agreements with another calculation[20] where the thermal conductivities of SnS and SnSe for the low-temperature *Pnma* phase are calculated with harmonic phonons and perturbative third-order force-constants. Theoretical calculations following the same procedure also show that the thermal conductivities of *Pnma* SnSe and SnS are very similar[23,45], in agreement with experiments[15,22]. Our calculations confirm that in the high-temperature *Cmcm* phase the thermal conductivity of these two compounds is also very similar. Both materials show a clear anisotropy between in-plane and out-of-plane calculations in agreement with experimental results[46] for the low-temperature phase close to the phase transition.

V. CONCLUSIONS

In conclusion, we have calculated the electronic and vibrational transport properties of *Cmcm* SnS using first-principles calculations. We have seen that the electronic transport properties of SnS and SnSe are comparable and that a similar power factor is expected for these isoelectronic and isostructural compounds. As in the case of SnSe, SnS suffers a second-order phase transition from the *Cmcm* to the *Pnma* phase driven by the collapse of a zone border phonon. We have also seen that SnS shows a strongly anharmonic phonon spectrum. Many phonon modes have a very large linewidth and show non-Lorentzian profiles in the spectral function. Finally, we have calculated the

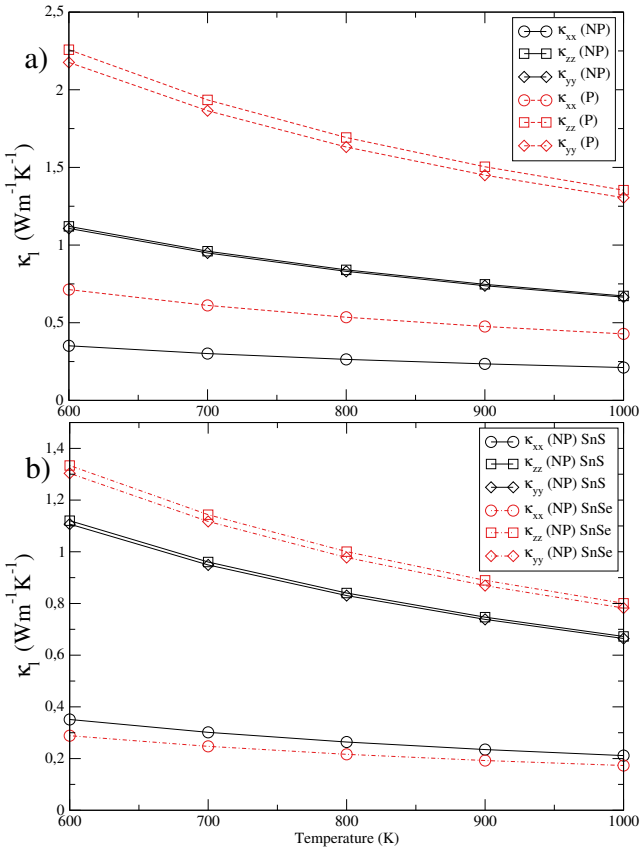

Figure 5. a) Lattice thermal conductivity of *Cmcm* SnS calculated within non-perturbative (NP) and perturbative (P) approaches. We have used $\tilde{\Omega}_\mu(\mathbf{q})$ at 800 K for both and $\overset{(3)}{\mathbf{\Phi}}$ at 800 K for the non-perturbative calculation in both cases. Calculations are within the LDA. b) Lattice thermal conductivity of *Cmcm* SnS and SnSe calculated within the non-perturbative (NP) approach.

lattice thermal conductivity of *Cmcm* SnS and we have seen that nonperturbative anharmonicity substantially corrects the third order force-constants. The thermal conductivity of both materials is very similar and ultralow. Therefore, by comparing the electronic and vibrational transport properties of SnS and SnSe in the *Cmcm* high-temperature phase, we conclude both should be good thermoelectrics. Thus, we suggest that SnS may be an earth-abundant very efficient high-temperature thermoelectric material. This work motivates more experimental effort in this regime for its characterization.

VI. ACKNOWLEDGMENTS

Financial support was provided by the Spanish Ministry of Economy and Competitiveness (FIS2016-76617-P); and the Department of Education, Universities and Research of the Basque Government and the University of the Basque Country (IT756-13). U.A. is also thankful to the Material Physics Center for a predoctoral fellowship. Computer facilities were provided by the Donostia International Physics Center (DIPC), PRACE (2017174186) and DARI (A0050901202).

[1] H. J. Goldsmid, *Introduction to thermoelectricity*, Vol. 121 (Springer, 2010).
[2] K. Behnia, *Fundamentals of thermoelectricity* (OUP Oxford, 2015).
[3] J. P. Heremans, V. Jovovic, E. S. Toberer, A. Saramat, K. Kurosaki, A. Charoenphakdee, S. Yamanaka, and G. J. Snyder, Science **321**, 554 (2008).
[4] Q. Zhang, B. Liao, Y. Lan, K. Lukas, W. Liu, K. Esfarjani, C. Opeil, D. Broido, G. Chen, and Z. Ren, Proceedings of the National Academy of Sciences **110**, 13261 (2013).
[5] S. H. Yang, T. Zhu, T. Sun, J. He, S. Zhang, and X. Zhao, Nanotechnology **19**, 245707 (2008).
[6] J. Cho, X. Shi, J. R. Salvador, G. P. Meisner, J. Yang, H. Wang, A. A. Wereszczak, X. Zhou, and C. Uher, Physical Review B **84**, 085207 (2011).
[7] O. Delaire, J. Ma, K. Marty, A. F. May, M. A. McGuire, M.-H. Du, D. J. Singh, A. Podlesnyak, G. Ehlers, M. Lumsden, *et al.*, Nature materials **10**, 614 (2011).
[8] C. W. Li, O. Hellam, J. May, A. F. May, H. B. Cao, X. Chen, A. D. Christianson, G. Thlers, D. J. Singh, and B. Sales, Phys. Rev. Lett. **112**, 175501 (2014).
[9] M. Iizumi, Y. Hamaguchi, K. F. Komatsubara, and Y. Kato, Journal of the Physical Society of Japan **38**, 443 (1975).
[10] C. D. O'Neill, D. A. Sokolov, A. Hermann, A. Bossak, C. Stock, and A. D. Huxley, Phys. Rev. B **95**, 144101 (2017).
[11] G. A. Ribeiro, L. Paulatto, R. Bianco, I. Errea, F. Mauri, and M. Calandra, Physical review B **97**, 014306 (2018).
[12] I. I. Ravich, *Semiconducting lead chalcogenides*, Vol. 5 (Springer Science & Business Media, 2013).
[13] K. F. Hsu, S. Loo, F. Guo, W. Chen, J. S. Dyck, C. Uher, T. Hogan, E. K. Polychroniadis, and M. G. Kanatzidis, Science **303**, 818 (2004), http://science.sciencemag.org/content/303/5659/818.full.pdf.
[14] D. M. Rowe, *Thermoelectrics handbook: macro to nano* (CRC press, 2018).

[15] L.-D. Zhao, S.-H. Lo, Y. Zhang, H. Sun, G. Tan, C. Uher, C. Wolverton, V. P. Dravid, and M. G. Kanatzidis, Nature **508**, 373 (2014).
[16] K. Adouby, Z. Kristallogr **213**, 343 (1998).
[17] T. Chattopadhyay, J. Pannetier, and H. Von Schnering, Journal of Physics and Chemistry of Solids **47**, 879 (1986).
[18] H. G. Von Schnering and H. Wiedemeier, Zeitschrift für Kristallographie-Crystalline Materials **156**, 143 (1981).
[19] U. Aseginolaza, R. Bianco, L. Monacelli, L. Paulatto, M. Calandra, F. Mauri, A. Bergara, and I. Errea, Physical Review Letters **122**, 075901 (2019).
[20] R. Guo, X. Wang, Y. Kuang, and B. Huang, Physical Review B **92**, 115202 (2015).
[21] W. He, D. Wang, J.-F. Dong, Y. Qiu, L. Fu, Y. Feng, Y. Hao, G. Wang, J. Wang, C. Liu, *et al.*, Journal of Materials Chemistry A **6**, 10048 (2018).
[22] Q. Tan, L.-D. Zhao, J.-F. Li, C.-F. Wu, T.-R. Wei, Z.-B. Xing, and M. G. Kanatzidis, Journal of Materials Chemistry A **2**, 17302 (2014).
[23] J. M. Skelton, L. A. Burton, S. C. Parker, A. Walsh, C.-E. Kim, A. Soon, J. Buckeridge, A. A. Sokol, C. R. A. Catlow, A. Togo, *et al.*, Physical review letters **117**, 075502 (2016).
[24] A. Dewandre, O. Hellman, S. Bhattacharya, A. H. Romero, G. K. Madsen, and M. J. Verstraete, Physical review letters **117**, 276601 (2016).
[25] I. Errea, M. Calandra, and F. Mauri, Physical Review B **89**, 064302 (2014).
[26] R. Bianco, I. Errea, L. Paulatto, M. Calandra, and F. Mauri, Physical Review B **96**, 014111 (2017).
[27] L. Monacelli, I. Errea, M. Calandra, and F. Mauri, Physical Review B **98**, 024106 (2018).
[28] T. J. Scheidemantel, C. Ambrosch-Draxl, T. Thonhauser, J. V. Badding, and J. O. Sofo, Phys. Rev. B **68**, 125210 (2003).
[29] R. Bianco, I. Errea, M. Calandra, and F. Mauri, Phys. Rev. B **97**, 214101 (2018).
[30] R. Bianco, I. Errea, L. Monacelli, M. Calandra, and F. Mauri, Nano Letters **19**, 3098 (2019), pMID: 30932501, https://doi.org/10.1021/acs.nanolett.9b00504.
[31] R. A. Cowley, Reports on Progress in Physics **31**, 123 (1968).
[32] A. Khitun and K. L. Wang, Applied Physics Letters **79**, 851 (2001), https://doi.org/10.1063/1.1391230.
[33] L. Paulatto, F. Mauri, and M. Lazzeri, Physical Review B **87**, 214303 (2013).
[34] J. P. Perdew and A. Zunger, Physical Review B **23**, 5048 (1981).
[35] J. P. Perdew, K. Burke, and M. Ernzerhof, Physical review letters **77**, 3865 (1996).
[36] P. Giannozzi, S. Baroni, N. Bonini, M. Calandra, R. Car, C. Cavazzoni, D. Ceresoli, G. L. Chiarotti, M. Cococcioni, I. Dabo, *et al.*, Journal of physics: Condensed matter **21**, 395502 (2009).
[37] P. Giannozzi, O. Andreussi, T. Brumme, O. Bunau, M. B. Nardelli, M. Calandra, R. Car, C. Cavazzoni, D. Ceresoli, M. Cococcioni, N. Colonna, I. Carnimeo, A. D. Corso, S. de Gironcoli, P. Delugas, R. A. DiStasio, A. Ferretti, A. Floris, *et al.*, Journal of Physics: Condensed Matter **29**, 465901 (2017).
[38] S. Baroni, S. De Gironcoli, A. Dal Corso, and P. Giannozzi, Reviews of Modern Physics **73**, 515 (2001).
[39] P. E. Blöchl, Physical review B **50**, 17953 (1994).
[40] G. K. Madsen and D. J. Singh, Computer Physics Communications **175**, 67 (2006).
[41] J. Vidal, S. Lany, M. d?Avezac, A. Zunger, A. Zakutayev, J. Francis, and J. Tate, Applied Physics Letters **100**, 032104 (2012).
[42] D. Orobengoa, C. Capillas, M. I. Aroyo, and J. M. Perez-Mato, Journal of Applied Crystallography **42**, 820 (2009).
[43] J. M. Perez-Mato, D. Orobengoa, and M. I. Aroyo, Acta Crystallographica Section A **66**, 558 (2010).
[44] L. Paulatto, I. Errea, M. Calandra, and F. Mauri, Physical Review B **91**, 054304 (2015).
[45] J. M. Skelton, L. A. Burton, A. J. Jackson, F. Oba, S. C. Parker, and A. Walsh, Physical Chemistry Chemical Physics **19**, 12452 (2017).
[46] D. Ibrahim, J.-B. Vaney, S. Sassi, C. Candolfi, V. Ohorodniichuk, P. Levinsky, C. Semprimoschnig, A. Dauscher, and B. Lenoir, Applied Physics Letters **110**, 032103 (2017).

Anharmonic melting of the charge density wave in single-layer $TiSe_2$

Jianqiang Sky Zhou,[1,*] Lorenzo Monacelli,[2] Raffaello Bianco,[3]
Ion Errea,[3,4,5] Francesco Mauri,[2,6] and Matteo Calandra[1,†]

[1] *Sorbonne Universitè, CNRS, Institut des Nanosciences de Paris, UMR7588, F-75252, Paris, France*
[2] *Dipartimento di Fisica, Università di Roma Sapienza, Piazzale Aldo Moro 5, I-00185 Roma, Italy*
[3] *Centro de Física de Materiales (CSIC-UPV/EHU), Manuel de Lardizabal pasealekua 5, 20018 Donostia-San Sebastián, Basque Country, Spain*
[4] *Fisika Aplikatua 1 Saila, Gipuzkoako Ingeniaritza Eskola, University of the Basque Country (UPV/EHU), Europa Plaza 1, 20018, Donostia-San Sebastián, Basque Country, Spain*
[5] *Donostia International Physics Center (DIPC), Manuel de Lardizabal pasealekua 4, 20018 Donostia-San Sebastián, Basque Country, Spain*
[6] *Graphene Labs, Fondazione Istituto Italiano di Tecnologia, Via Morego, I-16163 Genova, Italy*

(Dated: October 29, 2019)

Low dimensional systems with a vanishing band-gap and a large electron-hole interaction have been proposed to be unstable towards exciton formation. As the exciton binding energy increases in low dimension, conventional wisdom suggests that excitonic insulators should be more stable in 2D than in 3D. Here we study the effects of the electron-hole interaction and anharmonicity in single-layer $TiSe_2$. We find that, contrary to the bulk case and to the generally accepted picture, the electron-hole exchange interaction is much smaller in 2D than in 3D and it has negligible effects on phonon spectra. By calculating anharmonic phonon spectra within the stochastic self-consistent harmonic approximation, we obtain $T_{CDW}\approx$ 440K for an isolated and undoped single-layer and $T_{CDW}\approx$ 364K for an electron-doping $n = 4.6 \times 10^{13}$ cm^{-2}, close to the experimental result of $200-280$K on supported samples. Our work demonstrates that anharmonicity and doping melt the charge density wave in single-layer $TiSe_2$.

The occurrence of charge ordering in bulk $TiSe_2$ (see Fig. 1) and its possible interplay with electronic excitations has attracted increasing interest over the last years. Two scenarios for the occurrence of the charge density wave (CDW) have been proposed: the first one is purely electronic and is based on exciton condensation [1–5], while in the second the lattice plays a dominant role via the electron-phonon interaction [6–8]. However, both scenarios are incomplete, as there are currently no explanations of the strong temperature dependence of phonon spectra in the high-T [7] and low-T phases [9, 10] and of the magnitude of T_{CDW}. Surprisingly, little is known about anharmonicity and its effect on the CDW in $TiSe_2$.

From the theoretical point of view, it has been shown that harmonic calculations in bulk $TiSe_2$ including the electron-phonon interaction within density-functional perturbation theory (DFPT) [11] correctly reproduce the occurrence of a CDW with a $2\times2\times2$ periodicity [6, 8, 12]. However, the electronic structures of the high- and low-T phases as well as Raman and infrared spectra of the low-T phase at $T = 0$K can only be explained by including the electron-hole exchange interaction within hybrid functionals [8]. Density functional theory (DFT) with semi-local kernels leads to a metallic electronic structure, in disagreement with the angle-resolved photoemission spectroscopy (ARPES) experiments [6, 12, 13] that show a weakly doped semiconductor in both phases. Moreover, they underestimate the square of the electron-phonon deformation potential of a factor of 3 [8].

Recently, single-layer $TiSe_2$ was synthesized either by exfoliation or molecular beam epitaxy (MBE). It displays a 2×2 CDW with a T_{CDW} that is enhanced with respect to the bulk case ($T_{CDW}^{bulk} \approx 200$K) and is strongly substrate dependent [14–20]: single-layer $TiSe_2$ on top of insulating MoS_2 has $T_{CDW}=$ 280K [14], while on top of n-doped bilayer graphene or highly oriented pyrolytic graphite (HOPG) [14, 18–20] $T_{CDW}= 200-230$K. This strong variability of T_{CDW} has been tentatively ascribed to the different substrate dielectric constants in possible relation with an excitonic insulator picture [14]. Indeed, as the exciton binding energy increases in low dimension [1–4, 21], conventional wisdom suggests that excitonic insulators should be more stable in 2D than in 3D. However, other effects such as charge transfer from the substrate, the non-stoichiometry due to Se vacancies or doping could be very relevant. From theory, on the one hand the T_{CDW} of $TiSe_2$ monolayer has up to now only been estimated from a variation of the electronic temperature T_e. At the harmonic level this assumption predicts a $T_{CDW}\approx$ 1195K within PBE and $T_{CDW}\approx$ 1920K by including the exchange interaction via HSE06 [22], in complete disagreement with the experimental data and leading to an incorrect estimation of T_{CDW} of at least a factor of 5. On the other hand, little is known about the effects of electron-hole exchange interaction on the vibrational properties of single-layer $TiSe_2$ and its dependence on doping. It has been shown that, neglecting the spin-orbit coupling, semi-local functionals are successful in reproducing the semiconducting state of the low-T phase [23], contrary to what happens in the bulk case.

In this work we study the anharmonic phonon spectra of an isolated single-layer $TiSe_2$ within the stochastic self-consistent harmonic approximation (SSCHA) [24–27] that has been successfully applied to study the an-

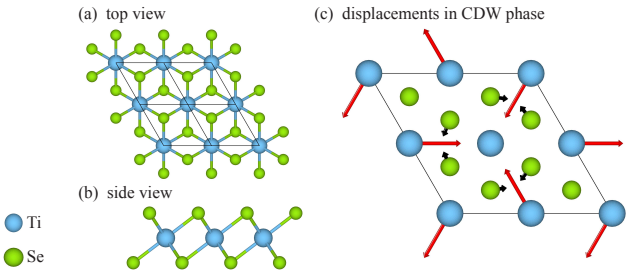

FIG. 1. (a) and (b): top and side schematic views of crystal structure of monolayer $TiSe_2$ in the high-T phase on a 2×2 cell. (c): top view of the atomic displacements of the low-T phase (i.e., the CDW phase) with respect to the high-T phase. Blue and green balls represent Ti and Se atoms, respectively.

harmonicity of other transition metal dichalcogenides [28, 29]. In particular, by including the exchange interaction via semi-local and hybrid functionals [30], we determine the CDW transition and demonstrate that its melting is determined by the combined effect of phonon-phonon scattering and electron doping and not by an excitonic mechanism.

ARPES measurements show that the high-T phase of single-layer $TiSe_2$ is a weakly n-doped semiconductor [18, 19, 31] with a 0.098 eV indirect band gap between the Γ (i.e., derived from Se $4p_{xy}$ states) and M (i.e., derived from Ti $3d$ states) points in the Brillion zone (BZ). In Fig. 2 (a) the calculated electronic band structures in both PBE and HSE06 approximations are presented. PBE predicts a metallic state with a negative band gap of -0.45 eV between the Γ and M points in BZ, in good agreement with previous calculations [23, 32, 33] but in disagreement with ARPES. The HSE06 yields a positive band gap of 0.092 eV, in perfect agreement with ARPES.

The PBE and HSE06 harmonic phonon dispersion are very similar, despite a different electronic structure, as shown in Fig. 2 (b). The A_{1u} mode at the M point is strongly unstable (imaginary phonon frequencies are represented as negative values in all dispersion plots), indicating formation of a 2×2 superstructure. The two functionals lead to ≈ 20 cm^{-1} (i.e., 12%) difference in the A_{1u} imaginary phonon frequency. Other modes at higher energy suffer of a somewhat stronger renormalization. In order to understand if the effect of exchange on the CDW is small, we also calculate the energy gain with respect to the displacement of Ti atoms corresponding to the CDW pattern (see Fig. 1) using the experimental ratio δTi/δSe = 3 [20, 34], as shown in the inset of Fig. 2 (b). Again, the two approximations yield a similar minimum indicating a similar CDW instability, which eventually confirms the negligible effect of electron-hole exchange in the soft-mode harmonic phonon bands. Interestingly, also the position of the energy minimum versus δTi is practically the same, indicative of an akin CDW structure. Note that in bulk $TiSe_2$, the energy gain for a distortion having modulation $\mathbf{q} = \mathbf{\Gamma L}$ in HSE06 is approximately three times larger than the PBE one [8] and the minimum occurs at substantially larger δTi in HSE06 than in PBE.

This puzzling difference between bulk and single layer can be understood by noting that in the former the strong electron-hole interaction is between the $4p_{xy}$ occupied states at zone center and some of the empty Ti $3d$ states at the L point. In the bulk, for a distortion having periodicity $\mathbf{q} = \mathbf{\Gamma M}$ (i.e., all the $TiSe_2$ layers distort in phase), and coupling the Brillouin zone regions around the A point with those around the L point, the energy gain by the distortion is reversed with respect to the case of a distortion having modulation $\mathbf{q} = \mathbf{\Gamma L}$, namely the PBE energy gain is much larger than the HSE06 one [22]. Thus, in the bulk, the exchange interaction effects depend crucially on the modulation of the distortion and on the electronic states involved. In the single layer, the electronic structure of the high-T phase along ΓM is very similar to the one of the undistorted bulk along the A-L line, with Γ and M in the single layer corresponding A and L in the bulk. For this reason, the effect of the exchange interaction on the phonon dispersion is much weaker for a $\mathbf{q} = \mathbf{\Gamma M}$ modulation in the single layer than for the case of a $\mathbf{q} = \mathbf{\Gamma L}$ distortion on the bulk. On top of that, other effects contribute to the different energy gain by the $\mathbf{q} = \mathbf{\Gamma M}$ distortion in bulk and single layer, such as the weak but non-negligible band dispersion along k_z close to the A and L high symmetry points in the bulk and the slightly different fillings of the Ti d-band at L in the bulk and M in the single layer. This explains why in single layer the effects of exchange on the charge density wave distortion are negligible and demonstrates how simple arguments based on isotropic coulomb interactions [1–4, 21] do not apply easily in layered materials with weak interlayer binding, such as $TiSe_2$.

Even if the two functionals give practically identical energy versus displacement profiles, this is not enough to conclude that the exchange interaction is irrelevant for the soft mode at the anharmonic level. For this purpose, we calculate the phonon dispersion including non-perturbative anharmonic effects within the SSCHA using both HSE06 and PBE as force engines. Namely, we evaluate the temperature dependent dynamical matrix $\boldsymbol{\mathcal{D}} = \mathbf{M}^{-\frac{1}{2}} \left. \frac{\partial^2 F}{\partial \boldsymbol{\mathcal{R}} \partial \boldsymbol{\mathcal{R}}} \right|_{\boldsymbol{\mathcal{R}}_{eq}} \mathbf{M}^{-\frac{1}{2}}$ where $\mathbf{M}$ is the matrix of the ionic masses M_a with $M_{ab} = \delta_{ab} M_a$ within the SSCHA. The free energy curvature with respect to the vector of the centroid positions $\boldsymbol{\mathcal{R}}$ reads [25]:

$$\frac{\partial^2 F}{\partial \boldsymbol{\mathcal{R}} \partial \boldsymbol{\mathcal{R}}} = \mathbf{\Phi} + \overset{(3)}{\mathbf{\Phi}} \mathbf{\Lambda}(0) \overset{(3)}{\mathbf{\Phi}} + \overset{(3)}{\mathbf{\Phi}} \mathbf{\Lambda}(0) \mathbf{\Theta} \mathbf{\Lambda}(0) \overset{(3)}{\mathbf{\Phi}} , \qquad (1)$$

where $\mathbf{\Phi}$ represents the SSCHA force constant, $\overset{(3)}{\mathbf{\Phi}} \mathbf{\Lambda}(0) \overset{(3)}{\mathbf{\Phi}}$ is the so-called "static bubble term", and $\overset{(3)}{\mathbf{\Phi}} \mathbf{\Lambda}(0) \mathbf{\Theta} \mathbf{\Lambda}(0) \overset{(3)}{\mathbf{\Phi}}$ contains the higher order terms. Here $\overset{(n)}{\mathbf{\Phi}}$ refers to the n-th order anharmonic force constants averaged over the density matrix of the SSCHA hamiltonian (see Ref. [25] for more details on notation). All

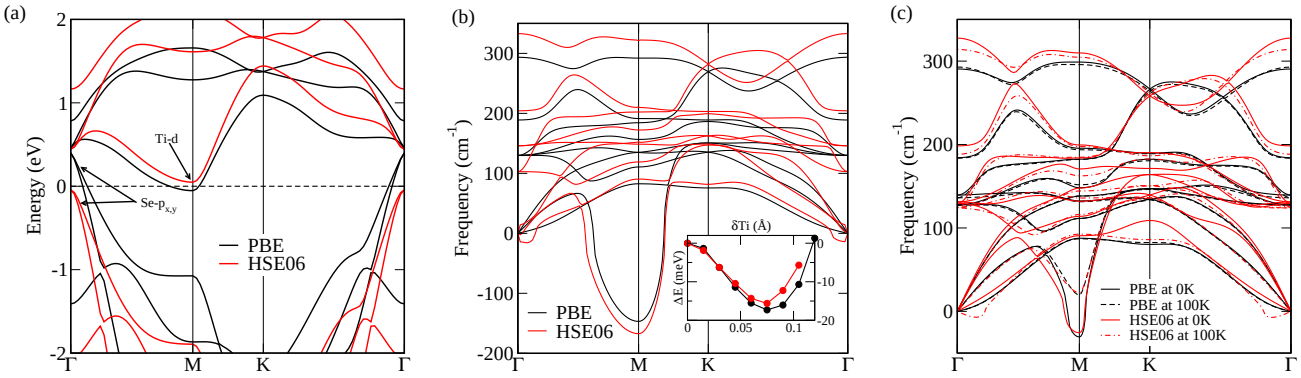

FIG. 2. (a) Electronic bands from PBE and HSE06 approximations. (b) The harmonic phonon bands calculated on a 4×4 supercell and the energy gain as a function of δTi where ΔE is the energy difference per 2×2 cell. (c) The anharmonic phonon dispersion on a 4×4 supercell at 0 and 100 Kelvin from PBE and HSE06 force engines. PBE and HES06 results are obtained from `QUANTUM ESPRESSO` and `CRYSTAL`, respectively.

these quantities can indeed be recasted as appropriate stochastic averages over the atomic forces. As the HSE06 calculation is computationally expensive, we perform the calculation on a 4×4 supercell (i.e., 48 atoms). Even if this supercell size is not completely converged and T_{CDW} is underestimated, as it will be shown later, it is clear from Fig. 2 (c) that PBE and HSE06 yield practically the same low energy dispersion around the M point even with full inclusion of anharmonicity. Moreover, the temperature dependence of the soft mode is also very similar, indicative of a practically identical T_{CDW} (i.e., identified as the point where the energy of the soft phonon at M crosses zero) for the two functionals on the 4×4 cell. Other phonon modes, particularly around zone center, suffer of a somewhat stronger renormalization by exchange (analogous to the harmonic case), however, as we are mainly interested in the CDW transition, we can stick to the PBE functional and proceed with calculations on larger supercells (see [22] for additional technical details and the magnitude of the different terms in Eq. (1)).

The anharmonic phonon spectrum obtained by evaluating Eq. (1) on a 8×8 supercell (i.e., 192 atoms) for several temperatures is shown in Fig. 3. As it can be seen, the harmonic phonon frequency of the lowest energy mode at M is $\omega_{A_{1u}} \approx -135$ cm^{-1}, while at 300K the anharmonic phonon frequency of the same mode is ≈ -26 cm^{-1}. Thus, already at room temperature, the anharmonic correction is of the same order of the harmonic phonon frequency. Between 400 and 500K, this phonon mode becomes positive, compatible with a CDW transition within this temperature range. Note that this transition temperature differs substantially with respect to the one on a 4×4 supercell which reflects the importance of cell size. To better illustrate this point, in the inset of Fig. 3 we show the convergence of the soft mode phonon frequency as a function of the cell size at 300K. The A_{1u} phonon frequency at M is fully converged on the 8×8 cell [22]. We can then obtain $T_{CDW} \approx$ 440K for a

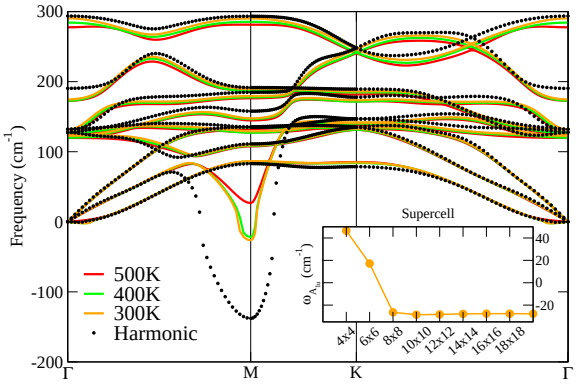

FIG. 3. Harmonic and anharmonic phonon dispersion on a 8×8 supercell. Inset: the convergence of the lowest phonon frequency at the M point $\omega_{A_{1u}}$ with respect to the size of the cell at 300K. The results of the cell larger than 8×8 come from the interpolation method detailed in [22].

suspended and undoped monolayer $TiSe_2$.

Our calculated T_{CDW} from first-principles SSCHA is 1.6-2.0 times higher than the measured one (depending on the substrate [14–16, 35]). However, our calculation is for an undoped isolated monolayer, the measured samples are instead supported by the substrate and substantially n-doped. In order to understand the origin of this discrepancy, we investigate the effect of electron-doping to see if it can be responsible for the decrease in T_{CDW}. To this end, we first determine the electron doping amount by performing HSE06 n-doped electronic structure calculations by changing the number of valence electrons and adding a compensating jellium (i.e., the virtual crystal approximation (VCA)) until the bands agree well with the ARPES spectra [19] (see [22] for details). With this electron density (i.e., 4.6×10^{13} cm^{-2} indicative of a substantial doping), we then perform a PBE linear response harmonic calculation to obtain the harmonic phonon dispersion shown in Fig. 4. It turns out that the harmonic

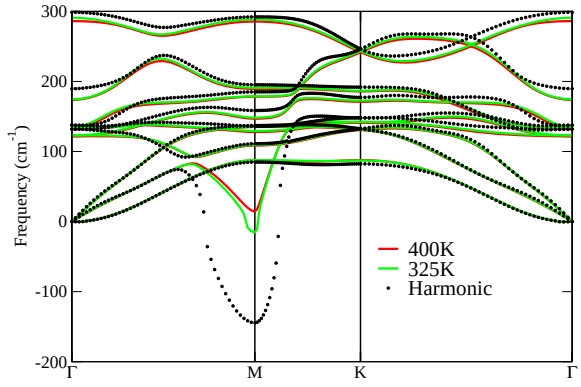

FIG. 4. Harmonic and anharmonic phonon spectra for doped ($n = 4.6 \times 10^{13}$cm^{-2}) samples calculated on a 8×8 supercell.

phonon dispersion (and consequently the effects of the electron-phonon interaction) are doping independent at this level of doping (by comparing the two black dotted curves in Figs. 3 and 4), consistent with an earlier study [23]. However, when anharmonicity is included, the electron-doping substantially suppresses the CDW instability as illustrated in Fig. 4 leading to $T_{CDW} \approx$ 364K for a suspended $TiSe_2$ monolayer, close to the experimental data of 280K on insulating MoS_2 substrate [14].

In conclusion, we study anharmonic effects in a free-standing $TiSe_2$ monolayer within the stochastic self-consistent harmonic approximation. We have shown that the electron-hole exchange plays only a marginal role on the vibrational properties of its high-T phase, at odds with its bulk counterpart where the exchange interaction is crucial. We showed that the weakening of the electron-hole interaction in single layer is related to the different periodicity of the modulation with respect to the bulk and the fact that it couples different states in the electronic structure. Our results upturns the conventional wisdom that the electron-hole interaction should be stronger in low dimension due to an increase in binding energy [1–4, 21], mainly because of the strong momentum dependence of the electron-hole interaction and the complex multiband nature of the electronic structure in $TiSe_2$. It also underlines that simple qualitative arguments based on the exciton binding energy and its dependence on the effective mass and on the screening (see Eq. (1) in Ref. [1]) do not easily apply since they are unable to explain the occurrence of charge density waves and the temperature dependence of phonon spectra when reducing the dimensionality.

By studying the temperature dependence of the A_{1u} soft mode at the M point, we find the T_{CDW} of an isolated and undoped single-layer to be $\approx$ 440K, while $T_{CDW} \approx$ 364K for an electron-doping $n = 4.6 \times 10^{13}$ cm^{-2}, close to the experimental value for supported sample. Thus, T_{CDW} is strongly doping dependent when including anharmonicity, an effect completely absent at the harmonic level as harmonic spectra are weakly doping dependent. Our work establishes phonon-phonon scattering and the density of carriers in the conduction band as the two mechanisms determining the melting of CDW in a single-layer $TiSe_2$.

Computational resources were granted by PRACE (Project No. 2017174186) and from IDRIS, CINES and TGCC (Grant eDARI 91202 and Grand Challenge Jean Zay). We acknowledge support from the Graphene Flaghisp core 2 (Grant No. 785219) and Agence nationale de la recherche (Grant No. ANR-17-CE24-0030). F. M. and L. M. acknowledge support by the MIUR PRIN-2017 program, project number 2017Z8TS5B. I.E. acknowledges financial support from the Spanish Ministry of Economy and Competitiveness (FIS2016-76617-P). We acknowledge U. Aseguinolaza for useful discussions.

* zhou@insp.jussieu.fr
† matteo.calandra@upmc.fr

[1] D. Sherrington and W. Kohn, Rev. Mod. Phys. **40**, 767 (1968).
[2] L. V. Keldish and A. N. Kozlov, Sov. Phys. JETP **27**, 521 (1968).
[3] Y. V. Keldysh, L. V. & Kopaev, Fiz. Tverd. Tela **6**, 2791 (1964), [Sov. Phys. Solid State 6, 2219 (1965)].
[4] D. Jérome, T. M. Rice, and W. Kohn, Phys. Rev. **158**, 462 (1967).
[5] A. Kogar, M. S. Rak, S. Vig, A. A. Husain, F. Flicker, Y. I. Joe, L. Venema, G. J. MacDougall, T. C. Chiang, E. Fradkin, J. van Wezel, and P. Abbamonte, Science (New York, N.Y.) **358**, 1314 (2017).
[6] M. Calandra and F. Mauri, Phys. Rev. Lett. **106**, 196406 (2011).
[7] F. Weber, S. Rosenkranz, J.-P. Castellan, R. Osborn, G. Karapetrov, R. Hott, R. Heid, K.-P. Bohnen, and A. Alatas, Phys. Rev. Lett. **107**, 266401 (2011).
[8] M. Hellgren, J. Baima, R. Bianco, M. Calandra, F. Mauri, and L. Wirtz, Phys. Rev. Lett. **119**, 176401 (2017).
[9] J. A. Holy, K. C. Woo, M. V. Klein, and F. C. Brown, Phys. Rev. B **16**, 3628 (1977).
[10] C. S. Snow, J. F. Karpus, S. L. Cooper, T. E. Kidd, and T.-C. Chiang, Phys. Rev. Lett. **91**, 136402 (2003).
[11] S. Baroni, S. de Gironcoli, A. Dal Corso, and P. Giannozzi, Rev. Mod. Phys. **73**, 515 (2001).
[12] R. Bianco, M. Calandra, and F. Mauri, Phys. Rev. B **92**, 094107 (2015).
[13] T. Rohwer, S. Hellmann, M. Wiesenmayer, C. Sohrt, A. Stange, B. Slomski, A. Carr, Y. Liu, L. M. Avila, M. Kalläne, S. Mathias, L. Kipp, K. Rossnagel, and M. Bauer, Nature **471**, 490 (2011).
[14] S. Kolekar, M. Bonilla, Y. Ma, H. C. Diaz, and M. Batzill, 2D Materials **5**, 015006 (2018).
[15] H. Wang, Y. Chen, M. Duchamp, Q. Zeng, X. Wang, S. H. Tsang, H. Li, L. Jing, T. Yu, E. H. T. Teo, and Z. Liu, Advanced Materials **30**, 1704382 (2018).
[16] L. J. Li, E. C. T. O'Farrell, K. P. Loh, G. Eda, B. Özyilmaz, and A. H. Castro Neto, Nature **529**, 185 (2016).

[17] D. L. Duong, G. Ryu, A. Hoyer, C. Lin, M. Burghard, and K. Kern, ACS Nano **11**, 1034 (2017).

[18] K. Sugawara, Y. Nakata, R. Shimizu, P. Han, T. Hitosugi, T. Sato, and T. Takahashi, ACS Nano **10**, 1341 (2016), pMID: 26624791, https://doi.org/10.1021/acsnano.5b06727.

[19] P. Chen, Y. H. Chan, X. Y. Fang, Y. Zhang, M. Y. Chou, S. K. Mo, Z. Hussain, A. V. Fedorov, and T. C. Chiang, Nature Communications **6**, 8943 (2015).

[20] X.-Y. Fang, H. Hong, P. Chen, and T.-C. Chiang, Phys. Rev. B **95**, 201409 (2017).

[21] D. Jérome, T. M. Rice, and W. Kohn, Phys. Rev. **158**, 462 (1967).

[22] See Supplementary material for theoretical and computational details and for additional results.

[23] B. Guster, E. Canadell, M. Pruneda, and P. Ordejón, 2D Materials **5**, 025024 (2018).

[24] I. Errea, M. Calandra, and F. Mauri, Phys. Rev. Lett. **111**, 177002 (2013).

[25] R. Bianco, I. Errea, L. Paulatto, M. Calandra, and F. Mauri, Phys. Rev. B **96**, 014111 (2017).

[26] I. Errea, M. Calandra, and F. Mauri, Phys. Rev. B **89**, 064302 (2014).

[27] L. Monacelli, I. Errea, M. Calandra, and F. Mauri, Phys. Rev. B **98**, 024106 (2018).

[28] U. Aseginolaza, R. Bianco, L. Monacelli, L. Paulatto, M. Calandra, F. Mauri, A. Bergara, and I. Errea, Phys. Rev. Lett. **122**, 075901 (2019).

[29] R. Bianco, I. Errea, L. Monacelli, M. Calandra, and F. Mauri, Nano Letters **19**, 3098 (2019), pMID: 30932501, https://doi.org/10.1021/acs.nanolett.9b00504.

[30] First-principles calculations are carried out using the bulk experimental lattice parameter ($a = 3.5398$ Å) [36]. This value agrees well with the one for single-layer $TiSe_2$ on top of bilayer graphene [19, 37]. The difference between the theoretical PBE ($a_{\mathrm{PBE}} = 3.5337$) and HSE06 ($a_{\mathrm{HSE06}} = 3.5546$) lattice parameters and experiments is below 0.2% and 0.6%, thus, marginal. We include a 12.01 Å vacuum region in out-of-plane direction to avoid interaction between periodic images. The atomic positions are fully relaxed using the PBE [38] and HSE06 [39, 40] approximations within DFT as implemented in `QUANTUM ESPRESSO` [41, 42] and `CRYSTAL` [43] packages, respectively. The harmonic phonon bands are computed within DFPT [11] in `QUANTUM ESPRESSO` and finite differences from analytic forces in `CRYSTAL`. Both codes give practically the same electronic and harmonic phonon bands at the PBE level. Anharmonic effects at non-perturbative level are obtained within SSCHA [24–27]. Additional computational details can be found in the supplemental material [22]. Finally, we neglect the spin-orbit coupling (SOC) as its effect on the phonon dispersion is marginal [22].

[31] P. Chen, Y.-H. Chan, M.-H. Wong, X.-Y. Fang, M. Y. Chou, S.-K. Mo, Z. Hussain, A.-V. Fedorov, and T.-C. Chiang, Nano Letters **16**, 6331 (2016), pMID: 27648493, https://doi.org/10.1021/acs.nanolett.6b02710.

[32] B. Singh, C.-H. Hsu, W.-F. Tsai, V. M. Pereira, and H. Lin, Phys. Rev. B **95**, 245136 (2017).

[33] D. Pasquier and O. V. Yazyev, Phys. Rev. B **98**, 235106 (2018).

[34] F. J. Di Salvo, D. E. Moncton, and J. V. Waszczak, Phys. Rev. B **14**, 4321 (1976).

[35] L. Sun, C. Chen, Q. Zhang, C. Sohrt, T. Zhao, G. Xu, J. Wang, D. Wang, K. Rossnagel, L. Gu, C. Tao, and L. Jiao, Angewandte Chemie International Edition **56**, 8981 (2017).

[36] C. Riekel, Journal of Solid State Chemistry **17**, 389 (1976).

[37] J.-P. Peng, J.-Q. Guan, H.-M. Zhang, C.-L. Song, L. Wang, K. He, Q.-K. Xue, and X.-C. Ma, Phys. Rev. B **91**, 121113 (2015).

[38] J. P. Perdew, K. Burke, and M. Ernzerhof, Phys. Rev. Lett. **77**, 3865 (1996).

[39] J. Heyd, G. E. Scuseria, and M. Ernzerhof, The Journal of Chemical Physics **118**, 8207 (2003), https://doi.org/10.1063/1.1564060.

[40] A. V. Krukau, O. A. Vydrov, A. F. Izmaylov, and G. E. Scuseria, The Journal of Chemical Physics **125**, 224106 (2006), https://doi.org/10.1063/1.2404663.

[41] P. Giannozzi, S. Baroni, N. Bonini, M. Calandra, R. Car, C. Cavazzoni, D. Ceresoli, G. L. Chiarotti, M. Cococcioni, I. Dabo, A. D. Corso, S. de Gironcoli, S. Fabris, G. Fratesi, R. Gebauer, U. Gerstmann, C. Gougoussis, A. Kokalj, M. Lazzeri, L. Martin-Samos, N. Marzari, F. Mauri, R. Mazzarello, S. Paolini, A. Pasquarello, L. Paulatto, C. Sbraccia, S. Scandolo, G. Sclauzero, A. P. Seitsonen, A. Smogunov, P. Umari, and R. M. Wentzcovitch, Journal of Physics: Condensed Matter **21**, 395502 (2009).

[42] P. Giannozzi, O. Andreussi, T. Brumme, O. Bunau, M. B. Nardelli, M. Calandra, R. Car, C. Cavazzoni, D. Ceresoli, M. Cococcioni, N. Colonna, I. Carnimeo, A. D. Corso, S. de Gironcoli, P. Delugas, R. A. DiStasio, A. Ferretti, A. Floris, G. Fratesi, G. Fugallo, R. Gebauer, U. Gerstmann, F. Giustino, T. Gorni, J. Jia, M. Kawamura, H.-Y. Ko, A. Kokalj, E. Kçkbenli, M. Lazzeri, M. Marsili, N. Marzari, F. Mauri, N. L. Nguyen, H.-V. Nguyen, A. O. de-la Roza, L. Paulatto, S. Poncé, D. Rocca, R. Sabatini, B. Santra, M. Schlipf, A. P. Seitsonen, A. Smogunov, I. Timrov, T. Thonhauser, P. Umari, N. Vast, X. Wu, and S. Baroni, Journal of Physics: Condensed Matter **29**, 465901 (2017).

[43] R. Dovesi, A. Erba, R. Orlando, C. M. Zicovich-Wilson, B. Civalleri, L. Maschio, M. Rrat, S. Casassa, J. Baima, S. Salustro, and B. Kirtman, Wiley Interdisciplinary Reviews: Computational Molecular Science **8**
https://onlinelibrary.wiley.com/doi/pdf/10.1002/wcms.1360.

THE JOURNAL OF PHYSICAL CHEMISTRY Letters

Letter

pubs.acs.org/JPCL

Manipulating Impulsive Stimulated Raman Spectroscopy with a Chirped Probe Pulse

Lorenzo Monacelli,[†] Giovanni Batignani,[†,‡] Giuseppe Fumero,[†,§] Carino Ferrante,[†] Shaul Mukamel,[∥] and Tullio Scopigno*[,†,⊥]

[†]Dipartimento di Fisica, Universitá di Roma "La Sapienza", Roma I-00185, Italy

[‡]Dipartimento di Scienze Fisiche e Chimiche, Universitá degli Studi dell'Aquila, L'Aquila I-67100, Italy

[§]Dipartimento di Scienze di Base e Applicate per l'Ingegneria, Universitá di Roma "La Sapienza", Roma I-00185, Italy

[∥]Department of Chemistry, University of California, Irvine, California 92697-2025, United States

[⊥]Istituto Italiano di Tecnologia, Center for Life Nano Science @Sapienza, Roma I-00161, Italy

Supporting Information

ABSTRACT: Photophysical and photochemical processes are often dominated by molecular vibrations in various electronic states. Dissecting the corresponding, often overlapping, spectroscopic signals from different electronic states is a challenge hampering their interpretation. Here we address impulsive stimulated Raman spectroscopy (ISRS), a powerful technique able to coherently stimulate and record Raman-active modes using broadband pulses. Using a quantum-mechanical treatment of the ISRS process, we show the mode-specific way the various spectral components of the broadband probe contribute to the signal generated at a given wavelength. We experimentally demonstrate how to manipulate the signal by varying the probe chirp and the phase-matching across the sample, thereby affecting the relative phase between the various contributions to the signal. These novel control knobs allow us to selectively enhance desired vibrational features and distinguish spectral components arising from different excited states.

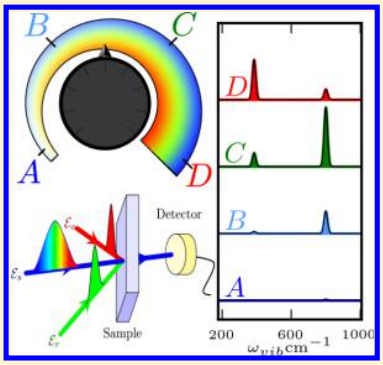

Ultrafast spectroscopy aims to study nonequilibrium atomic and molecular dynamics in the gas phase or the condensed phase on the femtosecond time scale.[1] This is most simply achieved by the pump−probe technique: an actinic pump beam prepares the sample in a nonstationary superposition state, while the transmission of a delayed probe subsequently reveals the state of the system at a given instant following photoexcitation. Ultrafast spectroscopy has witnessed a significant growth during the last two decades thanks to the development of temporal compression techniques, able to synthesize optical pulses with a few femtosecond duration and Fourier-transform-limited bandwidth.[2] This is a key tool for several spectroscopic approaches based on multiple pulses sequences, such as impulsive stimulated Raman spectroscopy (ISRS).[3−5]

The ISRS experiment exploits a time-domain *probe* protocol consisting of two temporally separated laser fields, the Raman and the probe pulses, to stimulate and read out vibrational coherences on a given electronic state, respectively. Consequently, it is not hampered by the background signals induced by the temporal overlap of multiple pulses, commonly affecting other kinds of ultrafast experiments.[6,7] The ISRS signal records the changes in the transmitted probe pulse as a function of its temporal delay with respect to the Raman pulse, T, and its wavelength λ_s, thereby resulting in a 2D signal. Fourier transforming over T recovers the spontaneous Raman spectrum. The heterodyne detection of ISRS spectra, engraved onto the highly directional probe field, suppresses fluorescence and other incoherent processes. The addition of a photochemical actinic *pump* allows for mapping out vibrational dynamics, triggering the system photoreaction with high temporal resolution.[8]

The power of ISRS has been recently demonstrated by investigating prototypical cases of photoinduced dynamics in Bacteriorhodopsin,[9] intermolecular vibrational motions in liquid CS_2,[10] isomerization of Channelrhodopsins,[11] and the excited-state proton transfer of green fluorescent protein.[12] The ISRS probing process is, in general, affected by concurring vibrational coherences from both the ground and excited states, and discerning the two is a most challenging task. Much effort has been made in this direction.[6] Strategies to identify the electronic state hosting a vibrational coherence at its generation have been proposed based on temporal dispersion by introducing a chirped resonant pump pulse.[13−15] Furthermore, ISRS extension to study the presence of electronic coherences in the X-ray domain[16,17] has been theoretically demonstrated.

Received: December 23, 2016
Accepted: February 8, 2017
Published: February 8, 2017

DOI: 10.1021/acs.jpclett.6b03027
J. Phys. Chem. Lett. 2017, 8, 966−974

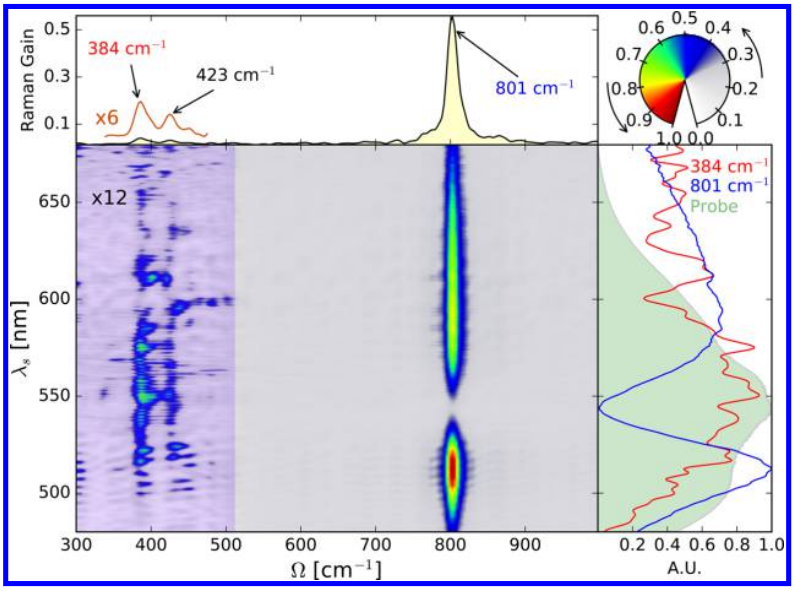

Figure 1. 2D broadband ISRS spectrum of cyclohexane as a function of the probe wavelength and the Raman frequency. The intensity of the 800 cm^{-1} mode exhibits a minimum in correspondence of the maximum probe intensity (reported in the right panel as green shaded area), with two maxima on the red and the blue sides of the probe central wavelength. The 384 cm^{-1} mode shows an opposite behavior, with the maximum in the center position. The top panel shows the marginal spectrum obtained by integrating over all probe wavelengths. The amplitude of the 384 and 800 cm^{-1} modes as a function of the probe wavelength is reported in the right panel (red and blue lines, respectively).

Here we study a three-beam experimental ISRS configuration. We start by a photoexcitation using a resonant actinic pulse (AP), followed by an ISRS detection, which combines an off-resonant Raman pulse (RP) and, critically, a properly shaped, chirped, broadband white-light continuum (WLC) probe. This allows us to unveil the undetermined population states following the photoreaction process triggered by the AP. Keeping the Raman pulse electronically off-resonant guarantees that the vibrational coherence is solely generated in the electronic state manifold involved in the photoreaction process, preventing contributions arising from additional electronic resonances. Moreover, taking advantage of a chirped WLC probe pulse provides access to the higher frequency region of the Raman spectrum (compared with a noncollinear optical parametric amplifier-based probe) without compromising the temporal resolution.[18] Last, but not least, introducing nonresonant chirped WLC, we demonstrate mode-selective enhancement of the ISRS signal.

We theoretically describe ISRS signals and their variation with the scattering geometry, elucidating the role of the phase-matching condition and the effect of a strongly chirped probe pulse. The response of the system is derived using a perturbative framework based on the diagrammatic expansion of the density matrix,[19,20] which allows us to take into account individually all of the nonlinear processes underlying the ISRS signal. Finally, we demonstrate how chirping and phase matching can be used to disentangle ground state from excited-state vibrational coherences.

The interpretation of broadband ISRS spectra is not easy, even in the apparently simple case of nonresonant probe pulses and in the absence of AP excitation reported in Figure 1. Here we show a broadband ISRS experiment, performed in a common solvent, liquid cyclohexane (C_6H_{12}). The ISRS signal intensity as a function of the probe wavelength, measured with an off-resonant Raman pulse, clearly reveals a different behavior of various vibrational ground-state modes. The 384 cm^{-1} mode has the maximum of its intensity around the center of the probe λ_s = 555 nm, while the 800 cm^{-1} mode shows a minimum in the same wavelength region. The behavior of the 800 cm^{-1} mode is well described by previous theoretical descriptions based on classical or semiclassical approaches,[5,21,22] which predict a bilobed profile in the probe-wavelength resolved 2D maps across each vibrational mode. In the time domain, this corresponds to an amplitude modulation of the probe pulse at the stimulated vibrational frequencies, which vanishes at the spectral maximum. Notably, the red and blue spectral wings oscillate with an opposite phase. However, the 384 cm^{-1} mode signal in Figure 1 behaves differently, suggesting a more complex underlying process. To understand these differences, we derive the ISRS spectral response, taking into account probe chirp and finite sample size effects, within a quantum perturbation theory framework.

In the dipole approximation,[23] the ISRS process is described by the dipole Power–Zienau[24] radiation–matter interaction Hamiltonian $H_I = \vec{\mu}\cdot\vec{E}$, where $\vec{\mu}$ and $\vec{E}$ are the dipole and the local electric field operators. $\vec{E}$ can be separated into creation and annihilation operators

$$\vec{E} = \sum_{j,\alpha} \hat{\epsilon}_\alpha [\mathcal{E}_j(\vec{r}, t) + \mathcal{E}_j^\dagger(\vec{r}, t)] \tag{1}$$

where $\hat{\epsilon}_\alpha$ and j run over the polarization and mode of the fields, respectively. The ISRS heterodyne-detected signal can be defined as the derivative of the mean number of photons N_s in mode s of the probe pulse[25,26]

$$S = \int_{-\infty}^{+\infty} \frac{d\langle N_s\rangle}{dt'} dt' = \frac{i}{\hbar}\langle (V + V^\dagger)(\mathcal{E}_s - \mathcal{E}_s^\dagger)\rangle \tag{2}$$

where V and $V^\dagger$ represent the molecule excitation lowering and raising operators (see Methods).

We consider here the ISRS pulse sequence shown in Figure 2a. The actinic pulse promotes the system into an electronic

DOI: 10.1021/acs.jpclett.6b03027
J. Phys. Chem. Lett. 2017, 8, 966–974

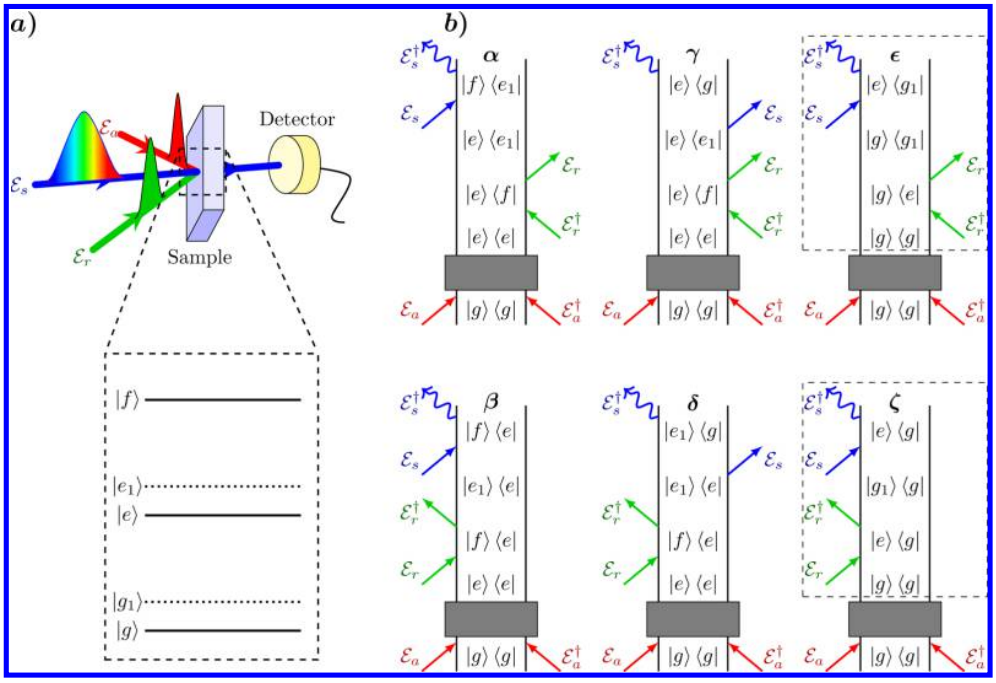

Figure 2. (a) ISRS experiment geometry and temporal envelopes of the laser fields are represented. Energy ladder scheme involved in the ISRS optical transitions is also indicated. We consider three electronic states g (ground), e, and f (excited); g_1 and e_1 are the corresponding vibrationally excited states. (b) Feynman diagrams for the ISRS process. Upon resonant actinic pump excitation, the system may evolve, ending up in an unknown population state (either the ground g or the electronically excited e) depending on the specific relaxation pathway (gray boxes). Dashed boxes represent the two ISRS signals surviving in the absence of actinic photoexcitation.

excited state, which can only relax (before the Raman pulse arrival time) down to the ground g or to the electronically excited state e, depending on its relaxation dynamics (indicated by the gray boxes in Figure 2b). At this point, the system could be vibrationally excited, as it happens in the presence of hot vibrational populations[27,28] or time-dependent frequencies along reaction coordinates.[29,30] However, for the sake of simplicity, we will consider in the following vibrationally relaxed cases. Accordingly, we will not include the actinic excitation pulse explicitly in the calculation, rather considering a molecular system characterized by three electronic levels g, e, and f and a single (common) vibrational mode (see Figure 2a). In this case, the ISRS signal is described by the six α–ζ diagrams in Figure 2b. The above possible extensions can be handled by evaluating additional diagrams originating from hot electronic states, weighted by the instantaneous thermal population, or by accounting for delay-dependent Green functions in eq 3.

Using the Heisenberg equation to calculate the derivative in eq 2,[20,31] the ISRS signal can be read out from the diagrams in Figure 2b

$$
\begin{aligned}
S(T,\omega_s) = \frac{2\mu_{ef}^2\mu_{e_1f}^2}{\hbar^4}\Im\Bigg\{ & \int_{-\infty}^{\infty}\int_{-\infty}^{\infty}\int_{-\infty}^{\infty} \mathrm{d}\omega_1\,\mathrm{d}\omega_2\,\mathrm{d}\omega_3\,\tilde{E}_r^*(\omega_1,T)\tilde{E}_r(\omega_2,T)\tilde{E}_s(\omega_3)\tilde{E}_s^*(\omega_s)\delta(\omega_s-\omega_3+\omega_2-\omega_1) \\
& \Big[\mathrm{Tr}\Big(VG_{fe_1}(\omega_3+\omega_2-\omega_1)V^\dagger G_{ee_1}(\omega_2-\omega_1)V^\dagger G_{ef}(-\omega_1)V\rho_{ee}\Big) \\
& +\mathrm{Tr}\Big(VG_{fe}(\omega_3-\omega_2+\omega_1)V^\dagger G_{e_1e}(\omega_1-\omega_2)VG_{fe}(\omega_1)V^\dagger\rho_{ee}\Big) \\
& -\mathrm{Tr}\Big(VG_{eg}(\omega_3+\omega_2-\omega_1)V^\dagger G_{ee_1}(\omega_2-\omega_1)V^\dagger G_{ef}(-\omega_1)V\rho_{ee}\Big) \\
& -\mathrm{Tr}\Big(VG_{e_1g}(\omega_3-\omega_2+\omega_1)V^\dagger G_{e_1e}(\omega_1-\omega_2)VG_{fe}(\omega_1)V^\dagger\rho_{ee}\Big) \\
& +\mathrm{Tr}\Big(VG_{eg_1}(\omega_3+\omega_2-\omega_1)V^\dagger G_{gg_1}(\omega_2-\omega_1)V^\dagger G_{ge}(-\omega_1)V\rho_{gg}\Big) \\
& +\mathrm{Tr}\Big(VG_{eg}(\omega_3-\omega_2+\omega_1)V^\dagger G_{g_1g}(\omega_1-\omega_2)VG_{eg}(\omega_1)V^\dagger\rho_{gg}\Big)\Big]\Bigg\}
\end{aligned}
\tag{3}
$$

where $G_{ij}(\omega) = (\omega-\omega_{ij}+i\eta)^{-1}$ is the matrix element of the frequency domain Green's function, η a positive infinitesimal

DOI: 10.1021/acs.jpclett.6b03027
J. Phys. Chem. Lett. 2017, 8, 966−974

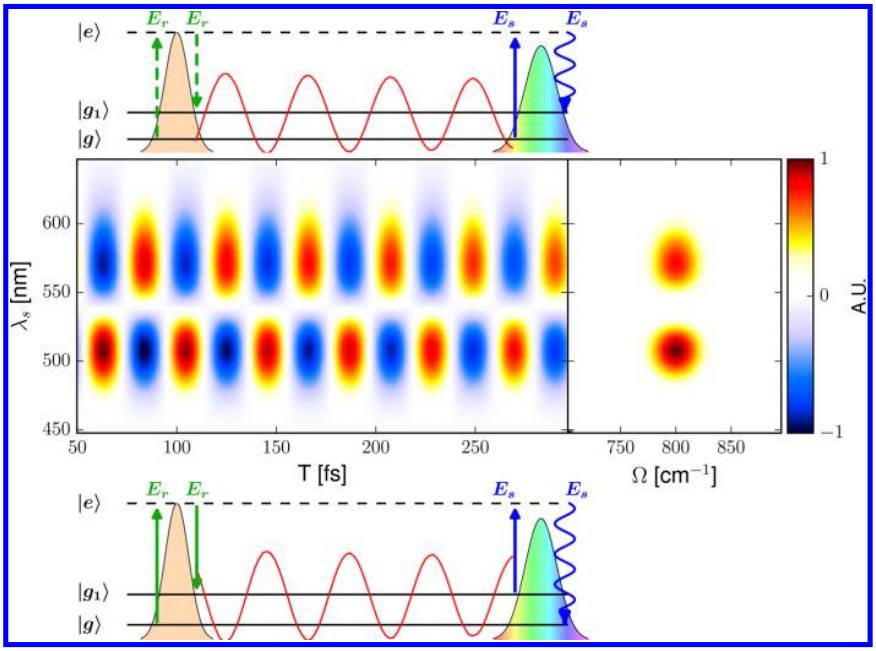

Figure 3. Simulation of the nonresonant third-order ISRS response (eq 4) for $\Delta k(\omega_1, \omega_2) = 0$ in the absence of actinic photoexcitation. Central panel: 2D map of $S(T, \lambda_s)$ and $S(\Omega, \lambda_s)$. The two energy ladder diagrams that describe the process, corresponding to the boxed section of the $\epsilon-\zeta$ Feynman diagrams in Figure 2b, are shown. The signal arises from the interference of these two pathways that generate time oscillations with opposite phases and cancel out in the central region of the spectrum, resulting in a bilobed profile along λ_s for each vibrational mode.

that ensures causality, and ρ_{ee} (ρ_{gg}) is the density matrix in the excited (ground) electronic state at the Raman pulse arrival time after the preparation process.

Calculating the matter correlation functions, taking into account for the finite sample length in a pencil shaped sample aligned with the probe pulse direction, as shown in the Methods section, eq 3 is recast as

$$S(T, \omega_s) = \frac{2\mu_{ef}^2\mu_{ef}^2}{\hbar^4}\Im\left\{\sum_{j=\alpha-\zeta}\int_{-\infty}^{\infty} d\omega_1\, d\omega_2\right.$$
$$\tilde{E}_r^*(\omega_1, T)\tilde{E}_r(\omega_2, T)\tilde{E}_s(\omega_s + \omega_1 - \omega_2)\tilde{E}_s^*(\omega_s)$$
$$\mathrm{sinc}\left[\frac{\Delta\vec{k}(\omega_1, \omega_2)\cdot\hat{z}L}{2}\right]\exp\left(i\frac{\overrightarrow{\Delta k}(\omega_1, \omega_2)}{2}\cdot\hat{z}L\right)$$
$$\left.P_j(-T)F_j(\omega_s, \omega_1, \omega_2)\right\} \quad (4)$$

where ω_s is the detected probe frequency, $\Im(z)$ indicates the imaginary part of z, $\tilde{E}_i$ stands for the spectral envelope of the i pulse, and $\tilde{\omega}_{ij} = \omega_i - \omega_j - i\gamma_{ij}$, where γ_{ij} is the dephasing rate of the vibrational coherence between i and j. $P_j(-T)$ indicates the population in the excited electronic state for diagrams $j = \alpha - \delta$ and in the ground state for diagrams $j = \epsilon - \zeta$ at the arrival time $(-T)$ of the Raman pulse. The correlation functions $F_j(\omega_s,\omega_1,\omega_2)$ contain the matter response, and $\Delta k(\omega_1,\omega_2)$ indicates the phase-matching condition for the six diagrams. Both are given in the Methods section, as well as the details of eq 4 derivation.[25]

We define the 2D signal $S(\Omega,\omega_s)$ as

$$S(\Omega, \omega_s) = \int_{-\infty}^{\infty} dT\ e^{i\Omega T}S(T, \omega_s) \quad (5)$$

In the following, we show experimental and simulated signals as a function of the wavelength $\lambda_s = \frac{2\pi}{\omega_s}$, instead of the angular frequency ω_s, to be consistent with the previous literature.[12,32]

To interpret the experimental results reported in Figure 1, eq 3 needs to be evaluated without the effect of the actinic photoexcitation and for off-resonant Raman and probe pulses. This is done by retaining the last two terms corresponding to the third-order processes indicated in the dashed boxes of the $\epsilon-\zeta$ diagrams in Figure 2b. Because the pulses wavelengths are far from any electronic transition, the rotating wave approximation (RWA) cannot be made and, in principle, six additional diagrams should be taken into account. However, as shown in the Supporting Information, they generate signals that are identical to those from ϵ and ζ diagrams.

At first, we neglect the dispersion in the sample and the chirp on the probe pulse and consider a collinear pulse geometry. Thus setting $\Delta k = 0$ in eq 4, we obtain the 2D signal shown in Figure 3. The two contributions oscillate with an opposite phase, in agreement with predictions of previous models.[22]

More generally, because of the finite sample length, the phase-matching condition can significantly influence the signal due to wave vector dispersion. For $\Delta k \neq 0$, it is possible to integrate eq 4 analytically for Lorentzian pulse envelopes (see the Supporting Information). This offers a test for the numerical integration in the case of general envelopes. A numerical integration of eq 5, performed using transform limited Gaussian envelopes, with λ_{WLC} = 540 nm, $\Delta\lambda_{WLC}$ = 100 nm, λ_{RP} = 545 nm, and $\Delta\lambda_{RP}$ = 60 nm in a noncollinear geometry (with an angle $\theta = 4°$ between the Raman pulse and the WLC), is reported Figure 4a,b.

DOI: 10.1021/acs.jpclett.6b03027
J. Phys. Chem. Lett. 2017, 8, 966−974

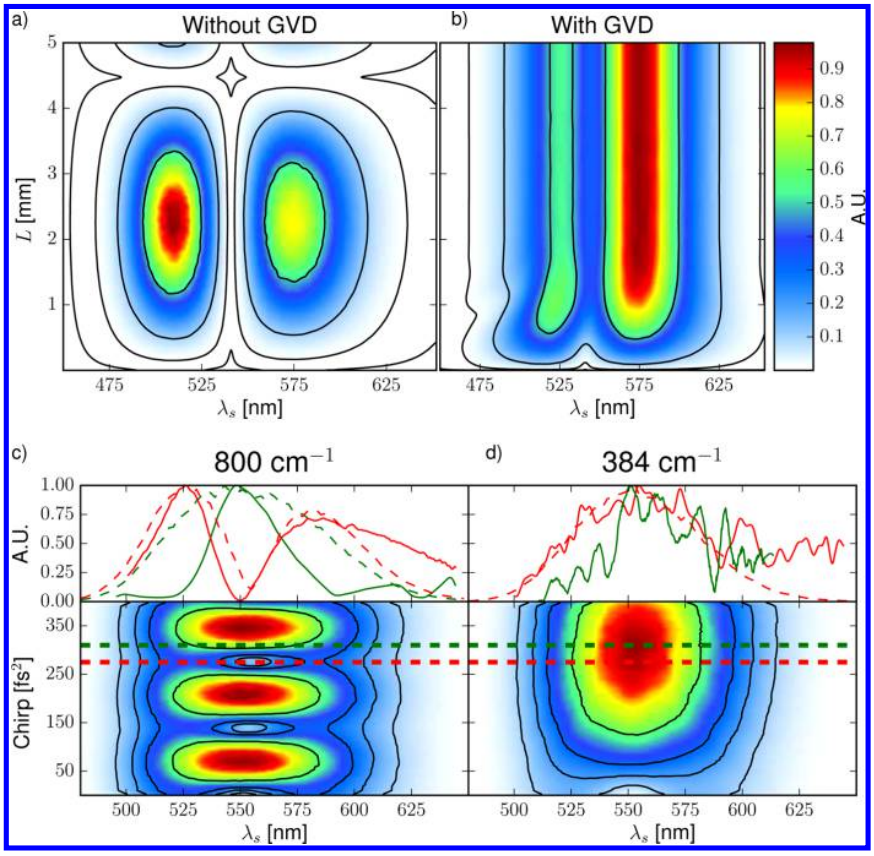

Figure 4. $S(\Omega = 800\ \mathrm{cm}^{-1}, \lambda_s)$, from eq 5, as a function of the sample length L and the probe chirp, for nonresonant ISRS in absence of actinic photoexcitation. In panel a, the sample is considered as a nondispersive medium (all spectral components propagate with the same velocity), and the phase-matching condition is ruled only by the relative angle between the Raman and probe pulses ($\theta = 4°$). Under this regime, the phase mismatch produces a wavelength-independent phase factor, periodically modulating the signal in L. In panel b, the dispersion curve of cyclohexane has been taken into account. While propagating in the sample, the Raman pulse undergoes a temporal broadening due to the group velocity dispersion; this reflects in a critical length beyond which the Raman pulse is longer than the vibrational mode period and the signal is no more generated, breaking the periodicity over L. Panels c and d depict the signal dependence on the probe chirp for two different vibrational modes. The experimental data (dashed lines in the plots) are overlapped with the theoretical simulations (solid lines) for two different values of the probe chirp, indicated by the dashed horizontal lines in the colormaps. The red features correspond to those presented in Figure 1.

In Figure 4a, we assume a nondispersive medium, with a dispersion curve $n(\lambda)$ constant over all wavelengths. The $\Delta k(\omega_1,\omega_2)$ term in eq 4 carries a wavelength-independent phase factor, which modulates the ISRS intensity over L but does not affect the spectral shape of the signal. In Figure 4b, the experimental dispersion curve of the cyclohexane[33] has been used to calculate the $\Delta k(\omega_1,\omega_2)$ function in eq 21. In this case, the spectral shape of the signal is affected by the group velocity dispersion (GVD), which acts asymmetrically for the two pathways ϵ and ζ that generate the signal. Because the phase mismatch is different for the two diagrams, they yield different amplitudes, resulting in the asymmetric double peak profile in Figure 4b. The presence of a phase factor between the two interfering diagrams also prevents a total cancellation of the ISRS signal around the central wavelength of the probe.

The GVD further induces a temporal broadening of the Raman and probe pulses, while propagating along the sample. When the duration of the Raman pulse is longer than the vibrational mode period ($T_{e_1e} = \frac{2\pi}{\omega_{e_1e}}$) the signal cannot be coherently generated. Hence, for sample size greater than a critical length (L_c, usually few millimeters), the signal reaches a stationary intensity. L_c depends on the Raman pulse initial duration, on the beam relative angle, on the vibrational mode frequency and on the sample group velocity dispersion. Notably, the suppression of the ISRS signal for $L > L_c$, as soon as the Raman pulse is temporal profile is stretched to a duration longer than T_{e_1e}, also sets an upper limit for the temporal resolution in ISRS-based pump−probe experiments. This is a useful advantage over other kinds of ultrafast measurements, where the temporal broadening of the pulses diminishes the temporal resolution.

Our results may be used to rationalize the experimental results reported by Kukura et. al,[3] who reported the ISRS spectral dependence on the sample size. They had pointed out that the intensity normalized by the number of molecules decreases as the sample length increases as a result of the combination between GVD and group velocity mismatch (GVM) between the Raman and the probe pulse. The intensity decrease with L can be also explained in the absence of these two phenomena (Figure 4a): the signal varies with the length of the sample in a sinusoidal fashion, while the number of molecules grows linearly. This would imply signal attenuation independent of the wavelength. Instead, Kukura et al. observed that the signal blue side is suppressed strongly:

DOI: 10.1021/acs.jpclett.6b03027
J. Phys. Chem. Lett. 2017, 8, 966−974

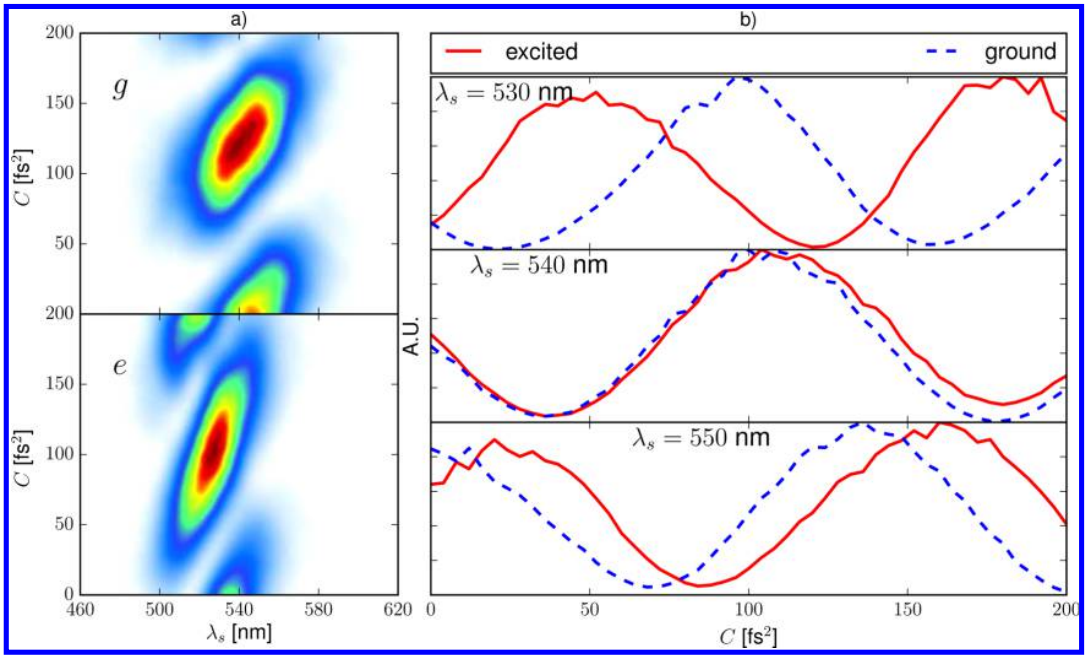

Figure 5. (a) $S(\Omega = 800\ \mathrm{cm}^{-1}, \lambda_s, C)$ ISRS signal intensity from eqs 5 and 6 for a 800 cm^{-1} vibrational mode as a function of the probed wavelength and the probe chirp, C, for the processes starting from the ground state $|g\rangle\langle g|$ (top panel and $\epsilon-\zeta$ diagrams) and the excited state $|e\rangle\langle e|$ (bottom panel and $\alpha-\beta-\gamma-\delta$ diagrams). The probe is tuned in resonance with all electronic transitions involved in the six diagrams. The shape of the signal is stretched along the chirp direction for vibrational coherences generated in the electronic excited state due to the destructive interference between $\alpha-\gamma$ and $\beta-\delta$ pathways. (b) Signal intensity as a function of C at selected probe wavelengths. The wavelength-dependent phase of Raman mode amplitude enables us to distinguish between the electronic levels in which the vibrational coherence is generated.

this can be explained as an effect of GVD that suppresses the blue-side peak (Figure 4b).

Remarkably, while the sample geometry and the GVD can significantly modulate the signal shape, because the two diagrams interfere destructively, they cannot generate single-lobe profiles centered around the maximum of the probe, such as reported in Figure 1.

The effect of a linear chirp of the probe can be taken into account in eq 4 by introducing a chirp (C) dependence in the probe electric field envelope

$$\tilde{E}_s(\omega, C) = \tilde{E}_s(\omega)e^{iC(\omega-\omega_0)^2} \quad (6)$$

where the leading frequency is indicated as ω_0 and $\tilde{E}_s(\omega) = \frac{1}{\sigma_s\sqrt{2\pi}}e^{-(\omega-\omega_0)^2/2\sigma_s^2}$ is the Gaussian envelope of the electric probe field (centered in ω_0).

As shown in Figure 4c,d, chirping the probe pulse strongly affects the spectral shape of the signal because it modifies the relative phase between the two Feynman diagrams ϵ and ζ. The 2D maps report the intensity of the 800 and 384 cm^{-1} modes of cyclohexane as a function of C and λ_s. On the top of Figure 4c,d, the experimental results (continuous lines) for two different chirped probe pulses are compared with the simulations (dashed lines), showing a good agreement. Modifying the chirp enables us to reshape and enhance the signal profile, in particular, switching from a bilobed to a monolobed dependence over the probe wavelength, as shown for the 800 cm^{-1} mode (red and green lines in of Figure 4c). This peculiar behavior can be easily interpreted. The ISRS signal is generated by the linear superposition of two Liouville pathways, represented by the Feynman diagrams ϵ and ζ in Figure 2b. Each diagram involves a different frequency component of the probe, which is shifted (with respect to the probed one) by the vibrational mode revealed by the signal. Consequently, on the tails of the probe spectrum, only one diagram dominates, the one generated by a frequency in which the probe is more intense. At the center of the probe spectrum, the two diagrams are in counter-phase and they cancel out. However, chirping the probe introduces a phase difference between the two contributions generating the signal. This means that there are some periodic values of the chirp in which the two diagrams constructively interfere, leading to a strong signal enhancement. Because the relative phase between the processes generating the ISRS response introduced by the WLC chirp depends quadratically on the observed vibrational frequency, the 384 cm^{-1} mode is much more weakly dependent on the probe chirp than the 800 cm^{-1}, as shown in Figure 4b,c. A small WLC chirp (50 fs^2) causes a relative phase between diagram $\epsilon-\zeta$ for the 384 cm^{-1} Raman mode, making the two components no longer opposite in phase and turning the bilobed shape into a (much more intense) monolobed one. This behavior survives even for much higher values of chirp (>400 fs^2), resulting in a monolobed profile for all explored chirp values. Only a higher value of C (~500 fs^2) would generate the bilobed profile, with destructive interference between ϵ and ζ.

Introducing a chirp on the probe pulse can be used to enhance specific vibrational modes and, most importantly, to separate contributions involving different potential energy surfaces upon resonant actinic excitation. Under such circumstances, the contributions from the two additional diagrams $\alpha-\beta$ in Figure 2b should be included in the ISRS response. Notably, the corresponding additional signals are identical to diagrams $\epsilon-\zeta$ and therefore do not allow us to discriminate between processes involving ground or excited states. This goal can be achieved by a resonant probe, which

DOI: 10.1021/acs.jpclett.6b03027
J. Phys. Chem. Lett. 2017, 8, 966−974

has two consequences: (i) the signals corresponding to $\alpha-\beta$ and $\epsilon-\zeta$ are no longer the same and (ii) two additional diagrams ($\gamma-\delta$) arise.

We now apply the proposed chirped probe scheme to the more challenging case of overlapping electronic resonances, where the resonance condition occurs in the same probe wavelength region, and hence the broadband nature of the probe could not be directly exploited to discriminate the involved electronic transition. The vibrational and electronic energy levels considered are shown in the diagram of Figure 2a, together with the pulse scheme used in the proposed experiment. In Figure 5, we show the corresponding ISRS response for a 800 cm^{-1} Raman mode, reproducing the vibrational peak amplitude as a function of the probe chirp C and wavelength λ_s. In the top panel of Figure 5a, only diagrams $\epsilon-\zeta$ for a system prepared in the electronic ground state are switched on, while in the bottom panel, the 2D signal is calculated for diagrams $\alpha-\delta$, where only the states prepared in the excited electronic state $|e\rangle\langle e|$ are interrogated by the ISRS process. As emphasized by the slices for fixed probed wavelength shown in Figure 5b, the specific involved electronic resonance introduces a wavelength-dependent phase shift on the chirp axis between the ISRS signal generated by a system prepared in the ground state and one in the excited state, as can be seen in eqs 15−20. Such a resonance-specific phase-factor can be conveniently sampled, taking advantage of the broadband nature of the probe pulse, which ensures us to access spectral regions strongly sensitive to the involved electronic level. This establishes a novel method to assign vibrational features to specific electronic states.

In summary, we have investigated the role of phase matching and probe chirp conditions in an ISRS experiment, through a diagrammatic treatment of the signal generation, enabling us to dissect the pathways that generate the nonlinear response and to rationalize the spectral dependence on the probe wavelength.

The ISRS signal, for a given detected wavelength, indeed results from the sum of concurring and distinct third-order processes, associated with photons, which are red- and blue-shifted by one vibrational quantum. This gives rise to contributions oscillating as a function of the time delay between the Raman and probe pulses.

In off-resonant ISRS with unchirped pulse, the two oscillations interfere destructively, explaining the strong signal suppression that can be observed in the central part of the spectrum. This explains why the weak Raman bands are often buried in the noise.

Our results suggest that an optimal probe chirping profile can be used to selectively enhance specific vibrational modes and are relevant for signal analysis improvement. The identification of the signal dependence on the probe wavelength for each mode indeed allows us to perform the correct weighted average over the entire probe spectrum, improving the signal-to-noise ratio.

Furthermore, our results establish a way to assign a given vibrational dynamics to the relevant potential energy surface: fine-tuning the relative phase between the processes contributing to the signal generation represents a powerful control knob to assign spectral features to specific electronic states, allowing for discerning excited from ground-state vibrational coherences.

METHODS

The $\vec{\mu}$ and $\vec{E}$ terms in the interaction Hamiltonian indicate the dipole and the local electric field operators and can be expressed as

$$\vec{\mu} = \sum_{i,j,i\neq j} \vec{\mu}_{ij}|i\rangle\langle j| \quad \vec{\mu}_{ij} = \langle i|e \sum_{\alpha} \vec{r}_{\alpha}|j\rangle \tag{7}$$

Here $|i\rangle$ indicates an eigenvector of the non interactive matter Hamiltonian and α is an index that runs over the atom positions.

The positive ($\mathcal{E}_j$) and negative ($\mathcal{E}_j^{\dagger}$) frequency components of the electric field can be expressed as

$$\mathcal{E}_j = \sqrt{\frac{\hbar\omega_j}{2\varepsilon_0 V}}\, a_j e^{-i(\omega_j t - \vec{k}_j\cdot\vec{r})} \quad \mathcal{E}_j^{\dagger} = \sqrt{\frac{\hbar\omega_j}{2\varepsilon_0 V}}\, a_j^{\dagger} e^{+i(\omega_j t - \vec{k}_j\cdot\vec{r})} \tag{8}$$

where j is the single mode of the electromagnetic radiation.

The time derivative of the number of photons in eq 2 has been computed using the Ehrenfest theorem,[20,31] and V is the molecular dipole transition operator

$$V = \sum_{i,j,j>i} \mu_{ij}|i\rangle\langle j| \qquad V + V^{\dagger} = \mu \tag{9}$$

We dropped the vectorial notation absorbing the thermodynamic average of the scalar product between the electric field polarization vector and the dipole in the symbol μ.

Considering an homogeneous 1D sample, the dipole operator is uniform

$$\mu(z) = \mu\theta(z)\theta(L - z) \tag{10}$$

where $\theta(z)$ is the Heaviside function. The coherent laser light state is an eigenvector of the electric field operator

$$\sum_j \mathcal{E}_j|E\rangle = E(t, \vec{r}, T)|E\rangle \tag{11}$$

Restricting along the z direction

$$E(t, \vec{r}, T) = \int_{-\infty}^{\infty} d\omega\, dk\, \tilde{E}(\omega, k, T) e^{-i\omega t + ikz\cos\vartheta} \tag{12}$$

Here ϑ is the angle between the chosen beam and the sample direction. The plane wave hypothesis leads to[19]

$$\tilde{E}(k, \omega, T) = \tilde{E}(\omega, T)\delta[k - k(\omega)] \tag{13}$$

where $k(\omega)$ contains the dispersion of the sample

$$k(\omega) = \frac{\omega}{c} n(\omega) \tag{14}$$

where n is the refractive index for the given frequency.

The density matrix formalism can be used to obtain the average in eq 2, through the relation $\langle O\rangle = \mathrm{Tr}[O\rho(t)]$, which holds for a generic operator O; here the time evolution of the density matrix $\rho(t)$ can be evaluated by the perturbative expansion of the Liouville equation. The correlation functions $F_j(\omega_s,\omega_1,\omega_2)$ in eq 4 are given by

$$F_{\alpha}(\omega_s, \omega_1, \omega_2) = \frac{1}{(\omega_s - \tilde{\omega}_{fe_1})(\omega_1 + \tilde{\omega}_{ef})(\omega_1 - \omega_2 + \tilde{\omega}_{ee_1})} \tag{15}$$

DOI: 10.1021/acs.jpclett.6b03027
J. Phys. Chem. Lett. 2017, 8, 966−974

$$F_{\beta}(\omega_s, \omega_1, \omega_2) = \frac{1}{(\omega_s - \tilde{\omega}_{fe})(\omega_2 - \tilde{\omega}_{fe})(\omega_2 - \omega_1 - \tilde{\omega}_{e_1e})} \quad (16)$$

$$F_{\gamma}(\omega_s, \omega_1, \omega_2) = \frac{-1}{(\omega_s - \tilde{\omega}_{eg})(\omega_1 + \tilde{\omega}_{ef})(\omega_1 - \omega_2 + \tilde{\omega}_{ee_1})} \quad (17)$$

$$F_{\delta}(\omega_s, \omega_1, \omega_2) = \frac{-1}{(\omega_s - \tilde{\omega}_{e_1g})(\omega_2 - \tilde{\omega}_{fe})(\omega_2 - \omega_1 - \tilde{\omega}_{e_1e})} \quad (18)$$

$$F_{\epsilon}(\omega_s, \omega_1, \omega_2) = \frac{1}{(\omega_s - \tilde{\omega}_{eg_1})(\omega_1 + \tilde{\omega}_{ge})(\omega_1 - \omega_2 + \tilde{\omega}_{gg_1})} \quad (19)$$

$$F_{\zeta}(\omega_s, \omega_1, \omega_2) = \frac{1}{(\omega_s - \tilde{\omega}_{eg})(\omega_2 - \tilde{\omega}_{eg})(\omega_2 - \omega_1 - \tilde{\omega}_{g_1g})} \quad (20)$$

and the $\Delta\vec{k}$ (ω_1, ω_2) phase mismatch is

$$\overrightarrow{\Delta k}(\omega_1, \omega_2) = -\vec{k}_a(\omega_1) + \vec{k}_a(\omega_2) + \vec{k}_s(\omega_s + \omega_1 - \omega_2) - \vec{k}_s(\omega_s) \quad (21)$$

The couples of eqs 15 and 16, 17 and 18, and 19 and 20 enlighten the fact that the resonance conditions for these diagrams, containing two distinct correlation functions, are different. In fact, considering, for example, eqs 15 and 16, the difference between ω_2 and ω_1 that maximizes the signal is, respectively, ω_{ee_1} and ω_{e_1e}. Remarkably, this leads to two different phase-matching condition in eq 21 for the two processes.

Moreover, the presence of different maximum conditions for these two diagrams ($\omega_1-\omega_2 = \omega_{ee_1}$ and $\omega_2-\omega_1 = \omega_{e_1e} \rightarrow \omega_1-\omega_2 = -\omega_{ee_1}$) rationalizes the π phase shift between the two pathways. In fact, in the off resonant regime, the imaginary parts of the denominator can be neglected, and hence the dominant contributions to the integrals in eq 4 are $\propto e^{i\omega_{ee1}T}$ and $\propto e^{-i\omega_{ee1}T}$, whose imaginary parts ($\sin[\omega_{ee_1}T]$ and $\sin[-\omega_{ee_1}T]$) oscillate with opposite phase.

Notably, when the probe wavelength is tuned to match the $e \rightarrow f$ electronic transition energy, the real part of the first denominators in eqs 15 and 16 cancels out, leaving an imaginary term proportional to the vibrational dephasing time. Hence, under resonant conditions, the leading contributions to the integral are $\propto i{\cdot}e^{i\omega_{ee1}T}$ and $\propto i{\cdot}e^{-i\omega_{ee1}T}$, whose imaginary parts ($\cos[\omega_{ee_1}T]$ and $\cos[-\omega_{ee_1}T]$) oscillate in phase. The analytic derivation of the phase relation between the Liouville pathways for Lorentzian pulse envelopes is reported in the Supporting Information.

The experimental setup exploited for the measurements on cyclohexane is based on a Ti:sapphire laser source that generates 3.6 mJ, 35 fs pulses at 800 nm and 1 kHz repetition rate. The Raman pulse is synthesized by a noncollinear optical parametric amplifier (NOPA) that produces tunable visible pulses in the range (500−700 nm) and compressed using chirped mirrors to ∼10 fs. The time interval between the Raman and probe pulses is settled by a computer-controlled delay line on the Raman pulse optical path. The WLC probe pulse is synthesized, focusing part of the source pulse on a nonlinear medium plate. The shape of the spectral envelope can be varied by changing the parameters of super continuum generation inside the nonlinear crystal, such as the pump power and the material used for the WLC generation. The time duration of the Raman pulse is measured by second-harmonic noncollinear autocorrelation, while the probe chirp can be estimated from the relative delay of the onset of oscillations at different probe wavelengths. Notably, as shown in the Supporting Information, a more accurate characterization of the chirp can be extracted using as a reference the coherent artifact between the two beams

A synchronized chopper blocks alternating Raman pulses to record the modification induced to transmitted WLC probe, which is frequency-dispersed by a spectrometer onto a CCD device. The Raman spectrum is obtained from the detected oscillating temporal signal using fast Fourier transform (FFT) algorithm. Zero padding algorithm and specific spectral Kaiser−Bessel windowing are exploited to enhance the spectral definition.[3,34]

■ ASSOCIATED CONTENT

Supporting Information

The Supporting Information is available free of charge on the ACS Publications website at DOI: 10.1021/acs.jpclett.6b03027.

Derivation of signal analytic integration protocols for specific spectral profiles. Comments on the non-RWA diagrams. Details of chirp and phase measurements. (PDF)

■ AUTHOR INFORMATION

Corresponding Author

*E-mail: tullio.scopigno@phys.uniroma1.it.

ORCID

Tullio Scopigno: 0000-0002-7437-4262

Notes

The authors declare no competing financial interest.

■ ACKNOWLEDGMENTS

S.M. gratefully acknowledges the support of the National Science Foundation through Grant No. CHE- 1361516 and the Chemical Sciences, Geosciences and Biosciences Division, Office of Basic Energy Sciences, Office of Science, U.S. Department of Energy through grant DE-FG02-04ER15571. The DOE grant and “Avvio alla Ricerca 2016” by Universitá di Roma “La Sapienza” had supported the visit of G.F. at UCI.

■ REFERENCES

(1) Zewail, A. H. Femtochemistry: Atomic-Scale Dynamics of the Chemical Bond. *J. Phys. Chem. A* **2000**, *104*, 5660−5694.

(2) Manzoni, C.; Mücke, O. D.; Cirmi, G.; Fang, S.; Moses, J.; Huang, S.-W.; Hong, K.-H.; Cerullo, G.; Kärtner, F. X. Coherent Pulse Synthesis: Towards Sub-Cycle Optical Waveforms. *Laser Photon. Rev.* **2015**, *9*, 129−171.

(3) Liebel, M.; Schnedermann, C.; Wende, T.; Kukura, P. Principles and Applications of Broadband Impulsive Vibrational Spectroscopy. *J. Phys. Chem. A* **2015**, *119*, 9506−9517.

(4) Tanimura, Y.; Mukamel, S. Two-Dimensional Femtosecond Vibrational Spectroscopy of Liquids. *J. Chem. Phys.* **1993**, *99*, 9496−9511.

(5) Yan, Y.-X.; Gamble, E. B.; Nelson, K. A. Impulsive Stimulated Scattering: General Importance in Femtosecond Laser Pulse

DOI: 10.1021/acs.jpclett.6b03027
J. Phys. Chem. Lett. 2017, 8, 966−974

Interactions with Matter, and Spectroscopic Applications. *J. Chem. Phys.* **1985**, *83*, 5391−5399.
(6) Liebel, M.; Kukura, P. Broad-Band Impulsive Vibrational Spectroscopy of Excited Electronic States in the Time Domain. *J. Phys. Chem. Lett.* **2013**, *4*, 1358−1364.
(7) Cheng, J.-X.; Xie, X. S. Coherent Anti-Stokes Raman Scattering Microscopy: Instrumentation, Theory, and Applications. *J. Phys. Chem. B* **2004**, *108*, 827−840.
(8) Tokmakoff, A.; Lang, M. J.; Larsen, D. S.; Fleming, G. R.; Chernyak, V.; Mukamel, S. Two-Dimensional Raman Spectroscopy of Vibrational Interactions in Liquids. *Phys. Rev. Lett.* **1997**, *79*, 2702−2705.
(9) Kahan, A.; Nahmias, O.; Friedman, N.; Sheves, M.; Ruhman, S. Following Photoinduced Dynamics in Bacteriorhodopsin with 7-fs Impulsive Vibrational Spectroscopy. *J. Am. Chem. Soc.* **2007**, *129*, 537−546.
(10) Ruhman, S.; Kohler, B.; Joly, A. G.; Nelson, K. A. Intermolecular Vibrational Motion in CS_2 Liquid at 165 ⩽ T⩾ 300 K Observed by Femtosecond Time-Resolved Impulsive Stimulated Scattering. *Chem. Phys. Lett.* **1987**, *141*, 16−24.
(11) Schnedermann, C.; Muders, V.; Ehrenberg, D.; Schlesinger, R.; Kukura, P.; Heberle, J. Vibronic Dynamics of the Ultrafast All- Trans to 13- Cis Photoisomerization of Retinal in Channelrhodopsin-1. *J. Am. Chem. Soc.* **2016**, *138*, 4757−4762.
(12) Fujisawa, T.; Kuramochi, H.; Hosoi, H.; Takeuchi, S.; Tahara, T. Role of Coherent Low-Frequency Motion in Excited-State Proton Transfer of Green Fluorescent Protein Studied by Time-Resolved Impulsive Stimulated Raman Spectroscopy. *J. Am. Chem. Soc.* **2016**, *138*, 3942−3945.
(13) Bardeen, C. J.; Wang, Q.; Shank, C. V. Selective Excitation of Vibrational Wave Packet Motion Using Chirped Pulses. *Phys. Rev. Lett.* **1995**, *75*, 3410−3413.
(14) Bardeen, C. J.; Wang, Q.; Shank, C. V. Femtosecond Chirped Pulse Excitation of Vibrational Wave Packets in LD690 and Bacteriorhodopsin. *J. Phys. Chem. A* **1998**, *102*, 2759−2766.
(15) Wand, A.; Kallush, S.; Shoshanim, O.; Bismuth, O.; Kosloff, R.; Ruhman, S. Chirp Effects on Impulsive Vibrational Spectroscopy: a Multimode Perspective. *Phys. Chem. Chem. Phys.* **2010**, *12*, 2149−2163.
(16) Biggs, J. D.; Zhang, Y.; Healion, D.; Mukamel, S. Multidimensional X-Ray Spectroscopy of Valence and Core Excitations in Cysteine. *J. Chem. Phys.* **2013**, *138*, 144303.
(17) Dorfman, K. E.; Bennett, K.; Mukamel, S. Detecting Electronic Coherence by Multidimensional Broadband Stimulated X-Ray Raman Signals. *Phys. Rev. A: At., Mol., Opt. Phys.* **2015**, *92*, 023826.
(18) Polli, D.; Brida, D.; Mukamel, S.; Lanzani, G.; Cerullo, G. Effective Temporal Resolution in Pump-Probe Spectroscopy with Strongly Chirped Pulses. *Phys. Rev. A: At., Mol., Opt. Phys.* **2010**, *82*, 053809.
(19) Mukamel, S. *Principles of Nonlinear Spectroscopy*; Oxford University Press, 1995.
(20) Rahav, S.; Mukamel, S. Ultrafast Nonlinear Optical Signals Viewed From the Molecule's Perspective: Kramers-Heisenberg Transition-Amplitudes Versus Susceptibilities. *Adv. At., Mol., Opt. Phys.* **2010**, *59*, 223−263.
(21) De Silvestri, S.; Fujimoto, J.; Ippen, E.; Gamble, E. B.; Williams, L. R.; Nelson, K. A. Femtosecond Time-Resolved Measurements of Optic Phonon Dephasing by Impulsive Stimulated Raman Scattering in α-Perylene Crystal From 20 to 300 K. *Chem. Phys. Lett.* **1985**, *116*, 146−152.
(22) Ruhman, S.; Joly, A.; Nelson, K. Coherent Molecular Vibrational Motion Observed in the Time Domain Through Impulsive Stimulated Raman Scattering. *IEEE J. Quantum Electron.* **1988**, *24*, 460−469.
(23) Babiker, M.; Loudon, R. Derivation of the Power-Zienau-Woolley Hamiltonian in Quantum Electrodynamics by Gauge Transformation. *Proc. R. Soc. London, Ser. A* **1983**, *385*, 439−460.
(24) Power, E. A.; Zienau, S. Coulomb Gauge in Non-Relativistic Quantum Electro-Dynamics and the Shape of Spectral Lines. *Philos. Trans. R. Soc., A* **1959**, *251*, 427−454.
(25) Dorfman, K. E.; Fingerhut, B. P.; Mukamel, S. Time-Resolved Broadband Raman Spectroscopies: a Unified Six-Wave-Mixing Representation. *J. Chem. Phys.* **2013**, *139*, 124113.
(26) Batignani, G.; Fumero, G.; Mukamel, S.; Scopigno, T. Energy Flow Between Spectral Components in 2D Broadband Stimulated Raman Spectroscopy. *Phys. Chem. Chem. Phys.* **2015**, *17*, 10454−10461.
(27) Ferrante, C.; Pontecorvo, E.; Cerullo, G.; Vos, M. H.; Scopigno, T. Direct Observation of Subpicosecond Vibrational Dynamics in Photoexcited Myoglobin. *Nat. Chem.* **2016**, *8*, 1137−1143.
(28) Leitner, D. M. Energy Flow in Proteins. *Annu. Rev. Phys. Chem.* **2008**, *59*, 233−259.
(29) Mukamel, S.; Biggs, J. D. Communication: Comment on the Effective Temporal and Spectral Resolution of Impulsive Stimulated Raman Signals. *J. Chem. Phys.* **2011**, *134*, 161101.
(30) Batignani, G.; Bossini, D.; Di Palo, N.; Ferrante, C.; Pontecorvo, E.; Cerullo, G.; Kimel, A.; Scopigno, T. Probing Ultrafast Photo-Induced Dynamics of the Exchange Energy in a Heisenberg Antiferromagnet. *Nat. Photonics* **2015**, *9*, 506−510.
(31) Fumero, G.; Batignani, G.; Dorfman, K. E.; Mukamel, S.; Scopigno, T. On the Resolution Limit of Femtosecond Stimulated Raman Spectroscopy: Modelling Fifth-Order Signals with Overlapping Pulses. *ChemPhysChem* **2015**, *16*, 3438−3443.
(32) Wende, T.; Liebel, M.; Schnedermann, C.; Pethick, R. J.; Kukura, P. Population-Controlled Impulsive Vibrational Spectroscopy: Background- and Baseline-Free Raman Spectroscopy of Excited Electronic States. *J. Phys. Chem. A* **2014**, *118*, 9976−9984.
(33) Kozma, I. Z.; Krok, P.; Riedle, E. Direct Measurement of the Group-Velocity Mismatch and Derivation of the Refractive-Index Dispersion for a Variety of Solvents in the Ultraviolet. *J. Opt. Soc. Am. B* **2005**, *22*, 1479−1485.
(34) Harris, F. On the Use of Windows for Harmonic Analysis with the Discrete Fourier Transform. *Proc. IEEE* **1978**, *66*, 51−83.

DOI: 10.1021/acs.jpclett.6b03027
J. Phys. Chem. Lett. 2017, 8, 966−974

Entropy evaluation sheds light on ecosystem complexity

Mattia Miotto* and Lorenzo Monacelli†
Department of Physics, University "Sapienza", Piazzale Aldo Moro 5, 00185, Rome, Italy

(Received 10 November 2017; published 3 October 2018)

Preserving biodiversity and ecosystem stability is a challenge that can be pursued through modern statistical mechanics modeling. Here we introduce a variational maximum entropy-based algorithm to evaluate the entropy of a minimal ecosystem on a lattice in which two species struggle for survival. The method quantitatively reproduces the scale-free law of the prey shoals size, where the simpler mean-field approach fails: the direct near-neighbor correlations are found to be the fundamental ingredient describing the system self-organized behavior. Furthermore, entropy allows the measurement of structural ordering we found to be a key ingredient in characterizing two different coexistence behaviors, one where predators form localized patches in a sea of preys and another where species display more complex patterns. The general nature of the introduced method paves the way for its application in many other systems of interest.

DOI: 10.1103/PhysRevE.98.042402

I. INTRODUCTION

The general formulation of statistical mechanics and information theory opened the way of physics to complex systems. The entropy definition is the basis of both theories. Although the concept of entropy was introduced in thermodynamics, it has been adapted to other fields of study, including economics, biophysics, and ecology.

In this work, we focus on an ecological system and its entropy, which we show to be pivotal in understanding how the phenotype, the characteristics of an organism resulting from the interaction between its genotype and the environment [1,2], discriminates and provides information about survival and extinction of species. This is a very important effort that must be pursued to prevent ecological disasters.

In a very general way, entropy is a property of the distribution function out of which the states of the system have been drawn. It is the capacity of the data to provide or convey information [3]. Consequently, knowing the entropy allows us to set limits on the information we can extract from observations and to the predictability of the system. It has been widely used to study information transport in neural networks [4,5] and in flocks of birds [6–8], complexity and hierarchy in written languages [9], and risk assessment in financial markets [10,11]. In particular, predictability plays a very important role in economics where the awareness of markets entropy allows one to maximize the investment profits [10]. Recently, entropy has been exploited in inference problems, with great results in biological phenomena, such as bacterial growth [12,13], evolution [14], and protein folding [15].

Here, we show how entropy is crucial also in the context of ecological systems. Ecosystems can be defined as a community of living organisms in conjunction with the environment [16,17], where the latter affects the organisms without being in turn influenced by them [18]. However, all living beings within the ecosystem are interdependent, in fact, variations in the size of one population influence all others. This is particularly clear for prey and predator dynamics. In fact, if the number of preys in an ecosystem grows, predators will respond to the supply of available food by increasing their number. The growth of predator number will reduce preys until the system can no longer sustain the predator population. The process has either to attain a steady state or to end in species extinction. To avoid extinction, both preys and predators need to optimize their phenotypes: predators must, for example, adapt for improving efficiency in hunting to catch enough food to ensure survival. Prey species, however, must be proficient in escaping their predators and reproduction; if enough of them are to survive for the species to endure [19–21]. Disturbances, which are perturbations that move the system away from its steady state [22], may affect species phenotypes. Such disturbances can originate from changing of environmental variables such as temperature and precipitation or in modifications of the populations, like the appearance or disappearance of a species. Besides the theoretical challenge of understanding the behavior of that kind of complex system, worthy of notice is also the practical importance of predicting the response to perturbations, particularly the ones produced by humans. Relevant cases are the fight against parasites in agriculture [23] and the perturbations in sea populations due to fishing activities [24]. From the groundbreaking works of Lotka [25] and Volterra [26], ecosystem modeling has been addressed in various ways, from sets of differential equations [27–29] to simulations on lattice [30–32].

Taking inspiration from the work of Dewdney [33], we modeled the simplest nontrivial ecosystem in which two species struggle for survival. Sharks (predators) and fishes (preys) occupy the nodes of the toroidal 2D lattice; they can move, reproduce, and hunt. The rules of the model resemble the ones described by Mobilia *et al.* [34] and are introduced in Sec. III A. This system has been extensively studied and several critical behaviors have been observed [35,36].

*mattia.miotto@roma1.infn.it
†lorenzo.monacelli@roma1.infn.it

Measuring the entropy of this kind of complex system without any explicit expression for a *prior* probability distribution is very challenging [37]. In fact, the Shannon definition of entropy relies on the system probability distribution P, which depends on all the degrees of freedom of the system [9]. The entropy measurement requires a fine sampling of this function, becoming not affordable even for small lattices.

The maximum entropy (MaxEnt) technique has been developed to obtain an approximation for the probability distribution. Given a set of observables x_i that partially describes the inquired system, MaxEnt algorithm allows one to find the less structured probability distribution that reproduces the chosen set of the real system observables. This technique was first introduced by Jaynes [38] in 1957, but it reached an outstanding interest only recently thanks to the availability of a huge amount of experimental and numerical data. MaxEnt has been successfully applied to countless problems, both in equilibrium and out-of-equilibrium systems [39]; among them, the prediction of protein amino acid contacts [15,40] and the analysis of neural networks [41] are of particular interest. However, even if MaxEnt provides an analytic expression for the probability distribution, computing the associated entropy is still a major issue [7].

In Sec. II A we outline how it is possible to obtain the exact entropy of the MaxEnt probability distribution taking advantage of all the data generated during the convergence of the algorithm, without any further time-consuming computation. Furthermore, in Sec. II B, we introduce a *least* entropy principle that justifies the use of the MaxEnt distribution as a truncation of a series that converges toward the real entropy of the system. Availing the variational principle, the approximation on the resulting entropy is of second order. While the method is formally derived for dealing with equilibrium systems, in Sec. III we apply it to the study of an ecosystem. In Sec. III D we examine the insights the entropy provides and discuss its limitations in the case of a nonequilibrium steady-state system, like the one we treat. Although we apply this method only to the introduced ecosystem, it is very general: it can be used whenever it is possible to define a probability distribution on a site model.

Maximum entropy

The MaxEnt framework we are going to discuss can deal with any stochastic process defined on a graph composed of M nodes. Each node is in one out of q possible states. If we indicate with P the probability that the system is in a given configuration the entropy is defined accordingly to Boltzmann-Shannon as

$$S[P] = -\langle \ln P \rangle_P \,, \tag{1}$$

where $\langle \cdot \rangle_P$ indicates the average over the P probability distribution.

The standard MaxEnt algorithm consists in maximizing $S[P]$ with respect to P in presence of a set of N constraints. The restraints are the set of observables $\{x\}_{i=1}^{N}$ that best describes the system; in other words, some degrees of freedom are fixed and the entropy is maximized among the remaining ones to have the broadest possible probability function. Each observable x_i is a generic function that associates any possible configuration of the system to a real number. Note that the index i identifies the observable in the set of constraints, not the specific site on the graph, as the x_i observable can be a function of more than one node, e.g., the average dimension of clusters of nodes in the same state.

Defining the auxiliary Lagrange functional Φ as

$$\Phi[P, \lambda_1, \cdots, \lambda_n] = -S[P] + \sum_{i=1}^{N} \lambda_i \langle x_i \rangle_P \,, \tag{2}$$

the correct constrained maximum entropy distribution P^* is found solving the set of equations:

$$\frac{\delta \Phi}{\delta P^*} = 0, \tag{3a}$$

$$\langle x_i \rangle_{P^*} = \bar{x}_i \quad \forall i = 1, \cdots, N, \tag{3b}$$

where $\bar{x}_i$ is the measured expected value of x_i. Equation (3) is very hard to solve, even numerically, since P depends still on q^M variables. P can be used to define an auxiliary effective Hamiltonian, according to the Boltzmann definition:

$$P(\vec{\sigma}) = \frac{e^{-H(\vec{\sigma})}}{Z},$$

where $\vec{\sigma}$ represents the configuration and Z the partition function that normalizes P.

Equation (3a) is solved by the Hamiltonian [38]:

$$H = \sum_{i=1}^{N} \lambda_i x_i, \tag{4}$$

where λ_i are fixed so that the expectation values of x_i respect the bounds over the real observables.

The values of λ_i can be obtained analytically only in very few cases. The simplest one is the mean-field solution, where only one-body observables are constrained, e.g., the numbers of nodes in each state. In the latter case, the number of observables is equal to the number of states q and the Lagrange multipliers that satisfy the imposed constraints are

$$\lambda_i = -\ln\left(\frac{\bar{x}_i}{M}\right). \tag{5}$$

The passages to prove Eq. (5) are sketched in Appendix A. In this case, the entropy per node is

$$S' = -\sum_{i=1}^{q} \left(\frac{\bar{x}_i}{M}\right) \ln\left(\frac{\bar{x}_i}{M}\right), \tag{6a}$$

$$S = M S'. \tag{6b}$$

This entropy evaluation corresponds to the standard one obtained by the Shannon-Fano algorithm [42,43]. This is a "Hartree-Fock" theory of the complex system, where the entropy is maximized using topology-independent Hamiltonians only. This framework paves the way to a more precise entropy computation.

II. ENTROPY ALGORITHM

The general solution of Eq. (3) has been matter of discussion [41,44–47]. On the way of Bialek and Ranganathan [47],

we introduce an auxiliary function $\tilde{\chi}^2$ whose global minimum coincides with the solution:

$$\tilde{\chi}^2 = \sum_{i=1}^{N} W_i(\langle x_i\rangle_H - \bar{x}_i)^2, \tag{7}$$

where $\langle x_i\rangle_H$ is the average of the x_i observable computed using the trial Hamiltonian H while $\bar{x}_i$ is the average over the real observable evaluated by the data. W_i are coefficients that do not affect the minimum of the χ^2, however, if wisely chosen, may accelerate the convergence process. The $\tilde{\chi}^2$ function defined in Eq. (7), in the minimum, is a random distributed Pearson variable only if all the observables are independent of each other and the W_i correspond to the inverses of the variances. This is not true in most MaxEnt applications, e.g., in the mean field case where the sum of the x_i is fixed to M.

We propose the introduction of a corrected χ^2 that takes into account linear correlations:

$$\chi^2 = \sum_{\substack{i=1\\ j=1}}^{N} (\bar{x}_i - \langle x_i\rangle_H)\left(\Sigma^{-1}\right)_{ij}(\bar{x}_j - \langle x_j\rangle_H), \tag{8}$$

where Σ is the covariance matrix between the N chosen observables. It must be stressed that Eq. (8) is still not a true χ^2 variable since we corrected only linear correlations. Moreover, eigenvectors of Σ will be uncorrelated, but not necessarily independent. However, the linear approximation for correlations between observables has a long history in statistical analysis [48,49] and usually leads to very good results.

Equation (8) is well defined only if Σ can be inverted. Diagonalizing the covariance matrix Σ, we can restrict the minimization only in the subspace spanned by its eigenvectors whose eigenvalues are greater than zero. Using these eigenvectors y_i as a basis, the Pearson χ^2 can be redefined as

$$\chi^2 = \sum_{i=1}^{N'} \frac{(\bar{y}_i - \langle y_i\rangle_H)^2}{\tilde{\sigma}_i^2}, \tag{9a}$$

$$N' = N - \dim\ker\Sigma, \tag{9b}$$

$$y_i = \sum_{j=1}^{N} S_{ij}x_j, \tag{9c}$$

where $\tilde{\sigma}_i^2$ is the ith eigenvalue of the Σ matrix and S is a $N' \times N$ matrix that diagonalizes Σ. The $\dim\ker\Sigma$ indicates the dimension of the Σ kernel.

The gradient of Eq. (8) can be computed as follows:

$$\frac{\partial\chi^2}{\partial\lambda_k} = -2\sum_{i=1}^{N'} \frac{(\bar{y}_i - \langle y_i\rangle_H)}{\tilde{\sigma}_i^2}\frac{\partial\langle y_i\rangle_H}{\partial\lambda_k}, \tag{10a}$$

$$\frac{\partial\langle y_i\rangle_H}{\partial\lambda_k} = \sum_{j=1}^{N} S_{ij}\frac{\partial\langle x_j\rangle_H}{\partial\lambda_k}, \tag{10b}$$

$$\frac{\partial\langle x_j\rangle_H}{\partial\lambda_k} = -\sigma_{jk}^{\mathrm{MC}}, \tag{10c}$$

where $\sigma_{jk}^{\mathrm{MC}}$ is the covariance matrix between observables x_j and x_k for the current Hamiltonian:

$$\sigma_{jk}^{\mathrm{MC}} = \langle x_j x_k\rangle_H - \langle x_j\rangle_H\langle x_k\rangle_H. \tag{11}$$

The final expression of the gradient is

$$\frac{\partial\chi^2}{\partial\lambda_k} = 2\sum_{i=1}^{N'} \frac{(\bar{y}_i - \langle y_i\rangle_H)}{\tilde{\sigma}_i^2}\sum_{j=1}^{N} S_{ij}\sigma_{jk}^{\mathrm{MC}}, \tag{12}$$

or, equivalently, in a compact form:

$$\vec{\nabla}\chi^2 = 2S^{\dagger}\sigma'_{\mathrm{MC}}\left(\frac{\vec{\Delta}y}{\sigma^2}\right), \tag{13}$$

where σ'_{MC} is the Monte Carlo covariance matrix in the non singular subspace and $\vec{\Delta}y/\sigma^2$ is the vector:

$$\left(\frac{\vec{\Delta}y}{\sigma^2}\right)_i = \frac{\bar{y}_i - \langle y_i\rangle_H}{\tilde{\sigma}_i^2}. \tag{14}$$

The minimization of Eq. (8) can be initialized by the mean-field solution Eq. (5), choosing zero for each λ_i associated with a non topology-independent observable. Equation (12) ensures that any standard gradient-based minimization algorithm can be used.

Moreover, to fasten the convergence [50], it is possible to derive the expression of the Hessian matrix in the minimum and utilize it as a precondition on the minimization:

$$D_{hk} = \left.\frac{\partial^2\chi^2}{\partial\lambda_k\partial\lambda_h}\right|_{\vec{\nabla}\chi^2=0}, \tag{15}$$

$$D_{hk} = 2\sum_{i=1}^{N'}\frac{1}{\tilde{\sigma}_i^2}\sum_{\substack{j=1\\ l=1}}^{N} S_{ij}S_{il}\sigma_{jk}^{\mathrm{MC}}\sigma_{hl}^{\mathrm{MC}}, \tag{16}$$

or, equivalently:

$$D = 2\sigma_{\mathrm{MC}}S^{\dagger}\Sigma^{-1}S\sigma_{\mathrm{MC}}. \tag{17}$$

A. Entropy evaluation

In usual MaxEnt implementations, minimization data are wasted and information about the system is inferred solely from the final probability distribution. Here we show how to recycle the whole minimization procedure to infer the entropy of the system. In fact, computing the entropy directly from the converged probability distribution is a very challenging task. However, entropy can be obtained from an adiabatic integration through the minimization path of the Hamiltonians. The values of the observables during the minimization can be used to obtain a measurement of the entropy of the system without any further Monte Carlo computations.

To compute entropy, it is convenient to define, as done for the effective Hamiltonian, an auxiliary function equivalent to the Helmholtz free energy:

$$F = -\ln Z,$$

which can be computed through a thermodynamic integration along the minimization path. Entropy is obtained by inverse Legendre transformation from the auxiliary free energy of the

system. Even if the free energy is not well defined (the energy is defined up to a constant), the entropy is.

The free energy at the final value of the minimization is

$$F(\xi = 1) = F_0 + \int_0^1 \frac{dF}{d\xi} d\xi, \tag{18}$$

where ξ is a variable that parametrizes the path of the Hamiltonian during the minimization. The F_0 value is the free energy at the starting condition, that is the noninteracting system:

$$F_0 = -M \ln \left(\sum_{j=1}^{q} e^{-\beta \lambda_j(0)} \right), \tag{19}$$

$$F_\xi = -\ln Z_\xi, \tag{20}$$

$$\frac{dF}{d\xi} = \left\langle \frac{dH_\xi}{d\xi} \right\rangle_\xi. \tag{21}$$

The integral can be done parametrizing the Hamiltonian as

$$H_\xi = \sum_{i=1}^{N} \lambda_i(\xi) x_i, \tag{22}$$

where x_i are the observables while λ_i are both the Lagrangian multipliers of the MaxEnt algorithm and the parameters through which the χ^2 function is minimized. Therefore, we get

$$\frac{dF}{d\xi} = \sum_{i=1}^{N} \frac{d\lambda_i}{d\xi} \langle x_i \rangle_\xi, \tag{23}$$

so that only the averages of the observables during the minimization are required to compute the free energy:

$$F = \langle H \rangle - TS, \tag{24a}$$

$$S = \frac{\langle H \rangle - F}{T}. \tag{24b}$$

Fixing $T = 1$, we obtain

$$S[\lambda_i(\xi)] = M \ln \left(\sum_{j=1}^{q} e^{-\lambda_j(0)} \right) + \sum_{i=1}^{N} \left[\lambda_i(1) \langle x_i \rangle_1 - \int_0^1 d\xi \frac{d\lambda_i}{d\xi}(\xi) \langle x_i \rangle_\xi \right]. \tag{25}$$

The only required quantities are the Hamiltonian during the minimization, i.e., the $\lambda_i(\xi)$, and the values of the observables $\langle x_i \rangle_\xi$, both already computed during the minimization. In addition, if all the configurations generated during the χ^2 minimization are stored, the importance sampling (IS) can be used to interpolate between different Monte Carlo points, providing a very good sampling of the integral. IS implementation for the minimization is discussed in Appendix B.

B. Least maximum entropy principle

Entropy can be defined in the framework of a least principle. The MaxEnt approach finds the probability distribution that maximizes the entropy on the subset where the expected values of the observables x_i are constrained. The entropy $S_{\rm ME}$ associated with the MaxEnt probability distribution is greater than the true entropy $S_{\rm real}$ of the system since the true P lies in the chosen subset:

$$S_{\rm real} \leqslant S_{\rm ME}. \tag{26}$$

Moreover, $S_{\rm ME}$ decreases whereas new constraints are added due to a contraction of the probability distribution space. In Appendix C we provide a rigorous proof that a set of constraints for which Eq. (26) becomes an equality exists. The true entropy of the system is then the least maximum entropy of all possible choices of the constraints.

Just like any variational least energy principle in physics, from Hartree-Fock to *density functional theory* (DFT), the energy (entropy in our case) and its derivatives are the targets of the theory, while the wave functions (probability distributions) are *side effects*. We want to remark that the error on the entropy due to the limited number of constraints is of second order, while the resulting probability distribution is affected by a first order error.

III. ECOSYSTEM ANALYSIS

Although the so far introduced method is quite general, we discuss its implication in ecosystems. In particular, we analyze a two dimensional model on a regular 2D lattice of edge L (number of nodes $M = L^2$), whose sites can either be empty or occupied by a fish or a shark. In the application of the MaxEnt algorithm, we limited the constraints x_i introduced in Eq. (2) to the numbers of preys and predators and near-neighbor fish-fish, shark-shark, and fish-shark couples. The corresponding MaxEnt Hamiltonian describes a three-state Potts model [51].

A. Model definition

Along the lines of Dewdney [33] and Mobilia *et al.* [34], we modeled a minimal ecosystem composed of two species interacting each other as a 2D lattice model. Each site can be occupied either by the environment or a fish or a shark, represented with the integers 0, 1, 2, respectively. At every time step, fishes can move, breed, or remain still with probability p_f^m, p_f^f, and $1 - p_f^m - p_f^f$. Sharks can move (p_s^m) or remain still ($1 - p_s^m$). Furthermore, sharks eat fishes whenever they step into a cell occupied by a prey. In this case, sharks can reproduce with probability p_s^f. If a shark does not eat a fish during its round, it can die with probability p_s^d. This set of rules defines a Markovian process described by the transition matrix $\Pi(\vec{\sigma}_i \to \vec{\sigma}_j)$. It gives the probability of the system to transit from the $\vec{\sigma}_i$ to the $\vec{\sigma}_j$ state, where $\vec{\sigma}_x$ identifies the values of all sites in the lattice. The probability to find the system in the $\vec{\sigma}_i$ state at the $t + 1$ time step is defined by

$$P(\vec{\sigma}_i, t+1) = \sum_{\vec{\sigma}_j} \Pi(\vec{\sigma}_j \to \vec{\sigma}_i) P(\vec{\sigma}_j, t). \tag{27}$$

Studying the time evolution of $P(\vec{\sigma}, t)$ through dynamical Monte Carlo simulations (see Appendix D), it is possible to

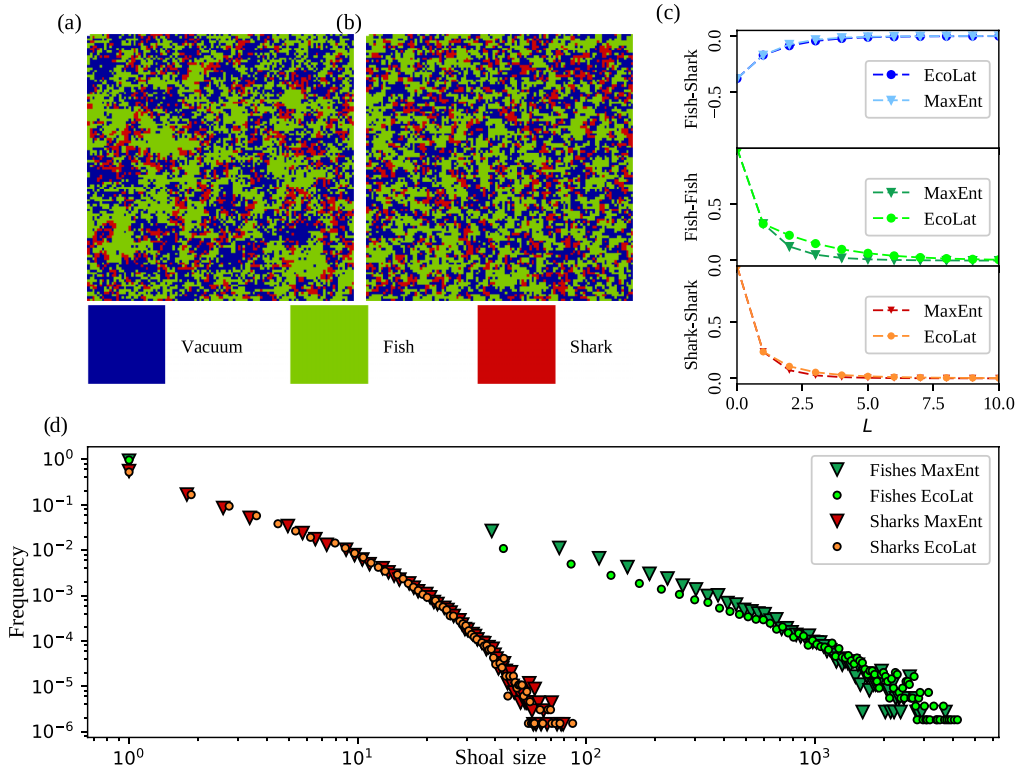

FIG. 1. Comparison between the *in silico* ecosystem (EcoLat) and the maximum entropy (MaxEnt) result. (a) Representation of an EcoLat snapshot in the steady-state regime. Fishes are colored in green, sharks in red, while blue represents the environment. Phenotypic parameters are reported in Appendix F. (b) A configuration extracted from the MaxEnt probability distribution obtained by constraining the numbers of fishes, sharks, and near-neighbor couples. Both simulations ran on a lattice of edge $L = 110$. (c) Spatial correlation functions of fish-shark (top), fish-fish (medium), and shark-shark (bottom). (d) Shoal-size distribution of fishes (green shades) and sharks (red shades) computed on EcoLat (circles) and MaxEnt (triangles) configurations. Fishes are power-law distributed, while sharks exhibit an exponential decay.

assess that the system reaches a steady-state distribution:

$$P(\vec{\sigma}_i) = \sum_{\vec{\sigma}_j} \Pi(\vec{\sigma}_j \to \vec{\sigma}_i) P(\vec{\sigma}_j). \tag{28}$$

Depending on the choice of the parameters, the system that we named EcoLat (*Eco*system on *Lat*tice) presents three different states: (i) fish saturation due to the extinction of sharks; (ii) life extinction, where sharks eat all fishes and then extinguish; (iii) nonequilibrium steady-state (NESS), in which fish and shark densities fluctuate around a constant value.

The probability distribution can be defined by extracting configurations from the evolving system after a transient time. Sampling configurations sufficiently distant in time it is possible to introduce an ergodic hypothesis (Appendix E), i.e., the so defined probability distribution is equivalent to the one of an infinite ensemble of independent systems. In this framework, the entropy becomes a well-defined quantity.

It is important to notice that such formulation neglects the time-correlations of the evolving configuration, i.e., it disregards the flux of probability distribution that uniquely characterizes the generic nonequilibrium steady state [52].

B. MaxEnt distribution benchmark

The configurations extracted from EcoLat are used to evaluate the constraints of the MaxEnt distribution (the number of fishes, sharks, and near-neighbor couples). We found a good agreement between EcoLat and MaxEnt distributions (Fig. 1).

In Figs. 1(a) and 1(b), two sample configurations are compared. The general aspect of the system is well reproduced by near neighbors MaxEnt, except the shape of the shoals that exhibits some differences. This is reflected by the spatial correlation functions in Fig. 1(c), computed as the Pearson coefficient:

$$f_{ij}(x) = \frac{\langle \sigma_i(X)\sigma_j(X+x)\rangle - \langle \sigma_i(X)\rangle \langle \sigma_j(X+x)\rangle}{\sqrt{(\langle \sigma_i(X)^2\rangle - \langle \sigma_i(X)\rangle^2)(\langle \sigma_j(X)^2\rangle - \langle \sigma_j(X)\rangle^2)}}, \tag{29}$$

where $\sigma_i(X)$ is one if the site X is occupied by the ith species; note that f_{ij} does not depend on X thanks to the translational symmetry of the system. MaxEnt approximation, although it maintains the qualitative agreement, predicts lower fish-fish spatial correlation at larger distances. This does not affect the cluster-size distribution, see Fig. 1(d), that decays with the same slope both in EcoLat and MaxEnt. The reason can be understood by looking at the snapshots of the configurations in Figs. 1(a) and 1(b), where fishes create shoals of similar size but having more roundish shapes in EcoLat than in MaxEnt configuration, explaining the higher spatial correlations even if shoals exhibit the same size distributions. This is a general feature of the system independent on the choice of the phenotypes. It unveils that, in the dynamical steady state, fishes

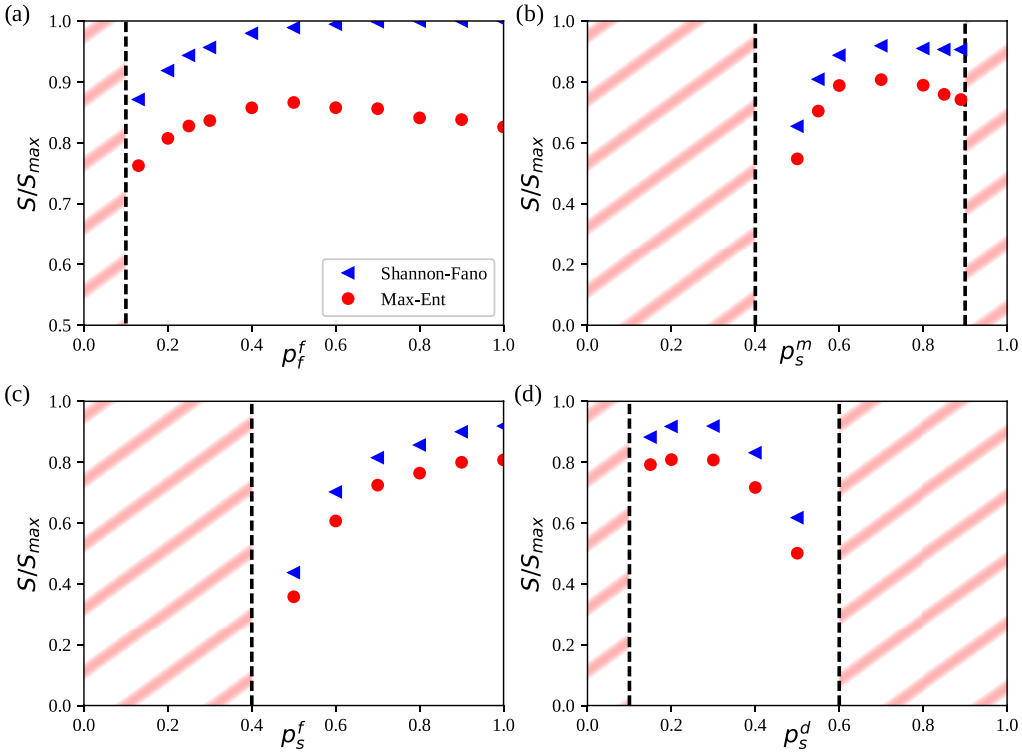

FIG. 2. Entropy per site as a function of species phenotypes. Blue triangles indicate the Shannon-Fano entropy Eq. (6a), while red circles indicate the MaxEnt entropy Eq. (25). The ranges of parameters that lead species to extinction are underlined by obliques lines. (a) Entropy vs. fish breading probability. A qualitative difference in the entropy behaviors appear when $p_f^f > 0.5$; MaxEnt entropy starts decreasing while Shannon-Fano one saturates to the maximum value. (b) Entropy vs. shark mobility. Also in this case a similar difference in behaviors manifests in the region $0.7 < p_s^m < 0.9$. These differences outline that structural ordering is occurring in the system. (c) Entropy vs. shark filiation. (d) Entropy vs. shark mortality. In these two cases, the Shannon-Fano approximation grasps qualitatively well the entropy trends, although the numerical values are overestimated.

cooperatively interact beyond near neighbors, while all other interactions seem operating on near-neighbor sites.

The power-law decay in EcoLat shoal size distribution [Fig. 1(d)] has been already observed [53] and assigned to a self-organized behavior of the system, moreover, it seems to be a general characteristic of several spatial ecology models [54].

The MaxEnt distribution is very close to a critical point. This can be checked by introducing a parameter T in analogy to the Boltzmann temperature; however, the T dependence alone is not an evidence of the criticality in the original system [55].

C. Entropic curves

Thanks to the method introduced in Eq. (25), it is possible to compute the entropy of the model and to shed light on several features of the ecosystem.

In Fig. 2 we report, as a function of the species relevant phenotypes, the entropy per site of the system normalized by its maximal value $\ln 3$. The entropy has been measured both through the mean-field Shannon-Fano algorithm Eq. (6a) and with the new approach based on the MaxEnt calculation of Eq. (25). The MaxEnt entropy estimation is always lower than the mean-field result, as expected due to the variational nature of the least-entropy-principle. Regions of phenotype values leading the system to extinction are filled with obliques lines. Figures 2(a) and 2(b), showing entropy curves as a function of p_f^f and p_s^m, respectively, manifest qualitative differences between Shannon-Fano and MaxEnt entropy trends. In particular, while Shannon-Fano predicted entropies reach a plateau whenever $p_f^f \gtrsim 0.5$ or $p_s^m \gtrsim 0.7$, MaxEnt ones display a maximum around those values. The increasing difference between Shannon-Fano and MaxEnt entropy is a clear sign that structural ordering is occurring since MaxEnt entropy is the exact entropy of the Potts-like Hamiltonian that takes into account spatial correlations even beyond near-neighbor ones [Fig. 1(c)].

This feature, particularly visible in Fig. 2(b), is related to the formation of waves of predator and preys [see snapshots in Fig. 3(b)].

Furthermore, extrapolation of Figs. 2(b)–2(d) entropy curves manifests sharp points in $p_s^m = 0.4$, $p_s^f = 0.4$, and $p_s^d = 0.6$, which are a peculiar sign of a second-order phase transition between coexistence and extinction. On the contrary, when $p_s^m = 0.9$ or $p_s^d = 0.1$ entropy displays a sudden jump into the extinction phase. This transition is due to a finite-size effect [56,57]: increasing the lattice size the probability of the system to extinguish in a fixed time becomes sharper as a function of the phenotypes but the transition threshold drifts to the bond value $p_s^m = 0$ in the thermodynamic limit.

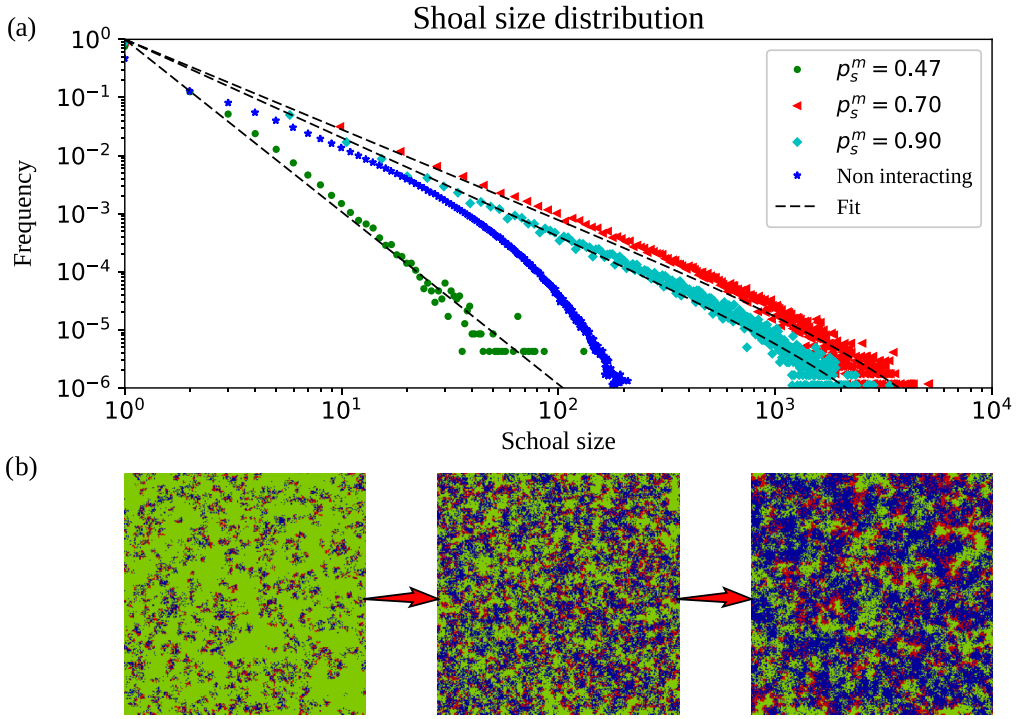

FIG. 3. (a) Distributions of prey shoal sizes for three different values of predator mobility (all parameters are reported in Appendix F). Distributions for $p_s^m = 0.47, 0.70, 0.90$ are shown in green dots, red triangles, and cyan diamonds, respectively. Blue stars represent the distribution of the independent-site model (Non interacting) with the fish density fixed to match the EcoLat one with $p_s^m = 0.7$. The EcoLat distributions have been fitted with a function $x^{-\gamma}\exp(x/\xi)$. The lower mobility case has $\xi = \infty$ and $\gamma = 2.97 \pm 0.04$, medium mobility has $\xi = 3450 \pm 220$ and $\gamma = 1.55 \pm 0.01$, while high shark motility gives a fish shoal distribution with $\xi = 2440 \pm 180$ and $\gamma = 1.69 \pm 0.01$. (b) Snapshots taken from the EcoLat steady-state distribution while tuning the shark mobility p_s^m from 0.47 (left) to 0.90 (right). Fishes are depicted in green, sharks in red, empty sites in blue.

D. Discussion

The measurement of disorder provides a new insight into the ecosystem. It allows us to recognize the second order phase transition near predator extinction threshold, to characterize the self-organized behavior of prey shoals, and to unveil the increase of structural ordering the system acquires improving the predator hunting capability. Here we discuss these findings following the ecosystem behavior while tuning the shark mobility (p_s^m) as in Fig. 2(b), since it is a particularly explicative parameter of the model. Increasing the shark mobility the system passes from an absorbing state where the lattice is crowded with preys to a phase in which sharks start appearing in small shoals swimming in a sea of fishes. This is a critical point known in literature [32,35,36] and it was characterized by its dynamical properties, where predator population decays in time with a power law, and it belongs to the directed percolation universality class. The criticality of this point is reflected in the entropy behavior which manifests a sharp point.

This phase transition, marking the passage between species coexistence and extinction, happens where the entropy reaches zero (sharp points in Figs. 2(b)–2(d) at $p_s^m = 0.4$, $p_s^f = 0.4$, and $p_s^d = 0.6$), and it can be attained diminishing the shark hunting ability as well as their fertility or increasing their mortality. The zero entropy of this critical point can be explained in a Shannon-Fano framework; in fact, the predominance of preys unbalances the average numbers of sharks and fishes.

Moving away from the aforesaid criticality, fish clusters acquire a power-law distribution [54] well described by the MaxEnt approximation (Fig. 1). Very interestingly, this kind of distribution cannot be simply explained in a Shannon-Fano framework. In fact, if we simulate an independent size model, fixing the densities as the real EcoLat ones, we obtain the cluster size distribution of Fig. 3(a) that does not match with the EcoLat one. Moreover, the Fisher exponent of the EcoLat distribution varies in the studied parameter ranges between 1.5 and 3 not matching with the fixed 2.05 one of the independent-site model at the percolation threshold (ordinary percolation). It is worth to notice that the observed power-law is completely accounted for and described by near-neighbor interactions, as the MaxEnt approach is able to quantitatively reproduce it [Fig. 1(d)]. Furthermore, the MaxEnt Hamiltonian is very close to a critical point. Even if this feature alone is not a signature that the real EcoLat is itself close to a criticality [55], the MaxEnt power-law cluster distribution is related to this criticality. Is the power-law distribution a marker of self-organized criticality in the EcoLat model? The excellent accordance with the critical MaxEnt power-law seems to support this hypothesis.

Increasing p_s^m from the directed percolation critical point we see the disorder growing [first two snapshots of Fig. 3(b)]. At first, the system starts getting rid of fish dominance (i.e.,

it moves away from direct percolation critical point) simply increasing the number of predators. Both the higher number of sharks and their increased motility make the ecosystem drift toward more disordered configurations (both Shannon-Fano and MaxEnt entropies increase). At a certain point, the interactions between species dominate and the system passes to a regime where it starts regaining order. From Figs. 2(b) and 3, we see that entropy discriminates these two distinct dynamical behaviours of species at coexistence: the one with a predominance of fishes and sharks grouping in small shoals, and the other where both preys and predators form elaborate shoals, characterized by a spreading wavelike fronts of fishes and sharks [32,58] with predators surrounding the shoals of preys [Fig. 3(b)]. Very interestingly, this crossover is clearly characterized by a decreasing MaxEnt entropy with respect to a constant Shannon-Fano one [Fig. 2(b)], remarking the structuring of the system and the impossibility of grasping this behavior just considering the mean-field approximation. The progressive reachievement of order can be visualized by looking at the last two EcoLat snapshots in the steady-state regime [Fig. 3(b)]. Notably, this new structural order is very different from the mean-field order close to the shark extinction threshold [last versus first snapshots of Fig. 3(b)]. The structural order can be measured as the difference between Shannon-Fano and MaxEnt entropy. In fact, Shannon-Fano order is a mean-field quantity that does not depend on the disposition of species in the lattice, while MaxEnt entropy considers the order resulting from all possible correlations reproduced by a three-state Potts model. An analogy with the Ising model (where the MaxEnt algorithm is exact) gives a clearer picture: in the overcritical region, $T > T_c$ and no external magnetic field, the Shannon-Fano entropy is always at its maximum value since there is an equal number of spin up and spin down. However, the true entropy decreases as $T \to T_c$ since ordered spin domains appear.

Finally, another transition between coexistence and extinction is reached by further increasing the shark mobility (as well as decreasing the fish fertility and shark mortality). Contrariwise to the first critical point, the entropy does not continuously go to zero in correspondence of the phase transition, but abruptly jumps to zero (Fig. 2). This is a finite-size effect [56,57] that disappears when $L \to \infty$. It is worth to notice that, at fixed L, it is possible to continuously tune the phenotype to get a steady-state metastable phase even in the extinction region that lives until a sufficiently large stochastic fluctuation causes a brutal extinction. This is very worrying; in fact, it is difficult to predict since no precursors are present and can bring to an ecological catastrophe.

IV. CONCLUSIONS

Entropy measurements in complex systems have always been challenging. MaxEnt is a powerful tool to obtain an estimation of the probability distribution of the system from simulations or experimental data. Until now, the information provided by the intermediate steps of the MaxEnt solution was wasted. We introduce a way to recycle it to directly evaluate the entropy of the system without any further time-consuming computation [Eq. (25)]. Thanks to the MaxEnt nature of the probability distribution, a variational principle for entropy evaluation of the real system can be formulated, which ensures that the obtained entropy is always greater or equal to its true value. Moreover, Eq. (25) is quite general, allowing us to compute entropy wherever it is possible to formulate a MaxEnt algorithm.

Among many possible applications, the knowledge of entropy in ecological systems plays a pivotal role describing the complexity due to the phenotype variability. In the studied prey-predator ecosystem, it sheds new light on the self-organizing behavior of preys. The direct near-neighbor correlations used in our MaxEnt approach are found to be the fundamental ingredient in this self-organized behavior: The MaxEnt Hamiltonian quantitatively reproduces the scale-free behavior of the prey shoals size, where the simpler mean-field approach fails. Furthermore, entropy allows the measurement of structural ordering, that is found to be a key ingredient in characterizing the crossover between two different coexistence behaviors, one where predators form localized patches (dominated by mean-field disorder) and another where predators chase preys in spreading prey-predator fronts (dominated by structural order).

As a matter of fact, the entropy curves reported in Fig. 2 are a powerful tool to investigate the system from quite different perspectives. This new tool will enable the study of entropic-driven phenomena, like entropic forces, already found to be of great importance in many biological systems as flocks of birds [7].

Furthermore, the general nature of the method encourages its application in many other systems of interest.

ACKNOWLEDGMENTS

The authors thank Francesca Tria, Vito D. P. Servedio, and Vittorio Loreto for useful insights and Andrea De Martino and Francesco Mauri for helpful discussions.

APPENDIX A: MEAN-FIELD MAXENT

Here we derive Eq. (5). In the mean-field approximation, only one-body observables $\{x_i\}_{i=1}^q$ are constrained, e.g., $\langle x_i \rangle$ is the average number of nodes in the ith state. Now, Eq. (4) describes a noninteracting effective Hamiltonian:

$$\langle x_i \rangle = \frac{1}{Z} \sum_{\sigma_1 \cdots \sigma_M} \left(\sum_{k=1}^{M} \delta_{\sigma_k,i} \right) \exp\left(- \sum_{h=1}^{q} \lambda_h \sum_{k=1}^{M} \delta_{\sigma_k,h} \right), \quad \text{(A1)}$$

where Z is the normalization of the probability distribution and we identified the configuration $\vec{\sigma}$ with its site values:

$$\vec{\sigma} = \begin{pmatrix} \sigma_1 \\ \sigma_2 \\ \vdots \\ \sigma_M \end{pmatrix}. \quad \text{(A2)}$$

The $(\sum_{k=1}^{M} \delta_{\sigma_k,i})$ is the application of the x_i observable on the $\vec{\sigma}$ state. Since x_i does not depend on the particular site k, we have

$$\langle x_i \rangle = M \frac{e^{-\lambda_i}}{\sum_{h=1}^{q} e^{-\lambda_h}}. \quad \text{(A3)}$$

Equation (A3) defines a complete set of linear equations. They are dependent since we have the constraint:

$$\sum_{i=1}^{q} \langle x_i \rangle = M. \tag{A4}$$

It is straightforward to show that the most general solution of the system is given by

$$\lambda_i = -\log\left(\frac{\langle x_i \rangle}{M}\right) + C, \tag{A5}$$

where C is an arbitrary constant that does not affect any physical quantity. For the sake of simplicity, in Eq. (5) we set $C = 0$.

APPENDIX B: IMPORTANCE SAMPLING

The minimization of Eq. (8) is computationally expensive. In each step, the expected values of the observables for the trial set of λ_i parameters must be computed through a Monte Carlo–metropolis integration. A natural extension of the Metropolis algorithm consists of re-weighting the extracted configurations at each step. This method takes the name of importance sampling (IS), and it has been widely applied in many physical applications [59,60]. It was introduced in MaxEnt by Broderick *et al.* [61].

The average of an observable with an Hamiltonian H' can be computed using a set uniform distributed configurations $\{c\}_{i=1}^{N_c}$ as follows:

$$\langle A \rangle_{H'} = \sum_{i=1}^{N_c} \left(A(c_i) \frac{P_{H'}(c_i)}{P_H(c_i)} \right) P_H(c_i) = \left\langle A \frac{P_{H'}}{P_H} \right\rangle_H. \tag{B1}$$

This average can be computed using Monte Carlo integration on a set of metropolis extracted configurations $\{c'\}_{i=1}^{N_c}$ with the H Hamiltonian:

$$\langle A \rangle_{H'} \approx \frac{1}{Z(N_c)} \sum_{i=1}^{N_c} A(c_i') e^{-\beta[H'(c_i') - H(c_i')]}, \tag{B2a}$$

$$Z(N_c) = \sum_{i=1}^{N_c} e^{-\beta[H'(c_i') - H(c_i')]}. \tag{B2b}$$

Handling with large lattices, energy differences can be considerable, and the exponential term may give rise to numerical instabilities. To correct these instabilities a constant factor a can be added to both exponential terms, equal to the maximum energy difference of all extracted configurations.

Estimating the goodness of IS in MaxEnt implementation can be difficult. In fact, we lack the *a priori* knowledge of the partition function of the original probability distribution. To upstage, the problem we implemented a new statistical evaluator for the MaxEnt algorithm and in general for IS Metropolis implementation. At each step the total extracted configurations are divided into two random groups and the normalization factors are compared:

$$\eta = \left| \frac{Z'(N_c/2)}{Z''(N_c/2)} - 1 \right|. \tag{B3}$$

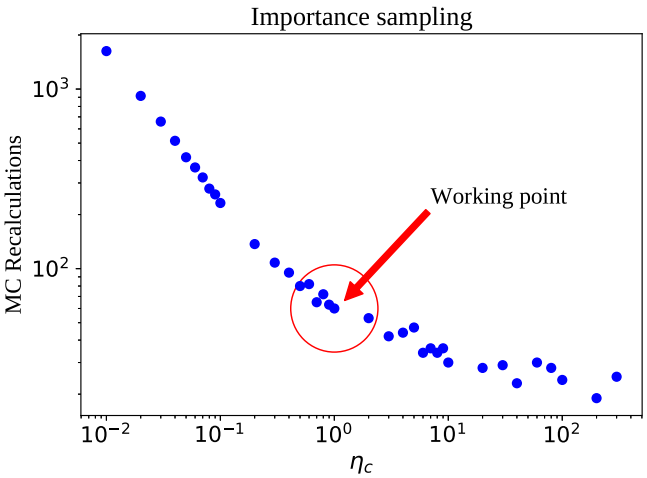

FIG. 4. Number of Monte Carlo simulations to reach convergence as a function of the η_c parameter Eq. (B3). The optimal working point lies in the marked region.

If η exceeds a critical value η_c, new configurations are extracted from the Metropolis algorithm. Figure 4 shows the performance of IS vs the η_c parameter. For $\eta_c \ll 1$, Eq. (B3) is symmetric with respect to Z' and Z''. For higher values of η_c the symmetry is recovered by random shuffling the configurations at each step.

APPENDIX C: PROOF OF THE LEAST MAXIMUM ENTROPY PRINCIPLE

By definition, the MaxEnt entropy is always greater than the true entropy:

$$S_{\text{real}} \leqslant S_{\text{ME}}[\{\hat{x}_i\}], \tag{C1}$$

where S_{real} is the real entropy of the system, while $S_{\text{ME}}[\{x_i\}]$ is the maximum entropy of all possible probability distributions that fix the set of $\hat{x}_i$ observables.

To prove the least maximum entropy principle, a set of observables $\hat{x}_i$ must exist so that Eq. (C1) is an equality. In any finite-size system, where configurations can be represented with a finite dimension vector, this is trivial, since it is possible to choose a set of observables $\hat{y}_i$ defined as

$$\hat{y}_i(\vec{\sigma}) = \delta(\vec{\sigma}, \vec{\sigma}_i), \tag{C2}$$

where $\vec{\sigma}$ is the configuration on which the observables act, $\vec{\sigma}_i$ is a particular configuration associated with the observable $\hat{y}_i$, and δ is the Kronecker symbol.

If two probability distributions are different, then a configuration $\vec{\sigma}_i$ must exist so that their probabilities differ:

$$p_1(\vec{\sigma}_i) \neq p_2(\vec{\sigma}_i). \tag{C3}$$

The two distributions give two distinct expected values for the corresponding $\hat{y}_i$ observable:

$$\langle y_i \rangle_{p_1} = \sum_j p_1(\vec{\sigma}_j)\delta(\vec{\sigma}_j, \vec{\sigma}_i) = p_1(\vec{\sigma}_i) \neq p_2(\vec{\sigma}_i) = \langle y_i \rangle_{p_2}. \tag{C4}$$

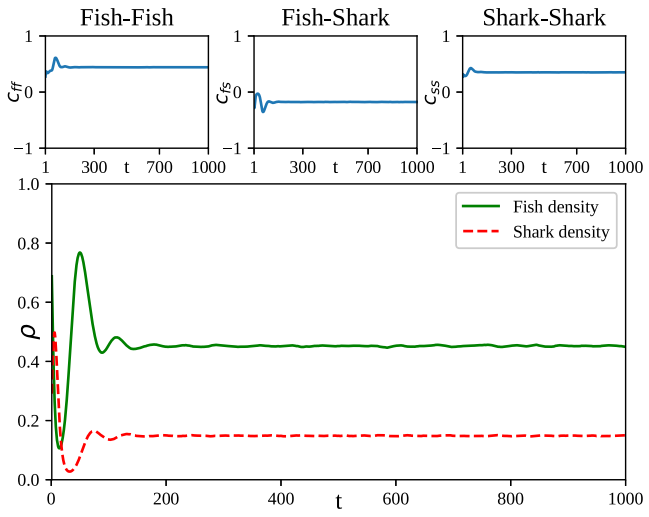

FIG. 5. Time evolution of the mean fish and shark densities and near-neighbor Pearson correlation coefficients computed on an ensemble composed by 100 replicas of the system. The simulation is prepared in an initial uniform distribution fixing the densities of preys and predators to $4/5$ and $1/5$, respectively.

The complete set of $\hat{y}_i$ fixes the probability distribution, so that

$$S_{\text{real}} = S_{\text{ME}}[\{\hat{y}_i\}]. \tag{C5}$$

Indeed, single-site density and couple density can be written as linear combination of the complete set of $\hat{y}_i$ observables. Therefore, the introduction of more independent constraints assures the convergence of the MaxEnt entropy toward the real entropy.

APPENDIX D: DYNAMICAL MONTE CARLO SIMULATIONS OF THE ECOLAT MODEL

Dynamical Monte Carlo allows us to simulate the EcoLat master equation [Eq. (27)]. Since the number of possible states is huge (3^M) it is impossible to numerically evolve the probability distribution. However, a stochastic solution of Eq. (27) is still possible: N replicas of the system, extracted according to an initial distribution $P(\vec{\sigma}, 0)$, can be evolved according to the transition matrix Π. The obtained time-dependent ensemble can be used to compute the averages of any observable as a function of time.

The EcoLat model reaches the asymptotic steady-state distribution described by Eq. (28). Figure 5 shows the time dependence of the mean density of preys and predators as well as the near-neighbor correlation coefficients [Eq. (29)].

Note that, although the time evolution of the single system continues to oscillate in the steady state, the correlation time is finite. This assures that, after a transient time, all the N simulations are independent and distributed according to the $P(\vec{\sigma})$ [Eq. (28)].

APPENDIX E: ERGODIC HYPOTHESIS

Here we discuss the stability of the steady-state distribution that depends on the ergodicity of the system [62]. Generally speaking, a system is ergodic if it can move between any couple of points in the phase space in a finite number of steps [63]. EcoLat does not satisfy this requirement; in fact, two traps are present in the phase space: if the system gets a configuration without preys or predators, it always evolves toward an absorbing state. However, in simulations, once the system has reached the nonabsorbing steady state (Fig. 5), it remains there during all the simulation time. So, we can postulate a weak ergodic hypothesis, where we imagine to restrict the feasible phase space excluding the absorbing traps. This is equivalent to neglecting the elements of the Π transition matrix that lead the system into the absorbing traps. Such an approximation makes sense if the lifetime τ of the metastable equilibrium is much larger than the typical time scales of the system. All the dynamical Monte Carlo simulations computed in Fig. 2 have $\tau \gg t_{\max}$, where $t_{\max}$ is the maximum simulation time (10^6).

APPENDIX F: SIMULATION DETAILS

Phenotypic parameters for the EcoLat simulation of Fig. 1 are: $p_f^f = 0.2$, $p_f^m = 0.8$, $p_s^m = 0.7$, $p_s^f = 1$, $p_s^d = 0.3$. Phenotypic parameters for the EcoLat simulation of Fig. 3 are the same apart for p_s^m that assumes the values of 0.47, 0.70, and 0.90.

All simulations and computations were carried out using authors handmade C and Python scripts. Python packages NumPy [64], SciPy [65], and MatPlotlib [66] were utilized during analysis and figure realization.

[1] W. Johannsen, Am. Nat. **45**, 129 (1911).
[2] F. B. Churchill, J. Hist. Biol. **7**, 5 (1974).
[3] W. Bialek, *Biophysics: Searching for Principles* (Princeton University Press, Princeton, NJ, 2012).
[4] S. P. Strong, R. Koberle, R. R. de Ruyter van Steveninck, and W. Bialek, Phys. Rev. Lett. **80**, 197 (1998).
[5] I. Nemenman, W. Bialek, and R. de Ruyter van Steveninck, Phys. Rev. E **69**, 056111 (2004).
[6] W. Bialek, A. Cavagna, I. Giardina, T. Mora, E. Silvestri, M. Viale, and A. M. Walczak, Proc. Natl. Acad. Sci. USA **109**, 4786 (2012).
[7] M. Castellana, W. Bialek, A. Cavagna, and I. Giardina, Phys. Rev. E **93**, 052416 (2016).
[8] W. Bialek, I. Nemenman, and N. Tishby, Neural Comput. **13**, 2409 (2001).
[9] C. E. Shannon, Bell Syst. Tech. J. **30**, 50 (1951).
[10] J. L. Kelly, Bell Syst. Tech. J. **35**, 917 (1956).
[11] G. C. Philippatos and C. J. Wilson, Appl. Econ. **4**, 209 (1972).
[12] D. De Martino, F. Capuani, and A. De Martino, Phys. Rev. E **96**, 010401 (2017).
[13] D. De Martino, F. Capuani, and A. De Martino, Phys. Biol. **13**, 036005 (2016).

[14] E. Kussell, Science **309**, 2075 (2005).
[15] M. Weigt, R. A. White, H. Szurmant, J. A. Hoch, and T. Hwa, Proc. Natl. Acad. Sci. USA **106**, 67 (2008).
[16] A. G. Tansley, Ecology **16**, 284 (1935).
[17] W. C. Allee, Ecol. Monogr. **4**, 541 (1934).
[18] F. S. Chapin, P. A. Matson, and P. M. Vitousek, *Principles of Terrestrial Ecosystem Ecology* (Springer, New York, 2011).
[19] W. Cooper and D. Blumstein, *Escaping From Predators: An Integrative View of Escape Decisions* (Cambridge University Press, Cambridge, 2015).
[20] B. A. Belgrad and B. D. Griffen, Proc. Roy. Soc. B: Biol. Sci. **283**, 20160408 (2016).
[21] R. S. Olson, A. Hintze, F. C. Dyer, D. B. Knoester, and C. Adami, J. Roy. Soc. Interf. **10**, 20130305 (2013).
[22] T. W. Swetnam and J. L. Betancourt, J. Clim. **11**, 3128 (1998).
[23] P. Kindlmann, H. Yasuda, Y. Kajita, S. Sato, and A. F. G. Dixon, Front. Ecol. Evol. **3**, 27 (2015).
[24] N. Bax, ICES J. Marine Sci. **55**, 997 (1998).
[25] A. J. Lotka, Proc. Natl. Acad. Sci. USA **6**, 410 (1920).
[26] V. Volterra, *Variations and Fluctuations of the Number of Individuals in Animal Species Living Together in Animal Ecology* (McGraw-Hill, New York, 1931).
[27] E. E. Holmes, M. A. Lewis, J. E. Banks, and R. R. Veit, Ecology **75**, 17 (1994).
[28] K. Kuto and Y. Yamada, J. Diff. Equ. **197**, 315 (2004).
[29] J. D. Ferreira, C. A. T. Salazar, and P. C. Tabxsares, Nonlin. Anal.: Real World Appl. **14**, 536 (2013).
[30] J. E. Satulovsky and T. Tomé, Phys. Rev. E **49**, 5073 (1994).
[31] A. Lipowski, Phys. Rev. E **60**, 5179 (1999).
[32] U. Dobramysl, M. Mobilia, M. Pleimling, and U. C. Täuber, J. Phys. A **51**, 063001 (2018).
[33] A. K. Dewdney, Sci. Am. **251**, 14 (1984).
[34] M. Mobilia, I. T. Georgiev, and U. C. Täuber, Phys. Rev. E **73**, 040903 (2006).
[35] T. Antal, M. Droz, A. Lipowski, and G. Ódor, Phys. Rev. E **64**, 036118 (2001).
[36] U. C. Täuber, J. Phys.: Conf. Ser. **319**, 012019 (2011).
[37] I. Nemenman, F. Shafee, and W. Bialek, in *Advances in Neural Information Processing Systems* (MIT Press, 2002), pp. 471–478.
[38] E. T. Jaynes, Phys. Rev. **106**, 620 (1957).
[39] A. Cavagna, I. Giardina, F. Ginelli, T. Mora, D. Piovani, R. Tavarone, and A. M. Walczak, Phys. Rev. E **89**, 042707 (2014).
[40] T. Mora, A. M. Walczak, W. Bialek, and C. G. Callan, Proc. Natl. Acad. Sci. USA **107**, 5405 (2010).
[41] E. Schneidman, M. J. Berry, R. Segev, and W. Bialek, Nature **440**, 1007 (2006).
[42] C. E. Shannon, Bell Syst. Tech. J. **27**, 379 (1948).
[43] R. M. Fano, *The Transmission of Information* (Massachusetts Institute of Technology, Cambridge, 1949).
[44] S. W. Lockless, Science **286**, 295 (1999).
[45] M. Socolich, S. W. Lockless, W. P. Russ, H. Lee, K. H. Gardner, and R. Ranganathan, Nature **437**, 512 (2005).
[46] W. P. Russ, D. M. Lowery, P. Mishra, M. B. Yaffe, and R. Ranganathan, Nature **437**, 579 (2005).
[47] W. Bialek and R. Ranganathan, arXiv:0712.4397 (2007).
[48] K. Pearson, Philos. Mag. Series 6 **2**, 559 (1901).
[49] H. Hotelling, J. Edu. Psychol. **24**, 417 (1933).
[50] S. G. Nash, SIAM J. Sci. Stat. Comput. **6**, 599 (1985).
[51] R. B. Potts and C. Domb, Math. Proc. Cambridge Philos. Soc. **48**, 106 (1952).
[52] R. K. P. Zia and B. Schmittmann, J. Stat. Mech.: Theory Exp. (2007) P07012.
[53] B. Sutherland and A. Jacobs, Complex Syst. **8**, 385 (1994).
[54] M. Pascual, M. Roy, F. Guichard, and G. Flierl, Philos. Trans. R. Soc. London B **357**, 657 (2002).
[55] I. Mastromatteo and M. Marsili, J. Stat. Mech.: Theory Exp. (2011) P10012.
[56] M. Parker and A. Kamenev, Phys. Rev. E **80**, 021129 (2009).
[57] A. Dobrinevski and E. Frey, Phys. Rev. E **85**, 051903 (2012).
[58] M. Mobilia, I. T. Georgiev, and U. C. Täuber, J. Stat. Phys. **128**, 447 (2007).
[59] G. Torrie and J. Valleau, J. Comput. Phys. **23**, 187 (1977).
[60] I. Errea, M. Calandra, and F. Mauri, Phys. Rev. B **89**, 064302 (2014).
[61] T. Broderick, M. Dudik, G. Tkacik, R. E. Schapire, and W. Bialek, arXiv:0712.2437 (2007).
[62] K. Huang, *Statistical Mechanics* (Wiley, New York, 2008).
[63] R. Palmer, Adv. Phys. **31**, 669 (1982).
[64] S. van der Walt, S. C. Colbert, and G. Varoquaux, Comput. Sci. Eng. **13**, 22 (2011).
[65] E. Jones, T. Oliphant, P. Peterson *et al.*, SciPy: Open source scientific tools for Python (2001), http://www.scipy.org/.
[66] J. D. Hunter, Comput. Sci. Eng. **9**, 90 (2007).

Gene heterogeneity drives the evolution of species

Mattia Miotto[a,1] **and Lorenzo Monacelli**[a,1,2]

[a] Department of Physics, "Sapienza" University of Rome, Piazzale Aldo Moro 5, 00185, Rome, Italy

This manuscript was compiled on November 3, 2019

We study a minimal model for the evolution of an ecosystem where two antagonist species struggle for survival on a lattice. Each specimen possesses a toy genome, encoding for its phenotype. The gene pool of the populations changes in time due to the effect of random mutations on genes (entropic force) and of interactions with the environment and between individuals (natural selection).

We prove that the relevance of each gene in the manifestation of the phenotype is a key feature for evolution. In presence of a uniform gene relevance, a mutational meltdown is observed. Natural selection acts quenching the ecosystem in a non-equilibrium state that slowly drifts, decreasing the fitness and leading to the extinction of the species.

Conversely, if a specimen is provided with a heterogeneous gene relevance, natural selection wins against entropic forces, and the species evolves increasing its fitness. We finally show that heterogeneity together with spatial correlations is responsible for spontaneous sympatric speciation.

Evolution | Heterogeneity | Sympatric speciation | Entropy

Evolution by natural selection shaped the marvelous biodiversity we presently observe in nature. Starting with one (or few) living organisms, the tree of life progressively branched as living beings managed to survive to different environments through adaptations and speciations (1).

Both processes arise by a complex interplay between intrinsic forces (e.g. mutations) and extrinsic ones, provided by the interactions between the different components of the ecosystem (2). This results in changes of behavior, morphology, and physiology (or combinations thereof) in the organisms.

Since its first formulation, the theory of evolution regarded natural selection, i.e. the effect of environment and interaction inter and intraspecies in selecting the organisms with maximum fitness, as the pivotal mechanisms of evolution. Several more years were required to clearly define the 'microscopic' role of genome mutations (alongside genetic drift, hitchhiking ext.) as the other main component of the evolutionary process (3–6).

Quantifying the simultaneous effects of natural selection and genomic mutations is far from being an easy task (5, 7–9). Its understanding is however not only a fascinating theoretical challenge but carries important practical implications. In fact, a continuously increasing literature highlights the connection between the rules governing ecology to the one regarding cell populations (10–12). Preeminent is the case of cancer cells, that are both subject to high entropic forces (fast mutation rates) and a strong natural selection, due to the selective pressure given by both the competition with the immune system and the effect of anti-cancer therapies. Bacteria drug resistance is under much scrutiny, too, since the selection done by antibiotics influences the evolution of resilient traits. Experimentally, the evolution of genomes during speciation has been studied only recently with the availability of next-generation sequencing technologies (13–15). In particular, recent findings highlighted how mutations on certain genes considerably enhance the speciation process (15). Also the increase of the genome length, due to duplication errors (e.g. the presence of redundant genes/chromosomes) has been pointed as one mechanism for evolution/speciation (16).

Parallel to experiments, several theoretical models were developed to study ecosystem dynamics(17, 18) and evolution, both at the molecular level (7, 19) and at the population level, such as population-environment interaction (20–23) and specie-species interactions (24–31).

In particular, agent-based models proved to be very efficient to include spatial information/features (32–36). Here, evolution is accounted either at phenotype level, i.e. the phenotype of a species is randomly modified generation by generation according to a particular law (20, 24, 37), or at genotype level, i.e. an evolution law is assumed for a genome upon which the phenotype is computed (38–41). More refined models have been considered accounting for dominant and recessive alleles, sex recombination (cross-over) or spatially resolved ecosystem dynamics (41–43).

This work aims to study how heterogeneity in gene relevance affects the evolution of the species. In particular, we study the evolution of a minimal ecosystem on a lattice, initially composed by one species of predators and one of preys. Each specimen possesses a toy genome composed of $3N$ genes that encode for three essential macro-phenotypic features of the animal: i) its capability of moving/hunting, ii) its fertility and iii) the mean life-time of the specimen (mortality).

The genome pool of the two prey-predator species can change in time due to random mutations at the level of the single genes (entropic force) and to predation/death events (selection force). Aiming at limiting the number of parameters and developing an evolutionary model as minimal as possible, we do not insert mating in the model, i.e. we have an asexual

Significance Statement

How genomes change to create new species is still a major question of evolutionary biology. Here, we identify heterogeneity in gene relevance as the control parameter that allows species to improve their fitness and originate new species. In fact, differentiating the contribution of genes to the phenotype prevents the accumulation of deleterious mutations (mutational meltdown), that in time leads species to extinction. At the same time, we found that gene heterogeneity and spatial correlations are the leading features for sympatric speciation. Altogether, we point to gene heterogeneity as a fundamental ingredient for the modern theory of evolution.

M.M. and L.M. conceived research, performed research and wrote the paper.

The authors declare no conflict of interest.

[1] M.M. and L.M. contributed equally to this work.

[2] To whom correspondence should be addressed. E-mail: author.twoemail.com

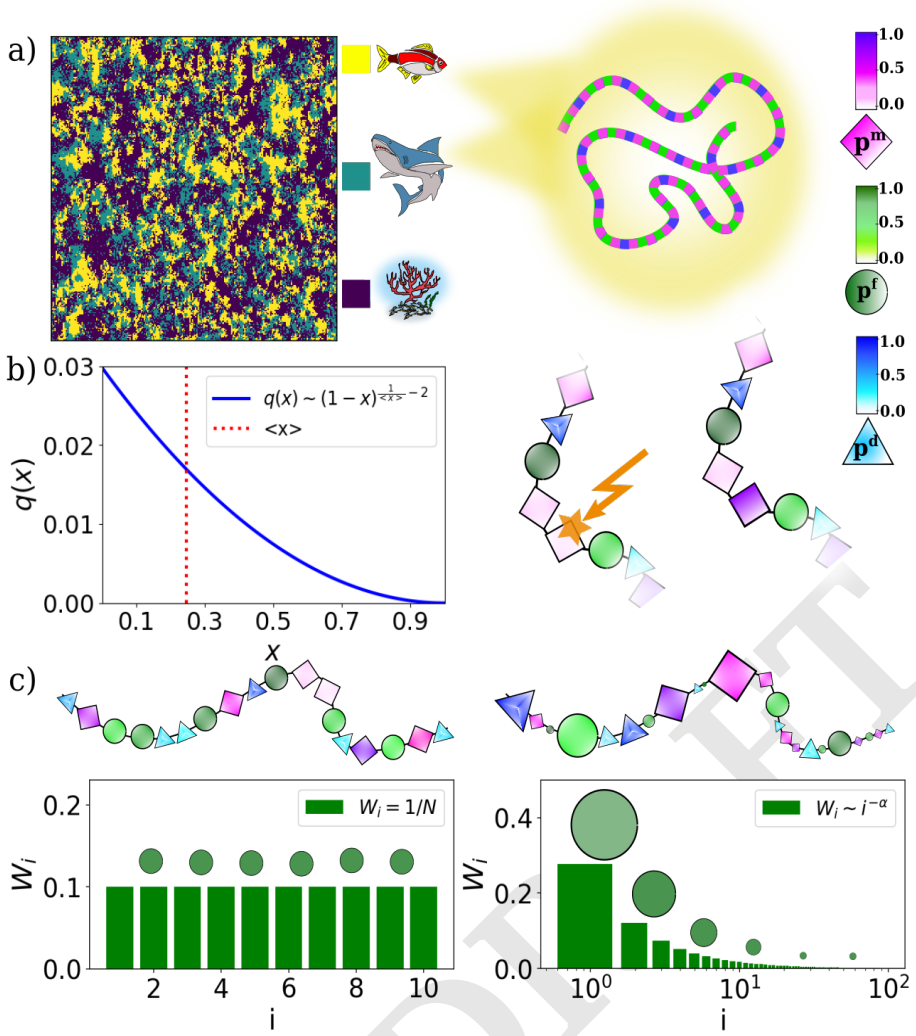

Fig. 1. Features of the EvoLat model. a) Snapshot of an EvoLat configuration in the steady-state regime. Fishes are colored in yellow, sharks in blue, while purple cells represent the environment. Each animal on the lattice possesses a toy genome, composed of $3N$ genes. Each gene is represented by a real number between 0 and 1 that concurs in manifesting three macro-phenotypes associated with the animals. Animal mobility is represented by the probability of moving, p^m, their fertility by the breeding probability (p^f) and their life-time by the death probability (p^d). **b)**Mutation events can happen with a rate, μ with equal probability on each gene. If one gene is subject to a mutation, a new value between 0 and 1 is extracted from the underline phenotype distribution $q(x)$, whose asymmetry accounts for the fact that mutations tend to be deleterious for the organisms. **c)** The phenotype of the individual is obtained as the weighted average over all the N independent genes encoding for it. In the present work, we assume two possible kinds of weights, uniform mean (all genes equally concur to the phenotype) or power-law weighted mean (some genes influence the phenotype more than others).

reproduction. Since mating is not taken into consideration, we will not look for speciation according to Mayr's Biology Speciation Concept, where different species are separated if mating does not produce fertile off-springs (4). Instead, we speak of speciation in terms of differences in phenotype distributions (44), where well-separated peaks can be interpreted as different species while the width of each peak accounts for the intra-species differentiation.

Two different kinds of genome are considered: i) a uniform genome (where all the genes have the same impact on the phenotype), and a heterogeneous genome (where each gene has a different weight on the overall phenotype). We show that, while in the first case entropy dominates, fostering the mutational meltdown (45–47), in the latter one natural selection allows the ecosystem to increase predator fitness. For each genome, we also look for the emergence of spontaneous speciation.

1. Model

We consider a variant of the EcoLat (Ecosystem on Lattice) model (34), where each site of a $L \times L$ square lattice can be occupied exclusively either by the environment or a prey or a predator. To use the same notation adopted in (34), we identify preys as fishes (f) and predators as sharks (s). At every discrete time step, fishes can move, breed or remain still with probability p_f^m, p_f^f and $1 - p_f^m - p_f^f$. Sharks can move (p_s^m) or remain still ($1 - p_s^m$). Furthermore, predators eat preys whenever they step into a cell occupied by a prey. In this case, sharks can reproduce with probability p_s^f. If a shark does not eat a fish during its round, it can die for starvation with probability p_s^d. We assumed that fishes may only die murdered by a predator (i.e. $p_f^d = 0$).

The set of three probabilities, $\{p^m_{(s,f)}, p^f_{(s,f)}, p^d_{(s,f)}\}$, constitutes the macro-phenotype of each individual, dictating the rates with which the specimen carries out three essential tasks of life.

Each specimen has a genome that codes the macro-phenotype of the individual. The macro-phenotype is obtained as a weighted averages over all the N genes (g_i) that code for a particular feature:

$$p_y = \sum_{i=1}^{N} g_{yi} W_i \qquad y = {}^{(m,f,d)}_{(s,f)}, \qquad [1]$$

where W_i expresses the weight of the i-th gene in the manifes-

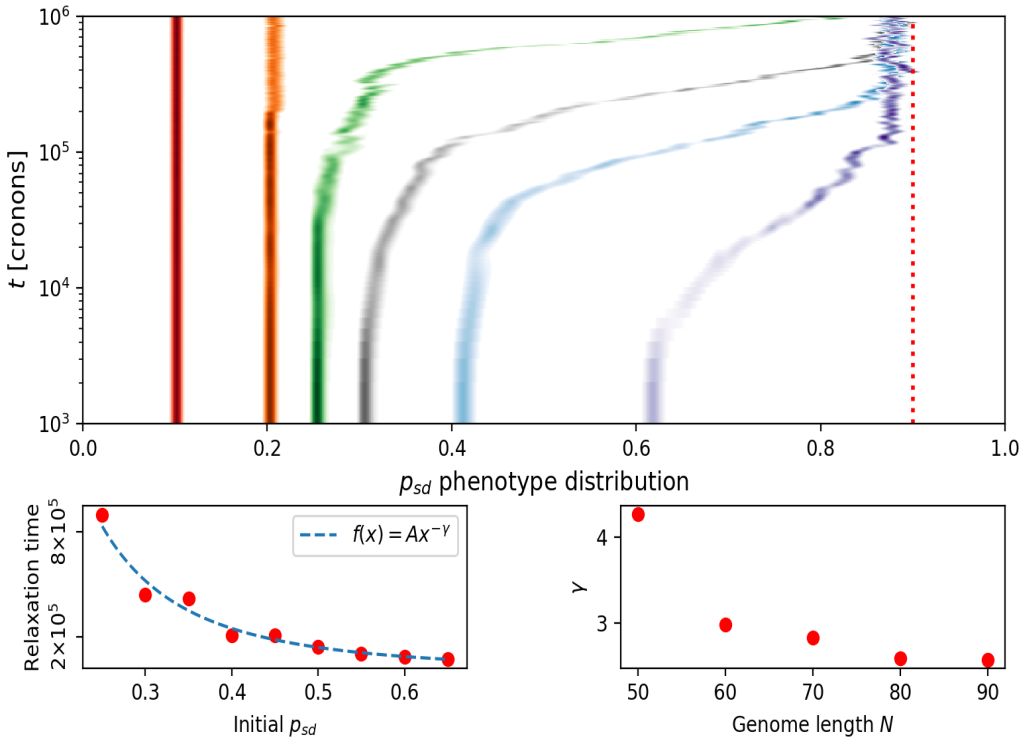

Fig. 2. Time evolution of predators death-rate after quenching. The predator relaxation time diverges as a power-law, in a way that resemble the dynamic of glassy systems. Different colors correspond to different simulations performed starting from several values of p_{sd}. a) Shark mortality distribution. The dashed vertical line is the stationary state for predator growing in a breeding farm (no natural selection).**b)** Relaxation time as a function of the initial phenotype. **c)** Exponent of the power law as a function of the genome length. It converges to a value of about 2.57. Simulation in panel a and b are performed with $N = 90$.

tation of the phenotype (see Figure 1*a*).

Genome is subject to point mutations, i.e. Poisson-distributed random events in time occurring with a constant rate for each gene every time a new individual is born (reproduction is asexual). If a mutation event occurs on a gene, its value is reset to a random number between 0 and 1. In order to tune the average value of the new mutated gene, we choose the new value $g_i = x$ according to the following probability distribution:

$$q(x) = \left(\frac{1}{\langle x\rangle} - 1\right)(1-x)^{\frac{1}{\langle x\rangle}-2} \qquad [2]$$

with $\langle x\rangle$ is a tunable parameter that determines the average value of the gene after the mutation (see Figure 1*b*). Such kind of asymmetric distributions is widely used for phenotype modeling, e.g. in the contest of bacterial growth rates, where slow rates dominate over fast ones (20, 48, 49). In this way, deleterious mutations can be enforced to be more common than favorable ones. This is quite reasonable, as a random mutation in the coding DNA produces a random change in the amino-acid chain of a protein, that is far more likely to produce an unfolded structure than a more functional one (50, 51).

Finally, in this work we will consider two weight distributions (see Figure 1*c*):

- a uniform distribution, where all genes equally contribute to manifest the phenotype (discussed in Sec. A)

$$W_i = \frac{1}{N}, \qquad [3]$$

- a power-law distribution allowing for the presence of preeminent genes, as discussed in Sec. B,

$$W_i \propto i^{-\alpha}. \qquad [4]$$

To assess the outcome of evolution, we define the fitness measured as the average size of the population. Such definition, profoundly linked with the usual fitness measurements (growth rate or the number of nephews per individual), is enforced by the finite carrying capacity, dictated by the lattice.

2. Results

A. Uniform genome. To begin with, we investigated the model behavior in presence of a uniform genome, where each phenotype is determined as the uniform average over all the genes associated to that phenotype (as given by Eq. (1) with Eq. (3)).

After preparing the ecosystem in a non-equilibrium steady state (NESS) with fixed initial phenotypes, we turned on mutations and followed the evolution of prey's and predator's traits on long periods. To prevent predators to acquire infinite lifetimes, we strongly favored deleterious mutations in the shark death rate (entropic force). This is achieved by tuning the $\langle x\rangle$ parameter in Eq. (2). In fact, if the average phenotype is above (or below) $\langle x\rangle$, random mutations will try to restore it around $\langle x\rangle$.

Fig. 2*a* shows the dynamic of the predator mortality distribution for various initial conditions (marked by different colors). In all simulations, sharks have a well-defined phenotype at each time step, so no speciation is observed. All distributions, even if with different timescales, tend at long times to converge toward a unique final distribution with a mean close to the average value chosen for the entropic force (dashed line in the figure). The time required to reach this value diverges quickly (following a power-law with exponent ~ 2.57), the farther we prepared the system from the final state. Note that the exponent of the power-law slightly de-

pends on the genome size N, as shown in Fig. 2*c*. This kind of dynamic reminds of a system close to a glassy phase (52) where the distance between the initial and final phenotypes plays the role of the difference between the quenched and equilibrium temperatures in a typical quenching experiment. Such behavior provides great insight into the evolutionary dynamics. Firstly, we observe the role natural selection plays in freezing the system into a meta-stable state for long times. In fact, phenotypes subject to the sole effect of entropic forces would converge to the steady-state exponentially fast (see SI). Furthermore, we see how the ecosystem and predators, in particular, react to negative mutations. In fact, shark fitness decreases due to the entropic force of the mutations (see SI for the anti-correlation between fitness and shark death-rate). If a population has a phenotype distribution whose mean is far from the mean entropy value ($\langle x \rangle$ in Eq. (2)), a mutation of the genome will tend to produce an individual with lower fitness than the rest of the population. The lowest the fitness the faster this individual will be suppressed by natural selection.

If the fitness worsens only slightly (the mutation is very soft), the specimen will reproduce and that deleterious mutation will remain inside the genome pool. On long timescales, the accumulations of these very soft negative mutations slowly drive the whole population toward the entropic limit. This phenomenon is observed in real ecosystems and is known as mutational meltdown(45–47). The meltdown we observe originates by the even impact genes have on the phenotype. We discuss how it scales with the system carrying capacity in SI.

Fig. 2 clearly show how evolution is not able to improve the fitness of predators. In fact, although natural selection is freezing the dynamics (strongly reducing the effect of genetic drift) if we wait for sufficient time, sharks will finally increase their death-rate, therefore reducing their fitness. This behavior is opposite to what is commonly observed in nature, where the combined effect of mutations and natural selection leads to an overall improvement of the fitness on long times.

This finding highlights the deleterious role of entropy in the evolution of the species. We will show in the next section that the capability to improve the fitness can be recovered even in the presence of a strong entropic force if genome variability is considered. This feature alone will be able both to allow predators to evolve and to provide a mechanism for spontaneous speciation.

B. Heterogeneous genome. To include the effect of genome heterogeneity in the simulation, i.e. the uneven impact that different genes have on the phenotype, we inserted a gene-dependent weight (Eq. (4)) in Eq. (1).

Fig. 3 depicts the time evolution of the distribution of shark's mortality starting from different initial values for two different exponent of Eq. (4), namely $\alpha = 1$ and $\alpha = 2$. The evolution is observed with both choices of exponents. Predators improve their expected life-time and the fitness (see SI) much above the equilibrium value obtained in Fig. 2.

Positive evolution occurs thank to the combination of two effects; i) the phenotype population is normally quenched (see Sec. A) and ii) genes exert a different role on the phenotype manifestation. The quenching allows the quasi-species to survive in an out-of-equilibrium situation where common random negative mutations usually kill the individuals. The species can survive long enough that a very rare, positive, mutation occurs in an important gene (with a big W_i), causing a discontinuity in the phenotype distribution and a sudden evolution of the population. This speciation creates two kinds of predators, with a quantitative different phenotype. The quasi-species which is more fitted to the environment very quickly gets fixed while the less fitted alleles vanish from the gene pool of the population.

Such a rare, discontinuous event is not possible in a uniform genome, where each gene has only a moderate impact on the overall phenotype and a massive number of positive mutations would be required to obtain the same shift (that is a so rare event that never occurs in practice). Conversely, heterogeneity allows the positive discontinuity in the phenotype to depend on the mutation of a relatively small number of genes, which is much more likely to occur.

Heterogeneity has another important effect on preys phenotype distribution. In Fig. 4 we show the preys breeding rate as it evolves as a function of time. After a while, the prey population splits into two well-separated traits. In particular, the two species have a different reproduction rate (p_f^f), respectively of 0.78 and 0.90, but they share the same fitness in the environment, therefore no one overcomes the other. This is a very important feature for sympatric speciation, and it is possible only thanks to the presence of the spatial organization of the animals. In fact, the species with a higher reproduction rate tend to regenerate the shoals faster, being, therefore, more prone to shark predation. This delicate trade-off between higher fertility and the different spatial organization of the shoal that favors predation stabilizes the two species, that can coexist. In a mean-field scenario, predators would hunt the two species in the same way, and this leads, at a long time, to a supremacy of the prey with the higher reproduction rate.

3. Discussion

We simulate the evolution of a minimal prey-predator system. Each species is characterized by a toy genome through which three macro-phenotypes manifest. Providing each specimen with N genes for each phenotype, we showed that the gene relevance (i.e. the weight of each gene according to Eq. 1) in coding for phenotypes is a key feature for evolution.

To survive, an organism must be robust to deleterious mutations. A convenient choice, the organism can opt for, could be to rely on many genes for the manifestation on one phenotype. If the information for the phenotype is evenly distributed in several genes, then a damage on some gene has the minimum impact on the resulting phenotype. As a counterpart, we showed that this condition favors the accumulation of detrimental mutations that lead to the mutational meltdown. Conversely, packing all the phenotype information in few genes enables abrupt variations of phenotype. This prevents the mutational meltdown, at the cost of reducing the differentiation between individuals and consequently the adaptability of the species. In this case, a drastic change in the environment would provoke a sudden extinction of the species.

Relying on a heterogeneous distribution of information in many genes assures both broad differentiation of a huge genome, and the possibility to have astonishing positive mutations that drive the evolution and prevents the mutational meltdown. EvoLat, albeit of representing a minimal model of an ecosystem, reproduces a rich variety of scenarios, upon varying a single parameter. In fact, tuning the α exponent in

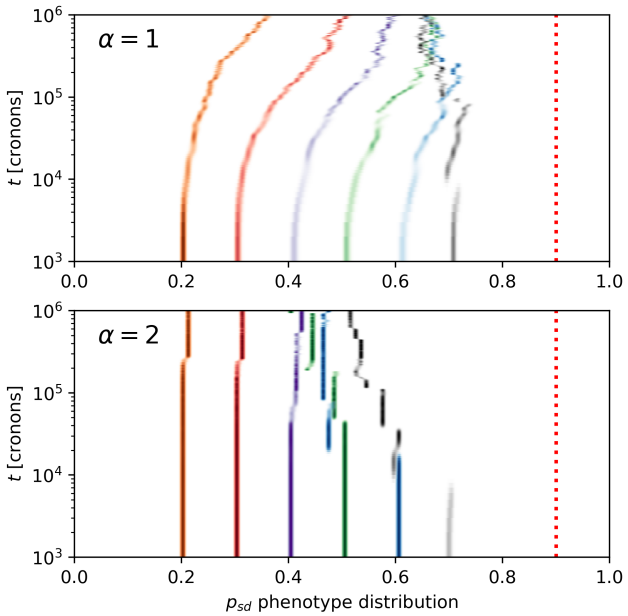

Fig. 3. Evolution of the shark death-probability distribution as a function of time, in presence of a heterogeneous genome. Heterogeneity allows the specie to evolve to higher average life-time, while this does not occur in presence of a uniform genome (Fig. 2). Different colors correspond to different starting values. The two simulation correspond to a different value of the power-law exponent α (see Eq. (4)). Both simulations exhibit a qualitative different behaviour if compared to a uniform genome. The less fitted individual can improve their fitness far above the entropic value.

Eq. 4, i.e. assigning different weights to genes associated to the same phenotype, the system exhibits different behaviors. Indeed, a uniform distribution of weights ($\alpha = 0$) leads to a progressive reduction of the fitness due to the accumulation of detrimental mutations (see Fig. 2). On the opposite side, if only one gene encodes for all the traits ($\alpha = \infty$) the mutational meltdown is prevented as species can improve their fitness. However, in this regime, there is no differentiation inside the same population, exposing the species to the threat of sudden environmental changes. Life lies in between, where the high impact of few genes prevents the mutational meltdown while the bulk of the remaining genes guarantees differentiation.

Notably, fishes provided with a heterogeneous genome respond to the fluctuation of the environment and to the natural selection operated by sharks by a sympatric speciation (53). Spontaneous speciation and in particular sympatric one is rarely reproduced (41) by models which manage to observe differentiation due to Mendelian inheritance (54). According to our simulations, two key ingredients are important to observe the emergence of sympatric speciations: the heterogeneity in gene relevance and the explicit spatial extension of the simulation. Moreover, our minimal model provides a theoretical framework to deal with the everlasting debate about the physical feasibility of evolution.

The idea that life had evolved by the combined action of mutations in the genome and natural selection of the most fitted individuals is accepted by a vast majority of scientists. Those, who are skeptics, argue that random mutations on the genome should progressively increase the disorder (entropy) and consequently be incompatible with life. Indeed, this happens only in case of a uniform genome, where mutations lead the phenotypes toward the entropic values. This argument is, therefore, based on the wrong assumption that all the genes equally contribute to the phenotype.

In our simple model, each part of the genetic sequence influences the phenotype with different weights. This is a coarse grain representation of the underlying biological mechanism through which the phenotype is manifested. In nature, only 2-3% of DNA is "coding" (it can be translated into mRNA and then into proteins). Several studies(55, 56) have shown that also the non-coding DNA (often referred to as *junk*) can affect the phenotype. This is a mechanism for strong heterogeneity in how the phenotype manifests from the underlying genetic sequence.

Overall, in our opinion, the most limiting choices we made were not to include sexual reproduction, correlations in gene expression and modifications in the food chain (a prey cannot become a predator). This limits the sources of variation between individuals only to the effect of mutations since both sexual recombination and gene flow are neglected together with the complex correlations between the expression of genes confers to the specimen. On the other hand, the reduced number of parameters allows one to look for general features of evolution.

In conclusion, we proved that heterogeneity in gene relevance is a key feature to prevent a mutational meltdown in a species. Moreover, we showed evidence that spatial correlations are fundamental to account for sympatric speciation. These findings contribute to disentangling how genomes change to create new species and provide a step forward in understanding the mechanisms of evolution.

ACKNOWLEDGMENTS. The authors are indebted with Giacinto De Vivo, Sergio Forcelloni and Noemi Panzironi for fruitful and enjoyable discussions.

1. D Howard, A Howard, S Berlocher, A Berlocher, *Endless Forms: Species and Speciation.* (Oxford University Press), (1998).
2. OF Cook, Factors of species formation. *Science* **23**, 506–507 (1906).
3. E Freese, A Yoshida, The role of mutations in evolution in *Evolving Genes and Proteins.* (Elsevier), pp. 341–355 (1965).
4. E Mayr, *What Makes Biology Unique?: Considerations on the Autonomy of a Scientific Discipline.* (Cambridge University Press), (2004).
5. M Nei, The new mutation theory of phenotypic evolution. *Proc. Natl. Acad. Sci.* **104**, 12235–12242 (2007).
6. M Kimura, The neutral theory of molecular evolution. *Camb. Univ. Press.* (1983).
7. M Eigen, Selforganization of matter and the evolution of biological macromolecules. *Die Naturwissenschaften* **58**, 465–523 (1971).
8. R Hershberg, Mutation—the engine of evolution: Studying mutation and its role in the evolution of bacteria: Figure 1. *Cold Spring Harb. Perspectives Biol.* **7**, a018077 (2015).
9. S Forcelloni, A Giansanti, Evolutionary forces on different flavors of intrinsic disorder in the human proteome. *bioRxiv* (2019).
10. Q Zhang, RH Austin, Physics of cancer: The impact of heterogeneity. *Annu. Rev. Condens. Matter Phys.* **3**, 363–382 (2012).
11. KS Korolev, JB Xavier, J Gore, Turning ecology and evolution against cancer. *Nat. Rev. Cancer* **14**, 371–380 (2014).
12. N McGranahan, C Swanton, Clonal heterogeneity and tumor evolution: Past, present, and the future. *Cell* **168**, 613–628 (2017).
13. D Cavalieri, JP Townsend, DL Hartl, Manifold anomalies in gene expression in a vineyard isolate of Saccharomyces cerevisiae revealed by DNA microarray analysis. *Proc. Natl. Acad. Sci.* **97**, 12369–12374 (2000).
14. BJ Shapiro, et al., Population genomics of early events in the ecological differentiation of bacteria. *Science* **336**, 48–51 (2012).
15. CR Campbell, JW Poelstra, AD Yoder, What is speciation genomics? the roles of ecology, gene flow, and genomic architecture in the formation of species. *Biol. J. Linnean Soc.* **124**, 561–583 (2018).
16. P J, H O, D S, LI J, Genome size diversity and its impact on the evolution of land plants. *Genes* **9**, 88 (2018).
17. A Lotka, Analytical note on certain rhythmic relations in organic systems. *Proc. Natl. Acad. Sci. U.S* (1920).
18. V Volterra, Variations and fluctuations of the number of individuals in animal species living together in animal ecology. *McGraw-Hill* (1931).

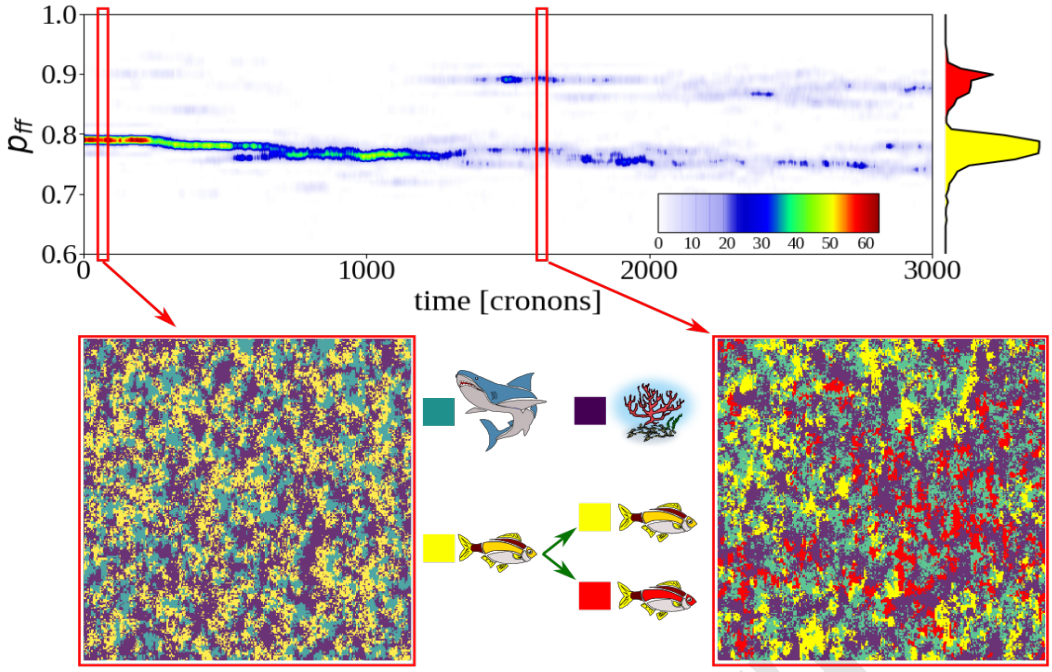

Fig. 4. Outcomes of evolution: speciation. a) Time evolution of the distribution of fish filiation probability. At time zero, the population of fishes is prepared with a filiation rate of 0.8. After about 1500 chronons, the population splits into two species with a well-separated trait. **b)** Snapshots of two EvoLat configurations during the evolution. In the left snapshot, only a species of fish is observed. In the right-side one, two fish species have formed. The spatial distribution of sharks differs in the proximity of the two species, spotting that sharks are adopting different hunting strategies.

19. D Bajić, JCC Vila, ZD Blount, A Sánchez, On the deformability of an empirical fitness landscape by microbial evolution. *Proc. Natl. Acad. Sci.* **115**, 11286–11291 (2018).
20. A De Martino, T Gueudré, M Miotto, Exploration-exploitation tradeoffs dictate the optimal distributions of phenotypes for populations subject to fitness fluctuations. *Phys. Rev. E* **99**, 012417 (2019).
21. E Kussell, Phenotypic diversity, population growth, and information in fluctuating environments. *Science* **309**, 2075–2078 (2005).
22. D De Martino, F Capuani, A De Martino, Growth against entropy in bacterial metabolism: the phenotypic trade-off behind empirical growth rate distributions in e . coli. *Phys. Biol.* **13** (2016).
23. I Bena, M Droz, J Szwabiński, A Pekalski, Complex population dynamics as a competition between multiple-time-scale phenomena. *Phys. Rev. E* **76** (2007).
24. NJ Savill, P Hogeweg, Spatially induced speciation prevents extinction: the evolution of dispersal distance in oscillatory predator-prey models. *Proc. Royal Soc. London. Ser. B: Biol. Sci.* **265**, 25–32 (1998).
25. M He, H Ruan, C Yu, A predator prey model based on the fully parallel cellular automata. *Int. J. Mod. Phys. C* **14**, 1237–1249 (2003).
26. M He, QH Pan, S Wang, Final state of ecosystem containing grass, sheep and wolves with aging. *Int. J. Mod. Phys. C* **16**, 177–190 (2005).
27. A Pekalski, M Droz, Self-organized packs selection in predator-prey ecosystems. *Phys. Rev. E* **73** (2006).
28. A Pérez-Escudero, J Friedman, J Gore, Preferential interactions promote blind cooperation and informed defection. *Proc. Natl. Acad. Sci.* **113**, 13995–14000 (2016).
29. GM Abernethy, M McCartney, DH Glass, The interaction between predator strategy and prey competition in a pair of multi-predator multi-prey lattices. *Commun. Nonlinear Sci. Numer. Simul.* **56**, 9–33 (2018).
30. M Barbier, JF Arnoldi, G Bunin, M Loreau, Generic assembly patterns in complex ecological communities. *Proc. Natl. Acad. Sci.* **115**, 2156–2161 (2018).
31. SMJ Portalier, GF Fussmann, M Loreau, M Cherif, The mechanics of predator–prey interactions: First principles of physics predict predator–prey size ratios. *Funct. Ecol.* **33**, 323–334 (2018).
32. Dewdney, Sharks and fish wage an ecological war on the toroidal planet wa-tor. *Sci. Am.* (1984).
33. T Antal, M Droz, A Lipowski, G Ódor, Critical behavior of a lattice prey-predator model. *Phys. Rev. E* **64** (2001).
34. M Miotto, L Monacelli, Entropy evaluation sheds light on ecosystem complexity. *Phys. Rev. E* **98**, 042402 (2018).
35. M Mobilia, IT Georgiev, UC Täuber, Fluctuations and correlations in lattice models for predator-prey interaction. *Phys. Rev. E* **73** (2006).
36. U Dobramysl, M Mobilia, M Pleimling, UC Täuber, Stochastic population dynamics in spatially extended predator-prey systems. *J. Phys. A: Math. Theor.* (2017).
37. E Kussell, Phenotypic diversity, population growth, and information in fluctuating environments. *Science* **309**, 2075–2078 (2005).
38. PAP Moran, Global stability of genetic systems governed by mutation and selection. *Math. Proc. Camb. Philos. Soc.* **80**, 331–336 (1976).
39. J Swetina, P Schuster, Self-replication with errors. *Biophys. Chem.* **16**, 329–345 (1982).
40. TJP Penna, A bit-string model for biological aging. *J. Stat. Phys.* **78**, 1629–1633 (1995).
41. J Friedman, EJ Alm, BJ Shapiro, Sympatric speciation: When is it possible in bacteria? *PLoS ONE* **8**, e53539 (2013).
42. AO Sousa, Sympatric speciation in an age-structured population living on a lattice. *The Eur. Phys. J. B* **39**, 521–525 (2004).
43. J Dalmau, Asymptotic behavior of eigen's quasispecies model. *Bull. Math. Biol.* **80**, 1689–1712 (2018).
44. J Garcia-Bernardo, MJ Dunlop, Phenotypic diversity using bimodal and unimodal expression of stress response proteins. *Biophys. J.* **110**, 2278–2287 (2016).
45. T OHTA, Slightly deleterious mutant substitutions in evolution. *Nature* **246**, 96–98 (1973).
46. M Lynch, J Conery, R Burger, Mutation accumulation and the extinction of small populations. *The Am. Nat.* **146**, 489–518 (1995).
47. A Grande-Perez, E Lazaro, P Lowenstein, E Domingo, SC Manrubia, Suppression of viral infectivity through lethal defection. *Proc. Natl. Acad. Sci.* **102**, 4448–4452 (2005).
48. DD Martino, F Capuani, AD Martino, Growth against entropy in bacterial metabolism: the phenotypic trade-off behind empirical growth rate distributions inE.coli. *Phys. Biol.* **13**, 036005 (2016).
49. D De Martino, F Capuani, A De Martino, Quantifying the entropic cost of cellular growth control. *Phys. Rev. E* **96** (2017).
50. S Cocco, C Feinauer, M Figliuzzi, R Monasson, M Weigt, Inverse statistical physics of protein sequences: a key issues review. *Reports on Prog. Phys.* **81**, 032601 (2018).
51. M Miotto, et al., Insights on protein thermal stability: a graph representation of molecular interactions. *Bioinformatics* (2018).
52. W Kob, F Sciortino, P Tartaglia, Aging as dynamics in configuration space. *Europhys. Lett. (EPL)* **49**, 590–596 (2000).
53. BM Fitzpatrick, JA Fordyce, S Gavrilets, What, if anything, is sympatric speciation? *J. Evol. Biol.* **21**, 1452–1459 (2008).
54. R Aguilée, A Lambert, D Claessen, Ecological speciation in dynamic landscapes. *J. Evol. Biol.* **24**, 2663–2677 (2011).
55. C Biémont, C Vieira, Junk dna as an evolutionary force. *Nature* **443**, 521 (2006).
56. S Prabhakar, et al., Human-specific gain of function in a developmental enhancer. *Science* **321**, 1346–1350 (2008).

Appendix B

SCHA calculation details

B.1 The SCHA gradients

Here I derive the equations for the gradient and introduce some useful formula for dealing with SCHA averages and derivatives.

First of all, lets derive the equations for computing the derivative of an observable with respect the atomic positions $\vec{\mathcal{R}}$ and the fluctuation matrix $\mathbf{\Phi}$.

$$\frac{\partial \langle O \rangle_{\rho_{\vec{\mathcal{R}},\mathbf{\Phi}}}}{\partial \mathcal{R}_a} = \frac{\partial}{\partial \mathcal{R}_a} \sqrt{\det\left(\mathbf{\Upsilon}/2\pi\right)} \int O(\vec{\mathcal{R}} + \vec{u}) \exp\left[-\frac{1}{2}\vec{u}\mathbf{\Upsilon}\vec{u}\right] \prod_a du_a \tag{B.1}$$

The derivative only acts on the probability distribution $\rho_{\vec{\mathcal{R}},\mathbf{\Phi}}$. However, we can perform a change of variable to normalize the $\rho_{\vec{\mathcal{R}},\mathbf{\Phi}}$, in this way we move the dependence of the $\vec{\mathcal{R}}$ and $\mathbf{\Phi}$ to the observable.

$$\vec{y} = \sqrt{\mathbf{\Upsilon}}\vec{u} \tag{B.2}$$

$$\prod dy = \det\sqrt{\mathbf{\Upsilon}} \prod du = \sqrt{\det \mathbf{\Upsilon}} \prod du \tag{B.3}$$

$$\langle O \rangle_{\rho_{\vec{\mathcal{R}},\mathbf{\Phi}}} = \frac{1}{\sqrt{(2\pi)^{3N}}} \int O\left(\vec{\mathcal{R}} + \sqrt{\mathbf{\Upsilon}}^{-1}\vec{y}\right) \prod_\mu e^{-\frac{y_\mu^2}{2}} dy_\mu \tag{B.4}$$

Eq. B.4 all the dependence from the minimization parameters have been moved inside the observable.

$$\begin{aligned} \frac{\partial \langle O \rangle_{\rho_{\vec{\mathcal{R}},\mathbf{\Phi}}}}{\partial \mathcal{R}_a} &= \frac{1}{\sqrt{(2\pi)^{3N}}} \int \frac{\partial O}{\partial R_a}(\vec{u}) \prod_\mu e^{-\frac{y_\mu^2}{2}} dy_\mu \\ &= \langle \frac{\partial O}{\partial R_a} \rangle_{\rho_{\vec{\mathcal{R}},\mathbf{\Phi}}} \end{aligned} \tag{B.5}$$

$$\frac{\partial \langle O \rangle_{\rho_{\vec{\mathcal{R}},\mathbf{\Phi}}}}{\partial \Phi_{ab}} = \frac{1}{\sqrt{(2\pi)^{3N}}} \sum_{cd} \frac{\partial \sqrt{\Upsilon}^{-1}{}_{cd}}{\partial \Phi_{ab}} \int y_d \frac{\partial O}{\partial R_c} \prod_\mu e^{-\frac{y_\mu^2}{2}} dy_\mu \tag{B.6}$$

$$\frac{\partial \langle O \rangle_{\rho_{\vec{\mathcal{R}},\mathbf{\Phi}}}}{\partial \Phi_{ab}} = \frac{1}{\sqrt{(2\pi)^{3N}}} \sum_{cdlm} \frac{\partial \sqrt{\Upsilon}^{-1}{}_{cd}}{\partial \Phi_{ab}} \int \sqrt{\Upsilon_{dl}} \sqrt{\Upsilon^{-1}}_{lm} y_m \frac{\partial O}{\partial R_c} \prod_{\mu} e^{-\frac{y_\mu^2}{2}} dy_\mu \quad \text{(B.7)}$$

$$\begin{aligned} \sum_{dl} \frac{\partial \sqrt{\Upsilon^{-1}}_{cd}}{\partial \Phi_{ab}} \sqrt{\Upsilon_{dl}} &= \sum_{dlhk} \frac{\partial \sqrt{\Upsilon^{-1}}_{cd}}{\partial \Phi_{ab}} \sqrt{\Upsilon^{-1}}_{dh} \sqrt{\Upsilon}_{hk} \sqrt{\Upsilon}_{kl} \\ &= \frac{1}{2} \sum_{ch} \frac{\partial \Upsilon^{-1}{}_{ch}}{\partial \Phi_{ab}} \Upsilon_{hl} \end{aligned} \quad \text{(B.8)}$$

$$\frac{\partial \langle O \rangle_{\rho_{\vec{\mathcal{R}},\mathbf{\Phi}}}}{\partial \Phi_{ab}} = \frac{1}{\sqrt{(2\pi)^{3N}}} \sum_{cdlm} \frac{1}{2} \frac{\partial \Upsilon^{-1}{}_{cd}}{\partial \Phi_{ab}} \Upsilon_{dl} \int \sqrt{\Upsilon^{-1}}_{lm} y_m \frac{\partial O}{\partial R_c} \prod_{\mu} e^{-\frac{y_\mu^2}{2}} dy_\mu \quad \text{(B.9)}$$

$$\frac{\partial \langle O \rangle_{\rho_{\vec{\mathcal{R}},\mathbf{\Phi}}}}{\partial \Phi_{ab}} = \sum_{cdl} \frac{1}{2} \frac{\partial \Upsilon^{-1}{}_{cd}}{\partial \Phi_{ab}} \Upsilon_{dl} \left\langle u_l \frac{\partial O}{\partial R_c} \right\rangle_{\rho_{\vec{\mathcal{R}},\mathbf{\Phi}}} \quad \text{(B.10)}$$

From Eq. B.5 it is possible to compute the free energy gradient with respect to the atomic position:

$$\mathcal{F}(\vec{\mathcal{R}}, \mathbf{\Phi}, \{\vec{a}_i\}) = F_{\mathbf{\Phi}} + \langle V - \mathcal{V} \rangle_{\rho_{\vec{\mathcal{R}},\mathbf{\Phi}}} \quad \text{(B.11)}$$

$$\frac{\partial \mathcal{F}(\vec{\mathcal{R}}, \mathbf{\Phi}, \{\vec{a}_i\})}{\partial \mathcal{R}_a} = \frac{\partial \langle V - \mathcal{V} \rangle_{\rho_{\vec{\mathcal{R}},\mathbf{\Phi}}}}{\partial \mathcal{R}_a} = - \langle f_a - f_{\mathcal{H}a} \rangle_{\rho_{\vec{\mathcal{R}},\mathbf{\Phi}}} \quad \text{(B.12)}$$

The gradient of the free energy with respect to the $\mathbf{\Phi}$ matrix is:

$$\frac{\partial \mathcal{F}(\vec{\mathcal{R}}, \mathbf{\Phi}, \{\vec{a}_i\})}{\partial \Phi_{ab}} = \frac{\partial F_{\mathbf{\Phi}}}{\partial \Phi_{ab}} - \left\langle \frac{\partial \mathcal{V}}{\partial \Phi_{ab}} \right\rangle_{\rho_{\vec{\mathcal{R}},\mathbf{\Phi}}} - \sum_{cdl} \frac{1}{2} \frac{\partial \Upsilon^{-1}{}_{cd}}{\partial \Phi_{ab}} \Upsilon_{dl} \langle u_l (f_c - f_{\mathcal{H}c}) \rangle_{\rho_{\vec{\mathcal{R}},\mathbf{\Phi}}} \quad \text{(B.13)}$$

we need first to compute the gradient of the harmonic free energy:

$$\frac{\partial F_{\mathbf{\Phi}}}{\partial \Phi_{ab}} = \sum_{\mu} \frac{\partial F_{\mathbf{\Phi}}}{\partial \omega_\mu^2} \frac{\partial \omega_\mu^2}{\partial \Phi_{ab}} \quad \text{(B.14)}$$

$$F_{\mathbf{\Phi}} = \sum_{\mu} \left[\frac{\omega_\mu}{2} + \frac{1}{\beta} \ln \left(1 + e^{-\beta \omega_\mu} \right) \right]$$

$$\frac{\partial F_{\mathbf{\Phi}}}{\partial \omega_\mu^2} = \frac{1}{2\omega_\mu} \frac{\partial F_{\mathbf{\Phi}}}{\partial \omega_\mu} = \frac{1}{2\omega_\mu} \left(\frac{1}{2} + n_\mu \right) \quad \text{(B.15)}$$

The other derivative can be computed with the inverse:

$$\frac{\partial \Phi_{ab}}{\partial \omega_\mu^2} = e_\mu^a e_\mu^b \cdot \sqrt{m_a m_b} \quad \text{(B.16)}$$

We can use the relation:

$$\sum_h \frac{\partial \omega_\mu^2}{\partial \Phi_{ah}} \frac{\partial \Phi_{hb}}{\partial \omega_\mu^2} = \delta_{ab} \tag{B.17}$$

to prove that

$$\frac{\partial \omega_\mu^2}{\partial \Phi_{ab}} = \frac{e_\mu^a e_\mu^b}{\sqrt{m_a m_b}} \tag{B.18}$$

$$\frac{\partial F_{\mathbf{\Phi}}}{\partial \Phi_{ab}} = \sum_\mu \frac{1+2n_\mu}{4\omega_\mu} \frac{e_\mu^a e_\mu^b}{\sqrt{m_a m_b}} = \frac{1}{2} \Upsilon^{-1}{}_{ab} \tag{B.19}$$

$$\mathcal{V} = \frac{1}{2} \sum_{ab} u_a \Phi_{ab} u_b$$

$$\frac{\partial \mathcal{V}}{\partial \Phi_{ab}} = \frac{1}{2} u_a u_b$$

$$\langle \frac{\partial \mathcal{V}}{\partial \Phi_{ab}} \rangle_{\rho_{\vec{\mathcal{R}},\mathbf{\Phi}}} = \frac{1}{2} \langle u_a u_b \rangle_{\rho_{\vec{\mathcal{R}},\mathbf{\Phi}}} = \frac{1}{2} \Upsilon^{-1}{}_{ab}$$

here we exploited the fact that $\mathbf{\Upsilon}$ is the inverse of the co-variance matrix.

From which we get that

$$\frac{\partial F_{\mathbf{\Phi}}}{\partial \Phi_{ab}} - \langle \frac{\partial \mathcal{V}}{\partial \Phi_{ab}} \rangle_{\rho_{\vec{\mathcal{R}},\mathbf{\Phi}}} = 0$$

Therefore,

$$\frac{\partial \mathcal{F}(\vec{\mathcal{R}}, \mathbf{\Phi}, \{\vec{a}_i\})}{\partial \Phi_{ab}} = -\sum_{cdl} \frac{1}{2} \frac{\partial \Upsilon^{-1}{}_{cd}}{\partial \Phi_{ab}} \Upsilon_{dl} \langle u_l (f_c - f_{\mathcal{H}c}) \rangle_{\rho_{\vec{\mathcal{R}},\mathbf{\Phi}}} \tag{B.20}$$

B.2 The hessian matrix of the SCHA minimization

In this appendix I derive the hessian matrix in the minimum for the SCHA minimization problem with respect to the fluctuations $\mathbf{\Phi}$. This work has been published in ref[25].

$$\boldsymbol{A}_{\mathbf{\Phi}}^{abcd} = \frac{\partial \mathcal{F}}{\partial \Phi_{ab} d\Phi_{cd}}$$

In this section, we provide an analytical guess of the free energy Hessian matrix $\boldsymbol{A}$ with respect to the minimization variable $\mathbf{\Phi}$. In general, this is not possible, since computing the real Hessian matrix corresponds to solving exactly the problem. However, we can perform the computation in an analytical test case that, hopefully, will enclose all the physics of the minimization problems incurred so far. This is a purely harmonic system, described by a harmonic Hamiltonian. From now on we introduce a compact notation to describe both Cartesian and atomic indices ($v_a = v_s^\alpha$).

$$H = \frac{1}{2} \sum_a \frac{(p_a)^2}{2m_a} + \frac{1}{2} \sum_{ab} u_a K_{ab} u_b, \tag{B.21}$$

The free energy Hessian matrix with respect to the $\mathbf{\Phi}$ variable can be computed analytically. The steps that lead to the following result are reported in B.2.1:

$$A^{abcd}_{\mathbf{\Phi}} = -\left.\frac{\partial^2 \mathcal{F}(\vec{\mathcal{R}}, \mathbf{\Phi}, \{\vec{a}_i\})}{\partial \Phi_{ab} \partial \Phi_{cd}}\right|_{\mathbf{\Phi}=\mathbf{K}} = \frac{1}{2}\mathcal{P}_{ab}\mathcal{P}_{cd}\left(\Lambda^{abcd} + \Lambda^{abdc}\right), \tag{B.22}$$

where the $\mathbf{\Lambda}$ 4-rank tensor is the same introduced by Bianco *et al.* [24], and $\mathcal{P}$ is a symmetrization factor

$$\Lambda^{abcd} = -\frac{\hbar}{4}\sum_{\mu\nu}\frac{1}{\omega_\mu\omega_\nu}\frac{e^a_\nu e^b_\mu e^c_\nu e^d_\mu}{\sqrt{m_a m_b m_c m_d}}\times \\ \times\begin{cases} \dfrac{2n_\nu+1}{2\omega_\nu} - \dfrac{dn_\nu}{d\omega_\mu} & \omega_\nu = \omega_\mu \\ \dfrac{n_\mu + n_\nu + 1}{\omega_\mu + \omega_\nu} - \dfrac{n_\mu - n_\nu}{\omega_\mu - \omega_\nu} & \omega_\nu \neq \omega_\mu \end{cases}, \tag{B.23}$$

$$\mathcal{P}_{ab} = \sqrt{2}\,(1-\delta_{ab}) + \delta_{ab}. \tag{B.24}$$

Here the ω_μ and $\vec{e}_\mu$ are the frequencies and polarization vectors of the $\boldsymbol{K}$ matrix. These are, indeed, equal to the $\mathbf{\Phi}$ matrix in the minimum of the SCHA free energy, and represent the real phonons of the system.

The $\mathbf{\Lambda}$ matrix can be diagonalized analytically if we consider the case of all equal masses

$$\sum_{cd}\Lambda^{abcd}e^c_\mu e^d_\nu = \tilde{\lambda}_{\mu\nu}e^a_\mu e^b_\mu. \tag{B.25}$$

We can obtain an easy expression of the spectrum of the Hessian matrix in the pure quantum limit $T \to 0$ and the pure classical limit $T \to \infty$:

$$\lim_{T\to 0}\tilde{\lambda}_{\mu\nu} = \frac{\hbar}{4m^2}\frac{1}{\omega_\mu\omega_\nu(\omega_\mu+\omega_\nu)}, \tag{B.26a}$$

$$\lim_{T\to\infty}\tilde{\lambda}_{\mu\nu} = \frac{1}{4\beta m^2}\frac{1}{\omega_\mu^2\omega_\nu^2}\left[1 + \frac{\omega_\mu\omega_\nu}{(\omega_\mu+\omega_\nu)^2}\right]. \tag{B.26b}$$

Therefore, the Hessiam matrix spectrum behaves as ω_μ^{-3} in the quantum limit and ω_ν^{-4} in the classical one. We can compute the condition numbers, as defined in Eq. (1.27):

$$C_{\mathbf{\Phi},T=0} \approx \left(\frac{\omega_{max}}{\omega_{min}}\right)^3, \tag{B.27a}$$

$$C_{\mathbf{\Phi},T\to\infty} \approx \left(\frac{\omega_{max}}{\omega_{min}}\right)^4. \tag{B.27b}$$

This unveils the pathology in the SSCHA minimization if the gradient is taken with respect to $\mathbf{\Phi}$ as presented in Ref.[22] for the mentioned systems: when we have a structural instability, there is a phonon mode that softens to zero ($\omega_{min} \to 0$), producing a diverging condition number $C \to \infty$. In the same way, molecular crystals have a broad spectrum, with a very large difference between the highest vibron modes and the lowest intermolecular ones (for example in common ice we

have $\omega_{max}/\omega_{min} \sim 10^3$). This yields extremely high values of the condition numbers, that makes the minimization really difficult and requires lots of energy and force recalculations to achieve a good minimization. This obviously hinders the application of the SSCHA method fully "ab-inito" in complex systems.

B.2.1 Detailed derivation of the Hessian matrix

In this section I report all the details of the calculations reported in appendix B.2.

The real and trial classical forces acting on each configuration identified by the displacements $\vec{u}$ are:

$$f_s^\alpha = -\frac{\partial V}{\partial u_s^\alpha} = -\sum_{t\beta} K_{st}^{\alpha\beta} u_t^\beta, \tag{B.28a}$$

$$f_{\mathcal{H}}{}_s^\alpha = -\frac{\partial \mathcal{V}_{\vec{\mathcal{R}},\mathbf{\Phi}}}{\partial u_s^\alpha} = -\sum_{t\beta} \Phi_{st}^{\alpha\beta} u_t^\beta. \tag{B.28b}$$

Defining $\delta\vec{f} = \vec{f} - \vec{f}_{\mathcal{H}}$ we have

$$\langle \delta f_s^\alpha u_t^\beta \rangle_{\rho_{\mathcal{H}}} = -\sum_{n\eta} (K_{sn}^{\alpha\eta} - \Phi_{sn}^{\alpha\eta}) \langle u_n^\eta u_t^\beta \rangle_{\rho_{\vec{\mathcal{R}},\mathbf{\Phi}}} . \tag{B.29}$$

From now on, we drop the subscript $\rho_{\vec{\mathcal{R}},\mathbf{\Phi}}$ for each average, and consider all the averages computed with respect to the trial density matrix. We further simplify the notation, introducing one index for each Cartesian and atomic coordinate, so $v_s^\alpha \to v_a$. In this new notation Eq. (B.29) reads:

$$\langle \delta f_a u_b \rangle = -\sum_{c=1}^{3N} (K_{ac} - \Phi_{ac}) \langle u_c u_b \rangle . \tag{B.30}$$

The average of the product between two displacements of a Gaussian distributed variable is the covariance between the two displacements (Eq. 1.13a):

$$\langle u_c u_b \rangle = \left(\mathbf{\Upsilon}^{-1}\right)_{cb} = \frac{1}{\sqrt{m_c m_b}} \sum_{\nu=1}^{3N} e_\nu^c e_\nu^b a_\nu^2, \tag{B.31}$$

where we introduce the mode length a_μ:

$$a_\mu = \sqrt{\frac{\hbar}{2\omega_\mu}(1 + 2n_\mu)}. \tag{B.32}$$

The gradient of the SCHA free energy functional with respect to $\mathbf{\Phi}$ is[22]:

$$\nabla_{\mathbf{\Phi}} \mathcal{F}_{\vec{\mathcal{R}},\mathbf{\Phi}} = -\sum_{ab\mu} \sqrt{\frac{m_a}{m_b}} \left(e_\mu^b \nabla_{\mathbf{\Phi}} \ln a_\mu + \nabla_{\mathbf{\Phi}} e_\mu^b \right) e_\mu^a \langle \delta f_b u_a \rangle . \tag{B.33}$$

Substituting the explicit expression of the forces we have:

$$\nabla_{\mathbf{\Phi}} \mathcal{F}(\vec{\mathcal{R}}, \mathbf{\Phi}, \{\vec{a}_i\}) = \sum_{abc\mu\nu} (K_{ac} - \Phi_{ac}) \left(e_\mu^a \nabla_{\mathbf{\Phi}} \ln a_\mu + \nabla_{\mathbf{\Phi}} e_\mu^a \right) \times \\ \times \frac{e_\mu^b e_\nu^c e_\nu^b a_\nu^2}{\sqrt{m_c m_a}}. \tag{B.34}$$

It is clear from Eq. (B.34) that in the minimum $\mathbf{\Phi} = \mathbf{K}$. Therefore, it is convenient to compact all the other terms into a symbol:

$$\frac{\partial \mathcal{F}(\vec{\mathcal{R}}, \mathbf{\Phi}, \{\vec{a}_i\})}{\partial \Phi_{cd}} = \sum_{ab} (K_{ab} - \Phi_{ab}) \, \mathcal{L}_{abcd}. \tag{B.35}$$

Here $\boldsymbol{\mathcal{L}}$ is a 4-rank tensor. Since we sum on all a and b indexes and $\boldsymbol{\mathcal{L}}$ 4-rank tensor multiplies a symmetrical matrix, it is convenient to recast it into a symmetrical form:

$$L_{abcd} = \sum_{k,\mu\nu} \left(e^a_\mu \frac{\partial \ln a_\mu}{\partial \Phi_{cd}} + \frac{\partial e^a_\mu}{\partial \Phi_{cd}} \right) e^k_\mu e^b_\nu e^k_\nu a^2_\nu, \tag{B.36}$$

$$\mathcal{L}_{abcd} = \frac{\mathcal{P}_{ab}}{\sqrt{m_a m_b}} \frac{L_{abcd} + L_{bacd}}{2}, \tag{B.37}$$

$$\mathcal{P}_{ab} = \sqrt{2}(1 - \delta_{ab}) + \delta_{ab}, \tag{B.38}$$

$$\mathcal{L}_{abcd} = \frac{\mathcal{P}_{ab}}{\sqrt{m_a m_b}} \sum_{\mu} \left[e^a_\mu e^b_\mu \frac{\partial \ln a_\mu}{\partial \Phi_{cd}} + \frac{1}{2} \frac{\partial (e^a_\mu e^b_\mu)}{\partial \Phi_{cd}} \right] a^2_\mu. \tag{B.39}$$

In the minimum the only non zero term of the hessian matrix is given by:

$$\left. \frac{\partial^2 \mathcal{F}(\vec{\mathcal{R}}, \mathbf{\Phi}, \{\vec{a}_i\})}{\partial \Phi_{ab} \partial \Phi_{cd}} \right|_{\mathbf{\Phi} = \mathbf{K}} = -\mathcal{L}_{abcd}, \tag{B.40}$$

$$\frac{\partial^2 \mathcal{F}(\vec{\mathcal{R}}, \mathbf{\Phi}, \{\vec{a}_i\})}{\partial \Phi_{ab} \partial \Phi_{cd}} = -\frac{\mathcal{P}_{ab}}{\sqrt{m_a m_b}} \sum_{\mu} \left[a_\mu e^a_\mu e^b_\mu \frac{\partial a_\mu}{\partial \Phi_{cd}} + \frac{1}{2} a^2_\mu \frac{\partial (e^a_\mu e^b_\mu)}{\partial \Phi_{cd}} \right]. \tag{B.41}$$

Let us start with the term inside the square brackets. The derivative of a_μ can be obtained with the chain rule:

$$\frac{\partial a_\mu}{\partial \Phi_{cd}} = \frac{\partial a_\mu}{\partial \omega_\mu} \frac{\partial \omega_\mu}{\partial \Phi_{cd}} = \frac{\mathcal{P}_{cd}}{2\omega_\mu} \frac{e^c_\mu e^d_\mu}{\sqrt{m_c m_d}} \frac{\partial a_\mu}{\partial \omega_\mu}. \tag{B.42}$$

The derivative of the polarization versors can be computed with first order perturbation theory:

$$\frac{\partial (e^a_\mu e^b_\mu)}{\partial \Phi_{cd}} = e^a_\mu \frac{\partial e^b_\mu}{\partial \Phi_{cd}} + e^b_\mu \frac{\partial e^a_\mu}{\partial \Phi_{cd}} = \frac{\mathcal{P}_{cd}}{\sqrt{m_c m_d}} \sum_{\nu}^{\nu \neq \mu} \frac{\left(e^a_\mu e^b_\nu + e^b_\mu e^a_\nu \right) \left(e^c_\nu e^d_\mu + e^c_\mu e^d_\nu \right)}{2(\omega^2_\mu - \omega^2_\nu)}. \tag{B.43}$$

We have a complete expression for the hessian matrix:

$$\begin{aligned} \frac{\partial^2 \mathcal{F}(\vec{\mathcal{R}}, \mathbf{\Phi}, \{\vec{a}_i\})}{\partial \Phi_{ab} \partial \Phi_{cd}} = -\frac{\mathcal{P}_{ab} \mathcal{P}_{cd}}{\sqrt{m_a m_b m_c m_d}} \Bigg[& \sum_{\mu} \frac{e^a_\mu e^b_\mu e^c_\mu e^d_\mu}{4\omega_\mu} \frac{\partial a^2_\mu}{\partial \omega_\mu} + \\ & + \sum_{\mu\nu}^{\mu \neq \nu} \frac{e^a_\mu e^b_\nu (e^c_\mu \varepsilon^d_\nu + e^c_\nu e^d_\mu)}{4} \left(\frac{a^2_\mu}{\omega^2_\mu - \omega^2_\nu} + \frac{a^2_\nu}{\omega^2_\nu - \omega^2_\mu} \right) \Bigg]. \end{aligned} \tag{B.44}$$

We can use the bosonic occupation number and write a_μ as a function of n_μ:

$$a_\mu = \sqrt{\frac{\hbar}{\omega_\mu} \left[n_\mu(\beta) + \frac{1}{2} \right]}, \tag{B.45a}$$

$$\frac{a_\mu}{2\omega_\mu}\frac{\partial a_\mu}{\partial \omega_\mu} = -\frac{\hbar}{8\omega_\mu^3}\left(2n_\mu + 1 + 2\beta\hbar\omega_\mu n_\mu^2 + 2\beta\hbar\omega n_\mu\right). \tag{B.45b}$$

Therefore we have:

$$\frac{\partial^2 \mathcal{F}(\vec{\mathcal{R}}, \mathbf{\Phi}, \{\vec{a}_i\})}{\partial \Phi_{ab}\partial\Phi_{cd}} = \frac{\hbar\,\mathcal{P}_{ab}\mathcal{P}_{cd}}{\sqrt{m_a m_b m_c m_d}}\left[\sum_\mu e_\mu^a e_\mu^b e_\mu^c e_\mu^d \frac{2n_\mu + 1 + 2\beta\hbar\omega_\mu n_\mu^2 + 2\beta\hbar\omega_\mu n_\mu}{8\omega_\mu^3} + \right.$$
$$\left. - \sum_{\mu\nu}^{\mu\neq\nu} \frac{e_\mu^a e_\nu^b (e_\mu^c e_\nu^d + e_\nu^c e_\mu^d)}{8(\omega_\mu^2 - \omega_\nu^2)}\left(\frac{2n_\mu + 1}{\omega_\mu} - \frac{2\omega_\nu + 1}{\omega_\nu}\right)\right] \tag{B.46}$$

It is clear from Eq. (B.46) that a $\mathbf{\Lambda}$ matrix can be introduced so that:

$$\frac{\partial^2 \mathcal{F}(\vec{\mathcal{R}}, \mathbf{\Phi}, \{\vec{a}_i\})}{\partial \Phi_{ab}\partial\Phi_{cd}} = -\frac{1}{2}\mathcal{P}_{ab}\mathcal{P}_{cd}\sum_{\mu\nu}\left(\Lambda_{\mu\nu}^{abcd} + \Lambda_{\mu\nu}^{abdc}\right), \tag{B.47}$$

where

$$\Lambda_{\mu\mu}^{abcd} = -\frac{\hbar e_\mu^a e_\mu^b e_\mu^c e_\mu^d}{\sqrt{m_a m_b m_c m_d}} \cdot \frac{2n_\mu + 1 + 2\beta\hbar\omega_\mu n_\mu^2 + 2\beta\hbar\omega_\mu n_\mu}{8\omega_\mu^3}, \tag{B.48a}$$

$$\Lambda_{\mu\nu}^{abcd} = \frac{\hbar}{\sqrt{m_a m_b m_c m_d}}\frac{e_\mu^a e_\nu^b e_\mu^c e_\nu^d}{(\omega_\mu - \omega_\nu)(\omega_\mu + \omega_\nu)}\frac{2n_\mu\omega_\nu - 2\omega_\mu n_\nu + \omega_\nu - \omega_\mu}{4\omega_\mu\omega_\nu}. \tag{B.48b}$$

To conclude the proof it is sufficient to show that the $\mathbf{\Lambda}$ matrix of Eq. (B.22) is equal to:

$$\Lambda^{abcd} = \sum_{\mu\nu}\Lambda_{\mu\nu}^{abcd}. \tag{B.49}$$

First, we introduce an auxiliary function $f(\omega_\mu, \omega_\nu)$ as

$$f(\omega_\mu, \omega_\nu) = \frac{2\omega_\nu n_\mu - 2\omega_\mu n_\nu + \omega_\nu - \omega_\mu}{4\omega_\mu\omega_\nu(\omega_\mu + \omega_\nu)(\omega_\mu - \omega_\nu)} = -\frac{1}{4\omega_\mu\omega_\nu}\left[\frac{n_\mu + n_\nu + 1}{\omega_\mu + \omega_\nu} - \frac{n_\mu - n_\nu}{\omega_\mu - \omega_\nu}\right]. \tag{B.50}$$

In the limit $\omega_\nu \to \omega_\mu$ we get:

$$f(\omega_\mu) = \lim_{\omega_\nu\to\omega_\mu} f(\omega_\mu, \omega_\nu) = -\frac{2n_\mu + 1 + 2\hbar\beta\omega_\mu n_\mu^2 + 2\hbar\beta n_\mu\omega_\mu}{8\omega_\mu^3} \tag{B.51}$$

$$f(\omega_\mu) = -\frac{1}{4\omega_\mu^2}\left[\frac{2n_\mu + 1}{2\omega_\mu} - \frac{\partial n}{\partial\omega}\right]. \tag{B.52}$$

So $\Lambda_{\mu\mu}^{abcd}$ is obtained as the continue limit of $\Lambda_{\mu\nu}^{abcd}$ when $\mu \to \nu$:

$$\Lambda_{\mu\nu}^{abcd} = \frac{\hbar e_\mu^a e_\mu^b e_\mu^c e_\mu^d}{\sqrt{m_a m_b m_c m_d}} f(\omega_\mu, \omega_\nu), \qquad \Lambda_{\mu\mu}^{abcd} = \frac{\hbar e_\mu^a e_\mu^b e_\mu^c e_\mu^d}{\sqrt{m_a m_b m_c m_d}} f(\omega_\mu). \tag{B.53}$$

Substituting Eq. (B.50) and (B.52) we finally get:

$$\Lambda_{\mu\nu}^{abcd} = -\frac{\hbar}{4\omega_\mu\omega_\nu}\frac{e_\mu^a e_\nu^b e_\mu^c e_\nu^d}{\sqrt{M_a M_b M_c M_d}} \times \begin{cases} \dfrac{n_\mu + n_\nu + 1}{\omega_\mu + \omega_\nu} - \dfrac{n_\mu - n_\nu}{\omega_\mu - \omega_\nu} & \omega_\mu \neq \omega_\nu \\ \dfrac{2n_\mu + 1}{2\omega_\mu} - \dfrac{\partial n_\mu}{\partial \omega_\mu} & \omega_\mu = \omega_\nu \end{cases}. \tag{B.54}$$

B.3 Condition number of the square/4-th root algorithm

The hessian matrix of the minimization problem using $\sqrt{\boldsymbol{\Phi}}$ or $\sqrt[4]{\boldsymbol{\Phi}}$ can be derived directly from $\boldsymbol{A}_{\boldsymbol{\Phi}}$ computed in appendix B.2.

This can be obtained exploiting the chain rule:

$$\boldsymbol{A}_{\sqrt{\boldsymbol{\Phi}}} = \frac{\partial^2 \mathcal{F}(\vec{\mathcal{R}}, \boldsymbol{\Phi}, \{\vec{a}_i\})}{\partial \sqrt{\boldsymbol{\Phi}} \partial \sqrt{\boldsymbol{\Phi}}} = \boldsymbol{\Phi}\boldsymbol{A}_{\boldsymbol{\Phi}} + 2\sqrt{\boldsymbol{\Phi}}\boldsymbol{A}_{\boldsymbol{\Phi}}\sqrt{\boldsymbol{\Phi}} + \boldsymbol{A}_{\boldsymbol{\Phi}}\boldsymbol{\Phi}, \tag{B.55}$$

where $\boldsymbol{A}_{\boldsymbol{\Phi}}$ is the 4-rank Hessian with respect $\boldsymbol{\Phi}$ (Eq. B.22). The procedure can be iterated to obtain any even root of $\boldsymbol{\Phi}$. Here we report also the $\sqrt[4]{\boldsymbol{\Phi}}$ expression, since, as we will show, it has a very favorable condition number:

$$\boldsymbol{A}_{\sqrt[4]{\boldsymbol{\Phi}}} = \sqrt{\boldsymbol{\Phi}}\boldsymbol{A}_{\sqrt{\boldsymbol{\Phi}}} + 2\sqrt[4]{\boldsymbol{\Phi}}\boldsymbol{A}_{\sqrt{\boldsymbol{\Phi}}}\sqrt[4]{\boldsymbol{\Phi}} + \boldsymbol{A}_{\sqrt{\boldsymbol{\Phi}}}\sqrt{\boldsymbol{\Phi}}. \tag{B.56}$$

We can easily compute the condition numbers in the new variables if all the masses are equal substituting Eq. (B.22) into (B.55) and (B.56) (recalling that $\boldsymbol{\Phi} \sim \omega^2$):

$$C_{\sqrt[2]{\boldsymbol{\Phi}}, T=0} \sim \left(\frac{\omega_{max}}{\omega_{min}}\right) \qquad C_{\sqrt[2]{\boldsymbol{\Phi}}, T\to\infty} \sim \left(\frac{\omega_{max}}{\omega_{min}}\right)^2, \tag{B.57}$$

$$C_{\sqrt[4]{\boldsymbol{\Phi}}, T=0} \sim 1 \qquad C_{\sqrt[4]{\boldsymbol{\Phi}}, T\to\infty} \sim \left(\frac{\omega_{max}}{\omega_{min}}\right). \tag{B.58}$$

Appendix C

Stress tensor calculation

To easily compute the derivative of the SCHA free energy functional with respect to the strain tensor, it is convenient to use the formalism introduced by Bianco *et al*[24]. The average of a generic observable can be written as:

$$\langle O \rangle_{\rho_{\vec{\mathcal{R}},\mathbf{\Phi}}} = \sqrt{\det\left(\frac{\mathbf{\Upsilon}}{2\pi}\right)} \int O(\vec{\mathcal{R}} + \vec{u}, \{\vec{a}_i\}) \exp\left(-\frac{1}{2}\vec{u}\,\mathbf{\Upsilon}\,\vec{u}\right) d^{3N}u, \tag{C.1}$$

In order to normalize the Gaussian integral a change of variable can be applied, so that:

$$u_s^\alpha = \sum_\mu J_{\mu_s}{}^\alpha y_\mu \qquad J_{\mu_s}{}^\alpha = \frac{e_{\mu_s}{}^\alpha}{\sqrt{m_s}} \sqrt{\frac{\hbar(1+n_\mu)}{2\omega_\mu}} \qquad \left(\mathbf{\Upsilon}^{-1}\right)_{st}^{\alpha\beta} = \sum_\mu J_{\mu_s}{}^\alpha J_{\mu_t}{}^\beta. \tag{C.2}$$

Then we have:

$$\langle O \rangle_{\rho_{\vec{\mathcal{R}},\mathbf{\Phi}}} = \int O(\vec{\mathcal{R}} + \mathbf{J}\vec{y}, \{\vec{a}_i\})\,[dy] \qquad [dy] = \prod_{\mu=1}^{3N} \frac{\exp\left(\frac{-y_\mu^2}{2}\right)}{\sqrt{2\pi}} dy_\mu. \tag{C.3}$$

Since we are deriving the $\mathcal{F}_{\vec{\mathcal{R}}}$ functional in the minimum (Eq. 1.9), the Hellman-Feynman (HF) theorem allows us to neglect the changes introduced by the strain on the dynamical matrix. Since we want the most general expression, even when $\vec{\mathcal{R}}$ is not in the minimum, we need to take into account how the atomic position changes when we apply the strain.

$$\frac{d\mathcal{F}(\vec{\mathcal{R}}, \{\vec{a}_i\})}{d\varepsilon_{\alpha\beta}} = \sum_{i=1}^{3} \left.\frac{\partial \mathcal{F}(\vec{\mathcal{R}}, \{\vec{a}_i\})}{\partial \vec{a}_i}\right|_{\substack{cart.\\coord.}} \frac{d\vec{a}_i}{d\varepsilon_{\alpha\beta}} + \frac{\partial \mathcal{F}(\vec{\mathcal{R}}, \{\vec{a}_i\})}{\partial \vec{\mathcal{R}}} \frac{d\vec{\mathcal{R}}}{d\varepsilon_{\alpha\beta}} \tag{C.4}$$

The last term is zero if we are in the minimum. This means that the final equation for the stress does not depend on the particular atomic deformation induced by the strain. This correspond in doing the derivative of the free energy keeping fixed the crystalline coordinates, that is:

$$\frac{d\mathcal{F}(\vec{\mathcal{R}}, \{\vec{a}_i\})}{d\varepsilon_{\alpha\beta}} = \sum_{i=1}^{3} \left.\frac{\partial \mathcal{F}(\vec{\mathcal{R}}, \{\vec{a}_i\})}{\partial \vec{a}_i}\right|_{\substack{cryst.\\coord.}} \frac{d\vec{a}_i}{d\varepsilon_{\alpha\beta}} \tag{C.5}$$

This expression is more convenient, as it coincides with the definition of stress tensor of a system whose atomic positions are out of equilibrium. The free energy functional is:

$$\mathcal{F}_{\vec{\mathcal{R}}} = F_{\mathbf{\Phi}(\vec{\mathcal{R}})} + \left\langle V - \mathcal{V}_{\vec{\mathcal{R}},\mathbf{\Phi}(\vec{\mathcal{R}})} \right\rangle_{\rho_{\vec{\mathcal{R}}}}, \tag{C.6}$$

where $\mathbf{\Phi}(\vec{\mathcal{R}})$ is the dynamical matrix that minimizes $\mathcal{F}(\vec{\mathcal{R}}, \mathbf{\Phi}, \{\vec{a}_i\})$ fixing the average atomic positions. The first term, $F_{\mathbf{\Phi}(\vec{\mathcal{R}})}$ is an explicit function only of the SCHA dynamical matrix, therefore does not contribute to the derivative.

$$\frac{d\mathcal{F}(\vec{\mathcal{R}}, \{\vec{a}_i\})}{d\varepsilon_{\alpha\beta}} = \sum_{i=1}^{3} \frac{\partial \left\langle V - \mathcal{V}_{\vec{\mathcal{R}},\mathbf{\Phi}(\vec{\mathcal{R}})} \right\rangle_{\rho_{\vec{\mathcal{R}}}}}{\partial \vec{a}_i}\bigg|_{\substack{cryst.\\coord.}} \frac{d\vec{a}_i}{d\varepsilon_{\alpha\beta}} \tag{C.7}$$

Joining Eq. (C.7) with Eq. (C.3) we can compute the derivative of an average in the SCHA ensemble with respect to the strain:

$$\frac{\partial \left\langle O \right\rangle_{\rho_{\vec{\mathcal{R}}}}}{\partial \varepsilon_{\alpha\beta}} = \frac{\partial}{\partial \varepsilon_{\alpha\beta}} \int O\left(\vec{\mathcal{R}}(\boldsymbol{\varepsilon}) + \boldsymbol{J}\vec{y}, \{\vec{a}_i(\varepsilon)\}\right)[dy] = \int \sum_{i\gamma} \frac{\partial O}{\partial a_i^\gamma}\bigg|_{\substack{cryst.\\coord.}} \frac{\partial a_i^\gamma}{\partial \varepsilon_{\alpha\beta}}[dy], \tag{C.8}$$

$$\frac{\partial \left\langle O \right\rangle_{\rho_{\vec{\mathcal{R}}}}}{\partial \varepsilon_{\alpha\beta}} = \Big\langle \sum_{i\gamma} \frac{\partial O}{\partial a_i^\gamma}\bigg|_{\substack{cryst.\\coord.}} \frac{\partial a_i^\gamma}{\partial \varepsilon_{\alpha\beta}} \Big\rangle_{\rho_{\vec{\mathcal{R}}}}. \tag{C.9}$$

$$\frac{\partial \left\langle V \right\rangle_{\rho_{\vec{\mathcal{R}}}}}{\partial \varepsilon_{\alpha\beta}} = \Big\langle \sum_{i\gamma} \frac{\partial V}{\partial a_i^\gamma}\bigg|_{\substack{cryst.\\coord.}} \frac{\partial a_i^\gamma}{\partial \varepsilon_{\alpha\beta}} \Big\rangle_{\rho_{\vec{\mathcal{R}}}} = -\Omega \left\langle P^H_{\alpha\beta} \right\rangle_{\rho_{\vec{\mathcal{R}}}}, \tag{C.10}$$

The term with the harmonic potential $\mathcal{V}$ can be derived writing its explicit dependence from the strain tensor $\boldsymbol{\varepsilon}$:

$$\mathcal{V}_{\vec{\mathcal{R}},\mathbf{\Phi}}(\boldsymbol{\varepsilon}) = \frac{1}{2}\left[(I+\boldsymbol{\varepsilon})\left(\vec{R}-\vec{\mathcal{R}}\right)\right]\mathbf{\Phi}\left[(I+\boldsymbol{\varepsilon})\left(\vec{R}-\vec{\mathcal{R}}\right)\right]^T \tag{C.11}$$

From which we immediately can write the derivative:

$$\begin{aligned}\frac{d\mathcal{V}_{\vec{\mathcal{R}},\mathbf{\Phi}}}{d\boldsymbol{\varepsilon}}\bigg|_{\varepsilon=0} &= \frac{1}{2}\left(\vec{R}-\vec{\mathcal{R}}\right)\otimes\mathbf{\Phi}\left(\vec{R}-\vec{\mathcal{R}}\right) + \frac{1}{2}\left(\vec{R}-\vec{\mathcal{R}}\right)\mathbf{\Phi}\otimes\left(\vec{R}-\vec{\mathcal{R}}\right) = \\ &= -\frac{1}{2}\left(\vec{R}-\vec{\mathcal{R}}\right)\otimes\vec{f_{\mathcal{H}s}} - \frac{1}{2}\vec{f_{\mathcal{H}s}}\otimes\left(\vec{R}-\vec{\mathcal{R}}\right)\end{aligned} \tag{C.12}$$

Where the outer product must be taken only on the Cartesian coordinates (as it is a consequence of the $\boldsymbol{\varepsilon}$ derivative). Explicitying the last equation in all cartesian and atomic indices it is:

$$\frac{d\mathcal{V}_{\vec{\mathcal{R}},\mathbf{\Phi}}}{d\varepsilon_{\alpha\beta}}\bigg|_{\varepsilon=0} = -\sum_{s=1}^{N_{atoms}} \frac{1}{2}\left(u_s^\alpha f_{\mathcal{H}_s}^\beta + u_s^\beta f_{\mathcal{H}_s}^\alpha\right) \tag{C.13}$$

From which we have:

$$\frac{d\left\langle \mathcal{V}_{\vec{\mathcal{R}},\mathbf{\Phi}} \right\rangle_{\rho_{\vec{\mathcal{R}}}}}{d\varepsilon_{\alpha\beta}} = -\frac{1}{2}\Big\langle \sum_{s=1}^{N_{atoms}} \left(u_s^\alpha f_{\mathcal{H}_s}^\beta + u_s^\beta f_{\mathcal{H}_s}^\alpha\right)\Big\rangle_{\rho_{\vec{\mathcal{R}}}} \tag{C.14}$$

$$\frac{d\mathcal{F}(\vec{\mathcal{R}},\{\vec{a}_i\})}{d\varepsilon_{\alpha\beta}} = -\Omega \left\langle P^H_{\alpha\beta} \right\rangle_{\rho_{\vec{\mathcal{R}}}} + \frac{1}{2} \Big\langle \sum_{s=1}^{N_{atoms}} \Big(u_s^\alpha f_{\mathcal{H}_s}^\beta + u_s^\beta f_{\mathcal{H}_s}^\alpha \Big) \Big\rangle_{\rho_{\vec{\mathcal{R}}}} \tag{C.15}$$

Therefore, the final expression of the stress tensor is:

$$P_{\alpha\beta} = -\frac{1}{\Omega} \frac{d\mathcal{F}(\vec{\mathcal{R}},\{\vec{a}_i\})}{d\varepsilon_{\alpha\beta}} \tag{C.16}$$

$$P_{\alpha\beta} = \langle P^H_{\alpha\beta} - \frac{1}{2\Omega} \sum_{s=1}^{N} \Big(f_{\mathcal{H}_s}^\alpha u_s^\beta + f_{\mathcal{H}_s}^\beta u_s^\alpha \Big) \rangle_{\rho_{\vec{\mathcal{R}}}} \tag{C.17}$$

It is interesting to notice that the "harmonic" contribution could also be computed analytically:

$$P^{\mathcal{H}}_{\alpha\beta} = -\frac{1}{2\Omega} \langle \sum_{s=1}^{N} \Big(f_{\mathcal{H}_s}^\alpha u_s^\beta + f_{\mathcal{H}_s}^\beta u_s^\alpha \Big) \rangle_{\rho_{\vec{\mathcal{R}}}} = -\frac{1}{\Omega} \sum_{\mu=1}^{3N} \sum_{s=1}^{N} \frac{\hbar\omega_\mu}{2\tanh\left(\frac{\beta\hbar\omega_\mu}{2}\right)} e_{\mu_s}^\alpha e_{\mu_s}^\beta, \tag{C.18}$$

Appendix D

TDSCHA

D.1 The Lambda matrix

In this section I prove the relation(3.13):

$$\Lambda^{abcd} = \frac{1}{2}\frac{\partial(\Upsilon^{-1})_{cd}}{\partial\Phi_{ab}}$$

We recall:

$$\Upsilon^{-1}{}_{cd} = \frac{1}{\sqrt{m_c m_d}}\sum_\mu e^c_\mu e^d_\mu \frac{1+2n_\mu}{2\omega_\mu} \tag{D.1}$$

$$\Phi_{ab} = \sqrt{m_a m_b}\sum_\mu \omega^2_\mu e^a_\mu e^b_\mu \tag{D.2}$$

Then we have:

$$\frac{\partial\Upsilon^{-1}{}_{cd}}{\partial\Phi_{ab}} = \sum_\mu \frac{\partial\Upsilon^{-1}{}_{cd}}{\partial\omega_\mu}\frac{\partial\omega_\mu}{\partial\Phi_{ab}} + \sum_{\mu hk}\frac{\partial\Upsilon^{-1}{}_{cd}}{\partial(e^k_\mu e^h_\mu)}\frac{\partial(e^k_\mu e^h_\mu)}{\partial\Phi_{ab}} \tag{D.3}$$

$$\frac{\partial\Phi_{ab}}{\partial\omega_\mu} = \sqrt{m_a m_b}\,2\omega_\mu e^a_\mu e^b_\mu \qquad \frac{\partial\omega_\mu}{\partial\Phi_{ab}} = \frac{e^a_\mu e^b_\mu}{2\omega_\mu\sqrt{m_a m_b}} \tag{D.4}$$

The derivative with respect of the perturbation vectors has been calculated in Eq. (B.43).

$$\frac{\partial(e^a_\mu e^b_\mu)}{\partial\Phi_{cd}} = \frac{\mathcal{P}_{cd}}{\sqrt{m_c m_d}}\sum_\nu^{\nu\neq\mu}\frac{\left(e^a_\mu e^b_\nu + e^b_\mu e^a_\nu\right)\left(e^c_\nu e^d_\mu + e^c_\mu e^d_\nu\right)}{2(\omega^2_\mu - \omega^2_\nu)}. \tag{D.5}$$

Lets compute some factors:

$$\frac{\partial n_\mu}{\partial\omega_\mu} = -\beta n^2_\mu e^{\beta\omega_\mu} \tag{D.6}$$

$$\frac{\partial}{\partial\omega_\mu}\left(\frac{1+2n_\mu}{2\omega_\mu}\right) = -\frac{2\beta\omega e^{\beta\omega}n^2_\mu + 1 + 2n_\mu}{2\omega^2_\mu} \tag{D.7}$$

$$= -\frac{2\beta\omega_\mu(e^{\beta\omega_\mu}-1)n^2_\mu + 2\beta\omega n^2_\mu + 1 + 2n_\mu}{2\omega^2_\mu} = \tag{D.8}$$

$$= -\frac{2\beta\omega n_\mu + 2\beta\omega n^2_\mu + 2n_\mu + 1}{2\omega^2_\mu} \tag{D.9}$$

$$\frac{\partial \Upsilon^{-1}{}_{cd}}{\partial \omega_\mu} = -\frac{1}{\sqrt{m_c m_d}} e^c_\mu e^d_\mu \frac{2\beta\omega n_\mu + 2\beta\omega n_\mu^2 + 2n_\mu + 1}{2\omega_\mu^2} \tag{D.10}$$

So the first part is computable easily:

$$\sum_\mu \frac{\partial \Upsilon^{-1}{}_{cd}}{\partial \omega_\mu} \frac{\partial \omega_\mu}{\partial \Phi_{ab}} = \frac{1}{\sqrt{m_c m_d}} \sum_\mu e^c_\mu e^d_\mu \frac{2\beta\omega n_\mu + 2\beta\omega n_\mu^2 + 2n_\mu + 1}{2\omega_\mu^2} \frac{e^a_\mu e^b_\mu}{2\omega_\mu \sqrt{m_a m_b}} \tag{D.11}$$

$$\sum_\mu \frac{\partial \Upsilon^{-1}{}_{cd}}{\partial \omega_\mu} \frac{\partial \omega_\mu}{\partial \Phi_{ab}} = \sum_\mu \frac{e^a_\mu e^b_\mu e^c_\mu e^d_\mu}{\sqrt{m_a m_b m_c m_d}} \frac{2\beta\omega n_\mu + 2\beta\omega n_\mu^2 + 2n_\mu + 1}{4\omega_\mu^3} \tag{D.12}$$

Now we compute the other part:

$$\frac{\partial \Upsilon^{-1}{}_{cd}}{\partial (e^k_\mu e^h_\mu)} = \frac{1}{\sqrt{m_c m_d}} \frac{1 + 2n_\mu}{2\omega_\mu} \left(\delta_{hc}\delta_{kd} + \delta_{hd}\delta_{kc}\right) \frac{\mathcal{P}_{cd}}{2} \tag{D.13}$$

$$\sum_{\mu hk} \frac{\partial \Upsilon^{-1}{}_{cd}}{\partial (e^k_\mu e^h_\mu)} \frac{\partial (e^k_\mu e^h_\mu)}{\partial \Phi_{ab}} = \sum_\mu \frac{\mathcal{P}_{ab}\mathcal{P}_{cd}}{\sqrt{m_a m_b m_c m_d}} \sum_\nu^{\nu \neq \mu} \frac{\left(e^c_\mu e^d_\nu + e^d_\mu e^c_\nu\right)\left(e^a_\nu e^b_\mu + e^a_\mu e^b_\nu\right)}{2(\omega_\mu^2 - \omega_\nu^2)} \frac{1 + 2n_\mu}{2\omega_\mu} \tag{D.14}$$

We can explicit the sum over ab by exchanging μ and ν:

$$\sum_{\mu hk} \frac{\partial \Upsilon^{-1}{}_{cd}}{\partial (e^k_\mu e^h_\mu)} \frac{\partial (e^k_\mu e^h_\mu)}{\partial \Phi_{ab}} = \frac{\mathcal{P}_{ab}\mathcal{P}_{cd}}{\sqrt{m_a m_b m_c m_d}} \sum_{\substack{\mu\nu \\ \nu \neq \mu}} \frac{\left(e^c_\mu e^d_\nu + e^d_\mu e^c_\nu\right) e^a_\mu e^b_\nu}{2(\omega_\mu^2 - \omega_\nu^2)} \left(\frac{1 + 2n_\mu}{2\omega_\mu} - \frac{1 + 2n_\nu}{2\omega_\nu}\right) \tag{D.15}$$

Joining Eq. (D.11) with Eq. (D.15) and comparing with Eq. (B.46) we recognize immediately that:

$$\frac{\partial \Upsilon^{-1}{}_{cd}}{\partial \Phi_{ab}} = 2\Lambda^{abcd} \tag{D.16}$$

D.2 Harmonic Green functions

Here we study an harmonic quantum crystal with Green functions. The green function for the phonons can be defined as the response function with respect to atomic displacements:

$$G_{ab}(t) = -i \left\langle \psi_0 | T \sqrt{m}_a [R_a(t) - \mathcal{R}_a] \sqrt{m}_b [R_b(0) - \mathcal{R}_b] | \psi_0 \right\rangle \tag{D.17}$$

Where the position operators $R_a(t)$ and $R_b(0)$ are in the Heisenberg picture

$$R_a(t) = e^{iHt} R_a e^{-iHt},$$

and T is the time-ordering operator.

We can express the position operator as a function of phonon creation and annihilation operators:

$$\sqrt{m_a}(R_a - \mathcal{R}_a) = \sum_\mu e^a_\mu \sqrt{\frac{1}{2\omega_\mu}} \left(c^\dagger_\mu + c_\mu\right) \tag{D.18}$$

Where μ are all the modes in the supercell. Substituting in the green function we get:

$$G_{ab}(t) = -i \sum_{\mu\nu} \frac{e^a_\mu e^b_\nu}{2\sqrt{\omega_\nu \omega_\mu}} \langle \psi_0 | T \left[c^\dagger_\mu(t) + c_\mu(t)\right] \left[c^\dagger_\nu + c_\nu\right] |\psi_0\rangle \tag{D.19}$$

From Eq. (D.19) it is clear that $\mu = \nu$. Harmonic phonons do not interact. The only non zero terms are those where a phonon is firstly created and then annihilated. In this case, thanks to the time ordering T operator, we have also a non vanishing backward propagation in time:

$$G_{ab}(t) = -i \sum_{\mu} \frac{e^a_\mu e^b_\mu}{2\omega_\mu} \langle \psi_0 | \left[c_\mu(t) c^\dagger_\mu \theta(t) + c_\mu c^\dagger_\mu(t)\theta(-t)\right] |\psi_0\rangle \tag{D.20}$$

This backward propagation is always present for Hermitian operators.

We can explicit the Heisenberg picture and compute the green function.

$$\langle \psi_0 | c_\mu c^\dagger_\mu | \psi_0 \rangle = 1$$

$$G_{ab}(\omega) = -i \sum_{\mu} \frac{e^a_\mu e^b_\mu}{2\omega_\mu} \left[\int_0^\infty e^{i(\omega - \omega_\mu + i0^+)t} dt + \int_{-\infty}^0 e^{i(\omega + \omega_\mu - i0^+)t} dt\right] \tag{D.21}$$

$$G_{ab}(\omega) = -i \sum_{\mu} \frac{e^a_\mu e^b_\mu}{2\omega_\mu} \left[\int_0^\infty e^{i(\omega - \omega_\mu + i0^+)t} dt + \int_0^\infty e^{-i(\omega + \omega_\mu - i0^+)t} dt\right] \tag{D.22}$$

From which we get

$$G_{ab}(\omega) = \sum_{\mu} \frac{e^a_\mu e^b_\mu}{2\omega_\mu} \left[\frac{1}{\omega - \omega_\mu + i0^+} - \frac{1}{\omega + \omega_\mu - i0^+}\right] \tag{D.23}$$

$$G_{ab}(\omega) = \sum_{\mu} \frac{e^a_\mu e^b_\mu}{2\omega_\mu} \frac{2(\omega_\mu - i0^+)}{\omega^2 - (\omega_\mu - i0^+)^2} \tag{D.24}$$

We can keep only first order poles. They are non vanishing only when $\omega = \pm\omega_\mu$, we can rewrite the equation as:

$$G_{ab}(\omega) = \sum_{\mu} e^a_\mu e^b_\mu \frac{1}{(\omega + i0^+)^2 - \omega^2_\mu} \tag{D.25}$$

Since this is diagonal in the eigenmode space, we can write it in matricial form:

$$D_{ab} = \sum_\mu e^a_\mu e^b_\mu \omega^2_\mu$$

$$\boldsymbol{G}(\omega) = \left[\omega^2 - \boldsymbol{D} + 2i\omega 0^+\right]^{-1} \tag{D.26}$$

D.3 Perturbation series

Here we want to derive the correct perturbation expansion (at $T = 0\,\mathrm{K}$ for simplicity) for the anharmonic problem:

$$V = \frac{1}{2}\sum_{ab}\sqrt{m_a m_b}\overset{(2)}{D}_{ab}\, u_a u_b + \frac{1}{6}\sum_{abc}\sqrt{m_a m_b m_c}\overset{(3)}{D}_{abc}\, u_a u_b u_c$$

We ignore higher order terms.

Here, the third order introduces a scattering channel between phonons. The interacting green function is, therefore:

$$G_{ab}(\omega) = -i\,\langle\psi_0|TS(\infty,-\infty)\sqrt{m_a}u_a(t)\sqrt{m_b}R_b(0)|\psi_0\rangle \tag{D.27}$$

Where $|\psi_0\rangle$ is the interacting ground state and $S(\infty,-\infty)$ is the propagator. We can expand the propagator in series

$$S(t,0) = T\exp\left\{-i\int_0^t dt'\frac{1}{6}\sum_{abc}\sqrt{m_a m_b m_c}\overset{(3)}{D}_{abc}\, u_a(t')u_b(t')u_c(t')\right\} \tag{D.28}$$

We can take the second order expansion of the propagator (the first order gives zero, as it contains an odd number of creation operators)

$$S(\infty,-\infty) \approx 1 - \frac{1}{36}\sum_{\substack{abc\\def}}\int_{-\infty}^{\infty}dt'\int_{-\infty}^{\infty}dt''\overset{(3)}{D}_{abc}\,\tilde{u}_a(t')\tilde{u}_b(t')\tilde{u}_c(t')\overset{(3)}{D}_{def}\,\tilde{u}_d(t'')\tilde{u}_e(t'')\tilde{u}_f(t'') \tag{D.29}$$

where $\tilde{u} = \sqrt{m}u$ for a more compact expression.

Substituting this inside the Green function we get:

$$\begin{aligned}G_{hk}(\omega) =& G^{(0)}_{hk}(\omega) + \frac{1}{36}\sum_{\substack{abc\\def}}\overset{(3)}{D}_{abc}\overset{(3)}{D}_{def}\int_{-\infty}^{\infty}e^{i\omega t}dt\int_{-\infty}^{\infty}dt'\int_{-\infty}^{\infty}dt''\\ &\langle\psi_0|Tu_h(t)u_a(t')u_b(t')u_c(t')u_d(t'')u_e(t'')u_f(t'')u_k(0)|\psi_0\rangle\end{aligned} \tag{D.30}$$

The last contraction can be evaluated using the Wick theorem. Among all possible contractions, we can easily see that the only non disconnected diagrams are of the type:

$$\langle u_h(t)u_a(t')\rangle\,\langle u_b(t')u_d(t'')\rangle\,\langle u_c(t')u_e(t'')\rangle\,\langle u_f(t'')u_k(0)\rangle$$

This diagram can be obtained also exchanging $a \leftrightarrow b \leftrightarrow c$, $d \leftrightarrow e \leftrightarrow f$. Therefore it appears 36 times in the summation. This diagram is the bubble. The other non vanishing diagram is the tadpole:

$$\langle u_h(t)u_a(t')\rangle\,\langle u_b(t')u_d(t'')\rangle\,\langle u_e(t'')u_f(t'')\rangle\,\langle u_c(t')u_k(0)\rangle$$

Also this diagram appears 36 times in the summation. We can cancel the 1/36 and the summation and account only for one diagram.

Here, I will consider only the bubble, as it is the term we find to be more interesting. We can make the following change of variables:

$$t'' = \tau_1 \qquad t' - t'' = \tau_2 \qquad t - t' = \tau_3$$

Since the times vary from $-\infty$ to ∞, so the τ variables do. Then the integral becomes:

$$\iiint_{-\infty}^{\infty} d\tau_3 d\tau_2 d\tau_1 e^{i\omega(\tau_1+\tau_2+\tau_3)} G^{(0)}_{ha}(\tau_3) G^{(0)}_{bd}(\tau_2) G^{(0)}_{ce}(\tau_2) G^{(0)}_{fk}(\tau_1) \tag{D.31}$$

We can call the two phonons propagator $\chi(\omega)$ as:

$$\frac{1}{2}\chi_{abcd}(\omega) = \int_{-\infty}^{\infty} dt e^{i\omega t} G^{(0)}_{ac}(t) G^{(0)}_{bd}(t) \tag{D.32}$$

And the bubble term is:

$$G_{hk}(\omega) = G^{(0)}_{hk}(\omega) + G^{(0)}_{ha}(\omega) \sum_{\substack{a\geq b\geq c \\ d\geq e\geq f}} \overset{(3)}{D}_{abc} \frac{1}{2}\chi_{bcde}(\omega) \overset{(3)}{D}_{def} G^{(0)}_{fk}(\omega) \tag{D.33}$$

Using a self-energy approach, we can extract the bubble self-energy:

$$\Pi(\omega) = -\sum_{\substack{a\geq b\geq c \\ d\geq e\geq f}} \overset{(3)}{D}_{abc} \frac{1}{2}\chi_{bcde}(\omega) \overset{(3)}{D}_{def} \tag{D.34}$$

And we get

$$\boldsymbol{G} = \boldsymbol{G}^{(0)} - \boldsymbol{G}^{(0)}\boldsymbol{\Pi}\boldsymbol{G} \tag{D.35}$$

$$(1 + \boldsymbol{G}^{(0)}\boldsymbol{\Pi})\boldsymbol{G} = \boldsymbol{G}^{(0)} \tag{D.36}$$

$$\boldsymbol{G} = (1 + \boldsymbol{G}^{(0)}\boldsymbol{\Pi})^{-1}\boldsymbol{G}^{(0)} \tag{D.37}$$

$$\boldsymbol{G}^{-1} = (\boldsymbol{G}^{(0)})^{-1}(1 + \boldsymbol{G}^{(0)}\boldsymbol{\Pi}) = (\boldsymbol{G}^{(0)})^{-1} + \boldsymbol{\Pi} \tag{D.38}$$

So now lets compute the two phonon propagator:

$$\frac{1}{2}\chi_{abcd}(\omega) = \int dt e^{i\omega t} G^{(0)}_{ac}(t) G^{(0)}_{bd}(t) \tag{D.39}$$

$$G^{(0)}_{ac}(t) = -i\sum_{\mu} \frac{e^a_\mu e^c_\mu}{2\omega_\mu}\left[\theta(t)e^{-i\omega_\mu t} + \theta(-t)e^{i\omega_\mu t}\right]$$

$$\frac{1}{2}\chi_{abcd}(\omega) = -i\sum_{\mu\nu} \frac{e^a_\mu e^c_\mu e^b_\nu e^d_\nu}{4\omega_\mu\omega_\nu}\left[\int_0^\infty dt e^{i(\omega-\omega_\mu-\omega_\nu+i0^+)t} + \int_0^\infty dt e^{-i(\omega+\omega_\mu+\omega_\nu-i0^+)t}\right] \tag{D.40}$$

So we have

$$\frac{1}{2}\chi_{abcd}(\omega) = \sum_{\mu\nu} \frac{e^a_\mu e^c_\mu e^b_\nu e^d_\nu}{4\omega_\mu\omega_\nu}\left[\frac{1}{\omega-\omega_\mu-\omega_\nu+i0^+} - \frac{1}{\omega+\omega_\mu+\omega_\nu-i0^+}\right] \tag{D.41}$$

$$\frac{1}{2}\chi_{abcd}(\omega) = \sum_{\mu\nu} \frac{e^a_\mu e^c_\mu e^b_\nu e^d_\nu}{4\omega_\mu\omega_\nu} \frac{1}{\omega^2 - (\omega_\mu+\omega_\nu-i0^+)^2} \tag{D.42}$$

D.4 Least action principle

We can split the action in the same way as done in the 1D case:

$$A_1 = \frac{1}{T}\int_0^T dt\, \langle \psi(t)|K|\psi(t)\rangle \tag{D.43}$$

$$A_2 = \frac{1}{T}\int_0^T dt\, \langle \psi(t)|V(t)|\psi(t)\rangle \tag{D.44}$$

$$A_3 = -\frac{i}{\hbar}\frac{1}{T}\int_0^T dt\, \langle \psi(t)|\frac{d}{dt}|\psi(t)\rangle \tag{D.45}$$

where K is an abbreviation for the kinetic energy operator:

$$K = \sum_{a=1}^{3N} \frac{P_a^2}{2m_a}$$

D.4.1 A_1 computation

The first term is just:

$$-\sum_i \frac{\hbar^2}{2m_i}\int d^{3N}R\psi^*(\vec{R},t)\frac{\partial^2\psi}{\partial R_i^2}(\vec{R},t) \tag{D.46}$$

$$\begin{aligned}\frac{\partial^2\psi}{\partial R_a^2} = \Big[&-\frac{\Upsilon_{aa}}{2} + 2i\mathcal{C}_{aa} + \frac{1}{4}\sum_{bc}\Upsilon_{ab}\Upsilon_{ac}(R_b-\mathcal{R}_b)(R_c-\mathcal{R}_c) - Q_a^2 - \\ &- 4\sum_{bc}\mathcal{C}_{ab}\mathcal{C}_{ac}(R_b-\mathcal{R}_b)(R_c-\mathcal{R}_c) - iQ_a\sum_b\Upsilon_{ab}(R_b-\mathcal{R}_b) - \\ &- 2i\sum_{bc}\Upsilon_{ab}\mathcal{C}_{ac}(R_b-\mathcal{R}_b)(R_c-\mathcal{R}_c) - 4Q_a\sum_b\mathcal{C}_{ab}(R_b-\mathcal{R}_b)\Big]\psi(\vec{R},t)\end{aligned} \tag{D.47}$$

when computing the integral all the terms linear in the displacement are cancelled, recalling that:

$$\int d^{3N}R\psi^*(\vec{R},t)(R_a-\mathcal{R}_a)(R_b-\mathcal{R}_b)\psi(\vec{R},t) = (\Upsilon^{-1})_{ab} \tag{D.48}$$

$$\int d^{3N}\psi^*(\vec{R},t)\frac{\partial^2\psi}{\partial R_a^2}(\vec{R},t) = -\frac{\Upsilon_{aa}}{4} - Q_a^2 - 4\sum_{bc}\mathcal{C}_{ab}(\Upsilon^{-1})_{bc}\mathcal{C}_{ca} \tag{D.49}$$

Then the kinetic term is:

$$\langle\psi|K|\psi\rangle = \hbar^2\sum_a\left[\frac{\Upsilon_{aa}}{8m_a} + \frac{Q_a^2}{2m_a} + \frac{2}{m_a}\sum_{bc}\mathcal{C}_{ab}(\Upsilon^{-1})_{bc}\mathcal{C}_{ca}\right] \tag{D.50}$$

From which we can get the first part of the action:

$$A_1 = \frac{\hbar^2}{T}\int_0^T dt\ \sum_a\left[\frac{\Upsilon_{aa}}{8m_a} + \frac{Q_a^2}{2m_a} + \frac{2}{m_a}\sum_{bc}\mathcal{C}_{ab}(\Upsilon^{-1})_{bc}\mathcal{C}_{ca}\right] \tag{D.51}$$

Now we can compute the variation of the action:

$$\frac{\delta A_1}{\delta Q_a} = \hbar^2 \frac{Q_a}{m_a} \qquad \frac{\delta A_1}{\delta \mathcal{R}_a} = 0 \tag{D.52}$$

$$\frac{\delta A_1}{\delta \mathcal{C}_{ab}} = \frac{2\hbar^2}{m_a} \sum_c (\Upsilon^{-1})_{bc} \mathcal{C}_{ca} + \frac{2\hbar^2}{m_b} \sum_c \mathcal{C}_{bc} (\Upsilon^{-1})_{ca} \tag{D.53}$$

Since each term is symmetric if I change a with b I can just take:

$$\frac{\delta A_1}{\delta \mathcal{C}_{ab}} = \frac{4\hbar^2}{m_a} \sum_c \left(\Upsilon^{-1}\right)_{bc} \mathcal{C}_{ca} \tag{D.54}$$

$$\frac{\delta A_1}{\delta \Phi_{ab}} = \sum_c \frac{\hbar^2}{m_c} \frac{1}{8} \frac{\partial \Upsilon_{cc}}{\partial \Phi_{ab}} + \sum_{cde} \frac{2\hbar^2}{m_c} \mathcal{C}_{cd} \frac{\partial (\Upsilon^{-1})_{de}}{\partial \Phi_{ab}} \mathcal{C}_{ec} \tag{D.55}$$

The last term can be rewritten as:

$$\frac{\partial \Upsilon_{cc}}{\partial \Phi_{ab}} = -\sum_{hk} \Upsilon_{ch} \Upsilon_{ck} \frac{\partial \Upsilon^{-1}_{hk}}{\partial \Phi_{ab}} \tag{D.56}$$

If $T = 0$ we have:

$$\sum_c \frac{\hbar^2}{4m_c} \Upsilon_{ac} \Upsilon_{cb} = \Phi_{ab} \tag{D.57}$$

$$\frac{\delta A_1}{\delta \Phi_{ab}} = -\sum_{de} \frac{1}{2} \Phi_{de} \frac{\partial \Upsilon^{-1}_{de}}{\partial \Phi_{ab}} + \sum_{cde} \frac{2\hbar^2}{m_c} \mathcal{C}_{cd} \frac{\partial (\Upsilon^{-1})_{de}}{\partial \Phi_{ab}} \mathcal{C}_{ec} \tag{D.58}$$

D.4.2 A_2 computation

To compute the action of the second term we must perform the derivatives of:

$$\delta A_2 = \delta \frac{1}{T} \int_0^T dt \, \langle \psi | V(t) | \psi \rangle \tag{D.59}$$

$$\frac{\delta A_2}{\delta \Phi_{ab}} = \frac{1}{2} \sum_{cd} \frac{\partial \Upsilon^{-1}_{cd}}{\partial \Phi_{ab}} \langle \frac{\partial^2 V}{\partial R_c \partial R_d} \rangle \tag{D.60}$$

It is quite easy to provide the derivative of both A_1 and A_2 respect to $\mathbf{\Phi}$ since it would be equal to the static free energy derivative in absence of the quadratic chirp $\mathcal{C}$.

$$\frac{\delta (A_1 + A_2)}{\delta \Phi_{ab}} = \sum_{cd} \frac{\partial \Upsilon^{-1}_{cd}}{\partial \Phi_{ab}} \left(\frac{1}{2} \langle \frac{\partial^2 V}{\partial R_c \partial R_d} \rangle - \frac{1}{2} \Phi_{cd} + \sum_e \frac{2\hbar^2}{m_e} \mathcal{C}_{ce} \mathcal{C}_{ed} \right) \tag{D.61}$$

It is interesting to notice how the old free energy gradient appears here:

$$\frac{\partial \mathcal{F}_{SCHA}}{\partial \Phi_{ab}} = \frac{1}{2} \sum_{cd} \frac{\partial \Upsilon^{-1}_{cd}}{\partial \Phi_{ab}} \left(\langle \frac{\partial^2 V}{\partial R_c \partial R_d} \rangle - \Phi_{cd} \right) \tag{D.62}$$

The derivative respect to $\mathcal{R}$ is trivial:

$$\frac{\delta A_2}{\delta \mathcal{R}_a} = -\langle f_a \rangle \tag{D.63}$$

The derivative respect to the two phases is zero:

$$\frac{\delta A_2}{\delta Q_a} = 0 \qquad \frac{\delta A_2}{\delta \mathcal{C}_{ab}} = 0 \tag{D.64}$$

D.4.3 A_3 computation

Let us compute the last term:

$$A_3 = -i\frac{\hbar}{T}\int_0^T dt\ \langle \psi(t)|\frac{d}{dt}|\psi(t)\rangle \tag{D.65}$$

$$\langle \psi(t)|\frac{d}{dt}|\psi(t)\rangle = \int d^{3N}R\ \psi^*(R,t)\frac{d}{dt}\psi(R,t) \tag{D.66}$$

If we consider the derivative on the real part of the wavefunction, we get zero, because for those term we have:

$$\int d^{3N}R\ \frac{d}{dt}|\psi(R,t)|^2 = \frac{d}{dt}\int d^{3N}R\ |\psi(R,t)|^2 = 0 \tag{D.67}$$

Therefore, only the derivative in the phase term will give a non zero contribution to the A_3 term:

$$\langle \psi(t)|\frac{d}{dt}|\psi(t)\rangle = -\sum_a iQ_a\dot{\mathcal{R}}_a + i\sum_{ab}\dot{\mathcal{C}}_{ab}(\Upsilon^{-1})_{ab} \tag{D.68}$$

We obtain the variation easily:

$$\frac{\delta A_3}{\delta Q_a} = -\hbar\dot{\mathcal{R}}_a \qquad \frac{\delta A_3}{\delta \mathcal{R}_a} = \hbar\dot{Q}_a \tag{D.69}$$

$$\frac{\delta A_3}{\delta \mathcal{C}_{ab}} = -\hbar\sum_{cd}\frac{\partial(\Upsilon^{-1})_{ab}}{\partial\Phi_{cd}}\dot{\Phi}_{cd} \qquad \frac{\delta A_3}{\delta\Phi_{ab}} = \hbar\sum_{cd}\dot{\mathcal{C}}_{cd}\frac{\partial(\Upsilon^{-1})_{cd}}{\partial\Phi_{ab}} \tag{D.70}$$

Putting all together we get:

$$\begin{cases} -\langle f_a\rangle + \hbar\dot{Q}_a = 0 \\ \\ -\hbar\dot{\mathcal{R}}_a + \hbar^2\dfrac{Q_a}{m_a} = 0 \\ \\ \dfrac{\partial\mathcal{F}_{SCHA}}{\partial\Phi_{ab}} + \displaystyle\sum_{cde}\frac{2\hbar^2}{m_c}\frac{\partial\Upsilon^{-1}_{de}}{\partial\Phi_{ab}}\mathcal{C}_{cd}\mathcal{C}_{ce} + \hbar\sum_{cd}\dot{\mathcal{C}}_{cd}\frac{\partial(\Upsilon^{-1})_{cd}}{\partial\Phi_{ab}} = 0 \\ \\ -\hbar\displaystyle\sum_{cd}\frac{\partial(\Upsilon^{-1})_{ab}}{\partial\Phi_{cd}}\dot{\Phi}_{cd} + \frac{4\hbar^2}{m_a}\sum_c(\Upsilon^{-1})_{bc}\mathcal{C}_{ca} = 0 \end{cases} \tag{D.71}$$

That are the equation of motion we presented in the main text.

D.5 Effective time-dependent Hamiltonian

In this section we want to prove that the equation of motion corresponds to a Gaussian wave-function evolving according to the SCHA Hamiltonian, as in the one dimensional case:

$$H\,|\psi\rangle = i\hbar \frac{d}{dt}\,|\psi\rangle \tag{D.72}$$

Where H is the SCHA Hamiltonian:

$$H = K + \frac{1}{2}\sum_{ab} \langle \frac{d^2V}{dR_a dR_b} \rangle \,(R_a - \mathcal{R}_a)(R_b - \mathcal{R}_b) - \sum_a \langle f_a \rangle \,(R_a - \mathcal{R}_a) \tag{D.73}$$

And $|\psi\rangle$ is the Gaussian wavepacket introduced in eq. (3.6).

We can derive the equations of motion by combining eq. (D.72), (D.73) and (3.6).

First of all, let us concentrate on the right hand side of eq. (D.72).

$$\langle \vec{R}|K|\psi\rangle = -\sum_a \frac{1}{2m_a}\frac{\partial^2 \psi}{\partial R_a^2} \tag{D.74}$$

$$\frac{\partial \psi}{\partial R_a} = \left[-\frac{1}{2}\sum_b \Upsilon_{ab}(R_b - \mathcal{R}_b) + iQ_a + 2i\sum_b \mathcal{C}_{ab}(R_b - \mathcal{R}_b) \right] \psi(\vec{R}) \tag{D.75}$$

$$\begin{aligned}\frac{\partial^2 \psi}{\partial R_a^2} = \Bigg\{ &\left[-\frac{1}{2}\sum_b \Upsilon_{ab}(R_b - \mathcal{R}_b) + iQ_a + 2i\sum_b \mathcal{C}_{ab}(R_b - \mathcal{R}_b) \right]^2 + \\ &+ \left[-\frac{1}{2}\Upsilon_{aa} + 2i\mathcal{C}_{aa} \right] \Bigg\} \psi(\vec{R})\end{aligned} \tag{D.76}$$

$$\begin{aligned}\frac{\partial^2 \psi}{\partial R_a^2} = \Bigg\{ &\sum_{bc} (R_b - \mathcal{R}_b)(R_c - \mathcal{R}_c) \left[\frac{\Upsilon_{ab}\Upsilon_{ac}}{4} - 4\mathcal{C}_{ab}\mathcal{C}_{ac} - 2i\Upsilon_{ab}\mathcal{C}_{ac} \right] + \\ &+ \sum_b (R_b - \mathcal{R}_b)\left[-iQ_a\Upsilon_{ab} - 4Q_a\mathcal{C}_{ab} \right] - \frac{1}{2}\Upsilon_{aa} + 2i\mathcal{C}_{aa} - Q_a^2 \Bigg\} \psi(\vec{R})\end{aligned} \tag{D.77}$$

Then, the potential part is:

$$\langle \vec{R}|V|\psi\rangle = \frac{1}{2}\sum_{ab} \langle \frac{d^2V}{dR_a dR_b} \rangle \,(R_a - \mathcal{R}_a)(R_b - \mathcal{R}_b)\psi(\vec{R}) - \sum_a \langle f_a \rangle \,(R_a - \mathcal{R}_a)\psi(\vec{R}) \tag{D.78}$$

We wrote the right-hand side of Eq. (D.72). Now we need to compute the time derivative:

$$N(t) = \sqrt[4]{\frac{\det \boldsymbol{\Upsilon}(t)}{2\pi}}$$

$$\frac{d\psi}{dt} = \left\{ \sum_{ab} (R_a - \mathcal{R}_a)(R_b - \mathcal{R}_b) \left[-\frac{\dot{\Upsilon}_{ab}}{4} + i\dot{\mathcal{C}}_{ab} \right] + \frac{d\ln N}{dt} - i \sum_a Q_a \dot{\mathcal{R}}_a + \right.$$
$$\left. + \sum_a (R_a - \mathcal{R}_a) \left[i\dot{Q}_a + \frac{1}{2} \sum_b \Upsilon_{ab} \dot{\mathcal{R}}_b - 2i \sum_b \mathcal{C}_{ab} \dot{\mathcal{R}}_b \right] \right\} \psi(\vec{R}) \tag{D.79}$$

Now we can join all together. These equations must hold separately for real/imaginary part and we can exploit the polinomy equivalence theorem. Then all the coefficients of the power of $(R - \mathcal{R})$ must be the same. We have the following equations:

$$\begin{cases} -\sum_c \frac{1}{2m_c} \left[\frac{\Upsilon_{ac}\Upsilon_{cb}}{4} - 4\mathcal{C}_{ca}\mathcal{C}_{cb} \right] + \frac{1}{2} \langle \frac{d^2V}{dR_a dR_b} \rangle = -\dot{\mathcal{C}}_{ab} \\ 2 \sum_c \frac{1}{2m_c} \Upsilon_{ca}\mathcal{C}_{cb} = -\frac{\dot{\Upsilon}_{ab}}{4} \\ \sum_a \frac{2Q_a\mathcal{C}_{ab}}{m_a} - \langle f_b \rangle = -\dot{Q}_b + 2 \sum_a \mathcal{C}_{ab} \dot{\mathcal{R}}_a \\ \sum_b \frac{Q_b \Upsilon_{ab}}{2m_b} = \frac{1}{2} \sum_b \Upsilon_{ab} \dot{\mathcal{R}}_b \\ \sum_a \frac{\Upsilon_{aa} + 2Q_a^2}{4m_a} = \sum_a Q_a \dot{\mathcal{R}}_a \\ -\sum_a \frac{\mathcal{C}_{aa}}{m_a} = \frac{d\ln N}{dt} \end{cases} \tag{D.80}$$

From the fourth equation we get:

$$\dot{\mathcal{R}}_b = \frac{Q_b}{m_b} \tag{D.81}$$

That is consistent with our dynamical equation of SCHA.

It is easy to show that:

$$\sum_c \frac{\Upsilon_{ac}\Upsilon_{cb}}{m_c} = \sqrt{m_a m_b} \sum_{\mu\nu c} 4\omega_\mu \omega_\nu e^a_\mu e^c_\mu e^c_\nu e^b_\nu = 4\Phi_{ab} \tag{D.82}$$

Therefore the first equation is:

$$-\frac{\Phi_{ab}}{2} + 2\sum_c \frac{\mathcal{C}_{ca}\mathcal{C}_{cb}}{m_c} + \frac{1}{2} \langle \frac{d^2V}{dR_a dR_b} \rangle = -\dot{\mathcal{C}}_{ab} \tag{D.83}$$

$$\frac{1}{2} \left[\langle \frac{d^2V}{dR_a dR_b} \rangle - \Phi_{ab} \right] + 2\sum_c \frac{\mathcal{C}_{ca}\mathcal{C}_{cb}}{m_c} = -\dot{\mathcal{C}}_{ab} \tag{D.84}$$

$$\sum_{ab} \frac{1}{2} \frac{\partial \Upsilon^{-1}_{ab}}{\partial \Phi_{cd}} \left[\langle \frac{d^2V}{dR_a dR_b} \rangle - \Phi_{ab} \right] + 2\sum_{ab} \frac{\partial \Upsilon^{-1}_{ab}}{\partial \Phi_{cd}} \sum_k \frac{\mathcal{C}_{ka}\mathcal{C}_{kb}}{m_k} = -\sum_{ab} \frac{\partial \Upsilon^{-1}_{ab}}{\partial \Phi_{cd}} \dot{\mathcal{C}}_{ab} \tag{D.85}$$

The gradient can be easily recognized by the Bianco eq.[24] (A18b)

$$\frac{\partial \mathcal{F}}{\partial \Phi_{ab}} + 2\sum_{ab} \frac{\partial \Upsilon^{-1}_{ab}}{\partial \Phi_{cd}} \sum_{k} \frac{\mathcal{C}_{ka}\mathcal{C}_{kb}}{m_k} + \sum_{ab} \frac{\partial \Upsilon^{-1}_{ab}}{\partial \Phi_{cd}} \dot{\mathcal{C}}_{ab} = 0 \tag{D.86}$$

That is exactly the other equation of the motion.

We can take the second equation:

$$4\sum_{c} \frac{\Upsilon_{ca}\mathcal{C}_{cb}}{m_c} = -\dot{\Upsilon}_{ab} \tag{D.87}$$

$$4\sum_{ca} \Upsilon^{-1}{}_{ka}\Upsilon_{ac}\frac{\mathcal{C}_{cb}}{m_c} = -\sum_{a} \Upsilon^{-1}{}_{ka}\dot{\Upsilon}_{ab} \tag{D.88}$$

$$4\frac{\mathcal{C}_{kb}}{m_k} = -\sum_{a} \Upsilon^{-1}{}_{ka}\dot{\Upsilon}_{ab} \tag{D.89}$$

$$4\sum_{b} \Upsilon^{-1}{}_{ab}\frac{\mathcal{C}_{kb}}{m_k} = -\sum_{bh} \Upsilon^{-1}{}_{ab}\Upsilon^{-1}{}_{kh}\dot{\Upsilon}_{hb} \tag{D.90}$$

We can easily recognize that

$$\frac{d}{dt}\left(\Upsilon^{-1}{}_{ab}\right) = -\sum_{cd} \Upsilon^{-1}{}_{ac}\Upsilon^{-1}{}_{bd}\frac{d\Upsilon_{cd}}{dt} \tag{D.91}$$

From which we get the equation:

$$4\sum_{k} \frac{\Upsilon^{-1}_{ak}\mathcal{C}_{bk}}{m_b} = \frac{d}{dt}\left(\Upsilon^{-1}{}_{ab}\right) = \sum_{cd} \frac{\partial \Upsilon^{-1}_{ab}}{\partial \Phi_{cd}}\dot{\Phi}_{cd} \tag{D.92}$$

Let us take the third equation.

$$\sum_{a} \mathcal{C}_{ab}\left(\frac{2Q_a}{m_a} - 2\dot{\mathcal{R}}_a\right) = \langle f_b \rangle - \dot{Q}_b \tag{D.93}$$

Recognizing the Eq. (D.81) we get:

$$\dot{Q}_a = \langle f_a \rangle \tag{D.94}$$

We recollected all the equations of motion, it only remains to check that also the last two equations are satisfied. But this is trivially true, since they represent the constraint of a Gaussian wavepacket in the time evolution with the Eq. (D.72). From the fifth equation we get:

$$\sum_{a} \frac{\Upsilon_{aa}}{m_a} = \sum_{a} \frac{Q_a^2}{2m_a} \tag{D.95}$$

This is just a gauge choice, as if we add a static energy to the Hamiltonian (or a global phase to the trial wavefunction) will change. And from the last equation we get:

$$\frac{d\ln N}{dt} = \frac{d}{dt}\left(\frac{1}{4}\sum_{a} \ln \lambda_a\right) \tag{D.96}$$

where λ_a is the a-th eigenvalue of the $\boldsymbol{\Upsilon}$ matrix. Inside the parenthesis the trace of the matrix $\ln \boldsymbol{\Upsilon}$ is written.

$$\frac{d \ln N}{dt} = \frac{1}{4} \frac{d}{dt} \mathrm{Tr} \left[\ln \boldsymbol{\Upsilon} \right] \tag{D.97}$$

We can bring the derivative inside the trace

$$\frac{d \ln N}{dt} = \frac{1}{4} \mathrm{Tr} \left[\frac{d}{dt} \ln \boldsymbol{\Upsilon} \right] \tag{D.98}$$

We can perform the derivative

$$\frac{d \ln N}{dt} = \frac{1}{4} \mathrm{Tr} \left[\boldsymbol{\Upsilon}^{-1} \cdot \dot{\boldsymbol{\Upsilon}} \right] \tag{D.99}$$

We can now perform the trace:

$$\frac{d \ln N}{dt} = \frac{1}{4} \sum_{ab} {\Upsilon^{-1}}_{ab} \dot{\Upsilon}_{ba} \tag{D.100}$$

Putting all togheter we have:

$$- \sum_a \frac{\mathcal{C}_{aa}}{m_a} = \frac{1}{4} \sum_{ab} \Upsilon^{-1}_{ab} \dot{\Upsilon}_{ba} \tag{D.101}$$

If we substitute the Eq. (D.87) we get

$$- \sum_a \frac{\mathcal{C}_{aa}}{m_a} = -\frac{1}{4} \sum_{ab} \Upsilon^{-1}_{ab} \left(4 \sum_c \frac{\Upsilon_{cb} \mathcal{C}_{ca}}{m_c} \right) \tag{D.102}$$

That is trivially always satisfied.

D.6 Average over the perturbed ensemble

Now we compute the quantity:

$$\langle O \rangle_{\rho^{(1)}} = \sum_a \frac{\partial \langle O \rangle}{\partial \mathcal{R}_a} \mathcal{R}^{(1)}_a + \sum_{ab} \frac{\partial \langle O \rangle}{\partial \Phi_{ab}} \Phi^{(1)}_{ab} \tag{D.103}$$

We can use the SCHA relations[24]:

$$\frac{\partial \langle O \rangle}{\partial \mathcal{R}_a} = \langle \frac{\partial O}{\partial R_a} \rangle \tag{D.104}$$

$$\frac{\partial \langle O \rangle}{\partial \Phi_{ab}} = \frac{1}{2} \sum_{cd} \frac{\partial {\Upsilon^{-1}}_{cd}}{\partial \Phi_{ab}} \langle \frac{\partial^2 O}{\partial R_c \partial R_d} \rangle \tag{D.105}$$

$$\langle \frac{\partial O}{\partial R_a} \rangle = \sum_b \Upsilon_{ab} \langle u_b O \rangle \tag{D.106}$$

Indeed $\rho^{(1)}(t)$ can be computed:

$$\rho(\vec{R}) \propto \exp\left[-\frac{1}{2}\sum_{ab}\left(\Upsilon^{(0)}_{ab}+\Upsilon^{(1)}_{ab}\right)(R_a-\mathcal{R}^{(0)}_a-\mathcal{R}^{(1)}_a)(R_b-\mathcal{R}^{(0)}_b-\mathcal{R}^{(1)}_b)\right] \quad \text{(D.107)}$$

we can split this exponential:

$$\rho(\vec{R}) = \rho^{(0)}(\vec{R})\exp\left[-\frac{1}{2}\sum_{ab}\Upsilon^{(1)}_{ab}u_a u_b + \frac{1}{2}\sum_{ab}\Upsilon^{(0)}_{ab}\left(u_b\mathcal{R}^{(1)}_a + u_a\mathcal{R}^{(1)}_b\right)\right] \quad \text{(D.108)}$$

$$\rho(\vec{R}) = \rho^{(0)}(\vec{R})\left[1-\frac{1}{2}\sum_{ab}\Upsilon^{(1)}_{ab}u_a u_b + \frac{1}{2}\sum_{ab}\Upsilon^{(0)}_{ab}\left(u_b\mathcal{R}^{(1)}_a + u_a\mathcal{R}^{(1)}_b\right)\right] \quad \text{(D.109)}$$

From which it is trivial to obtain the perturbation term of the density matrix:

$$\rho^{(1)}(\vec{R},t) = \frac{1}{2}\rho^{(0)}(\vec{R})\sum_{ab}\left[\Upsilon^{(0)}_{ab}\left(u_a\mathcal{R}^{(1)}_b(t)+\mathcal{R}^{(1)}_a(t)u_b\right)-\Upsilon^{(1)}_{ab}(t)u_a u_b\right] \quad \text{(D.110)}$$

Then the average of an observable becomes:

$$\langle O(\vec{u})\rangle_{\rho^{(1)}(t)} = \frac{1}{2}\sum_{ab}\left[\Upsilon^{(0)}_{ab}\left(\langle Ou_a\rangle\,\mathcal{R}^{(1)}_b(t)+\mathcal{R}^{(1)}_a(t)\,\langle Ou_b\rangle\right)-\Upsilon^{(1)}_{ab}(t)\,\langle u_a O u_b\rangle\right] \quad \text{(D.111)}$$

We can recognize that the first term is a symmetric matrix Υ_{ab} multiplied with the symmetrized version of another matrix $\langle Ou_a\rangle\,\mathcal{R}^{(1)}_b$. Since an asymmetric matrix times a symmetric ones is always zero, we can add the asymmetric part of that matrix and simplify the expression:

$$\langle O(\vec{u})\rangle_{\rho^{(1)}} = \sum_{ab}\left[\Upsilon_{ab}\,\langle Ou_a\rangle\,\mathcal{R}^{(1)}_b - \frac{1}{2}\Upsilon^{(1)}_{ab}\,\langle u_a O u_b\rangle\right] \quad \text{(D.112)}$$

we can exploit the SCHA formalism in order to write them in a much better way:

$$\sum_b \Upsilon^{(0)}_{ab}\,\langle Ou_b\rangle = \langle\frac{\partial O}{\partial R_a}\rangle \quad \text{(D.113)}$$

Then the equation for the averages becomes:

$$\langle O\rangle_{\rho^{(1)}} = \sum_a \mathcal{R}^{(1)}_a(t)\,\langle\frac{\partial O}{\partial R_a}\rangle - \frac{1}{2}\sum_{ab}\Upsilon^{(1)}_{ab}\,\langle u_a O u_b\rangle \quad \text{(D.114)}$$

Then we can substitute

$$\begin{aligned}\dot{\mathcal{C}}^{(1)}_{hk} =& \frac{1}{2\hbar}\langle\frac{\partial f^{(1)}_k}{\partial R_h}\rangle_{\rho^{(0)}} + \frac{1}{2\hbar}\Phi^{(1)}_{hk} \\ &+ \frac{1}{2\hbar}\sum_{abc}\Upsilon_{ha}\Upsilon_{bc}\,\langle u_c u_a \delta f_k\rangle_{\rho^{(0)}}\,\mathcal{R}^{(1)}_b + \\ &- \frac{1}{4\hbar}\sum_{abc}\Upsilon_{ha}\Upsilon^{(1)}_{bc}\,\langle u_b u_c u_a \delta f_k\rangle\end{aligned}$$

Using the notation introduced in ref. [24] we recognize:

$$\overset{(3)}{\Phi}_{abc} = -\sum_{pq} \Upsilon_{ap}\Upsilon_{bq} \langle u_p u_q \delta f_c \rangle \tag{D.115}$$

$$\overset{(4)}{\Phi}_{abcd} = -\sum_{pqr} \Upsilon_{ap}\Upsilon_{bq}\Upsilon_{cr} \langle u_p u_q u_r \delta f_d \rangle \tag{D.116}$$

Then we can unwrap the $\Upsilon^{(1)}_{bc}$ with the following:

$$\sum_b \Upsilon_{ab}\Upsilon^{-1}_{bc} = \delta_{ac} \tag{D.117}$$

Applying the derivative we get:

$$\sum_b \left[\Upsilon^{(1)}_{ab}\Upsilon^{-1}_{bc} + \Upsilon_{ab}\Upsilon^{-1}{}^{(1)}_{bc} \right] = 0 \tag{D.118}$$

$$\sum_b \Upsilon^{(1)}_{ab} \underbrace{\sum_c \Upsilon^{-1}_{bc}\Upsilon_{cd}}_{\delta_{bd}} = -\sum_{bc} \Upsilon_{ab}\Upsilon^{-1}{}^{(1)}_{bc}\Upsilon_{cd} \tag{D.119}$$

$$\Upsilon^{(1)}_{ad} = -\sum_{bc} \Upsilon_{ab}\Upsilon_{cd}\Upsilon^{-1}{}^{(1)}_{bc} \tag{D.120}$$

We get

$$\dot{\mathcal{C}}^{(1)}_{hk} = \frac{1}{2\hbar}\left(\langle \frac{\partial f^{(1)}_k}{\partial R_h} \rangle_{\rho^{(0)}} + \Phi^{(1)}_{hk} \right) - \frac{1}{2\hbar}\sum_b \overset{(3)}{\Phi}_{hkb} \mathcal{R}^{(1)}_b - \frac{1}{4\hbar}\sum_{pq} \overset{(4)}{\Phi}_{hpqk} \Upsilon^{-1}{}^{(1)}_{pq} \tag{D.121}$$

The advantage of having the perturbation written in $\boldsymbol{\Upsilon}^{-1}$ instead of $\boldsymbol{\Upsilon}$ not only simplifies the expression allowing for the reconstruction of $\overset{(4)}{\Phi}$ but can also be expressed in terms of $\boldsymbol{\Phi}$:

$$\dot{\mathcal{C}}^{(1)}_{hk} = \frac{1}{2\hbar}\left(\langle \frac{\partial f^{(1)}_k}{\partial R_h} \rangle_{\rho^{(0)}} + \Phi^{(1)}_{hk} \right) - \frac{1}{2\hbar}\sum_b \overset{(3)}{\Phi}_{hkb} \mathcal{R}^{(1)}_b - \frac{1}{4\hbar}\sum_{pqcd} \overset{(4)}{\Phi}_{hpqk} \frac{\partial \Upsilon^{-1}{}_{pq}}{\partial \Phi_{cd}} \Phi^{(1)}_{cd} \tag{D.122}$$

$$\dot{\mathcal{C}}^{(1)}_{hk} = \frac{1}{2\hbar}\left[\langle \frac{\partial f^{(1)}_k}{\partial R_h} \rangle_{\rho^{(0)}} + \Phi^{(1)}_{hk} - \sum_b \overset{(3)}{\Phi}_{hkb} \mathcal{R}^{(1)}_b - \sum_{pqcd} \overset{(4)}{\Phi}_{hpqk} \Lambda^{cdpq} \Phi^{(1)}_{cd} \right] \tag{D.123}$$

In a very interesting way we can obtain the static limit of the equation when a constant electric field is applied to the system. The time derivative of the chirp is zero and we get:

$$\Phi^{(1)}_{hk} = \sum_b \overset{(3)}{\Phi}_{hkb} \mathcal{R}^{(1)}_b + \sum_{pqcd} \overset{(4)}{\Phi}_{hpqk} \Lambda^{cdpq} \Phi^{(1)}_{cd} \tag{D.124}$$

Then if we derive for the $\mathcal{R}$ vector we get:

$$\frac{\partial \Phi_{hk}}{\partial \mathcal{R}_a} = \overset{(3)}{\Phi}_{hka} + \sum_{pqcd} \overset{(4)}{\Phi}_{hpqk} \Lambda^{cdpq} \frac{\partial \Phi_{cd}}{\partial \mathcal{R}_a} \tag{D.125}$$

That coincides with the equation (A27) from ref. [24].

D.6.1 Final equation for the perturbated average

We can join all the equations of the previous section to provide the solution of the average of an observable over the perturbed ensemble.

$$\langle O\rangle_{\rho^{(1)}} = \sum_{ab} \Upsilon_{ab} \langle u_a O\rangle \mathcal{R}_b^{(1)} + \sum_{bcdpq} \Upsilon_{ac} \langle u_a u_b O\rangle \Upsilon_{bd} \Lambda^{pqcd} \Phi_{pq}^{(1)} - \langle O\rangle \sum_{abcd} \Lambda^{abcd} \Phi_{cd}^{(1)} \tag{D.126}$$

D.6.2 Perturbations in Φ

The last perturbation that remains to be taken into account to close the system is the $\Phi^{(1)}$ one.

Rewriting the Φ equation of motion we have.

$$\sum_{cd} \Lambda^{cdab} \dot{\Phi}_{cd} = \sum_{c} \frac{2\hbar}{m_a} \Upsilon_{bc}^{-1} \mathcal{C}_{ca} \tag{D.127}$$

Since in the unperturbed state $\dot{\mathbf{\Phi}}$ and $\boldsymbol{\mathcal{C}}$ are zero, the only first order terms that survive in perturbation theory are:

$$\sum_{cd} \Lambda^{cdab} \dot{\Phi}_{cd}^{(1)} = \sum_{c} \frac{2\hbar}{m_a} \Upsilon_{bc}^{-1} \mathcal{C}_{ca}^{(1)} \tag{D.128}$$

Now that we isolate the time dependence in $\dot{\mathbf{\Phi}}^{(1)}$ and $\boldsymbol{\mathcal{C}}^{(1)}$, it is possible to derive to couple this equation with the chirp:

$$\sum_{cd} \Lambda^{cdab} \ddot{\Phi}_{cd}^{(1)} = \sum_{c} \frac{2\hbar}{m_a} \Upsilon_{bc}^{-1} \dot{\mathcal{C}}_{ca}^{(1)} \tag{D.129}$$

Now we can substitute the $\dot{\boldsymbol{\mathcal{C}}}$ equation (D.123).

$$\begin{aligned}\sum_{cd} \Lambda^{cdab} \ddot{\Phi}_{cd}^{(1)} = -\sum_{c} \frac{2\hbar}{m_a} \Upsilon_{bc}^{-1} \frac{1}{2\hbar} \Big[&- \langle \frac{\partial f_c^{(1)}}{\partial R_a} \rangle_{\rho^{(0)}} - \Phi_{ca}^{(1)} + \\ &+ \sum_{h} \overset{(3)}{\Phi}_{cah} \mathcal{R}_h^{(1)} + \sum_{rstd} \overset{(4)}{\Phi}_{cars} \Lambda^{tdrs} \Phi_{td}^{(1)} \Big]\end{aligned} \tag{D.130}$$

$$\begin{aligned}\sum_{cd} \Lambda^{cdab} \ddot{\Phi}_{cd}^{(1)} = -\sum_{c} \frac{\Upsilon_{bc}^{-1}}{m_a} \Big[&- \langle \frac{\partial f_c^{(1)}}{\partial R_a} \rangle_{\rho^{(0)}} - \Phi_{ca}^{(1)} + \\ &+ \sum_{h} \overset{(3)}{\Phi}_{cah} \mathcal{R}_h^{(1)} + \sum_{rstd} \overset{(4)}{\Phi}_{cars} \Lambda^{tdrs} \Phi_{td}^{(1)} \Big]\end{aligned} \tag{D.131}$$

D.7 Link with the dynamical ansatz

Here we prove that the (4.30) is equivalent to the dynamical ansatz reported in ref. [24].

We can pass in matrix notation:

$$\left(\boldsymbol{A} - \omega^2 \boldsymbol{\Lambda}\right) \tilde{\boldsymbol{\Phi}}(\omega) = \boldsymbol{A} \left[\overset{(3)}{\boldsymbol{\Phi}} \vec{\mathcal{R}} + \overset{(4)}{\boldsymbol{\Phi}} \boldsymbol{\Lambda} \tilde{\boldsymbol{\Phi}}(\omega) \right] \tag{D.132}$$

$$\tilde{\boldsymbol{\Phi}}(\omega) = \left(\boldsymbol{A} - \omega^2 \boldsymbol{\Lambda}\right)^{-1} \boldsymbol{A} \left[\overset{(3)}{\boldsymbol{\Phi}} \vec{\mathcal{R}} + \overset{(4)}{\boldsymbol{\Phi}} \boldsymbol{\Lambda} \tilde{\boldsymbol{\Phi}}(\omega) \right] \tag{D.133}$$

$$\tilde{\boldsymbol{\Phi}}(\omega) = \left(\boldsymbol{A} - \omega^2 \boldsymbol{\Lambda}\right)^{-1} \boldsymbol{A} \overset{(3)}{\boldsymbol{\Phi}} \vec{\mathcal{R}} + \left(\boldsymbol{A} - \omega^2 \boldsymbol{\Lambda}\right)^{-1} \boldsymbol{A} \overset{(4)}{\boldsymbol{\Phi}} \boldsymbol{\Lambda} \tilde{\boldsymbol{\Phi}}(\omega) \tag{D.134}$$

Then the first equation becomes:

$$\sum_b \left(\frac{1}{m_a} \Phi_{ab} + \frac{1}{m_a} \sum_{pqcd} \overset{(3)}{\Phi}_{acd} \Lambda^{pqcd} \frac{\partial \tilde{\Phi}_{pq}}{\partial \tilde{\mathcal{R}}_b} - \omega^2 \delta_{ab} \right) \tilde{\mathcal{R}}_b = \frac{\mathcal{Z}_a E_a}{2m_a} \tag{D.135}$$

To symmetrize the problem with respect to the masses we can define the displacements in unit of mass, and divide the perturbation by the mass of the index:

$$\sum_b \left(\frac{\Phi_{ab}}{\sqrt{m_a m_b}} + \frac{1}{\sqrt{m_a m_b}} \sum_{pqcd} \overset{(3)}{\Phi}_{acd} \Lambda^{pqcd} \frac{\partial \tilde{\Phi}_{pq}}{\partial \tilde{\mathcal{R}}_b} - \omega^2 \delta_{ab} \sqrt{\frac{m_a}{m_b}} \right) \sqrt{m_b} \tilde{\mathcal{R}}_b = \frac{\mathcal{Z}_a E_a}{2\sqrt{m_a}} \tag{D.136}$$

The $\sqrt{\frac{m_a}{m_b}}$ that multiply the δ_{ab} is of course 1. Therefore we get:

$$\boldsymbol{G}^{-1}(\omega) \left(\sqrt{m} \tilde{\mathcal{R}} \right) = -\frac{\mathcal{Z} \vec{E}}{2\sqrt{m}} \tag{D.137}$$

Where $\boldsymbol{G}(\omega)$ is the dynamical Green function.

$$\boldsymbol{G}^{-1}(\omega) = \boldsymbol{I}\omega^2 - \boldsymbol{M}^{-\frac{1}{2}} \left[\boldsymbol{\Phi} + \overset{(3)}{\boldsymbol{\Phi}} \boldsymbol{\Lambda} \left(\boldsymbol{A} - \omega^2 \boldsymbol{\Lambda}\right)^{-1} \boldsymbol{A} \overset{(3)}{\boldsymbol{\Phi}} + \overset{(3)}{\boldsymbol{\Phi}} \boldsymbol{\Lambda} \boldsymbol{\Theta}(\omega) (\boldsymbol{A} - \omega^2 \boldsymbol{\Lambda})^{-1} \boldsymbol{A} \overset{(3)}{\boldsymbol{\Phi}} \right] \boldsymbol{M}^{-\frac{1}{2}} \tag{D.138}$$

where the $\boldsymbol{\Theta}$ tensor inverts the $\tilde{\boldsymbol{\Phi}}$ equation.

$$\boldsymbol{\Theta}(\omega) = \left(\boldsymbol{I} - (\boldsymbol{A} - \omega^2 \boldsymbol{\Lambda})^{-1} \boldsymbol{A} \overset{(4)}{\boldsymbol{\Phi}} \boldsymbol{\Lambda} \right)^{-1} \tag{D.139}$$

From which, if we define the self-energy as:

$$\boldsymbol{G}^{-1}(\omega) = \boldsymbol{G}^{(0)\,-1} - \boldsymbol{\Pi}(\omega) \tag{D.140}$$

The sscha unperturbed green function is:

$$\boldsymbol{G}^{(0)\,-1} = \boldsymbol{I}\omega^2 - \boldsymbol{D}^{(s)} = \boldsymbol{I}\omega^2 - \boldsymbol{M}^{-\frac{1}{2}} \boldsymbol{\Phi} \boldsymbol{M}^{-\frac{1}{2}} \tag{D.141}$$

From which we get the self-energy:

$$\boldsymbol{\Pi}(\omega) = \boldsymbol{\Pi}^{(B)}(\omega) + \boldsymbol{M}^{-\frac{1}{2}} \left[\overset{(3)}{\boldsymbol{\Phi}} \boldsymbol{\Lambda} \boldsymbol{\Theta}(\omega) (\boldsymbol{A} - \omega^2 \boldsymbol{\Lambda})^{-1} \boldsymbol{A} \overset{(3)}{\boldsymbol{\Phi}} \right] \boldsymbol{M}^{-\frac{1}{2}} \tag{D.142}$$

If anharmonicities are not too high, it is sufficient to evaluate the Bubble term:

$$\boldsymbol{\Pi}^{(B)}(\omega) = \boldsymbol{M}^{-\frac{1}{2}} \overset{(3)}{\boldsymbol{\Phi}} \boldsymbol{\Lambda} \left(\boldsymbol{A} - \omega^2 \boldsymbol{\Lambda} \right)^{-1} \boldsymbol{A} \overset{(3)}{\boldsymbol{\Phi}} \boldsymbol{M}^{-\frac{1}{2}} \tag{D.143}$$

This is equal to the Raffaello's expression if we are able to prove the relation:

$$\boldsymbol{\Lambda}(\omega) = \boldsymbol{\Lambda}(0) \left[\boldsymbol{A} - \omega^2 \boldsymbol{\Lambda}(0) \right]^{-1} \boldsymbol{A} \tag{D.144}$$

This equation must be taken with care, as in the whole discussion we neglected acoustic modes. They make it impossible to define the inverse, as the Kernel of the operators are not empty. However, we are not interested in the acoustic mode projection at gamma, therefore the inversion must be defined within the space without translations.

We can start proving the limit. As already shown, the static limit is correctly satisfied. We can try to prove the $\omega \to \infty$ limit, that is the strong off-resonant limit:

$$\lim_{\omega \to \infty} \boldsymbol{\Lambda}(\omega) = -\frac{1}{\omega^2} \boldsymbol{A} \tag{D.145}$$

We can resemble the $T = 0$ equation for $\boldsymbol{\Lambda}(\omega)$ as it is in the Raffaello's paper:

$$\Lambda_{abcd}(\omega) = -\sum_{\mu\nu} \frac{F(\omega, \omega_\mu, \omega_\nu)}{8\omega_\mu \omega_\nu} \frac{e^a_\mu e^b_\nu e^c_\mu e^d_\nu}{\sqrt{M_a M_b M_c M_d}} \tag{D.146}$$

where

$$F(\omega, \omega_\mu, \omega_\nu) = 2 \frac{(\omega_\mu + \omega_\nu)}{(\omega_\mu + \omega_\nu)^2 - \omega^2} \tag{D.147}$$

$$\lim_{\omega \to \infty} F(\omega, \omega_\mu, \omega_\nu) = -\frac{2(\omega_\mu + \omega_\nu)}{\omega^2} \tag{D.148}$$

$$\lim_{\omega \to \infty} \Lambda_{abcd}(\omega) = \frac{1}{\omega^2} \sum_{\mu\nu} \frac{\omega_\mu + \omega_\nu}{4\omega_\mu \omega_\nu} \frac{e^a_\mu e^b_\nu e^c_\mu e^d_\nu}{\sqrt{M_a M_b M_c M_d}} \tag{D.149}$$

Combining with eq. (D.145)

$$A^{abcd} = -\sum_{\mu\nu} \frac{\omega_\mu + \omega_\nu}{4\omega_\mu \omega_\nu} \frac{e^a_\mu e^b_\nu e^c_\mu e^d_\nu}{\sqrt{M_a M_b M_c M_d}} \tag{D.150}$$

If this is true, it is trivial to prove analytically equation (D.144). In fact the term:

$$\boldsymbol{A} - \omega^2 \boldsymbol{\Lambda}(0) \tag{D.151}$$

Can be explicited as

$$A^{abcd} - \omega^2 \Lambda^{abcd} = \sum_{\mu\nu} \left(-\frac{\omega_\mu + \omega_\nu}{4\omega_\mu \omega_\nu} + \frac{\omega^2}{4\omega_\mu \omega_\nu (\omega_\mu + \omega_\nu)} \right) \frac{e^a_\mu e^b_\nu e^c_\mu e^d_\nu}{\sqrt{m_a m_b m_c m_d}} \tag{D.152}$$

This can be inverted symbolically as:

$$\left[\boldsymbol{A} - \omega^2 \boldsymbol{\Lambda} \right]^{-1}_{abcd} = -\sum_{\mu\nu} \frac{4\omega_\mu \omega_\nu (\omega_\mu + \omega_\nu)}{(\omega_\mu + \omega_\nu)^2 - \omega^2} e^a_\mu e^b_\nu e^c_\mu e^d_\nu \sqrt{m_a m_b m_c m_d} \tag{D.153}$$

If we contract this supermatrix on the left with $\boldsymbol{\Lambda}$ and on the right with $\boldsymbol{A}$ we can exploit the fact that they are expressed in the opposite polarization/mass vectors, therefore they select the same $\mu\nu$ for all the matrices. Then we get the solution:

$$\left[\boldsymbol{\Lambda}\left(\boldsymbol{A}-\omega^2\boldsymbol{\Lambda}\right)^{-1}\boldsymbol{A}\right]_{abcd} = -\sum_{\mu\nu}\frac{1}{4\omega_\mu\omega_\nu}\frac{\omega_\mu+\omega_\nu}{(\omega_\mu+\omega_\nu)^2-\omega^2}\frac{e^a_\mu e^b_\nu e^c_\mu e^d_\nu}{\sqrt{m_a m_b m_c m_d}} \tag{D.154}$$

That is indeed $\boldsymbol{\Lambda}(\omega)$.

Therefore the final proof of the equivalence with the Raffaello's ansatz can be achieved by proving eq. (D.150)

Then let us check the $\boldsymbol{A}$ matrix. Lets rewrite equation (4.28).

$$A^{cdab} = -\frac{1}{2}\left[\frac{\delta_{ad}\Upsilon^{-1}_{bc}}{\sqrt{m_a m_d}}+\frac{\delta_{bc}\Upsilon^{-1}_{ad}}{\sqrt{m_b m_c}}\right] \tag{D.155}$$

$$-\frac{\delta_{ad}\Upsilon^{-1}_{bc}}{\sqrt{m_a m_d}} = -\sum_{\mu\nu}\frac{e^a_\mu e^d_\mu}{\sqrt{m_a m_d}}\frac{e^b_\nu e^c_\nu}{\sqrt{m_b m_c}}\frac{1}{2\omega_\nu} \tag{D.156}$$

$$A^{cdab} = -\frac{1}{2}\sum_{\mu\nu}\frac{e^a_\mu e^b_\nu e^c_\mu e^d_\nu}{\sqrt{m_a m_b m_c m_d}}\left[\frac{1}{2\omega_\mu}+\frac{1}{2\omega_\nu}\right] \tag{D.157}$$

$$A^{cdab} = -\sum_{\mu\nu}\frac{e^a_\mu e^b_\nu e^c_\mu e^d_\nu}{\sqrt{m_a m_b m_c m_d}}\frac{\omega_\mu+\omega_\nu}{4\omega_\nu\omega_\mu} \tag{D.158}$$

D.8 The Lanczos matrix

First of all we need to compute the matrix $\boldsymbol{\mathcal{L}}$ as a symmetric matrix. We first introduce the non symmetrix $\boldsymbol{\mathcal{L}}'$ matrix, that works in the $\sqrt{m}\vec{\mathcal{R}}$ and $\boldsymbol{D}$ variables, then we introduce a change of variables in which our system becomes symmetric and defines the $\boldsymbol{\mathcal{L}}$ matrix. We can rewrite the system in a more convenient case. From now on we use greek letters for indices of a matrix: $\Phi_{ab} = \Phi_\alpha$ while we use latin letters for vectors. Let us also define the D matrix as the dynamical matrix, i.e. the force constant matrix divided by the masses:

$$D_{ab} = \frac{\Phi_{ab}}{\sqrt{m_a m_b}} \qquad \overset{(3)}{D}_{abc} = \frac{\overset{(3)}{\Phi}_{abc}}{\sqrt{m_a m_b m_c}} \qquad \overset{(4)}{D}_{abcd} = \frac{\overset{(4)}{\Phi}_{abcd}}{\sqrt{m_a m_b m_c m_d}} \tag{D.159}$$

And, following the Raffaello notation, we can also redefine:

$$\chi_{\alpha\beta} = -2M_\alpha\Lambda^{\alpha\beta}M_\beta \qquad \chi_{abcd} = -2\sqrt{m_a m_b m_c m_d}\Lambda^{abcd} \tag{D.160}$$

And the new $\mathcal{A}$ matrix:

$$\mathcal{A}_{\alpha\beta} = M_\alpha A^{\alpha\beta}M_\beta \qquad \mathcal{A}_{abcd} = \sqrt{m_a m_b m_c m_d}A^{abcd} \tag{D.161}$$

Then the first equation reads as:

$$-\omega^2\sqrt{m_a}\tilde{\mathcal{R}}_a = v_a - \sum_b D_{ab}\sqrt{m_b}\tilde{\mathcal{R}}_b - \sum_{\alpha\beta}\overset{(3)}{D}_{a\alpha}\left(-\frac{1}{2}\chi_{\alpha\beta}\right)\tilde{D}_\beta \tag{D.162}$$

In the same way the second equation reads:

$$-\omega^2\tilde{D}_\alpha = \sum_{\beta\gamma}\left(-\frac{1}{2}\chi_{\alpha\beta}\right)^{-1}\mathcal{A}^{\beta\gamma}\left[-\tilde{D}_\gamma + \sum_a \overset{(3)}{D}_{\gamma a}\sqrt{m}_a\tilde{\mathcal{R}}_a + \sum_{\lambda\eta}\overset{(4)}{D}_{\gamma\eta}\left(-\frac{1}{2}\chi_{\eta\lambda}\right)\tilde{D}_\lambda\right] \tag{D.163}$$

$$-\omega^2\tilde{D}_\alpha = -2\sum_{\beta\gamma}\chi^{-1}_{\alpha\beta}\mathcal{A}^{\beta\gamma}\left[-\tilde{D}_\gamma + \sum_a \overset{(3)}{D}_{\gamma a}\sqrt{m}_a\tilde{\mathcal{R}}_a - \frac{1}{2}\sum_{\lambda\eta}\overset{(4)}{D}_{\gamma\eta}\chi_{\eta\lambda}\tilde{D}_\lambda\right] \tag{D.164}$$

Let us compute the matrix multiplication between χ and $\mathcal{A}$.

$$\mathcal{A}^{abcd} = -\sum_{\mu\nu} e^a_\mu e^b_\nu e^c_\mu e^d_\nu \frac{\omega_\mu + \omega_\nu}{4\omega_\nu\omega_\mu} \tag{D.165}$$

$$\chi^{-1}_{abcd} = \sum_{\mu\nu} e^a_\mu e^b_\nu e^c_\mu e^d_\nu 2\omega_\mu\omega_\nu(\omega_\mu + \omega_\nu) \tag{D.166}$$

Summing them together we get:

$$\sum_{cd}\chi^{-1}_{abcd}A^{cdef} = -\sum_{cd}\sum_{\mu\nu\eta\lambda} e^a_\mu e^b_\nu e^c_\mu e^d_\nu e^c_\lambda e^d_\eta e^e_\lambda e^f_\eta 2\omega_\mu\omega_\nu(\omega_\mu+\omega_\nu)\frac{\omega_\lambda+\omega_\eta}{4\omega_\lambda\omega_\eta} \tag{D.167}$$

The summation over cd gives us $\delta_{\lambda\mu}\delta_{\eta\nu}$

$$\sum_{cd}\chi^{-1}_{abcd}A^{cdef} = -\frac{1}{2}\sum_{cd}\sum_{\mu\nu} e^a_\mu e^b_\nu e^e_\mu e^f_\nu(\omega_\mu+\omega_\nu)^2 \tag{D.168}$$

We can define a new matrix $\mathcal{B}$ as:

$$\mathcal{B}_{abcd} = \frac{1}{2}\sum_{\mu\nu} e^a_\mu e^b_\nu e^c_\mu e^d_\nu(\omega_\mu+\omega_\nu)^2 \tag{D.169}$$

From this it is trivial to see that thee supermatrices $\mathcal{B}$, χ and $\mathcal{A}$ commute.

With this convention we have the second equation:

$$-\omega^2\tilde{D}_\alpha = 2\sum_\gamma \mathcal{B}^{\alpha\gamma}\left[-\tilde{D}_\gamma + \sum_a \overset{(3)}{D}_{\gamma a}\sqrt{m}_a\tilde{\mathcal{R}}_a - \frac{1}{2}\sum_{\lambda\eta}\overset{(4)}{D}_{\gamma\eta}\chi_{\eta\lambda}\tilde{D}_\lambda\right] \tag{D.170}$$

Now we can compute all the elements of the $\boldsymbol{\mathcal{L}}'$ matrix.

$$\mathcal{L}_{ab}{}' = D_{ab} \tag{D.171}$$

$$\mathcal{L}_{a\alpha}{}' = -\frac{1}{2}\sum_\beta \overset{(3)}{D}_{a\beta}\,\chi^{\beta\alpha} \tag{D.172}$$

$$\mathcal{L}_{\alpha a}{}' = -2\sum_\gamma \mathcal{B}^{\alpha\gamma}\overset{(3)}{D}_{\gamma a} \tag{D.173}$$

$$\mathcal{L}_{\alpha\beta}{}' = 2\mathcal{B}_{\alpha\beta} + \sum_{\gamma\delta}\mathcal{B}^{\alpha\gamma}\overset{(4)}{D}_{\gamma\delta}\,\chi^{\delta\beta} \tag{D.174}$$

This matrix is not symmetric so its inversion is not so easy. However the asymmetry is only with regards of the greek letter indices, i.e. the responce of the fluctuations. I can rewrite the Eq. D.170 as:

$$-\omega^2 \sum_{\alpha} \sqrt{\frac{\chi}{4\mathcal{B}}}_{\alpha\beta} \tilde{D}_\alpha = \sum_{\gamma} \sqrt{\chi\mathcal{B}}_{\beta\gamma} \left[-\tilde{D}_\gamma + \sum_a \overset{(3)}{D}_{\gamma a} \sqrt{m}_a \tilde{\mathcal{R}}_a - \sum_{\lambda\eta\delta} \overset{(4)}{D}_{\gamma\eta} \sqrt{\mathcal{B}\chi}_{\eta\lambda} \sqrt{\frac{\chi}{4\mathcal{B}}}_{\lambda\delta} \tilde{D}_\delta \right] \tag{D.175}$$

We can use the same trick on the other equation:

$$-\omega^2 \sqrt{m}_a \tilde{\mathcal{R}}_a = v_a - \sum_b D_{ab} \sqrt{m}_b \tilde{\mathcal{R}}_b + \frac{1}{2} \sum_{\alpha\beta\gamma} \overset{(3)}{D}_{a\alpha} \sqrt{4\chi\mathcal{B}}_{\alpha\beta} \sqrt{\frac{\chi}{4\mathcal{B}}}_{\beta\gamma} D_\gamma \tag{D.176}$$

With this trick we symmetrized the equation, now we can study the perturbation against $\sqrt{m}\tilde{\mathcal{R}}$ and $\sqrt{\frac{\chi}{4\mathcal{B}}}D$ Then the matrix of our inversion problem becomes:

$$\mathcal{L}_{ab} = D_{ab} \tag{D.177}$$

$$\mathcal{L}_{a\alpha} = -\sum_{\beta} \overset{(3)}{D}_{a\beta} \sqrt{\chi\mathcal{B}}_{\beta\alpha} \tag{D.178}$$

$$\mathcal{L}_{\alpha a} = -\sum_{\gamma} \sqrt{\chi\mathcal{B}}_{\alpha\gamma} \overset{(3)}{D}_{\gamma a} \tag{D.179}$$

$$\mathcal{L}_{\alpha\beta} = 2\mathcal{B}_{\alpha\beta} + \sum_{\gamma\lambda} \sqrt{\chi\mathcal{B}}_{\alpha\gamma} \overset{(4)}{D}_{\gamma\lambda} \sqrt{\mathcal{B}\chi}_{\lambda\beta} \tag{D.180}$$

As can be seen now the $\boldsymbol{\mathcal{L}}$ is a symmetric matrix, therefore we can use it to apply the Lanczos algorithm. For sake of completeness it can be noticed that $\sqrt{\chi\mathcal{B}} = \sqrt{-\mathcal{A}}$. This change of variables that brought the $\boldsymbol{\mathcal{L}}'$ matrix to be symmetric does not affect the perturbation or the responce vectors, as they are defined in the block $\sqrt{m}\mathcal{R}$.

D.9 Lanczos and the Static theory

To convince ourselves of what we are doing, we can invert the lanczos superoperator $\boldsymbol{\mathcal{L}}$ in a symbolic way. We can write the superoperator as matrix of matrices:

$$\boldsymbol{\mathcal{L}} = \begin{pmatrix} A & B \\ B^\dagger & C \end{pmatrix} \tag{D.181}$$

where A is a $N \times N$ matrix (N = number of modes in the supercell), B is a $N^2 \times N$. and C is a $N^2 \times N^2$ matrix. We are interested on the responce function of only in the upper left block of the matrix. Therefore we need to compute:

$$\boldsymbol{G}(\omega = 0) = \boldsymbol{\mathcal{L}}_{0,0}^{-1} \tag{D.182}$$

The free energy curvature is the inverse of the static green function:

$$D_{odd} = \left[\boldsymbol{\mathcal{L}}_{0,0}^{-\mathbf{1}} \right]^{-1} \tag{D.183}$$

Using the matrix theory we can write explicitly this inverse as a function of the A, B, C.

$$D_{odd} = A - BC^{-1}B^{\dagger} \tag{D.184}$$

Now we have:

$$A_{ab} = D_{ab} \qquad B_{a(bc)} = -\sum_{\beta} \overset{(3)}{D}_{a\beta} \sqrt{\chi\mathcal{B}}_{\beta(bc)} \tag{D.185}$$

$$C_{(ab)(cd)} = 2\mathcal{B}_{(ab)(cd)} + \sum_{\gamma\lambda} \sqrt{\chi\mathcal{B}}_{(ab)\gamma} \overset{(4)}{D}_{\gamma\lambda} \sqrt{\mathcal{B}\chi}_{\lambda(cd)} \tag{D.186}$$

$$C^{-1}_{(ab)(cd)} = \frac{1}{2}\sqrt{\mathcal{B}}^{-1} \left[1 + \sqrt{\frac{1}{2}\boldsymbol{\chi}} \overset{(4)}{D} \sqrt{\frac{1}{2}\boldsymbol{\chi}}\right]^{-1} \sqrt{\mathcal{B}}^{-1} \tag{D.187}$$

Let's recall the definition from the Bianco paper:

$$W = \sqrt{\frac{1}{2}\boldsymbol{\chi}} \tag{D.188}$$

from which we get the same equation as Bianco:

$$D_{odd} = D - \overset{(3)}{D} \sqrt{\boldsymbol{\chi}}\frac{1}{2} \left[1 + \sqrt{\frac{1}{2}\boldsymbol{\chi}} \overset{(4)}{D} \sqrt{\frac{1}{2}\boldsymbol{\chi}}\right]^{-1} \sqrt{\boldsymbol{\chi}} \overset{(3)}{D} \tag{D.189}$$

$$D_{odd} = D - \overset{(3)}{D} W \left[1 + W \overset{(4)}{D} W\right]^{-1} W \overset{(3)}{D} \tag{D.190}$$

From which we got the right limit.

D.9.1 Lanczos in the polarization basis

To further simplify the Lanczos procedure we can write it in the polarization basis:

$$\mathcal{L}'_{ab} = \delta_{ab}\omega_a\omega_b \tag{D.191}$$

$$\mathcal{L}'_{a(bc)} = -\frac{1}{2} \overset{(3)}{D}_{a(bc)} \sqrt{\frac{\omega_b + \omega_c}{\omega_b\omega_c}} \tag{D.192}$$

$$\mathcal{L}'_{(ab)(cd)} = \delta_{ac}\delta_{bd}(\omega_a + \omega_b)^2 + \frac{1}{4}\sqrt{\frac{(\omega_a + \omega_b)(\omega_c + \omega_d)}{\omega_a\omega_b\omega_c\omega_d}} \overset{(4)}{D}_{(ab)(cd)} \tag{D.193}$$

We can convert easily the third and fourth rank matrices in the polarization basis:

$$\overset{(4)}{D}_{abcd} = \sum_{uvwz} \frac{\overset{(4)}{\Phi}_{uvwz}}{\sqrt{m_u m_v m_w m_z}} e^u_a e^v_b e^w_c e^z_d \tag{D.194}$$

$$\overset{(4)}{D}_{abcd} = -\sum_{uvwz} \frac{\sum_{pqr} \Upsilon_{up}\Upsilon_{vq}\Upsilon_{wr} \langle u_p u_q u_r \delta f_z\rangle}{\sqrt{m_u m_v m_w m_z}} e^u_a e^v_b e^w_c e^z_d \tag{D.195}$$

$$\overset{(4)}{D}_{abcd} = -\sum_{uvwz} \frac{\sum_{pqr\mu\nu\eta} \sqrt{m_p m_q m_r} e^u_\mu e^p_\mu e^v_\nu e^q_\nu e^r_\eta e^w_\eta 8\omega_\mu\omega_\nu\omega_\eta \langle u_p u_q u_r \delta f_z\rangle}{\sqrt{m_z}} e^u_a e^v_b e^w_c e^z_d \tag{D.196}$$

$$\overset{(4)}{D}_{abcd} = -\sum_{z} \frac{\sum_{pqr} \sqrt{m_p m_q m_r} e^p_a e^q_b e^r_c 8\omega_a\omega_b\omega_c \langle u_p u_q u_r \delta f_z\rangle}{\sqrt{m_z}} e^z_d \tag{D.197}$$

To speedup the calculation of the $\overset{(4)}{D}$ matrix we can define the forces and displacements in the polarization basis.

$$X_a = \sum_v \sqrt{m_v} u_v e^v_a \qquad Y_a = \sum_v \frac{e^v_a}{\sqrt{m_v}} \delta f_v \tag{D.198}$$

From which we get the $\overset{(4)}{D}$ tensor:

$$\overset{(4)}{D}_{abcd} = -8\omega_a\omega_b\omega_c \langle X_a X_b X_c Y_d\rangle \tag{D.199}$$

In the same way the third order tensor can be calculated:

$$\overset{(3)}{D}_{abc} = -4\omega_a\omega_b \langle X_a X_b Y_c\rangle \tag{D.200}$$

D.9.2 Symmetries in the polarization basis

The Lanczos algorithm is very efficient only if the application of $\boldsymbol{\mathcal{L}}$ matrix to a vector scales as a scalar product. In other words, Lanczos is good only if the $\boldsymbol{\mathcal{L}}$ matrix is sparse, that means that most of its values are zero.

In principle, from equation (D.199), all the values of $\overset{(4)}{D}$ are different from zero and are needed to be computed. This is the most time consuming part. However, symmetries come in our help, as they allow us to set to zero some terms.

Let us first check how a symmetry is applied to the force constant matrix.

$$\Phi_{ab} = \sum_{cd} S_{ac} S_{bd} \Phi_{cd} \tag{D.201}$$

Here the S matrix is a $3N \times 3N$ unitary matrix that represents the symmetry of the crystal. We can write Φ in the polarization basis:

$$\Phi_{ab} = \sum_\mu \omega^2_\mu e^a_\mu e^b_\mu \sqrt{m_a m_b} = \sum_{\mu cd} \omega^2_\mu S_{ac} e^c_\mu \sqrt{m_c} S_{bd} e^d_\mu \sqrt{m_d} \tag{D.202}$$

We immediately see how the polarization vectors must change under the generic symmetry operation of the crystal: In absence of degeneracy the symmetry can at most change the sign of the polarization vector:

$$e^a_\mu \sqrt{m_a} = \pm \sum_b S_{ab} e^b_\mu \sqrt{m_b} \qquad \text{if } \omega_\mu \neq \omega_\nu \ \forall \nu \tag{D.203}$$

In presence of degeneracy, the symmetry can rotate the vector in the degenerate subspace:

$$\boldsymbol{S} e_\mu \sqrt{m} \in \text{Span}\left\{e_\nu \sqrt{m}\right\} \qquad \forall \nu \mid : \omega_\nu = \omega_\mu \tag{D.204}$$

Now we can apply this definition to the third order force constant:

$$\overset{(3)}{\Phi}_{abc} = \sum_{uvz} S_{au} S_{bv} S_{cz} \overset{(3)}{\Phi}_{uvz} \tag{D.205}$$

$$\overset{(3)}{\Phi}_{abc} = \sum_{\alpha\beta\gamma} \overset{(3)}{D}_{\alpha\beta\gamma} \, e^a_\alpha e^b_\beta e^c_\gamma \sqrt{m_a m_b m_c} = \sum_{\substack{uvz \\ \alpha\beta\gamma}} \overset{(3)}{D}_{\alpha\beta\gamma} \, S_{au} S_{bv} S_{cz} e^u_\alpha e^v_\beta e^z_\gamma \sqrt{m_u m_v m_z} \tag{D.206}$$

If we have no degenerate mode then each symmetry operation of the vector will at most change the sign. If we indicate with s_α the sign of the application of the S symmetry on the α polarization mode we have:

$$\sum_{\alpha\beta\gamma} \overset{(3)}{D}_{\alpha\beta\gamma} \, e^a_\alpha e^b_\beta e^c_\gamma \sqrt{m_a m_b m_c} = \sum_{\alpha\beta\gamma} \overset{(3)}{D}_{\alpha\beta\gamma} \, e^a_\alpha e^b_\beta e^c_\gamma \sqrt{m_a m_b m_c} s_\alpha s_\beta s_\gamma \tag{D.207}$$

Since all the vectors are independent the equality holds for each mode:

$$\overset{(3)}{D}_{\alpha\beta\gamma} = \overset{(3)}{D}_{\alpha\beta\gamma} \, s_\alpha s_\beta s_\gamma \tag{D.208}$$

$$\overset{(3)}{D}_{\alpha\beta\gamma} = 0 \qquad \text{if } s_\alpha s_\beta s_\gamma = -1 \tag{D.209}$$

So if we have no degeneracy, each symmetry operation would reduce by a factor 2 the number of non zero elements of the matrix. The same indeed holds for the fourth order tensor.

$$\overset{(4)}{D}_{\alpha\beta\gamma\delta} = 0 \qquad \text{if } s_\alpha s_\beta s_\gamma s_\delta = -1 \tag{D.210}$$

Let us now extend this behaviour in case of degeneracy: we can exploit the fact that the polarization vector is in the subspace of the degeneracy after the application of the S matrix.

$$\sum_b S_{ab} e^b_\mu \sqrt{m_b} = \sum_{\substack{\nu \\ \omega_\nu = \omega_\mu}} s_{\mu\nu} e^a_\nu \sqrt{m_a} \tag{D.211}$$

From which we get a direct expression for the $s_{\mu\nu}$ matrix:

$$s_{\mu\nu} = \sum_{ab} S_{ab} e^a_\mu e^b_\nu \sqrt{\frac{m_b}{m_a}} \tag{D.212}$$

$$\sum_{\alpha\beta\gamma} \overset{(3)}{D}_{\alpha\beta\gamma} \, e^a_\alpha e^b_\beta e^c_\gamma \sqrt{m_a m_b m_c} = \sum_{\alpha\beta\gamma} \sum_{\substack{\lambda\mu\nu \\ \omega_\lambda = \omega_\alpha \\ \omega_\mu = \omega_\beta \\ \omega_\nu = \omega_\gamma}} s_{\alpha\lambda} s_{\beta\mu} s_{\gamma\nu} e^a_\lambda e^b_\mu e^c_\nu \sqrt{m_a m_b m_c} \overset{(3)}{D}_{\alpha\beta\gamma} \tag{D.213}$$

We can exchage the greek letters in the right-hand side summations:

$$\overset{(3)}{D}_{\alpha\beta\gamma} = \sum_{\substack{\lambda\mu\nu \\ \omega_\lambda = \omega_\alpha \\ \omega_\mu = \omega_\beta \\ \omega_\nu = \omega_\gamma}} \overset{(3)}{D}_{\lambda\mu\nu} \, s_{\lambda\alpha} s_{\mu\beta} s_{\nu\gamma} \tag{D.214}$$

This trivially reduces to Eq. (D.209) in case of no degeneracy, and can be trivially extended to the fourth-order tensor:

$$\overset{(4)}{D}_{\alpha\beta\gamma\delta} = \sum_{\substack{\lambda\mu\nu\eta \\ \omega_\lambda = \omega_\alpha \\ \omega_\mu = \omega_\beta \\ \omega_\nu = \omega_\gamma \\ \omega_\eta = \omega_\delta}} \overset{(4)}{D}_{\lambda\mu\nu\delta} \; s_{\lambda\alpha} s_{\mu\beta} s_{\nu\gamma} s_{\eta\delta} \tag{D.215}$$

These equations for the symmetrization are much better than the original ones in real space, as the small s matrices are block diagonal in the space of modes. It, therefore, mixes very few elements of the original matrix, forcing some of the others to zero. Moreover, it could be possible to chose the polarization so that they diagonalize the $s_{\alpha\beta}$ matrices for a particular symmetry operation. In this case we will set to zero other elements.

D.9.3 Translational symmetries and momentum conservation

A very important consequence of the translational symmetry is the momentum conservation. If the $\overset{(3)}{D}$ or $\overset{(4)}{D}$ is written in momentum space, then we have:

$$\overset{(3)}{D}_{abc}(\vec{q}_1, \vec{q}_2, \vec{q}_3) \propto \delta(\vec{q}_1 + \vec{q}_2 + \vec{q}_3 + \vec{G}) \tag{D.216}$$

where $\vec{G}$ is a generic reciprocal lattice vector. This has an important consequence of reducing the number of indices by one of the $\overset{(3)}{D}$ or $\overset{(4)}{D}$ computation. Indeed, since we work on real polarization vector in real space, they violate the translational symmetry, so it is impossible to assign a specific $\vec{q}$ at a given polarization vector. However, we can always define the polarization vector in the supercell starting from the polarization vector in the momentum space as::

$$e_\mu^{a\,(1)} = \Re\left(e_{q\nu}^{\tilde{a}} e^{i\vec{q}\cdot\vec{R}_a}\right) \qquad e_\mu^{a\,(2)} = \Im\left(e_{q\nu}^{\tilde{a}} e^{i\vec{q}\cdot\vec{R}_a}\right) \tag{D.217}$$

Where $\tilde{a}$ is the unit cell atom-cartesian coordinate of a (supercell), $\vec{R}_a$ is the supercell lattice vector of the a coordinate:

$$\vec{r}_a = \vec{R}_a + \vec{\tau}_a$$

In this way, the supercell polarization vector e_μ^a is a linear combination of two q points: q and $-q$. This leads immediately to an approximate momentum conservation law:

$$\overset{(3)}{D}_{\alpha\beta\gamma} \propto \delta(\pm\vec{q}_\alpha \pm \vec{q}_\beta \pm \vec{q}_\gamma + \vec{G}) \tag{D.218}$$

A pure translational symmetry will act in the supercell exchanging the indices of equivalent atoms in different unit cells.

$$\sum_b S_{ab}^T R_b = R_a + T_a$$

Where T_a is the a coordinate of the unit cell translation identified by the S^T symmetry

So, if we apply such a symmetry to a vector defined according to Eq. (D.217) we get:

$$\sum_b S^T_{ab} e^b_\mu = \sum_b \Re\left(e^{\tilde{a}}_{q\nu} e^{i\vec{q}\cdot S^T_{ab}\vec{R}_b}\right) \tag{D.219}$$

This is again a vector of periodicity $\vec{q}$ but with a phase factor:

$$\sum_b S^T_{ab} e^b_\mu = \Re\left(e^{\tilde{a}}_{q\nu} e^{i\vec{q}\cdot\vec{R}_a + i\vec{q}\cdot\vec{T}_a}\right) \tag{D.220}$$

$$\sum_b S^T_{ab} e^b_\mu = \Re\left(e^{\tilde{a}}_{q\nu} e^{i\vec{q}\cdot\vec{R}_a}\right)\cos(\vec{q}\cdot\vec{T}_a) - \Im\left(e^{\tilde{a}}_{q\nu} e^{i\vec{q}\cdot\vec{R}_a}\right)\sin(\vec{q}\cdot\vec{T}_a) \tag{D.221}$$

$$\sum_b S^T_{ab} e^{b\,(1)}_\mu = e^{a\,(1)}_\mu \cos(\vec{q}\cdot\vec{T}_a) - e^{a\,(2)}_\mu \sin(\vec{q}\cdot\vec{T}_a) \tag{D.222}$$

$$\sum_b S^T_{ab} e^{b\,(2)}_\mu = e^{a\,(1)}_\mu \sin(\vec{q}\cdot\vec{T}_a) + e^{a\,(2)}_\mu \cos(\vec{q}\cdot\vec{T}_a) \tag{D.223}$$

The translational symmetry is a rotation in the polarization space defined by our two vectors. This also clearly shows that does not exist any real basis that allows to diagonalize the translations.

Lets apply the translational symmetry to the $\overset{(2)}{D}_{\alpha\beta\gamma}$, where now this is a 2x2 tensor (each α has two components)

$$\overset{(2)}{D}_{\alpha\beta} = \sum_{\alpha'\beta'} S_{\alpha\alpha'}(\vec{q}_\alpha\cdot\vec{T}) S_{\beta\beta'}(\vec{q}_\beta\cdot\vec{T})\ \overset{(2)}{D}_{\alpha'\beta'} \tag{D.224}$$

$$\begin{aligned}\overset{(2)}{D}_{\alpha\beta} =& \overset{(2)}{D}_{\alpha\beta}\cos(\phi_\alpha)\cos(\phi_\beta) + (-1)^{s_{\alpha'}}\sin(\phi_\alpha)\cos(\phi_\beta)\ \overset{(2)}{D}_{\alpha'\beta} + \\ &+ (-1)^{s_\beta}\cos(\phi_\alpha)\sin(\phi_\beta)\ \overset{(2)}{D}_{\alpha\beta'} + (-1)^{s_{\alpha'}+s_{\beta'}}\sin(\phi_\alpha)\sin(\phi_\beta)\ \overset{(2)}{D}_{\alpha'\beta'}\end{aligned}$$

This equation admits a non trivial (all zero) solution if, and only if, the system it defines has a zero determinant. The matrix of coefficients is:

$$A = \begin{pmatrix} 1-\cos(\phi_\alpha)\cos(\phi_\beta) & -\sin(\phi_\alpha)\cos(\phi_\beta) & -\cos(\phi_\alpha)\sin(\phi_\beta) & \sin(\phi_\alpha)\sin(\phi_\beta) \\ \sin(\phi_\alpha)\cos(\phi_\beta) & 1-\cos(\phi_\alpha)\cos(\phi_\beta) & -\sin(\phi_\alpha)\sin(\phi_\beta) & -\cos(\phi_\alpha)\sin(\phi_\beta) \\ \cos(\phi_\alpha)\sin(\phi_\beta) & -\sin(\phi_\alpha)\sin(\phi_\beta) & 1-\cos(\phi_\alpha)\cos(\phi_\beta) & -\sin(\phi_\alpha)\cos(\phi_\beta) \\ \sin(\phi_\alpha)\sin(\phi_\beta) & \cos(\phi_\alpha)\sin(\phi_\beta) & \sin(\phi_\alpha)\cos(\phi_\beta) & 1-\cos(\phi_\alpha)\cos(\phi_\beta) \end{pmatrix} \tag{D.225}$$

This ugly big matrix is the tensor product between two rotation matrices, so its calculation can be trivially extended for 3 or 4-rank tensors. To have a solution different from zero, we need to impose $\det A = 0$. This leads to:

$$4[1-\cos(\phi_\alpha+\phi_\beta)][1-\cos(\phi_\alpha-\phi_\beta)] = 0$$

whose solution is $\phi_\alpha = \pm\phi_\beta$

Indeed, one can extend this to a generic n-rank matrix. In the case of th 3-rank matrix the $\det A = 0$ equation is:

$$0 = [1 - \cos(\phi_\alpha + \phi_\beta + \phi_\gamma)][1 - \cos(\phi_\alpha + \phi_\beta - \phi_\gamma))]\cdot$$
$$\cdot [1 - \cos(\phi_\alpha - \phi_\beta + \phi_\gamma)][1 - \cos(\phi_\alpha - \phi_\beta - \phi_\gamma)]$$

That leads to the result:

$$\phi_\alpha = \pm\phi_\beta \pm \phi_\gamma \tag{D.226}$$

Since this must hold for all the possible translations, this condition on the angles leads to the condition of the $\vec{q}$ vectors:

$$\vec{q}_1 = \pm\vec{q}_2 \pm \vec{q}_3 + \vec{G} \tag{D.227}$$

From this calculation we learned a new interesting info about how the symmetries with a irreducible representation size bigger than one can lead to zero mixing between sub-spaces of degenerate modes, if the determinant of the tensor product between the symmetry in the polarization vectors minus the identity is different from zero.

Appendix E

Simulation parameters

In this appendix, I report all the parameters used for the simulations.

E.1 Data on ice

Here I discuss the simulation details of Figure 2.1. The BO landscape is approximated with DFT-PBE exchange correlation, with ultra-soft pseudo-potential, as implemented in Quantum ESPRESSO. The simulation is performed only at gamma for the vibrational properties, while electronic properties are computed on a K mesh 4x4x4, an offset of 0,0,1. The plane-wave basis set is trucated to 110 Ry for the wavefunctions and 1100 Ry for the electronic density. For the quasi-Harmonic calculation, harmonic dynamical matrices are computed using linear response theory. A K mesh of 6x6x6 is used with a cutoff of 180 Ry for the wavefunctions and 1800 Ry for the electronic density. The SSCHA stress tensor is computed with 40000 ab-initio configurations.

E.2 Data on hydrogen

All the simulations are performed using density functional theory (DFT). The exchange correlation functional is BLYP[50]. The pseudo-potential used for the hydrogen atoms is a norm conserving from Pseudo-Dojo library[74]. The basis set is plane-wave, with a cutoff of 60 Ry for the SSCHA relaxation and 80 Ry for the final energy calculation.

The phonon properties have been calculated on supercells of 96 atoms. To check the convergence, the harmonic part of the free energy is extrapolated to infinite volume. This resulted in a difference less than 1 meV per atom. To account for metalization in the distorted atomic configurations, we use a Marzari-Vanderbilt smearing of 0.03 Ry.

The program used to carry out the DFT simulations is Quantum Espresso[68] (versions 6.2.1 and 6.4).

The SSCHA minimization where carried out using 1000/4000 configurations per population (depending on the number of symmetries). The typical calculation requires about 20 populations to be converged with variable cell relaxation.

The final Lanczos algorithm to study structure stability as well as Raman and IR spectrum has been computed using from 10000 to 40000 configurations (depending on the pressure, configurations where increased doubling the size of the ensemble, starting from 5000 up to convergence).

The dielectric properties where averaged on many randomly displaced configurations. To achieve convergence, with the 432 atoms cell only 5 configurations where sufficient as they well represent the thermodynamic limit (in which 1 configuration is enough).

E.2.1 Properties of phase III

The parameters of the data reported in Figure 5.2. The static calculation are performed with a K mesh of 12x12x6 with a 1,1,1 offset, a cutoff of 80 Ry for the wavefunctions and 320 for the electronic density. The SSCHA calculations with variable cell are firstly performed on a 1x1x1 phonon mesh, then interpolated in a 2x2x1 mesh and relaxed with the variable cell algorithm. Each step is done with 4000 configurations. The DFT calculations for the SSCHA are done using a 4x4x4 K mesh on the 2x2x1 supercell, with 1,1,1 offset, and a cutoff of 60 Ry for the wavefunctions and 240 Ry for the electron density.

The parameters of Figure 5.3,5.4 are obtained using the Lnaczos algorithm. I truncated the iterations after 100 iterations, with the terminator averaged over the 5 last values of the a_n and b_n coefficients, and a smearing of $0.1\,\mathrm{cm}^{-1}$. The result is obtained including $\overset{(4)}{\mathbf{\Phi}}$. In Figure 5.3 both Raman and IR are obtained only considering polarized light along the x direction (parallel to the planes).

Figure 5.5 is obtained using the SSCHA static dynamical matrix in the 2x2x1 supercell, computing the IR spectra using the effective charges computed for 10 randomly distorted configurations. Effective charges are computed using linear response theory, as implemented in the PHonon package of quantum espresso.

The peak positions and widths reported in Figure 5.6,5.7,5.8 are computed as the highest peak in the dynamical Green function above $2500\,\mathrm{cm}^{-1}$ and the full width at half maximum.

The dielectric calculation in Figure 5.11,5.10, 5.9,5.12,5.17,5.16 and 5.15 are computed using displaced configurations in supercells of 2x2x1 (96 atoms) and 3x3x2 (432 atoms), with K meshes of 10x10x10 and 7x7x5 respectively and a random offset. The self-consistent calculation are computed using a Gaussian smearing of 0.03 Ry. The dielectric properties in the Eq. (5.2) are computed with the smearing of 0.1 eV and electronic temperature of 300 K. The dielectric function is averaged over 5 configurations.

E.2.2 The phase diagram

The phase diagrams of Figure 6.10,Figure 6.11, Figure 6.12, and Figure 6.14 are obtained using a plane-wave cutoff of 80 Ry and 320 Ry for the density. The details of the K mesh used for all the structures are reported in Table E.1.

The data of Figure 6.13 are obtained using the Lanczos static algorithm including the $\overset{(4)}{\mathbf{\Phi}}$. 40000, 20000 and 10000 configurations are used to converge 250 GPa, 350 GPa

Structure	N atm/cell	Ks static	Qs SSCHA	Ks SSCHA	offset
C2/c-24	24	12x12x6	2x2x1	6x6x6	1,1,1
P62/c-24	24	12x12x6	2x2x1	6x6x6	1,1,1
Ibam-8	16	12x18x6	2x3x1	6x6x6	1,1,1
Cmca-12	12	12x12x12	2x2x2	6x6x6	1,1,1
Pc-48	48	12x6x6	2x1x1	6x6x6	1,1,1
P2/c-48	48	12x6x6	2x1x1	6x6x6	1,1,1
C2/c-16	16	6x24x12	1x3x2	6x6x6	1,1,1
Cs-IV	2	32x32x32	3x3x3	16x16x16	1,1,1

Table E.1. The K meshes (electrons) and Q meshes (phonon) used for the static and the SSCHA phase diagrams.

and 450 GPa respectively. Neither the terminator nor the smearing are used. The forces of the ab-initio configurations are computed using cutoffs of 60 Ry for the wave-function and 240 Ry for the electron density and a K mesh of 4x4x4 with 1,1,1 as offset.

The dielectric properties discussed in Figure 6.16,6.15,6.18, and 6.17 are computed with the same parameters as the C2/c-24 discussed in E.2.1. For the Cmca-12, the K mesh used in the 2x2x2 and 3x3x3 phonon supercell are, respectively, 10x10x10 and 7x7x7.

Appendix F

Dielectric function

The dielectric function can be computed directly as the from the response function when we apply an external electric field:

$$\varepsilon(\omega) = 1 + 4\pi\chi(\omega)$$

The energy depends on the external electric field as:

$$V_{ext} = e\vec{r}\cdot\vec{E}$$

Therefore the response function can be computed using the Kubo formula:

$$\chi_{\alpha\beta}(t) = e^2 \left\langle [r_\alpha(t), r_\beta(0)] \right\rangle \theta(t) \tag{F.1}$$

Now, $\vec{r}$ behaves very badly in a system with periodic boundary conditions, therefore we use a trick to rewrite it:

$$[\vec{r}, H]\,|hm\rangle = \frac{\vec{p}}{m}\,|hm\rangle \tag{F.2}$$

$$\vec{r}|hm\rangle = (\varepsilon_{hm} - H)^{-1}\,\frac{\vec{p}}{m}\,|hm\rangle \tag{F.3}$$

Now we can write the operator using the second quantization formalism:

$$\vec{r} \Longrightarrow \frac{1}{m}\frac{1}{\sqrt{N_k\Omega}} \sum_{\substack{hm \\ kn\neq hm}} \frac{\langle kn|\vec{p}|hm\rangle}{\varepsilon_{hm} - \varepsilon_{kn}} c^\dagger_{kn} c_{hm} \tag{F.4}$$

From which we have the correlation function.

$$\chi_{\alpha\beta}(t) = \frac{e^2}{m^2 N_k\Omega} \sum_{\substack{hkmn \\ h'k'm'n'}} \frac{\langle hm|p_\alpha|kn\rangle \langle h'm'|p_\beta|k'n'\rangle}{(\varepsilon_{hm} - \varepsilon_{kn})(\varepsilon_{h'm'} - \varepsilon_{k'n'})} \left\langle [c^\dagger_{hm}(t)c_{kn}(t), c^\dagger_{h'm'}c_{k'n'}] \right\rangle \theta(t) \tag{F.5}$$

Since we are studying a system of non interacting fermions, the t evolution can be explicated:

$$c^\dagger_{hm}(t)c_{kn}(t) = e^{-i(\varepsilon_{kn} - \varepsilon_{hm})t} c^\dagger_{hm} c_{kn} \tag{F.6}$$

The commutator in Eq. F.5 is non zero only if:

$$h'm' = kn \qquad k'n' = hm$$

Therefore we can eliminate the summation over the primate indices.

$$\chi_{\alpha\beta}(t) = -\frac{e^2}{m^2 N_k \Omega} \sum_{hkmn} \frac{\langle hm|p_\alpha|kn\rangle \langle kn|p_\beta|hm\rangle}{(\varepsilon_{hm} - \varepsilon_{kn})^2} \langle [c^\dagger_{hm} c_{kn}, c^\dagger_{kn} c_{hm}]\rangle \, e^{-i(\varepsilon_{kn} - \varepsilon_{hm})t} \theta(t) \tag{F.7}$$

Now we can compute explicitly the commutator:

$$\langle [c^\dagger_{hm} c_{kn}, c^\dagger_{kn} c_{hm}]\rangle = \langle c^\dagger_{hm} c_{kn} c^\dagger_{kn} c_{hm}\rangle - \langle c^\dagger_{kn} c_{hm} c^\dagger_{hm} c_{kn}\rangle \tag{F.8}$$

To compute these thermal averages we need to consider all the possible states. Here we have two fermionic states hm and kn; they can be either 0 or 1. We recall that:

$$\langle O\rangle = \frac{\mathrm{Tr}\left[e^{-\beta H} O\right]}{\mathrm{Tr}\left[e^{-\beta H}\right]}$$

The energies are:

$$|00\rangle \qquad e^{-\beta\varepsilon_{hm}}|10\rangle \qquad e^{-\beta\varepsilon_{kn}}|01\rangle \qquad e^{-\beta(\varepsilon_{kn}+\varepsilon_{hm})}|11\rangle$$

Thus the trace over $e^{-\beta H}$ on these states is:

$$1 + e^{-\beta\varepsilon_{hm}} + e^{-\beta\varepsilon_{kn}} + e^{-\beta(\varepsilon_{kn}+\varepsilon_{hm})} = (1 + e^{-\beta\varepsilon_{hm}})(1 + e^{-\beta\varepsilon_{kn}})$$

The creation and annihilation operators select only one state, with coefficient 1 in both cases. The first one of Eq. (F.8) selects a state with $|hm = 1, kn = 0\rangle$ where $e^{-\beta H}$ acts as $e^{-\beta\varepsilon_{hm}}$ while the second one selects the state with $|hm = 0, kn = 1\rangle$ with energy $e^{-\beta\varepsilon_{kn}}$. Thus we get:

$$\langle [c^\dagger_{hm} c_{kn}, c^\dagger_{kn} c_{hm}]\rangle = \frac{e^{-\beta\varepsilon_{hm}}}{(1 + e^{-\beta\varepsilon_{hm}})(1 + e^{-\beta\varepsilon_{kn}})} - \frac{e^{-\beta\varepsilon_{kn}}}{(1 + e^{-\beta\varepsilon_{hm}})(1 + e^{-\beta\varepsilon_{kn}})} \tag{F.9}$$

Defining the Fermi function as:

$$f(x) = \frac{1}{e^{\beta x} + 1}$$

we can rewrite the average.

$$\langle [c^\dagger_{hm} c_{kn}, c^\dagger_{kn} c_{hm}]\rangle = [1 - f(\xi_{kn})] f(\xi_{hm}) - [1 - f(\xi_{hm})] f(\xi_{kn}) = f(\xi_{hm}) - f(\xi_{kn}) \tag{F.10}$$

In frequency domain:

$$\chi_{\alpha\beta}(\omega) = -i\frac{e^2}{m^2 N_k \Omega} \sum_{hkmn} \frac{\langle hm|p_\alpha|kn\rangle \langle kn|p_\beta|hm\rangle}{(\varepsilon_{hm} - \varepsilon_{kn})^2} \int_0^\infty e^{-i(\varepsilon_{kn} - \varepsilon_{hm} - \omega)t} \left[f(\xi_{hm}) - f(\xi_{kn})\right] \tag{F.11}$$

$$\chi_{\alpha\beta}(\omega) = \frac{e^2}{m^2 N_k \Omega} \sum_{hkmn}^{hm \neq kn} \frac{\langle hm|p_\alpha|kn\rangle \langle kn|p_\beta|hm\rangle}{(\varepsilon_{hm} - \varepsilon_{kn})^2} \frac{f(\xi_{hm}) - f(\xi_{kn})}{\varepsilon_{kn} - \varepsilon_{hm} - \omega - i0^+} \tag{F.12}$$

This is the standard expression for the interband susceptibility tensor. We can manipulate it a bit. First of all, the $\vec{p}$ operator is diagonal in the block space. This selects only vertical transitions with $k = h$.

$$\chi_{\alpha\beta}(\omega) = \frac{e^2}{m^2 N_k \Omega} \sum_{kmn}^{m\neq n} \frac{\langle km|p_\alpha|kn\rangle \langle kn|p_\beta|km\rangle}{(\varepsilon_{km} - \varepsilon_{kn})^2} \frac{f(\xi_{km}) - f(\xi_{kn})}{\varepsilon_{kn} - \varepsilon_{km} - \omega - i0^+} \tag{F.13}$$

This equation suffers a problem if we have spaghetti like bands. In such cases it is difficult to distinguish between interband and intraband transition and the denominator diverges when two states are very close in energy. However, this divergence disappears if we have a finite frequency. To spotlight on this, we must rearrange terms in the summation. For brevity, we define:

$$f_{mn} = f(\xi_{km}) - f(\xi_{kn}) \qquad \varepsilon_{mn} = \varepsilon_{km} - \varepsilon_{kn}$$
$$z = \omega + i0^+$$

Then we have

$$\chi_{\alpha\beta}(z) = -\frac{e^2}{m^2 N_k \Omega} \sum_{kmn}^{m\neq n} \frac{f_{mn}}{\varepsilon_{mn}} \frac{\langle km|p_\alpha|kn\rangle \langle kn|p_\beta|km\rangle}{\varepsilon_{mn}} \frac{1}{\varepsilon_{mn} + z} \tag{F.14}$$

This summation acts twice, as we have both $m > n$ and $n > m$. The matrix elements are the same, as the $\vec{p}$ operator is Hermitian, while the $f_{mn}/\varepsilon_{mn}^2$ changes the sign. Therefore we can restrict the summation only when $n > m$:

$$\chi_{\alpha\beta}(z) = -\frac{e^2}{m^2 N_k \Omega} \sum_{kmn}^{n>m} \frac{f_{mn}}{\varepsilon_{mn}} \frac{\langle km|p_\alpha|kn\rangle \langle kn|p_\beta|km\rangle}{\varepsilon_{mn}} \left[\frac{1}{\varepsilon_{mn} + z} - \frac{1}{\varepsilon_{nm} + z}\right] \tag{F.15}$$

$$\begin{aligned} \frac{1}{\varepsilon_{mn} + z} - \frac{1}{\varepsilon_{nm} + z} &= \frac{1}{\varepsilon_{mn} + z} + \frac{1}{\varepsilon_{mn} - z} \\ &= \frac{2\varepsilon_{mn}}{\varepsilon_{mn}^2 - z^2} \end{aligned} \tag{F.16}$$

From which we can substitute back in the original formula.

$$\chi_{\alpha\beta}(z) = -2\frac{e^2}{m^2 N_k \Omega} \sum_{kmn}^{n>m} \frac{f_{mn}}{\varepsilon_{mn}} \frac{\langle km|p_\alpha|kn\rangle \langle kn|p_\beta|km\rangle}{\varepsilon_{mn}^2 - z^2} \tag{F.17}$$

Now this equation does not diverge if $\varepsilon_{mn} \to 0$. if $z \neq 0$. This means that we can now even insert intraband transition with $m = n$ if we allow z to have an imaginary part.

This expression is very convenient as it unifies the inter-band and intra-band transition. In disordered systems, or systems where phonon are present, these transition are not very well defined, Brilluine zone is refolded and many bands overlaps. In a metal, this means that many transition within the same band are possible, where ε_{mn} is small. Indeed, here a factor 2 from the spin multiplicity is missing. Therefore the last equation is:

$$\chi_{\alpha\beta}(z) = -4\frac{e^2}{m^2 N_k \Omega} \sum_{kmn}^{n\geq m} \frac{f(\xi_{km}) - f(\xi_{hm})}{\xi_{km} - \xi_{hn}} \frac{\langle km|p_\alpha|kn\rangle \langle kn|p_\beta|km\rangle}{(\varepsilon_{km} - \varepsilon_{kn})^2 - z^2} \tag{F.18}$$

Bibliography

[1] V. L. Ginzburg, "Nobel lecture: On superconductivity and superfluidity (what i have and have not managed to do) as well as on the "physical minimum" at the beginning of the xxi century," *Rev. Mod. Phys.*, vol. 76, pp. 981–998, Dec 2004.

[2] R. Dias, O. Noked, and I. F. Silvera, "New low temperature phase in dense hydrogen: The phase diagram to 421 gpa," *arXiv preprint arXiv:1603.02162*, 2016.

[3] R. P. Dias and I. F. Silvera, "Observation of the wigner-huntington transition to metallic hydrogen," *Science*, vol. 355, pp. 715–718, jan 2017.

[4] M. I. Eremets, A. P. Drozdov, P. P. Kong, and H. Wang, "Semimetallic molecular hydrogen at pressure above 350 GPa," *Nature Physics*, sep 2019.

[5] P. Loubeyre, F. Occelli, and P. Dumas, "Observation of a first order phase transition to metal hydrogen near 425 gpa," *arXiv preprint arXiv:1906.05634*, 2019.

[6] E. Wigner and H. B. Huntington, "On the possibility of a metallic modification of hydrogen," *The Journal of Chemical Physics*, vol. 3, pp. 764–770, dec 1935.

[7] N. W. Ashcroft, "Metallic hydrogen: A high-temperature superconductor?," *Phys. Rev. Lett.*, vol. 21, pp. 1748–1749, Dec 1968.

[8] S. T. Weir, A. C. Mitchell, and W. J. Nellis, "Metallization of fluid molecular hydrogen at 140 gpa (1.4 mbar)," *Phys. Rev. Lett.*, vol. 76, pp. 1860–1863, Mar 1996.

[9] A. P. Drozdov, M. I. Eremets, I. A. Troyan, V. Ksenofontov, and S. I. Shylin, "Conventional superconductivity at 203 kelvin at high pressures in the sulfur hydride system," *Nature*, vol. 525, pp. 73–76, aug 2015.

[10] P. Kong, V. Minkov, M. Kuzovnikov, S. Besedin, A. Drozdov, S. Mozaffari, L. Balicas, F. Balakirev, V. Prakapenka, E. Greenberg, *et al.*, "Superconductivity up to 243 k in yttrium hydrides under high pressure," *arXiv preprint arXiv:1909.10482*, 2019.

[11] P. Dalladay-Simpson, R. T. Howie, and E. Gregoryanz, "Evidence for a new phase of dense hydrogen above 325 gigapascals," *Nature*, vol. 529, pp. 63–67, jan 2016.

[12] M. Eremets, I. Troyan, and A. Drozdov, "Low temperature phase diagram of hydrogen at pressures up to 380 gpa. a possible metallic phase at 360 gpa and 200 k," *arXiv preprint arXiv:1601.04479*, 2016.

[13] M. I. Eremets and A. P. Drozdov, "Comments on the claimed observation of the Wigner-Huntington Transition to Metallic Hydrogen," *ArXiv e-prints*, Feb. 2017.

[14] P. Loubeyre, F. Occelli, and P. Dumas, "Comment on: Observation of the Wigner-Huntington transition to metallic hydrogen," *ArXiv e-prints*, Feb. 2017.

[15] A. F. Goncharov and V. V. Struzhkin, "Comment on "observation of the wigner-huntington transition to metallic hydrogen"," *Science*, vol. 357, no. 6353, 2017.

[16] C. J. Pickard and R. J. Needs, "Structure of phase III of solid hydrogen," *Nature Physics*, vol. 3, pp. 473–476, may 2007.

[17] C. J. Pickard, M. Martinez-Canales, and R. J. Needs, "Density functional theory study of phase iv of solid hydrogen," *Phys. Rev. B*, vol. 85, p. 214114, Jun 2012.

[18] J. Kohanoff, S. Scandolo, G. L. Chiarotti, and E. Tosatti, "Solid molecular hydrogen: The broken symmetry phase," *Physical Review Letters*, vol. 78, pp. 2783–2786, apr 1997.

[19] R. T. Howie, C. L. Guillaume, T. Scheler, A. F. Goncharov, and E. Gregoryanz, "Mixed molecular and atomic phase of dense hydrogen," *Physical Review Letters*, vol. 108, mar 2012.

[20] B. Monserrat, N. D. Drummond, P. Dalladay-Simpson, R. T. Howie, P. L. Ríos, E. Gregoryanz, C. J. Pickard, and R. J. Needs, "Structure and metallicity of phase v of hydrogen," *Physical Review Letters*, vol. 120, jun 2018.

[21] B. Monserrat, N. D. Drummond, and R. J. Needs, "Anharmonic vibrational properties in periodic systems: energy, electron-phonon coupling, and stress," *Phys. Rev. B*, vol. 87, p. 144302, Apr 2013.

[22] I. Errea, M. Calandra, and F. Mauri, "Anharmonic free energies and phonon dispersions from the stochastic self-consistent harmonic approximation: Application to platinum and palladium hydrides," *Physical Review B*, vol. 89, feb 2014.

[23] I. Errea, M. Calandra, C. J. Pickard, J. Nelson, R. J. Needs, Y. Li, H. Liu, Y. Zhang, Y. Ma, and F. Mauri, "High-pressure hydrogen sulfide from first principles: A strongly anharmonic phonon-mediated superconductor," *Physical Review Letters*, vol. 114, apr 2015.

[24] R. Bianco, I. Errea, L. Paulatto, M. Calandra, and F. Mauri, "Second-order structural phase transitions, free energy curvature, and temperature-dependent anharmonic phonons in the self-consistent harmonic approximation: Theory and stochastic implementation," *Physical Review B*, vol. 96, jul 2017.

[25] L. Monacelli, I. Errea, M. Calandra, and F. Mauri, "Pressure and stress tensor of complex anharmonic crystals within the stochastic self-consistent harmonic approximation," *Phys. Rev. B*, vol. 98, p. 024106, Jul 2018.

[26] W. H. Press, *Numerical recipes 3rd edition: The art of scientific computing*. Cambridge university press, 2007.

[27] S. Baroni, P. Giannozzi, and E. Isaev, "Density-functional perturbation theory for quasi-harmonic calculations," *Reviews in Mineralogy and Geochemistry*, vol. 71, pp. 39–57, jan 2010.

[28] I. Errea, F. Belli, L. Monacelli, A. Sanna, T. Koretsune, T. Tadano, R. Bianco, M. Calandra, R. Arita, F. Mauri, *et al.*, "Quantum crystal structure in the 250 k superconducting lanthanum hydride," *arXiv preprint arXiv:1907.11916*, 2019.

[29] T. Tadano and S. Tsuneyuki, "Self-consistent phonon calculations of lattice dynamical properties in cubic $SrTiO_3$ with first-principles anharmonic force constants," *Phys. Rev. B*, vol. 92, p. 054301, Aug 2015.

[30] A. Kong, J. S. Liu, and W. H. Wong, "Sequential imputations and bayesian missing data problems," *Journal of the American Statistical Association*, vol. 89, pp. 278–288, mar 1994.

[31] W. H. Press, *Numerical Recipes: The Art of Scientific Computing, Third Edition*. Cambridge University Press, 3 ed., 2017.

[32] U. Aseginolaza, R. Bianco, L. Monacelli, L. Paulatto, M. Calandra, F. Mauri, A. Bergara, and I. Errea, "Phonon collapse and second-order phase transition in thermoelectric SnSe," *Physical Review Letters*, vol. 122, feb 2019.

[33] U. Aseginolaza, R. Bianco, L. Monacelli, L. Paulatto, M. Calandra, F. Mauri, A. Bergara, and I. Errea, "Strong anharmonicity and high thermoelectric efficiency in high temperature sns from first-principles," *arXiv preprint arXiv:1906.02047*, 2019.

[34] I. J. Onuorah, P. Bonfà, R. D. Renzi, L. Monacelli, F. Mauri, M. Calandra, and I. Errea, "Quantum effects in muon spin spectroscopy within the stochastic self-consistent harmonic approximation," *Physical Review Materials*, vol. 3, jul 2019.

[35] R. Bianco, I. Errea, L. Monacelli, M. Calandra, and F. Mauri, "Quantum enhancement of charge density wave in NbS2 in the two-dimensional limit," *Nano Letters*, vol. 19, pp. 3098–3103, apr 2019.

[36] J. S. Zhou, L. Monacelli, R. Bianco, I. Errea, F. Mauri, and M. Calandra, "Anharmonic melting of the charge density wave in single-layer tise2," *arXiv preprint arXiv:1910.12709*, 2019.

[37] A. D. Fortes, "Accurate and precise lattice parameters of H_2O and D_2O ice I*h* between 1.6 and 270K from high-resolution time-of-flight neutron powder diffraction data," *Acta Crystallographica Section B*, vol. 74, pp. 196–216, Apr 2018.

[38] M. K. Gupta, R. Mittal, B. Singh, S. K. Mishra, D. T. Adroja, A. D. Fortes, and S. L. Chaplot, "Phonons and anomalous thermal expansion behavior of h2o and d2o ice ih," *Physical Review B*, vol. 98, Sept. 2018.

[39] L. Monacelli, G. Batignani, G. Fumero, C. Ferrante, S. Mukamel, and T. Scopigno, "Manipulating impulsive stimulated raman spectroscopy with a chirped probe pulse," *The Journal of Physical Chemistry Letters*, vol. 8, pp. 966–974, feb 2017.

[40] C. Schnedermann, V. Muders, D. Ehrenberg, R. Schlesinger, P. Kukura, and J. Heberle, "Vibronic dynamics of the ultrafast all- trans to 13- cis photoisomerization of retinal in channelrhodopsin-1," *J. Am. Chem. Soc.*, vol. 138, no. 14, pp. 4757–4762, 2016.

[41] S. Ruhman, B. Kohler, A. G. Joly, and K. A. Nelson, "Intermolecular vibrational motion in CS_2 liquid at $165 \leqslant t \geqslant 300$ K observed by femtosecond time-resolved impulsive stimulated scattering," *Chem. Phys. Let.*, vol. 141, no. 1-2, pp. 16–24, 1987.

[42] T. Fujisawa, H. Kuramochi, H. Hosoi, S. Takeuchi, and T. Tahara, "Role of coherent low-frequency motion in excited-state proton transfer of green fluorescent protein studied by time-resolved impulsive stimulated raman spectroscopy," *Journal of the American Chemical Society*, vol. 138, pp. 3942–3945, Mar. 2016.

[43] R. Mankowsky, A. Subedi, M. Först, S. O. Mariager, M. Chollet, H. T. Lemke, J. S. Robinson, J. M. Glownia, M. P. Minitti, A. Frano, M. Fechner, N. A. Spaldin, T. Loew, B. Keimer, A. Georges, and A. Cavalleri, "Nonlinear lattice dynamics as a basis for enhanced superconductivity in YBa2cu3o6.5," *Nature*, vol. 516, pp. 71–73, dec 2014.

[44] M. Mitrano, A. Cantaluppi, D. Nicoletti, S. Kaiser, A. Perucchi, S. Lupi, P. D. Pietro, D. Pontiroli, M. Riccò, S. R. Clark, D. Jaksch, and A. Cavalleri, "Possible light-induced superconductivity in k3c60 at high temperature," *Nature*, vol. 530, pp. 461–464, feb 2016.

[45] P. Hohenberg and W. Kohn, "Inhomogeneous electron gas," *Physical Review*, vol. 136, pp. B864–B871, nov 1964.

[46] W. Kohn and L. J. Sham, "Self-consistent equations including exchange and correlation effects," *Physical Review*, vol. 140, pp. A1133–A1138, nov 1965.

[47] W. Foulkes, L. Mitas, R. Needs, and G. Rajagopal, "Quantum monte carlo simulations of solids," *Reviews of Modern Physics*, vol. 73, no. 1, p. 33, 2001.

[48] R. J. Bartlett and M. Musiał, "Coupled-cluster theory in quantum chemistry," *Reviews of Modern Physics*, vol. 79, no. 1, p. 291, 2007.

[49] J. P. Perdew, K. Burke, and M. Ernzerhof, "Generalized gradient approximation made simple," *Physical Review Letters*, vol. 77, pp. 3865–3868, oct 1996.

[50] B. Miehlich, A. Savin, H. Stoll, and H. Preuss, "Results obtained with the correlation energy density functionals of becke and lee, yang and parr," *Chemical Physics Letters*, vol. 157, no. 3, pp. 200–206, 1989.

[51] R. C. Clay, J. Mcminis, J. M. McMahon, C. Pierleoni, D. M. Ceperley, and M. A. Morales, "Benchmarking exchange-correlation functionals for hydrogen at high pressures using quantum monte carlo," *Physical Review B*, vol. 89, may 2014.

[52] N. D. Drummond, B. Monserrat, J. H. Lloyd-Williams, P. L. Ríos, C. J. Pickard, and R. J. Needs, "Quantum monte carlo study of the phase diagram of solid molecular hydrogen at extreme pressures," *Nature Communications*, vol. 6, jul 2015.

[53] G. Rillo, M. A. Morales, D. M. Ceperley, and C. Pierleoni, "Coupled electron-ion monte carlo simulation of hydrogen molecular crystals," *The Journal of Chemical Physics*, vol. 148, p. 102314, mar 2018.

[54] J. R. Trail, P. L. Ríos, and R. J. Needs, "Energetics of h2 clusters from density functional and coupled cluster theories," *Physical Review B*, vol. 95, mar 2017.

[55] S. Azadi, B. Monserrat, W. Foulkes, and R. Needs, "Dissociation of high-pressure solid molecular hydrogen: A quantum monte carlo and anharmonic vibrational study," *Physical Review Letters*, vol. 112, apr 2014.

[56] J. McMinis, R. C. Clay, D. Lee, and M. A. Morales, "Molecular to atomic phase transition in hydrogen under high pressure," *Physical Review Letters*, vol. 114, mar 2015.

[57] J. Kohanoff, S. Scandolo, S. de Gironcoli, and E. Tosatti, "Dipole-quadrupole interactions and the nature of phase III of compressed hydrogen," *Physical Review Letters*, vol. 83, pp. 4097–4100, nov 1999.

[58] I. B. Magdău and G. J. Ackland, "Identification of high-pressure phases III and IV in hydrogen: Simulating raman spectra using molecular dynamics," *Physical Review B*, vol. 87, may 2013.

[59] S. Azadi and T. D. Kühne, "Unconventional phase iii of high-pressure solid hydrogen," *arXiv preprint arXiv:1906.10854*, 2019.

[60] S. Azadi, R. Singh, and T. D. Kühne, "Nuclear quantum effects induce metallization of dense solid molecular hydrogen," *Journal of Computational Chemistry*, vol. 39, pp. 262–268, nov 2017.

[61] R. Singh, S. Azadi, and T. D. Kühne, "Anharmonicity and finite-temperature effects on the structure, stability, and vibrational spectrum of phase III of solid molecular hydrogen," *Physical Review B*, vol. 90, jul 2014.

[62] C. Ji, B. Li, W. Liu, J. S. Smith, A. Majumdar, W. Luo, R. Ahuja, J. Shu, J. Wang, S. Sinogeikin, Y. Meng, V. B. Prakapenka, E. Greenberg, R. Xu, X. Huang, W. Yang, G. Shen, W. L. Mao, and H.-K. Mao, "Ultrahigh-pressure

isostructural electronic transitions in hydrogen," *Nature*, vol. 573, pp. 558–562, Sept. 2019.

[63] M. Borinaga, P. Riego, A. Leonardo, M. Calandra, F. Mauri, A. Bergara, and I. Errea, "Anharmonic enhancement of superconductivity in metallic molecularCmca - 4 hydrogen at high pressure: a first-principles study," *Journal of Physics: Condensed Matter*, vol. 28, p. 494001, oct 2016.

[64] P. Loubeyre, F. Occelli, and R. LeToullec, "Optical studies of solid hydrogen to 320 GPa and evidence for black hydrogen," *Nature*, vol. 416, pp. 613–617, apr 2002.

[65] S. Azadi and G. J. Ackland, "The role of van der waals and exchange interactions in high-pressure solid hydrogen," *Physical Chemistry Chemical Physics*, vol. 19, no. 32, pp. 21829–21839, 2017.

[66] M. Zacharias, C. E. Patrick, and F. Giustino, "Stochastic approach to phonon-assisted optical absorption," *Physical Review Letters*, vol. 115, oct 2015.

[67] P. Giannozzi, S. Baroni, N. Bonini, M. Calandra, R. Car, C. Cavazzoni, D. Ceresoli, G. L. Chiarotti, M. Cococcioni, I. Dabo, A. D. Corso, S. de Gironcoli, S. Fabris, G. Fratesi, R. Gebauer, U. Gerstmann, C. Gougoussis, A. Kokalj, M. Lazzeri, L. Martin-Samos, N. Marzari, F. Mauri, R. Mazzarello, S. Paolini, A. Pasquarello, L. Paulatto, C. Sbraccia, S. Scandolo, G. Sclauzero, A. P. Seitsonen, A. Smogunov, P. Umari, and R. M. Wentzcovitch, "QUANTUM ESPRESSO: a modular and open-source software project for quantum simulations of materials," *Journal of Physics: Condensed Matter*, vol. 21, p. 395502, sep 2009.

[68] P. Giannozzi, O. Andreussi, T. Brumme, O. Bunau, M. B. Nardelli, M. Calandra, R. Car, C. Cavazzoni, D. Ceresoli, M. Cococcioni, N. Colonna, I. Carnimeo, A. D. Corso, S. de Gironcoli, P. Delugas, R. A. DiStasio, A. Ferretti, A. Floris, G. Fratesi, G. Fugallo, R. Gebauer, U. Gerstmann, F. Giustino, T. Gorni, J. Jia, M. Kawamura, H.-Y. Ko, A. Kokalj, E. Küçükbenli, M. Lazzeri, M. Marsili, N. Marzari, F. Mauri, N. L. Nguyen, H.-V. Nguyen, A. O. de-la Roza, L. Paulatto, S. Poncé, D. Rocca, R. Sabatini, B. Santra, M. Schlipf, A. P. Seitsonen, A. Smogunov, I. Timrov, T. Thonhauser, P. Umari, N. Vast, X. Wu, and S. Baroni, "Advanced capabilities for materials modelling with quantum ESPRESSO," *Journal of Physics: Condensed Matter*, vol. 29, p. 465901, oct 2017.

[69] Y. Akahama and H. Kawamura, "Pressure calibration of diamond anvil raman gauge to 310gpa," *Journal of Applied Physics*, vol. 100, p. 043516, aug 2006.

[70] Y. Akahama and H. Kawamura, "Pressure calibration of diamond anvil raman gauge to 410 GPa," *Journal of Physics: Conference Series*, vol. 215, p. 012195, mar 2010.

[71] I. F. Silvera and R. Dias, "Comment on: Observation of a first order phase transition to metal hydrogen near 425 gpa," 2019.

[72] M. B. Trevino, *Hydrogen and lithium under high pressure, Superconductivity and other emerging properties*. PhD thesis, Universidad del Pais Vasco, July 2018. Supervised by Aitor Bergara and Ion Errea.

[73] V. Kapil, E. Engel, M. Rossi, and M. Ceriotti, "An assessment of approximate methods for anharmonic free energies," *arXiv preprint arXiv:1906.06524*, 2019.

[74] M. van Setten, M. Giantomassi, E. Bousquet, M. Verstraete, D. Hamann, X. Gonze, and G.-M. Rignanese, "The PseudoDojo: Training and grading a 85 element optimized norm-conserving pseudopotential table," *Computer Physics Communications*, vol. 226, pp. 39–54, may 2018.